

**ISTANBUL TECHNICAL UNIVERSITY ★ GRADUATE SCHOOL OF SCIENCE**  
**ENGINEERING AND TECHNOLOGY**

**ENERGY DISSIPATOR STEEL CUSHIONS**

**M.Sc. THESIS**

**Arastoo KHAJEHDEHI**

**Department of Civil Engineering**

**Structural Engineering Programme**

**JANUARY 2015**



**ISTANBUL TECHNICAL UNIVERSITY ★ GRADUATE SCHOOL OF SCIENCE**  
**ENGINEERING AND TECHNOLOGY**

**ENERGY DISSIPATOR STEEL CUSHIONS**

**M.Sc. THESIS**

**Arastoo KHAJEHDEHI**  
**(501121004)**

**Department of Civil Engineering**

**Structural Engineering Programme**

**Thesis Advisor: Assoc. Prof. Dr. Ercan YÜKSEL**

**JANUARY 2015**



**İSTANBUL TEKNİK ÜNİVERSİTESİ ★ FEN BİLİMLERİ ENSTİTÜSÜ**

**ENERJİ SÖNÜMLEYİCİ ÇELİK YASTIKLAR**

**YÜKSEK LİSANS TEZİ**

**Arastoo KHAJEHDEHI  
(501121004)**

**İnşaat Mühendisliği Anabilim Dalı**

**Yapı Mühendisliği Programı**

**Tez Danışmanı: Doç. Dr. Ercan YÜKSEL**

**OCAK 2015**



**Arastoo KHAJEHDEHI**, a M.Sc. student of ITU **Graduate School of SCIENCE ENNGINEERING AND TECHNOLOGY** student ID **501121004** successfully defended the **thesis/dissertation** entitled “**ENERGY DISSIPATOR STEEL CUSHIONS**”, which he prepared after fulfilling the requirements specified in the associated legislations, before the jury whose signatures are below.

**Thesis Advisor :**      **Assoc. Prof. Dr. Ercan YÜKSEL**      .....

Istanbul Technical University

**Jury Members :**      **Asst. Prof. Dr. A. Anıl DİNDAR**      .....

Istanbul Kültür University

**Asst. Prof. Dr. Burcu GÜNEŞ**      .....

Istanbul Technical University

**Date of Submission : 15 December 2014**

**Date of Defense : 19 January 2015**



*To my family,*



## **FOREWORD**

It is an honor for me to heartily thank my advisor, Assoc. Prof. Dr. Ercan Yüksel, whose encouragement, patience and generous support from the beginning to the very last days enabled me to develop an understanding of the subject. Assoc. Prof. Dr. Ercan Yüksel who has the attitude and substance of an effective supervisor has continually conveyed a spirit of research in regard to this topic. I must honestly say that without his help this thesis would not have been completed.

I also express my warm thanks to dear Prof. Dr. Hüseyin Faruk Karadoğan for his encouragement, insightful comments and his never-ending support and guidance.

Last but not least, I offer my best regards and blessings to my family especially my dad, Dr. Ali Khajehdehi, M.D., and all of those who supported me in any respect towards the completion of my thesis.

January 2015

Arastoo KHAJEHDEHI  
(Civil Engineer)



## TABLE OF CONTENTS

<b>FOREWORD</b> .....	<b>ix</b>
<b>TABLE OF CONTENTS</b> .....	<b>xi</b>
<b>ABBREVIATIONS</b> .....	<b>xvii</b>
<b>LIST OF TABLES</b> .....	<b>xix</b>
<b>LIST OF FIGURES</b> .....	<b>xxi</b>
<b>SUMMARY</b> .....	<b>xxxix</b>
<b>ÖZET</b> .....	<b>xli</b>
<b>1. INTRODUCTION</b> .....	<b>1</b>
1.1 Purpose of Thesis .....	2
1.2 General Definition and Concepts .....	2
1.2.1 Dissipated energy .....	2
1.2.2 Equivalent viscous damping .....	4
1.2.3 Effective (secant) stiffness .....	4
1.3 Literature Review .....	5
<b>2. UNIAXIAL TESTS</b> .....	<b>19</b>
2.1 Introduction .....	19
2.2 Coupon Test of Specimens .....	20
2.3 Uniaxial Shear Test .....	21
2.3.1 Shear test-loading protocol .....	23
2.3.2 Experimental results of cyclic and monotonic shear tests .....	24
2.3.2.1 Force-Displacement relation .....	25
2.3.2.2 Cyclic and monotonic shear tests envelop .....	29
2.3.2.3 Energy dissipation .....	30
2.3.2.4 Equivalent viscous damping .....	33
2.3.2.5 Effective (secant) stiffness .....	35
2.3.2.6 Strain history .....	37
2.3.3 Evaluation of experimental results for three specific specimens under shear loading .....	38
2.3.3.1 Ductility .....	39
2.3.3.2 Yield force and yield displacement .....	39
2.3.3.3 Maximum shear force .....	40
2.3.3.4 Initial stiffness .....	41
2.4 Uniaxial Axial Test .....	41
2.4.1 Axial test loading protocol .....	43
2.4.2 Experimental results of cyclic and monotonic axial tests .....	44
2.4.2.1 Force-Displacement relation .....	44
2.4.2.2 Cyclic and monotonic axial tests envelop .....	47
2.4.2.3 Energy dissipation .....	47
2.4.2.4 Equivalent viscous damping .....	48
2.4.2.5 Effective (secant) stiffness .....	49

2.4.2.6 Strain history .....	49
2.4.3. Evaluation of experimental results for three specific specimens under axial loading.....	50
2.4.3.1 Ductility.....	51
2.4.3.2 Yield force and yield displacement.....	52
2.4.3.3 Maximum shear force.....	53
2.4.3.4 Initial stiffness .....	54
<b>3. Bi-DIRECTIONAL CYCLIC SHEAR AND AXIAL TEST .....</b>	<b>55</b>
3.1 Introduction .....	55
3.2 Experimental Results of Bi-Directional Test under Shear + Tension Loading. ....	58
3.2.1 Force-Displacement relation .....	58
3.2.2 Energy dissipation .....	66
3.2.3 Equivalent viscous damping.....	72
3.2.4 Effective (secant) stiffness .....	78
3.3 Evaluation of Experimental Results for Three Specific Specimens under Bi-Directional Shear + Tension Loading .....	80
3.3.1 Ductility.....	80
3.3.2 Yield force and yield displacement.....	81
3.3.3 Initial stiffness .....	83
3.3.4 Maximum shear force.....	85
3.4 Experimental Results of Bi-directional Test under Shear + Compression Loading .....	87
3.4.1 Force-Displacement relation .....	87
3.4.2 Energy dissipation .....	94
3.4.3 Equivalent viscous damping.....	100
3.4.4 Effective (secant) stiffness .....	107
3.5 Evaluation of Experimental Results for Three Specific Specimens under Bi-Directional Shear + Compression Loading.....	108
3.5.1 Ductility.....	109
3.5.2 Yield force and yield displacement.....	110
3.5.3 Initial stiffness .....	113
3.5.4 Maximum shear force.....	114
3.6 Interaction Diagrams .....	116
<b>4. CYCLIC TEST OF CLADDING PANELS EQUIPPED WITH STEEL CUSHIONS (SYSTEM TESTS).....</b>	<b>117</b>
4.1 Introduction .....	117
4.2 System Test Set-Up .....	118
4.3 System Test Loading Protocol.....	123
4.4 System Test I (Single Cushion Test) .....	124
4.4.1 Evaluation of experimental results obtained from system test I .....	125
4.4.1.1 Actuator force-top displacement relation.....	125
4.4.1.2 Energy dissipation .....	126
4.4.1.3 Equivalent viscous damping.....	127
4.4.1.4 Effective (secant) stiffness .....	128
4.4.1.5 Relative vertical displacement of panel to panel steel cushions .....	128
4.4.1.6 Relative horizontal displacement of panel to support steel cushions. ....	131
4.4.1.7 Relative horizontal displacement of panel to beam steel cushions ..	135
4.4.1.8 Cladding panels rotation.....	137



4.8.2.3 Equivalent viscous damping.....	193
4.8.2.4 Effective (secant) stiffness .....	194
4.8.2.5 Relative vertical displacement of panel to panel steel cushions .....	195
4.8.2.6 Relative horizontal displacement of panel to support steel cushions. .....	195
4.8.2.7 Maximum rotation of cladding panels .....	196
4.8.3 Comparison of system test II and III experimental results.....	196
4.8.3.1 Actuator force-top displacement relation.....	196
4.8.3.2 Energy dissipation .....	197
4.8.3.3 Equivalent viscous damping.....	198
4.8.3.4 Effective (secant) stiffness .....	198
4.8.3.5 Relative vertical displacement of panel to panel steel cushions .....	199
4.8.3.6 Relative horizontal displacement of panel to support steel cushions .....	200
4.8.3.7 Maximum rotation of cladding panels .....	200
4.8.4 Comparison of system test III and IV experimental results .....	200
4.8.4.1 Actuator force-top displacement relation.....	201
4.8.4.2 Energy dissipation .....	201
4.8.4.3 Equivalent viscous damping.....	202
4.8.4.4 Effective (secant) stiffness .....	203
4.8.4.5 Relative vertical displacement of panel to panel steel cushions .....	204
4.8.4.6 Relative horizontal displacement of panel to support steel cushions. .....	204
4.8.4.7 Maximum rotation of cladding panels .....	205
<b>5. ANALYTICAL STUDY OF CONCRETE CLADDING PANELS EQUIPPED WIT ENERGY DISSIPATIVE STEEL CUSHIONS.....</b>	<b>207</b>
5.1 Introduction .....	207
5.2 SeismoStruct Program Version 6.0 .....	207
5.3 Response Curve for Modeling Shear and Axial behavior Behaviors of Steel Cushions.....	208
5.3.1 Response curve for modeling shear behavior of steel cushions.....	208
5.3.1.1 Comparison of analytical and experimental results for three distinct steel cushions under shear effect.....	211
5.3.2 Response curve for modeling axial behavior of steel cushions .....	212
5.3.2.1 Comparison of analytical and experimental results for three distinct steel cushions under axial effect .....	213
5.4 Analytical Study of System Tests.....	215
5.4.1 Analytical study of system test I .....	215
5.4.1.1 Definition of link elements.....	216
5.4.1.2 Actuator force-top displacement relation.....	217
5.4.1.3 Force-Displacement relation of panel to panel steel cushion.....	218
5.4.1.4 Force-Displacement relation of panel to support steel cushion .....	219
5.4.1.5 Rotation of cladding panels.....	220
5.4.1.6 Moment-Rotation relation of cladding panels.....	221
5.4.1.7 Energy analysis .....	221
5.4.1.8 Deformed shape of structural system .....	222
5.4.2 Analytical study of system test II.....	222
5.4.2.1 Definition of link elements.....	223
5.4.2.2 Actuator force-top displacement relation.....	224
5.4.2.3 Force-Displacement relation of panel to panel steel cushion.....	225

5.4.2.4 Force-Displacement relation of panel to support steel cushion .....	226
5.4.2.5 Rotation of cladding panels.....	227
5.4.2.6 Moment-Rotation relation of cladding panels .....	228
5.4.2.7 Energy analysis .....	229
5.4.2.8 Deformed shape of structural system.....	230
5.4.3 Analytical study of system test III .....	230
5.4.3.1 Definition of link elements .....	230
5.4.3.2 Actuator force-top displacement relation.....	232
5.4.3.3 Force-Displacement relation of panel to panel steel cushion .....	232
5.4.3.4 Force-Displacement relation of panel to support steel cushion .....	233
5.4.3.5 Rotation of cladding panels.....	235
5.4.3.6 Moment-Rotation relation of cladding panels .....	236
5.4.3.7 Energy analysis .....	236
5.4.3.8 Deformed shape of structural system.....	237
5.4.4 Analytical study of system test IV .....	237
5.4.4.1 Definition of link elements .....	237
5.4.4.2 Actuator force-top displacement relation.....	239
5.4.4.3 Force-Displacement relation of panel to panel steel cushion .....	239
5.4.4.4 Force-Displacement relation of panel to support steel cushion .....	240
5.4.4.5 Rotation of cladding panels.....	242
5.4.4.6 Moment-Rotation relation of cladding panels .....	243
5.4.4.7 Energy analysis .....	243
5.4.4.8 Deformed shape of structural system.....	244
<b>6. Conclusions and Recommendations .....</b>	<b>245</b>
6.1 Conclusions .....	245
6.1.1 Uniaxial test .....	245
6.1.2 Bi-directional shear and axial test.....	245
6.1.3 System test and analytical study .....	246
6.2 Recommendations .....	247
<b>REFERENCES.....</b>	<b>249</b>
<b>CURRICULUM VITAE.....</b>	<b>251</b>



## ABBREVIATIONS

<b>FP7</b>	: 7th Framework Program for Research Funded by European Union
<b>JRC</b>	: Joint Research Centre
<b>ITU</b>	: Istanbul Technical University
<b>m</b>	: Mass
<b>c</b>	: Damping coefficient
<b><math>f_s</math></b>	: Resisting force
<b><math>\dot{u}</math></b>	: Relative velocity
<b><math>\ddot{u}</math></b>	: Relative acceleration
<b><math>\ddot{u}_g</math></b>	: Ground acceleration
<b><math>E_I</math></b>	: Input energy
<b><math>E_K</math></b>	: Kinetic energy
<b><math>E_D</math></b>	: Damping energy
<b><math>E_Y</math></b>	: Energy dissipated by yielding
<b><math>E_S</math></b>	: Strain energy
<b><math>\zeta_{eq}</math></b>	: Equivalent damping
<b><math>E_D</math></b>	: Energy loss
<b><math>E_{S0}</math></b>	: Maximum strain energy
<b><math>u_0</math></b>	: Displacement amplitude
<b><math>K_{eff}</math></b>	: Effective (secant) stiffness
<b><math>P_{max}</math></b>	: Maximum target force
<b><math>P_{min}</math></b>	: Minimum target force
<b><math>D_{max}</math></b>	: Maximum target displacement
<b><math>D_{min}</math></b>	: Minimum target displacement
<b>S1</b>	: Steel cushions beneath panel 1
<b>S2</b>	: Steel cushions beneath panel 2
<b>S3</b>	: Steel cushions beneath panel 3
<b>S4</b>	: Steel cushions beneath panel 4
<b>S12</b>	: Steel cushion in panel 1 to panel 2 connection
<b>S34</b>	: Steel cushion in panel 3 to panel 4 connection
<b>S1*</b>	: Steel cushion in panel 1 to beam connection
<b>S2*</b>	: Steel cushion in panel 2 to beam connection
<b>S3*</b>	: Steel cushion in panel 3 to beam connection
<b>S4*</b>	: Steel cushion in panel 4 to beam connection
<b><math>\Theta</math></b>	: Rotation
<b><math>\Delta</math></b>	: Vertical displacement



## LIST OF TABLES

	<u>Page</u>
<b>Table 2.1</b> : Summary of uniaxial tests performed on the steel cushions.....	19
<b>Table 2.2</b> : Ratio of displacements amplitudes. ....	23
<b>Table 2.3</b> : Displacement targets of uniaxial shear test.....	23
<b>Table 2.4</b> : Summary of experimental results derived from cyclic shear test for three.....	38
<b>Table 2.5</b> : Ratio of displacements amplitudes. ....	43
<b>Table 2.6</b> : Displacement targets of uniaxial axial test. ....	43
<b>Table 2.7</b> : Summary of test results under compression stress. ....	50
<b>Table 2.8</b> : Summary of test results for under tensile stress.....	51
<b>Table 3.1</b> : Experimental program summary in the bi-directional tests.....	57
<b>Table 3.2</b> : Summary of experimental results derived from bi-directional cyclic shear and tensile axial test.....	80
<b>Table 3.3</b> : Summary of experimental results derived from bi-directional cyclic shear and compressive axial test for.....	108
<b>Table 4.1</b> : Relative loading history deformation amplitude.....	123
<b>Table 4.2</b> : Displacement target values. ....	123
<b>Table 4.3</b> : Summary of test results obtained from system test I. ....	126
<b>Table 4.4</b> : Summary of test results obtained from system test II.....	142
<b>Table 4.5</b> : Summary of test results obtained from system test III. ....	158
<b>Table 4.6</b> : Summary of test results obtained from system test IV. ....	174
<b>Table 4.7</b> : Experimental results derived from system tests I and II.....	188
<b>Table 4.8</b> : Maximum rotation of panels obtained from system test I and II.....	192
<b>Table 4.9</b> : Experimental results derived from system tests I and III. ....	193
<b>Table 4.10</b> : Maximum rotation of panels obtained from system test I and III.....	196
<b>Table 4.11</b> : Experimental results derived from system tests II and III. ....	197
<b>Table 4.12</b> : Maximum rotation of panels obtained from system test II and III. ....	200
<b>Table 4.13</b> : Experimental results derived from system tests III and IV.....	201
<b>Table 4.14</b> : Maximum rotation of panels obtained from system test III and IV....	205
<b>Table 5.1</b> : Ramberg-Osgood curve parameters for 3mm specimens. ....	211
<b>Table 5.2</b> : Ramberg-Osgood curve parameters for 5mm specimens. ....	212
<b>Table 5.3</b> : Ramberg-Osgood curve parameters for 8mm specimens. ....	212
<b>Table 5.4</b> : Asymmetric bi-linear curve parameters for t=3mm specimens.....	214
<b>Table 5.5</b> : Asymmetric bi-linear curve parameters for t=5mm specimens.....	214
<b>Table 5.6</b> : Asymmetric bi-linear curve parameters for t=8mm specimens.....	215



## LIST OF FIGURES

	Page
<b>Figure 1.1</b> : Typical dimension of steel cushion. ....	2
<b>Figure 1.2</b> : General view of 3, 5 and 8mm thick steel cushions. ....	2
<b>Figure 1.3</b> : Fixed base single degree of freedom system. ....	3
<b>Figure 1.4</b> : Energy dissipated and strain energy in a cycle. ....	4
<b>Figure 1.5</b> : Effective stiffness in a cycle. ....	5
<b>Figure 1.6</b> : U-Shaped strip type steel elements. ....	5
<b>Figure 1.7</b> : Jointed wall equipped with shear connector. ....	6
<b>Figure 1.8</b> : Pre-WEC System concept. ....	7
<b>Figure 1.9</b> : Oval-shaped shear connectors and Pre-WEC test set-up. ....	8
<b>Figure 1.10</b> : Overview of passive steel slit damper. ....	8
<b>Figure 1.11</b> : Application of steel slit damper in framed structures. ....	9
<b>Figure 1.12</b> : Overview of test set-up. ....	9
<b>Figure 1.13</b> : Failure of test specimens. ....	10
<b>Figure 1.14</b> : Overview of yielding shear panel device, (a) Elevation, (b) Top view. ....	10
<b>Figure 1.15</b> : Overview of test set-up. ....	11
<b>Figure 1.16</b> : Overview of test specimens. ....	11
<b>Figure 1.17</b> : General view of the optimized steel slit device. ....	12
<b>Figure 1.18</b> : Deformed shape of the optimized steel slit device. ....	12
<b>Figure 1.19</b> : Overview of the test set-up. ....	13
<b>Figure 1.20</b> : Deformed shape of filled steel pipe. ....	14
<b>Figure 1.21</b> : Schematic drawing of hybrid damper and deformed shape of hybrid damper. ....	14
<b>Figure 1.22</b> : Test set-up and loading history. ....	15
<b>Figure 1.23</b> : Cracking pattern in CRB and HDB specimens. ....	15
<b>Figure 1.24</b> : Deformed shape of hybrid damper. ....	16
<b>Figure 1.25</b> : Dual-pipe damper. ....	16
<b>Figure 1.26</b> : Test set-up. ....	16
<b>Figure 1.27</b> : Deformed shape of the dual-pipe damper. ....	17
<b>Figure 1.28</b> : U-shaped energy dissipative device. ....	18
<b>Figure 1.29</b> : Schematic drawing of the test set-up. ....	18
<b>Figure 2.1</b> : Coupon test of 5mm and 8mm thick specimens. ....	20
<b>Figure 2.2</b> : Fractures of two distinct specimens. ....	20
<b>Figure 2.3</b> : Stress-Strain relation obtained from coupon test. ....	21
<b>Figure 2.4</b> : Stress-Strain relation obtained from coupon test. ....	21
<b>Figure 2.5</b> : Final displacement target of shear test. ....	22
<b>Figure 2.6</b> : General view of test set-up. ....	22
<b>Figure 2.7</b> : Technical drawing of test set-up. ....	23
<b>Figure 2.8</b> : Drift based cyclic loading protocol applied to steel cushions at cyclic shear test. ....	24

<b>Figure 2.9</b> : Drift based monotonic loading protocol applied to cushions at monotonic shear test. ....	24
<b>Figure 2.10</b> : Force-Displacement relation for 3mm thick specimen derived from cyclic shear test. ....	25
<b>Figure 2.11</b> : Force-Displacement relation for 5mm thick specimen derived from cyclic shear test. ....	25
<b>Figure 2.12</b> : Force-Displacement relation for 8mm thick specimen derived from cyclic shear test. ....	26
<b>Figure 2.13</b> : Damages occurred on the welding location at 5mm and 8mm thick specimens in the cyclic shear test. ....	26
<b>Figure 2.14</b> : Sharp increase of force value in force-vertical displacement relation derived from cyclic shear test. ....	27
<b>Figure 2.15</b> : Force-Displacement relation for 3mm thick specimen derived from monotonic shear test. ....	27
<b>Figure 2.16</b> : Force-Displacement relation for 5mm thick specimen derived from monotonic shear test. ....	28
<b>Figure 2.17</b> : Force-Displacement relation for 8mm thick specimen derived from monotonic shear test. ....	28
<b>Figure 2.18</b> : Envelop of cyclic shear test in comparison with monotonic shear test for 3mm thick specimens. ....	29
<b>Figure 2.19</b> : Envelop of cyclic shear test in comparison with monotonic shear test for 5mm thick specimens. ....	29
<b>Figure 2.20</b> : Envelop of cyclic shear test in comparison with monotonic shear test for 8mm thick specimens. ....	30
<b>Figure 2.21</b> : Envelop of cyclic shear test in comparison with monotonic shear test for 8mm thick specimens. ....	30
<b>Figure 2.22</b> : Energy per loop and Cumulative Dissipated energy value for 3mm thick steel specimen under shear effect. ....	31
<b>Figure 2.23</b> : Cumulative energy-vertical displacement relation for 3mm thick specimens derived from cyclic shear test. ....	31
<b>Figure 2.24</b> : Cumulative energy-vertical displacement relation for 5mm thick specimens derived from cyclic shear test. ....	32
<b>Figure 2.25</b> : Cumulative energy-vertical displacement relation for 8mm thick specimens derived from cyclic shear test. ....	32
<b>Figure 2.26</b> : Comparison of cumulative energy-vertical displacement for three distinct specimens under shear effect. ....	33
<b>Figure 2.27</b> : Equivalent viscous damping ratio-vertical displacement relation for 3mm thick specimens derived from cyclic shear test. ....	33
<b>Figure 2.28</b> : Equivalent viscous damping ratio-vertical displacement relation for 5mm thick specimens derived from cyclic shear test. ....	34
<b>Figure 2.29</b> : Equivalent viscous damping ratio-vertical displacement relation for 8mm thick specimens derived from cyclic shear test. ....	34
<b>Figure 2.30</b> : Comparison of equivalent viscos damping ratio for three distinct specimens under shear effect. ....	35
<b>Figure 2.31</b> : Comparison of the Ksecant for three distinct specimen under shear effect. ....	35
<b>Figure 2.32</b> : Ratio of Ksecant to k initial for 3mm thick specimens derived from cyclic shear test. ....	36
<b>Figure 2.33</b> : Ratio of Ksecant to k initial for 5mm thick specimens derived from cyclic shear test. ....	36

<b>Figure 2.34</b> : Ratio of $K_{secant}$ to $k$ initial for 8mm thick specimens derived from cyclic shear test. ....	36
<b>Figure 2.35</b> : Comparison of normalized stiffness ratio for three distinct specimens under shear effect. ....	37
<b>Figure 2.36</b> : Location of Strain gages on the test specimens under shear effect. ....	37
<b>Figure 2.37</b> : Comparison bottom strain versus drift relation for 3mm and 5mm thick specimens at cyclic shear test. ....	38
<b>Figure 2.38</b> : Comparison bottom strain versus drift relation for 5mm and 8mm thick specimens at cyclic shear test. ....	38
<b>Figure 2.39</b> : Relation between ductility and specimens thickness for three distinct thicknesses under shear effect. ....	39
<b>Figure 2.40</b> : Relation between yield force and specimens thickness for three distinct thicknesses under shear effect. ....	40
<b>Figure 2.41</b> : Relation between yield displacement and specimens thickness for three distinct thicknesses under shear effect. ....	40
<b>Figure 2.42</b> : Relation between maximum shear force and specimens thickness for three distinct thicknesses under shear effect. ....	40
<b>Figure 2.43</b> : Relation between initial stiffness and specimens thickness for three distinct thicknesses under shear effect. ....	41
<b>Figure 2.44</b> : Monotonic and cyclic axial test. ....	42
<b>Figure 2.45</b> : General view of testing set-up. ....	42
<b>Figure 2.46</b> : Technical drawing of test set-up. ....	42
<b>Figure 2.47</b> : Drift based cyclic loading protocol applied to steel cushions at cyclic axial test. ....	44
<b>Figure 2.48</b> : Drift based monotonic loading protocol applied to steel cushions at axial test. ....	44
<b>Figure 2.49</b> : Cyclic axial test performed on $t=3\text{mm}$ steel cushion. ....	45
<b>Figure 2.50</b> : Cyclic axial test performed on $t=5\text{mm}$ steel cushion. ....	45
<b>Figure 2.51</b> : Cyclic axial test performed on $t=8\text{mm}$ steel cushion. ....	45
<b>Figure 2.52</b> : Force-Displacement relation for 3mm thick specimen derived from monotonic axial test. ....	46
<b>Figure 2.53</b> : Force-Displacement relation for 5mm thick specimen derived from monotonic axial test. ....	46
<b>Figure 2.54</b> : Force-Displacement relation for 8mm thick specimen derived from monotonic axial test. ....	47
<b>Figure 2.55</b> : Comparison of monotonic test results with cyclic force-displacement hysteresis for $t=3\text{mm}$ , 5mm and 8mm thick specimens. ....	47
<b>Figure 2.56</b> : Cumulative energy dissipation capacity for three distinct specimens derived from cyclic axial test. ....	48
<b>Figure 2.57</b> : Equivalent damping ratio in term of Displacement for three distinct specimens derived from cyclic axial test. ....	48
<b>Figure 2.58</b> : Comparison of normalized stiffness ratio versus displacement derived from cyclic axial test for three specific specimens. ....	49
<b>Figure 2.59</b> : Location of strain gages at monotonic and cyclic axial test. ....	49
<b>Figure 2.60</b> : Comparison of strain histories in terms of drift for $t=3\text{mm}$ and 5mm thick specimens derived from cyclic axial test. ....	50
<b>Figure 2.61</b> : Comparison of strain histories in terms of drift for $t=5\text{mm}$ and 8mm thick specimens derived from cyclic axial test. ....	50
<b>Figure 2.62</b> : Ductility in term of specimen thickness for three distinct specimens in compression part. ....	51

<b>Figure 2.63</b> : Ductility in term of specimens thickness for three distinct specimens in tension part. ....	51
<b>Figure 2.64</b> : Yield force in terms of specimen thickness for three distinct specimens in compression part. ....	52
<b>Figure 2.65</b> : Yield force in terms of specimen thickness for three distinct specimens in tension part. ....	52
<b>Figure 2.66</b> : Yield displacement in terms of specimen thickness for three distinct specimens in compression part. ....	53
<b>Figure 2.67</b> : Yield displacement in terms of specimen thickness for three distinct specimens in tension part. ....	53
<b>Figure 2.68</b> : Maximum force in terms of specimen thickness for three distinct specimens in compression part. ....	53
<b>Figure 2.69</b> : Maximum force in terms of specimen thickness for three distinct specimens in tension part. ....	54
<b>Figure 2.70</b> : Initial stiffness in terms of specimen thickness for three distinct specimens in compression part. ....	54
<b>Figure 2.71</b> : Initial stiffness in terms of specimen thickness for three distinct specimens in tension part. ....	54
<b>Figure 3.1</b> : Steel cushions configuration on the precast structure. ....	56
<b>Figure 3.2</b> : General view of test set-up. ....	56
<b>Figure 3.3</b> : General dimension of test set-up. ....	56
<b>Figure 3.4</b> : Plan view of test set-up. ....	56
<b>Figure 3.5</b> : Bi-Axial test under varied level of constant axial tension and compression load. ....	57
<b>Figure 3.6</b> : Direction of applied loads. ....	58
<b>Figure 3.7</b> : Location of transducers and load cells. ....	58
<b>Figure 3.8</b> : Force-Displacement relation of 3mm thick specimen under tensile axial load of $N/N_0=25\%$ . ....	59
<b>Figure 3.9</b> : Force-Displacement relation of 3mm thick specimen under tensile axial load of $N/N_0=50\%$ . ....	59
<b>Figure 3.10</b> : Force-Displacement relation of $t= 3\text{mm}$ thick specimens under tensile axial load of $N/N_0=75\%$ KN. ....	59
<b>Figure 3.11</b> : Comparison of force-displacement relation for 3mm thick specimens under tensile axial stress. ....	60
<b>Figure 3.12</b> : Force-Displacement relation of 5mm thick specimen under tensile axial load of $N/N_0=25\%$ . ....	60
<b>Figure 3.13</b> : Force-Displacement relation of 5mm thick specimen under tensile axial load of $N/N_0=50\%$ . ....	61
<b>Figure 3.14</b> : Rupture occurred at the final displacement target in 5mm steel cushion under tensile axial stress of 15 KN. ....	61
<b>Figure 3.15</b> : Force-Displacement relation of 5mm thick specimen under tensile axial load of $N/N_0=75\%$ . ....	61
<b>Figure 3.16</b> : Rupture occurred at the final displacement target in 5mm steel cushion under tensile axial stress of 25 KN. ....	62
<b>Figure 3.17</b> : Comparison of force-displacement relation for 5mm thick specimens under tensile axial stress. ....	62
<b>Figure 3.18</b> : Force-Displacement relation of 8mm thick specimens under tensile axial load of $N/N_0=25\%$ . ....	63
<b>Figure 3.19</b> : Rupture occurred at the final displacement target in 8mm steel cushion under tensile axial stress of 25 KN. ....	63

<b>Figure 3.20</b> : Force-Displacement relation of 8mm thick specimens under tensile axial load of $N/N_0=50\%$ .....	63
<b>Figure 3.21</b> : Rupture occurred at the final displacement target in 8mm steel cushion under tensile axial stress of 50 KN. ....	64
<b>Figure 3.22</b> : Force-Displacement relation of 8mm thick specimens under tensile axial load of $N/N_0=75\%$ .....	64
<b>Figure 3.23</b> : Rupture occurred at the final displacement target in 8mm steel cushion under tensile axial stress of 75KN. ....	64
<b>Figure 3.24</b> : Comparison of force-displacement relation for 8mm thick specimens under tensile axial stress. ....	65
<b>Figure 3.25</b> : Comparison of force-displacement relation in terms of different thicknesses under constant level of tensile axial load. ....	65
<b>Figure 3.26</b> : Cumulative energy in terms of displacement for $t=3\text{mm}$ thick steel cushions under constant tensile load of $N=2.5\text{ KN}$ . ....	66
<b>Figure 3.27</b> : Cumulative energy in terms of displacement for 3mm thick steel cushions under constant tensile load of $N=5.0\text{ KN}$ . ....	66
<b>Figure 3.28</b> : Cumulative energy in terms of displacement for 3mm thick steel cushions under constant tensile load of $N=2.50\text{ KN}$ . ....	67
<b>Figure 3.29</b> : Comparison of energy dissipation capacity for 3mm thick specimens under tensile axial stress in two extreme axial loads.....	67
<b>Figure 3.30</b> : Cumulative energy in terms of displacement for 5mm thick steel cushions under constant tensile load of $N=7.5\text{ KN}$ . ....	68
<b>Figure 3.31</b> : Cumulative energy in terms of displacement for 5mm thick steel cushions under constant tensile load of $N=15\text{ KN}$ . ....	68
<b>Figure 3.32</b> : Cumulative energy in terms of displacement for 5mm thick steel cushions under constant tensile load of $N=25\text{ KN}$ . ....	69
<b>Figure 3.33</b> : Comparison of energy dissipation capacity for 5mm thick specimens under tensile axial stress in two extreme axial loads.....	69
<b>Figure 3.34</b> : Cumulative energy in terms of displacement for 8mm thick steel cushions under constant tensile load of $N=25\text{ KN}$ . ....	70
<b>Figure 3.35</b> : Cumulative energy in terms of displacement for 8mm thick steel cushions under constant tensile load of $N=50\text{ KN}$ . ....	70
<b>Figure 3.36</b> : Cumulative energy in terms of displacement for 8mm thick steel cushions under constant tensile load of $N=75\text{ KN}$ . ....	71
<b>Figure 3.37</b> : Comparison of energy dissipation capacity for 8mm thick specimens under tensile axial stress in two extreme axial loads.....	71
<b>Figure 3.38</b> : Equivalent damping ratio in terms of displacement for 3mm thick steel cushions under constant tensile load of $N=2.5\text{ KN}$ . ....	72
<b>Figure 3.39</b> : Equivalent damping ratio in terms of displacement for 3mm thick steel cushions under constant tensile load of $N=5\text{ KN}$ . ....	72
<b>Figure 3.40</b> : Equivalent damping ratio in terms of displacement for 3mm thick steel cushions under constant tensile load of $N=7.5\text{ KN}$ . ....	73
<b>Figure 3.41</b> : Comparison of equivalent damping ratio for $t= 3\text{mm}$ thick specimens under two extreme tensile axial loads. ....	73
<b>Figure 3.42</b> : Equivalent damping ratio in terms of displacement for 5mm thick steel cushions under constant tensile load of $N=7.5\text{ KN}$ . ....	74
<b>Figure 3.43</b> : Equivalent damping ratio in terms of displacement for 5mm thick steel cushions under constant tensile load of $N=15\text{ KN}$ . ....	74
<b>Figure 3.44</b> : Equivalent damping ratio in terms of displacement for 5mm thick steel cushions under constant tensile load of $N=25\text{ KN}$ . ....	75

<b>Figure 3.45</b> : Comparison of equivalent damping ratio for 5mm thick specimens under two extreme tensile axial loads.....	75
<b>Figure 3.46</b> : Equivalent damping ratio in terms of displacement for 8mm thick steel cushions under constant tensile load of N=25 KN.....	76
<b>Figure 3.47</b> : Equivalent damping ratio in terms of displacement for 8mm thick steel cushions under constant tensile load of N=50 KN.....	76
<b>Figure 3.48</b> : Equivalent damping ratio in terms of displacement for 8mm thick steel cushions under constant tensile load of N=75 KN.....	77
<b>Figure 3.49</b> : Comparison of equivalent damping ratio for 8mm thick specimens under two extreme tensile axial loads.....	77
<b>Figure 3.50</b> : Comparison of equivalent damping ratio for three distinct thicknesses under two extreme tensile axial loads. ....	78
<b>Figure 3.51</b> : Comparison of normalized Stiffness ratio in terms of displacement for 3mm thick specimen under constant tensile axial loads. ....	78
<b>Figure 3.52</b> : Comparison of normalized Stiffness ratio in terms of displacement for 5mm thick specimen under constant tensile axial loads. ....	79
<b>Figure 3.53</b> : Comparison of normalized Stiffness ratio in terms of displacement for 8mm thick specimen under constant tensile axial loads. ....	79
<b>Figure 3.54</b> : Ductility trend for 3mm thick specimen under increase of tensile axial load.....	80
<b>Figure 3.55</b> : Ductility trend for 5mm thick specimen under increase of tensile axial load.....	81
<b>Figure 3.56</b> : Ductility trend for 8mm thick specimen under increase of tensile axial load.....	81
<b>Figure 3.57</b> : Yield force trend for 8mm thick specimen under increase of tensile axial load.....	82
<b>Figure 3.58</b> : Yield displacement trend for 3mm thick specimen under increase of tensile axial load. ....	82
<b>Figure 3.59</b> : Yield displacement trend for 5mm thick specimen under increase of tensile axial load. ....	83
<b>Figure 3.60</b> : Yield displacement trend for 8mm thick specimen under increase of tensile axial load. ....	83
<b>Figure 3.61</b> : Initial stiffness trend for 3mm thick specimen under increase of tensile axial load. ....	84
<b>Figure 3.62</b> : Initial stiffness trend for 5mm thick specimen under increase of tensile axial load. ....	84
<b>Figure 3.63</b> : Initial stiffness trend for 8mm thick specimen under increase of tensile axial load. ....	85
<b>Figure 3.64</b> : Maximum force trend for 3mm thick specimen under increase of tensile axial load. ....	85
<b>Figure 3.65</b> : Maximum force trend for 5mm thick specimen under increase of tensile axial load. ....	86
<b>Figure 3.66</b> : Maximum force trend for 8mm thick specimen under increase of tensile axial load. ....	86
<b>Figure 3.67</b> : Force-Displacement relation of 3mm thick specimens under compressive axial load of N/N <sub>0</sub> =25%.....	87
<b>Figure 3.68</b> : Force-Displacement relation of 3mm thick specimens under compressive axial load of N/N <sub>0</sub> =50%.....	88
<b>Figure 3.69</b> : Force-Displacement relation of 3mm thick specimens under compressive axial load of N/N <sub>0</sub> =75%.....	88

<b>Figure 3.70</b> : Comparison of force-displacement relation for $t= 3\text{mm}$ thick specimens under compressive axial stress.....	89
<b>Figure 3.71</b> : Force-Displacement relation for $5\text{mm}$ thick specimens under compressive axial load of $N/N_0=25\%$ .....	89
<b>Figure 3.72</b> : Force-Displacement relation for $5\text{mm}$ thick specimens under compressive axial load of $N/N_0=50\%$ .....	90
<b>Figure 3.73</b> : Force-Displacement relation for $5\text{mm}$ thick specimens under compressive axial load of $N/N_0=75\%$ .....	90
<b>Figure 3.74</b> : Comparison of force-displacement relation for $5\text{mm}$ thick specimens under compressive axial stress. ....	91
<b>Figure 3.75</b> : Force-Displacement relation for $8\text{mm}$ thick specimens under compressive axial load of $N/N_0=25\%$ .....	91
<b>Figure 3.76</b> : Comparison of force-displacement relation for $8\text{mm}$ thick specimens under compressive axial load of $N/N_0=50\%$ . ....	92
<b>Figure 3.77</b> : Rupture occurred at the final displacement target in $8\text{mm}$ steel cushion under tensile axial stress of $50\text{ KN}$ . ....	92
<b>Figure 3.78</b> : Force-Displacement relation for $8\text{mm}$ thick specimens under compressive axial load of $N/N_0=75\%$ .....	92
<b>Figure 3.79</b> : Rupture occurred at the final displacement target in $8\text{mm}$ steel cushion under tensile axial force of $75\text{ KN}$ . ....	93
<b>Figure 3.80</b> : Comparison of force-displacement relation for $8\text{mm}$ thick specimens under compressive axial stress. ....	93
<b>Figure 3.81</b> : Comparison of force-displacement relation in terms of different thicknesses under compressive axial load. ....	94
<b>Figure 3.82</b> : Cumulative energy in terms of displacement for $3\text{mm}$ thick steel cushions under compressive load of $N=2.5\text{ KN}$ .....	94
<b>Figure 3.83</b> : Cumulative energy in terms of displacement for $3\text{mm}$ thick steel cushions under compressive load of $N=7.5\text{ KN}$ .....	95
<b>Figure 3.84</b> : Cumulative energy in terms of displacement for $3\text{mm}$ thick steel cushions under compressive load of $N=10\text{ KN}$ .....	95
<b>Figure 3.85</b> : Comparison of energy dissipation capacity for $3\text{mm}$ thick specimens under compressive axial stress in two extreme axial loads. ....	96
<b>Figure 3.86</b> : Cumulative energy in terms of displacement for $5\text{mm}$ thick steel cushions under compressive load of $N=7.5\text{ KN}$ .....	96
<b>Figure 3.87</b> : Cumulative energy in terms of displacement for $5\text{mm}$ thick steel cushions under c compressive load of $N=15\text{ KN}$ . ....	97
<b>Figure 3.88</b> : Cumulative energy in terms of displacement for $5\text{mm}$ thick steel cushions under compressive load of $N=25\text{ KN}$ .....	97
<b>Figure 3.89</b> : Comparison of energy dissipation capacity for $5\text{mm}$ thick specimens under compressive axial stress in two extreme axial loads. ....	98
<b>Figure 3.90</b> : Cumulative energy in terms of displacement for $8\text{mm}$ thick steel cushions under compressive load of $N=25\text{ KN}$ .....	98
<b>Figure 3.91</b> : Cumulative energy in terms of displacement for $8\text{mm}$ thick steel cushions under compressive load of $N=50\text{ KN}$ .....	99
<b>Figure 3.92</b> : Cumulative energy in terms of displacement for $8\text{mm}$ thick steel cushions under compressive load of $N=75\text{ KN}$ .....	99
<b>Figure 3.93</b> : Comparison of energy dissipation capacity for $t= 8\text{mm}$ thick specimens under two extreme axial loads. ....	100
<b>Figure 3.94</b> : Equivalent damping ratio in terms of displacement for $3\text{mm}$ thick steel cushions under compressive load of $N=2.5\text{ KN}$ . ....	100

<b>Figure 3.95</b> : Equivalent damping ratio in terms of displacement for 3mm thick steel cushions under compressive load of N=7.5KN.....	101
<b>Figure 3.96</b> : Equivalent damping ratio in terms of displacement for 3mm thick steel cushions under compressive load of N=10 KN.....	101
<b>Figure 3.97</b> : Comparison of equivalent damping ratio for 3mm thick specimens under two extreme compressive axial loads. ....	102
<b>Figure 3.98</b> : Equivalent damping ratio in terms of displacement for 5mm thick steel cushions under compressive load of N=7.5 KN.....	102
<b>Figure 3.99</b> : Equivalent damping ratio in terms of displacement for 5mm thick steel cushions under compressive load of N=15 KN.....	103
<b>Figure 3.100</b> : Equivalent damping ratio in terms of displacement for 5mm thick steel cushions under compressive load of N=25 KN.....	103
<b>Figure 3.101</b> : Comparison of equivalent damping ratio for 5mm thick specimens under two extreme compressive axial loads. ....	104
<b>Figure 3.102</b> : Equivalent damping ratio in terms of displacement for 8mm thick steel cushions under compressive load of N=25 KN.....	104
<b>Figure 3.103</b> : Equivalent damping ratio in terms of displacement for 8mm thick steel cushions under compressive load of N=50 KN.....	105
<b>Figure 3.104</b> : Equivalent damping ratio in terms of displacement for 8mm thick steel cushions under compressive load of N=75 KN.....	105
<b>Figure 3.105</b> : Comparison of equivalent damping ratio for 8mm thick specimens under two extreme compressive axial loads. ....	106
<b>Figure 3.106</b> : Comparison of equivalent damping ratio for three distinct thicknesses under two extreme compressive axial loads. ....	106
<b>Figure 3.107</b> : Comparison of normalized Stiffness ratio in terms of displacement for 3mm thick specimen under compressive axial loads. ....	107
<b>Figure 3.108</b> : Comparison of normalized Stiffness ratio in terms of displacement for 5mm thick specimen under compressive axial loads. ....	107
<b>Figure 3.109</b> : Comparison of normalized Stiffness ratio in terms of displacement for 8mm thick specimen under compressive axial loads. ....	108
<b>Figure 3.110</b> : Ductility trend for 3mm thick specimen under increase of compressive axial load. ....	109
<b>Figure 3.111</b> : Ductility trend for 5mm thick specimen under increase of compressive axial load. ....	109
<b>Figure 3.112</b> : Ductility trend for 8mm thick specimen under increase of compressive axial load. ....	110
<b>Figure 3.113</b> : Yield force trend for 3mm thick specimen under increase of compressive axial load. ....	110
<b>Figure 3.114</b> : Yield force trend for 5mm thick specimen under increase of compressive axial load. ....	111
<b>Figure 3.115</b> : Yield force trend for 8mm thick specimen under increase of tensile axial load. ....	111
<b>Figure 3.116</b> : Yield displacement trend for 3mm thick specimen under increase of compressive axial load. ....	112
<b>Figure 3.117</b> : Yield displacement trend for 5mm thick specimen under increase of compressive axial load. ....	112
<b>Figure 3.118</b> : Yield displacement trend for 8mm thick specimen under increase of compressive axial load. ....	112
<b>Figure 3.119</b> : Initial stiffness trend for 3mm thick specimen under increase of compressive axial load. ....	113

<b>Figure 3.120</b> : Initial stiffness trend for 5mm thick specimen under increase of compressive axial load.....	113
<b>Figure 3.121</b> : Initial stiffness trend for 8mm thick specimen under increase of compressive axial load.....	114
<b>Figure 3.122</b> : Maximum force trend for 3mm thick specimen under increase of compressive axial load.....	114
<b>Figure 3.123</b> : Maximum force trend for 5mm thick specimen under increase of compressive axial load.....	115
<b>Figure 3.124</b> : Maximum force trend for 8mm thick specimen under increase of compressive axial load.....	115
<b>Figure 3.125</b> : Interaction diagram for three distinct specimens.....	116
<b>Figure 4.1</b> : Double and single cushion tests .....	117
<b>Figure 4.2</b> : Typical dimension of single cushion test set-up. ....	118
<b>Figure 4.3</b> : Typical dimension of double cushion test set-up. ....	119
<b>Figure 4.4</b> : Steel bracing in the loading frame. ....	119
<b>Figure 4.5</b> : Two pairs of concrete panel at two sides.....	120
<b>Figure 4.6</b> : Loading actuator. ....	120
<b>Figure 4.7</b> : Lateral truss system. ....	121
<b>Figure 4.8</b> : Typical dimension of concrete cladding panels. ....	121
<b>Figure 4.9</b> : Reinforcement details in concrete panel.....	122
<b>Figure 4.10</b> : Reinforcement details in concrete panel.....	122
<b>Figure 4.11</b> : Drift based cyclic loading protocol. ....	123
<b>Figure 4.12</b> : Arrangements of steel cushions in system test I.....	124
<b>Figure 4.13</b> : Location of strain assessment devices in system test I.....	124
<b>Figure 4.14</b> : Location of transducers in side 1 in system test I.....	125
<b>Figure 4.15</b> : Location of transducers in side 2 in system test I.....	125
<b>Figure 4.16</b> : Force-Top displacement Relation obtained from system test I. ....	126
<b>Figure 4.17</b> : Force-Drift angle curve obtained from system test I.....	126
<b>Figure 4.18</b> : Cumulative energy vs drift curve obtained from system test I.....	127
<b>Figure 4.19</b> : Equivalent damping ratio vs drift curve obtained from system test I. ....	127
<b>Figure 4.20</b> : Secant stiffness vs drift relation obtained from system test I.....	128
<b>Figure 4.21</b> : Actuator force vs relative displacement relation for steel cushion in panel 1 to panel 2 connection obtained from system test I.....	128
<b>Figure 4.22</b> : Strain gages location on steel cushions in panel-to-panel connection obtained from system test I. ....	129
<b>Figure 4.23</b> : Strain vs drift angle relation for steel cushion in panel 1 to panel 2 connection obtained from system test I.....	129
<b>Figure 4.24</b> : Actuator force vs relative displacement relation for steel cushion in panel 3 to panel 4 connection obtained from system test I.....	130
<b>Figure 4.25</b> : Strain vs drift angle relation for steel cushion in panel 3 to panel4 connection obtained from system test I.....	130
<b>Figure 4.26</b> : Comparison of actuator force vs relative displacement of S12 and S34 obtained from system test I. ....	130
<b>Figure 4.27</b> : Actuator force vs relative displacement relation for steel cushion beneath panel 1 obtained from system test I. ....	131
<b>Figure 4.28</b> : Strain gage location steel cushions in panel to support connection obtained from system test I. ....	131
<b>Figure 4.29</b> : Actuator force vs relative displacement relation for steel cushion beneath panel 2 obtained from system test I. ....	132

<b>Figure 4.30</b> : Actuator force vs relative displacement relation for steel cushion beneath panel 3 obtained from system test I.....	133
<b>Figure 4.31</b> : Actuator force vs relative displacement relation for steel cushion beneath panel 4 obtained from system test I.....	133
<b>Figure 4.32</b> : Comparison of actuator force-relative displacement relation for S1 and S4 obtained from system test I.....	134
<b>Figure 4.33</b> : Comparison of actuator force-relative displacement relation for S2 and S3 obtained from system test I.....	134
<b>Figure 4.34</b> : Relation of the Actuator force vs relative displacement between panel 1 and beam obtained from system test I.....	135
<b>Figure 4.35</b> : Relation of the Actuator force vs relative displacement between panel 1 and beam obtained from system test I.....	136
<b>Figure 4.36</b> : Top view of S3* at final displacement target obtained from system test I. ....	136
<b>Figure 4.37</b> : Top view of S4* at final displacement target obtained from system test I. ....	136
<b>Figure 4.38</b> : Strain gage location of steel devices in panel to beam connection obtained from system test I.....	137
<b>Figure 4.39</b> : Cladding panels rotation. ....	137
<b>Figure 4.40</b> : Rotation in terms of step numbers for panel 3.....	138
<b>Figure 4.41</b> : Rotation in terms of step numbers for panel 4.....	138
<b>Figure 4.42</b> : Deformed shape of cladding panels obtained from system test I. ....	138
<b>Figure 4.43</b> : Out of plane displacement of panel 3 in terms of in plane displacement obtained from system test I.....	139
<b>Figure 4.44</b> : Out of plane displacement of panel 4 in terms of in plane displacement obtained from system test I.....	139
<b>Figure 4.45</b> : Arrangements of steel cushions in system test II. ....	140
<b>Figure 4.46</b> : Location of strain assessment devices in system test II.....	140
<b>Figure 4.47</b> : Location of transducers in side 1 in system test II. ....	141
<b>Figure 4.48</b> : Location of transducers in side 2 in system test II. ....	141
<b>Figure 4.49</b> : Force-Top Displacement Relation obtained from system test II. ....	142
<b>Figure 4.50</b> : Force-Drift angle curve obtained from system test II.....	142
<b>Figure 4.51</b> : Cumulative energy vs drift curve obtained from test II.....	143
<b>Figure 4.52</b> : Equivalent damping ratio vs drift curve obtained from system test II. ....	144
<b>Figure 4.53</b> : Secant stiffness vs drift relation obtained from system test II.....	144
<b>Figure 4.54</b> : Actuator force vs relative displacement relation for steel cushion in panel 1 to panel 2 connection obtained from system test II. ....	145
<b>Figure 4.55</b> : Strain gages location on steel cushions in panel-to-panel connection obtained from system test II. ....	145
<b>Figure 4.56</b> : Strain vs drift angle relation for steel cushion in panel 1 to panel 2 connection obtained from system test II.....	145
<b>Figure 4.57</b> : Actuator force vs relative displacement relation for steel cushion in panel 3 to panel 4 connection obtained from system test II. ....	146
<b>Figure 4.58</b> : Strain vs drift angle relation for steel cushion in panel 3 to panel 4 connection obtained from system test II.....	146
<b>Figure 4.59</b> : Comparison of actuator force vs relative displacement of S12 and S34 obtained from system test II. ....	147
<b>Figure 4.60</b> : Actuator force vs relative horizontal displacement relation for steel cushions beneath panel 1 obtained from system test II. ....	147

<b>Figure 4.61</b> : Location of strain gages on steel cushions in panel to support connection obtained from system test II.....	148
<b>Figure 4.62</b> : Actuator force vs relative horizontal displacement relation for steel cushions beneath panel 2 obtained from system test II. ....	148
<b>Figure 4.63</b> : Actuator force vs relative horizontal displacement relation for steel cushions beneath panel 3 obtained from system test II. ....	149
<b>Figure 4.64</b> : Actuator force vs relative horizontal displacement relation for steel cushions beneath panel 4 obtained from system test II. ....	150
<b>Figure 4.65</b> : Comparison of actuator force-relative displacement relation for steel cushions beneath panel 1 and panel 4 obtained from system test II. ....	151
<b>Figure 4.66</b> : Comparison of actuator force-relative displacement relation for steel cushions beneath panel 2 and panel 3 obtained from system test II. ....	151
<b>Figure 4.67</b> : Relation of the Actuator force vs relative displacement between panel 1 and beam obtained from system test II. ....	152
<b>Figure 4.68</b> : Relation of the Actuator force vs relative displacement between panel 2 and beam obtained from system test II. ....	152
<b>Figure 4.69</b> : Top view of S3* at final displacement target obtained from system test II. ....	153
<b>Figure 4.70</b> : Top view of S4* at final displacement target obtained from system test II. ....	153
<b>Figure 4.71</b> : location of strain gages on steel device in system test II.....	153
<b>Figure 4.72</b> : Rotation in terms of step numbers for panel 3. ....	154
<b>Figure 4.73</b> : Rotation in terms of step numbers for panel 4. ....	154
<b>Figure 4.74</b> : Out of plane displacement of panel 3 in terms of in plane displacement obtained from system test II. ....	155
<b>Figure 4.75</b> : Out of plane displacement of panel 4 in terms of in plane displacement obtained from system test II. ....	155
<b>Figure 4.76</b> : Arrangements of steel cushions in system test III. ....	156
<b>Figure 4.77</b> : Location of strain assessment devices in system test III. ....	156
<b>Figure 4.78</b> : Location of transducers in side 1 in system test III. ....	157
<b>Figure 4.79</b> : Location of transducers in side 2 in system test III. ....	157
<b>Figure 4.80</b> : Force-Top Displacement Relation obtained from system test III. ....	158
<b>Figure 4.81</b> : Force-Drift angle curve obtained from system test III. ....	158
<b>Figure 4.82</b> : Cumulative energy vs drift curve obtained from system test III. ....	159
<b>Figure 4.83</b> : Equivalent damping ratio vs drift curve obtained from system test III. ....	159
<b>Figure 4.84</b> : Secant stiffness vs drift relation obtained from system test III. ....	160
<b>Figure 4.85</b> : Actuator force vs relative displacement relation for steel cushion in panel 1 to panel 2 connection obtained from system test III. ....	160
<b>Figure 4.86</b> : Strain gages location on steel cushions in panel-to-panel connection obtained from system test III. ....	161
<b>Figure 4.87</b> : Strain vs drift angle relation for steel cushion in panel 1 to panel 2 connection obtained from system test III. ....	161
<b>Figure 4.88</b> : Actuator force vs relative displacement relation for steel cushion in panel 3 to panel 4 connection obtained from system test III. ....	161
<b>Figure 4.89</b> : Strain vs drift angle relation for steel cushion in panel 3 to panel 4 connection obtained from system test III. ....	162

<b>Figure 4.90</b> : Comparison of actuator force vs relative displacement of S12 and S34 obtained from system test III. ....	162
<b>Figure 4.91</b> : Actuator force vs relative horizontal displacement relation for steel cushions beneath panel 1 obtained from system test III. ....	163
<b>Figure 4.92</b> : Location of strain gages on steel cushions in panel to support connection obtained from system test III. ....	163
<b>Figure 4.93</b> : Actuator force vs relative horizontal displacement relation for steel cushions beneath panel 2 obtained from system test III. ....	164
<b>Figure 4.94</b> : Actuator force vs relative horizontal displacement relation for steel cushions beneath panel 3 obtained from system test III. ....	165
<b>Figure 4.95</b> : Location of strain gages on steel cushions in panel to support connection obtained from system test III. ....	165
<b>Figure 4.96</b> : Actuator force vs relative horizontal displacement relation for steel cushions beneath panel 4 obtained from system test III. ....	166
<b>Figure 4.97</b> : Comparison of actuator force-relative displacement relation for steel cushions beneath panel 1 and panel 4 obtained from system test III. ....	166
<b>Figure 4.98</b> : Comparison of actuator force-relative displacement relation for steel cushions beneath panel 2 and panel 3 obtained from system test III. ....	167
<b>Figure 4.99</b> : Relation of the Actuator force vs relative displacement between panel 1 and beam obtained from system test III. ....	167
<b>Figure 4.100</b> : Relation of the Actuator force vs relative displacement between panel 2 and beam obtained from system test III. ....	168
<b>Figure 4.101</b> : Top view of S3* at final displacement target obtained from system test III. ....	168
<b>Figure 4.102</b> : Top view of S4* at final displacement target obtained from system test III. ....	169
<b>Figure 4.103</b> : location of strain gages on steel device in system test III. ....	169
<b>Figure 4.104</b> : Rotation in terms of step numbers for panel 3. ....	169
<b>Figure 4.105</b> : Rotation in terms of step numbers for panel 4. ....	170
<b>Figure 4.106</b> : Out of plane displacement of panel 3 in terms of in plane displacement obtained from system test III. ....	170
<b>Figure 4.107</b> : Out of plane displacement of panel 4 in terms of in plane displacement obtained from system test III. ....	171
<b>Figure 4.108</b> : Deformed shape of the steel cushions obtained from system test III. ....	171
<b>Figure 4.109</b> : Arrangements of steel cushions in system test IV. ....	172
<b>Figure 4.110</b> : Location of strain assessment devices in system test IV. ....	172
<b>Figure 4.111</b> : Location of transducers in side 1 in system test IV. ....	173
<b>Figure 4.112</b> : Location of transducers in side 2 in system test IV. ....	173
<b>Figure 4.113</b> : Force-Top Displacement Relation obtained from system test IV. ..	174
<b>Figure 4.114</b> : Force-Drift angle curve obtained from system test IV. ....	174
<b>Figure 4.115</b> : Cumulative energy vs drift curve obtained from system test IV. ....	175
<b>Figure 4.116</b> : Equivalent damping ratio vs drift curve obtained from system test IV. ....	175
<b>Figure 4.117</b> : Secant stiffness vs drift relation obtained from system test IV. ....	176
<b>Figure 4.118</b> : Actuator force vs relative displacement relation for steel cushion in panel 1 to panel 2 connection obtained from system test IV. ....	176

<b>Figure 4.119</b> : Strain gages location on steel cushions in panel to panel connection obtained from system test IV. ....	177
<b>Figure 4.120</b> : Strain vs drift angle relation for steel cushion in panel 1 to panel 2 connection obtained from system test IV. ....	177
<b>Figure 4.121</b> : Actuator force vs relative displacement relation for steel cushion in panel 3 to panel 4 connection obtained from system test IV.....	177
<b>Figure 4.122</b> : Strain vs drift angle relation for steel cushion in panel 3 to panel 4 connection obtained from system test IV. ....	178
<b>Figure 4.123</b> : Comparison of actuator force vs relative displacement of S12 and S34 obtained from system test IV.....	178
<b>Figure 4.124</b> : Actuator force vs relative horizontal displacement relation for steel cushions beneath panel 1 obtained from system test IV. ....	179
<b>Figure 4.125</b> : Location of strain gages on steel cushions in panel to support connection obtained from system test IV. ....	179
<b>Figure 4.126</b> : Actuator force vs relative horizontal displacement relation for steel cushions beneath panel 2 obtained from system test IV. ....	180
<b>Figure 4.127</b> : Actuator force vs relative horizontal displacement relation for steel cushions beneath panel 3 obtained from system test IV. ....	181
<b>Figure 4.128</b> : Location of strain gages on steel cushions in panel to support connection obtained from system test IV. ....	181
<b>Figure 4.129</b> : Actuator force vs relative horizontal displacement relation for steel cushions beneath panel 4 obtained from system test IV. ....	182
<b>Figure 4.130</b> : Comparison of actuator force-relative displacement relation for steel cushions beneath panel 1 and panel 4 obtained from system test IV. ....	182
<b>Figure 4.131</b> : Comparison of actuator force-relative displacement relation for steel cushions beneath panel 2 and panel 3 obtained from system test IV. ....	183
<b>Figure 4.132</b> : Relation of the Actuator force vs relative displacement between panel 1 and beam obtained from system test IV.....	183
<b>Figure 4.133</b> : Relation of the Actuator force vs relative displacement between panel 2 and beam obtained from system test IV.....	184
<b>Figure 4.134</b> : Top view of S3* at final displacement target obtained from system test IV. ....	184
<b>Figure 4.135</b> : Top view of S4* at final displacement target obtained from system test IV. ....	185
<b>Figure 4.136</b> : location of strain gages on steel device in system test IV. ....	185
<b>Figure 4.137</b> : Rotation in terms of step numbers for panel 3. ....	185
<b>Figure 4.138</b> : Rotation in terms of step numbers for panel 4. ....	186
<b>Figure 4.139</b> : Out of plane displacement of panel 3 in terms of in plane displacement obtained from system test IV.....	186
<b>Figure 4.140</b> : Out of plane displacement of panel 4 in terms of in plane displacement obtained from system test IV.....	187
<b>Figure 4.141</b> : Deformed shape of the steel cushions obtained from system test IV. ....	187
<b>Figure 4.142</b> : Comparison of actuator force vs drift relations of system test I and II. ....	188
<b>Figure 4.143</b> : Comparison of energy dissipation capacity in terms of drift for system test I and II.....	189
<b>Figure 4.144</b> : Comparison of equivalent damping ratios in terms of drift for system test I and II.....	189

<b>Figure 4.145</b> : Comparison of secant stiffness in terms of drift for of system test I and II. ....	190
<b>Figure 4.146</b> : Comparison of normalized stiffness in terms of drift for system test I and II. ....	190
<b>Figure 4.147</b> : Comparison of relative vertical displacements in S12 elements in system test I and II. ....	191
<b>Figure 4.148</b> : Comparison of relative horizontal displacements in panel to support steel devices in system test I and II. ....	191
<b>Figure 4.149</b> : Comparison of actuator force vs drift relations of system test I and II. ....	192
<b>Figure 4.150</b> : Comparison of energy dissipation capacity in terms of drift for system test I and III. ....	193
<b>Figure 4.151</b> : Comparison of equivalent damping ratios in terms of drift for system test I and III. ....	194
<b>Figure 4.152</b> : Comparison of secant stiffness in terms of drift for of system test I and III. ....	194
<b>Figure 4.153</b> : Comparison of normalized stiffness in terms of drift for system test I and III. ....	195
<b>Figure 4.154</b> : Comparison of relative vertical displacements in the steel cushions in panel-to-panel connection in system test I and III. ....	195
<b>Figure 4.155</b> : Comparison of relative horizontal displacements in panel to support steel devices in system test I and III. ....	196
<b>Figure 4.156</b> : Comparison of actuator force vs drift relations of system test II and III. ....	197
<b>Figure 4.157</b> : Comparison of energy dissipation capacity in terms of drift for system test II and III. ....	197
<b>Figure 4.158</b> : Comparison of equivalent damping ratios in terms of drift for system test II and III. ....	198
<b>Figure 4.159</b> : Comparison of secant stiffness in terms of drift for of system test II and III. ....	198
<b>Figure 4.160</b> : Comparison of normalized stiffness in terms of drift for system test II and III. ....	199
<b>Figure 4.161</b> : Comparison of relative vertical displacements in S34 elements in system test II and III. ....	199
<b>Figure 4.162</b> : Comparison of relative horizontal displacements in panel to support steel devices in system test II and III. ....	200
<b>Figure 4.163</b> : Comparison of actuator force vs drift relations of system test III and IV. ....	201
<b>Figure 4.164</b> : Comparison of energy dissipation capacity in terms of drift for system test III and IV. ....	202
<b>Figure 4.165</b> : Comparison of equivalent damping ratios in terms of drift for system test III and IV. ....	202
<b>Figure 4.166</b> : Comparison of secant stiffness in terms of drift for of system test III and IV. ....	203
<b>Figure 4.167</b> : Comparison of normalized stiffness in terms of drift for system test III and IV. ....	203
<b>Figure 4.168</b> : Comparison of relative vertical displacements in S34 elements in system test III and IV. ....	204
<b>Figure 4.169</b> : Comparison of relative horizontal displacements in panel to support steel devices in system test III and IV. ....	204

<b>Figure 5.1</b> : Structure of software.....	207
<b>Figure 5.2</b> : Ramberg-Osgood curve.....	208
<b>Figure 5.3</b> : Required parameters for definition of Ramberg-Osgood curve.....	208
<b>Figure 5.4</b> : Degree of freedoms for definition of element.....	209
<b>Figure 5.5</b> : Analytical model for definition of steel cushions under shear effect..	209
<b>Figure 5.6</b> : Definition of structural and non-structural nods.....	210
<b>Figure 5.7</b> : Definition of elastic and link element.....	210
<b>Figure 5.8</b> : Comparison of experimental and analytical force-displacement relation for 3mm thick steel cushions under shear effects.....	211
<b>Figure 5.9</b> : Comparison of experimental and analytical force-displacement relation for 5mm thick steel cushions under shear effects.....	211
<b>Figure 5.10</b> : Comparison of experimental and analytical force-displacement relation for 8mm thick steel cushions under shear effects.....	212
<b>Figure 5.11</b> : Analytical model for definition of steel cushions under axial effect.	212
<b>Figure 5.12</b> : Asymmetric bi-linear curve.....	213
<b>Figure 5.13</b> : Required parameters for definition of asymmetric bi-linear curve..	213
<b>Figure 5.14</b> : Comparison of experimental and analytical force-displacement relation for 3mm thick steel cushions under axial effect.....	214
<b>Figure 5.15</b> : Comparison of experimental and analytical force-displacement relation for 5mm thick steel cushions under axial effect.....	214
<b>Figure 5.16</b> : Comparison of experimental and analytical force-displacement relation for 8mm thick steel cushions under axial effect.....	215
<b>Figure 5.17</b> : Definition of the support link elements for system test I.....	216
<b>Figure 5.18</b> : Definition of the panel-to-panel link elements for system test I.....	216
<b>Figure 5.19</b> : Definition of the panel to beam link elements for system test I.....	217
<b>Figure 5.20</b> : Comparison of the experimental and analytical actuator force-top displacement relations in the system test I.....	217
<b>Figure 5.21</b> : Analytical force versus vertical displacement relation for panel-to- panel steel cushion in system test I.....	218
<b>Figure 5.22</b> : Comparison of the experimental and analytical relative vertical displacement history in the panel-to-panel steel cushion.....	218
<b>Figure 5.23</b> : Force-Displacement relation panel to support link element under the rotation of the panel 1 for system test I.....	219
<b>Figure 5.24</b> : Force-Displacement relation panel to support link element under the rotation of the panel 2 for system test I.....	219
<b>Figure 5.25</b> : Comparison of the experimental and analytical rotation history for panel 3 in system test I.....	220
<b>Figure 5.26</b> : Comparison of the experimental and analytical rotation history for panel 4 in system test I.....	220
<b>Figure 5.27</b> : Moment-Rotation relation at the base of panel 3 in system test I....	221
<b>Figure 5.28</b> : Moment-Rotation relation at the base of panel 4 in system test I....	221
<b>Figure 5.29</b> : Deformed shape of the structural system I.....	222
<b>Figure 5.30</b> : Overview of the mathematical model for system test II.....	222
<b>Figure 5.31</b> : Definition of the support link elements for system test II.....	223
<b>Figure 5.32</b> : Definition of the panel-to-panel link elements for system test II.....	223
<b>Figure 5.33</b> : Definition of the panel to beam link elements for system test II.....	224
<b>Figure 5.34</b> : Comparison of the experimental and analytical actuator force-top displacement relations in the system test II.....	224
<b>Figure 5.35</b> : Analytical force versus vertical displacement relation for panel-to- panel steel cushion in system test II.....	225

<b>Figure 5.36</b> : Comparison of the experimental and analytical relative vertical displacement history in the panel-to-panel steel cushion. ....	225
<b>Figure 5.37</b> : Force-Displacement relation panel to support link element in under the rotation of the panel 1 for system test II. ....	226
<b>Figure 5.38</b> : Force-Displacement relation panel to support link element under the rotation of the panel 1 for system test II. ....	226
<b>Figure 5.39</b> : Force-Displacement relation panel to support link element under the rotation of the panel 2 for system test II. ....	227
<b>Figure 5.40</b> : Force-Displacement relation panel to support link element under the rotation of the panel 2 for system test II. ....	227
<b>Figure 5.41</b> : Comparison of the experimental and analytical rotation history for panel 3 in system test II. ....	228
<b>Figure 5.42</b> : Comparison of the experimental and analytical rotation history for panel 4 in system test II. ....	228
<b>Figure 5.43</b> : Moment-Rotation relation at the base of panel 3 in system test II. ...	229
<b>Figure 5.44</b> : Moment-Rotation relation at the base of panel 4 in system test II. ...	229
<b>Figure 5.45</b> : Deformed shape of the structural system II. ....	230
<b>Figure 5.46</b> : Definition of the support link elements for system test III. ....	230
<b>Figure 5.47</b> : Definition of the panel-to-panel link elements for system test III. ....	231
<b>Figure 5.48</b> : Definition of the panel to beam link elements for system test III. ....	231
<b>Figure 5.49</b> : Comparison of the experimental and analytical actuator force-displacement relations in the system test III. ....	232
<b>Figure 5.50</b> : Analytical force versus vertical displacement relations for panel-to-panel steel cushion in system test III. ....	232
<b>Figure 5.51</b> : Comparison of the experimental and analytical relative vertical displacement history in the panel-to-panel link element. ....	233
<b>Figure 5.52</b> : Force-Displacement relation panel to support link element under the rotation of the panel 1 for system test III. ....	233
<b>Figure 5.53</b> : Force-Displacement relation panel to support link element under the rotation of the panel 1 for system test III. ....	234
<b>Figure 5.54</b> : Force-Displacement relation panel to support link element under the rotation of the panel 2 for system test III. ....	234
<b>Figure 5.55</b> : Force-Displacement relation panel to support link element under the rotation of the panel 2 for system test III. ....	234
<b>Figure 5.56</b> : Comparison of the experimental and analytical rotation history for panel 3 in system test III. ....	235
<b>Figure 5.57</b> : Comparison of the experimental and analytical rotation for panel 4 in system test III. ....	235
<b>Figure 5.58</b> : Moment-Rotation relation at the base of panel 3 in system test III. ...	236
<b>Figure 5.59</b> : Moment-Rotation relation at the base of panel 4 in system test III. ...	236
<b>Figure 5.60</b> : Deformed shape of the structural system III. ....	237
<b>Figure 5.61</b> : Definition of the support link elements for system test IV. ....	237
<b>Figure 5.62</b> : Definition of the panel-to-panel link elements for system test IV. ...	238
<b>Figure 5.63</b> : Definition of the panel to beam link elements for system test IV. ....	238
<b>Figure 5.64</b> : Comparison of the experimental and analytical actuator force-top displacement relations in the system test IV. ....	239
<b>Figure 5.65</b> : Analytical force versus vertical displacement relations for panel-to-panel steel cushion in system test IV. ....	239
<b>Figure 5.66</b> : Comparison of the experimental and analytical relative vertical displacement history in the panel-to-panel steel cushion. ....	240

<b>Figure 5.67</b> : Force-Displacement relation panel to support link element under the rotation of the panel 1 for system test IV. ....	240
<b>Figure 5.68</b> : Force-Displacement relation panel to support link element under the rotation of the panel 1 for system test IV. ....	241
<b>Figure 5.69</b> : Force-Displacement relation panel to support link element under the rotation of the panel 2 for system test IV. ....	241
<b>Figure 5.70</b> : Force-Displacement relation panel to support link element under the rotation of the panel 2 for system test IV. ....	241
<b>Figure 5.71</b> : Comparison of the experimental and analytical rotation history for panel 3 in system test IV. ....	242
<b>Figure 5.72</b> : Comparison of the experimental and analytical rotation history for panel 4 in system test IV. ....	242
<b>Figure 5.73</b> : Moment-Rotation relation at the base of panel 3 in system test IV. .	243
<b>Figure 5.74</b> : Moment-Rotation relation at the base of panel 4 in system test IV. .	243
<b>Figure 5.75</b> : Deformed shape of the structural system IV. ....	244



## **ENERGY DISSIPATOR STEEL CUSHIONS**

### **SUMMARY**

The observation on the severely damaged precast concrete industrial buildings after the destructive L'Aquila Earthquake (2009) demonstrated the inadequate seismic performance of connecting elements between cladding panels and other structural elements, which leading to collapse of many panels. Moreover, the cladding walls lack the sufficient energy dissipation capacity, requiring the supplementary energy dissipative component to improve the energy dissipation capability.

SAFECLADDING a research study was initiated in the scope of FP7 with collaboration of some European Union universities such as, Istanbul Technical University, Polytechnic University of Milan, University of Ljubljana, National Technical University of Athens, Joint Research Centre - Elsa Laboratory (JRC), and some construction companies from Italy and Turkey, aiming to design the innovative energy dissipative steel connector and to investigate the seismic performance of the Cladding panels equipped with steel connectors. A brand new oval shaped low-cost steel connector was developed in Structural and Earthquake Engineering Laboratory of ITU to be utilized as a connecting element between adjacent panels, panel to beam and panel to support connections of industrial buildings.

The experimental and analytical studies were conducted in the scope of this thesis. The experimental studies were performed in two different phases namely; steel cushion tests and system tests. In the first phase, a series of experimental study was performed to investigate the uniaxial and bi-axial behavior of steel cushions with three distinct thicknesses. The high deformation capacity, and high-energy dissipation capability and stable hysteretic curves are the common properties observed from the uniaxial tests. In addition, the performed bi-directional tests showed that the direction of the applied axial load affects the general behavior of the steel cushions, so that with increment of applied compressive axial load the energy dissipation capacity of specimens increase while the relation is inverse in the case of tension type axial load. The interaction curves are plotted for each specific thickness of specimens as well.

In the second phase, the system tests were carried out. The testing set up consisted of RC cladding panels and fully pinned swaying steel frame to transfer the lateral load to RC walls. The steel devices were positioned at different locations, in panel to support, in panel to panel between two adjacent panels and in panel to beam connections. In this study, two kinds of test carried out named single cushion test and double cushion test according to the number of steel connector placed as the support per panel. The experimental study was performed to evaluate the energy dissipation capacity and performance of cladding panels equipped with steel devices. The results indicate that the double cushion type tests have higher energy dissipation capacity in comparison with single cushion test type, resulting to appropriate performance of whole system.

In the analytical part, the steel cushions are modeled with link elements in the finite element program of SeismoStruct v 6.0. Ramberg-Osgood and asymmetric bi-linear response curves are suggested for modeling of shear and axial behavior of steel cushions analytically as link elements. The mathematical models for system tests are set and experimental and analytical results are compared. In addition force-displacement relation of each steel cushions at different position in the system tests are obtained and their contribution in the energy dissipation capacity are calculated. The results showed that the steel cushions in panel-to-panel and panel to support connections, contribute in the energy dissipation capacity with their shear and axial behavior respectively.

## ENERJİ SÖNÜMLEYİCİ ÇELİK YASTIKLAR

### ÖZET

L'Aquila depremi, L'Aquila kasabasını 2009 yılında vurdu. Richter ölçeğine göre depremin yıkıcı gücü 5.8, büyüklüğü 6.3 ve yatay pik ivmesi 0.35 ve 0.40 g arasındaydı. Deprem, birçok prefabrik yapının yıkımına yol açtı.

Depremden sonra bir grup araştırmacı yapıların davranışını incelemek için kasabaya gitti. Araştırmacılar, birçok endüstriyel binanın yeterli yapı davranışı gösterdiğini, fakat prekast cephe panellerin davranışının yeterli olmadığını gözlemlediler.

Bu gözlemler, mafsalı kırılgan yapılar için prefabrik iskeletli yapıların sismik tasarımının güvenilir olduğunu, fakat cephe panelleri ile diğer yapı elemanları arasındaki bağlantı elemanlarının sismik performansının yetersiz olduğunu göstermiştir.

Bağlantı elemanlarının yetersiz sismik performansa sahip oldukları, panellerinin yeterli mevcut yatay yük taşıma potansiyellerinin kullanılmadığı, enerji tüketme kapasitesini geliştirmek için yeni birleşim elemanı tasarımına ihtiyaç olduğuna göstermiştir.

İstanbul Teknik Üniversitesi, Milan Politeknik Üniversitesi, Ljubljana Üniversitesi, Atina Ulusal Teknik Üniversitesi, Joint Research Centre - Elsa Laboratory (JRC) gibi araştırma kurumları ile İtalya ve Türkiye'den Prefabrik Birliklerinin işbirliğiyle, yeni birleşim metodları ve elemanları tasarlamak ve bu bağlantı elemanları ile donatılmış cephe panellerinin sismik performansını araştırmak için FP7 kapsamında SAFECLADDING isimli bir araştırma projesi başlatılmıştır.

3, 5 ve 8 mm olmak üzere üç farklı kalınlıktaki yeni oval düşük maliyetli çelik bağlantı elemanı, endüstriyel binaların bitişik panelleri, panel-kiriş ve panel-mesnet bağlantıları arasında bağlantı elemanı olarak kullanılmak üzere İTÜ Yapı ve Deprem Mühendisliği Laboratuvarında geliştirmiştir.

Enerji sönmüleyici çelik bağlantı elemanları deprem enerjisinin bir bölümünü sönmüleyebilir, yapısal ve yapısal olmayan elemanlardaki hasar miktarını sınırlayabilir.

Bu tez kapsamında deneysel ve analitik çalışmalar yürütülmüştür. Deneysel çalışmalar çelik yastık testleri ve sistem testleri olmak üzere iki farklı aşamada gerçekleştirilmiştir.

Çelik yastıklar cephe panellerin üzerinde farklı konumlara yerleştirilmiştir. Yerleşim. Davranışta değişiklikler gözlemlendiğinden farklı yük kombinasyonlarıyla çok sayıda test yapmak gerekmiştir.

İlk aşamada, üç farklı kalınlıktaki çelik yastığın tek eksenli ve iki eksenli davranışını araştırmak için bir dizi deney yapılmıştır.

Tek eksenli testler, kesme ve tek eksenli kuvvet testlerinden oluşmaktadır. Tek eksenli testleri yapmak için, özel test düzenleri tasarlanmış ve yaptırılmıştır.

Çelik yastıkların çevrimsel davranışını ve enerji tüketme kapasitesini değerlendirmek için 3, 5 ve 8 mm'lik numuneler üzerinde toplam 15 adet tek eksenli kesme testi yapılmıştır.

Kesme testleri, enerji sönümlenme yastıklarının yüksek deformasyon kapasitesine, yüksek enerji sönümlenme kabiliyetine ve kararlı çevrimsel eğrilere sahip olduklarını göstermiştir. Çelik yastıkların kalınlığı, genel davranışını etkilemektedir. Kalın çelik yastıklar daha fazla mukavemet, sertlik ve enerji tüketme kapasitesine sahiptir. Ayrıca, çelik yastıkların sünekliği, artan kalınlıkla birlikte artmaktadır.

Çelik yastıkların eksenel davranışını ve enerji sönümlenme kapasitesini değerlendirmek için 3, 5 ve 8 mm'lik numuneler üzerinde toplam 9 adet tek eksenli eksenel yükleme testi yapılmıştır. Sistem testlerinde ve gerçek yapıdaki numuneler, beton panellerin ağırlığını taşımaktadır. Dolayısıyla çelik yastıkların eksenel davranışını belirlemek önemlidir.

Eksenel yükleme testleri, enerji sönümleyici yastıkların yüksek deformasyon kapasitesine ve yüksek enerji sönümlenme kabiliyetine sahip olduklarını göstermiştir. Çelik yastıkların kalınlığı, çelik yastıkların genel davranışını etkilemektedir. Kalın çelik yastıklar daha fazla mukavemet, sertlik ve enerji sönümlenme kapasitesine sahiptir. Ayrıca, çelik yastıkların sünekliği, artan kalınlıkla birlikte artmaktadır.

Farklı sabit eksenel gerilme etkisine tabi tutulan çelik yastıkların kesme davranışını incelemek için toplam 82 adet iki eksenli test yapılmıştır.

Çift eksenli testler büyük öneme sahiptir, çünkü çelik yastıklar endüstriyel binalarda panel-mesnet, panel-panel ve panel-kiriş bağlantıları olarak kullanılmak üzere tasarlanmıştır. Bu nedenle, çelik yastıklar farklı tipte yük kombinasyonlarıyla karşılaşmaktadır. Özellikle tabanda, çelik yastıklar mesnet işlevi sağladıklarından, yatay yük altında kesme deformasyonuna ve aynı zamanda cephe panellerinin kendi ağırlığı altında eksenel deformasyona tabi olurlar.

Eksenel kuvvetler, testler boyunca sabit tutulmuştur. Eksenel kuvvetlerin değerleri,  $N/N_0$  oranına göre seçilmiştir. Burada  $N_0$ , monoton eksenel yükleme testlerinden elde edilen nihai eksenel kuvvettir. Uygulanan eksenel yükler,  $N_0$ 'ın %25, %50 ve %75 ine karşı gelmektedir.

Yapılan iki eksenli testler, yükleme yönünün farklı kalınlıktaki çelik yastıkların genel davranışı üzerinde etkili bir faktör olduğunu; sıkışma yükünün artmasıyla sönüm oranı ve enerji sönümlenme kapasitesinin arttığını, çekmede ise, sönüm oranı ve enerji sönümlenme kapasitesinin düştüğünü göstermiştir. Ayrıca, optimum eksenel yük seviyesinin maksimum eksenel yük kapasitesinin  $\pm\%25$ 'i olduğu gösterilmiştir. Çünkü daha yüksek seviyelerde, çelik yastıkların genel davranışı etkilenebilmektedir.

3, 5 ve 8 mm kalınlıkta çelik yastıklar için etkileşim diyagramları oluşturulmuştur. Etkileşim diyagramlarına göre, kalın çelik yastık, ince çelik yastığa göre daha geniş çevrelenmiş alana sahiptir.

İkinci aşamada, toplam 4 adet sistem testi yapılmıştır. Test düzeni, betonarme cephe panelleri ve yanal yükün betonarme cephe panellere transferi için tam mafsallı bir çelik çerçeveden oluşmaktadır.

Çelik yastıklar farklı konumlarda, panel-mesnet, iki bitişik panel arası panel-panel ve panel-kiriş bağlantılarına yerleştirilmiştir.

Bu deneysel çalışmada, her panel için mesnet olarak kullanılan çelik bağlantı sayısına göre, tek yastık testi ve çift yastık testi olmak üzere iki tür test yapılmıştır.

Çelik yastıklarla donatılmış cephe panellerinin enerji sönümlenme kapasitesi ve performansı değerlendirilmiştir. FEMA-461'de önerilen deneylerde yer değiştirme protokolü kullanılmıştır.

Plastikleşmeler çelik yastıkların üzerinde yoğunlaştığından, yapısal elemanlarda hasar veya çatlak gözlenmemiştir.

Tüm sistem testlerinde, beton panelin dönmesi hemen hemen aynı olurken, tabandaki panellerin yatay ötelenmesi ihmal edilebilir düzeydedir. Bu da panellerin baskın davranışının dönme olduğunu göstermektedir. Dolayısıyla, enerji sönümlenme kapasitesine en büyük katkı, panel-panel bağlantılarında çelik yastıkların kesme davranışı ve panel-mesnet bağlantılarında çelik yastıkların eksenel davranışından sağlanmaktadır.

Tek yastık testinde, sistemin genel davranışını etkileyen düzlem dışı hareket olmakla beraber, yüksek enerji sönme kapasitesi vardır.

Panel-kiriş bağlantılarındaki çelik yastık akmaya erişmemiştir, dolayısıyla sistemin enerji sönümlenme kapasitesine hiçbir katkısı olmamıştır, basit mafsal bağlantısı gibi hareket etmiştir.

Analiz kısmında ise, çelik yastıklar SeismoStruct v 6.0 yazılımı modellenmiştir. Çelik yastıkların kesme ve eksenel davranışının modellenmesi için Ramberg-Osgood ve asimetrik bilinear davranış eğrileri önerilmektedir.

Sistem testlerine karşı gelen matematik modeller oluşturularak , deneysel ve sayısal sonuçlar karşılaştırılmıştır.

Sistem testlerinde farklı pozisyonlardaki her bir çelik yastığın kuvvet-yerdeğiştirme ilişkileri elde edilmiştir ve enerji sönümlenme kapasitesine katkıları hesaplanmıştır.

Sonuçlar, panel-panel ve panel-mesnet bağlantılarında çelik yastıkların, sırasıyla kesme ve eksenel davranış ile sistem enerji sönümlenme kapasitesine büyük katkı sağladıklarını göstermiştir.



## **1. INTRODUCTION**

Large experimental campaigns were performed during two years from 2012 until 2014 in the Structural and Earthquake Laboratory of Istanbul Technical University, within the framework of FP7 project, named SAFECLADDING.

The experimental works consist of two stages, element test and system tests. During the first stage, the new low-cost energy dissipative cushions, which were made of mild steel, with different thickness of 3, 5, and 8mm, were developed. They were called steel cushions. In addition, a complete set of Quasi-static uniaxial and bi-directional tests were conducted on the steel cushions with different thickness to investigate the uniaxial and biaxial behavior of steel cushions.

Steel cushions made of mild steel were developed to utilize in cladding panels of precast structure. They can be used at different locations such as, between adjacent cladding panels, in beam to cladding panel connections and cladding panel to foundation connections. The steel cushions have various advantages, such as they can provide additional source of energy dissipation, they can be replaced easily after an earthquake and their manufacturing is simple.

At the second stage, the cladding panel and loading frame were designed and the cladding panels were equipped with steel cushions. A series of cyclic tests were performed on the precast concrete cladding panels equipped with steel cushions to understand the behavior of cladding-to-cladding, cladding to beam and cladding to foundation connections.

Finally, analytical study were carried out on the steel cushions and cladding panels equipped with steel cushions.

In the scope of this thesis, the experimental and analytical studies, which were conducted on the steel cushions, and cladding panels equipped with steel cushions have been discussed. The steel cushions and their typical dimensions are shown in Figure 1.1 and 1.2.

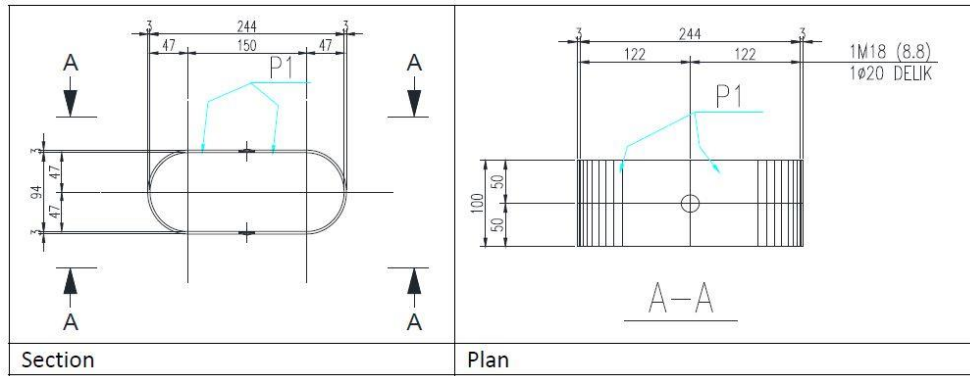


**Figure 1.1 :** Typical dimension of steel cushion.



**Figure 1.2 :** General view of 3, 5 and 8mm thick steel cushions.

## 1.1 Purpose of Thesis

The purpose of thesis is to investigate the uniaxial and biaxial behavior of the steel cushions, which are designed to utilize as a connection in panel to support, panel to panel and panel to beam connections in precast industrial buildings. In addition, in the analytical part the link element models are suggested for modeling of the steel cushions under the uniaxial and bi-axial stresses.

## 1.2 General Definition and Concepts

In this part, the general concepts of dissipative energy, equivalent viscous damping and effective stiffness are described.

### 1.2.1 Dissipated Energy

Viscous damping and yielding dissipate the input energy in inelastic system caused by earthquake excitation. The input energy subdivided into several energy terms, each energy terms can be directly obtained through integrating of the equation of motion, and the energy balance equation (Chopra, 1995) is presented in Equation (1.1).

$$\int_0^u m \ddot{u}(t) du + \int_0^u c \dot{u}(t) du + \int_0^u f_s(u) du = - \int_0^u m \ddot{u}_g(t) \quad (1.1)$$

Where,  $m$  is the mass of structure,  $c$  is the damping coefficient,  $f_s$  is the resisting force. The terms of  $\dot{u}(t)$ ,  $\ddot{u}(t)$  and  $\ddot{u}_g(t)$  are relative velocity, relative acceleration and the ground acceleration at any instant in the single degree of freedom system as shown in Figure 1.3.

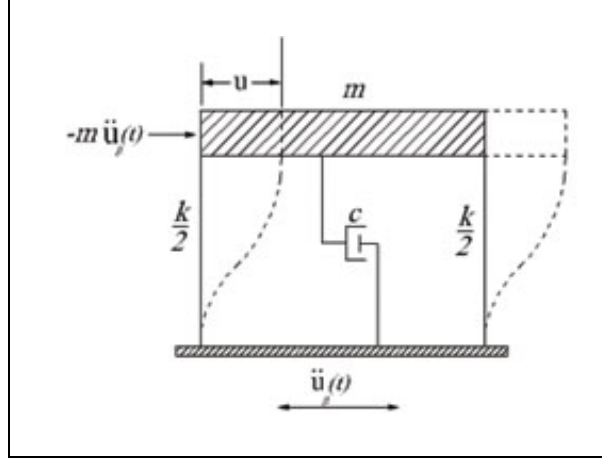


**Figure 1.3 :** Fixed base single degree of freedom system.

The right side of Equation 1.1, is the input energy ( $E_I$ ), which consists of kinetic energy ( $E_K$ ), energy dissipated by viscous damping ( $E_D$ ) and energy dissipated by yielding ( $E_Y$ ) and strain energy ( $E_S$ ). Thus, the energy balance equation can be written as Equation (1.2).

$$E_K(t) + E_D(t) + E_S(t) + E_Y(t) = E_I(t) \quad (1.2)$$

The strain energy is calculated with the following relation

$$E_S(t) = \frac{u^2(t)}{2K} \quad (1.3)$$

Where,  $k$  is the elastic stiffness of the system. Therefore, the energy dissipated by yielding can be obtained from the Equation (1.4), (Chopra, 1995).

$$E_Y(t) = \int_0^u f_s(u) du - E_S(t) \quad (1.4)$$

In the inelastic systems, more energy is dissipated by the yielding energy ( $E_Y$ ) than damping energy. In contrast, in the elastic systems, nearly all of the energy is dissipated by damping, as the yielding does not exist. The energy dissipated by kinetic energy and strain energy is negligible in both elastic and in elastic systems, (Chopra, 1995).

### 1.2.2 Equivalent Viscous Damping

The most common method to calculate the equivalent-damping ratio is presented by Equation (1.5), (Chopra, 1995).

$$\zeta_{eq} = \frac{1}{4\pi} \frac{E_D}{E_{S0}} \quad (1.5)$$

Where,  $E_D$  is the energy dissipated in a cycle of force-displacement hysteresis obtained from experiments as illustrated in Figure 1.4.  $E_D$  is equaled to the enclosed area of the each hysteresis loop and  $E_{S0}$  is the maximum strain energy, and can be determined from the Equation (1.6), (Chopra, 1995).

$$E_{S0} = \frac{kU_0^2}{2} \quad (1.6)$$

Where  $k$  is stiffness obtained from the experiment and  $u_0$  is the displacement amplitude in each hysteresis cycle.

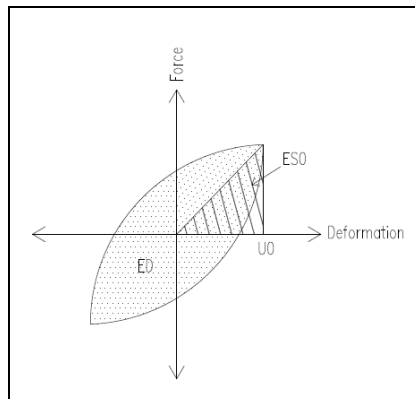


**Figure 1.4 :** Energy dissipated and strain energy in a cycle.

### 1.2.3 Effective (Secant) Stiffness

Effective stiffness can be calculated from the force-displacement hysteresis, which is obtained from the experiment, this is the displacement dependent parameter. The effective stiffness is calculated through the Equation (1.7).

$$k_{eff} = \frac{|P_{max}| - |P_{min}|}{|D_{max}| - |D_{min}|} \quad (1.7)$$

Where  $P_{max}$  and  $P_{min}$  are maximum and minimum target force in the force-displacement hysteresis,  $D_{max}$ , and  $D_{min}$  are the maximum and minimum displacements in the force-displacement hysteresis, as shown in Figure 1.5.

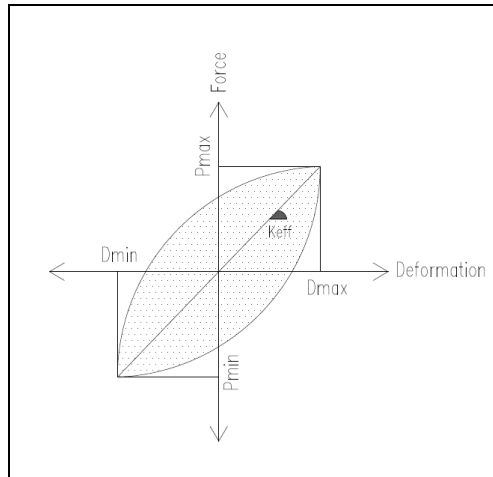


**Figure 1.5 :** Effective stiffness in a cycle.

### 1.3 Literature Review

Numerous experimental and analytical studies have been performed since 1972 until now in order to determine the seismic performance of the passive energy dissipater devices.

Kelly et. al. (1972) performed elementary tests on the flat U shaped strip type steel elements, which is presented in Figure 1.6. The relative motion of steel elements is directed parallel between adjacent surfaces, which might be significant energy absorption source by means of rolling, and bending. This study highlighted the significance of steel bent plates, which might be incorporated in structures for absorption of energy generated by earthquake effects.

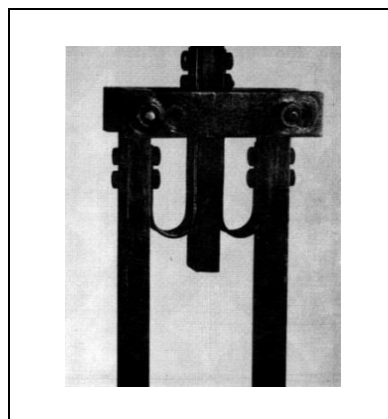


**Figure 1.6 :** U-Shaped strip type steel elements, (Kelly et. al, 1972).

The energy dissipater type steel members in jointed wall system of two or more precast concrete walls, post-tensioned to the foundation using unbonded tendons, and connected along the vertical joints with special energy dissipating shear

connectors were studied in the content of Precast Seismic Structural Systems (PRESSSS) program, by (Priestley et al, 1991). The jointed wall equipped with shear connector in the PREESS study is presented in Figure 1.7.

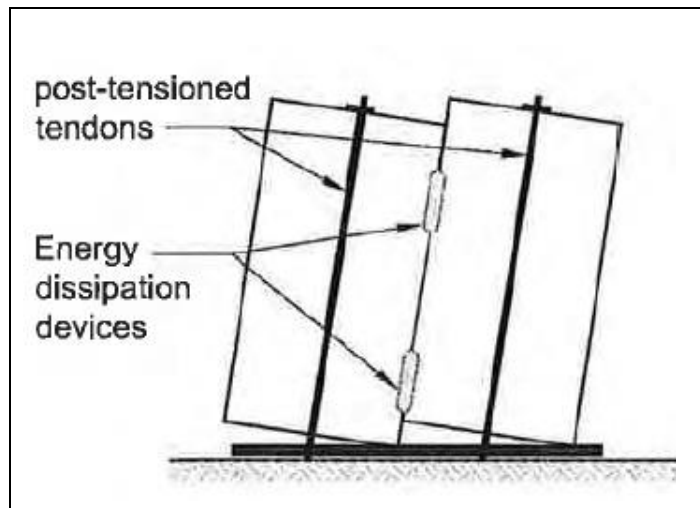


**Figure 1.7 :** Jointed wall equipped with shear connector, (Priestley et al, 1991).

Shultz et al. (1996) conducted a series of experimental studies in order to determine the energy dissipation behavior of shear connectors, and to find out the inelastic flexural deformation capacity of U- shaped plates, which are mobilized through the rolling action. As the connector bends and unbends, the source of resistance and hysteretic energy dissipation is turn out to be improving seismic resistance of precast shear walls by increasing overall system toughness and energy dissipation.

Magana and Shultz (1996) as a part of the PRESSSS program conducted an experimental study on the determination of behavior of various shear connectors under reverse cyclic vertical displacement history. The U-shaped flexural plate was found out by Shultz as the most appropriate shear connector which was utilized in jointed wall system of PRESS test building.

Nakaki and Stanton (1999) used a self-centering concept, in the development of the post-tensioned split rocking wall systems. Energy dissipation can be introduced by grouting reinforcing bars into vertical ducts at the edges of the wall, so that they yield in tension and compression cycles during an earthquake.

Several self-centering systems as part of the co-coordinated PRESSSS research program phases on precast concrete systems were studied. Appropriate level of hysteretic damping was added to the wall system through the connection devices located at the vertical joint between the panels. U-shaped rolling stainless steel plates

were designed for energy dissipation and used to couple the walls. A new low-damage structural system that uses self-centering design, called Pre-WEC that consisted of precast wall with end columns, was proposed by (Henry et.al, 2008). The Pre-WEC system was designed to overcome the deficiencies of previous low-damage wall system by increasing the moment capacity in a cost effective way, so that the Pre-WEC system is comparable to the traditional reinforced concrete construction in addition to providing superior seismic resistance. The Pre-WEC system is displayed in Figure 1.8. The finite element analysis were conducted, leading to design of the oval shaped shear connectors, as the oval shaped connectors represented the most appropriate response. The general view of O-Connector and Pre-WEC test set-up are demonstrated in Figure 1.9. O-connectors performed with stable response with adequate energy dissipation capability and high displacement capacity. In addition, it was found that the O-Connectors produced nearly 17% viscous damping.

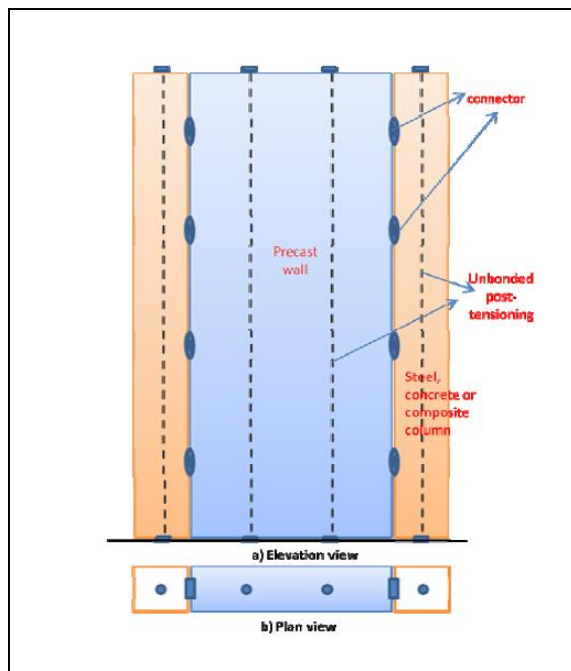


**Figure 1.8 :** Pre-WEC System concept, (Henry et.al, 2008).

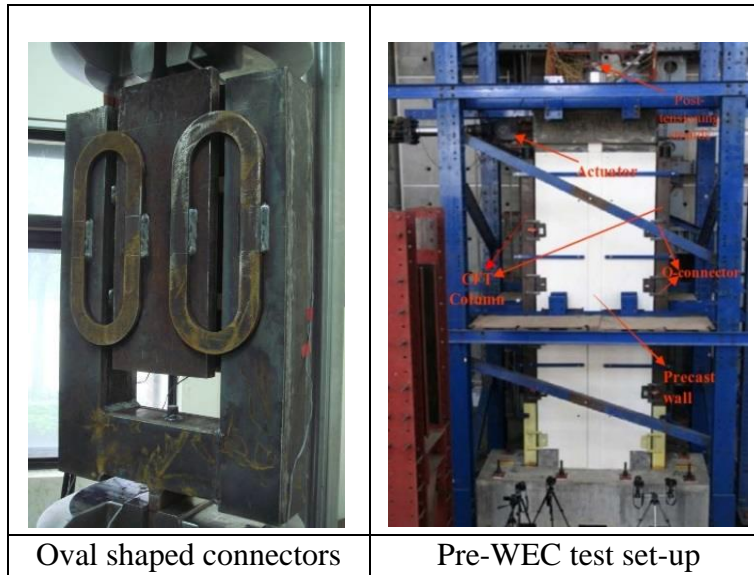


**Figure 1.9 :** Oval-shaped shear connectors and Pre-WEC test set-up, (Henry et.al, 2008).

Chan and Albermani (2007) developed the new Passive Steel Slit Damper (PSSD). This device was fabricated from standard wide flange section with numbers of slit cut from the web, which remains the strips between two flanges. The device is shown in Figure 1.10. Steel slit device dissipated energy through the flexural yielding of strips under the inelastic cyclic deformation. Steel slit damper can be utilized in inverted brace-to-beam connection in framed structures as displayed in Figure 1.11.

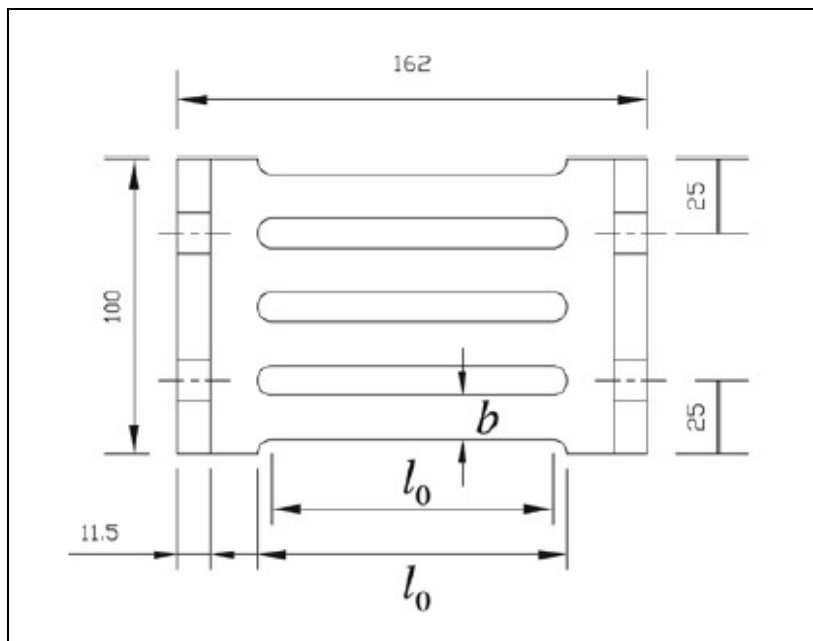


**Figure 1.10 :** Overview of passive steel slit damper, (Chan and Albermani, 2007).

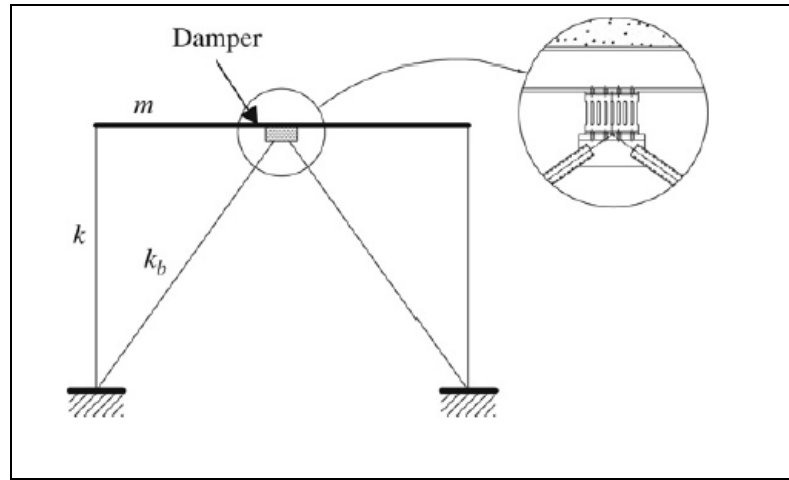


**Figure 1.11** : Application of steel slit damper in framed structures, (Chan and Albermani, 2007).

Eight cyclic and one monotonic test were performed on the PSSD with varied slit length. The test set-up is shown in Figure 1.12.

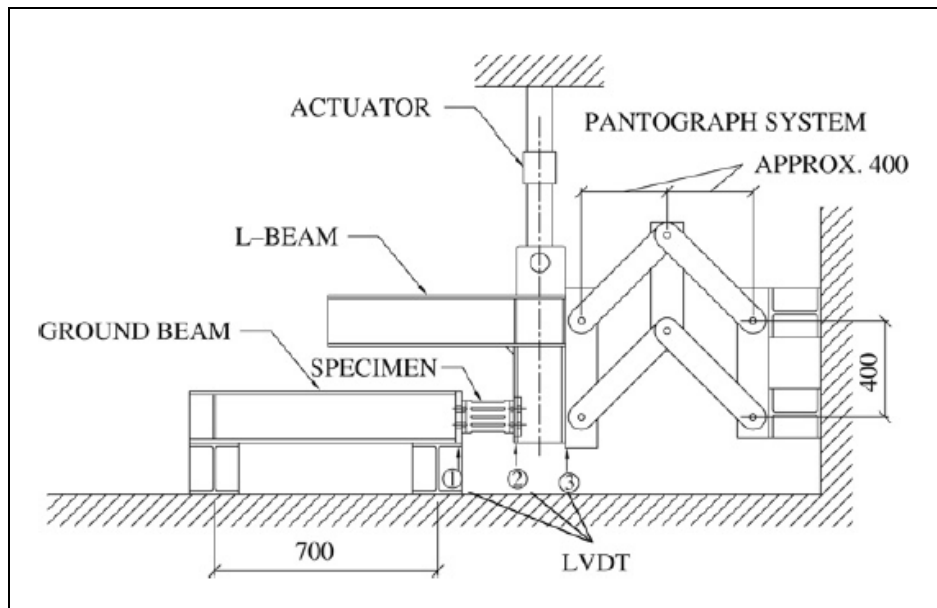


**Figure 1.12** : Overview of test set-up, (Chan and Albermani, 2007).

The tests demonstrated the stable hysteresis and high-energy dissipation capability and high ductility of steel slit device. However, the device with longer and wider slit length represented behavior that is more flexible, whereas the steel device with shorter and narrower slit length had the more stiffness and higher energy dissipation capacity although the failure occurred earlier with respect to former steel device. The failures of steel devices are displayed in Figure 1.13.

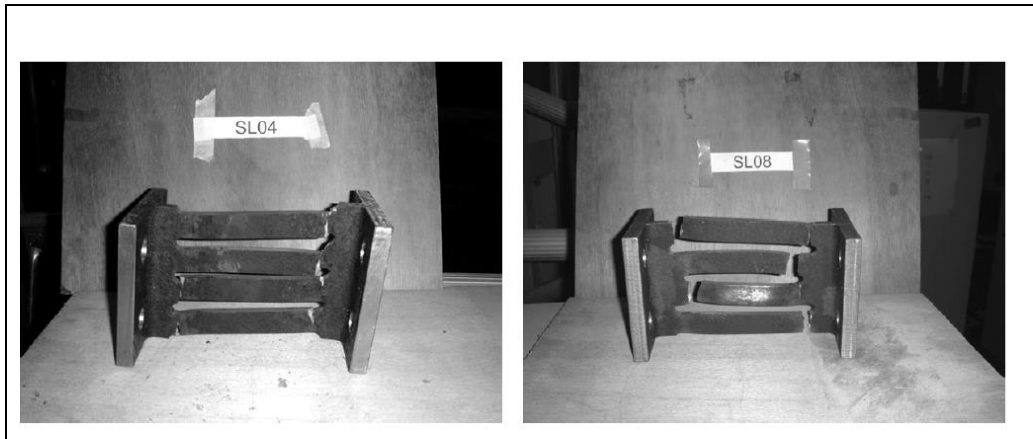


**Figure 1.13 :** Failure of test specimens, (Chan and Albermani, 2007).

Nineteen monotonic and cyclic tests were performed on the half scaled yielding shear panel devices (YSPD) by (Chan et.al, 2009). The yielding steel panel device is presented in Figure 1.14. It is the square hollow section, with steel diaphragm plate welded inside it. These devices can be installed in inverted brace to beam connection or in floor beam to concert panel connection. The size of the squares ( $D$ ) was either 100 or 120 mm and the thicknesses of diaphragm plates ( $t$ ) were 2, 3 or 4 mm.

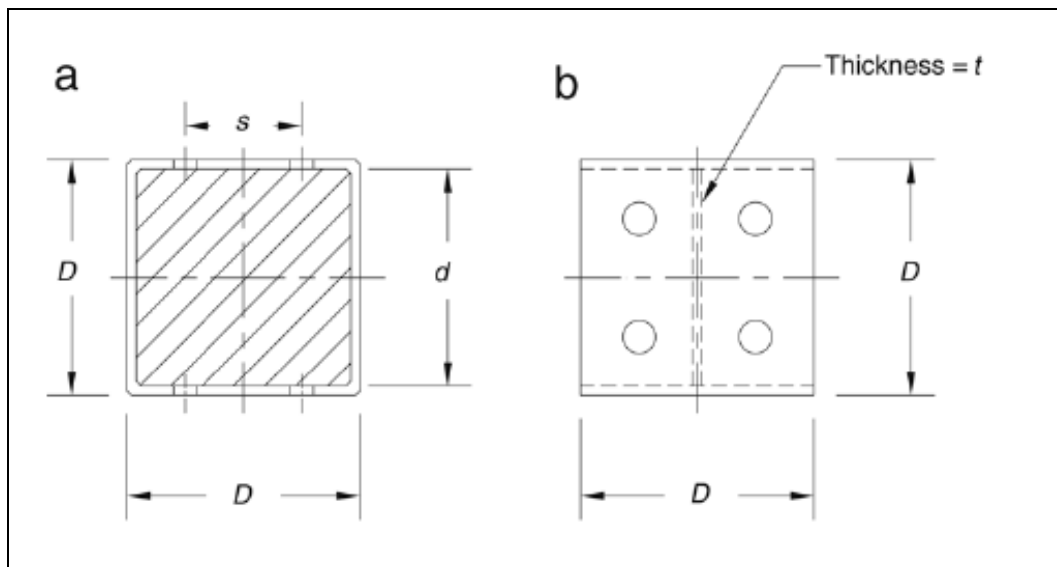


**Figure 1.14 :** Overview of yielding shear panel device, (a) Elevation, (b) Top view, (Chan et.al, 2009).

The yielding shear panel device is dissipated energy by plastic distortion of the diaphragm plate under the large displacement. The main parameters in the tests were the plate slenderness in the range of 24-59 and device configuration. The test set up is shown in Figure 1.15.

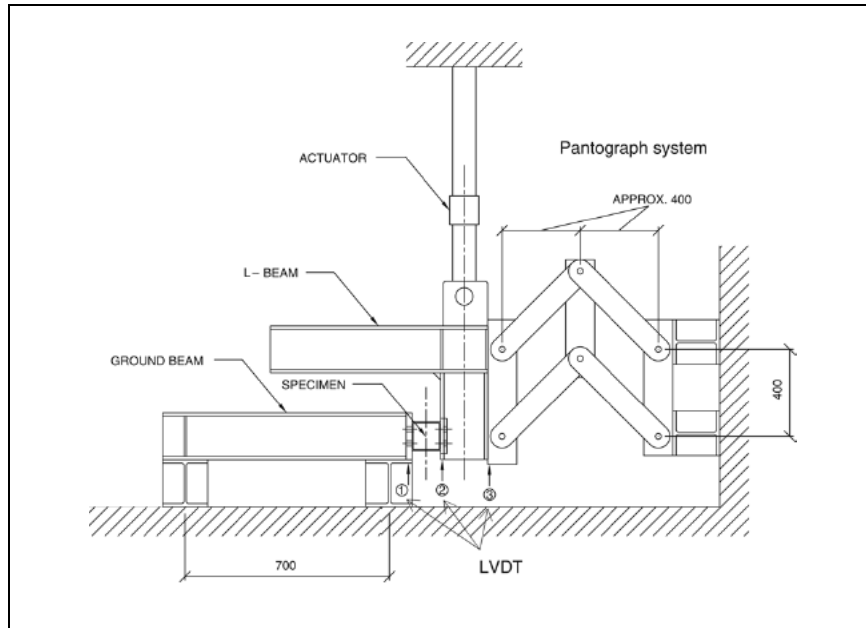


**Figure 1.15 :** Overview of test set-up, (Chan et.al, 2009).

The study showed that the diaphragm plate with high slenderness provide the greater energy dissipation capability, strength and ductility. The stability of the hysteresis can be provided by Stiffening the flange of the square hollow section although it reduce the energy dissipation capacity. The deformed shapes of test specimens are presented in Figure 1.16.

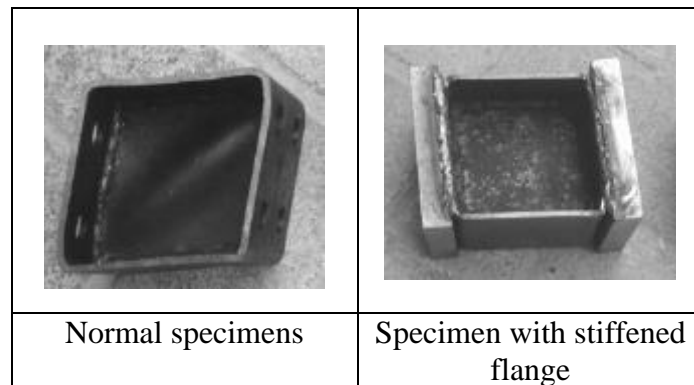


**Figure 1.16 :** Overview of test specimens, (Chan et.al, 2009).

The shape of initial steel slit damper proposed by (Chan and Albermani, 2007), optimized through Bi-directional evolutionary structural optimization method (BESO) by (Ghabraie et.al, 2010) to increase the energy dissipation capacity, stress distribution and resistance against the low cycle fatigue by means of curbing stress concentration. According this method, the insufficient parts of steel damper were removed by contrast the sufficient parts were strengthening by adding the materials. Afterwards analytical studies were performed on the optimized steel slit dampers.

The optimized shape of specimens consisted the diamond shaped slits in the middle of the specimens with different material volume. The analytical study showed the significant increase in the energy dissipation capacity the increase of 56%-96%. In addition, the results were demonstrated that the tapered slit provides the even stress distribution and eliminates the stress concentration with respect to the common steel slit dampers. Three optimized steel slit specimens were tested under cyclic load history to predict the failure and fatigue of the steel slit dampers. The test set-up is similar with the previous research test set-up. According to experimental studies, the optimized steel slit specimens delayed the low cycle fatigue. The optimized steel slit specimen dimension and its deformed shape are displayed in Figure 1.17 and 1.18 respectively.

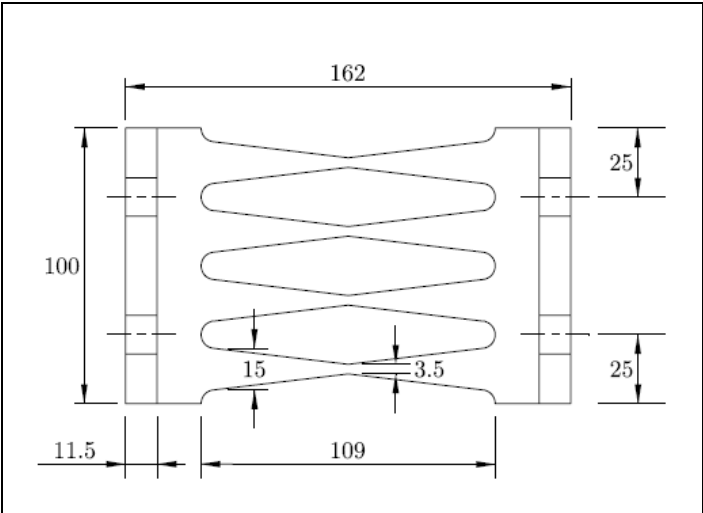


**Figure 1.17 :** General view of the optimized steel slit device, (Ghabraie et.al, 2010).



**Figure 1.18 :** Deformed shape of the optimized steel slit device, (Ghabraie et.al, 2010).

Filled and unfilled steel pipes were tested under the monotonic and cyclic shear loading by (Maleki and Bagheri, 2010). The experimental and analytical studies were performed to investigate the possible application of steel pipes as the metallic yielding damper. The filled steel pipes were filled by concrete and tested under the cyclic and monotonic test while the unfilled steel pipes were tested under cyclic shear test. The general view of test set-up is shown in Figure 1.19. The test parameter was the geometrical properties of the steel pipe.

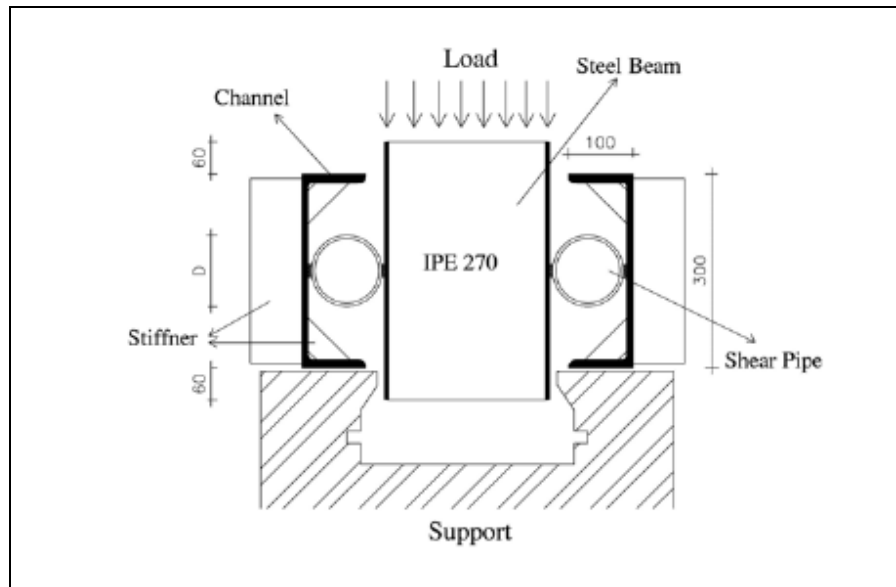


**Figure 1.19 :** Overview of the test set-up, (Maleki and Bagheri, 2010).

The filled steel pipes behaved in brittle way because of concrete crushing although the steel pipes remained undamaged in contrast the bared steel pipes represented the suitable hysteresis behavior and can be the appropriate option as a yielding device damper. The bared steel pipes pose the high viscous damping ratio of 40%. The deformed shape of the filled steel pipes are displayed in Figure 1.20. The analytical studies were conducted and the behavior of the steel pipes were simulated by means of finite element program ANSYS. Bi-linear model was proposed to obtain the effect of the geometrical properties on the hysteresis behavior of the steel pipes. According to the analytical studies the strength and stiffness increase linearly as the length of steel pipe raises. In addition, the strength and the stiffness increase as the steel pipes thickness increases or the diameter of steel pipes declines.



**Figure 1.20 :** Deformed shape of filled steel pipe, (Maleki and Bagheri , 2010).

The quasi-static tests were performed on the conventional coupled RC shear walls (CRB) and RC shear walls connected by hybrid energy dissipative coupling beam whose consist of U-shaped steel plate with high damping rubber (HDB) and their hysteresis behaviors were compared by (Joon Kim et.al, 2012). The coupling beam with hybrid damper is displayed in Figure 1.21.

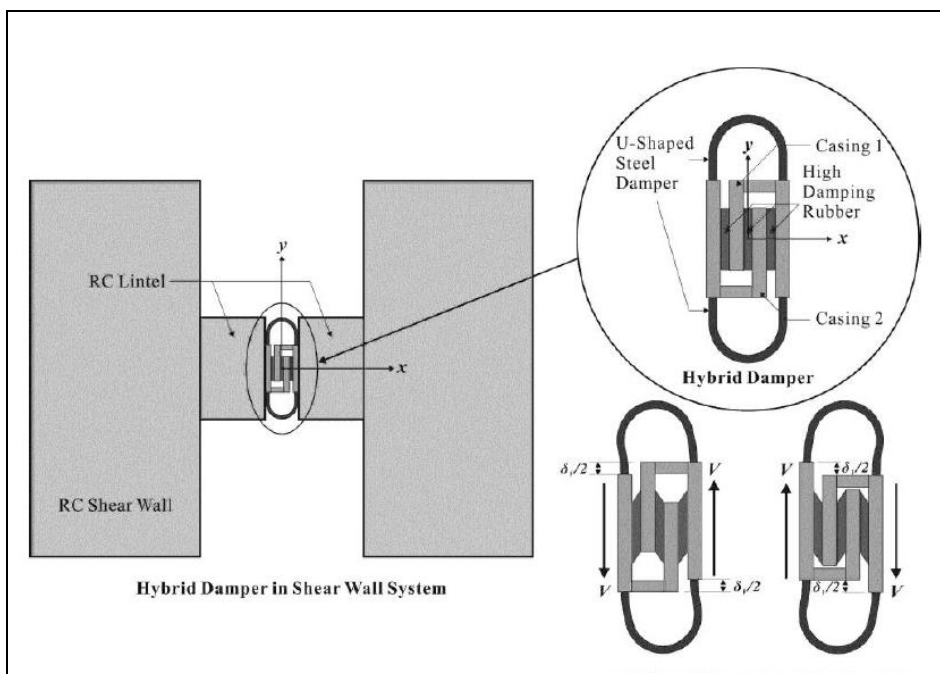


**Figure 1.21 :** Schematic drawing of hybrid damper and deformed shape of hybrid damper, (Joon Kim et.al, 2012).

The test set up and cyclic loading histories are presented in Figure 1.22.

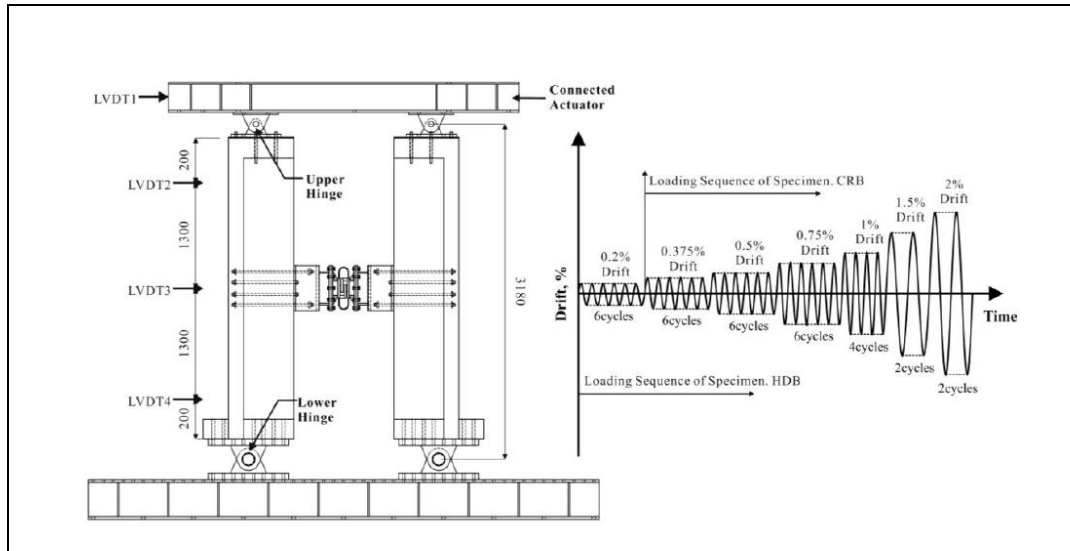


**Figure 1.22 :** Test set-up and loading history, (Joon Kim et.al, 2012).

In the CRB specimens the diagonal cracking occurred in the coupled beam leading to brittle shear failure afterward the strength degradation occurred while in the HDB specimens any major cracking were not observed in structural element, except the hybrid damping device. The cracking pattern in the CRB and HDB specimens are displayed in Figure 1.23. The HDB specimens behaved in a ductile manner. Any strength degradation was not observed in the force- drift angle of the HDB specimens. The HDB specimens pose higher energy dissipative capability and equivalent viscous damping in comparison with the CRB specimens. The deformed shape of the hybrid energy dissipative damper is shown in Figure 1.24.

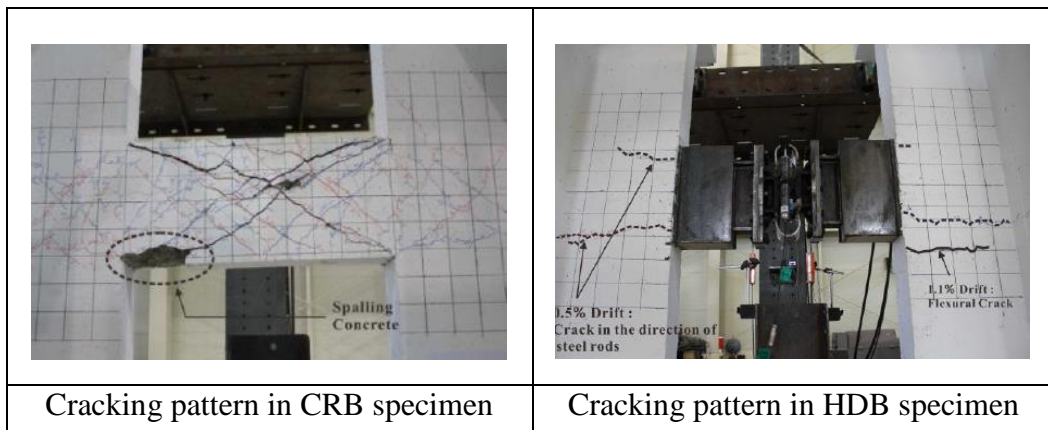


**Figure 1.23 :** Cracking pattern in CRB and HDB specimens, (Joon Kim et.al, 2012).

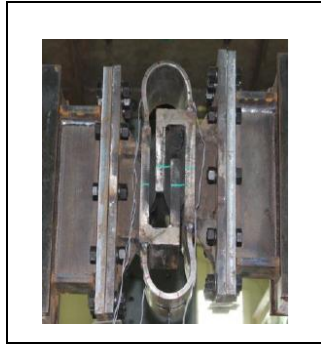


**Figure 1.24 :** Deformed shape of hybrid damper, (Joon Kim et.al, 2012).

Maleki and Mahjoubi (2013) conducted the experimental and analytical studies on the passive energy dissipative device called the dual-pipe damper (DPD). DPD device comprises of the two welded pipes. The DPD device is displayed in Figure 1.25.

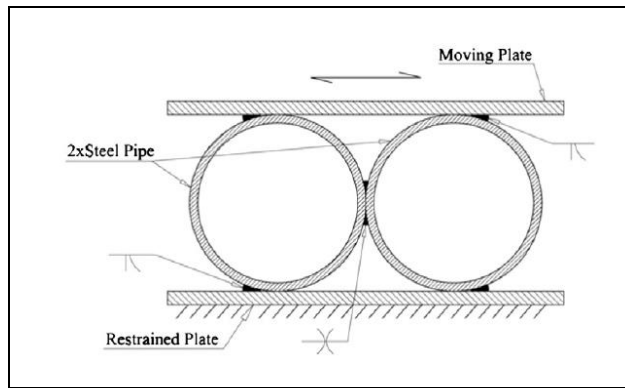


**Figure 1.25 :** Dual-pipe damper, (Maleki and Mahjoubi, 2013).

The dual-pipe dampers dissipate energy by flexural deformation of the pipes. The cyclic quasi-static test were conducted on the four specimens, the test set-up is displayed in Figure 1.26.

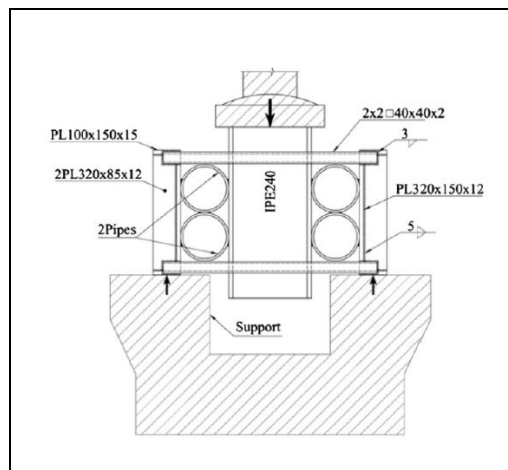


**Figure 1.26 :** Test set-up, (Maleki and Mahjoubi, 2013).

The experimental results showed that the strength, stiffness and energy dissipation values in DPD device are higher than the corresponding values obtained for two individual steel pipes. In addition, the DPD device poses the high displacement capacity up to the 36% its height. The length of the damper does not affect the hysteresis behavior considerably. The deformed shape of the dual-pipe damper is displayed in Figure 1.27.



**Figure 1.27 :** Deformed shape of the dual-pipe damper, (Maleki and Mahjoubi, 2013).

The analytical studies were performed to examine the varying geometrical properties influence on the hysteresis behavior of the dual-pipe damper. According to analytical studies, the energy hysteresis capability merely depends on the pipe length and pipe thickness, in the constant diameter with increase of the pipe thickness the energy dissipative capacity increases. The deformation capacity decreases with decreasing  $D/t$  ratio. The ductility decreases with increasing  $D/t$  ratio. The elastic stiffness only depends on the pipe length and the  $D/t$  ratio, in the constant length as the  $D/t$  ratio increases the stiffness declines.

The quasi-static and uni-directional tests were performed on the full-scaled single bay single story precast concrete frame with and without precast cladding panel by (Baird et.al, 2013) in which, the innovative U-shape energy dissipative device was utilized in panel to beam connection and the hysteresis behavior of the bare and equipped frame structure was compared. The U-shaped energy dissipative device dissipates wind or earthquake input energy by its inelastic flexural deformation. The U-shaped energy dissipative device is shown in Figure 1.28.

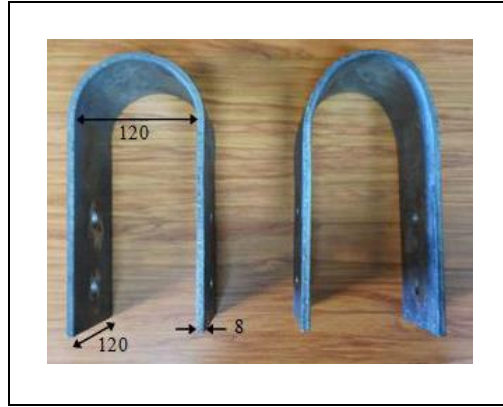


**Figure 1.28** : U-shaped energy dissipative device, (Baird et.al, 2013).

The cladding panel has the thickness of 120 mm, 3.0 m long and 2.0 m wide. The cladding panel is connected to the top beam by U-shaped energy dissipative device whereas; it is connected to the base level beam by means of fixed bearing connection as displayed in Figure 1.29. The experimental study showed that the strength and energy dissipation capability increase without any damages on the structural elements and strength degradation.

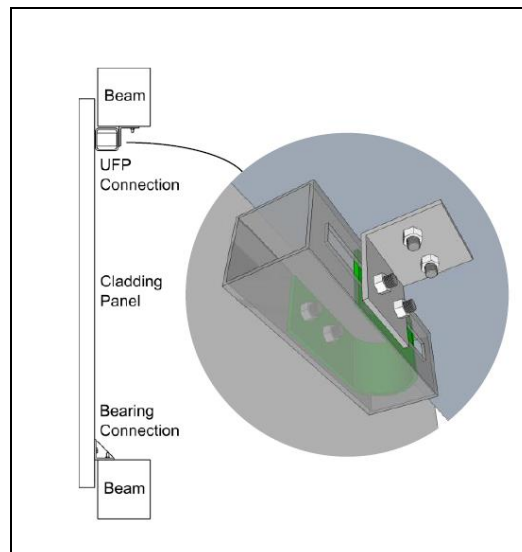


**Figure 1.29** : Schematic drawing of the test set-up, (Baird et.al, 2013).

## 2. UNIAXIAL TESTS

The steel cushions are developed to be utilized in the industrial buildings in panel to support, panel to panel and panel to beam connections. Since the steel cushions positioned on several locations through the cladding edges, this causes changes in the behavior during the excitation and thus it was an obligation to perform several tests with different load combinations, such as cyclic shear and axial tests. In particular in panel to support connections, the steel cushions are subjected to axial stress under self-weight of panel and in the panel-to-panel connection; the steel cushion is subjected to shear effect under the lateral loading.

### 2.1 Introduction

In this chapter the uniaxial behavior of the steel cushions with three distinct thicknesses of 3, 5 and 8mm are investigated. This chapter is divided into two sections. In the first section, the cyclic and monotonic shear tests are discussed and in the second section, cyclic and monotonic axial tests are discussed. The experimental works are summarized in Table 2.1.

**Table 2.1** : Summary of uniaxial tests performed on the steel cushions.

Test Type	t= 3mm	t= 5mm	t= 8mm
Cyclic Shear	4	4	4
Cyclic Axial	1	1	1
Monotonic Shear	1	1	1
Monotonic Axial Compression	1	1	1
Monotonic Axial Tension	1	1	1
Total Experimental works	9	9	9

**2.2 Coupon Test of Specimens**

A total numbers of twelve tests were conducted on three distinct specimens. Four tests per specific thicknesses of 3mm, 5mm and 8mm, were performed. The coupon tests for 5mm and 8mm thick specimens are illustrated in Figure 2.1 and 2.2. The average ultimate strengths were 410 MPa, 390 MPa and 450 MPa with ultimate strains levels of 28%, 40% and 40% for 3mm, 5mm and 8mm coupon specimens respectively. The stress-strain relation obtained from coupon tests are illustrated in Figure 2.3 and 2.4.

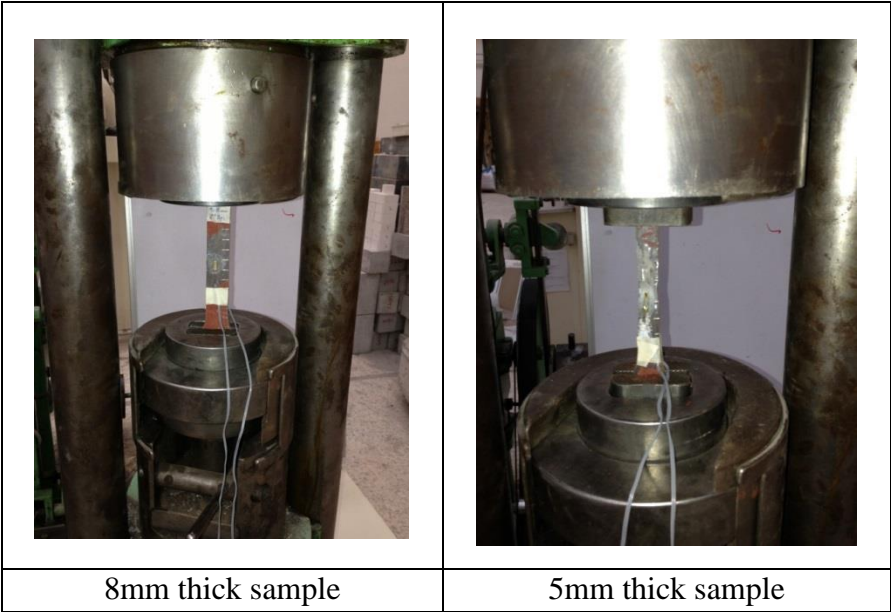


**Figure 2.1 :** Coupon test of 5mm and 8mm thick specimens.

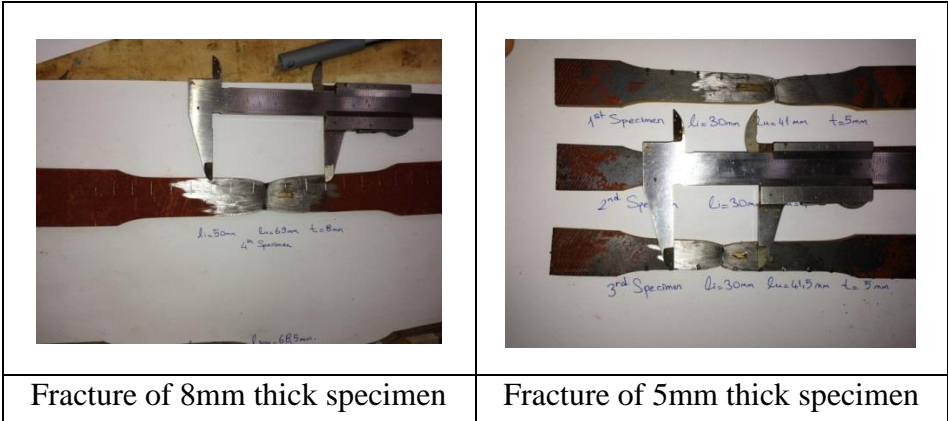


**Figure 2.2 :** Fractures of two distinct specimens.

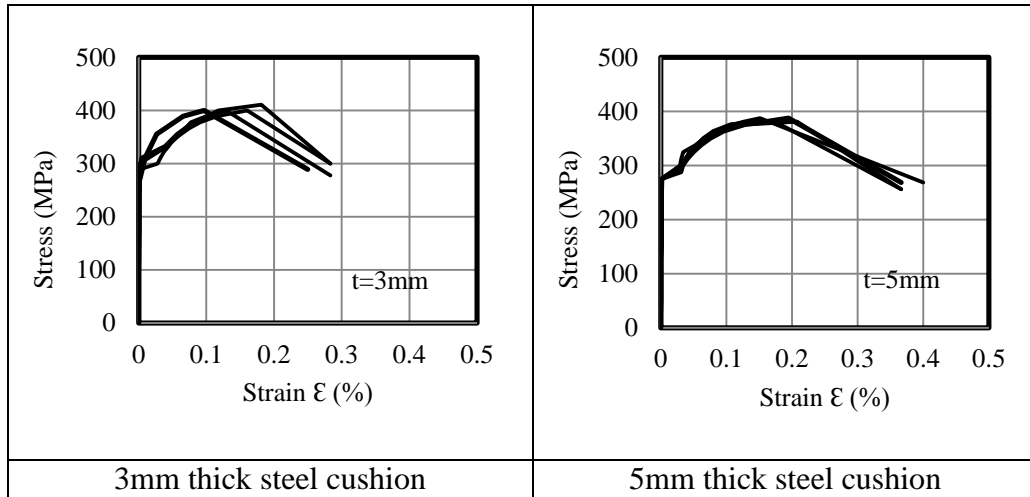


**Figure 2.3 :** Stress-Strain relation obtained from coupon test.

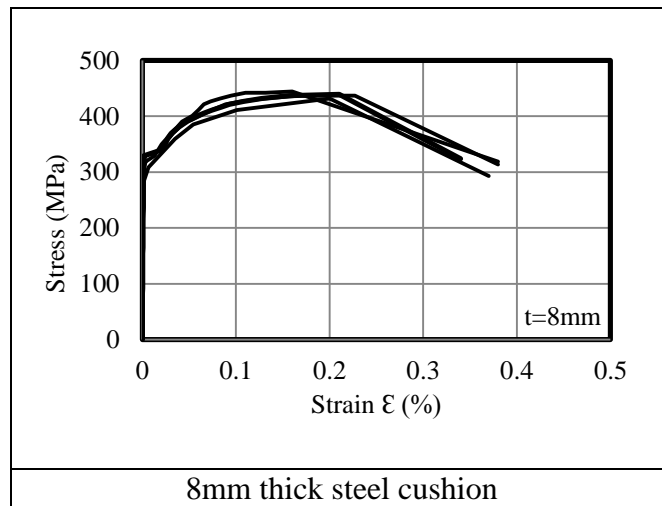


**Figure 2.4 :** Stress-Strain relation obtained from coupon test.

### 2.3 Uniaxial Shear Test

A total number of 15 uniaxial shear tests performed on specimens of 3, 5 and 8mm, to evaluate hysteresis behavior and energy dissipation capacity of steel cushions. In addition, because of sliding of two adjacent panels and panel with respect to beam this test is necessary. The number of four cyclic tests and one monotonic test were performed per specimen with specific thicknesses, to reduce probable errors and acquire precise results. The testing set-up consists of two cantilever sides, right and left hand sides; right hand cantilever acts as a fixed support whereas the left hand one has the role of connection Figure 2.5. The right hand side is fixed to the short column, while the left hand one is able to move in vertical direction. Thus, the vertical actuator connects to this part and displacement protocol applied in this segment vertically somehow; the specimen has shearing movement Figure 2.6. A

second thick-sectioned profile was welded to right hand part to restrict the lateral displacement and strengthen the testing set-up. Also to avoid the rotation of the actuator the outer restrainer was utilized as it is shown at Figure 2.7 the specimens connected to each side through bolting, the diameter of hole on each cushion is 20mm for 3 and 5 mm thick specimens, 29mm for 8mm thick specimens respectively. The main parameter of test was specimen thickness. During the shear tests the several measurements were taken from different location of the specimen. Six strain gages were placed per specimen. A string transducer measured the vertical displacement of actuator. One transducer per side measured the lateral displacement of left and right hand side of testing set-up, in addition one transducer was utilized to measure vertical displacement of base plate. The locations of transducers are displayed at Figure 2.7.

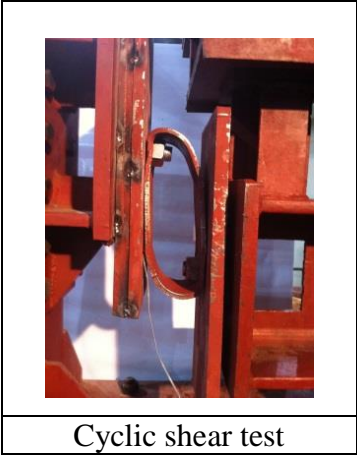


**Figure 2.5:** Final displacement target of shear test.



**Figure 2.6 :** General view of test set-up.

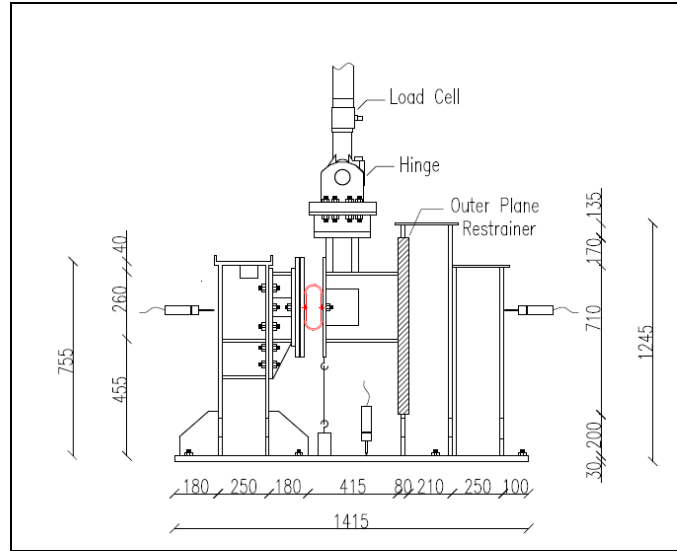


**Figure 2.7 :** Technical drawing of test set-up.

### 2.3.1 Shear test-loading protocol

The testing protocols selected in accordance with the recommendations placed in FEMA 461, this actually based on the expected maximum drift ratios. The dimensions of the steel cushions are 100 mm in width and 250 mm in depth. In considering the expected deformability of the cushion, the target displacements derived by multiplying the “ $a_i/a_{10}$ ” ratios with the specimen length of 250 mm in its lateral axis. As it was impossible to apply the 250 mm displacement on the tests’ specimens for the sake of bolt contact with the specimen’s vertices, 220 mm was considered as a target displacement in instead of 250 mm. The ratios to determine target displacement amplitudes defined in Table 2.2. Ten diverse amplitude levels exist in the table. Two full cycles applied for each displacement target. The displacement targets values are shown in Table 2.3. The complete loading protocol presented in Figure 2.8.

**Table 2.2 :** Ratio of displacements amplitudes, (FEMA 461, 2007).

step	1	2	3	4	5	6	7	8	9	10
$a_i/a_{10}$	0.048	0.068	0.095	0.133	0.186	0.260	0.364	0.510	0.714	1.000

**Table 2.3 :** Displacement targets of uniaxial shear test.

step	1	2	3	4	5	6	7	8	9	10
Displacement Target (mm)	10.56	14.96	20.90	29.26	40.92	57.20	80.08	112.20	157.08	220.00

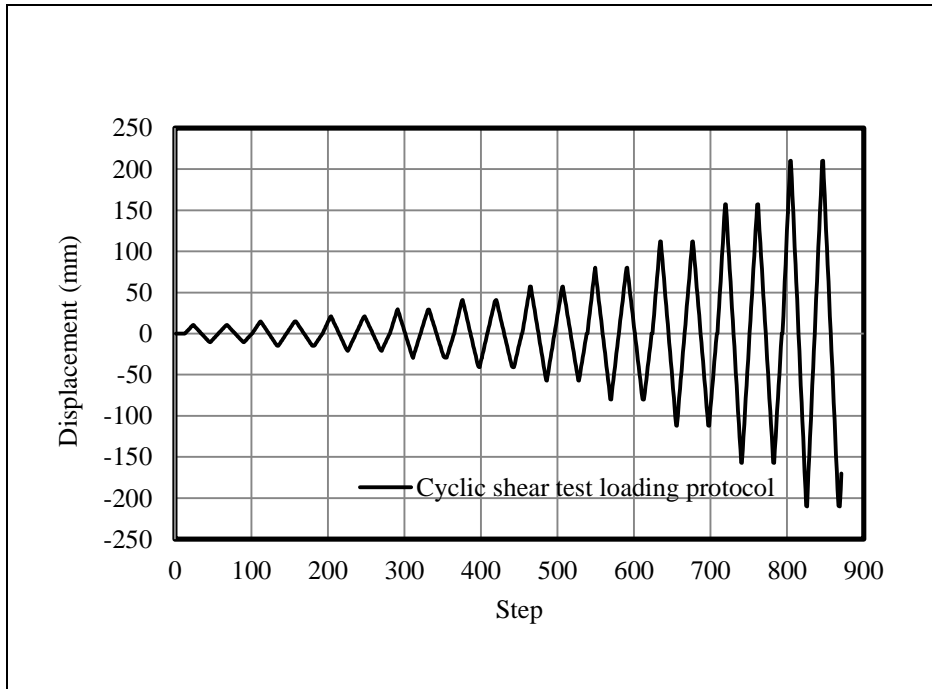


**Figure 2.8 :** Drift based cyclic loading protocol applied to steel cushions at cyclic shear test.

In the monotonic tests the same target displacements were applied Figure 2.9.

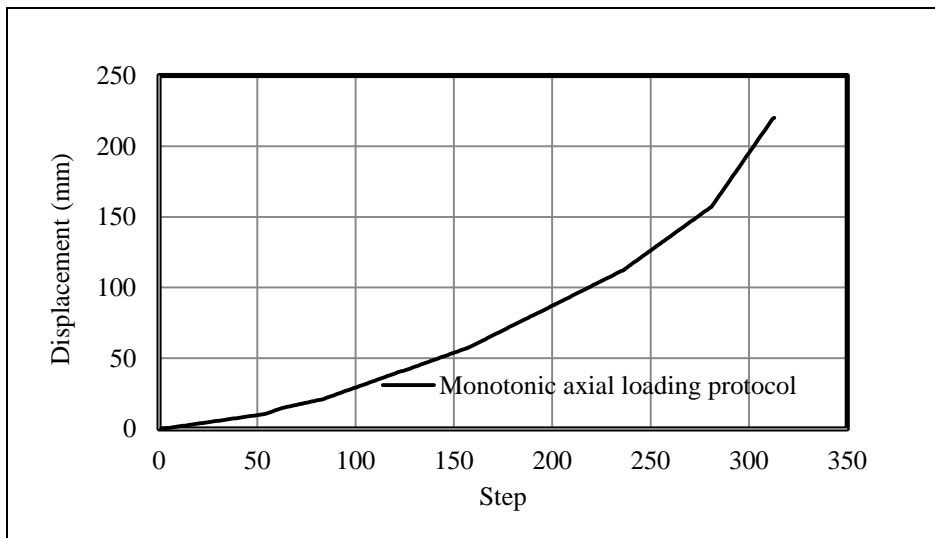


**Figure 2.9 :** Drift based monotonic loading protocol applied to cushions at monotonic shear test.

### 2.3.2 Experimental results of cyclic and monotonic shear tests

The experimental results were obtained from the recorded data by loading hydraulic jack and measurements tool such as transducers and strain gages which all of data were transferred in EXCEL version 2010 and MATLAB version 7.0 programs to form pertinent graphs.

### 2.3.2.1 Force-Displacement relation

Force versus displacement cycles and the relevant deformed shape of the specimens having thickness of 3mm, 5mm and 8mm obtained from cyclic shear tests are illustrated in Figure 2.10, 2.11 and 2.12 respectively.

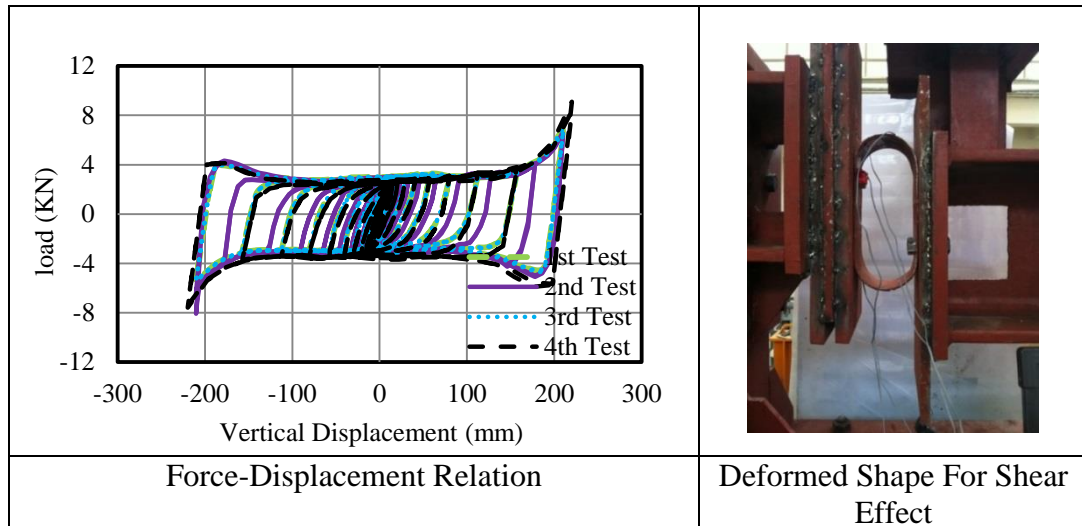


**Figure 2.10 :** Force-Displacement relation for 3mm thick specimen derived from cyclic shear test.

3mm thick specimens behaved symmetrically under cyclic shear effect. The nominal strengths for 3mm thick steel cushions are 3KN this parameter would be utilized in definition of link element in the mathematical model. No damages observed during the test in 3mm thick steel cushions. It should be mentioned that the values of drift angle and vertical displacement of specimens are equal, since the depth of specimens are 100mm.

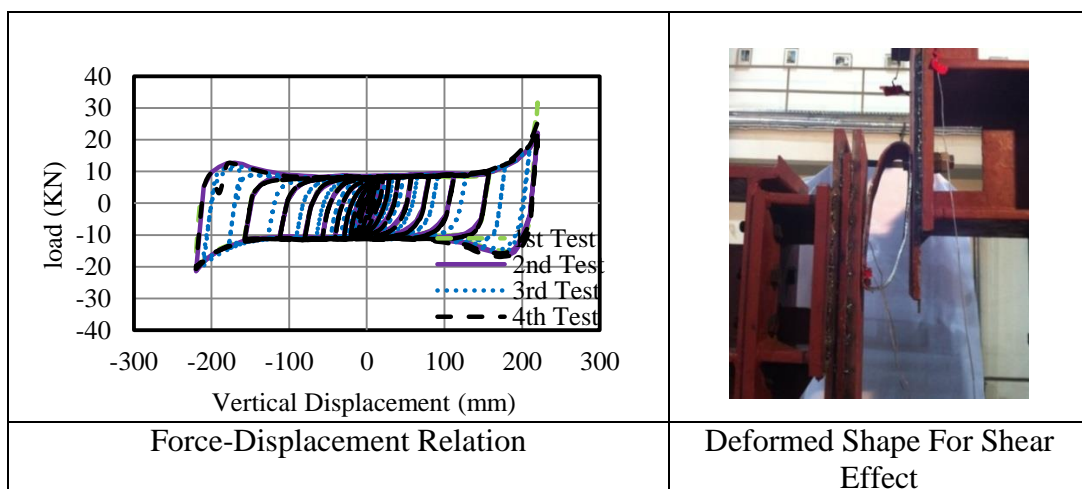


**Figure 2.11 :** Force-Displacement relation for 5mm thick specimen derived from cyclic shear test.

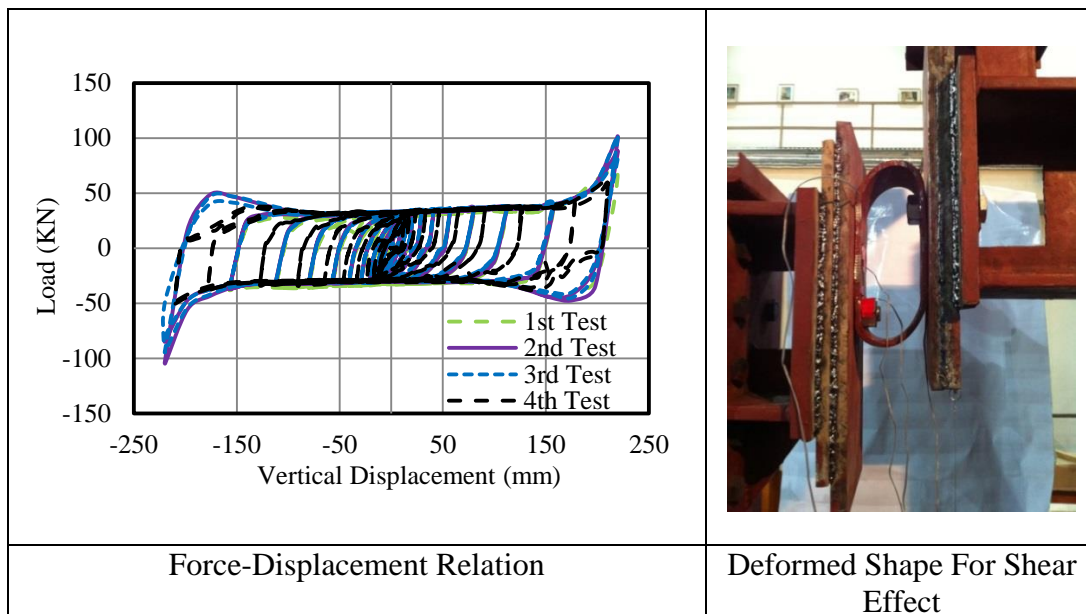


**Figure 2.12 :** Force-Displacement relation for 8mm thick specimen derived from cyclic shear test.

The specimens having 5mm and 8mm thickness had nominal strength of 10 KN and 35 KN respectively. Which directly indicate that with increasing of specimen thickness, the nominal strength of specimen rises. The specimens behaved symmetrically under shear effect. Moreover cracking observed at displacement target of 157mm, leading to rupture at the final displacement target of 220 mm at specimens having 5mm and 8mm thickness. As it is shown in Figure, 2.13. It should be mentioned that, damages were occurred on the welding location where two side of specimen linked to each other.

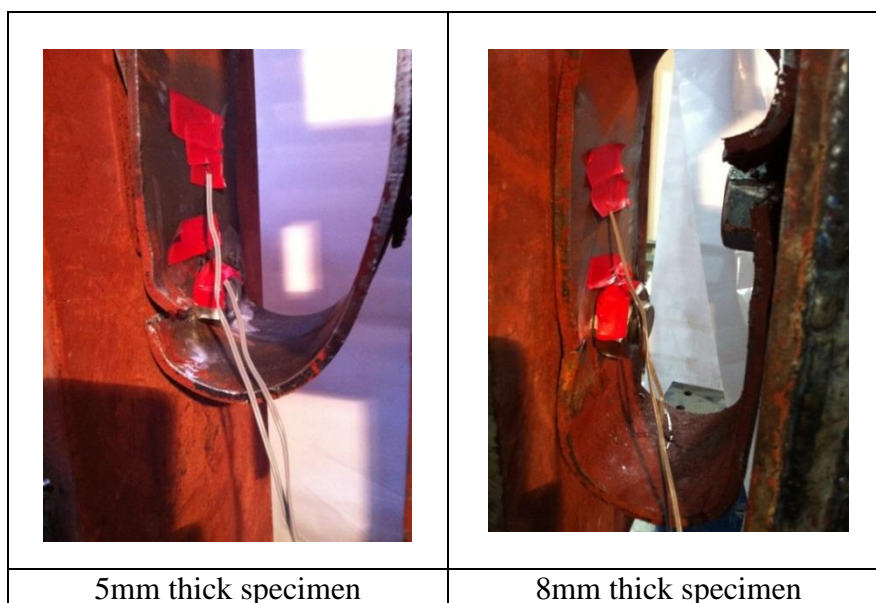


**Figure 2.13 :** Damages occurred on the welding location at 5mm and 8mm thick specimens in the cyclic shear test.

The sudden sharp increase of the force in the Force-Displacement curve is due to contact of bolt with the vertices of specimen as it is shown in Figure 2.14.

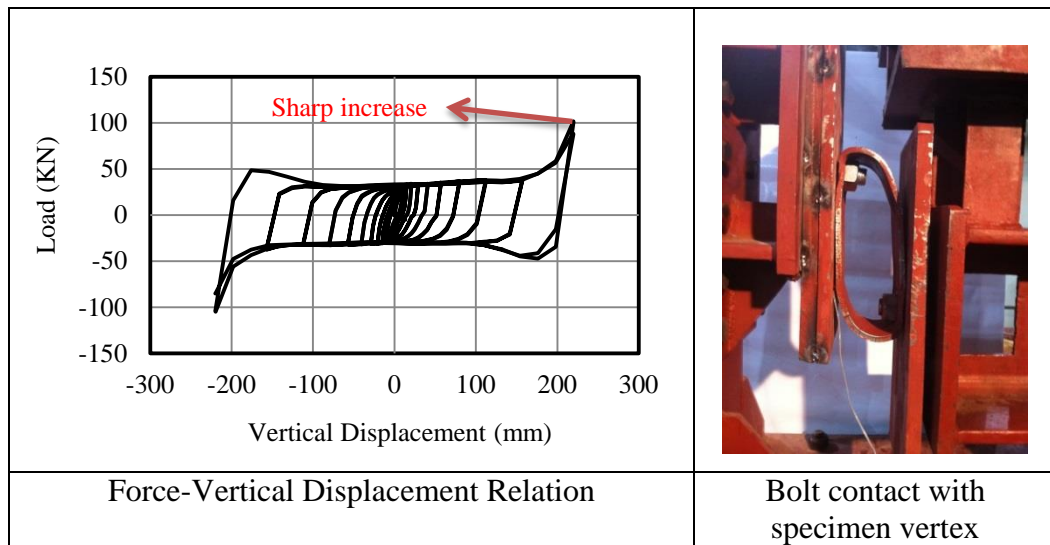


**Figure 2.14 :** Sharp increase of force value in force-vertical displacement relation derived from cyclic shear test.

The force displacement relation obtained from monotonic test for 3mm, 5mm and 8mm thick specimens are presented in Figure 2.15, 2.16 and 2.17 respectively. According to Figure 2.15, the nominal shear yield strength of 3mm thick specimen is 4.11 KN and the yield displacement is 17.66 mm, the value of ultimate strength is 8.25 KN.

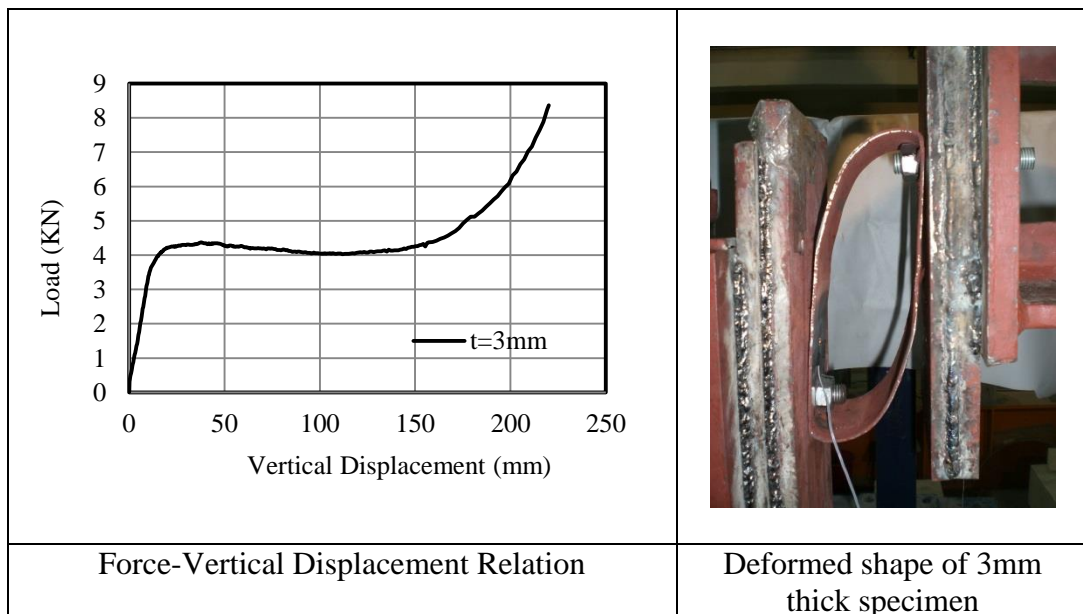


**Figure 2.15 :** Force-Displacement relation for 3mm thick specimen derived from monotonic shear test.

According to Figure 2.16, the nominal shear strength of 5mm thick specimen is 10.42 KN and the yield displacement is 12.75 mm, the value of ultimate strength is 24.18 KN.

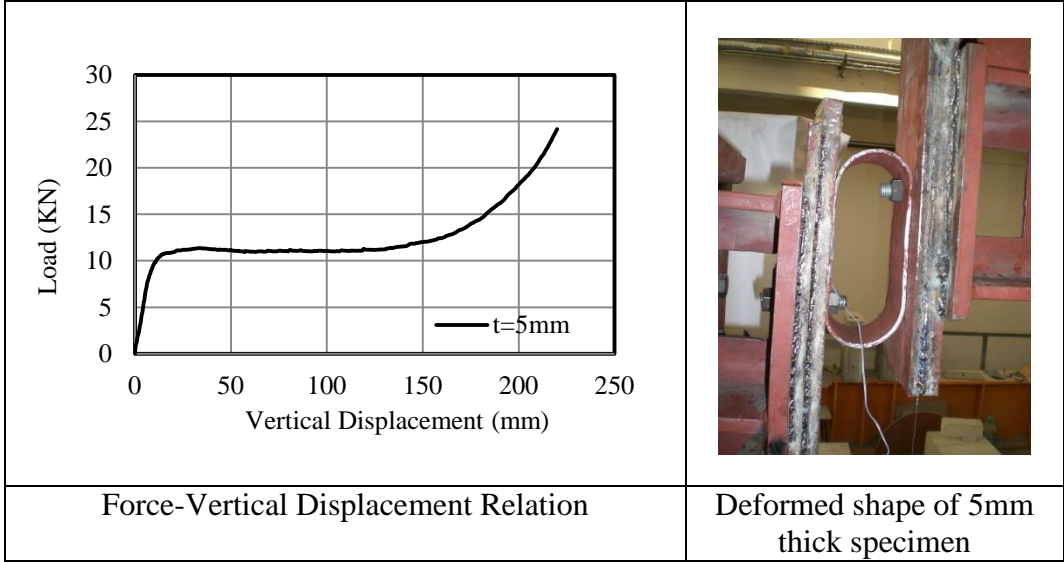


**Figure 2.16 :** Force-Displacement relation for 5mm thick specimen derived from monotonic shear test.

According to Figure 2.17, the nominal shear yield strength of 8mm thick specimen is 28.46 KN and the yield displacement is 12.59 mm, the value of ultimate strength is 138.09 KN. It should be noted the sharp increase at the ultimate strength is because of bolt contact with specimen vertex.

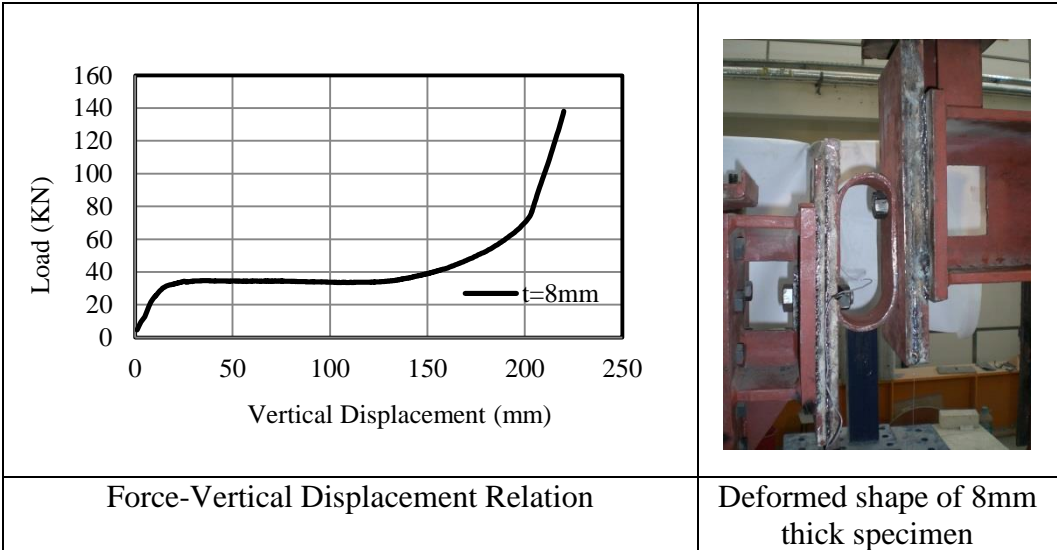


**Figure 2.17 :** Force-Displacement relation for 8mm thick specimen derived from monotonic shear test.

### 2.3.2.2 Cyclic and monotonic shear tests envelop

The cyclic shear test's envelopes are compared with monotonic shear test results for each distinct specimen, as expected each monotonic shear test results comprise cyclic shear test force-displacement envelope, as shown in Figure 2.18, 2.19 and Figure 2.20 for 3mm, 5mm and 8mm thick specimen respectively.

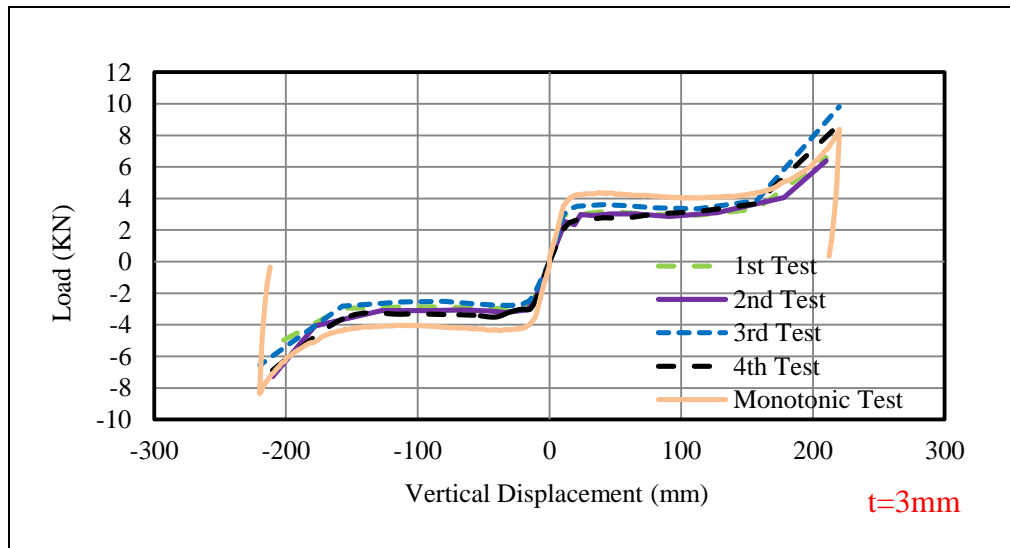


**Figure 2.18 :** Envelop of cyclic shear test in comparison with monotonic shear test for 3mm thick specimens.

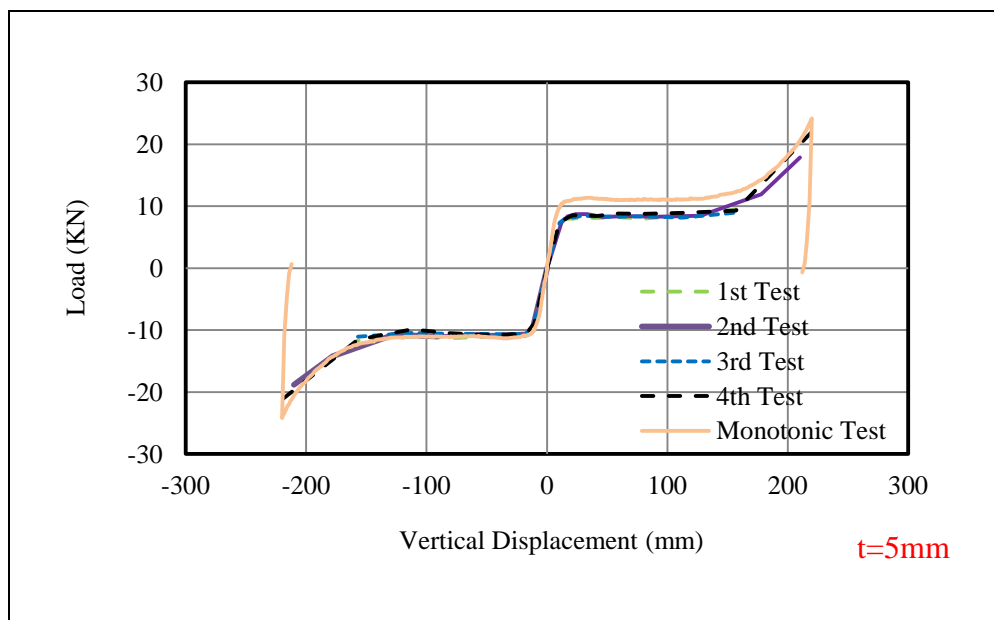


**Figure 2.19 :** Envelop of cyclic shear test in comparison with monotonic shear test for 5mm thick specimens.

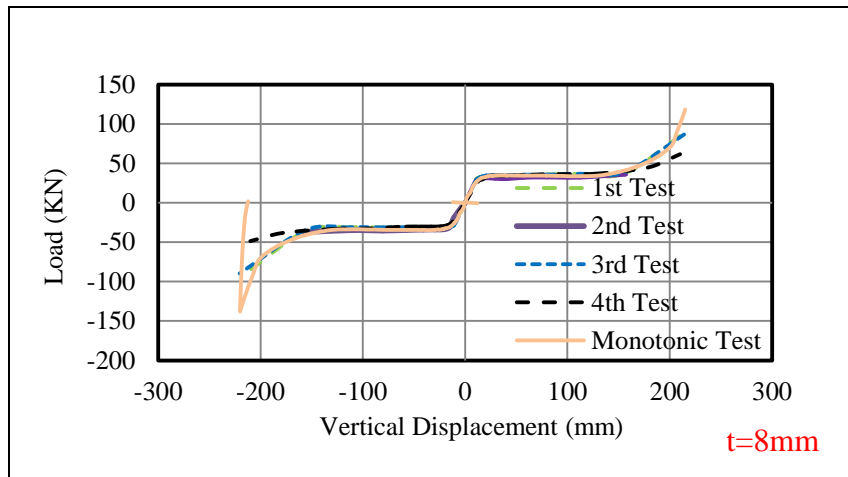


**Figure 2.20** : Envelop of cyclic shear test in comparison with monotonic shear test for 8mm thick specimens.

### 2.3.2.3 Energy dissipation

Steel specimens have high-energy dissipation capability under the seismic or wind actions, through the formation of hysteresis in Force-Displacement curve. The dissipative energy for each loop is equal to area of pertinent loop. With the aid of Matlab v 7 program (Dindar, 2009) dissipated energy was calculated per loop by separation of hysteresis and calculation of the corresponding loop's area, afterwards each loop's dissipative energy amount added together which leads to cumulative energy, in other word, this cumulative energy is the energy dissipation capacity of steel cushions. Arbitrarily as the depth of the specimens is 100mm, therefore there is no difference between displacement and drift angle.

The dissipated energy of one loop and cumulative dissipated energy for 3mm thick steel specimen, which is the Matlab program output, are illustrated in Figure 2.21 and 2.22.

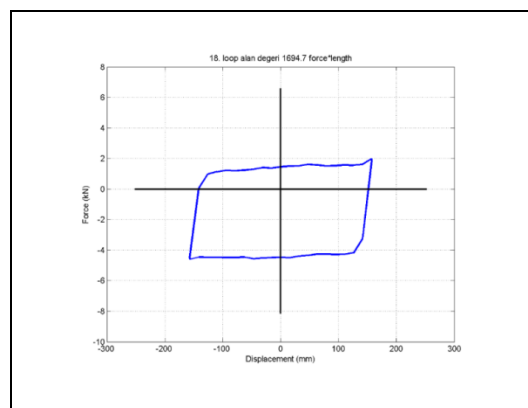


**Figure 2.21** : Envelop of cyclic shear test in comparison with monotonic shear test for 8mm thick specimens.

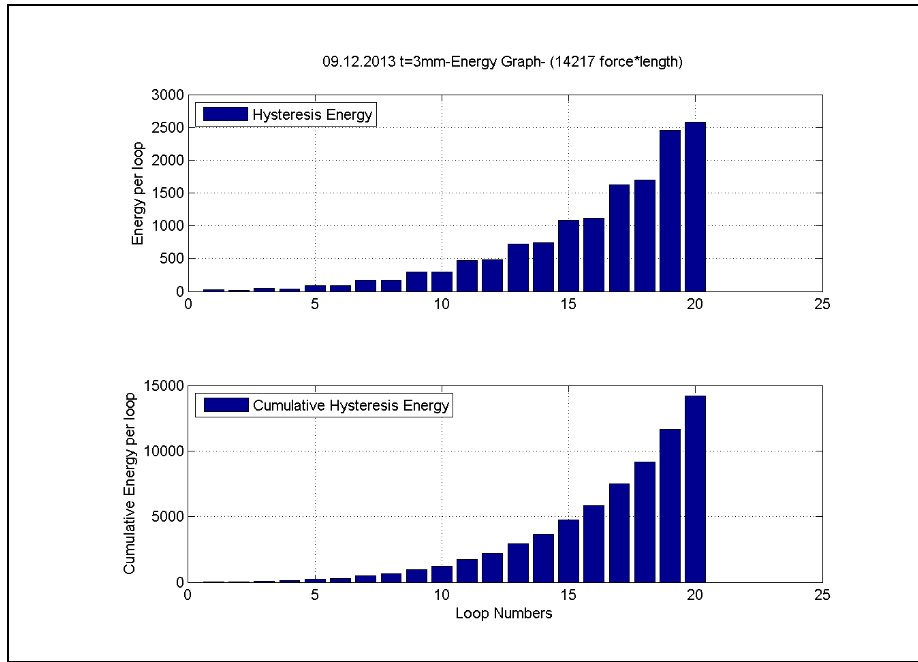


**Figure 2.22 :** Energy per loop and cumulative dissipated energy value for 3mm thick steel specimen under shear effect.

The cumulative energy versus displacement graphs for 3mm, and 5mm thick steel cushions are illustrated in Figure 2.23, and Figure 2.24. The average cumulative energy value is 149034 KN.mm and 42959 KN.mm for  $t=3\text{mm}$  and 8mm thick specimens respectively.

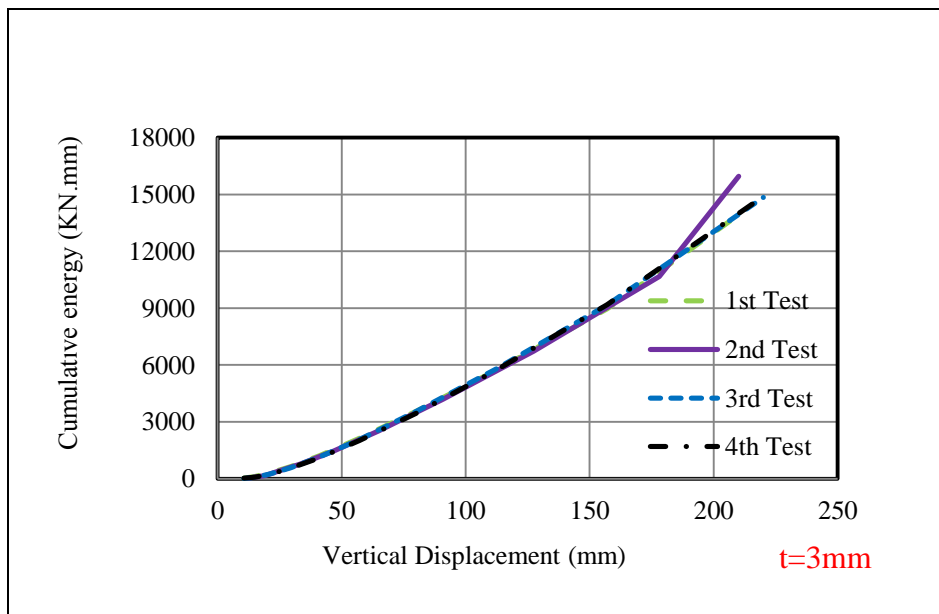


**Figure 2.23 :** Cumulative energy-vertical displacement relation for 3mm thick specimens derived from cyclic shear test.

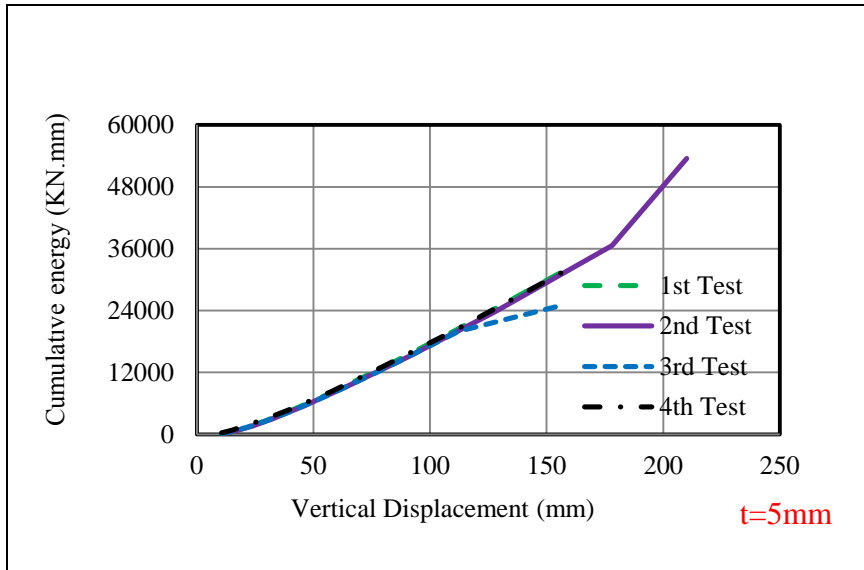


**Figure 2.24 :** Cumulative energy-verticle displacement relation for 5mm thick specimens derived from cyclic shear test.

The cumulative energy versus displacement graphs for 8mm thick steel cushions is illustrated in Figure 2.25. The average cumulative energy value is 113215 KN.mm for  $t=8\text{mm}$  thick specimens.

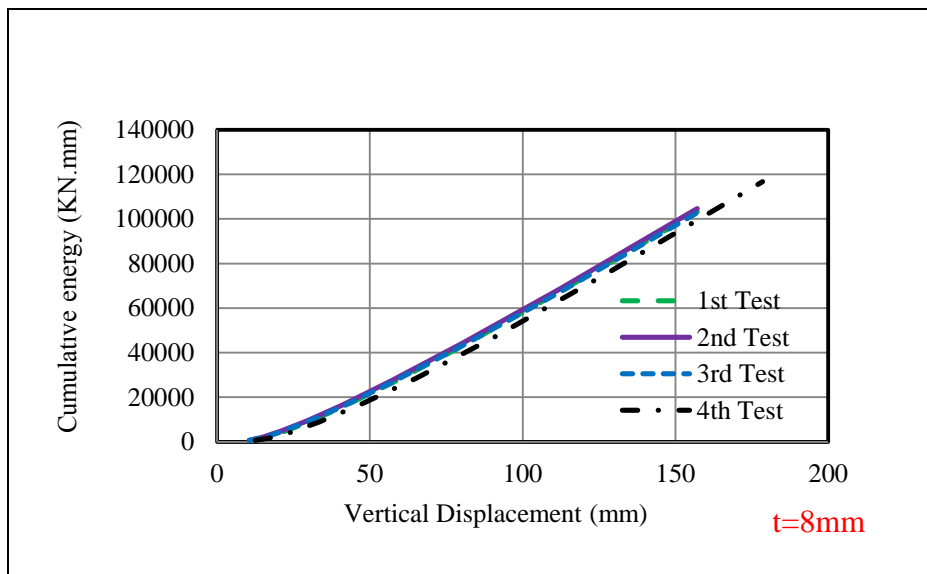


**Figure 2.25 :** Cumulative energy-verticle displacement relation for 8mm thick specimens derived from cyclic shear test.

As it is apparent from the cumulative dissipated energy curve for the varied thicknesses the amount of dissipated energy increase significantly, with rising of the thicknesses, in fact these energy dissipation value represents the amount of energy absorption of each specimen subjected to excitation. The comparisons of the dissipated energy value for three specific thicknesses are illustrated in Figure 2.26.

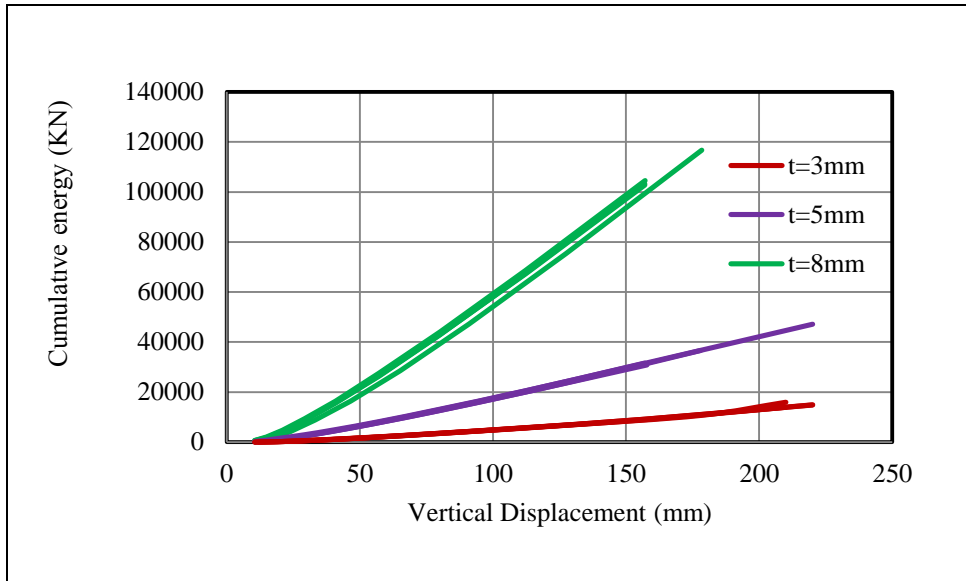


**Figure 2.26 :** Comparison of cumulative energy-vertical displacement for three distinct specimens under shear effect.

### 2.3.2.4 Equivalent viscous damping

Equivalent viscous damping is calculated per specimen as well. The calculations are based on the equivalent damping ratio relation (Chopra, 1995) the pertinent explanation exists in the first chapter. The equivalent damping ratio versus displacement curve for  $t=3\text{mm}$  specimen is illustrated in Figure 2.27. The average damping ratio 50.25% for  $t=3\text{mm}$  thick specimens.

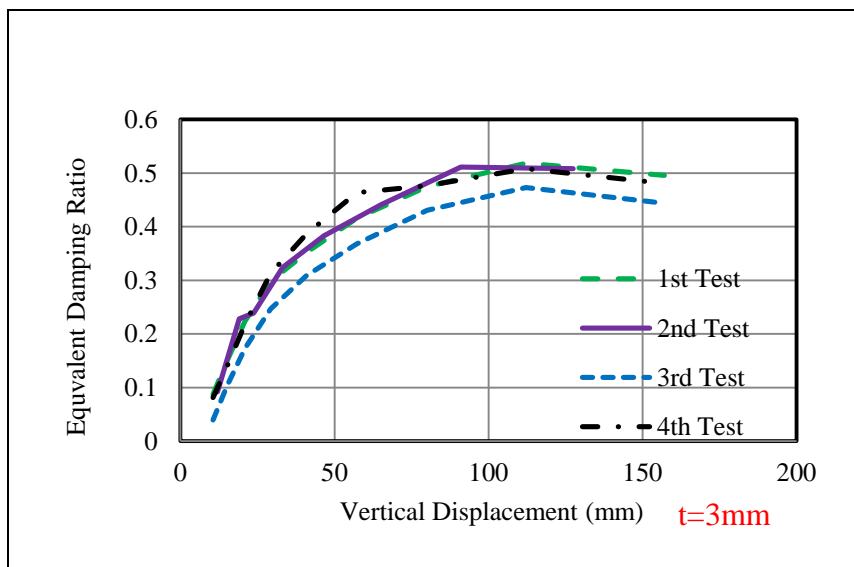


**Figure 2.27 :** Equivalent viscous damping ratio-vertical displacement relation for 3mm thick specimens derived from cyclic shear test.

Equivalent viscous Damping ratio versus Displacement curves for  $t=5\text{mm}$  and  $t=8\text{mm}$  specimens are illustrated in Figure 2.28. and Figure 2.29, respectively.

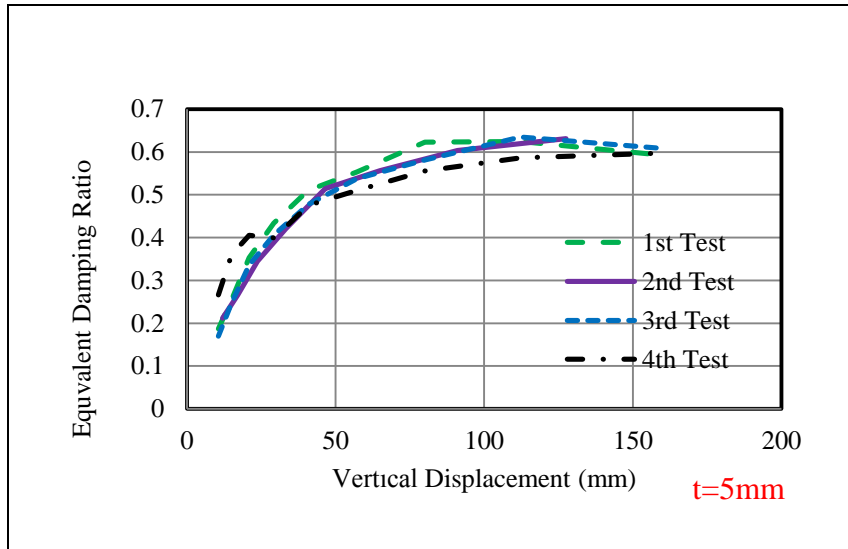


**Figure 2.28 :** Equivalent viscous damping ratio-vertical displacement relation for 5mm thick specimens derived from cyclic shear test.

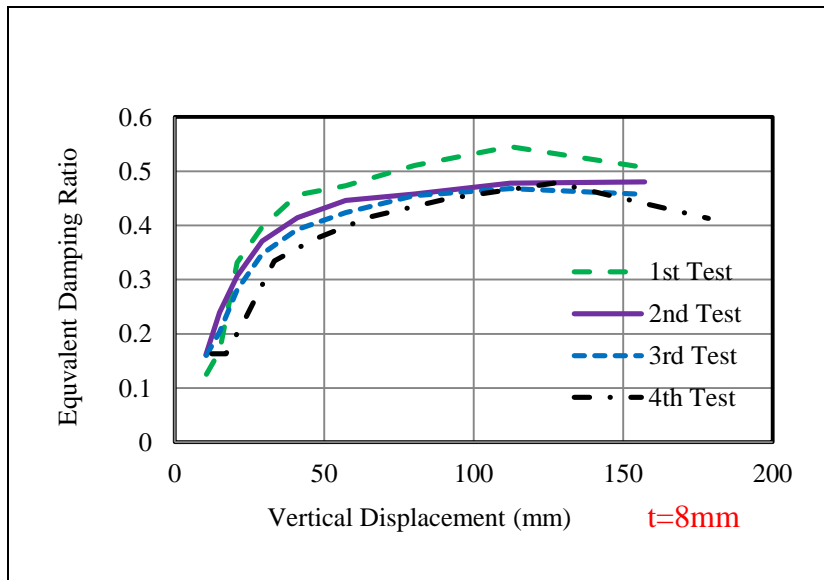


**Figure 2.29 :** Equivalent viscous damping ratio-vertical displacement relation for 8mm thick specimens derived from cyclic shear test.

The average equivalent damping ratios are 62.16% and 49.31%, for  $t=5\text{mm}$  and  $t=8\text{mm}$  thick specimens respectively. Also in some tests, the maximum displacement reached the 157mm, while the final displacement target is 220mm this is due to the ruptures during applying the last target, thereby the test was terminated. The comparisons of the equivalent damping for three distinct specimens are shown at Figure 2.30. According to Figure 2.30 the specimens having 5mm thickness have maximum equivalent viscous damping ratio and specimens having 3mm thickness have the least corresponding ratio, while 8mm thick specimens have the equivalent viscous damping ratio between 3mm thick and 5mm thick specimens damping ratio.

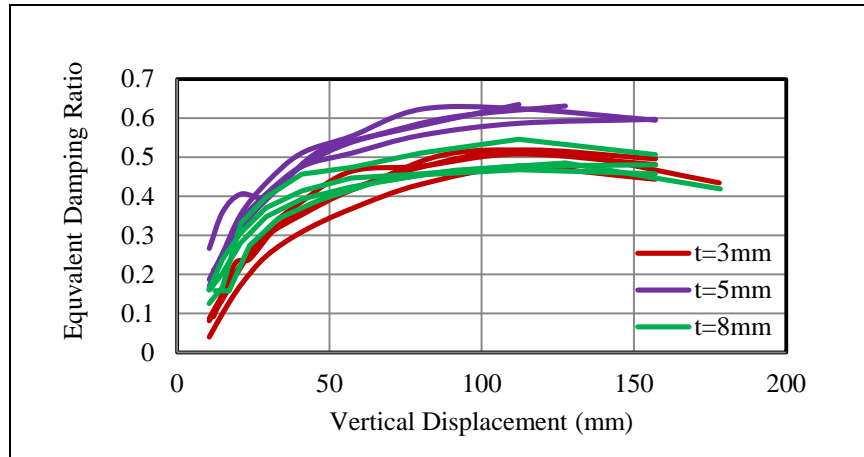


**Figure 2.30 :** Comparison of equivalent viscos damping ratio for three distinct specimens under shear effect.

### 2.3.2.5 Effective (secant) stiffness

Curves of effective stiffness versus displacement for 3mm, 5mm and 8mm steel cushions are compared in Figure 2.31. According to Figure 2.31 8mm, thick specimens have the secant stiffness value higher than 5mm and 3mm thick specimens, and 3mm thick specimens have the secant stiffness value less than 5mm thick specimen, corresponding value does. Thus as the specimens thickness increases the secant stiffness value rises.

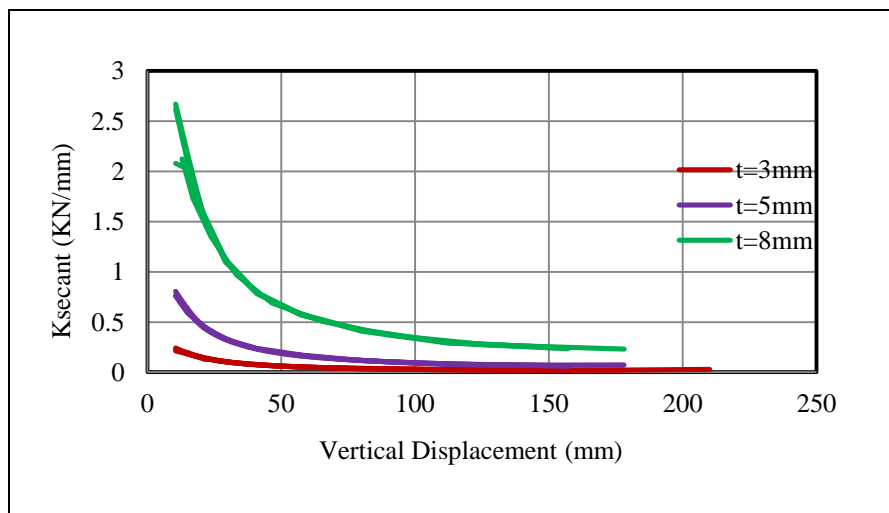


**Figure 2.31 :** Comparison of the  $K_{secant}$  for three distinct specimen under shear effect.

Effective stiffness is normalized by initial stiffness to evaluate the rate of stiffness decadence. Normalized stiffness ratio versus displacement curves for 3mm, 5mm and 8mm thick specimens are presented in Figure 2.32, 2.33 and Figure 2.34 respectively.

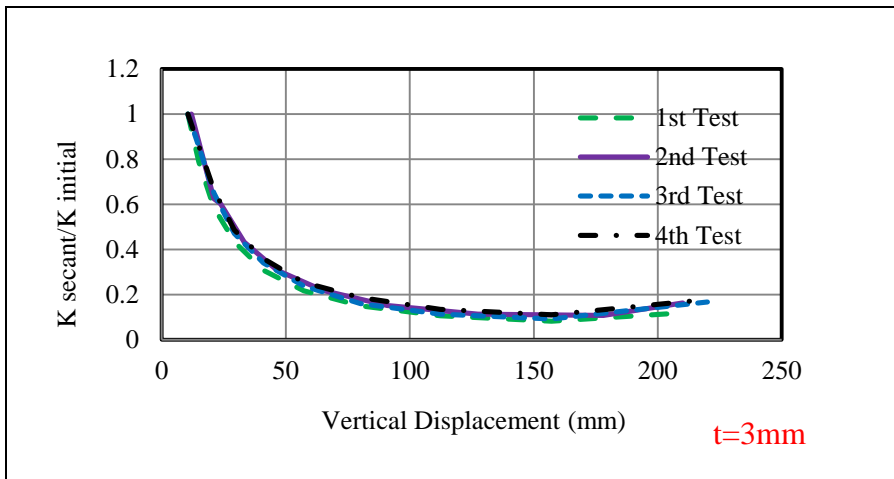


**Figure 2.32** : Ratio of Ksecant to k initial for 3mm thick specimens derived from cyclic shear test.

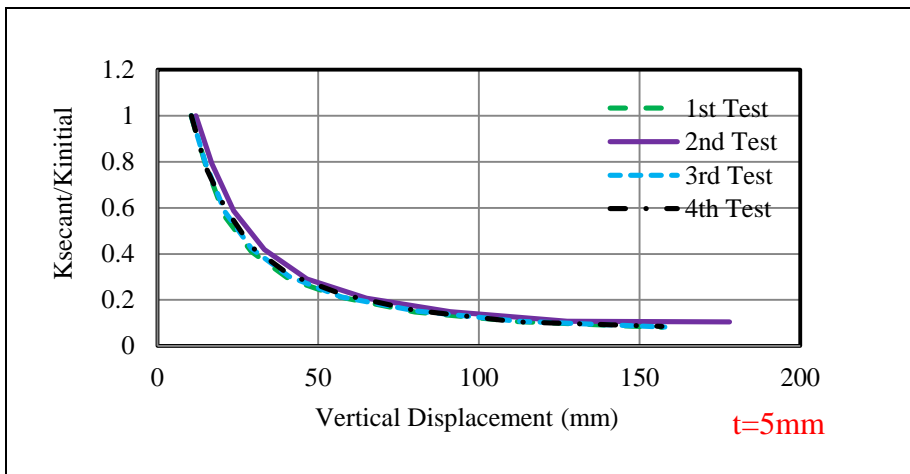


**Figure 2.33** : Ratio of Ksecant to k initial for 5mm thick specimens derived from cyclic shear test.

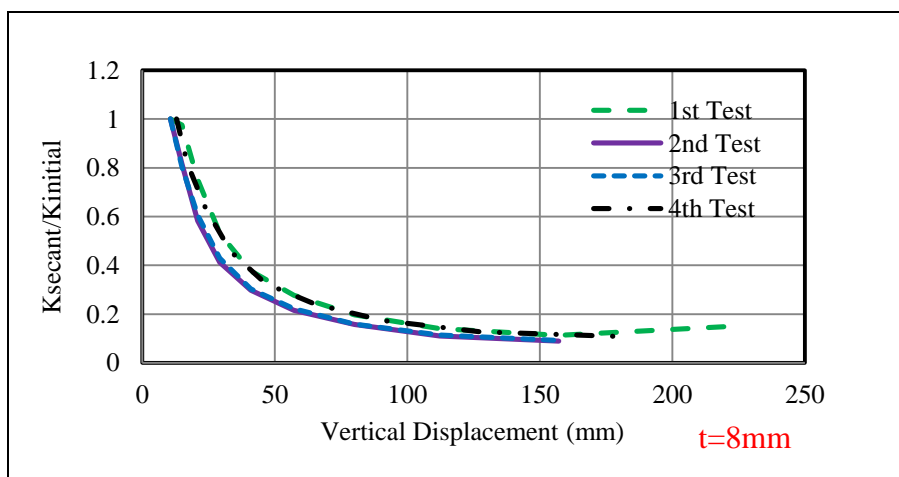


**Figure 2.34** : Ratio of Ksecant to k initial for 8mm thick specimens derived from cyclic shear test.

The comparisons of the  $K_{secant} / K_{initial}$  for three specific steel cushions are presented in Figure 2.35.

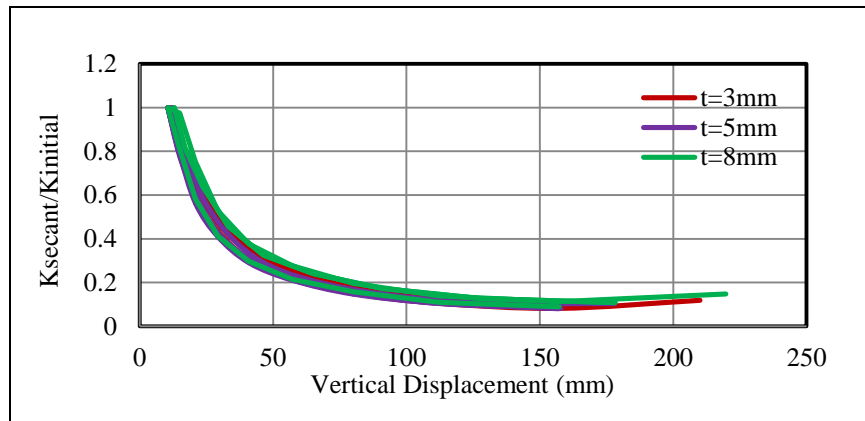


**Figure 2.35 :** Comparison of normalized stiffness ratio for three distinct specimens under shear effect.

These results indicate that the decaying rate of stiffness during the tests is independent of specimen thickness. In fact, these decaying rates are identical for all of three distinct specimens.

### 2.3.2.6 Strain history

The strain values are measured from the strain gages located at the critical points. The locations of strain gages are shown in Figure 2.36. The location of first yielding was at SG#3 at all of the distinct specimens. The obtained strain histories versus drift angle of three distinct specimens are compared in Figure 2.37 and 2.38. The red line in the Figures indicates the yielding strain. In SG#3 point, the yielding strain range is between 2500 and 3000 $\mu_s$ . There is a relation between the strain values and equivalent viscos-damping ratio. 5mm thick, specimens have higher strain values and damping ratio with respect to the 3mm and 8mm thick specimens and the 8mm thick specimens have higher strain values and damping ratio next to the 3mm thick ones. The average yield displacements are 15.64mm, 10.97mm and 11.039mm for t=3mm, 5mm and t=8mm thick specimens respectively.

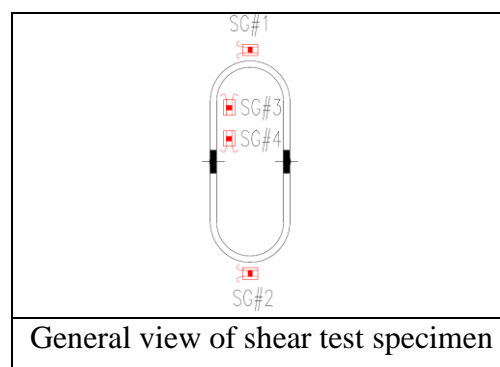


**Figure 2.36 :** Location of Strain gages on the test specimens under shear effect.

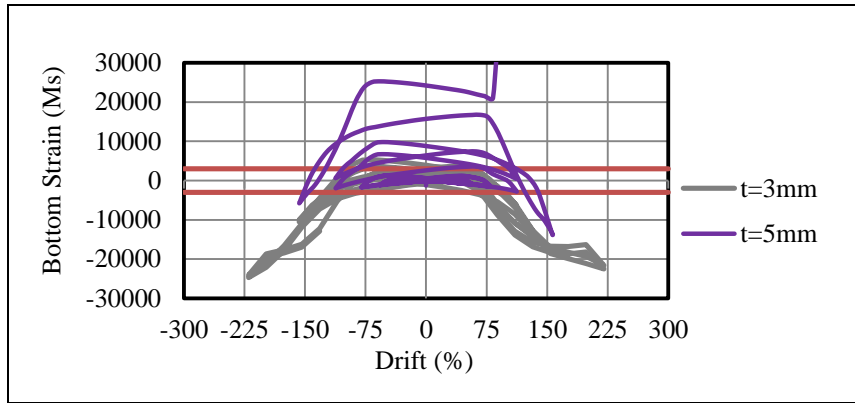


**Figure 2.37 :** Comparison bottom strain versus drift relation for 3mm and 5mm thick specimens at cyclic shear test.

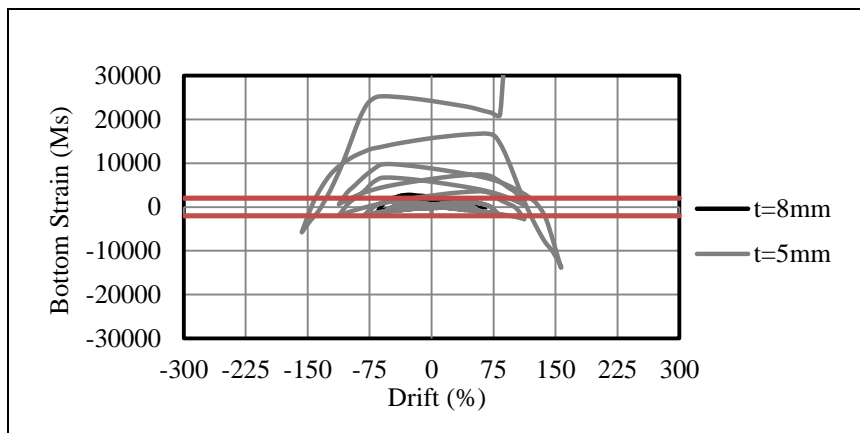


**Figure 2.38 :** Comparison bottom strain versus drift relation for 5mm and 8mm thick specimens at cyclic shear test.

### 2.3.3 Evaluation of experimental results for three specific specimens under shear loading

The experimental results derived from the cyclic shear tests for three different specimens are summarized at Table 2.4.

**Table 2.4 :** Summary of experimental results derived from cyclic shear test for three.

Specimen Type	Test number	Initial stiffness $K_0$ KN/mm	Yield Force (KN)	Max Force (KN)	Yield Displacement $D_y$ (mm)	Ultimate Displacement $D_u$ (mm)	Ductility $\mu$
3mm thick Cushion	1	0.13	2.94	4.25	22.03	178.12	8.09
	2	0.17	1.82	4.12	10.59	157.09	14.83
	3	0.21	3.03	3.81	14.97	157.08	10.50
	4	0.18	2.70	3.48	14.95	156.90	10.50
5mm thick Cushion	1	0.66	6.93	11.73	10.55	157.45	14.93
	2	0.82	9.82	14.25	12.01	178.05	14.83
	3	0.70	7.36	11.38	10.55	157.88	14.96
	4	0.68	7.23	11.80	10.56	157.18	14.88
8mm thick Cushion	1	2.01	24.17	45.62	12.0	178.71	14.90
	2	2.71	28.63	40.24	10.56	157.15	14.89
	3	2.84	29.95	38.45	10.56	157.08	14.88
	4	2.71	28.52	38.24	10.53	156.82	14.89

### 2.3.3.1 Ductility

The ductility is the ratio between  $\Delta u$  to  $\Delta y$  (ultimate displacement to yield displacement). It should be noted that four tests were performed per thickness, but as most of values are so closed for each thickness, the ductility values overlap with each other in specific thickness. The relation between thickness and ductility of three distinct specimens is illustrated by trend line in Figure 2.39.

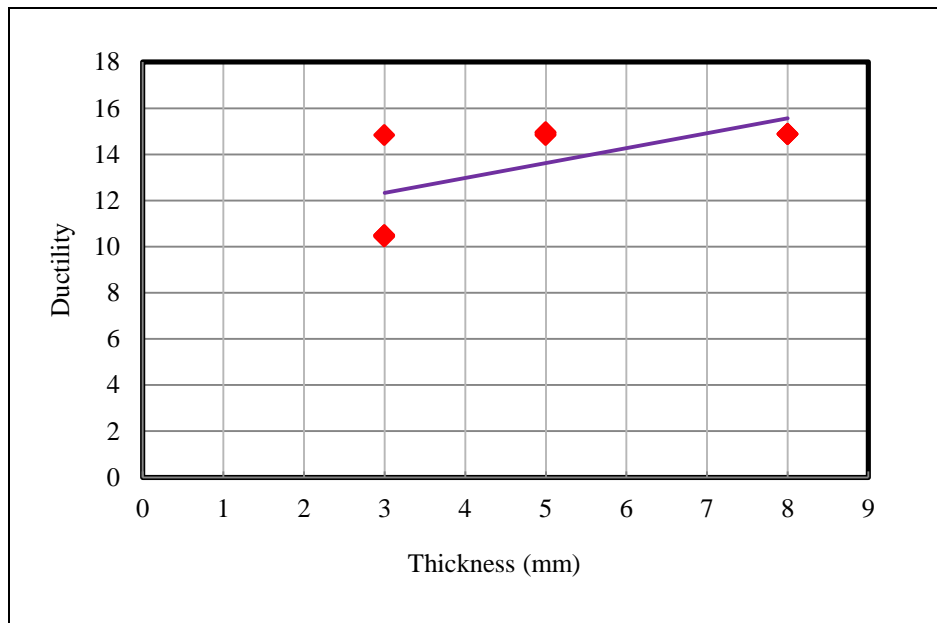


**Figure 2.39 :** Relation between ductility and specimens thickness for three distinct thicknesses under shear effect.

Figure 2.39 indicates that ductility increases with raising of thickness, therefore the specimens with larger thicknesses have the higher ductility next to smaller thicknesses.

### 2.3.3.2 Yield force and yield displacement

The yield force and yield displacement can be obtained by means of strain history evaluation for three distinct specimens. The relations between yield force/yield displacement and specimen thickness are presented by trend line in Figure 2.40 and 2.41. According to Figure 2.40 and 2.41, yield Force increases with rising of specimen thickness, whereas yield displacement declines with rising of specimen thickness.

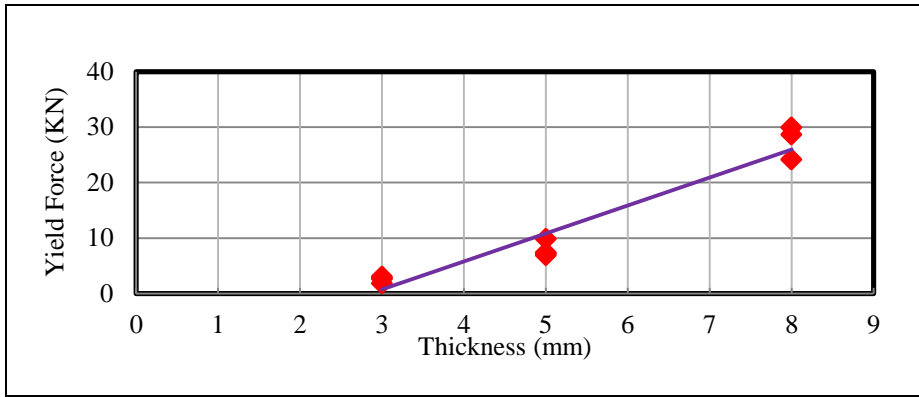


**Figure 2.40 :** Relation between yield force and specimens thickness for three distinct thicknesses under shear effect.

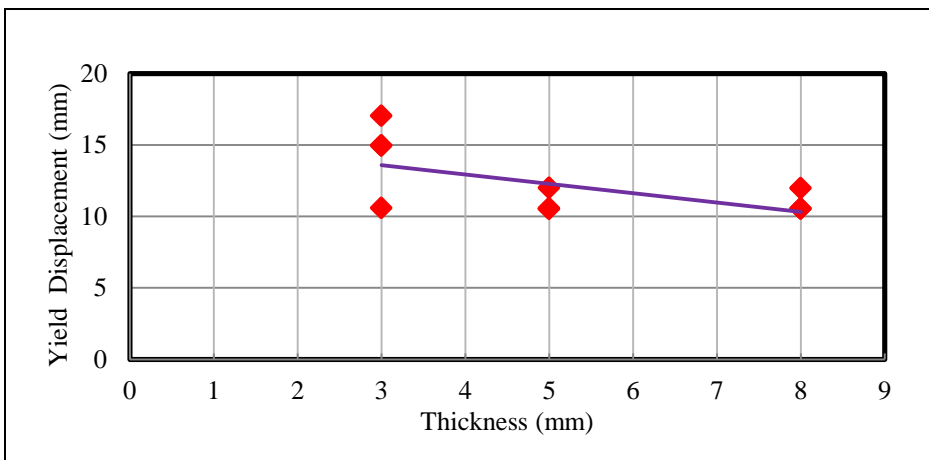


**Figure 2.41 :** Relation between yield displacement and specimens thickness for three distinct thicknesses under shear effect.

### 2.3.3.3 Maximum shear force

The relation between maximum shear force and specimens thickness is presented by trend line in Figure 2.42. The maximum shear force rises with the increase of specimen thickness.

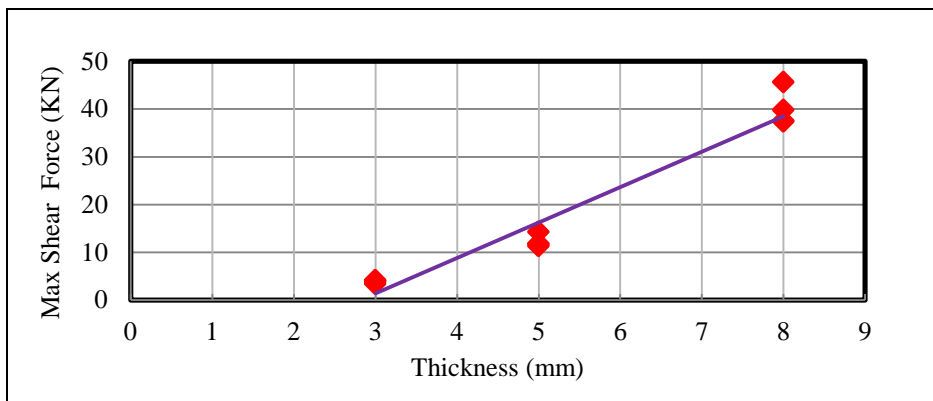


**Figure 2.42 :** Relation between maximum shear force and specimens thickness for three distinct thicknesses under shear effect.

### 2.3.3.4 Initial stiffness

The relation of the initial stiffness versus thicknesses is shown in Figure 2.43. As expected, initial stiffness increases as specimen's thickness rises.

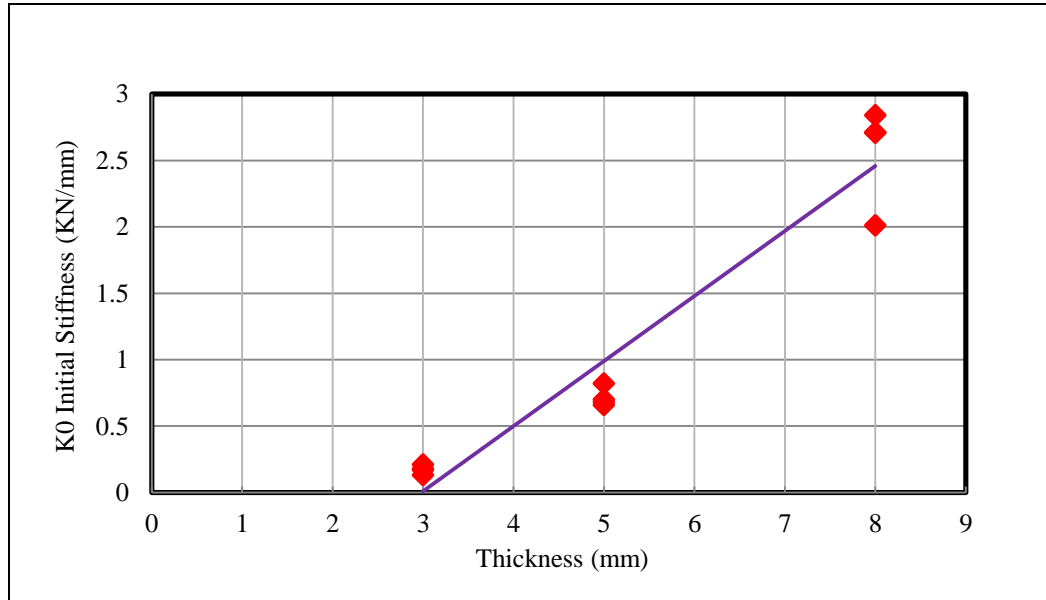


**Figure 2.43 :** Relation between initial stiffness and specimens thickness for three distinct thicknesses under shear effect.

### 2.4 Uniaxial Axial Test

A set of cyclic and monotonic tension and compression axial tests were carried out as shown in Figure 2.44. For each thickness, two monotonic tests (one tension and one compression) and one cyclic test were performed; the main parameter for each test was the specimen thicknesses. The tests were conducted to investigate the cyclic and monotonic axial behavior of steel specimens. The specimens in the following system tests and real structure are located at the base of concrete cladding panels under weight of concrete panels, thus it is essential to determine the axial behavior of steel cushions. Also because of probable out of plane movement or asymmetric behavior of concert panels, application of the axial test is compulsory for the steel cushions, in panel to beam connections in the system test and real structure. The test set-up is the same as the cyclic shear test, only the left short column of set up was utilized, and it played the role of base support for steel cushions in this test. The out of plane restrainers were used to avoid the probable rotation of the actuator head. The monotonic and cyclic protocol were applied by vertical actuator. One transducer was utilized to measure the lateral displacement of base plate and two numbers of

transducers were installed in each side of the actuator head to capture possible rotation would be any rotation of actuator head or not. The test set-up and the transducers location are presented in Figure 2.45 and 2.46 respectively.

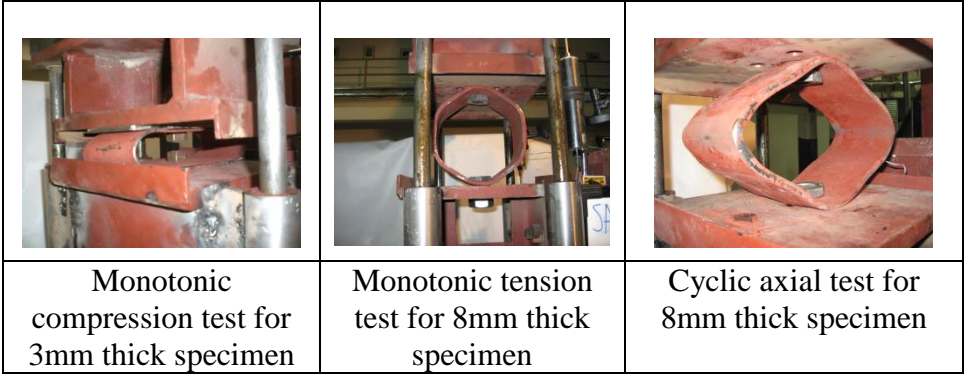


Figure 2.44 : Monotonic and cyclic axial test.

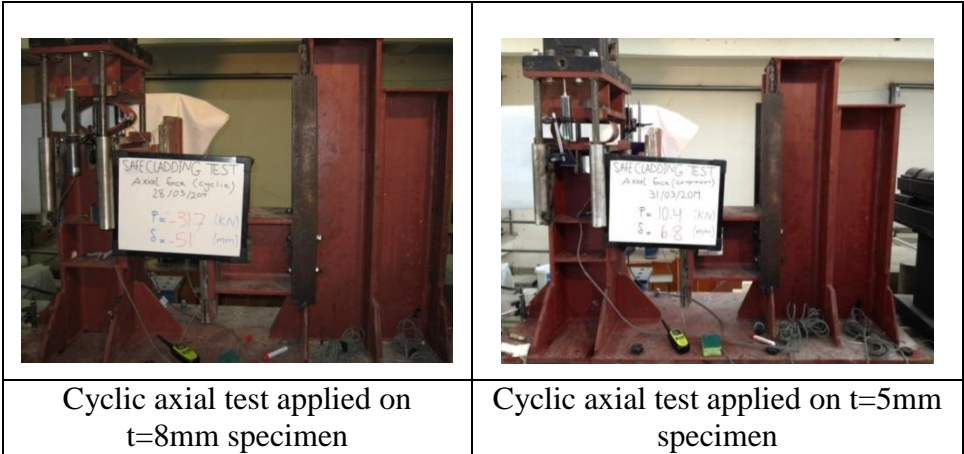


Figure 2.45 : General view of testing set-up.

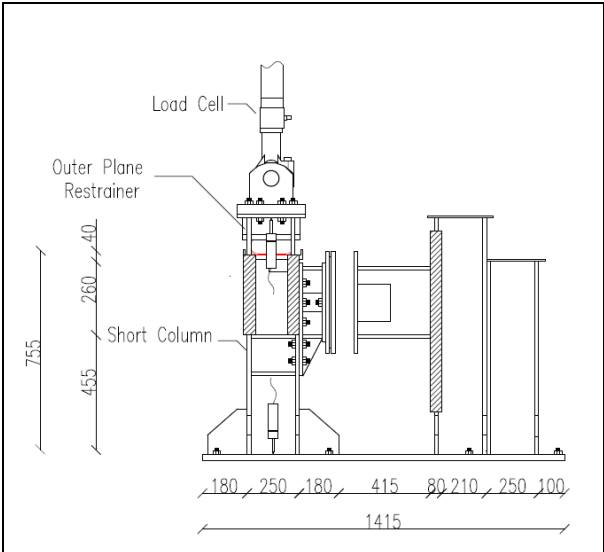


Figure 2.46 : Technical drawing of test set-up.

### 2.4.1 Axial test loading protocol

The testing protocols selected in accordance with the recommendations placed in FEMA 461, which actually is based on the expected maximum drift ratios. The dimensions of the steel cushions are 250 mm in width and 100 mm in depth. In considering the expected deformability of the cushions, the target displacements derived by multiplying the “ $a_i/a_{10}$ ” ratios with the specimen height of 100 mm in its vertical axis. The maximum target displacement was considered 64.44 mm instead of 100mm, because of bolt contacts to each other. The ratios to determine target displacement amplitudes are defined in Table 2.5. Ten diverse amplitude levels exist in the table. Two full cycles applied for each displacement target. The displacement targets values are shown in Table 2.6.

**Table 2.5 :** Ratio of displacements amplitudes, (FEMA 461 , 2007).

step	1	2	3	4	5	6	7	8	9	10
$a_i/a_{10}$	0.048	0.068	0.095	0.133	0.186	0.260	0.364	0.510	0.714	1.000

**Table 2.6 :** Displacement targets of uniaxial axial test.

step	1	2	3	4	5	6	7	8	9
Displacement Target (mm)	4.8	6.8	9.5	13.3	18.6	26.0	36.4	51.0	66.4

The complete loading protocol is presented in Figure 2.47. In the monotonic tests, the same target displacements were applied as shown in Figure 2.48. It is worthy to mention that in the monotonic tension test to determine the tensile strength of specimens the applied ultimate displacement target exceeded with respect to corresponding ultimate displacement target in the cyclic axial test. Since, there was not any restriction to precede the test, whereas in the monotonic compression axial test the ultimate target was identical with the cyclic axial test ultimate displacement target, because of top and bottom bolts contact with each other.

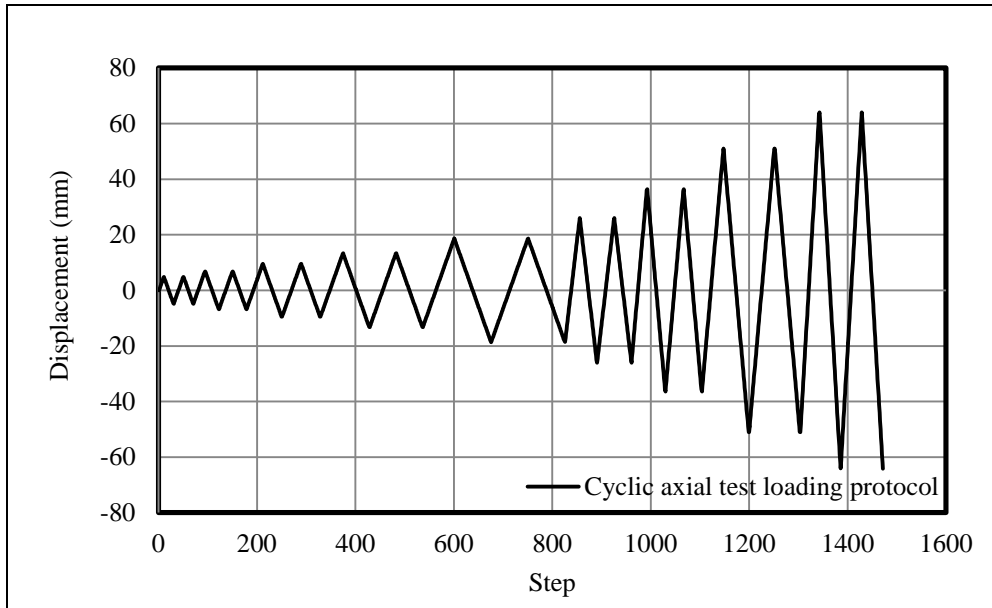


**Figure 2.47 :** Drift based cyclic loading protocol applied to steel cushions at cyclic axial test.

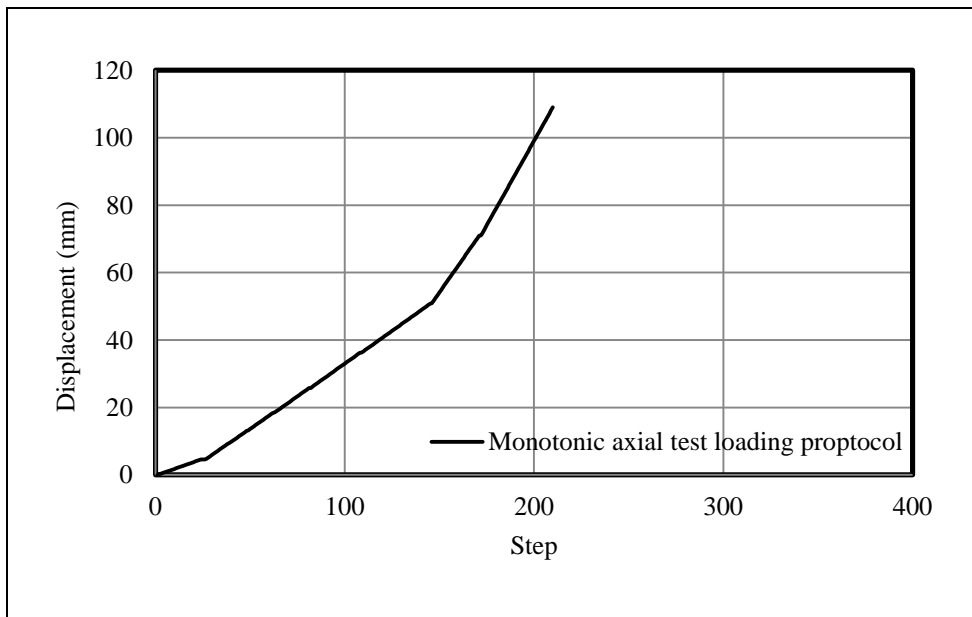


**Figure 2.48 :** Drift based monotonic loading protocol applied to steel cushions at axial test.

## 2.4.2 Experimental results of cyclic and monotonic axial tests

### 2.4.2.1 Force-Displacement relation

The force-displacement relation, which obtained from the cyclic axial tests for 3mm, 5mm and 8mm thick specimens are presented in Figure 2.49, 2.50 and Figure 2.51 respectively.

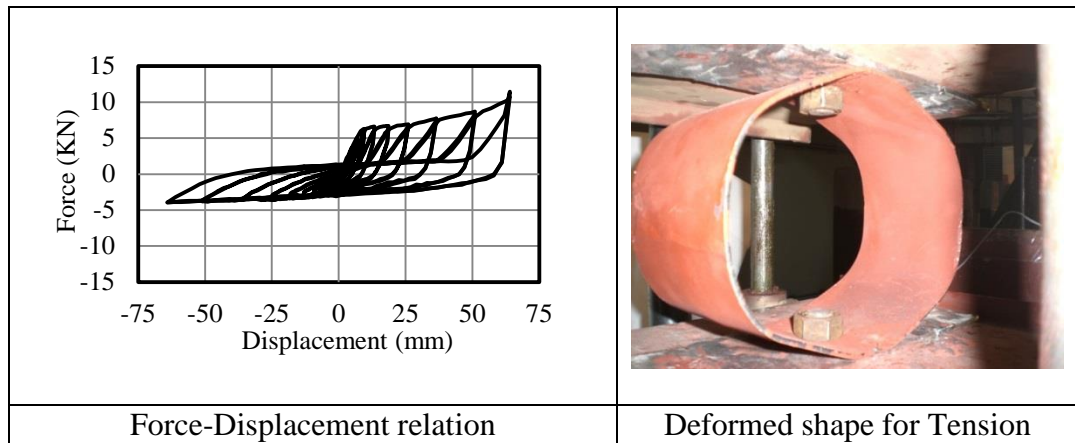


**Figure 2.49 :** Cyclic axial test performed on t=3mm steel cushion.

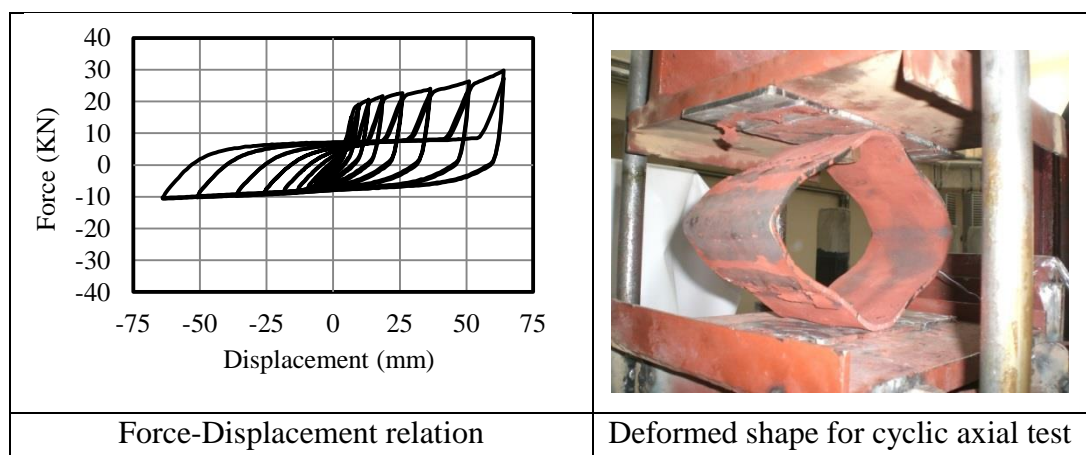


**Figure 2.50 :** Cyclic axial test performed on t=5mm steel cushion.

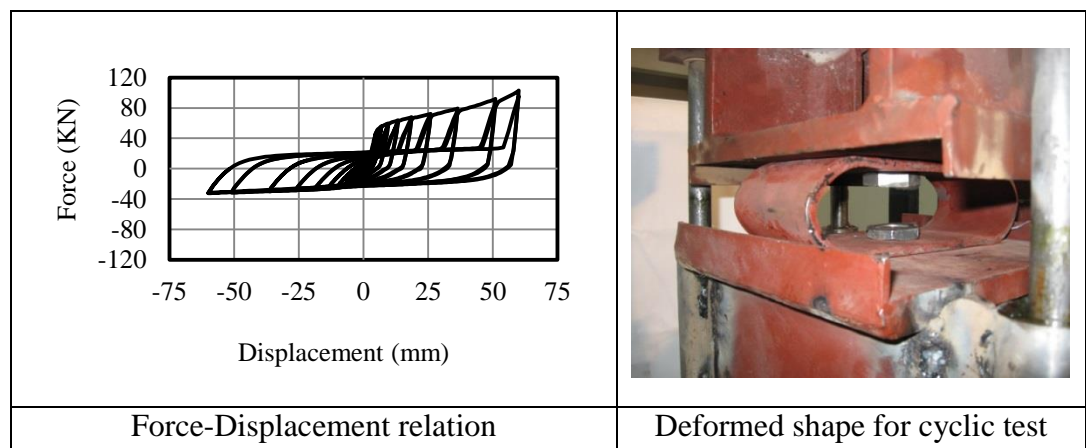


**Figure 2.51 :** Cyclic axial test performed on t=8mm steel cushion.

The nominal compression yield strength is 8 KN, 15 KN and 45 KN, The ultimate compression strength is 10 KN, 30 KN, and 100 KN for t=3mm, 5mm and 8mm specimens, respectively. The nominal tension yield strengths are 3KN, 6KN, and 16KN, the ultimate tension strength is 4 KN, 11 KN, and 32KN for 3mm, 5mm and 8mm thick specimens respectively. The values of strength for compression tests are

higher than the tension tests because the stiffness of specimens under the compression effect is higher than corresponding value under the tension tests. The specimens behaved asymmetrically under cyclic axial loading. After yielding, force increases at both compression and tension parts.

The force displacement relation obtained from monotonic compression and tension axial tests for 3mm, 5mm and 8mm thick specimens are presented in Figure 2.52, 2.53 and 2.54 respectively. According to Figure 2.52, the axial yield strengths of 3mm thick specimen are 2.89 KN, 6.79 KN, the yield displacement is 14.30 mm, and 12.02 mm, the value of ultimate strength is 5.40 KN and 11.85 KN, in monotonic tension and compression tests respectively. It should be noted that in compression test after 64 mm the top and bottom bolts were contacted with each other, therefore the test terminated at this point.

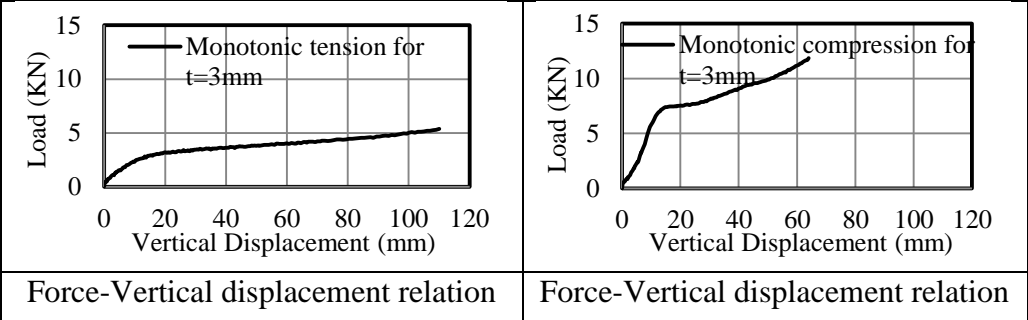


**Figure 2.52 :** Force-Displacement relation for 3mm thick specimen derived from monotonic axial test.

According to Figure 2.53, the axial yield strength of 5mm thick specimen is 6.09 KN, 16.87 KN, the yield displacement is 11.09 mm, and 10.72 mm, the value of ultimate strength is 11.70 KN and 25.12 KN, in monotonic tension and compression tests respectively.

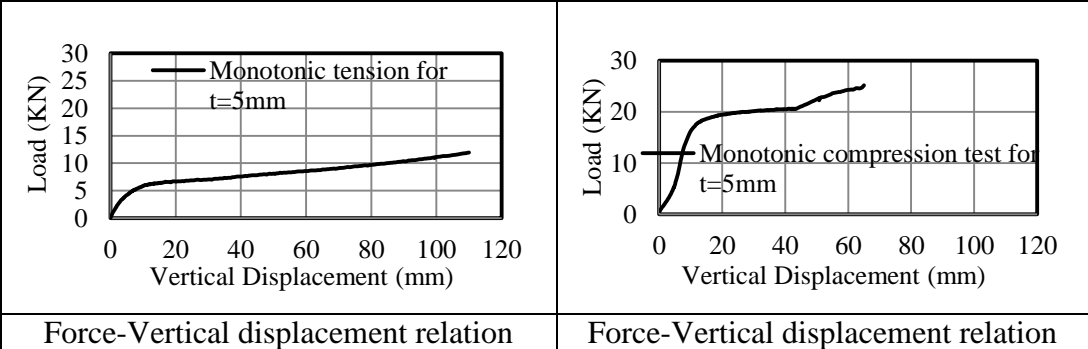


**Figure 2.53 :** Force-Displacement relation for 5mm thick specimen derived from monotonic axial test.

According to Figure 2.54 the axial yield strength of 8mm thick specimen is 22.90 KN, 49.83 KN, the yield displacement is 10.60 mm, and 5.20 mm, the value of ultimate strength is 51.50 KN and 156.87 KN, in monotonic tension compression and tests respectively.

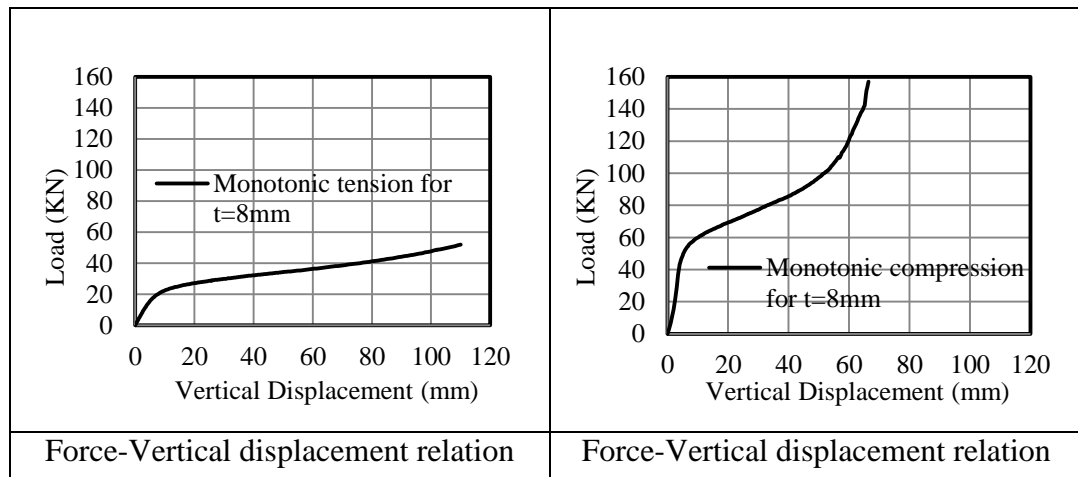


**Figure 2.54 :** Force-Displacement relation for 8mm thick specimen derived from monotonic axial test.

#### 2.4.2.2 Cyclic and monotonic axial tests envelop

The monotonic tests envelop results are compared with cyclic force-displacement hysteresis in Figure 2.55. As expected, the monotonic test results generate the cyclic force-displacement hysteresis envelop for each specific specimen.

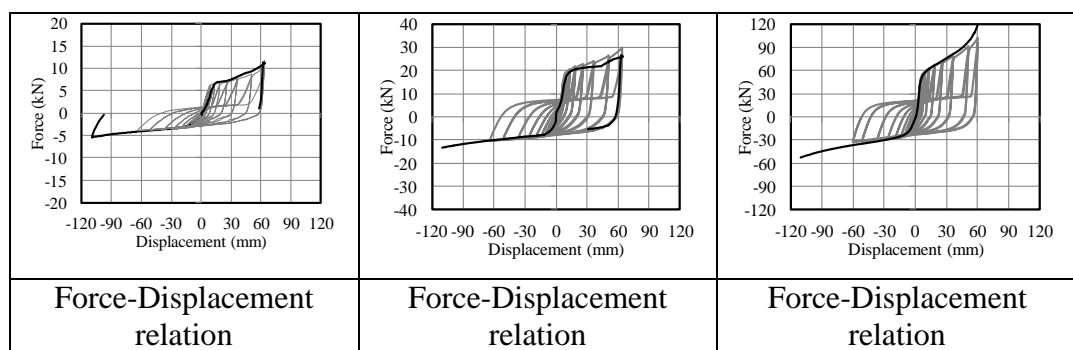


**Figure 2.55 :** Comparison of monotonic test results with cyclic force-displacement hysteresis for t=3mm, 5mm and 8mm thick specimens.

#### 2.4.2.3 Energy dissipation

The energy dissipation capacity for three specific specimens subjected to axial loads is illustrated in Figure 2.56. According to the Figure 2.56, there is a relation between energy dissipation capacity and thickness, the energy dissipation capacity increases with increasing thickness. 3mm, 5mm and 8mm thick specimens have maximum

energy dissipation capacity of 2759, 9865 and 26987 KN.mm respectively, at maximum displacement target.

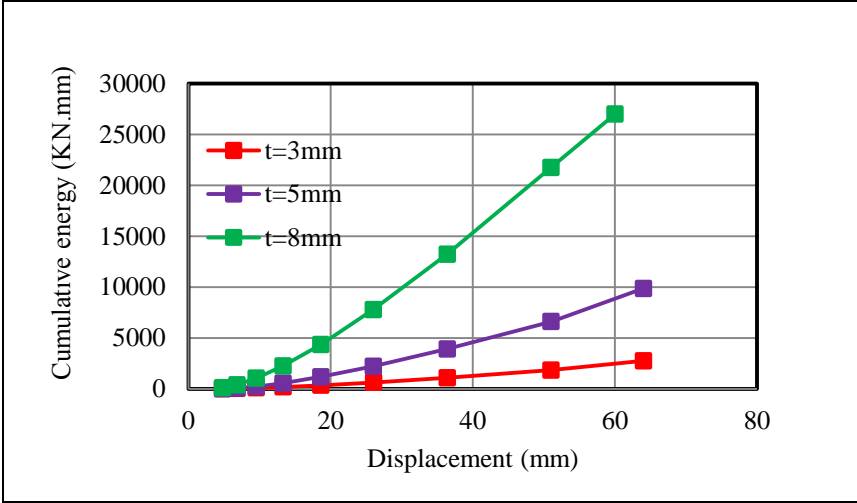


**Figure 2.56 :** Cumulative energy dissipation capacity for three distinct specimens derived from cyclic axial test.

**2.4.2.4 Equivalent viscous damping**

The calculated equivalent damping ratio for three specific specimens subjected to axial loading are presented in Figure 2.57. According this Figure the damping ratio does not increase with increasing of thickness. The specimen having the highest damping ratio is 5mm thick specimen and the least one is 3mm thick specimen while 8mm thick specimen is located between two specimens. The maximum damping ratio for t=3mm thick specimen is 14.48%, for t=5mm thick specimen this value is 16.48% and for t=8mm thick specimen is 13.33%.

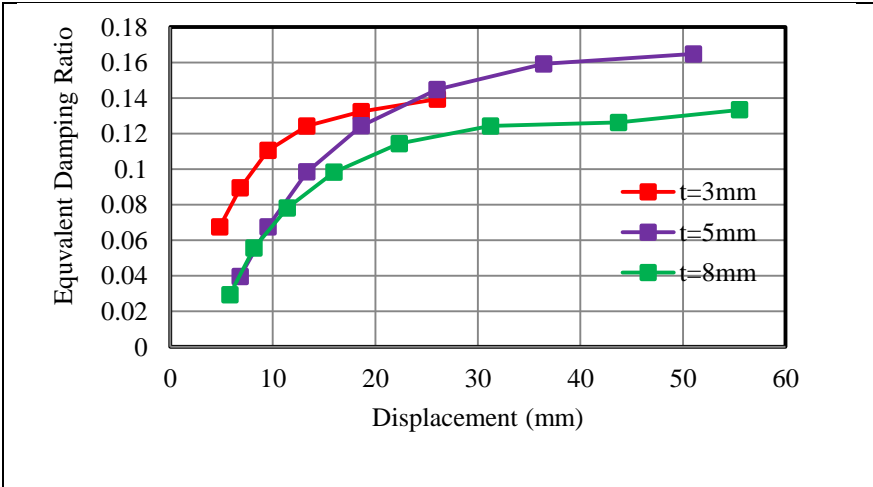


**Figure 2.57 :** Equivalent damping ratio in term of displacement for three distinct specimens derived from cyclic axial test.

### 2.4.2.5 Effective (secant) stiffness

The comparison of the normalized stiffness ratio vs. displacement, for three specific specimens is presented in Figure 2.58. These results indicate that the decaying rate of stiffness during the tests is independent of specimen thickness. In fact, these decaying rates are identical for all of three distinct specimens. It should be noted that the normalized stiffness ratio for 5mm thick specimen is higher than corresponding value for 3mm thick specimen and normalized stiffness ratio for 3mm thick specimen is higher than corresponding value for 8mm thick specimen.

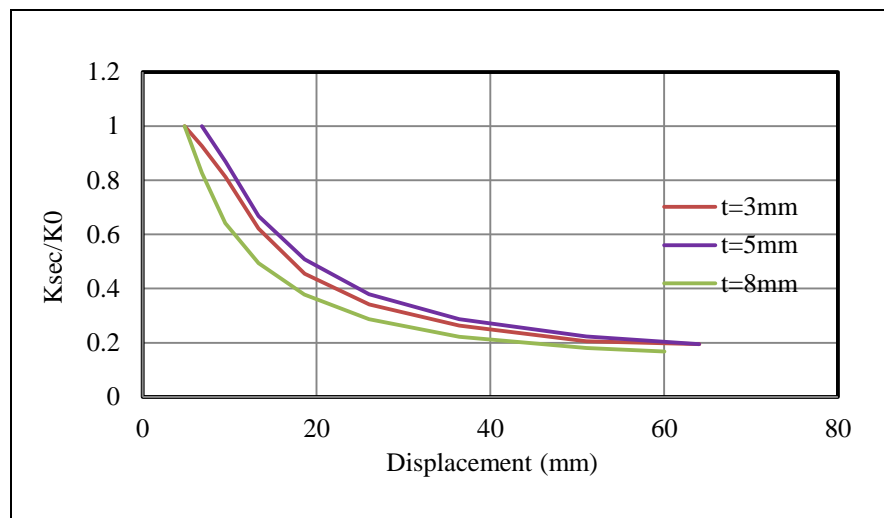


**Figure 2.58 :** Comparison of normalized stiffness ratio versus displacement derived from cyclic axial test for three specific specimens.

### 2.4.2.6 Strain history

The strain gage placements for the specimen, are shown in Figure 2.59. The strain histories for the critical point are compared for three distinct specimens in Figure 2.60 and 2.61. There is the relation between the obtained equivalent damping ratio and strain values. 5mm thick specimen gives higher strain values and damping ratio next to 3mm and 8mm. The yielding level of steel cushions is relevant to hysteresis damping directly.

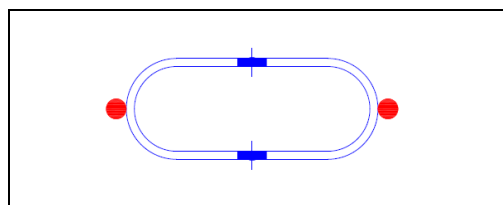


**Figure 2.59 :** Location of strain gages at monotonic and cyclic axial test.

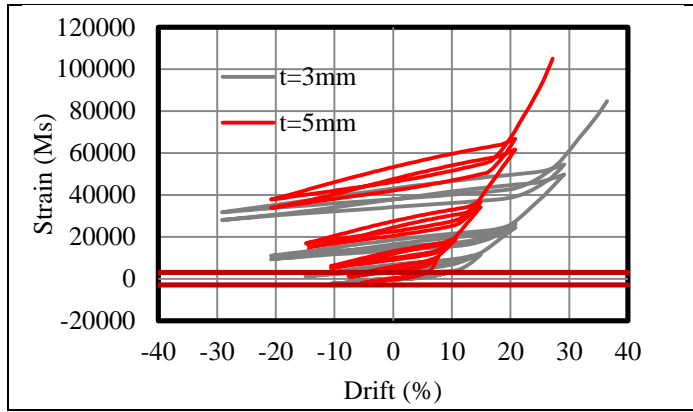


**Figure 2.60** : Comparison of strain histories in terms of drift for t=3mm and 5mm thick specimens derived from cyclic axial test.

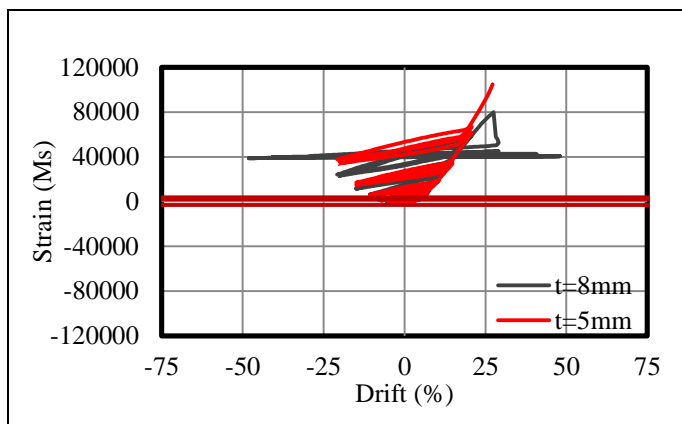


**Figure 2.61** : Comparison of strain histories in terms of drift for t=5mm and 8mm thick specimens derived from cyclic axial test.

### 2.4.3. Evaluation of experimental results for three specific specimens under axial loading

The experimental results derived from the cyclic axial tests for three different specimens are summarized at Table 2.7 and 2.8. As the specimens behaved asymmetrically under axial effect, the results are given for tension and compression parts individually.

**Table 2.7** : Summary of test results under compression stress.

Specimen thickness	Initial stiffness $K_0$ KN/mm	Yield Force (KN)	Max Force (KN)	Yield Displacement $D_y$ (mm)	Ultimate Displacement $D_u$ (mm)	Ductility $\mu$
t=3mm	0.64	6.11	10.21	9.52	62.98	6.62
t=5mm	1.96	18.65	27.34	9.53	63.99	6.72
t=8mm	8.78	51.02	98.37	5.81	58.05	9.99

**Table 2.8 :** Summary of test results for under tensile stress.

Specimen thickness	Initial stiffness $K_0$ KN/mm	Yield Force (KN)	Max Force (KN)	Yield Displacement $D_y$ (mm)	Ultimate Displacement $D_u$ (mm)	Ductility $\mu$
t=3mm	0.29	2.77	3.88	9.50	61.96	6.52
t=5mm	0.79	7.47	10.58	9.49	61.98	6.53
t=8mm	2.60	21.18	32.00	8.14	56.99	7.00

### 2.4.3.1 Ductility

The relation between ductility and specimen thickness for cyclic axial tests are presented by linear trend in Figure 2.62 and 2.63, for compression and tension parts respectively. As it is obvious from the Figure 2.62, the ductility increases with increase of thickness so that, thicker specimen has more ductility; conversely, the thinner specimen has smaller ductility.

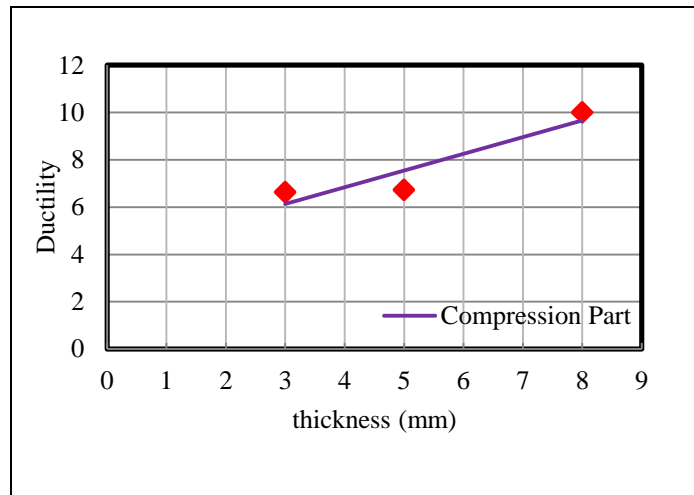


**Figure 2.62 :** Ductility in term of specimen thickness for three distinct specimens in compression part.

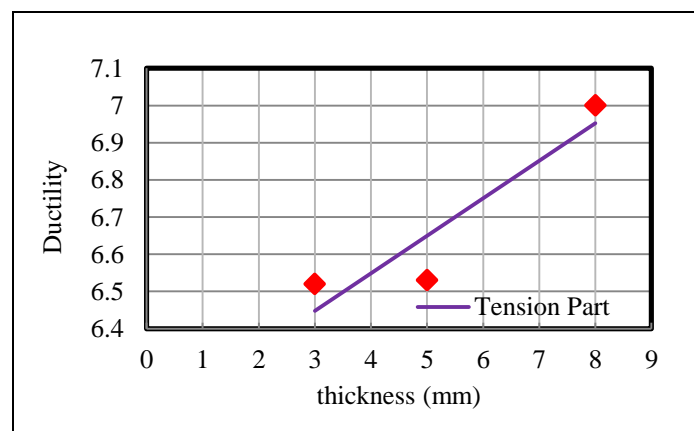


**Figure 2.63 :** Ductility in term of specimens thickness for three distinct specimens in tension part.

The ductility increases with increasing thickness in tension part.

**2.4.3.2 Yield force and yield displacement**

Trend line in Figure 2.64 and 2.65, for compression and tension part respectively, demonstrate yield force in terms of specimen thickness. There is the direct relation between yield force and specimens thickness, so that the yield forces increase directly with rising thickness at both tension and compression part.

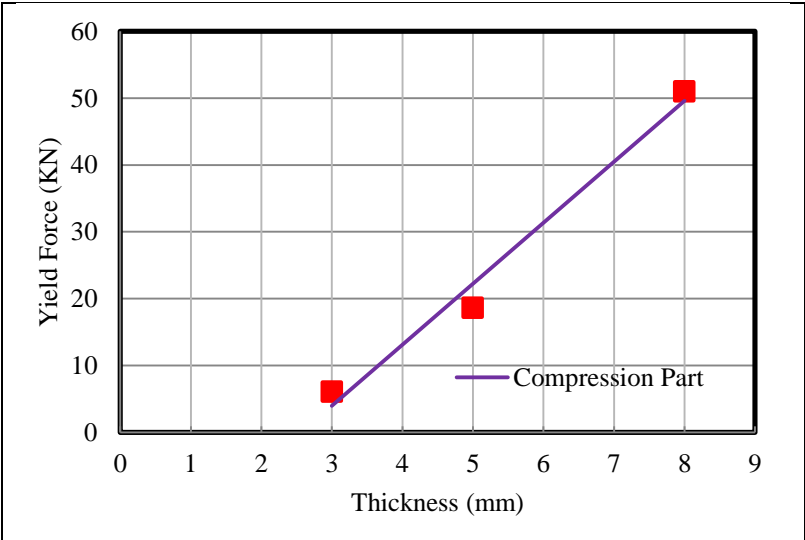


**Figure 2.64 :** Yield force in terms of specimen thickness for three distinct specimens in compression part.

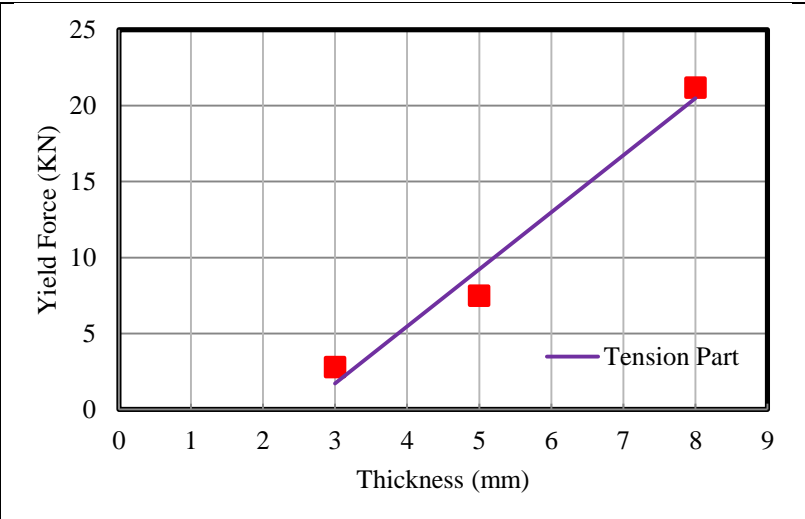


**Figure 2.65 :** Yield force in terms of specimen thickness for three distinct specimens in tension part.

Trend line in Figure 2.66 and 2.67, for compression and tension part respectively, demonstrate yield displacements in terms of specimen thickness. In compression and tension part, yield displacement decreases with increasing thickness.

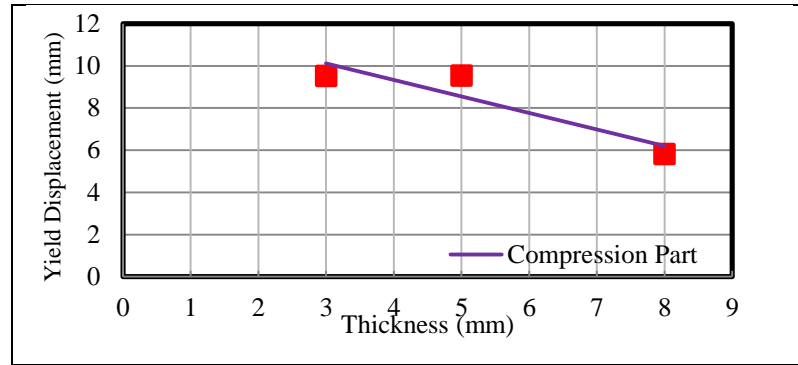


**Figure 2.66 :** Yield displacement in terms of specimen thickness for three distinct specimens in compression part.

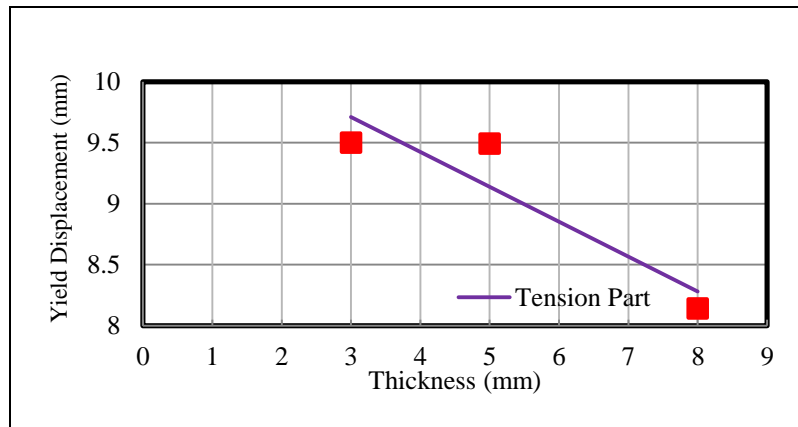


**Figure 2.67 :** Yield displacement in terms of specimen thickness for three distinct specimens in tension part.

#### 2.4.3.3 Maximum shear force

The relation between maximum force and specimen thickness in compression and tension parts under axial effect is shown by trend line in Figure 2.68 and 2.69. This force is the maximum shear force obtained in the axial test for three specific thicknesses in each part. As it is clear in Figure 2.68 and 2.69, maximum shear force increases as specimen thickness increases.

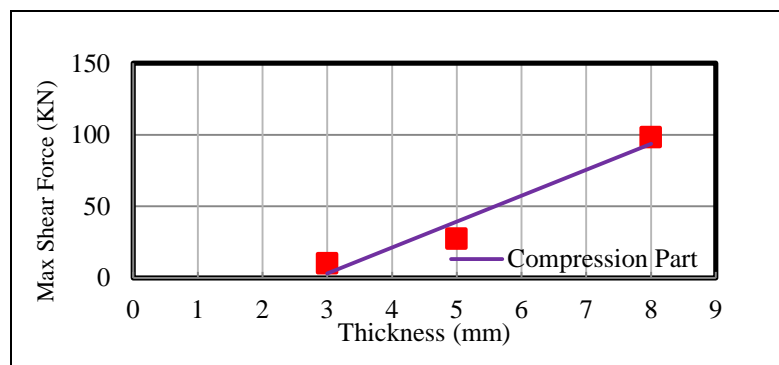


**Figure 2.68 :** Maximum force in terms of specimen thickness for three distinct specimens in compression part.

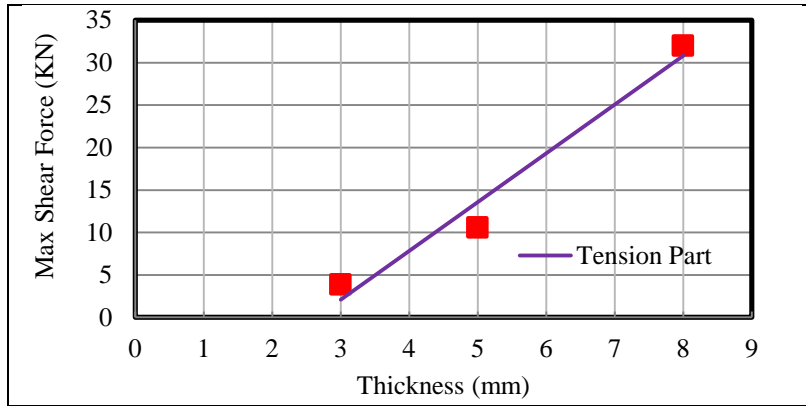


**Figure 2.69 :** Maximum force in terms of specimen thickness for three distinct specimens in tension part.

#### 2.4.3.4 Initial stiffness

Initial stiffness trends in term of specimen thickness are demonstrated in Figure 2.70 and 2.71, for compression and tension part, respectively. Initial stiffness increases directly with increasing thickness, at both tension and compression part.

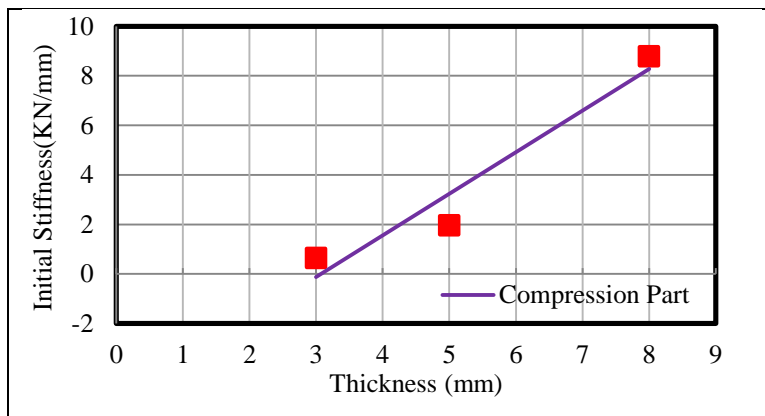


**Figure 2.70 :** Initial stiffness in terms of specimen thickness for three distinct specimens in compression part.

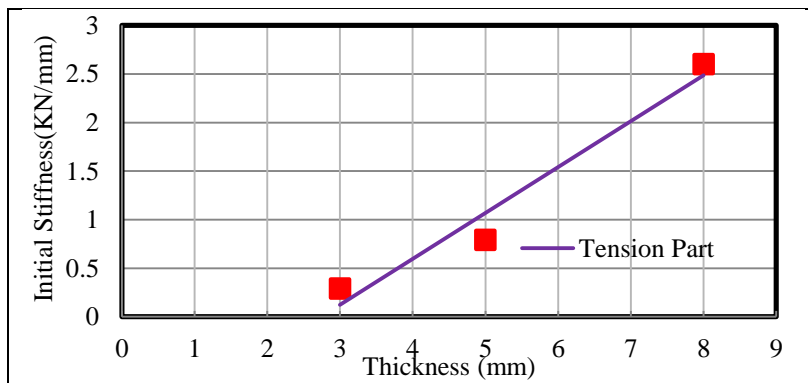


**Figure 2.71 :** Initial stiffness in terms of specimen thickness for three distinct specimens in tension part.

### **3. Bi-DIRECTIONAL CYCLIC SHEAR AND AXIAL TEST**

In this chapter the bi-axial behavior of steel cushions with thicknesses of 3, 5, and 8mm are investigated. This chapter is divided into two sections. In the first section the bi-directional cyclic shear and tension axial test is discussed and in the second section, the bi-directional cyclic shear and compression axial test is discussed. In the last part, the interaction diagrams for three distinct specimens are presented as well.

#### **3.1 Introduction**

The large experimental campaigns were conducted to examine the cyclic shear behavior of steel cushion subjected to constant axial tension or compression effects. The bi-axial tests are in great importance, since the steel cushions were designed to be utilized as panel to support, panel-to-panel and panel to beam connections in the industrial buildings, as shown in Figure 3.1. Thus, the steel devices encounter with different types of load combinations. In particular, at the base, the steel cushions play the role of support; they are subjected to shear deformation under lateral load and axial deformation under the self-weight of cladding panels simultaneously. In addition, the axial force can be altered from tension to compression or vice versa, because of panels racking. The special test set-up was design to perform the biaxial tests. The test set-up consisted of two main parts , in the right hand side the horizontal actuators was used to apply the axial tension or compression force and this forces were tried to be kept constant during the tests. In the left hand side, the vertical actuator applied the drift base cyclic displacement protocol. To avoid the out of plane displacement of vertical and horizontal actuator the out of plane restrainer were utilized. The general views and technical drawing of the test set-up are presented in Figure 3.2, 3.3 and Figure 3.4.

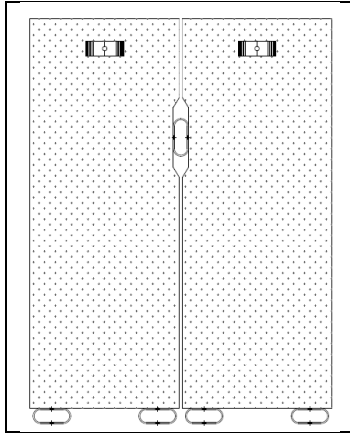


**Figure 3.1 :** Steel cushions configuration on the precast structure.

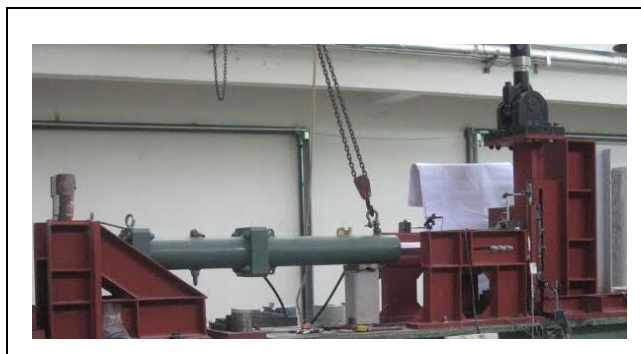


**Figure 3.2 :** General view of test set-up.

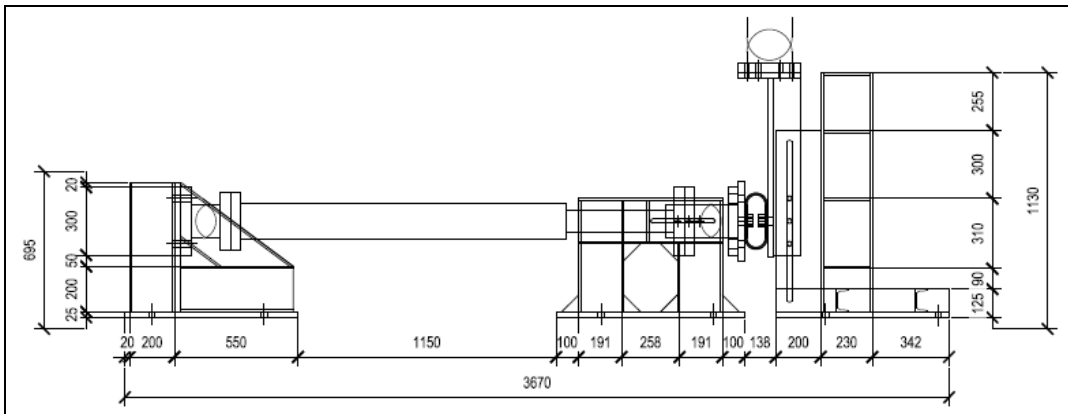


**Figure 3.3 :** General dimension of test set-up.

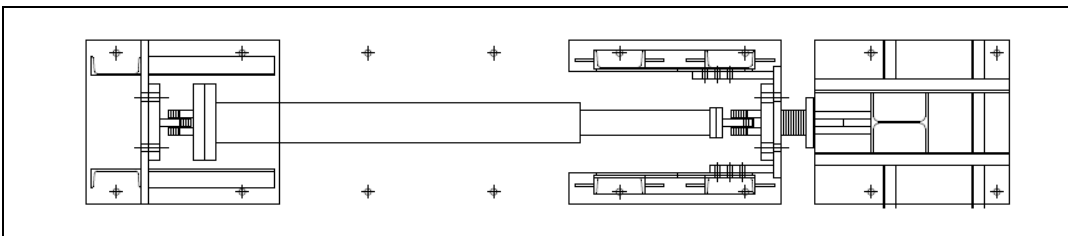


**Figure 3.4 :** Plan view of test set-up.

The maximum axial tension and compression capacity of three distinct steel cushions were determined in the uni-axial monotonic tests. The values of the applied constant tension or compression axial loads were 25%, 50% and 75% of the maximum axial capacity per distinct specimen. Figure 3.5 presents the deformed shape of steel cushions under bi-axial effects.

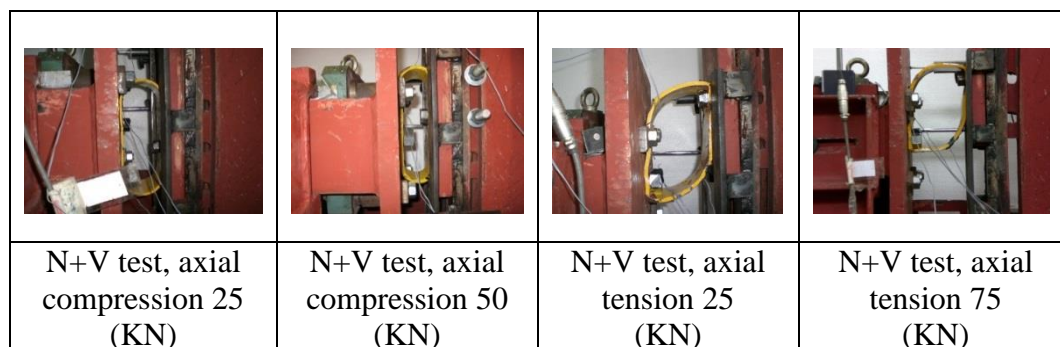


**Figure 3.5 :** Bi-Axial test under varied level of constant axial tension and compression load.

The total numbers of 42 biaxial tests were performed. The summary of the experimental campaign are summarized at Table 3.1. The main parameters of the tests were the specimen thickness and the value of constant axial force.

**Table 3.1 :** Experimental program summary in the bi-directional tests.

Test Type	Test Scheme	t= 3 mm				t= 5 mm				t= 8 mm				Total Number
	N/N <sub>0</sub> (%)	0	2	5	7	0	2	5	7	0	2	5	7	
Cyclic shear and constant axial compression		1	2	2	2	1	2	2	2	1	2	2	2	21
Cyclic shear and constant axial tension		1	2	2	2	1	2	2	2	1	2	2	2	21

The displacement protocol was similar with the uni-axial shear test protocol and was applied by vertical actuator. The horizontal actuator, as shown in Figure 3.6 applied the constant axial load. Two transducers were used to measure rotation of vertical plate connected to horizontal jack to control the uniform distribution of axial force and one transducer was used to measure the vertical displacement of plate connected to the horizontal jack. The value of axial load at any time was measured through the load cell on the horizontal actuator. The transducer locations are illustrated in Figure 3.7.

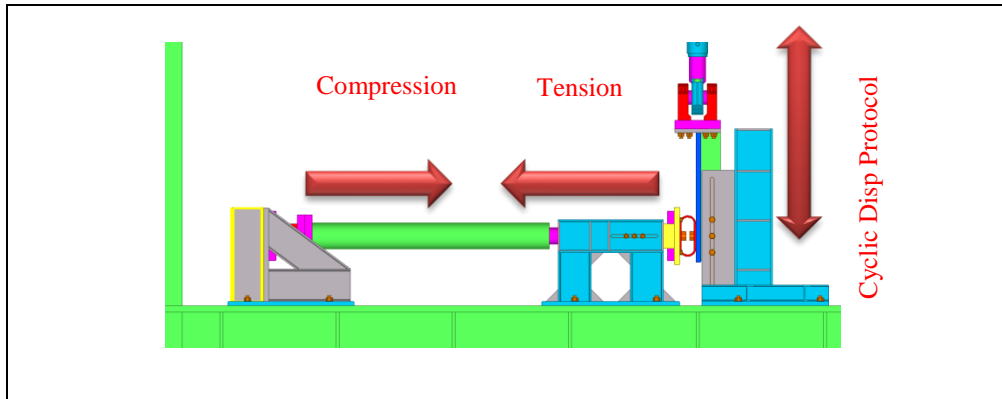


**Figure 3.6 :** Direction of applied loads.

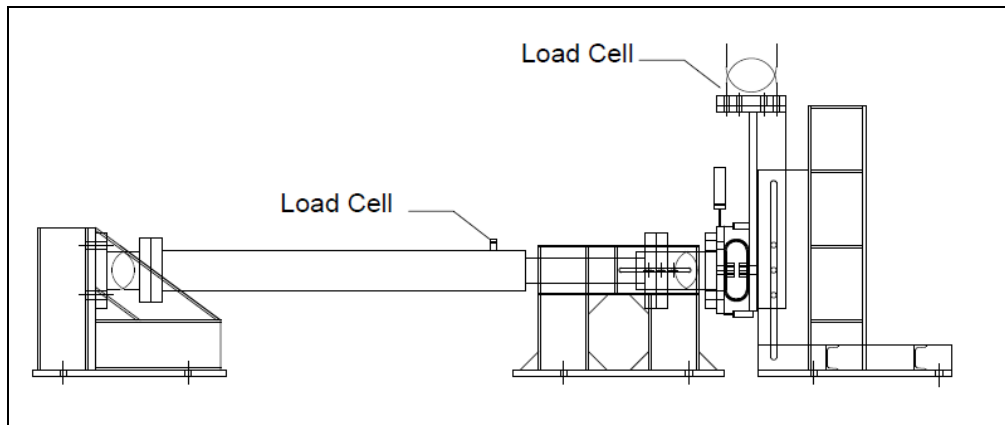


**Figure 3.7 :** Location of transducers and load cells.

### **3.2 Experimental Results of Bi-directional Test under Shear + Tension Loading**

In this section, the experimental results obtained from bi-directional cyclic shear and axial tension tests are discussed. It is worthy to mention that axial tension forces were constant during the tests. The values of the axial tension forces are selected based on the proportion of the  $N/N_0$  in which  $N_0$  is the axial ultimate tension strength obtained from the monotonic axial tension tests. The applied axial loads were 25%, 50% and 75% of  $N_0$ .

#### **3.2.1 Force-Displacement relation**

The force - displacement relations which obtained from bi-directional shear and axial tension tests are presented in Figure 3.8, 3.9 and Figure 3.10 for  $t=3\text{mm}$  thick steel cushion subjected to  $N/N_0 = 25\%$ ,  $N/N_0 = 50\%$  and  $N/N_0 = 75\%$  respectively, the corresponding axial load values are 2.5, 5, and 7.5 KN.

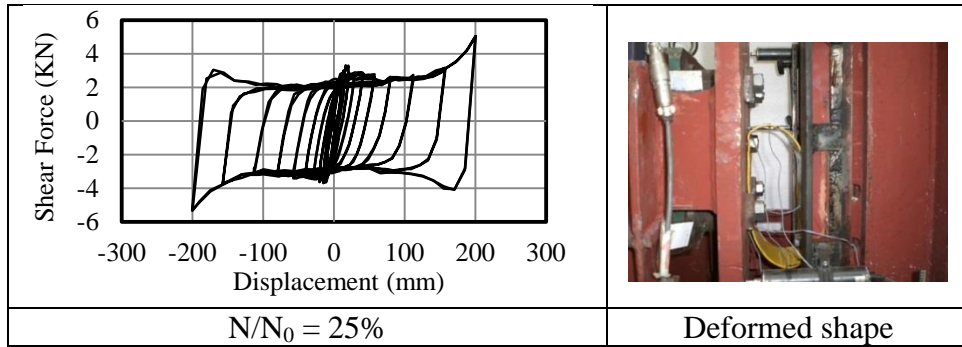


**Figure 3.8 :** Force-Displacement relation of 3mm thick specimen under tensile axial load of  $N/N_0=25\%$ .

The nominal yield strength is about 2.18KN in tension part and 3.22KN in compression part under the axial load of 2.50 KN. In this level of constant tensile axial load, the steel cushion behaved asymmetrically. There is no any reduction in the displacement capacity.

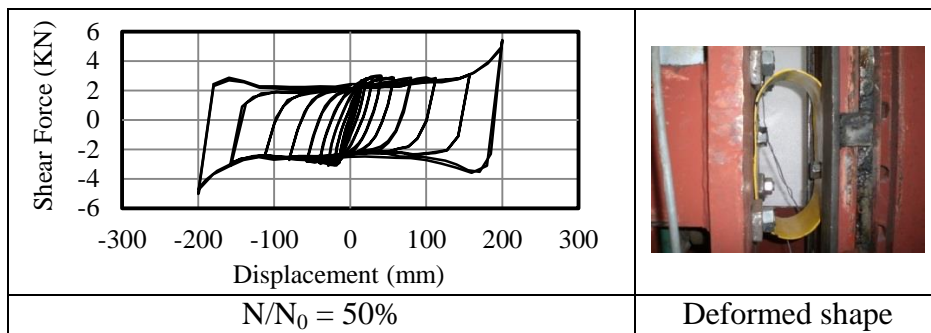


**Figure 3.9 :** Force-Displacement relation of 3mm thick specimen under tensile axial load of  $N/N_0=50\%$ .

The nominal yield strength is about 2.28 KN in tension part and 2.63KN in compression part under the axial load of 5.0 KN. In this level of constant tensile axial load, the steel cushions behaved symmetrically. There is no any reduction in the displacement capacity.

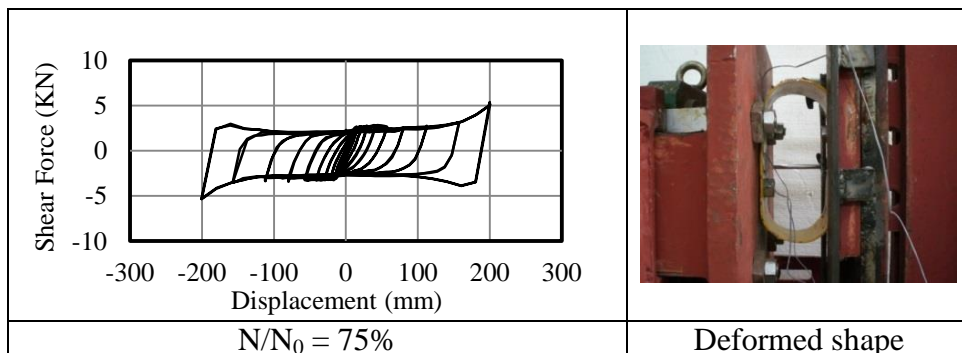


**Figure 3.10 :** Force-Displacement relation of  $t= 3\text{mm}$  thick specimens under tensile axial load of  $N/N_0=75\%$  KN.

The nominal yield strength is about 2.04 KN in tension part and nearly 2.90 KN in compression part under the axial load of 7.50 KN. In this level of constant tensile axial load, the steel cushion behaved asymmetrically. There is no any reduction in the displacement capacity.

The force-displacement relations t=3mm thick specimen are compared in Figure 3.11 with each other in two extreme states under N= 2.5 KN and N= 7.5 KN to show the effect of axial load in shear capacity. The nominal yield strength decreases up to 6.4% as the axial constant load increases. There is no any change in the displacement capacity.

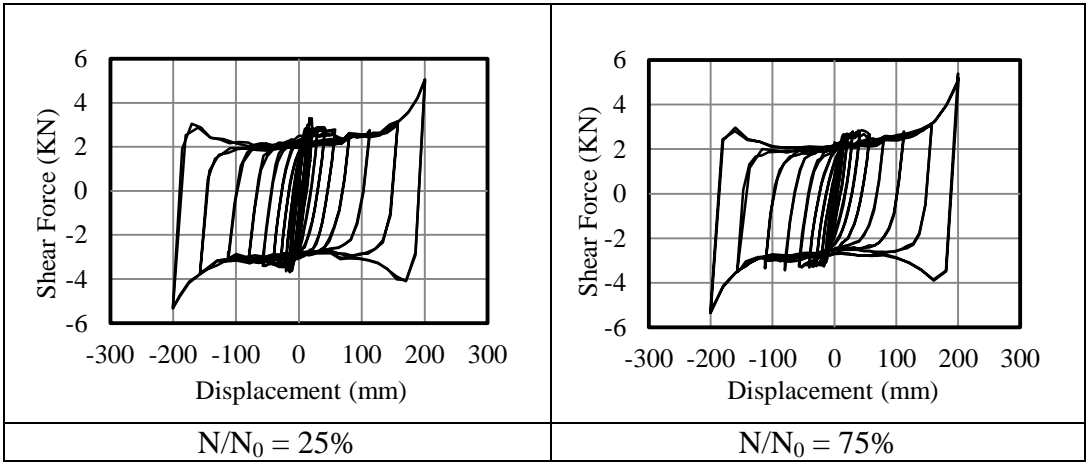


**Figure 3.11 :** Comparison of force-displacement relation for 3mm thick specimens under tensile axial stress.

The force - displacement relations which obtained from bi-directional shear and axial tension tests are presented in Figure 3.12, 3.13 and Figure 3.15 for t=5mm thick steel cushion subjected to  $N/N_0 = 25\%$ ,  $N/N_0 = 50\%$  and  $N/N_0 = 75\%$  respectively, the corresponding axial load values are 7.5, 15, and 25 KN.

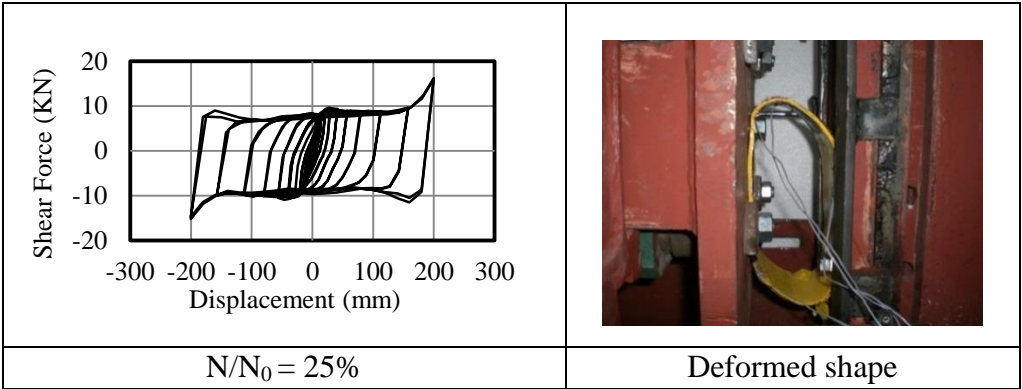


**Figure 3.12 :** Force-Displacement relation of 5mm thick specimen under tensile axial load of  $N/N_0=25\%$ .

The nominal yield strength is about 7.86 KN in tension part and 9.93KN in compression part under the axial load of 7.5 KN. In this level of constant tensile axial load, the steel cushion behaved asymmetrically. There is no any reduction in the displacement capacity.

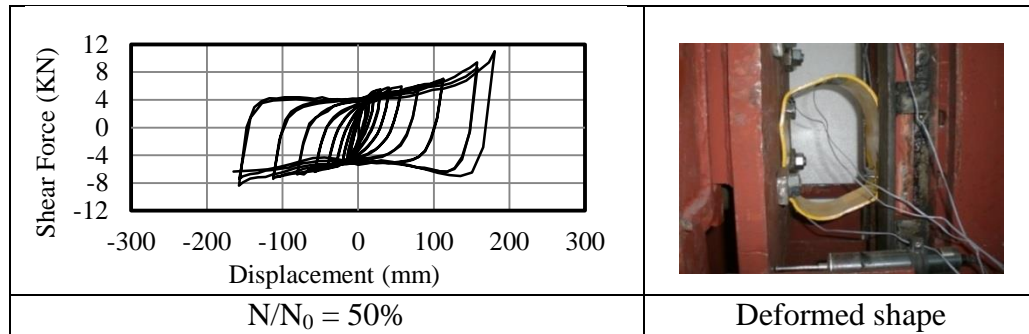


**Figure 3.13 :** Force-Displacement relation of 5mm thick specimen under tensile axial load of  $N/N_0=50\%$ .

The nominal yield strength is about 4 KN in tension part and 5.22 KN in compression part under the axial load of 15 KN. In this level of constant tensile axial load, the steel cushion behaved asymmetrically. In addition, rupture occurred in the final target displacement 200mm as it is shown in Figure 3.14.



**Figure 3.14 :** Rupture occurred at the final displacement target in 5mm steel cushion under tensile axial stress of 15 KN.

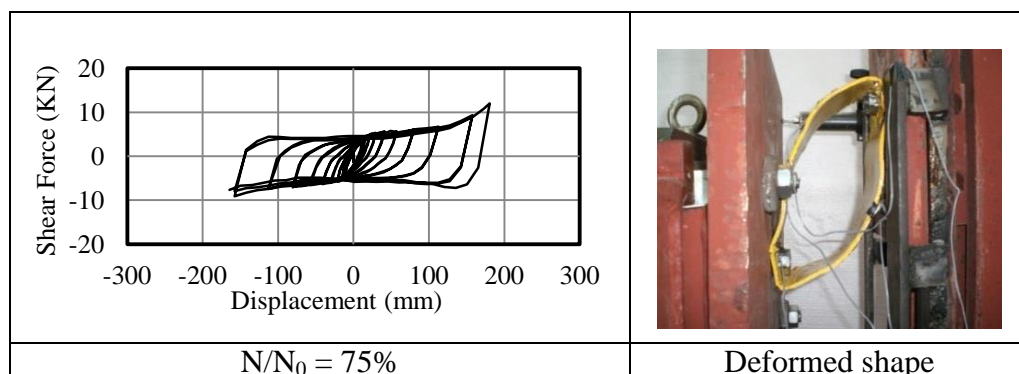


**Figure 3.15 :** Force-Displacement relation of 5mm thick specimen under tensile axial load of  $N/N_0=75\%$ .

The nominal yield strength is about 3.55KN in tension part and 5.19KN in compression part under the axial load of 25 KN. In this level of constant tensile axial load, the steel cushion behaved asymmetrically. In addition, cracking and rupture occurred in the final target displacement 200mm as it is shown in Figure 3.16.

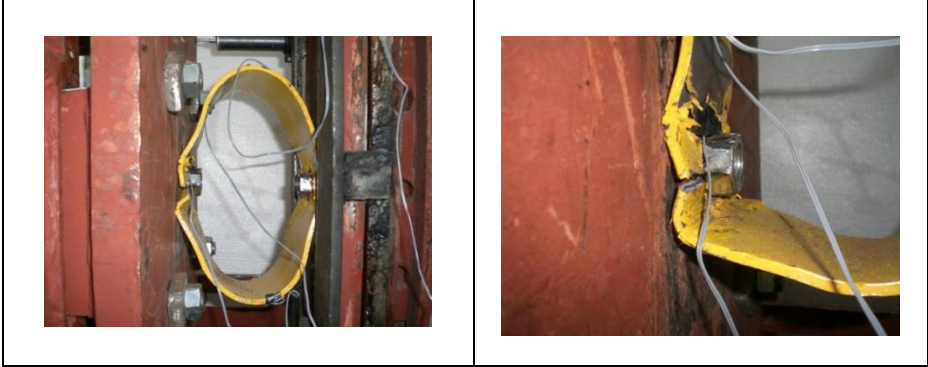


**Figure 3.16 :** Rupture occurred at the final displacement target in 5mm steel cushion under tensile axial stress of 25 KN.

The force-displacement relations  $t=5\text{mm}$  thick specimen are compared in Figure 3.17 with each other in two extreme states under  $N= 7.5 \text{ KN}$  and  $N= 25 \text{ KN}$  to show the effect of axial load in shear capacity. The nominal yield strength decreases up to 41% as the axial load increases. In addition, the increase of the tensile axial load causes a reduction in the displacement capacity.

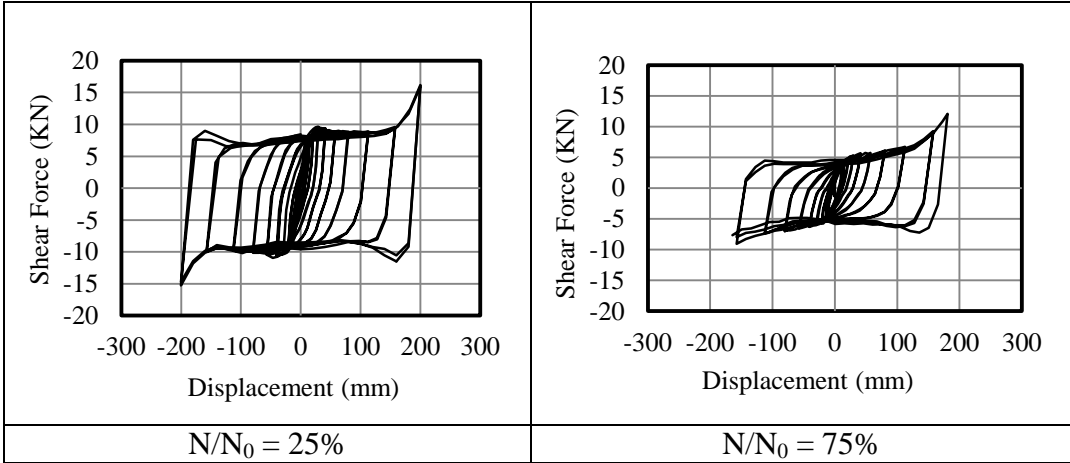


**Figure 3.17 :** Comparison of force-displacement relation for 5mm thick specimens under tensile axial stress.

The force - displacement relations which obtained from bi-directional shear and tensile axial tests are presented in Figure 3.18, 3.20 and Figure 3.22 for  $t=8\text{mm}$  thick steel cushion subjected to  $N/N_0 = 25\%$ ,  $N/N_0 = 50\%$  and  $N/N_0 = 75 \%$  respectively , the corresponding axial load values are 25, 50, and 75 KN.

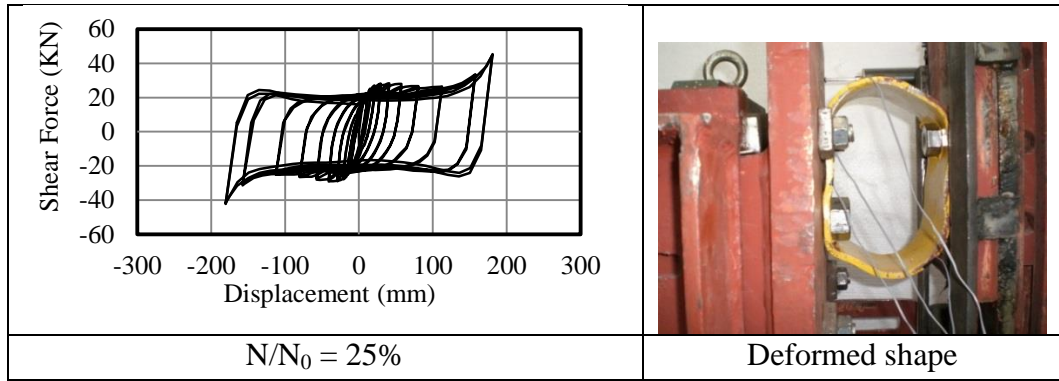


**Figure 3.18 :** Force-Displacement relation of 8mm thick specimens under tensile axial load of  $N/N_0=25\%$ .

The nominal yield strength is about 25.86KN in tension part and 25.68KN in compression part under the axial load of 25 KN. In this level of constant tensile axial load, the steel cushion behaved symmetrically. In addition, at the final displacement target of 200mm rupture occurred as it is shown in Figure 3.19.



**Figure 3.19 :** Rupture occurred at the final displacement target in 8mm steel cushion under tensile axial stress of 25 KN.

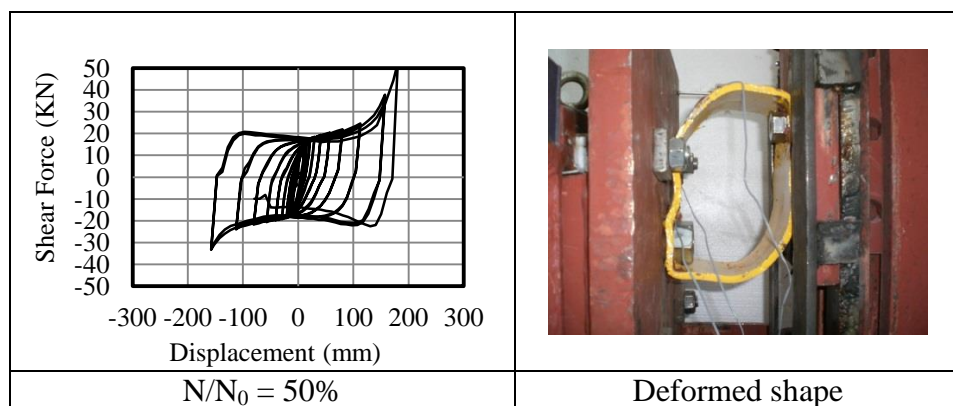


**Figure 3.20 :** Force-Displacement relation of 8mm thick specimens under tensile axial load of  $N/N_0=50\%$ .

The nominal yield strength is about 16.86KN in tension part and 16.86KN in compression part under the axial load of 50 KN. In this level of constant tensile axial

load the steel cushion behaved symmetrically. In addition, at the final displacement target of 200mm rupture occurred as it is shown in Figure 3.21.

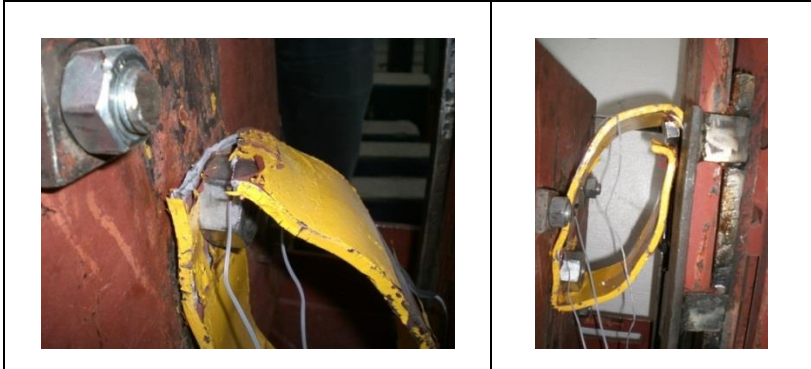


**Figure 3.21 :** Rupture occurred at the final displacement target in 8mm steel cushion under tensile axial stress of 50 KN.

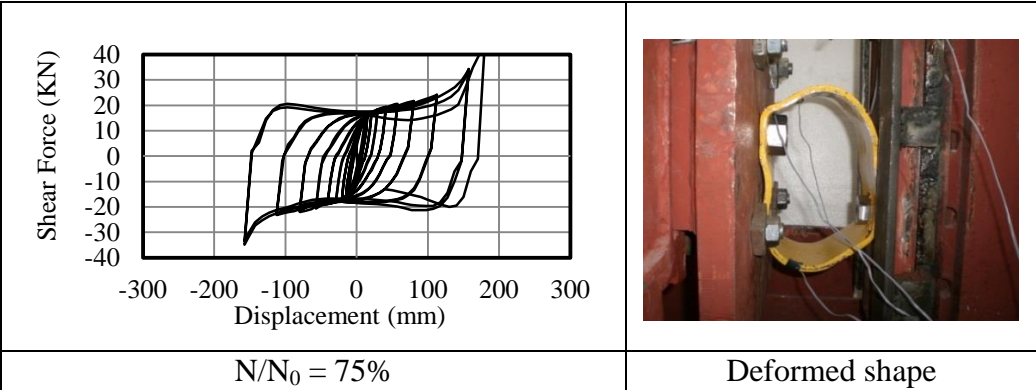


**Figure 3.22 :** Force-Displacement relation of 8mm thick specimens under tensile axial load of  $N/N_0=75\%$ .

The nominal yield strength is about 16.03KN in tension part and 17.03KN in compression part under the axial load of 75 KN. In this, level of constant tensile axial load the steel cushion behaved symmetrically. In addition, at the final displacement target of 200mm rupture occurred as it is shown in Figure 3.23.



**Figure 3.23 :** Rupture occurred at the final displacement target in 8mm steel cushion under tensile axial stress of 75KN.

The force-displacement relations for  $t=8\text{mm}$  thick specimens are compared in Figure 3.24 with each other in two extreme states under  $N=25\text{ KN}$  and  $N=75\text{ KN}$  to show the effect of axial load in shear capacity. The nominal yield strength decreases up to 36% as the axial constant load increases. In addition, there is reduction in the displacement capacity in the both cases.

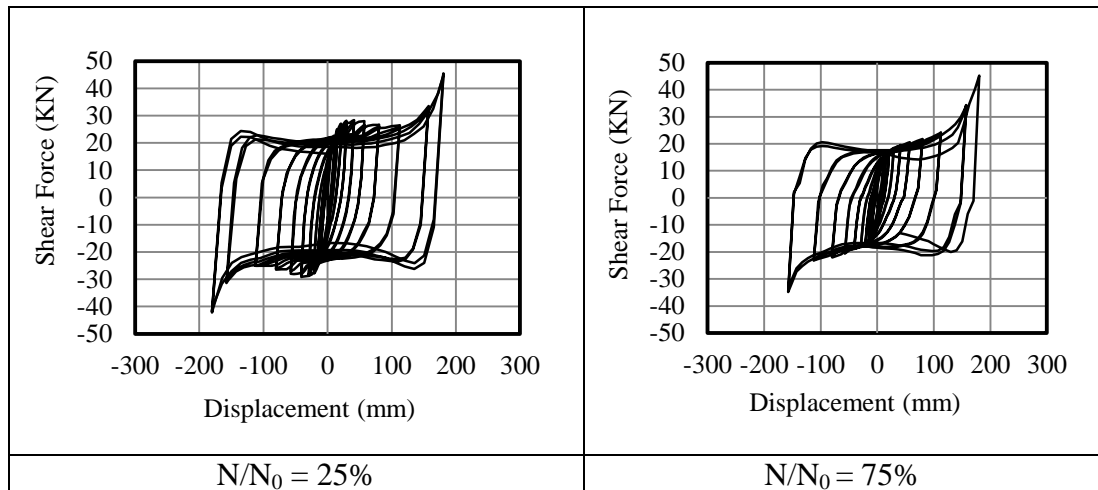


**Figure 3.24 :** Comparison of force-displacement relation for 8mm thick specimens under tensile axial stress.

The force-displacement relations for steel cushions in three distinct thicknesses under two extreme axial forces are compared in Figure 3.25. According to Figure 3.25, as the thickness increases, the shear yield strength increases as well.

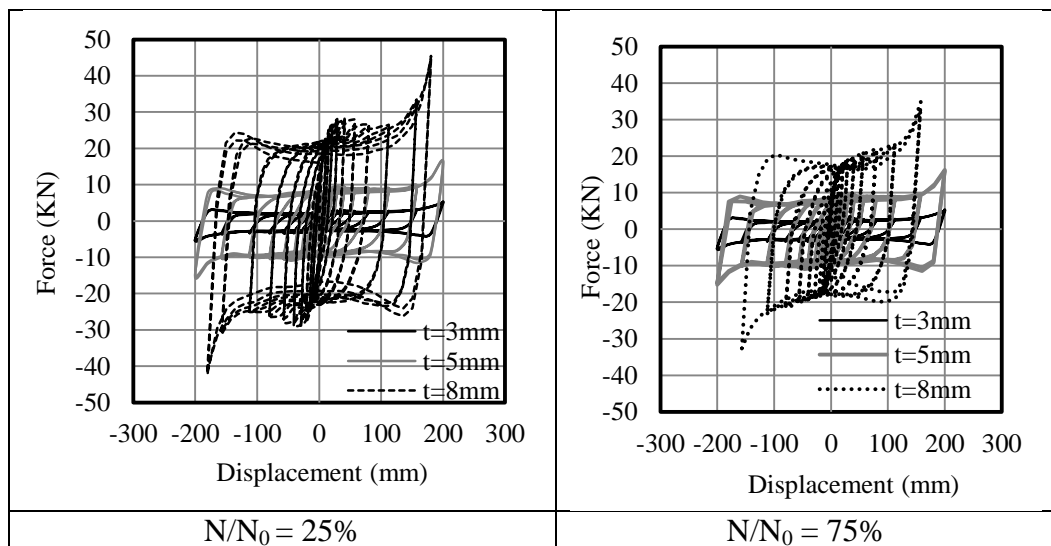


**Figure 3.25 :** Comparison of force-displacement relation in terms of different thicknesses under constant level of tensile axial load.

**3.2.2 Energy dissipation**

The cumulative energy in terms of displacement for t=3mm thick specimen subjected to constant tensile axial loads of N=2.5 KN, N=5 KN, and N=7.5 KN are displayed at Figure 3.26, 3.27, and Figure 3.28, respectively the corresponding axial load values are 2.5, 5 and 7.5 KN.

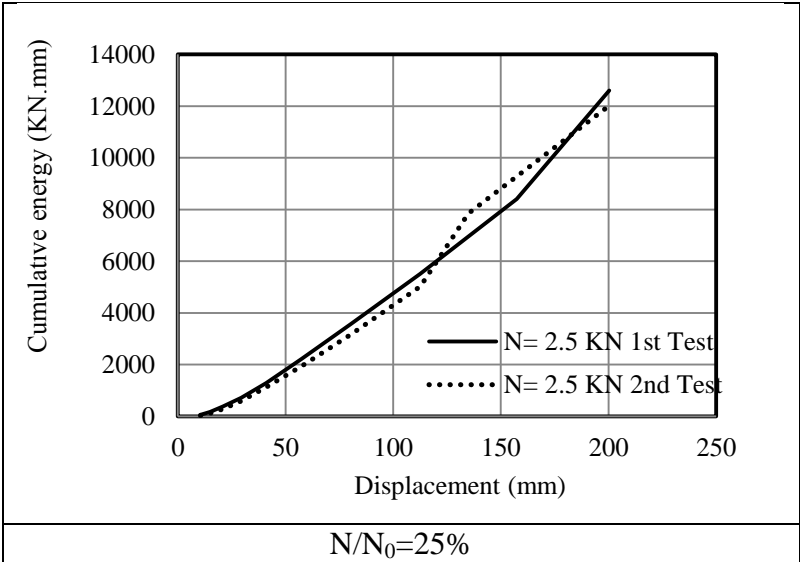


**Figure 3.26 :** Cumulative energy in terms of displacement for t=3mm thick steel cushions under constant tensile load of N=2.5 KN.

The cumulative energy capacity is 12603 and 12048 KN.mm for 3mm thick specimen in the first and second test respectively.

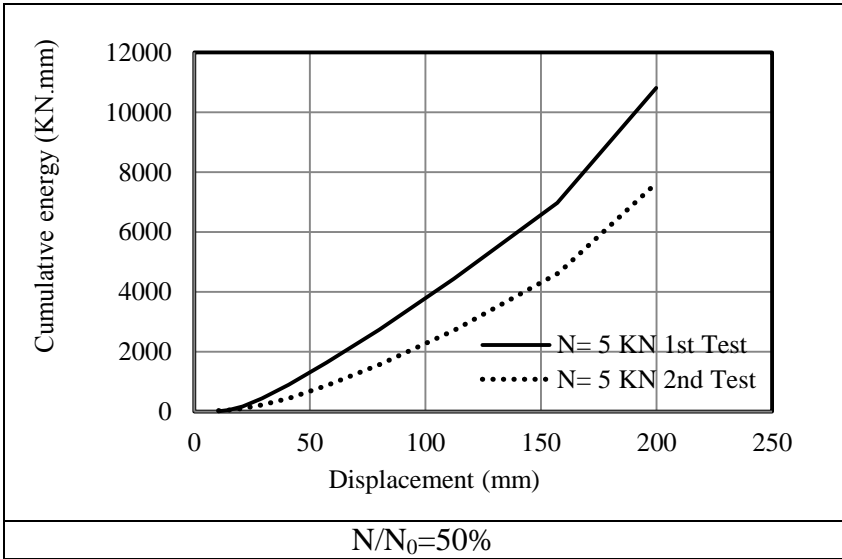


**Figure 3.27 :** Cumulative energy in terms of displacement for 3mm thick steel cushions under constant tensile load of N=5.0 KN.

The cumulative energy capacity is 10818 and 7672 KN.mm for 3mm thick specimen in the first and second test, respectively. This difference in the energy capacity can be because of experimental errors.

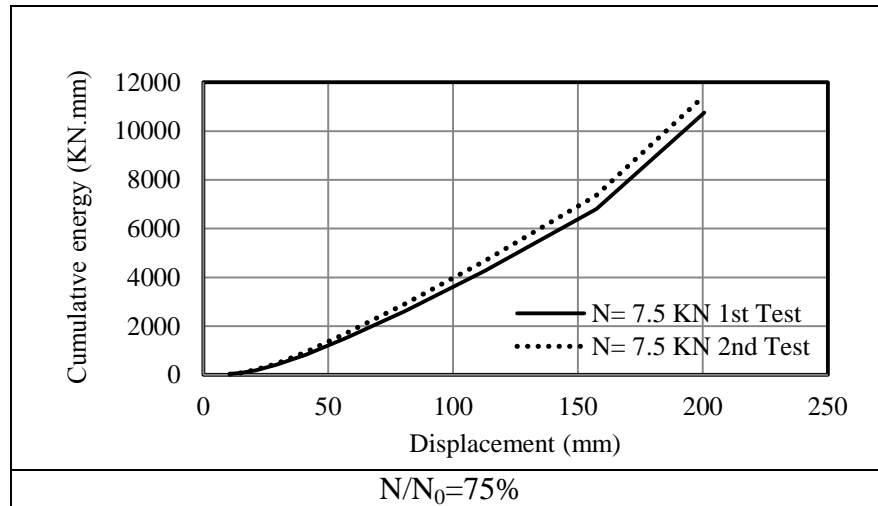


**Figure 3.28 :** Cumulative energy in terms of displacement for 3mm thick steel cushions under constant tensile load of  $N=2.50$  KN.

The cumulative energy capacity is 10754 and 11419KN.mm for 3mm thick specimen in the first and second test, respectively.

The cumulative capacity for  $t=3$ mm thick steel cushions in two extreme tensile axial load level of  $N/N_0=25\%$  and  $N/N_0=75\%$  are compared to show the effect of the tensile axial load in Figure 3.29.

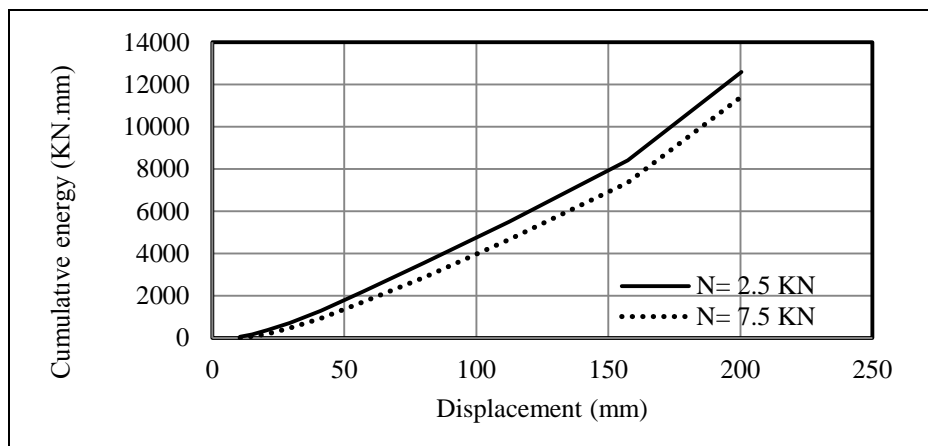


**Figure 3.29 :** Comparison of energy dissipation capacity for 3mm thick specimens under tensile axial stress in two extreme axial loads.

The increase of tensile axial load has the negative effect it reduces the cumulative energy capacity, however this reduction is not significant for  $t=3$ mm thick steel cushions according to the Figure 3.29.

The cumulative energy in terms of displacement for t=5mm thick specimen subjected to constant tensile axial loads of N=7.5 KN, N=15 KN, and N=25 KN are displayed at Figure 3.30, 3.31, and Figure 3.32 respectively, the corresponding axial load values are 7.5, 15 and 25 KN.

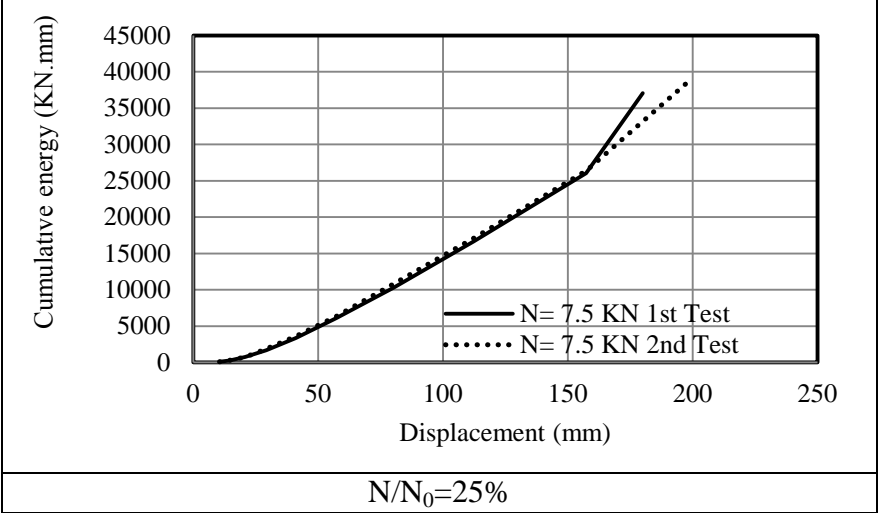


**Figure 3.30 :** Cumulative energy in terms of displacement for 5mm thick steel cushions under constant tensile load of N=7.5 KN.

The cumulative energy capacity is 37053 and 39158 KN.mm for 5mm thick specimen in the first and second test respectively.

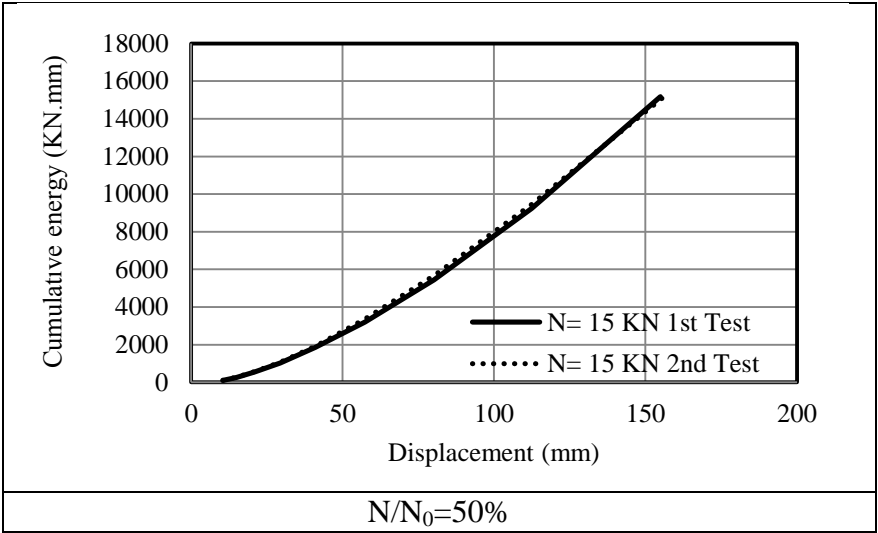


**Figure 3.31 :** Cumulative energy in terms of displacement for 5mm thick steel cushions under constant tensile load of N=15 KN.

The cumulative energy capacity is 15299 KN.mm for 5mm thick specimen in the first and second test.

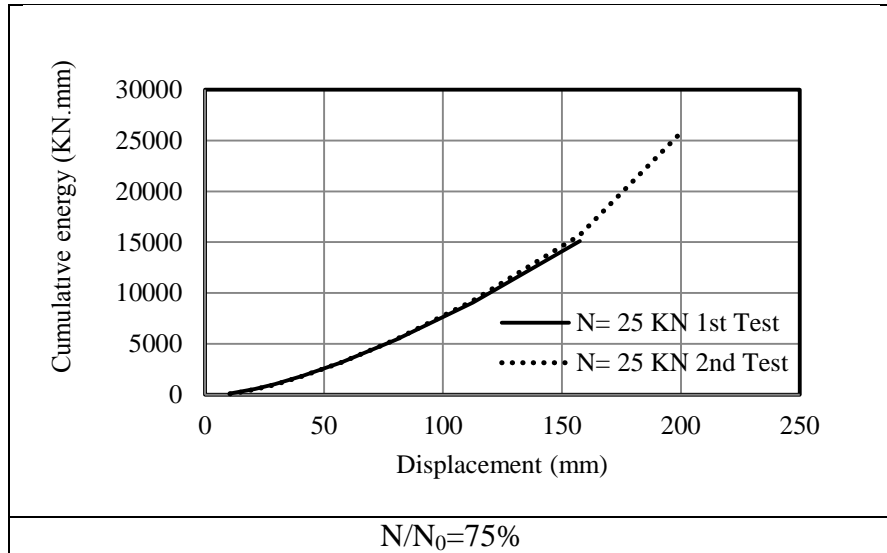


**Figure 3.32 :** Cumulative energy in terms of displacement for 5mm thick steel cushions under constant tensile load of  $N=25$  KN.

The cumulative energy capacity is 15658 and 25744 KN.mm for 5mm thick specimen in the first and second test, respectively. It should be noted that the rupture occurred at the first test in the final displacement targets.

The cumulative capacity for  $t=5$ mm thick steel cushions in two extreme tensile axial load level of  $N/N_0=25\%$  and  $N/N_0=75\%$  are compared to show the effect of the tensile axial load in Figure 3.33.

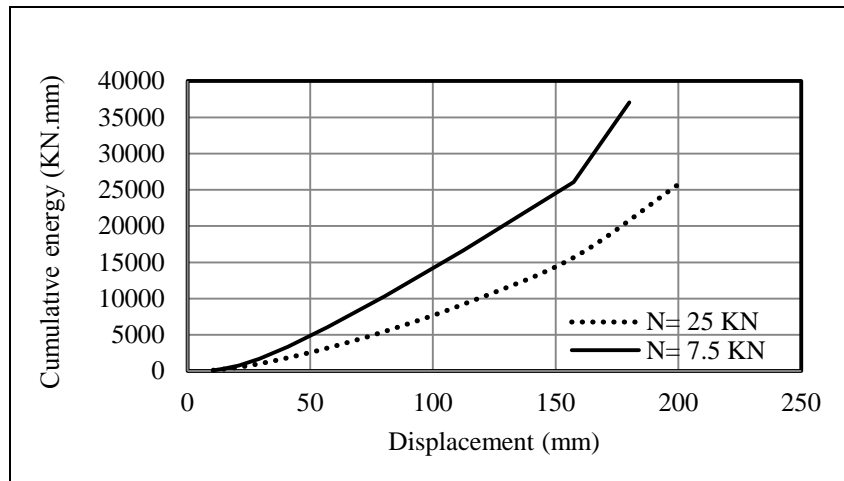


**Figure 3.33 :** Comparison of energy dissipation capacity for 5mm thick specimens under tensile axial stress in two extreme axial loads.

The increase of tensile axial load has the negative effect it reduces the cumulative energy capacity up to 30.5 % for  $t=5$ mm thick steel cushions according to the Figure 3.33. It should be noted that the rupture occurred at the first test in the final displacement target.

The cumulative energy in terms of displacement for t=8mm thick specimen subjected to constant tensile axial loads of N=25.0 KN, N=50.0 KN, and N=75.0 KN are displayed at Figure 3.34, 3.35 and Figure 3.36, respectively, the corresponding axial load values are 25, 50 and 75 KN.

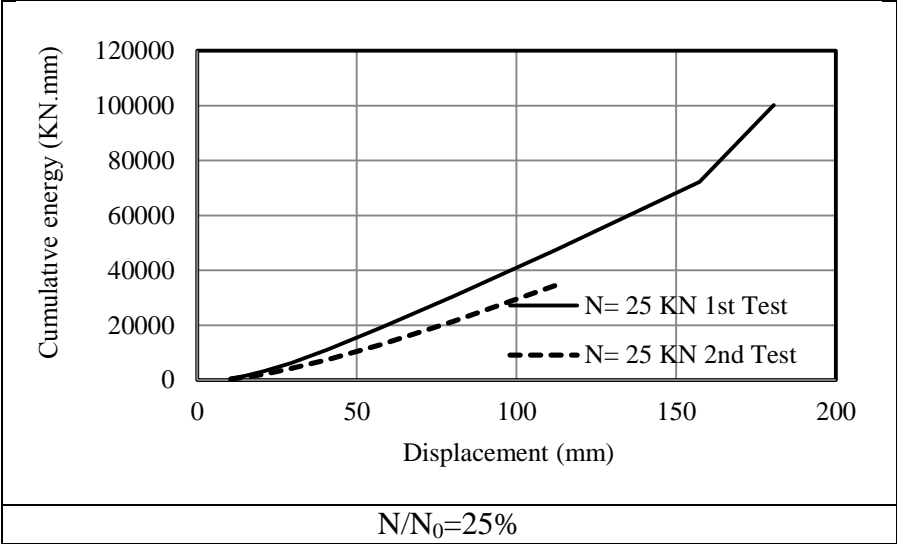


**Figure 3.34 :** Cumulative energy in terms of displacement for 8mm thick steel cushions under constant tensile load of N=25 KN.

The cumulative energy capacity is 100179 and 34488 KN.mm for 8mm thick specimen in the first and second test, respectively. It should be noted that the rupture occurred at the second test in the final displacement targets.

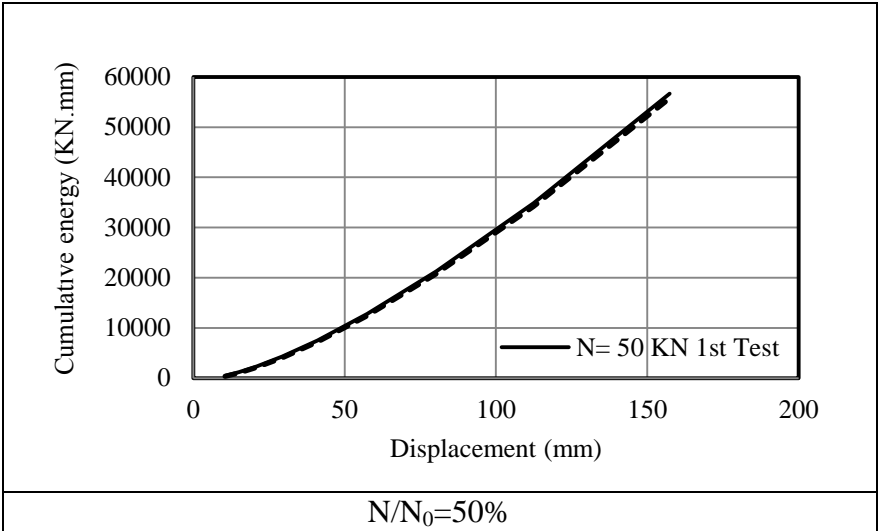


**Figure 3.35 :** Cumulative energy in terms of displacement for 8mm thick steel cushions under constant tensile load of N=50 KN.

The cumulative energy capacity is 55625 KN.mm for 8mm thick specimen in the first and second test.

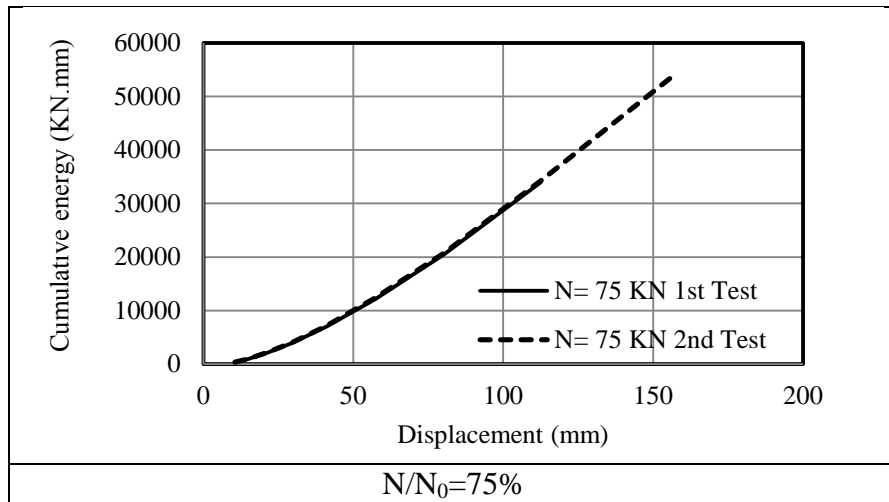


**Figure 3.36 :** Cumulative energy in terms of displacement for 8mm thick steel cushions under constant tensile load of N=75 KN.

The cumulative energy capacity is 34025 and 54118 KN.mm for 5mm thick specimen in the first and second test, respectively. It should be noted that the rupture occurred at the second test in the final displacement targets.

The cumulative capacity for t=8mm thick steel cushions in two extreme tensile axial load level of  $N/N_0=25\%$  and  $N/N_0=75\%$  are compared to show the effect of the tensile axial load in Figure 3.37.

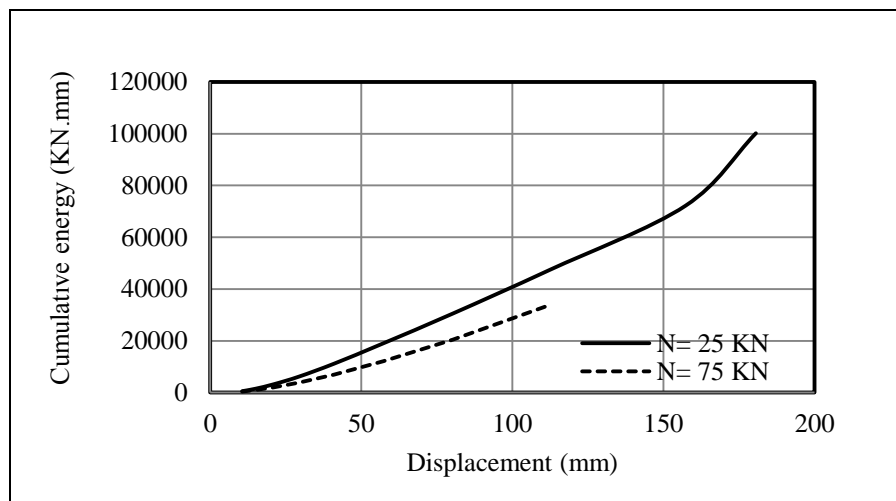


**Figure 3.37 :** Comparison of energy dissipation capacity for 8mm thick specimens under tensile axial stress in two extreme axial loads.

The increase of tensile axial load has the negative effect it reduces the cumulative energy capacity up to 66 % for t=8mm thick steel cushions according to the Figure 3.37. It should be noted that the rupture occurred under the axial load level of 75 KN in 8mm thick specimen in the final displacement targets.

### 3.2.3 Equivalent viscous damping

The equivalent damping in terms of displacement for  $t=3\text{mm}$  thick specimen subjected to constant tensile axial loads of  $N=2.5\text{ KN}$ ,  $N=5.0\text{ KN}$ , and  $N=7.5\text{ KN}$  are displayed at Figure 3.38, 3.39 and Figure 3.40 respectively.

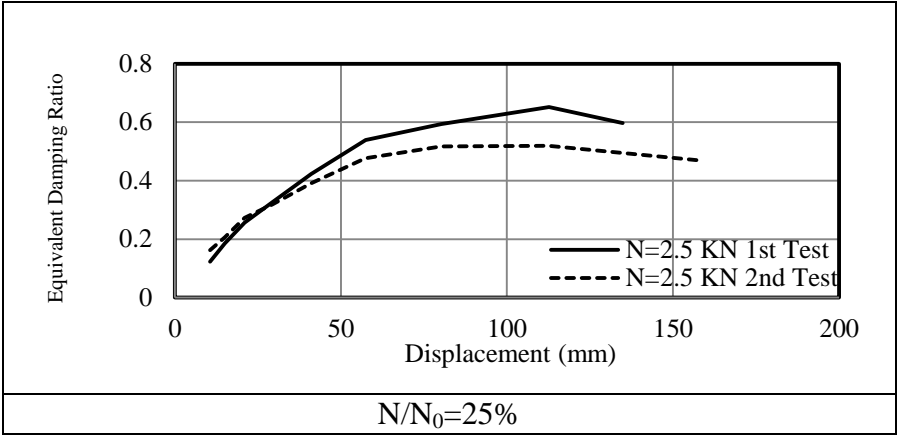


**Figure 3.38 :** Equivalent damping ratio in terms of displacement for 3mm thick steel cushions under constant tensile load of  $N=2.5\text{ KN}$ .

The maximum equivalent damping ratio is 65% and 52% for 3mm thick specimen in the first and second test respectively. It should be noted that the falling section of the equivalent damping ratio curves are not plotted up to final displacement target since the maximum equivalent damping is important.

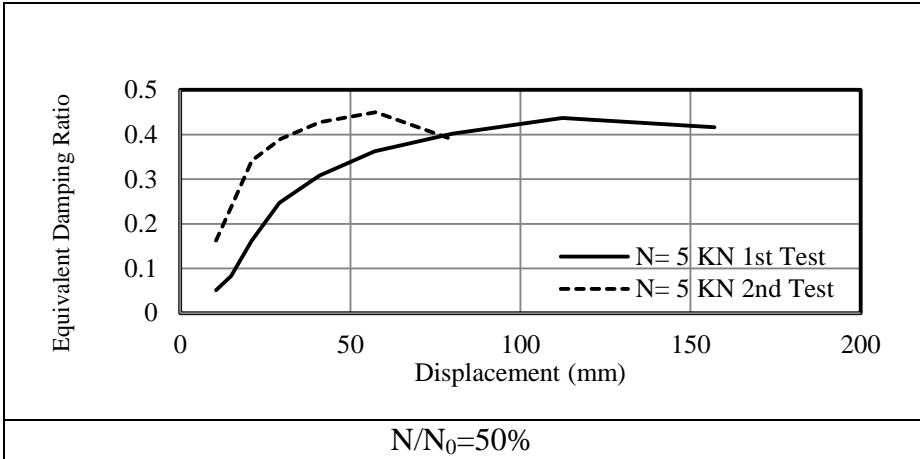


**Figure 3.39 :** Equivalent damping ratio in terms of displacement for 3mm thick steel cushions under constant tensile load of  $N=5\text{ KN}$ .

The maximum equivalent damping ratio is 44% and 45% for 3mm thick specimen in the first and second test respectively. It should be noted that the falling section of the equivalent damping ratio curves are not plotted up to final displacement target since the maximum equivalent damping is important.

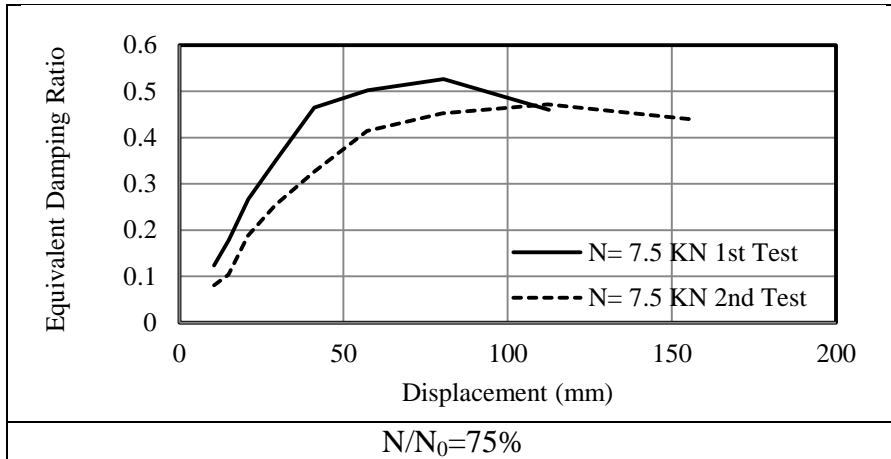


**Figure 3.40 :** Equivalent damping ratio in terms of displacement for 3mm thick steel cushions under constant tensile load of  $N=7.5$  KN.

The maximum equivalent damping ratio is 53% and 47% for 3mm thick specimen in the first and second test respectively. It should be noted that the falling section of the equivalent damping ratio curves are not plotted up to final displacement target since the maximum equivalent damping is important.

The equivalent damping ratio for  $t=3$ mm thick steel cushions in two extreme tensile axial load level of  $N/N_0=25\%$  and  $N/N_0=75\%$  are compared to show the effect of the tensile axial load in Figure 3.41.

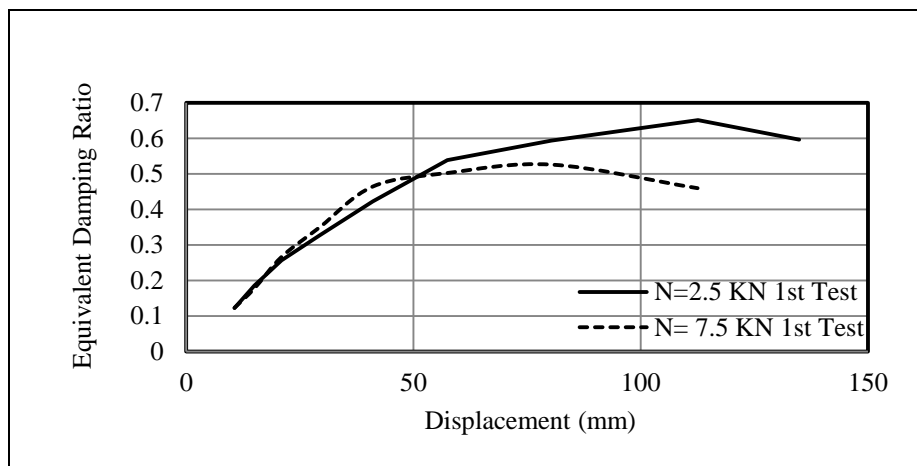


**Figure 3.41 :** Comparison of equivalent damping ratio for  $t= 3$ mm thick specimens under two extreme tensile axial loads.

The tensile axial load has the negative effect as it increases from 2.5 KN to 7.5 KN the maximum equivalent damping ratio decreases from 65% to 53% in  $t=3$ mm thick steel cushions according to the Figure 3.41. It should be noted that the falling section of the equivalent damping ratio curves are not plotted up to final displacement target since the maximum equivalent damping is important.

The equivalent damping in terms of displacement for  $t=5\text{mm}$  thick specimen subjected to constant tensile axial loads of  $N=7.5\text{ KN}$ ,  $N=15\text{ KN}$ , and  $N=25\text{ KN}$  are displayed at Figure 3.42, 3.43 and Figure 3.44, respectively.

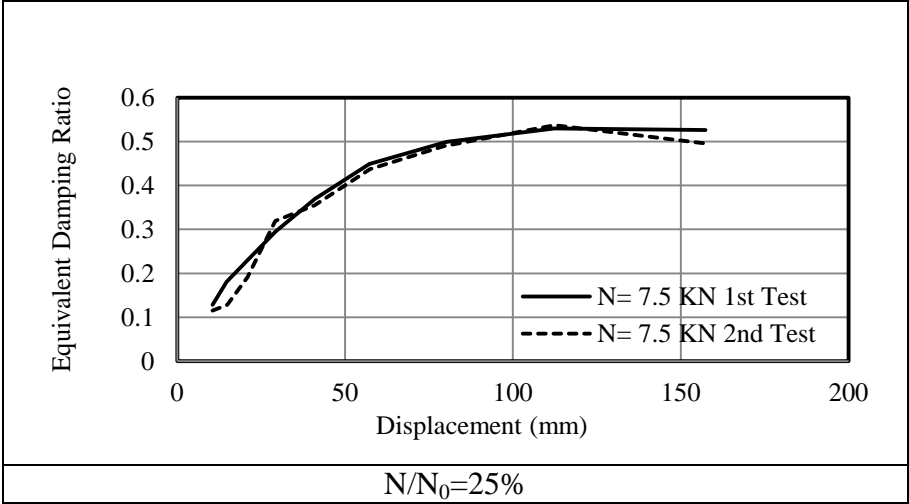


**Figure 3.42 :** Equivalent damping ratio in terms of displacement for 5mm thick steel cushions under constant tensile load of  $N=7.5\text{ KN}$ .

The maximum equivalent damping ratio is 54% for 5mm thick specimen in the first and second test.

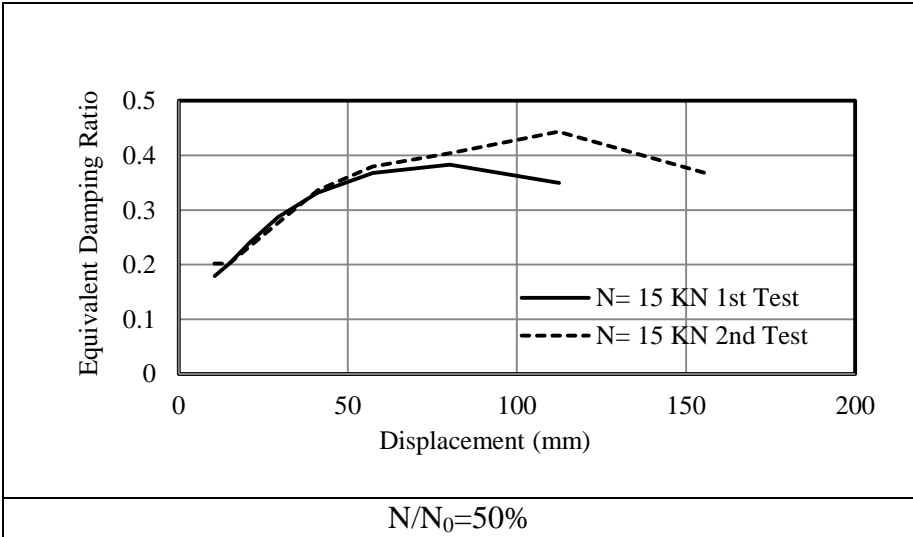


**Figure 3.43 :** Equivalent damping ratio in terms of displacement for 5mm thick steel cushions under constant tensile load of  $N=15\text{ KN}$ .

The maximum equivalent damping ratio is 38% and 44% for 5mm thick specimen in the first and second test respectively. It should be noted that the falling section of the equivalent damping ratio curves are not plotted up to final displacement target since the maximum equivalent damping is important.

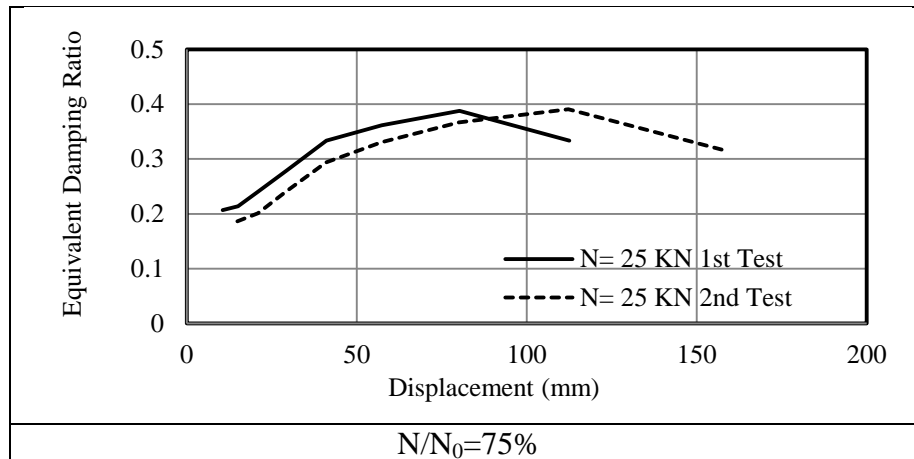


**Figure 3.44 :** Equivalent damping ratio in terms of displacement for 5mm thick steel cushions under constant tensile load of  $N=25$  KN.

The maximum equivalent damping ratio is 38% and 39% for 5mm thick specimen in the first and second test respectively. It should be noted that the falling section of the equivalent damping ratio curves are not plotted up to final displacement target since the maximum equivalent damping is important.

The equivalent damping ratio for  $t=5$ mm thick steel cushions in two extreme tensile axial load level of  $N/N_0=25\%$  and  $N/N_0=75\%$  are compared in Figure 3.45 to show the effect of the tensile axial load.

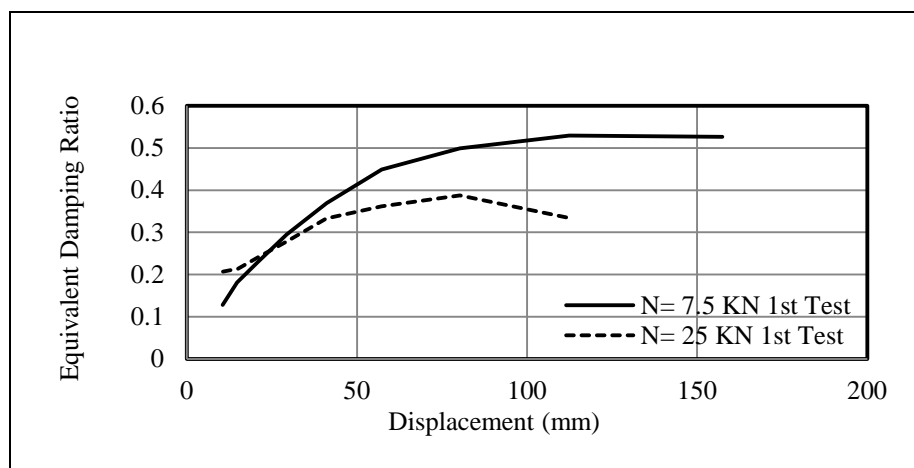


**Figure 3.45 :** Comparison of equivalent damping ratio for 5mm thick specimens under two extreme tensile axial loads.

The tensile axial load has the negative effect as it increases, the maximum equivalent damping ratio decreases from 53% to 39% in  $t=5$ mm thick steel cushions according to the Figure 3.45. It should be noted that the falling section of the equivalent damping ratio curves are not plotted up to final displacement target since the maximum equivalent damping is important.

The equivalent damping in terms of displacement for  $t=8\text{mm}$  thick specimen subjected to constant tensile axial loads of  $N=25\text{ KN}$ ,  $N=50\text{ KN}$ , and  $N=75\text{ KN}$  are displayed at Figure 3.46, 3.47 and Figure 3.48, respectively.

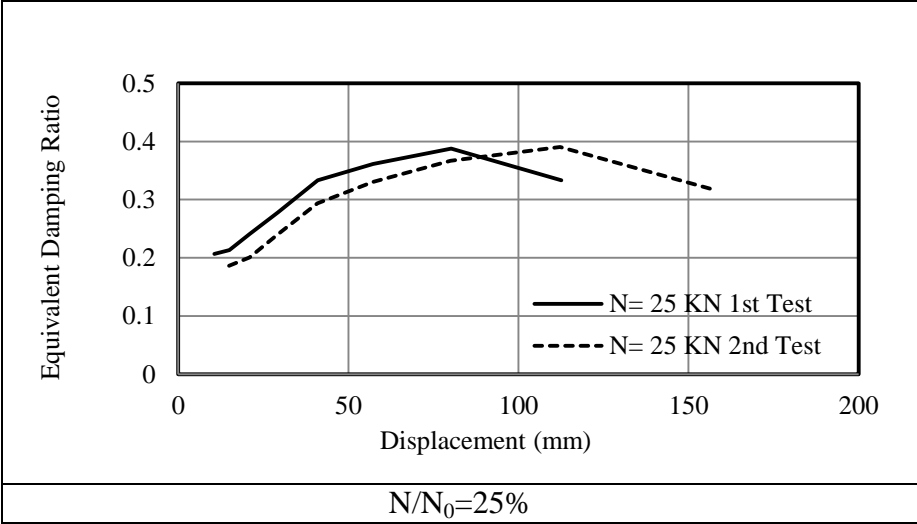


**Figure 3.46 :** Equivalent damping ratio in terms of displacement for 8mm thick steel cushions under constant tensile load of  $N=25\text{ KN}$ .

The maximum equivalent damping ratio is 37% and 39% for 5mm thick specimen in the first and second test respectively. It should be noted that the falling section of the equivalent damping ratio curves are not plotted up to final displacement target since the maximum equivalent damping is important.

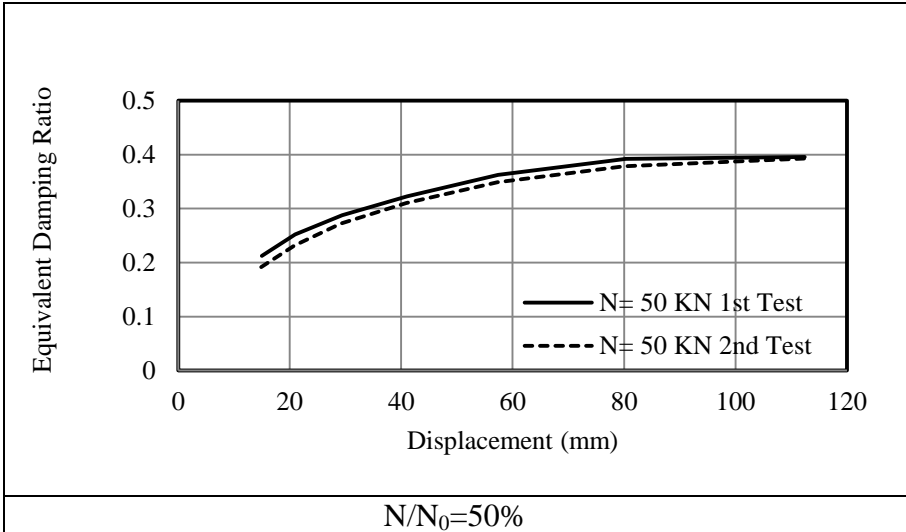


**Figure 3.47 :** Equivalent damping ratio in terms of displacement for 8mm thick steel cushions under constant tensile load of  $N=50\text{ KN}$ .

The maximum equivalent damping ratio is 39% for 5mm thick specimen in the first and second test.

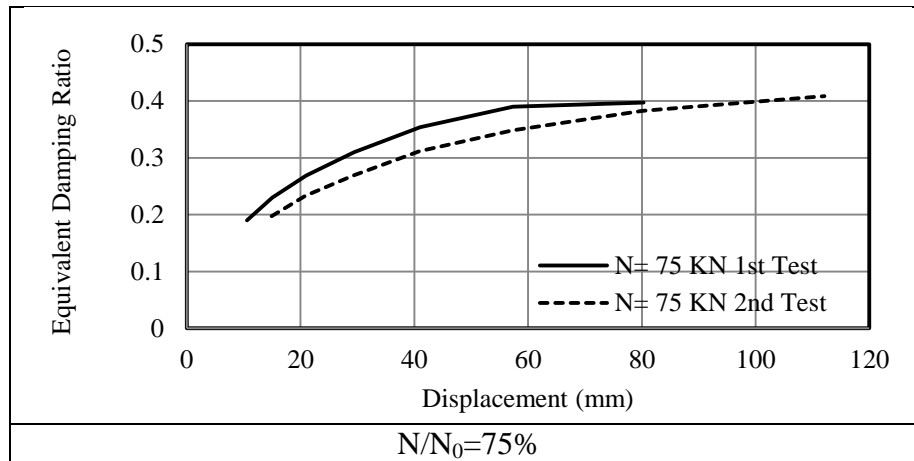


**Figure 3.48 :** Equivalent damping ratio in terms of displacement for 8mm thick steel cushions under constant tensile load of  $N=75$  KN.

The maximum equivalent damping ratio is 39% and 41% for 5mm thick specimen in the first and second test respectively. It should be noted that the falling section of the equivalent damping ratio curves are not plotted up to final displacement target since the maximum equivalent damping is important.

The equivalent damping ratio for  $t=8$ mm thick steel cushions in two extreme tensile axial load level of  $N/N_0=25\%$  and  $N/N_0=75\%$  are compared to show the effect of the tensile axial load in Figure 3.49.

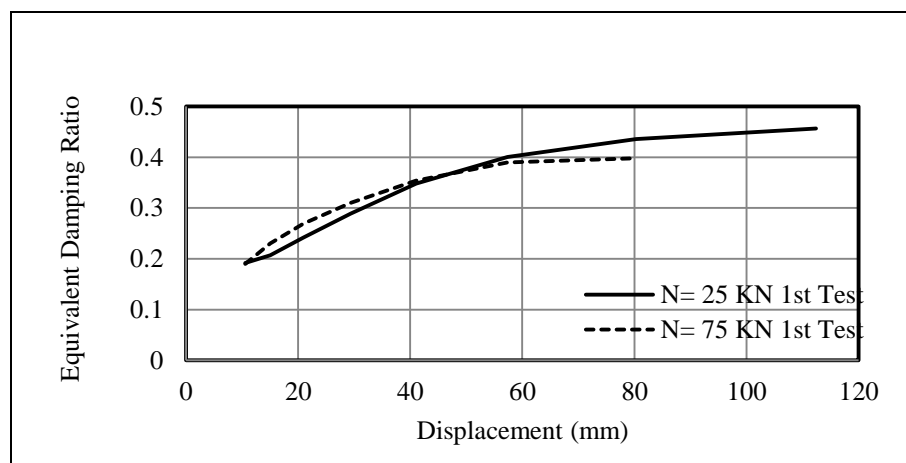


**Figure 3.49 :** Comparison of equivalent damping ratio for 8mm thick specimens under two extreme tensile axial loads.

The tensile axial load has the negative effect as it increases, the maximum equivalent damping ratio decreases from 46% to 40% in  $t=8$ mm thick steel cushions according to the Figure 3.49. It should be noted that the falling section of the equivalent damping ratio curves are not plotted up to final displacement target since the maximum equivalent damping is important.

The equivalent damping ratio for three distinct thicknesses in two extreme axial loads of  $N/N_0=25\%$  and  $N/N_0=75\%$  are compared in Figure 3.50.

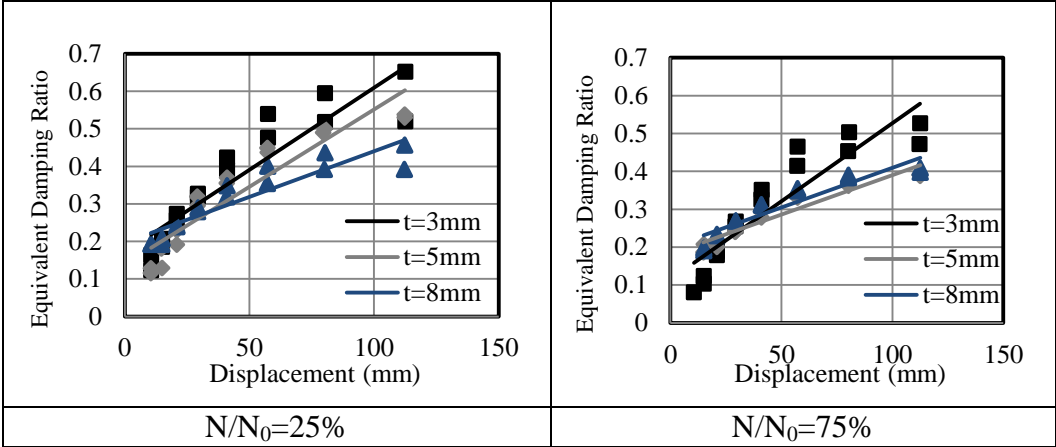


**Figure 3.50 :** Comparison of equivalent damping ratio for three distinct thicknesses under two extreme tensile axial loads.

In the case of  $N/N_0=25\%$  the equivalent damping ratio increases with increasing thickness. In the case of  $N/N_0 = 75\%$ , as the axial load increases from 25% to 75% the damping ratios arrangement does not change significantly.

**3.2.4 Effective (secant) stiffness**

The relationship between the ratio of  $K_{secant}$  to  $K_{initial}$  versus displacement for three specific specimens with thickness of  $t= 3\text{mm}$ ,  $5\text{mm}$  and  $8\text{mm}$  subjected to tensile axial loads of  $N/N_0=25\%$ ,  $50\%$  and  $75\%$  are compared in Figure 3.51, 3.52 and Figure 3.53 respectively this ratio in fact represents the velocity of the stiffness decadence.

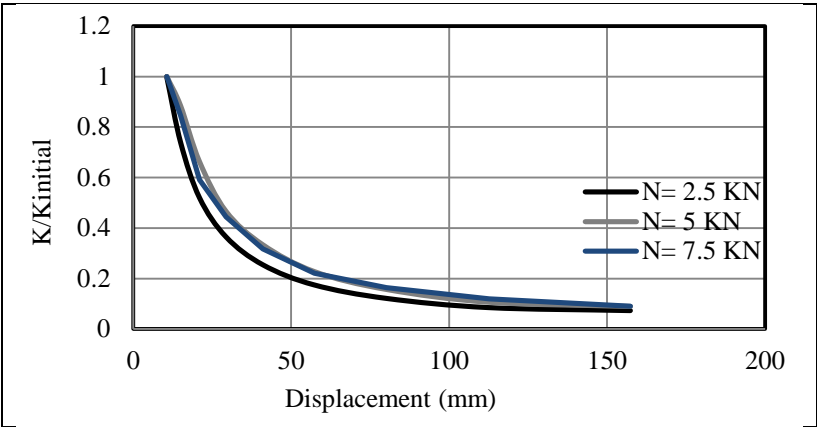


**Figure 3.51 :** Comparison of normalized stiffness ratio in terms of displacement for 3mm thick specimen under constant tensile axial loads.

According to Figure 3.51 the rate of stiffness decrease are independent of axial load value. Since, in all three states the mentioned rates are nearly identical.

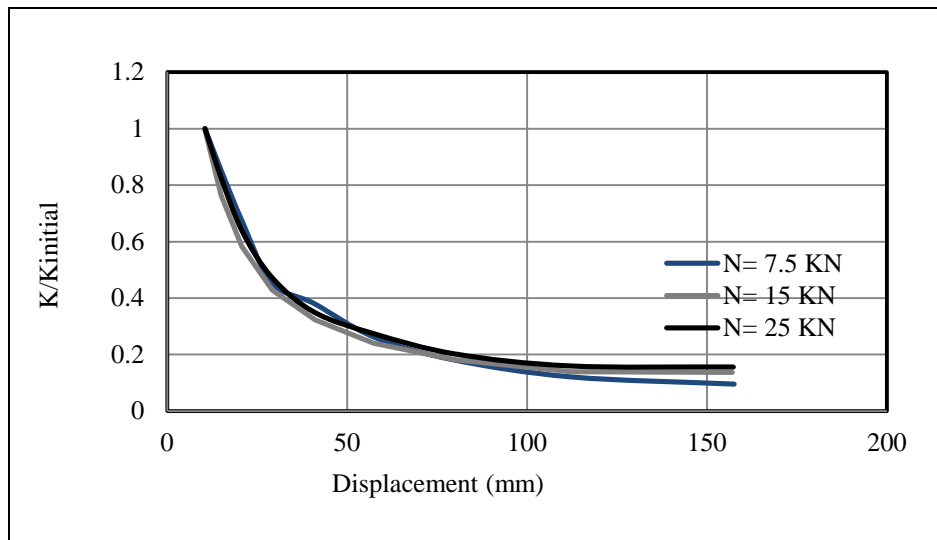


**Figure 3.52 :** Comparison of normalized stiffness ratio in terms of displacement for 5mm thick specimen under constant tensile axial loads.

According to Figure 3.52 the rate of stiffness decrease are independent of axial load value for  $t=5\text{mm}$  as well. Since, in all three states the mentioned rates are nearly identical.

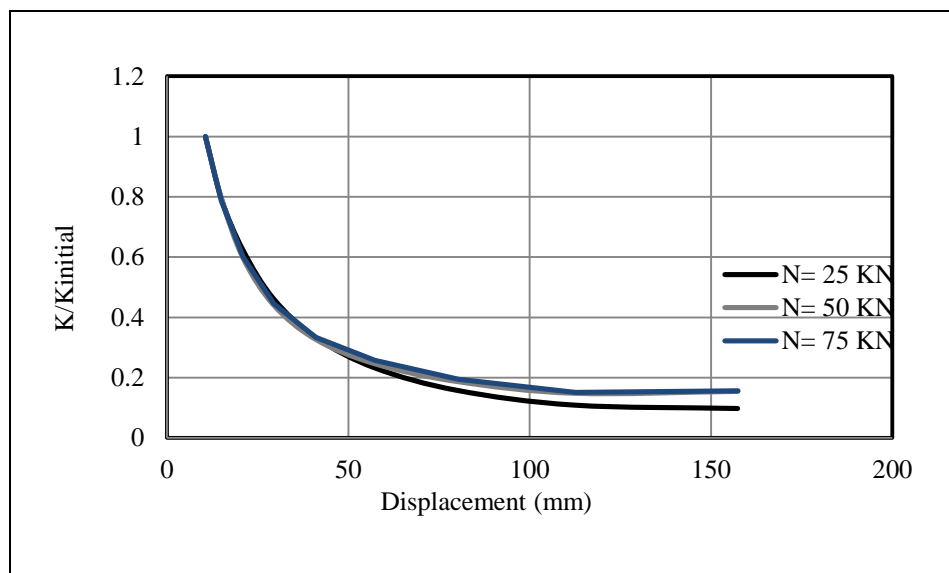


**Figure 3.53 :** Comparison of normalized stiffness ratio in terms of displacement for 8mm thick specimen under constant tensile axial loads.

In 8mm thick specimen the same logic exists similar to 5mm and 3mm thick specimens.

### 3.3 Evaluation of Experimental Results for Three Specific Specimens under Bi-Directional Shear + Tension Loading

The experimental results derived from the bi-directional cyclic shear and tensile axial test for three different specimens are summarized at Table 3.2.

**Table 3.2 :** Summary of experimental results derived from bi-directional cyclic shear and tensile axial test.

Specimen Type	Axial Load Ratio $N/N_0$	Initial stiffness $K_0$ KN/mm	Yield Force (KN)	Max Force (KN)	Yield Displacement $D_y$ (mm)	Ultimate Displacement $D_u$ (mm)	Ductility $\mu$
3mm thick Specimen	25%	0.26	3.97	4.10	15.0	157.71	10.51
	25%	0.33	3.44	3.76	10.57	157.47	14.90
	50%	0.15	3.10	3.13	20.91	157.42	7.53
	50%	0.07	0.70	3.43	10.58	157.58	14.89
	75%	0.26	2.73	3.74	10.61	157.74	14.87
	75%	0.18	2.67	3.51	14.96	157.28	10.52
5mm thick Specimen	25%	0.51	5.39	10.47	10.51	157.48	14.98
	25%	0.54	8.01	10.94	14.93	157.56	10.55
	50%	0.19	5.67	9.40	29.32	152.54	5.20
	50%	0.39	4.10	10.0	10.49	157.53	15.02
	75%	0.39	4.14	9.28	10.58	157.57	14.89
	75%	0.33	3.45	10.33	10.50	157.33	15.0
8mm thick Specimen	25%	2.09	22.14	33.52	10.57	157.59	14.91
	25%	1.39	14.61	35.02	10.51	157.19	14.95
	50%	1.33	14.11	37.75	10.59	157.50	14.88
	50%	1.28	14.09	35.25	11.0	157.44	15.0
	75%	1.27	13.34	34.92	10.48	157.43	15.02
	75%	1.32	13.95	34.83	10.59	157.43	14.87

#### 3.3.1 Ductility

The trend line of ductility for 3mm, 5mm and 8mm thick specimens under increase of tensile axial loads from  $N/N_0=25\%$ , to  $75\%$  in bi-directional cyclic shear and axial test are displayed test in Figure 3.54, 3.55 and Figure 3.56, respectively. The ductility remains constant for 3mm thick specimen as tensile axial load increases, as shown in Figure 3.54.

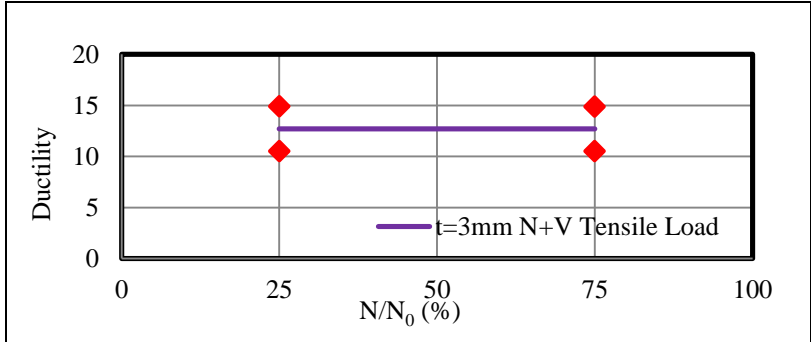


**Figure 3.54 :** Ductility trend for 3mm thick specimen under increase of tensile axial load.

The ductility increases for 5mm thick specimen under increase of tensile axial load, as shown in Figure 3.55.

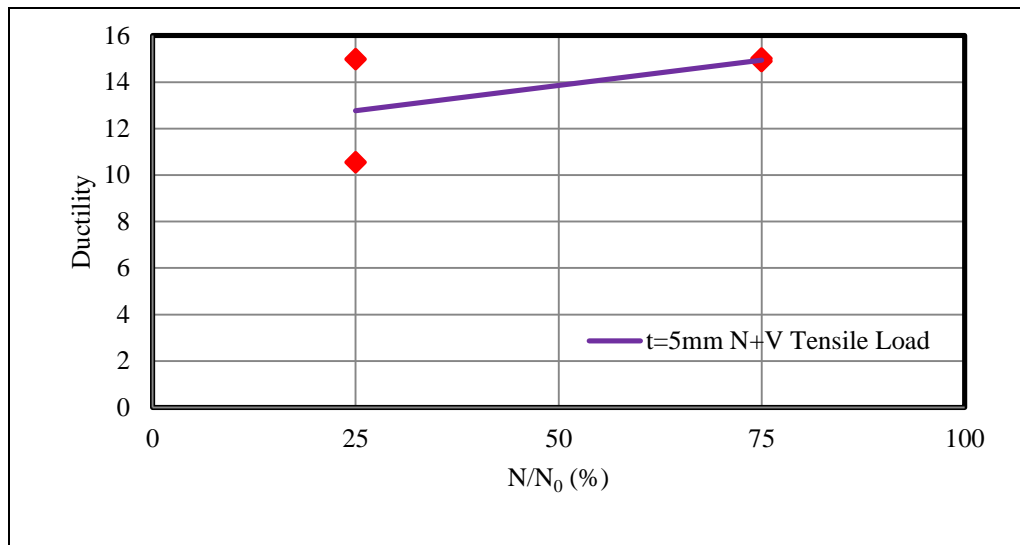


**Figure 3.55** : Ductility trend for 5mm thick specimen under increase of tensile axial load.

The ductility increases for 8mm thick specimen under increase of tensile axial load, as shown in Figure 3.56.

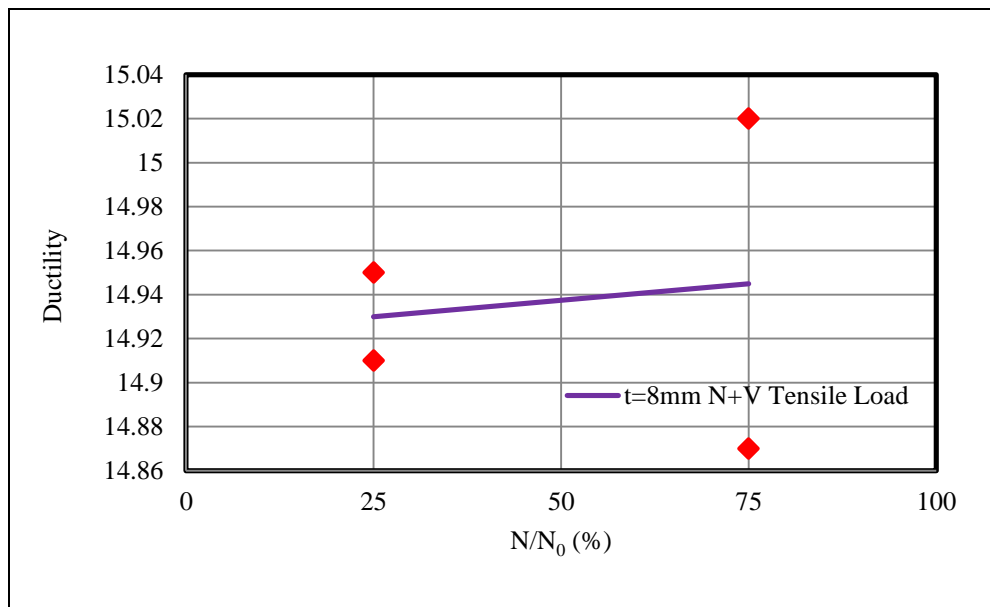


**Figure 3.56** : Ductility trend for 8mm thick specimen under increase of tensile axial load.

### 3.3.2 Yield force and yield displacement

The yield force decreases for 8mm thick specimen as tensile axial load increases up to 50% as shown in Figure 3.57.

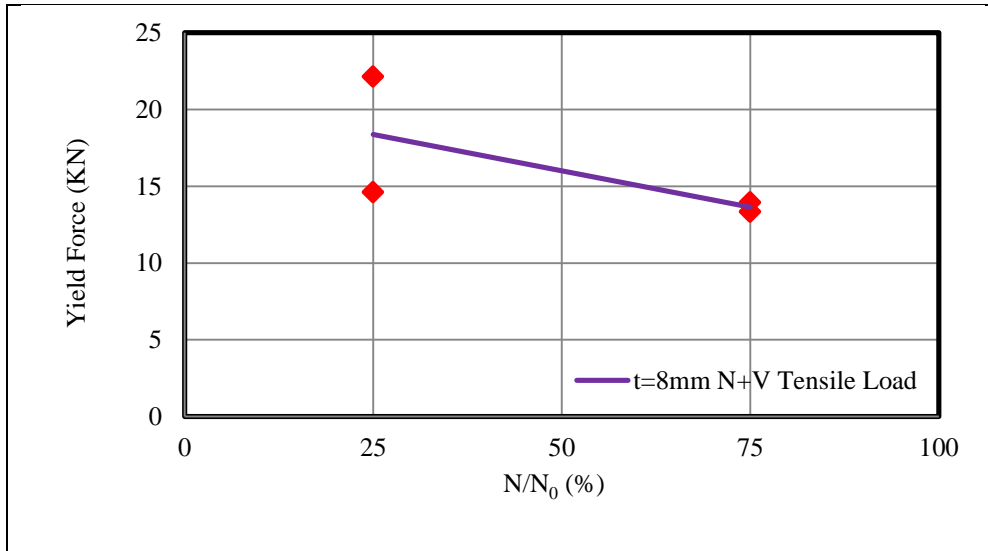


**Figure 3.57 :** Yield force trend for 8mm thick specimen under increase of tensile axial load.

The trend line of yield displacement for 3mm, 5mm and 8mm thick specimens under increase of tensile axial loads from  $N/N_0=25\%$ , to  $75\%$  in bi-directional cyclic shear and axial test are displayed test in Figure 3.58, 3.59 and Figure 3.60, respectively.

The yield displacement remains constant for 3mm thick specimen as tensile axial load increases, as shown in Figure 3.58.

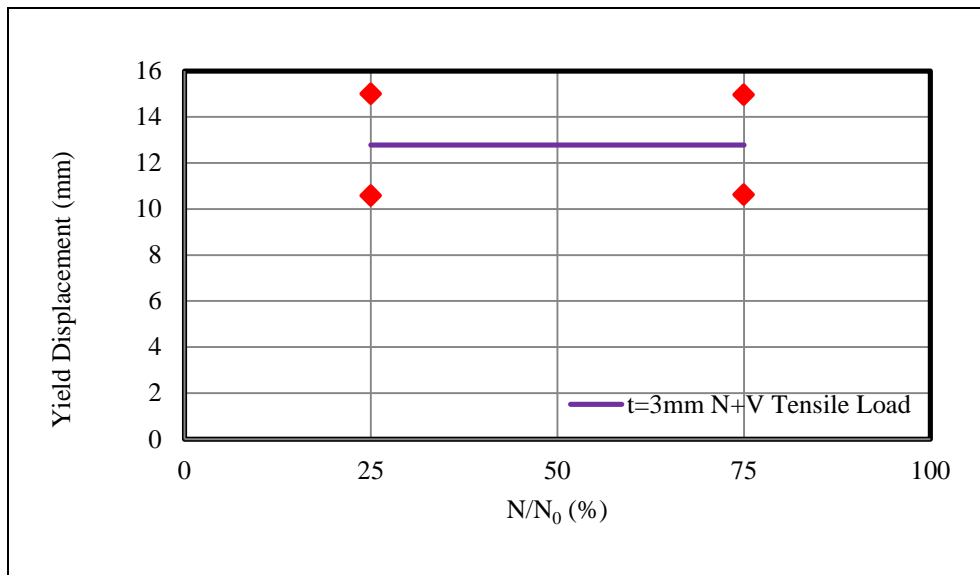


**Figure 3.58 :** Yield displacement trend for 3mm thick specimen under increase of tensile axial load.

The yield displacement decreases for 5mm thick specimen under increase of tensile axial load, as shown in Figure 3.59.

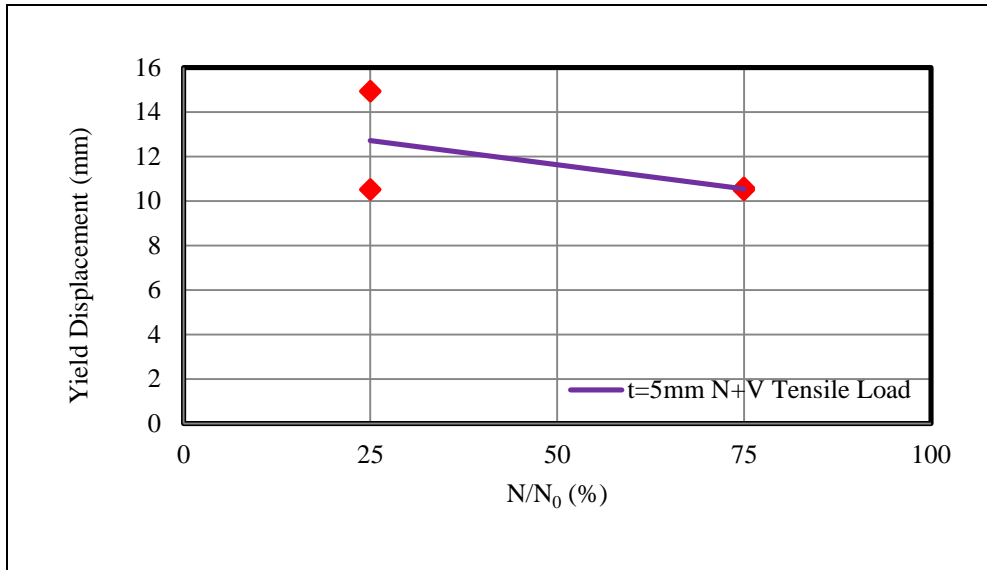


**Figure 3.59 :** Yield displacement trend for 5mm thick specimen under increase of tensile axial load.

The yield displacement decreases for 8mm thick specimen under increase of tensile axial load, as shown in Figure 3.60.

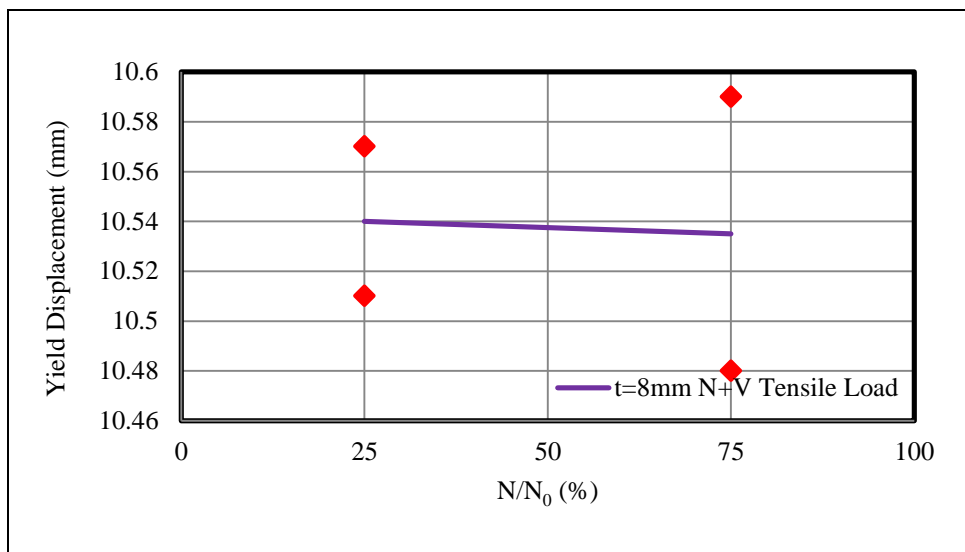


**Figure 3.60 :** Yield displacement trend for 8mm thick specimen under increase of tensile axial load.

### 3.3.3 Initial stiffness

The trend line of initial stiffness for 3mm, 5mm and 8mm thick specimens under increase of tensile axial loads from  $N/N_0=25\%$ , to  $75\%$  in bi-directional cyclic shear and axial test are displayed test in Figure 3.61, 3.62 and Figure 3.63 respectively.

The initial stiffness decreases for 3mm thick specimen under increase of tensile axial load, as shown in Figure 3.61.

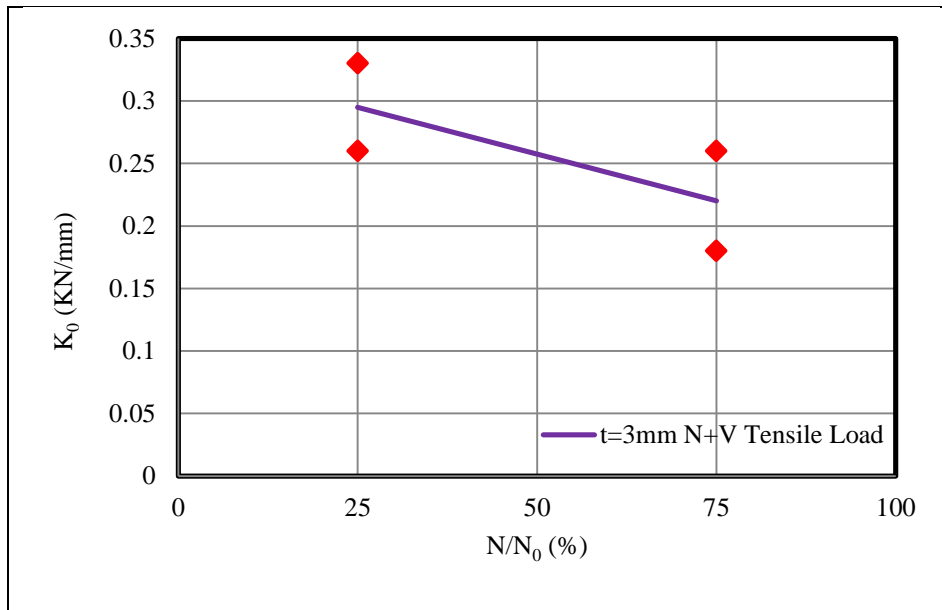


**Figure 3.61** : Initial stiffness trend for 3mm thick specimen under increase of tensile axial load.

The initial stiffness decreases for 5mm thick specimen under increase of tensile axial load, as shown in Figure 3.62.

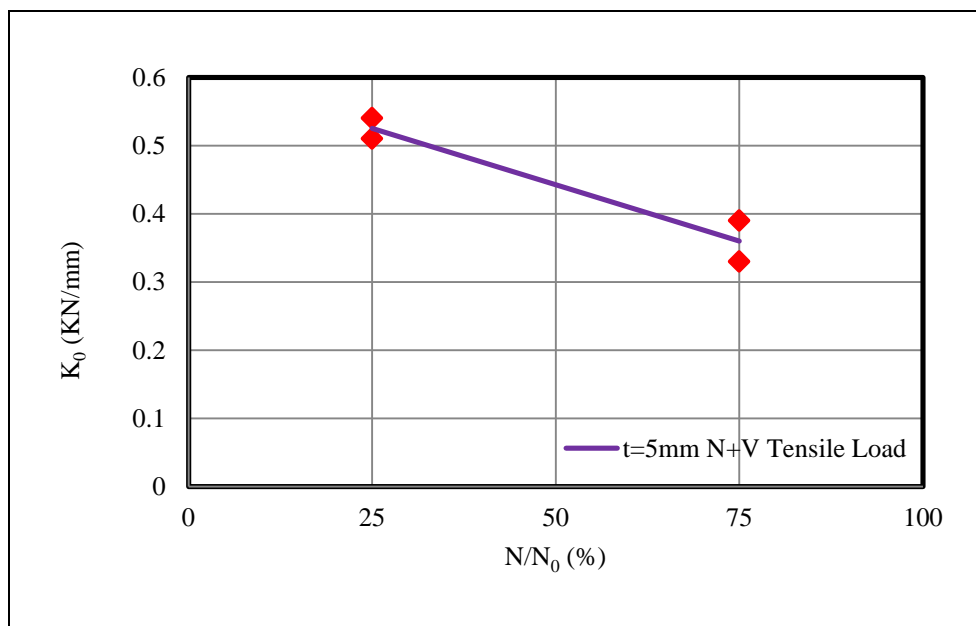


**Figure 3.62** : Initial stiffness trend for 5mm thick specimen under increase of tensile axial load.

The initial stiffness decreases for 8mm thick specimen under increase of tensile axial load, as shown in Figure 3.63.

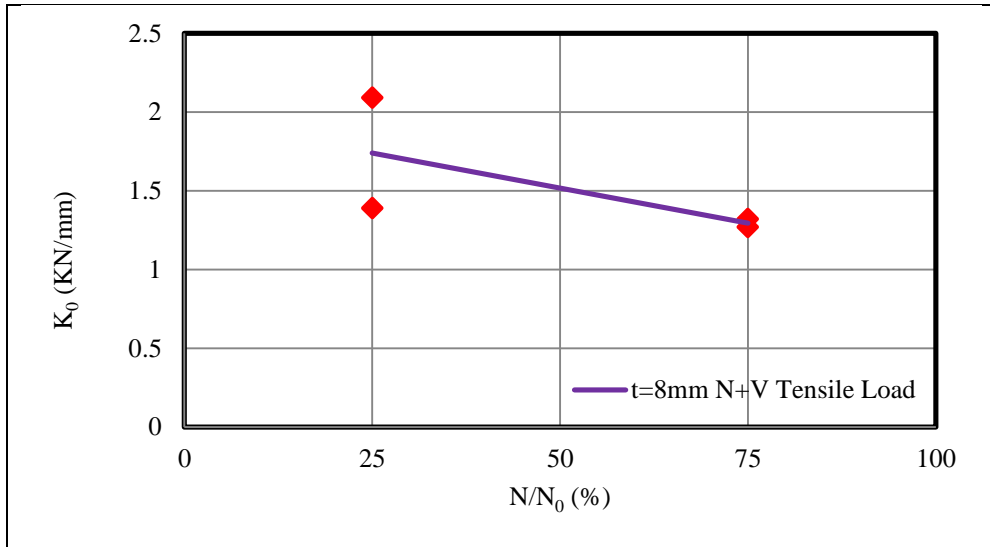


**Figure 3.63 :** Initial stiffness trend for 8mm thick specimen under increase of tensile axial load.

### 3.3.4 Maximum shear force

The trend line of maximum force for 3mm, 5mm and 8mm thick specimens under increase of tensile axial loads from  $N/N_0=25\%$ , to  $75\%$  in bi-directional cyclic shear and axial test are displayed test in Figure 3.64, 3.65 and Figure 3.66, respectively.

The maximum force decreases for 3mm thick specimen as tensile axial load increases, as shown in Figure 3.64.

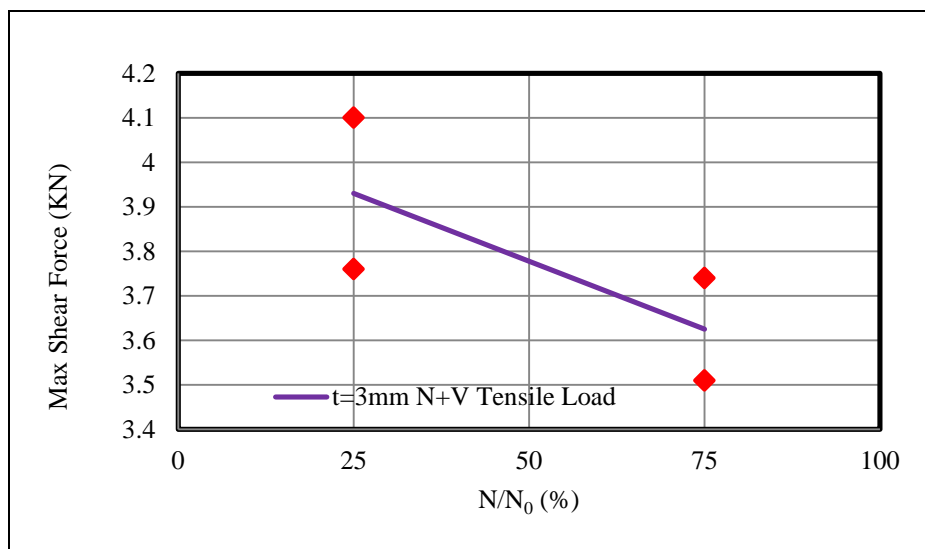


**Figure 3.64 :** Maximum force trend for 3mm thick specimen under increase of tensile axial load.

The maximum force decreases for 5mm thick specimen under increase of tensile axial load, as shown in Figure 3.65.

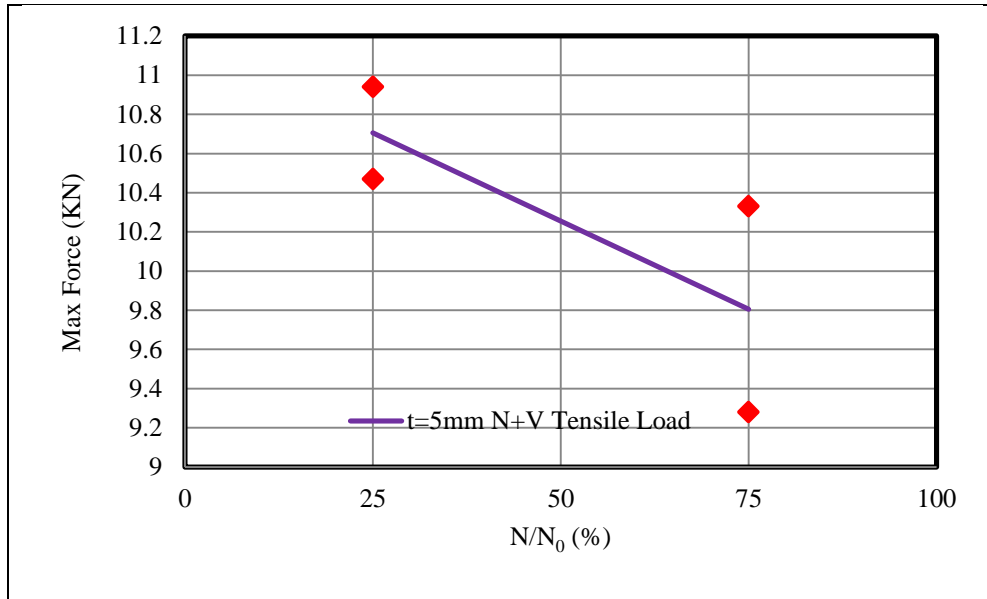


**Figure 3.65** : Maximum force trend for 5mm thick specimen under increase of tensile axial load.

The maximum force increases for 8mm thick specimen under increase of tensile axial load, as shown in Figure 3.66.

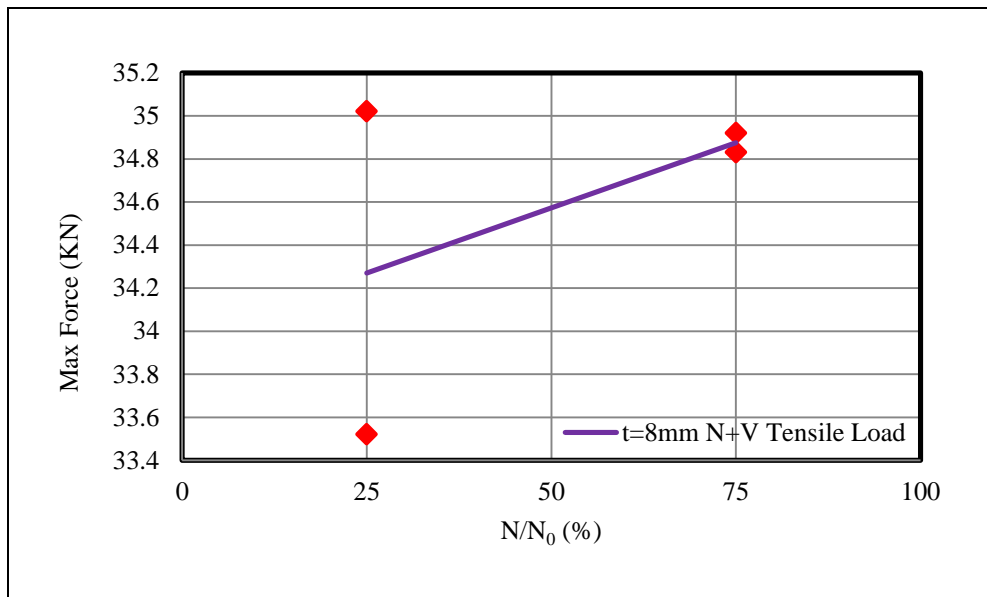


**Figure 3.66** : Maximum force trend for 8mm thick specimen under increase of tensile axial load.

### 3.4 Experimental Results of Bi-directional Test under Shear + Compression Loading

In this section, the experimental results obtained from bi-directional cyclic shear and axial compression tests are discussed. It is worthy to mention that axial compression forces were constant during the tests. The values of the axial compression forces are selected based on the proportion of the  $N/N_0$  in which  $N_0$  is the axial ultimate compression strength obtained from the monotonic axial tension tests. The applied axial loads were 25%, 50% and 75% of  $N_0$ .

#### 3.4.1 Force-Displacement relation

The force-displacement relations which obtained from bi-directional test under shear and compression loading are presented in Figure 3.67, 3.68 and Figure 3.69 for  $t=3\text{mm}$  thick steel cushion subjected to  $N/N_0 = 25\%$ ,  $N/N_0 = 50\%$  and  $N/N_0 = 75\%$ , respectively. The corresponding axial load values are 2.5, 7.5 and 10 KN.

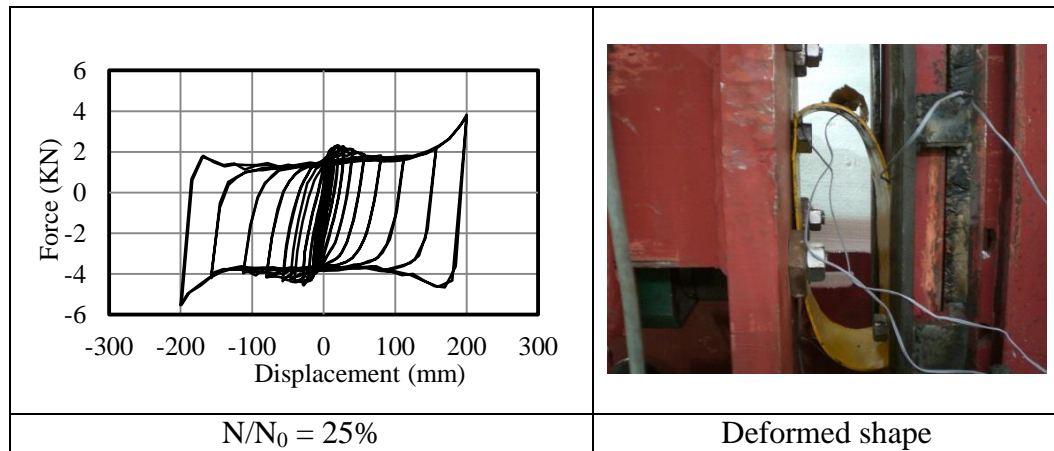


**Figure 3.67 :** Force-Displacement relation of 3mm thick specimens under compressive axial load of  $N/N_0=25\%$ .

The nominal yield strength is about 1.85KN in tension part and 4.19KN in compression part under the axial load of 2.5 KN. In this level of constant tensile axial load, the steel cushion behaved asymmetrically. There is no any reduction in the displacement capacity.

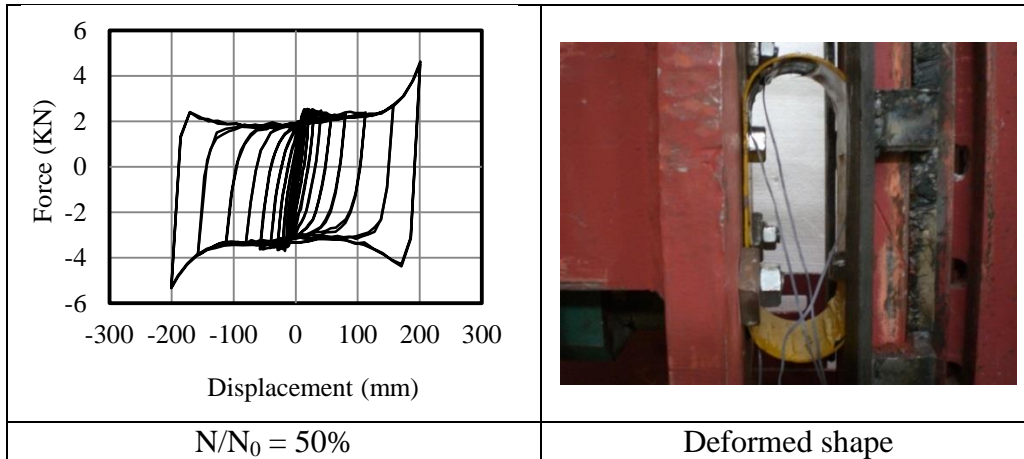


**Figure 3.68 :** Force-Displacement relation of 3mm thick specimens under compressive axial load of  $N/N_0=50\%$ .

The nominal yield strength is about 2.5 KN in tension part and 3.55 KN in compression part under the axial load of 7.5 KN. In this level of constant tensile axial load, the steel cushion behaved asymmetrically. There is no any reduction in the displacement capacity.

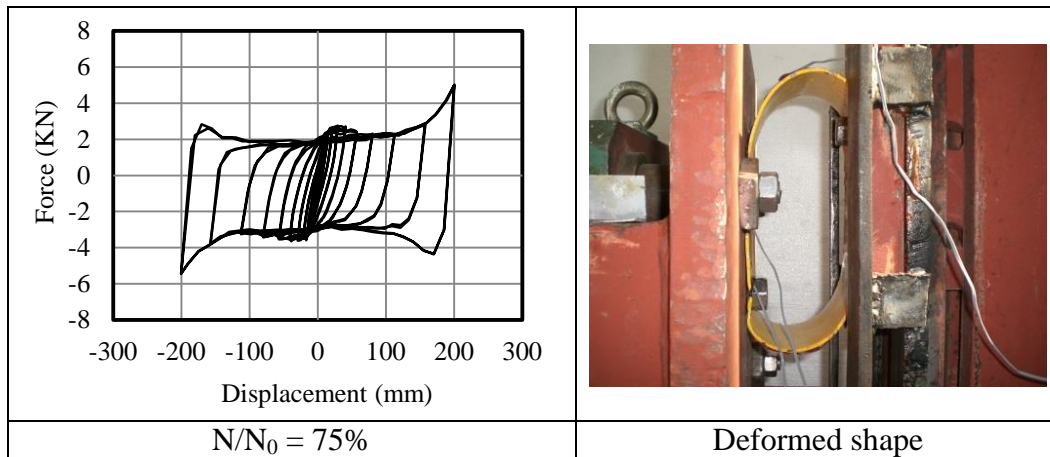


**Figure 3.69 :** Force-Displacement relation of 3mm thick specimens under compressive axial load of  $N/N_0=75\%$ .

The nominal yield strength is about 2.53 KN in tension part and 3.52 KN in compression part under the axial load of 10 KN. In this level of constant tensile axial load, the steel cushion behaved asymmetrically. There is no any reduction in the displacement capacity.

The force-displacement relations for  $t=3\text{mm}$  thick specimen are compared in Figure 3.70 with each other in two extreme states under  $N= 2.5 \text{ KN}$  and  $N= 10.0 \text{ KN}$  to show the effect of compressive axial load in shear capacity. As it is obvious, the nominal yield strength increases up to 37 % as the axial constant load increases. There is no any change in capacity.

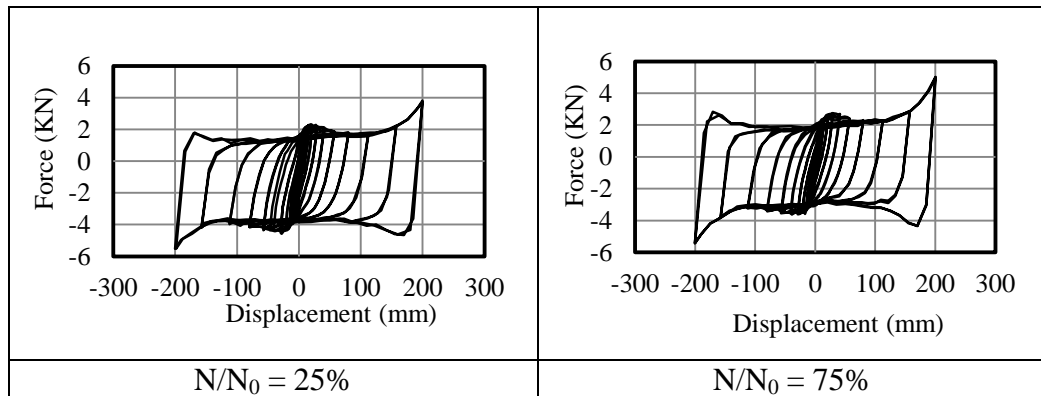


**Figure 3.70 :** Comparison of force-displacement relation for  $t= 3\text{mm}$  thick specimens under compressive axial stress.

The force-displacement relations which obtained from bi-directional shear and compressive axial tests are presented in Figure 3.71, 3.72 and Figure 3.73 for  $t=5\text{mm}$  thick steel cushion subjected to  $N/N_0 = 25\%$ ,  $N/N_0 = 50\%$  and  $N/N_0 = 75\%$ , respectively. The corresponding axial load values are 7.5, 15 and 25 KN.

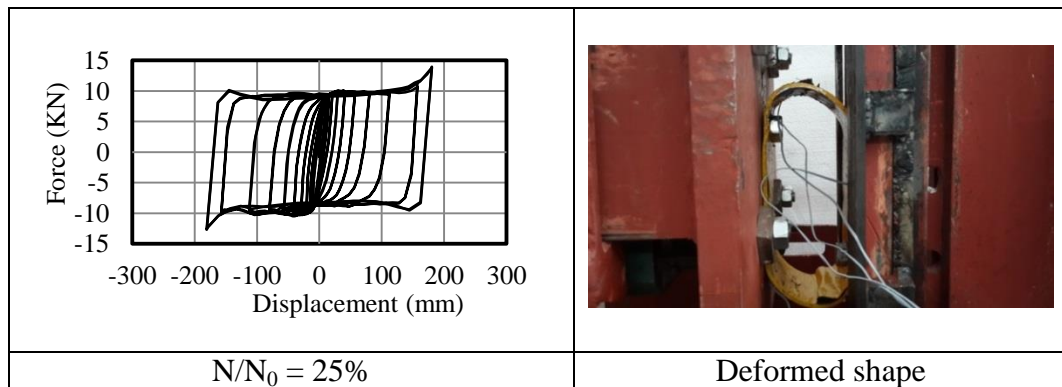


**Figure 3.71 :** Force-Displacement relation for 5mm thick specimens under compressive axial load of  $N/N_0=25\%$ .

The nominal yield strength is about 9.83 KN in tension part and 10.1 KN in compression part under the axial load of 7.5 KN. In this level of constant tensile axial load, the steel cushion behaved asymmetrically. There is no any reduction in the displacement capacity.

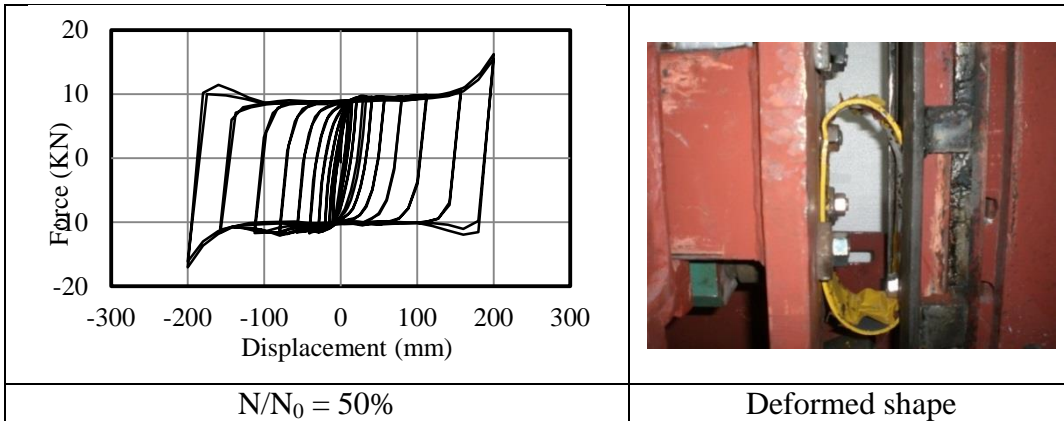


**Figure 3.72 :** Force-Displacement relation for 5mm thick specimens under compressive axial load of  $N/N_0=50\%$ .

The nominal yield strength is about 9.50 KN in tension part and 11.48 KN in compression part under the axial load of 15 KN. In this level of constant tensile axial load, the steel cushion behaved asymmetrically. There is no any reduction in the displacement capacity.

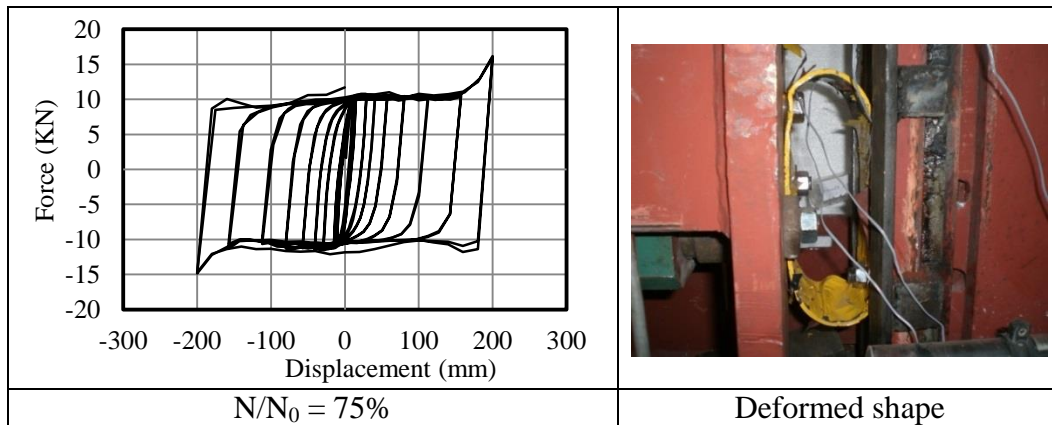


**Figure 3.73 :** Force-Displacement relation for 5mm thick specimens under compressive axial load of  $N/N_0=75\%$ .

The nominal yield strength is about 10.43 KN in tension part and 11.14 KN in compression part under the axial load of 25 KN. In this level of constant tensile axial load, the steel cushion behaved symmetrically. There is no any reduction in the displacement capacity.

The force-displacement relations for  $t=5\text{mm}$  thick specimen are compared in Figure 3.74 with each other in two extreme states under  $N= 7.5 \text{ KN}$  and  $N= 25 \text{ KN}$  to show the effect of compressive axial load in shear capacity. As it is obvious, the nominal yield strength increases up to 6 % as the axial constant load increases. There is no any change in capacity.

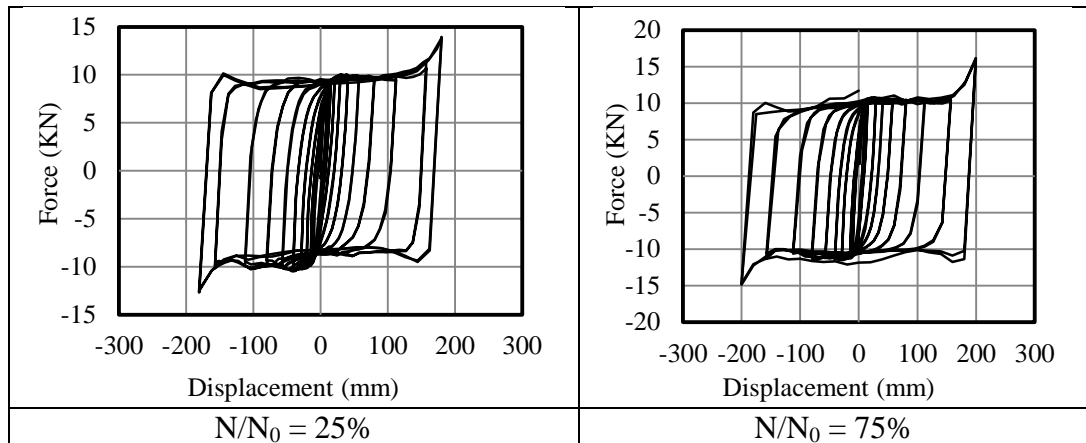


**Figure 3.74 :** Comparison of force-displacement relation for 5mm thick specimens under compressive axial stress.

The force-displacement relations which obtained from bi-directional shear and compressive axial tests are presented in Figure 3.75, 3.76 and Figure 3.78 for  $t=8\text{mm}$  thick steel cushion subjected to  $N/N_0 = 25\%$ ,  $N/N_0 = 50\%$  and  $N/N_0 = 75\%$  respectively. The corresponding axial load values are 25, 50 and 75 KN.

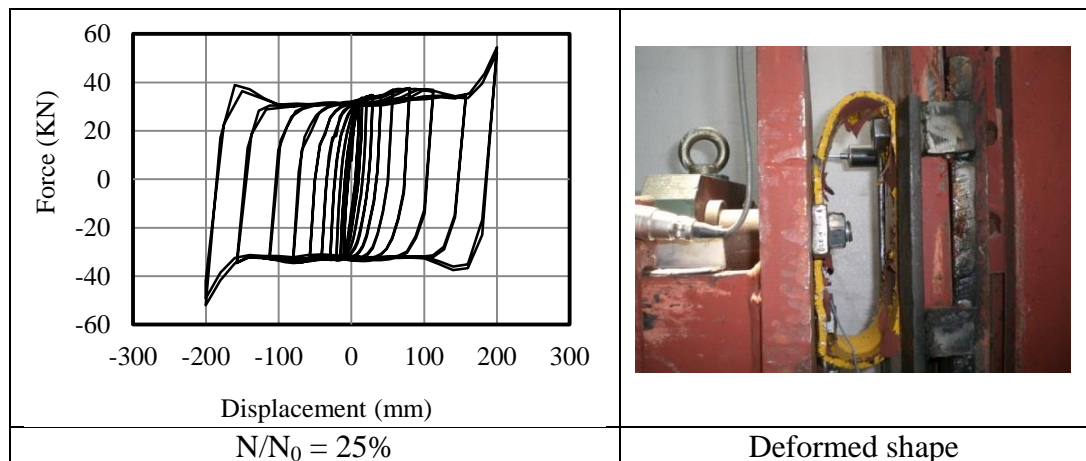


**Figure 3.75 :** Force-Displacement relation for 8mm thick specimens under compressive axial load of  $N/N_0=25\%$ .

The nominal yield strength is about 34.37 KN in tension part and 33.02 KN in compression part under the axial load of 25 KN. In this level of constant tensile axial load, the steel cushion behaved symmetrically. There is no any reduction in the displacement capacity.

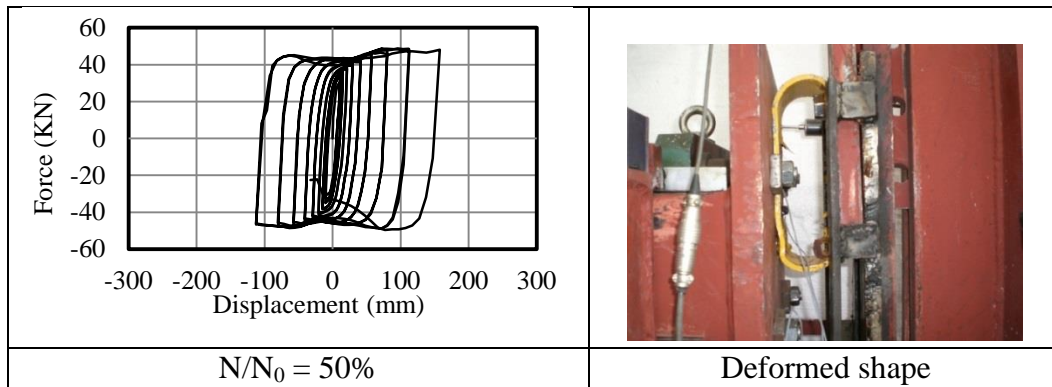


**Figure 3.76 :** Comparison of force-displacement relation for 8mm thick specimens under compressive axial load of  $N/N_0=50\%$ .

The nominal yield strength is about 43.88 KN in compression part and 42.17 KN in tension part under the axial load of 50 KN. In this level of constant tensile axial load, the steel cushion behaved symmetrically. In addition, at the displacement target of 200mm rupture occurred as it is shown in Figure 3.77.



**Figure 3.77 :** Rupture occurred at the final displacement target in 8mm steel cushion under tensile axial stress of 50 KN.

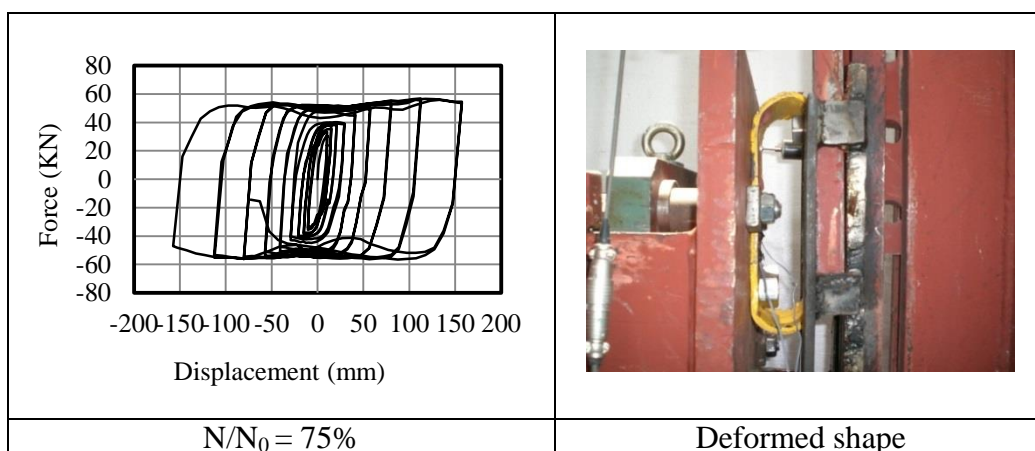


**Figure 3.78 :** Force-Displacement relation for 8mm thick specimens under compressive axial load of  $N/N_0=75\%$ .

The nominal yield strength is about 51.52 KN in tension part and 52.66 KN in compression part under the axial load of 75 KN. In this level of constant tensile axial load, the steel cushion behaved symmetrically. In addition, at the final displacement target of 200mm rupture occurred as it is shown in Figure 3.79.

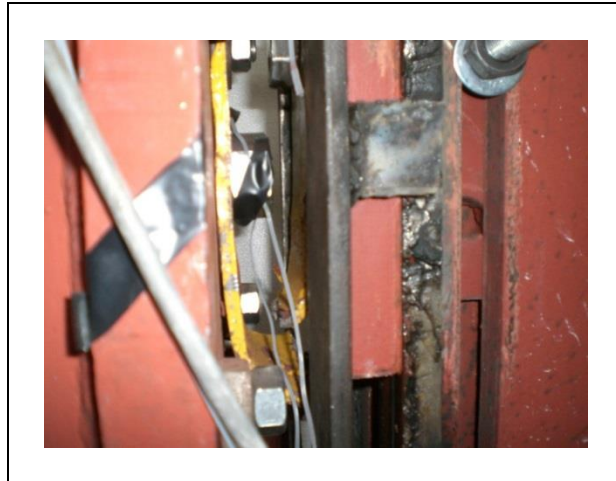


**Figure 3.79** : Rupture occurred at the final displacement target in 8mm steel cushion under tensile axial force of 75 KN.

The force-displacement relations for t=8mm thick specimen are compared in Figure 3.80 with each other in two extreme states under  $N= 25$  KN and  $N= 75$  KN to show the effect of compressive axial load in shear capacity. As it is obvious, the nominal yield strength increases up to 50% as the axial constant load increases. In addition, the displacement capacity declines as the compressive axial load increases.

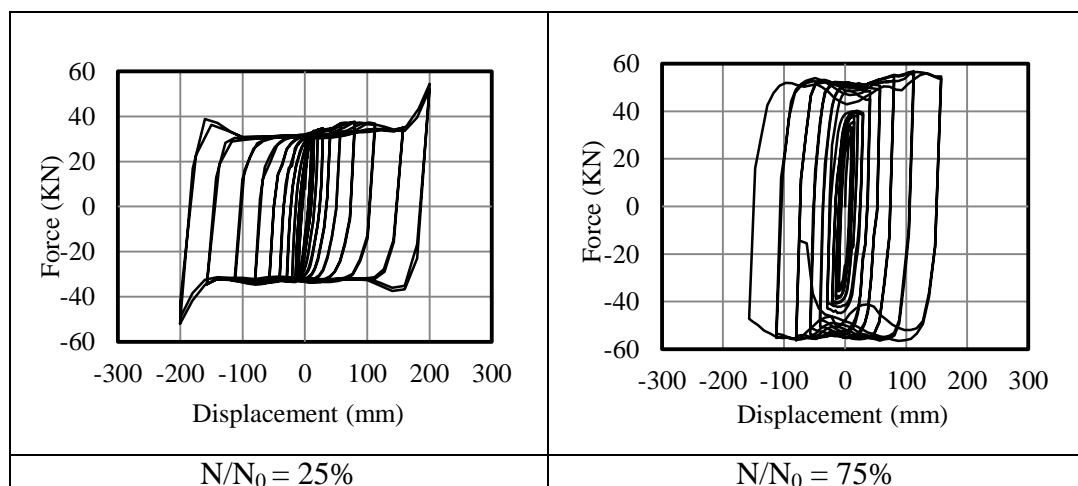


**Figure 3.80** : Comparison of force-displacement relation for 8mm thick specimens under compressive axial stress.

The force-displacement relations for steel cushions in three distinct thicknesses subjected two extreme axial forces are compared in Figure 3.81. According these Figures as the thickness increases the shear strength increases as well.

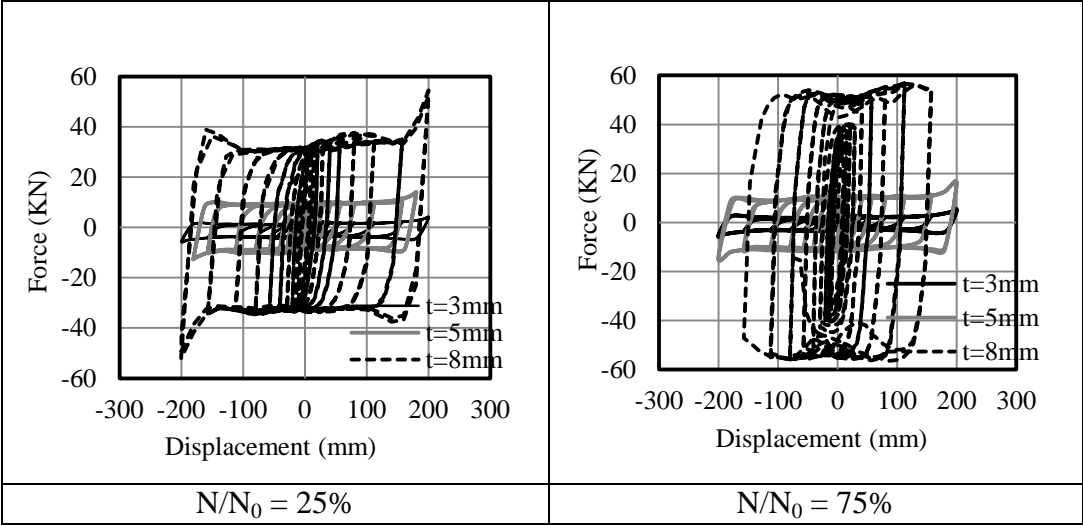


**Figure 3.81 :** Comparison of force-displacement relation in terms of different thicknesses under compressive axial load.

**3.4.2 Energy dissipation**

The cumulative energy in terms of displacement for t=3mm thick specimen subjected to constant tensile axial loads of N=2.5 KN, N=7.5 KN, and N=10.0 KN are displayed at Figure 3.82, 3.83 and Figure 3.84 respectively.

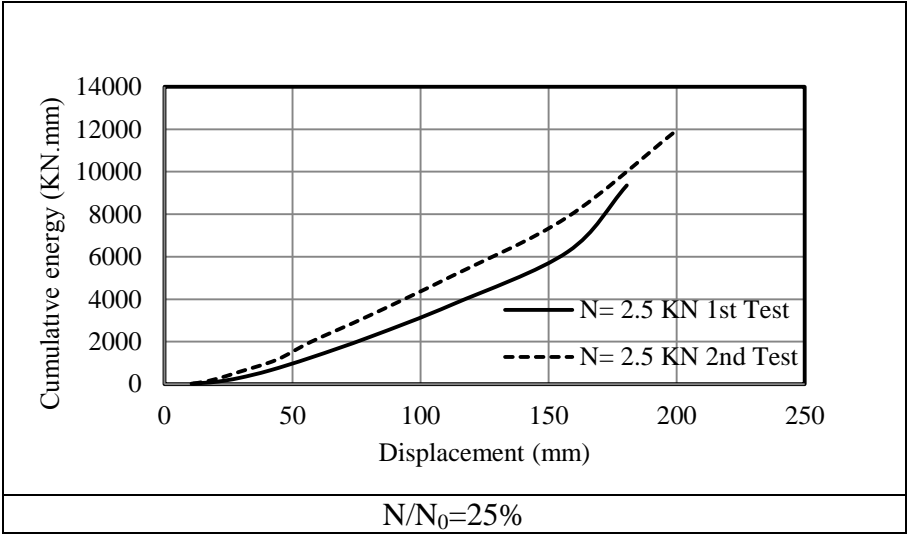


**Figure 3.82 :** Cumulative energy in terms of displacement for 3mm thick steel cushions under compressive load of N=2.5 KN.

The cumulative energy capacity is 9356 and 11888 KN.mm for 3mm thick specimen in the first and second test respectively.

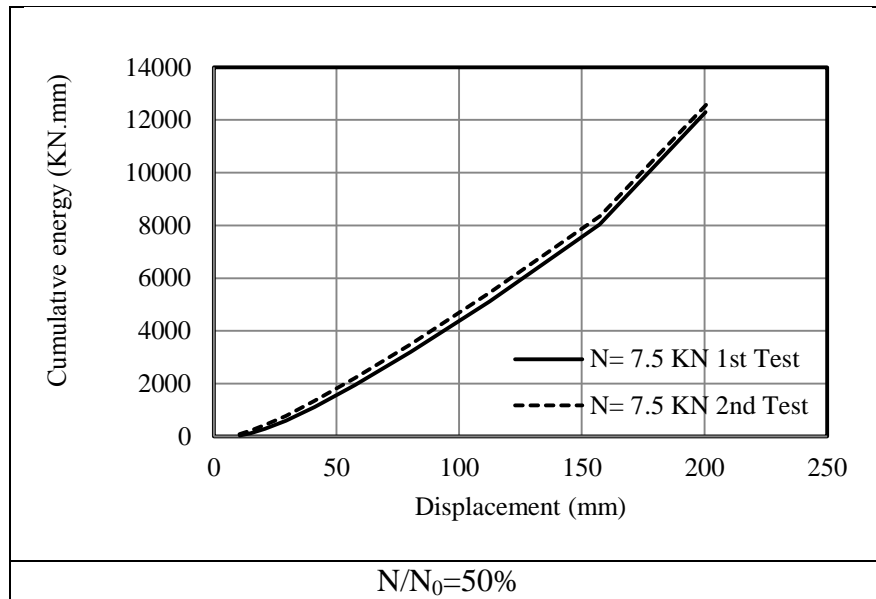


**Figure 3.83 :** Cumulative energy in terms of displacement for 3mm thick steel cushions under compressive load of  $N=7.5$  KN.

The cumulative energy capacity is 12581 KN.mm for 3mm thick specimen in the first and second test.

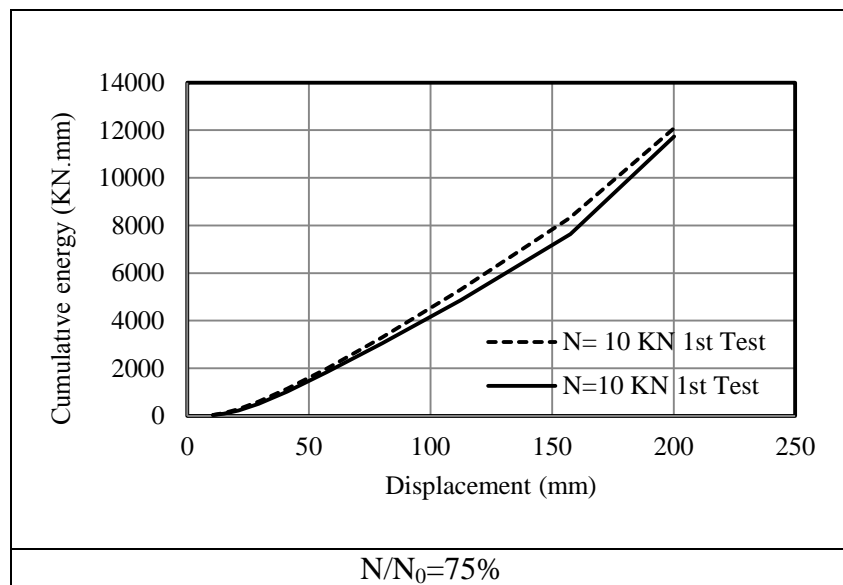


**Figure 3.84 :** Cumulative energy in terms of displacement for 3mm thick steel cushions under compressive load of  $N=10$  KN.

The cumulative energy capacity is 9356 and 11888 KN.mm for 3mm thick specimen in the first and second test respectively.

The cumulative capacity for  $t=3$ mm thick steel cushions in two extreme compressive axial load level of  $N/N_0=25\%$  and  $N/N_0=75\%$  are compared to show the effect of the tensile axial load in Figure 3.85.

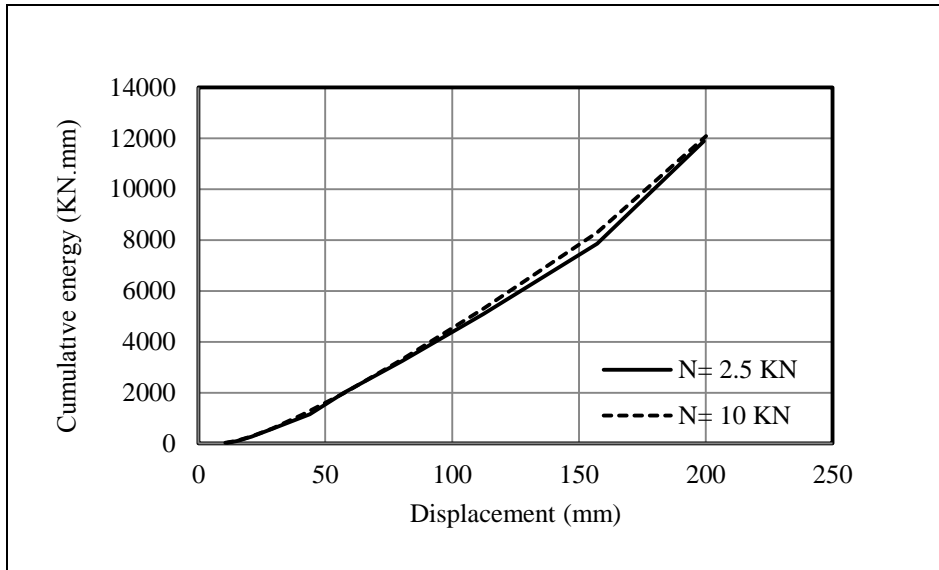


**Figure 3.85 :** Comparison of energy dissipation capacity for 3mm thick specimens under compressive axial stress in two extreme axial loads.

The compressive axial load has the positive effect it increases the cumulative energy capacity up to 1.62 % for  $t=3\text{mm}$  thick steel cushions according to the Figure 3.85.

The cumulative energy in terms of displacement for  $t=5\text{mm}$  thick specimen subjected to constant tensile axial loads of  $N=7.5\text{ KN}$ ,  $N=15\text{ KN}$  and  $N=25\text{ KN}$  are displayed at Figure 3.86, 3.87, and Figure 3.88 respectively.

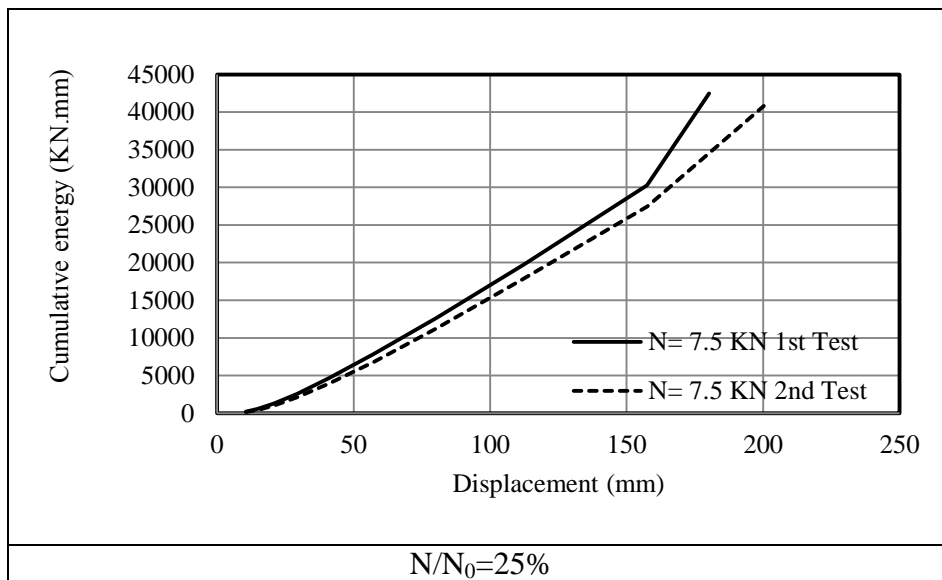


**Figure 3.86 :** Cumulative energy in terms of displacement for 5mm thick steel cushions under compressive load of  $N=7.5\text{ KN}$ .

The cumulative energy capacity is 42484 and 40818 KN.mm for 5mm thick specimen in the first and second test respectively.

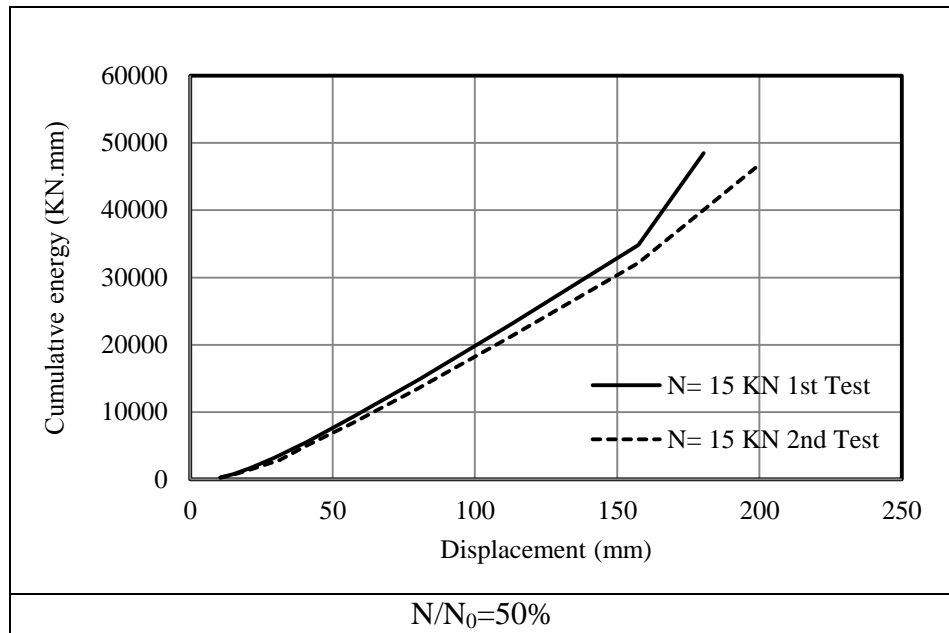


**Figure 3.87 :** Cumulative energy in terms of displacement for 5mm thick steel cushions under a compressive load of N=15 KN.

The cumulative energy capacity is 48516 and 46849 KN.mm for 5mm thick specimen in the first and second test respectively.

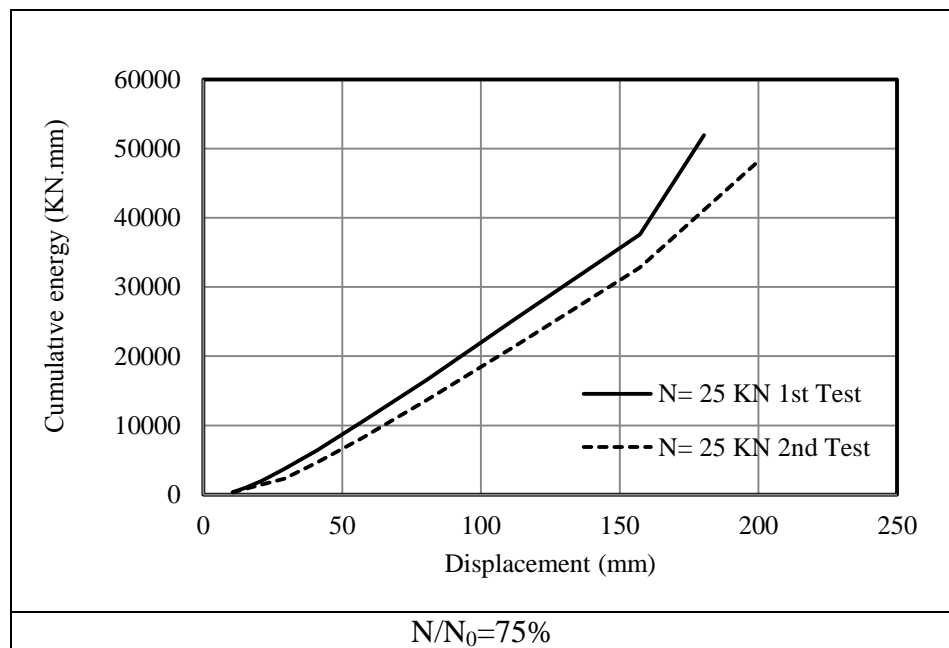


**Figure 3.88 :** Cumulative energy in terms of displacement for 5mm thick steel cushions under a compressive load of N=25 KN.

The cumulative energy capacity is 51920 and 48166 KN.mm for 5mm thick specimen in the first and second test respectively.

The cumulative capacity for t=5mm thick steel cushions in two extreme compressive axial load level of  $N/N_0=25\%$  and  $N/N_0=75\%$  are compared to show the effect of the tensile axial load in Figure 3.89.

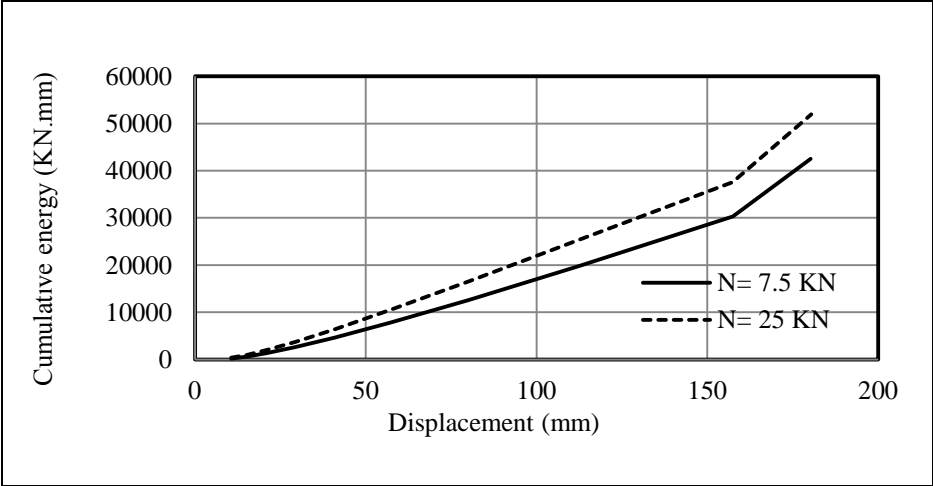


**Figure 3.89 :** Comparison of energy dissipation capacity for 5mm thick specimens under compressive axial stress in two extreme axial loads.

The compressive axial load has the positive effect it increases the cumulative energy capacity up to 22.21 % for t=5mm thick steel cushions according to the Figure 3.89.

The cumulative energy in terms of displacement for t=8mm thick specimen subjected to constant tensile axial loads of N=25 KN, N=50 KN and N=75 KN are displayed at Figure 3.90, 3.91, and Figure 3.92 respectively.

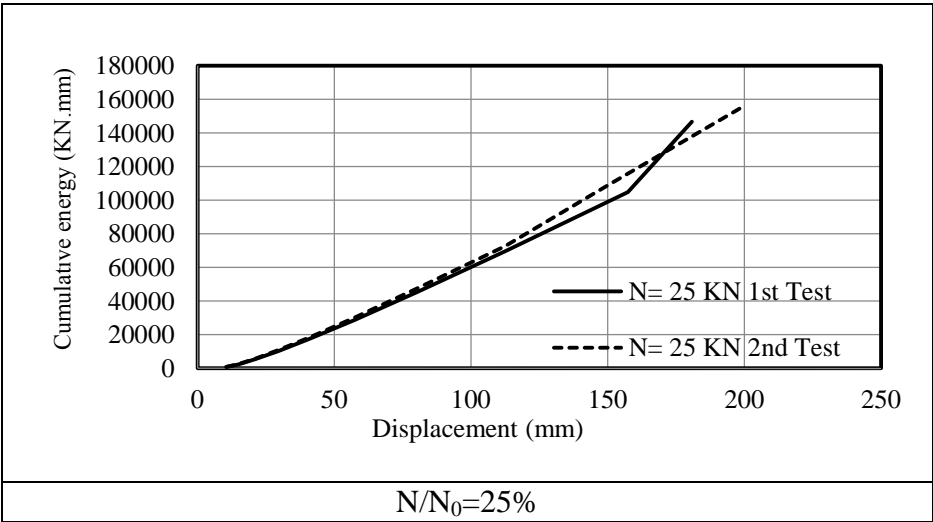


**Figure 3.90 :** Cumulative energy in terms of displacement for 8mm thick steel cushions under compressive load of N=25 KN.

The cumulative energy capacity is 156103 and 146695 KN.mm for 8mm thick specimen in the first and second test respectively.

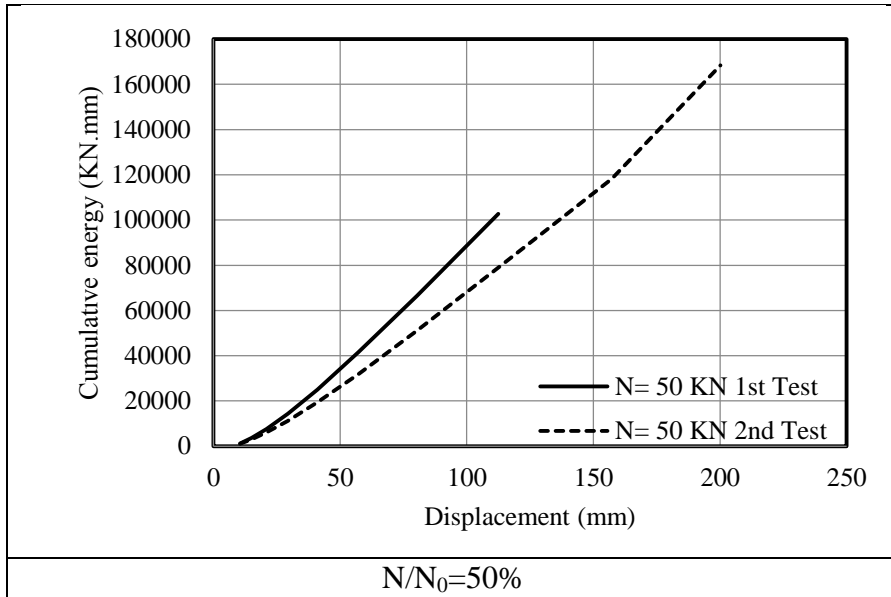


**Figure 3.91 :** Cumulative energy in terms of displacement for 8mm thick steel cushions under compressive load of N=50 KN.

The cumulative energy capacity is 102765 and 168354 KN.mm for 8mm thick specimen in the first and second test respectively.

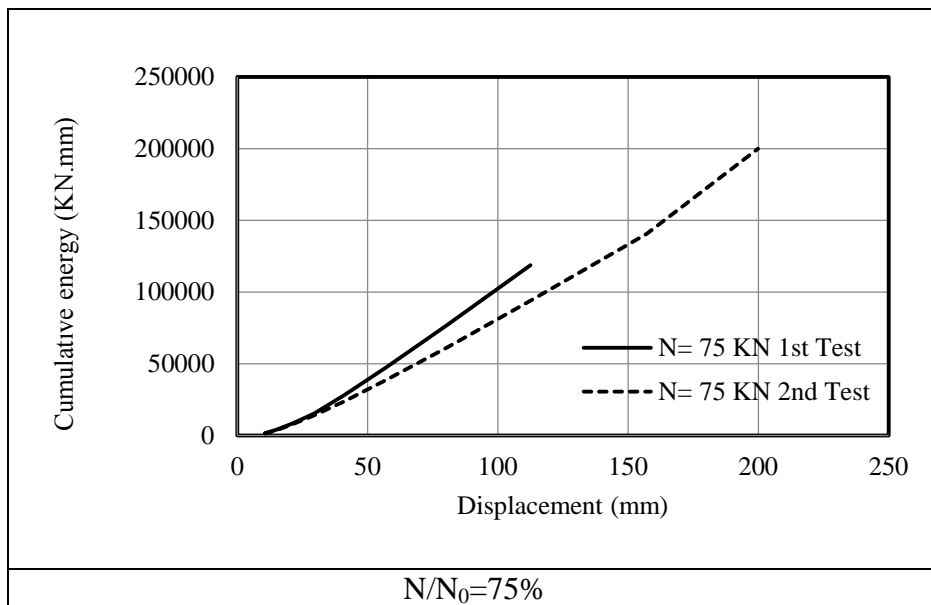


**Figure 3.92 :** Cumulative energy in terms of displacement for 8mm thick steel cushions under compressive load of N=75 KN.

The cumulative energy capacity is 118763 and 199937 KN.mm for 8mm thick specimen in the first and second test respectively.

The cumulative capacity for t=8mm thick steel cushions in two extreme compressive axial load level of  $N/N_0=25\%$  and  $N/N_0=75\%$  are compared to show the effect of the tensile axial load in Figure 3.93.

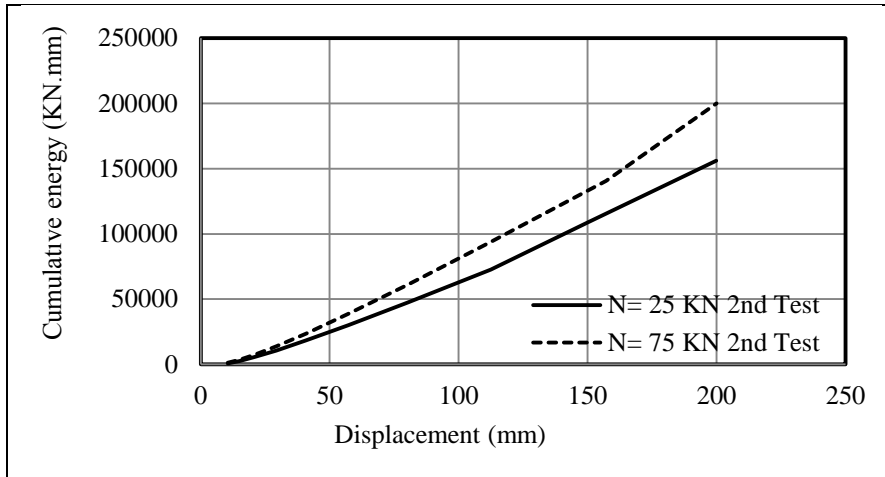


**Figure 3.93 :** Comparison of energy dissipation capacity for  $t= 8\text{mm}$  thick specimens under two extreme axial loads.

The compressive axial load has the positive effect it increases the cumulative energy capacity up to 28.08% for  $t=8\text{mm}$  thick steel cushions according to Figure 3.93.

### 3.4.3 Equivalent viscous damping

The equivalent damping in terms of displacement for  $t=3\text{mm}$  thick specimen subjected to constant compressive axial loads of  $N=2.5\text{ KN}$ ,  $N=7.5\text{ KN}$  and  $N=10\text{ KN}$  are displayed at Figure 3.94, 3.95 and Figure 3.96, respectively.

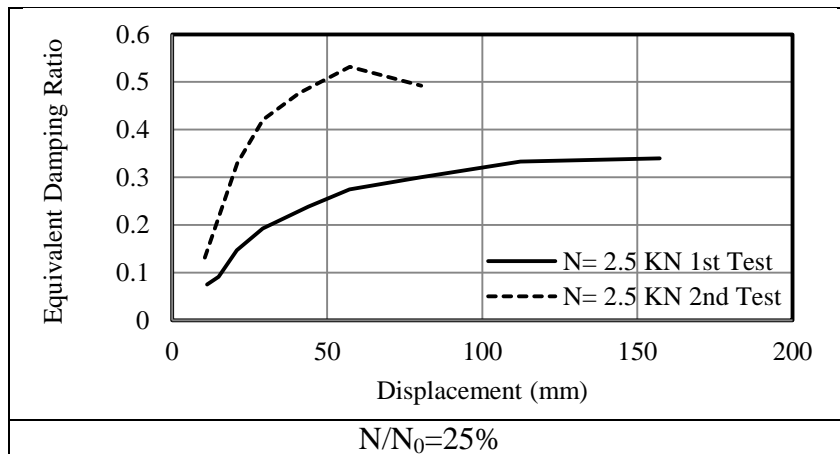


**Figure 3.94 :** Equivalent damping ratio in terms of displacement for  $3\text{mm}$  thick steel cushions under compressive load of  $N=2.5\text{ KN}$ .

The maximum equivalent damping ratio is 34% and 53% for  $3\text{mm}$  thick specimen in the first and second test respectively. It should be noted that the falling section of the equivalent damping ratio curves are not plotted up to ultimate displacement target.

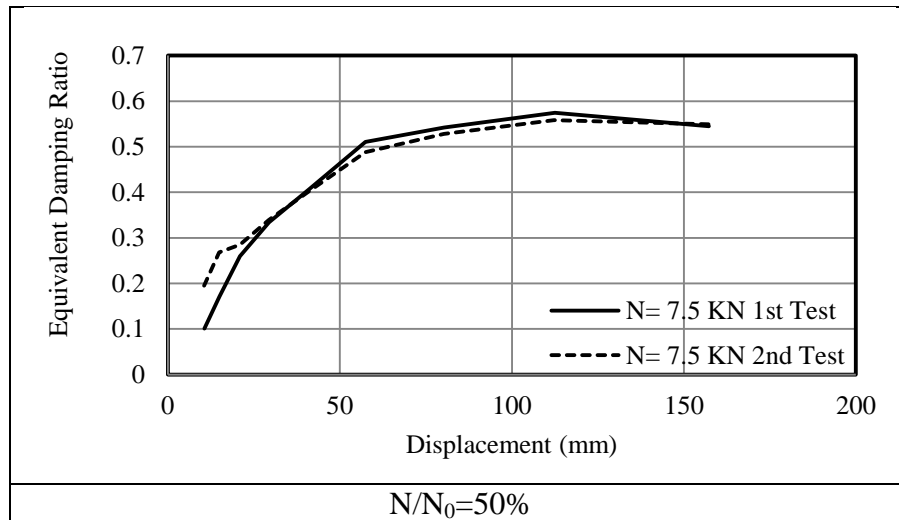


**Figure 3.95 :** Equivalent damping ratio in terms of displacement for 3mm thick steel cushions under compressive load of  $N=7.5\text{KN}$ .

The maximum equivalent damping ratio is 57% and 55% for 3mm thick specimen in the first and second test respectively.

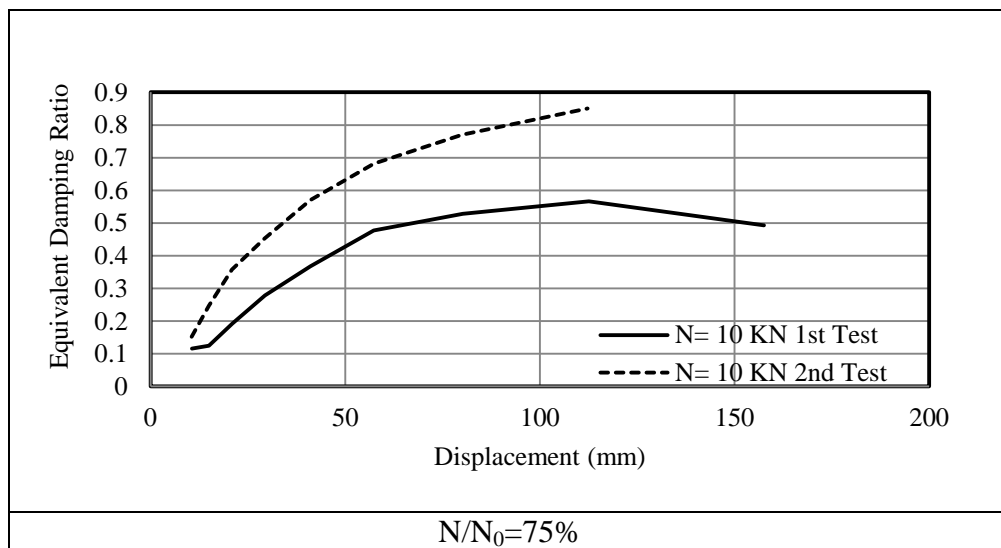


**Figure 3.96 :** Equivalent damping ratio in terms of displacement for 3mm thick steel cushions under compressive load of  $N=10\text{KN}$ .

The maximum equivalent damping ratio is 57% and 85% for 3mm thick specimen in the first and second test respectively. It should be noted that the falling section of the equivalent damping ratio curves are not plotted up to final displacement target since the maximum equivalent damping is important.

The equivalent damping ratio for  $t=3\text{mm}$  thick steel cushions in two extreme compressive axial load level of  $N/N_0=25\%$  and  $N/N_0=75\%$  are compared to show the effect of the tensile axial load in Figure 3.97.

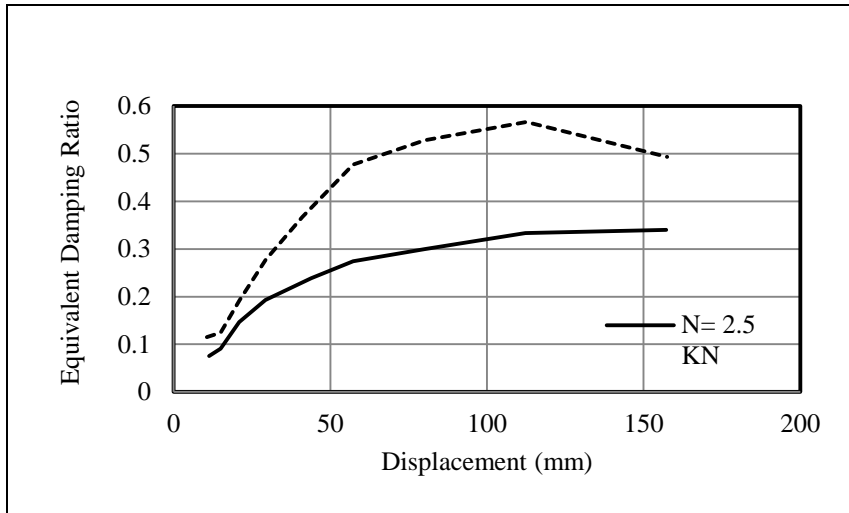


**Figure 3.97 :** Comparison of equivalent damping ratio for 3mm thick specimens under two extreme compressive axial loads.

The compressive axial load has the positive effect as it increases up to 50% the equivalent damping ratio increases as well from 34% to 57% in  $t=3\text{mm}$  thick steel cushions according to the Figure 3.97.

The equivalent damping in terms of displacement for  $t=5\text{mm}$  thick specimen subjected to constant compressive axial loads of  $N=7.5\text{ KN}$ ,  $N=15\text{ KN}$ , and  $N=25\text{KN}$  are displayed at Figure 3.98, 3.99 and Figure 3.100, respectively.

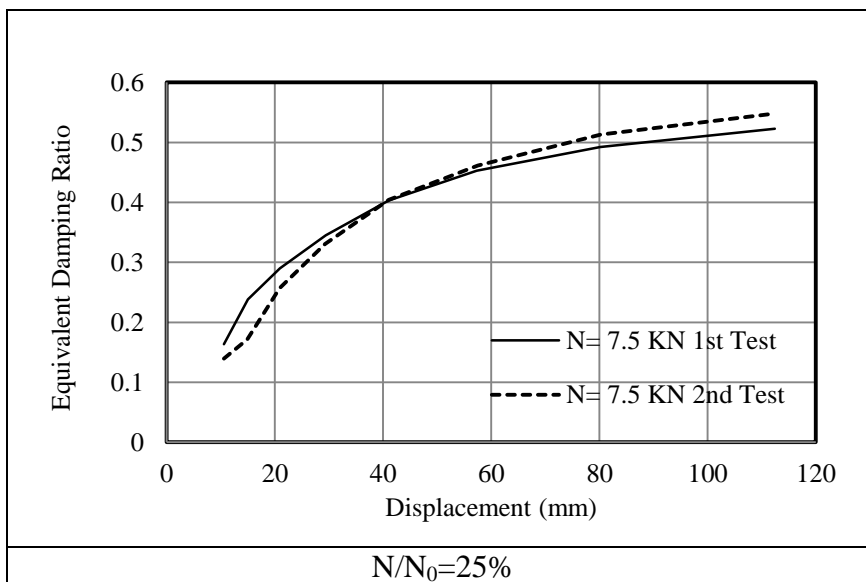


**Figure 3.98 :** Equivalent damping ratio in terms of displacement for 5mm thick steel cushions under compressive load of  $N=7.5\text{ KN}$ .

The maximum equivalent damping ratio is 52% and 55% for 5mm thick specimen in the first and second test respectively.

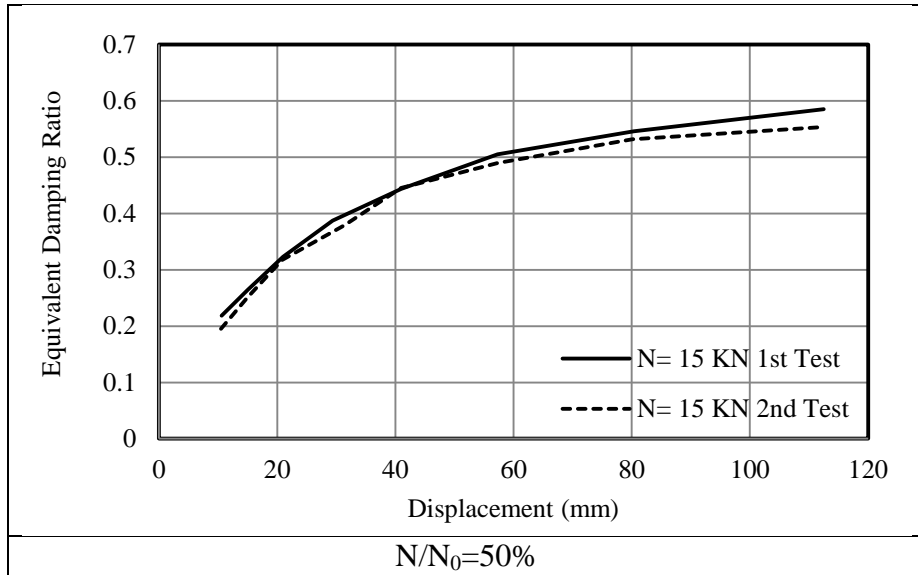


**Figure 3.99 :** Equivalent damping ratio in terms of displacement for 5mm thick steel cushions under compressive load of  $N=15$  KN.

The maximum equivalent damping ratio is 59% and 55% for 5mm thick specimen in the first and second test respectively.

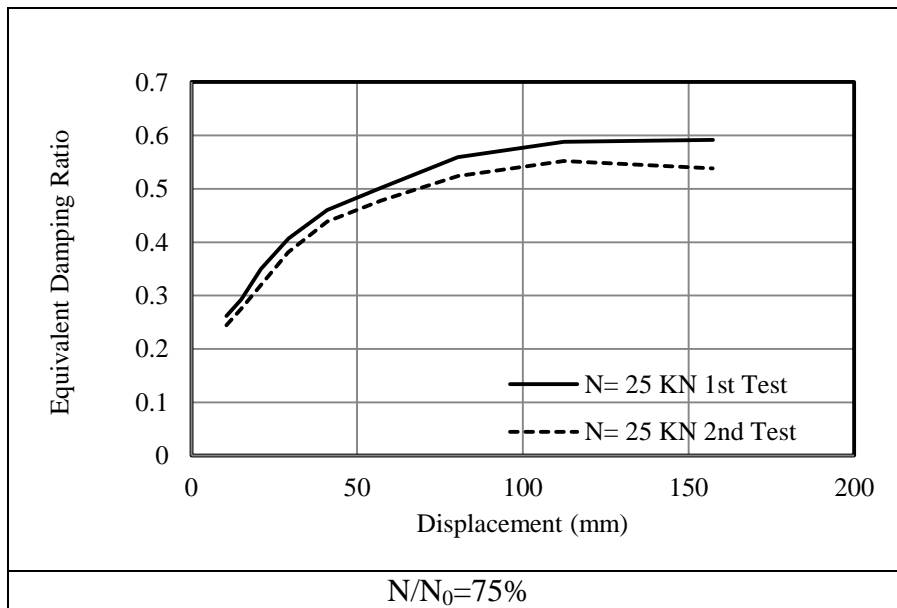


**Figure 3.100 :** Equivalent damping ratio in terms of displacement for 5mm thick steel cushions under compressive load of  $N=25$  KN.

The maximum equivalent damping ratio is 59% and 54% for 5mm thick specimen in the first and second test respectively.

The equivalent damping ratio for  $t=5$ mm thick steel cushions in two extreme compressive axial load level of  $N/N_0=25\%$  and  $N/N_0=75\%$  are compared to show the effect of the tensile axial load in Figure 3.101.

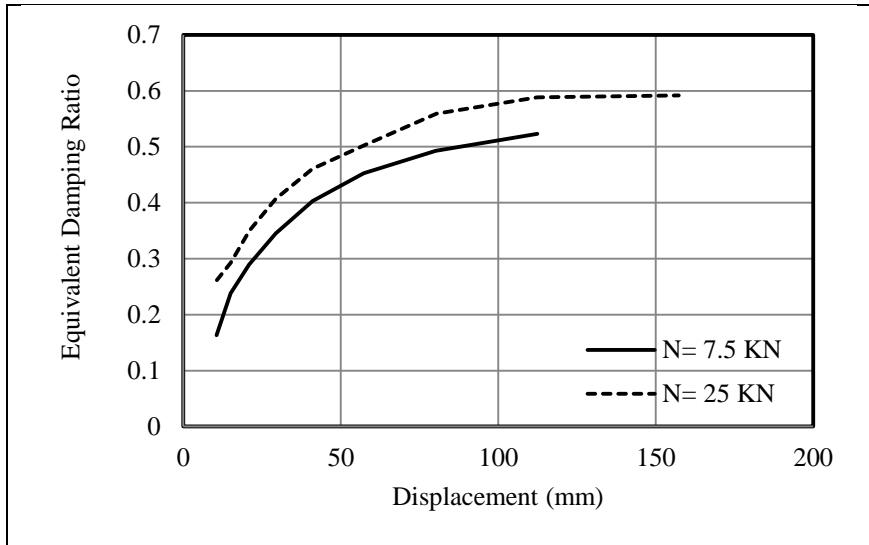


**Figure 3.101 :** Comparison of equivalent damping ratio for 5mm thick specimens under two extreme compressive axial loads.

The compressive axial load has the positive effect as it increases up to 50% the equivalent damping ratio increases as well from 52% to 59% in  $t=5\text{mm}$  thick steel cushions according to the Figure 3.101.

The equivalent damping in terms of displacement for  $t=8\text{mm}$  thick specimen subjected to constant compressive axial loads of  $N=25\text{ KN}$ ,  $N=50\text{ KN}$ , and  $N=75\text{ KN}$  are displayed at Figure 3.102, 3.103 and Figure 3.104, respectively.

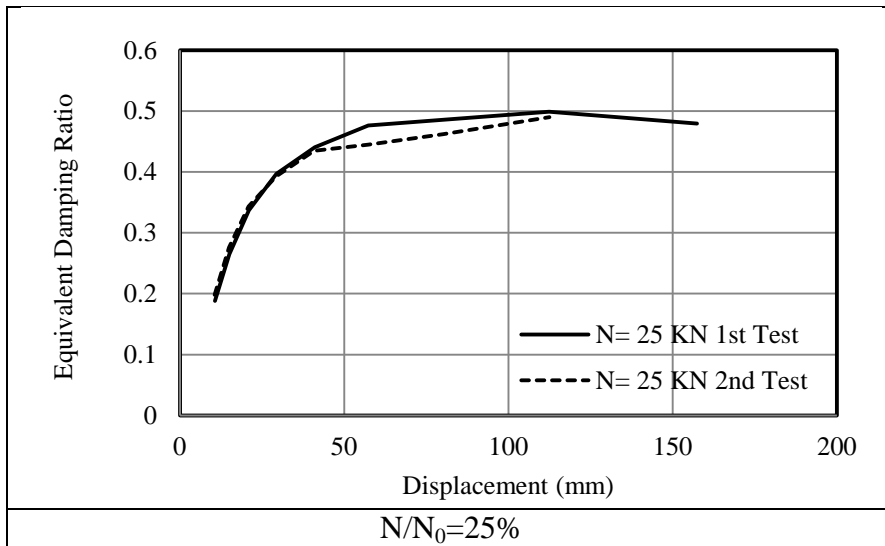


**Figure 3.102 :** Equivalent damping ratio in terms of displacement for 8mm thick steel cushions under compressive load of  $N=25\text{ KN}$ .

The maximum equivalent damping ratio is 49% and 47% for 8mm thick specimen in the first and second test respectively.

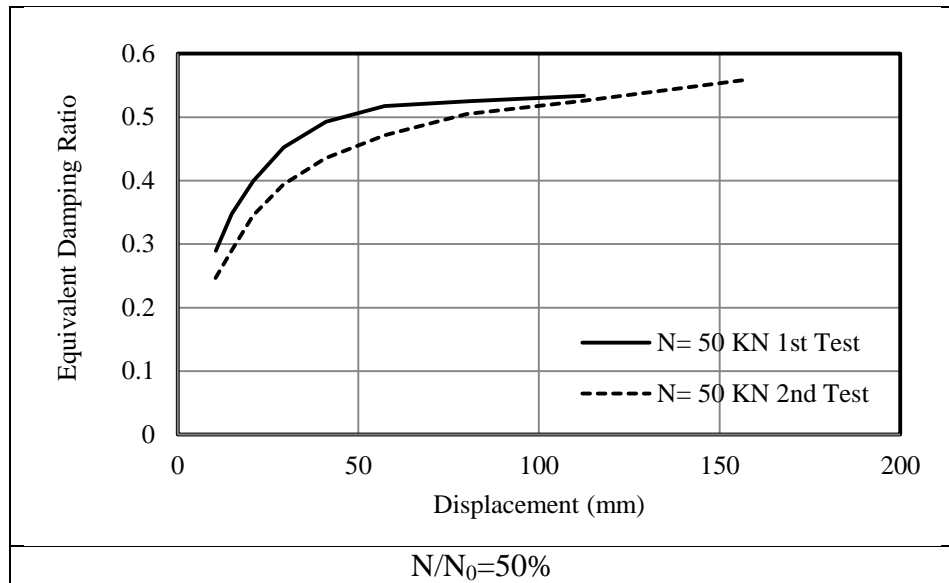


**Figure 3.103 :** Equivalent damping ratio in terms of displacement for 8mm thick steel cushions under compressive load of N=50 KN.

The maximum equivalent damping ratio is 53% and 56% for 8mm thick specimen in the first and second test respectively.

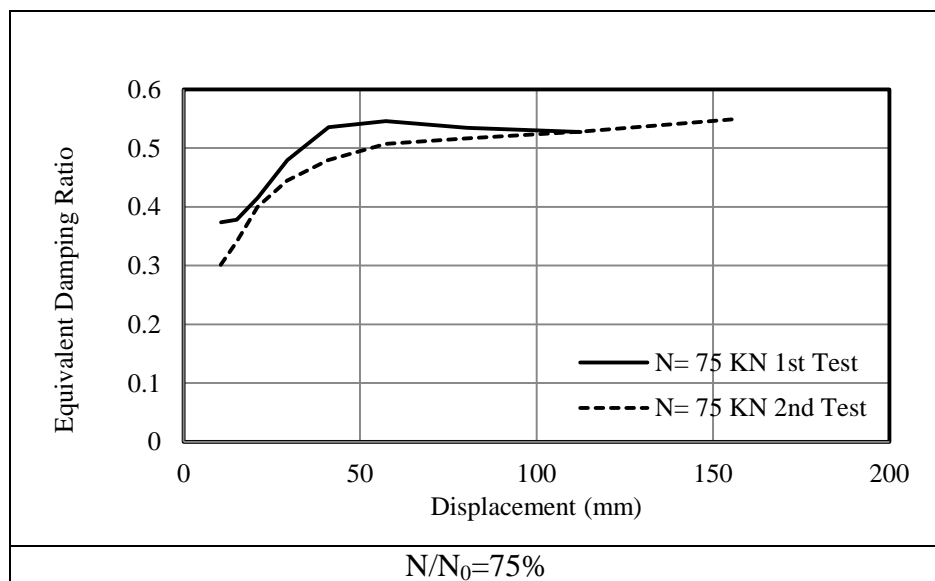


**Figure 3.104 :** Equivalent damping ratio in terms of displacement for 8mm thick steel cushions under compressive load of N=75 KN.

The maximum equivalent damping ratio is 55% for 8mm thick specimen in the first and second test.

The equivalent damping ratio for t=8mm thick steel cushions in two extreme compressive axial load level of  $N/N_0=25\%$  and  $N/N_0=75\%$  are compared to show the effect of the tensile axial load in Figure 3.105.

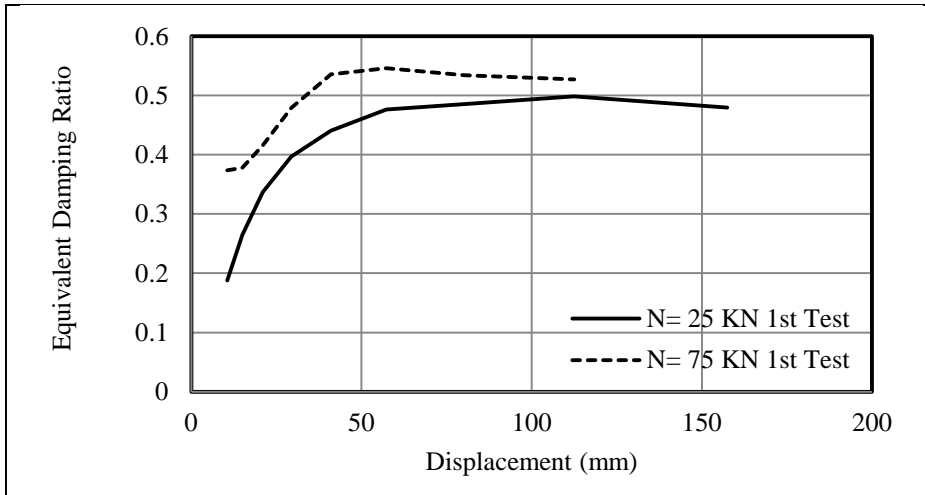


**Figure 3.105 :** Comparison of equivalent damping ratio for 8mm thick specimens under two extreme compressive axial loads.

The compressive axial load has the positive effect as it increases up to 50%, the maximum equivalent damping ratio increases as well from 50% to 55% in  $t=8\text{mm}$  thick steel cushions according to Figure 3.105.

The equivalent damping ratio for three distinct thicknesses in two extreme axial loads of  $N/N_0=25\%$  and  $N/N_0=75\%$  are compared in Figure 3.106.

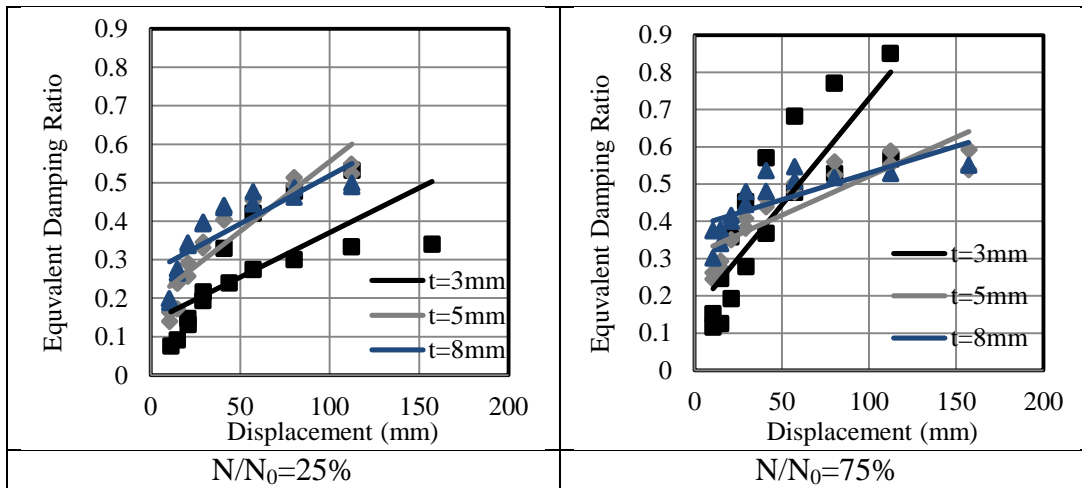


**Figure 3.106 :** Comparison of equivalent damping ratio for three distinct thicknesses under two extreme compressive axial loads.

In the case of  $N/N_0=25\%$  the maximum equivalent damping ratio increases with increasing thickness although 5mm thick specimen damping ratio after the displacement of 52mm is higher than 8mm thick specimen. In the case of  $N/N_0=75\%$ , as the axial load increases up to 50% the damping ratios of 3mm thick specimen is the least ratio up to displacement of 50 mm after this value 3mm thick specimens damping ratio is the largest value.

### 3.4.4 Effective (secant) stiffness

The relationship between the ratio of  $K_{\text{secant}}$  to  $K_{\text{initial}}$  versus displacement for three specific specimens with thickness of  $t= 3\text{mm}$ ,  $5\text{mm}$  and  $t= 8\text{mm}$  subjected to compressive axial loads of  $N/N_0=25\%$ ,  $50\%$  and  $75\%$  are compared in Figure 3.107, 3.108 and Figure 3.109 respectively this ratio in fact represents the velocity of the stiffness decaying.

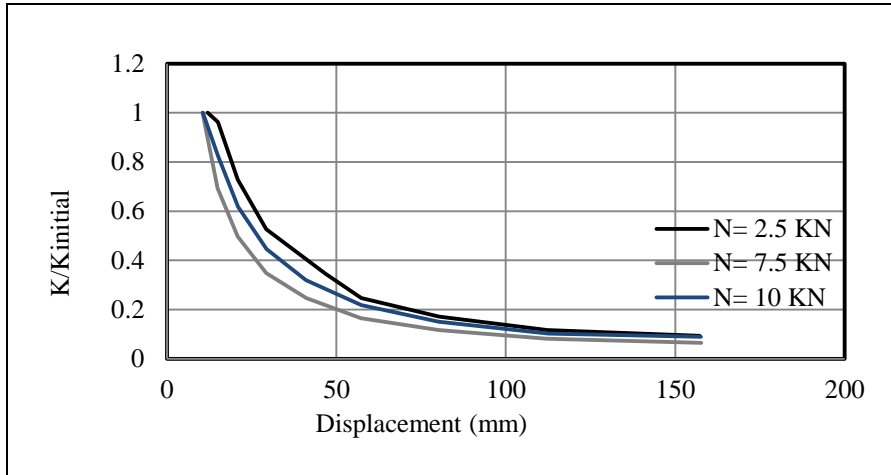


**Figure 3.107 :** Comparison of normalized stiffness ratio in terms of displacement for 3mm thick specimen under compressive axial loads.

According to Figure 3.107 the rate of stiffness decrease are independent of axial load value. Since, in all three states the mentioned rates are nearly identical.

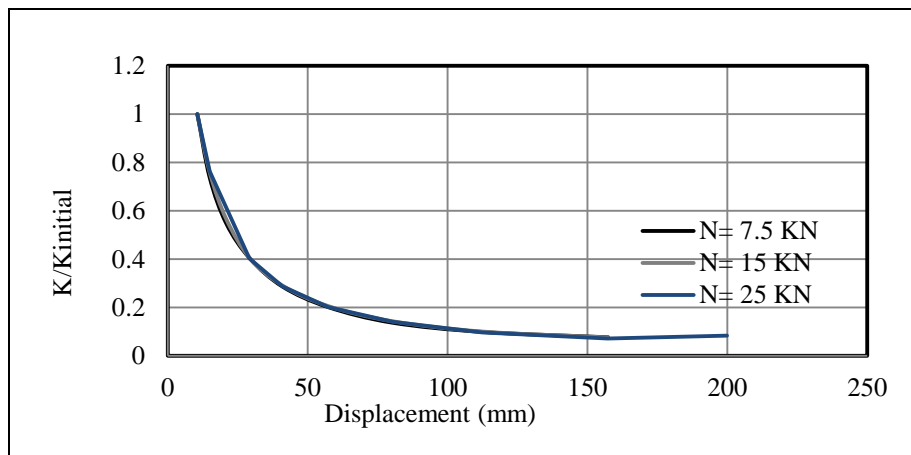


**Figure 3.108 :** Comparison of normalized stiffness ratio in terms of displacement for 5mm thick specimen under compressive axial loads.

According to Figure 3.108 the rate of stiffness decrease are independent of axial load value. Since, in all three states the mentioned rates are nearly identical.

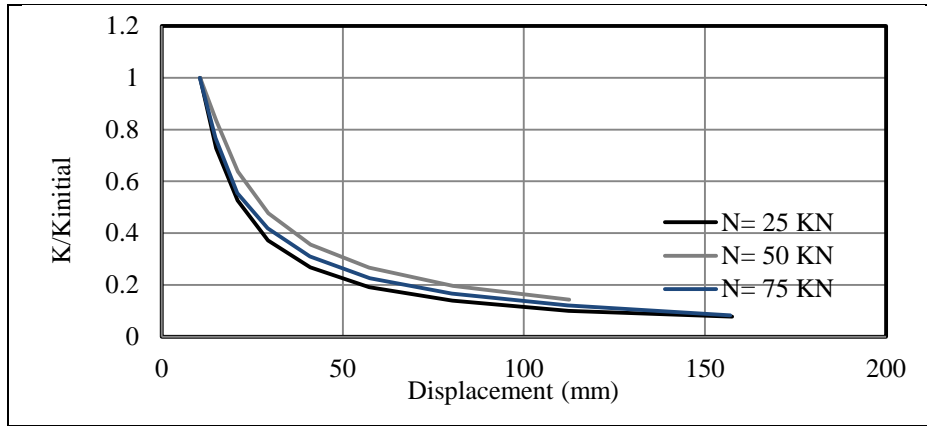


**Figure 3.109 :** Comparison of normalized stiffness ratio in terms of displacement for 8mm thick specimen under compressive axial loads.

In 8mm, thick specimen the same logic exists similar to 5mm and 3mm thick specimens. It seems that in the case of compressive axial force at the one displacement point the stiffness decadent rate for specimens are different while this case does not exist in specimens under tensile axial load.

### 3.5 Evaluation of Experimental Results for Three Specific Specimens under Bi-Directional Shear + Compression Loading

The experimental results derived from the bi-directional cyclic shear and compressive axial test for three different specimens are summarized at Table 3.3.

**Table 3.3 :** Summary of experimental results derived from bi-directional cyclic shear and compressive axial test for.

Specimen Type	Axial Load Ratio N/N <sub>0</sub>	Initial stiffness K <sub>0</sub> KN/mm	Yield Force (KN)	Max Force (KN)	Yield Displacement Dy (mm)	Ultimate Displacement Du (mm)	Ductility $\mu$
3mm thick Specimen	25%	0.07	0.72	3.62	10.60	157.59	14.86
	25%	0.20	2.14	4.57	10.58	157.53	14.89
	50%	0.23	3.47	3.87	14.97	157.43	10.52
	50%	0.28	2.93	4.18	10.49	157.72	15.04
	75%	0.22	3.25	3.80	14.99	157.65	10.52
	75%	0.15	1.6	4.48	10.49	157.49	15.02
5mm thick Specimen	25%	0.83	8.83	11.36	10.59	157.46	14.86
	25%	0.58	8.64	10.82	14.90	157.55	10.58
	50%	1.0	10.66	12.10	10.57	157.48	14.90
	75%	0.90	9.58	13.0	10.60	157.69	14.87
	75%	0.85	8.95	11.50	10.49	157.66	15.03
8mm thick Specimen	25%	2.20	32.94	37.80	14.99	157.61	10.51
	25%	3.13	32.91	37.73	10.51	157.54	14.99
	50%	3.31	34.96	48.74	10.57	112.56	10.65
	50%	2.86	30.0	38.91	10.49	157.39	15.0
	75%	2.26	23.91	56.87	10.58	112.58	10.64
	75%	2.96	31.13	45.26	10.50	157.34	14.99

### 3.5.1 Ductility

The trend of ductility for 3mm, 5mm and 8mm thick specimens under increase of compressive axial loads from  $N/N_0=25\%$ , to 75% in bi-directional cyclic shear and axial test are displayed test in Figure 3.110, 3.111 and Figure 3.112, respectively. The ductility decreases for 3mm thick specimen as compressive axial load decreases, as shown in Figure 3.110.

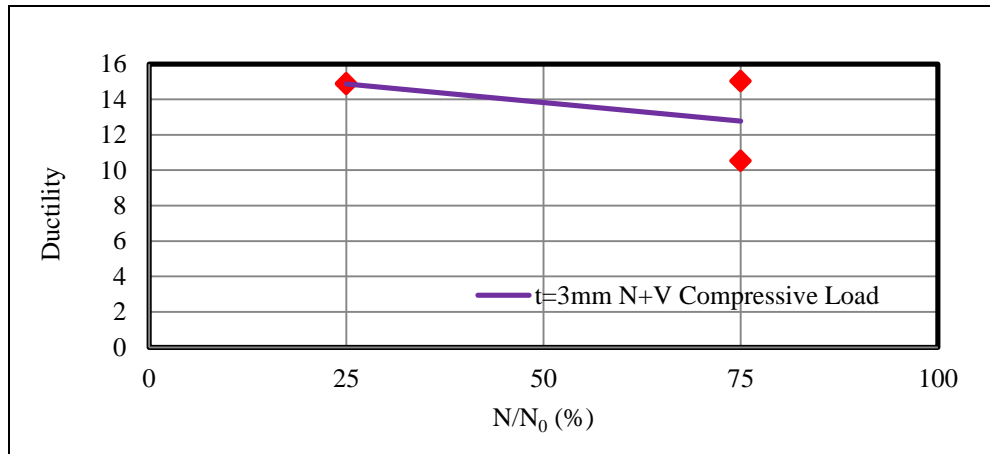


**Figure 3.110 :** Ductility trend for 3mm thick specimen under increase of compressive axial load.

The ductility increases for 5mm thick specimen as compressive axial load increases, as shown in Figure 3.111.

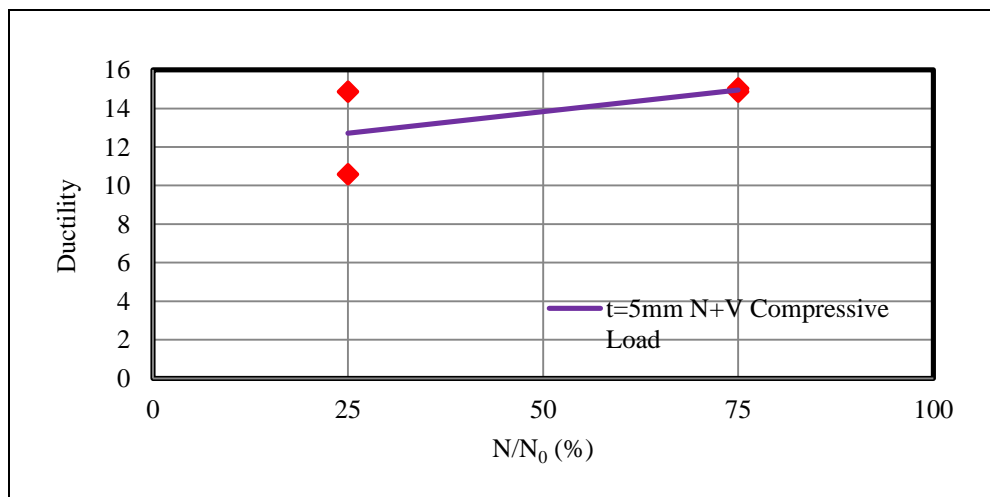


**Figure 3.111 :** Ductility trend for 5mm thick specimen under increase of compressive axial load.

The ductility remains constant for 8mm thick specimen as compressive axial load increases, as shown in Figure 3.112.

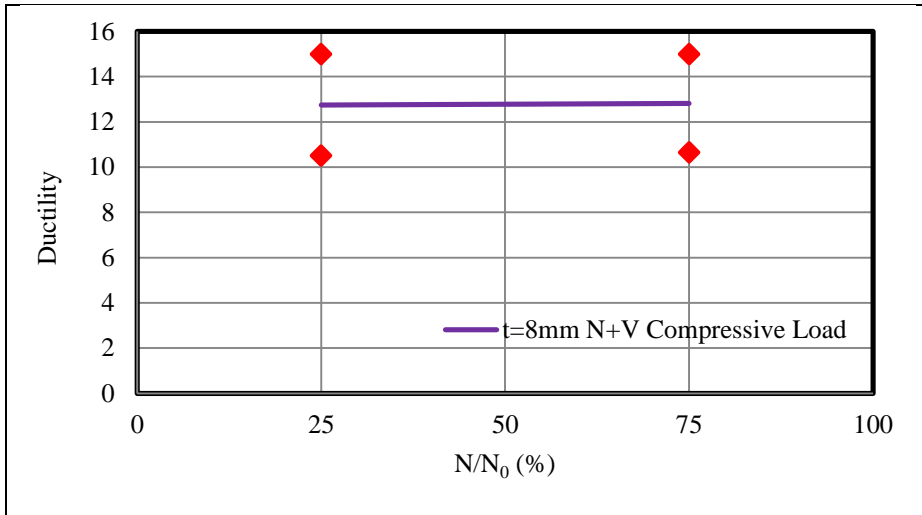


**Figure 3.112 :** Ductility trend for 8mm thick specimen under increase of compressive axial load.

### 3.5.2 Yield force and yield displacement

The trend line of yield force for 3mm, 5mm and 8mm thick specimens under increase of compressive axial loads from  $N/N_0=25\%$  to  $75\%$  in bi-directional cyclic shear and axial test are displayed test in Figure 3.113, 3.114 and Figure 3.115 respectively.

The yield force increases for 3mm thick specimen as compressive axial load increases, as shown in the Figure 3.113.

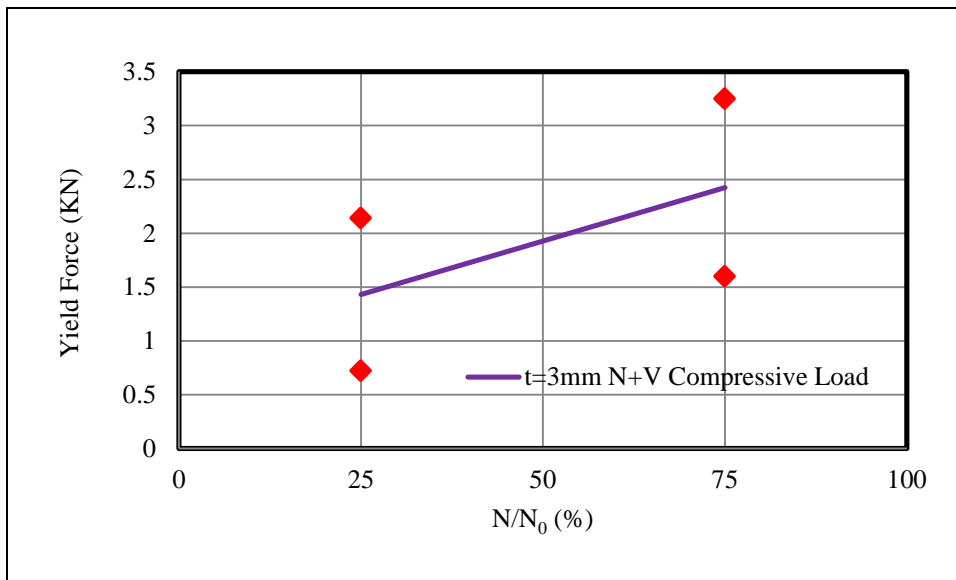


**Figure 3.113 :** Yield force trend for 3mm thick specimen under increase of compressive axial load.

The yield force increases for 5mm thick specimen as compressive axial load increases, as shown in Figure 3.114.

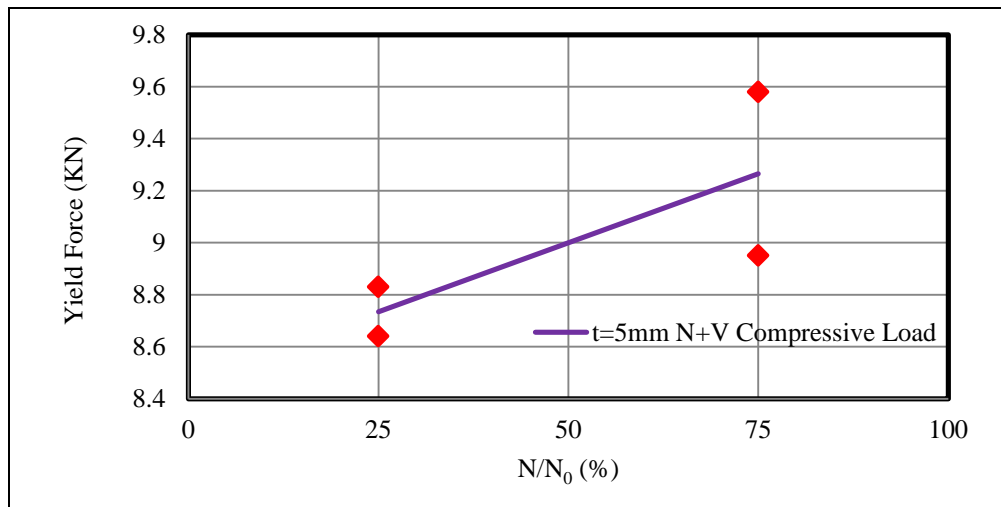


**Figure 3.114 :** Yield force trend for 5mm thick specimen under increase of compressive axial load.

The yield force decreases for 8mm thick specimen as compressive axial load increases, as shown in Figure 3.115.

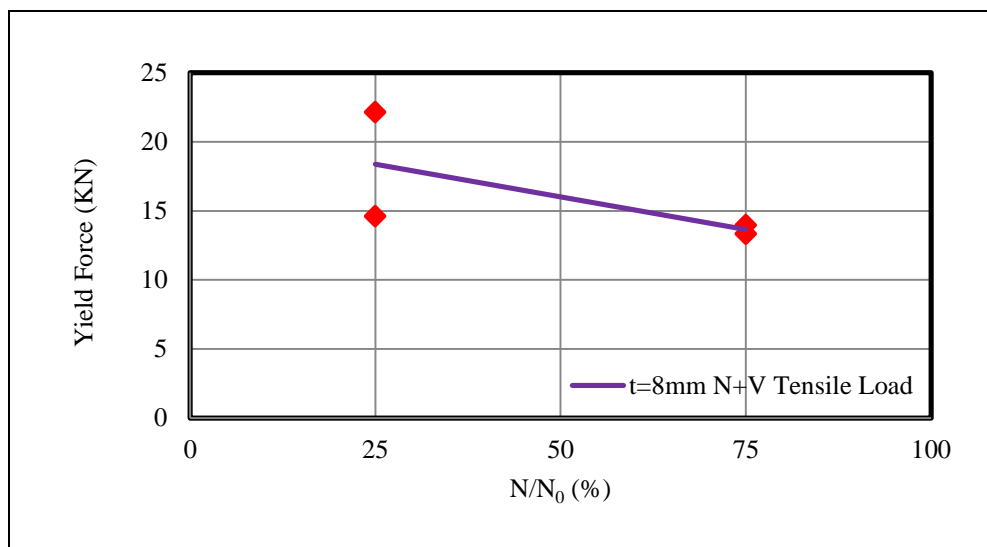


**Figure 3.115 :** Yield force trend for 8mm thick specimen under increase of tensile axial load.

The trend line of yield displacement for 3mm, 5mm and 8mm thick specimens under increase of compressive axial loads from  $N/N_0=25\%$ , to  $75\%$  in bi-directional cyclic shear and axial test are displayed test in Figure 3.116, 3.117 and Figure 3.118 respectively. The yield displacement increases for 3mm thick specimen as compressive axial load increases, as shown in Figure 3.116.

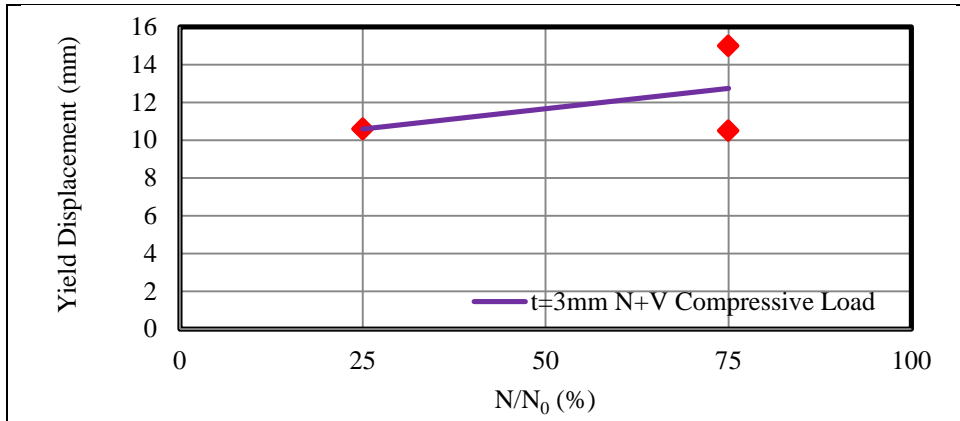


**Figure 3.116 :** Yield displacement trend for 3mm thick specimen under increase of compressive axial load.

The yield displacement decreases for 5mm thick specimen as compressive axial load increases, as shown in Figure 3.117.

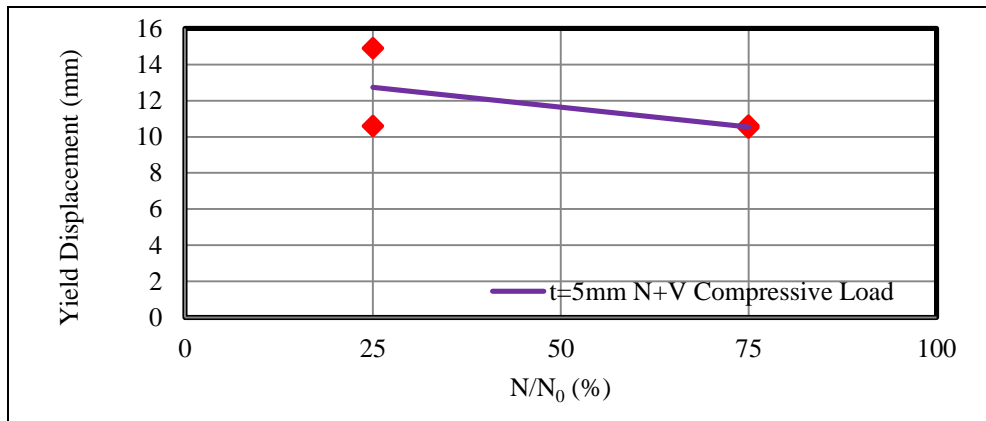


**Figure 3.117 :** Yield displacement trend for 5mm thick specimen under increase of compressive axial load.

The yield displacement decreases for 8mm thick specimen as compressive axial load increases, as shown in Figure 3.118.

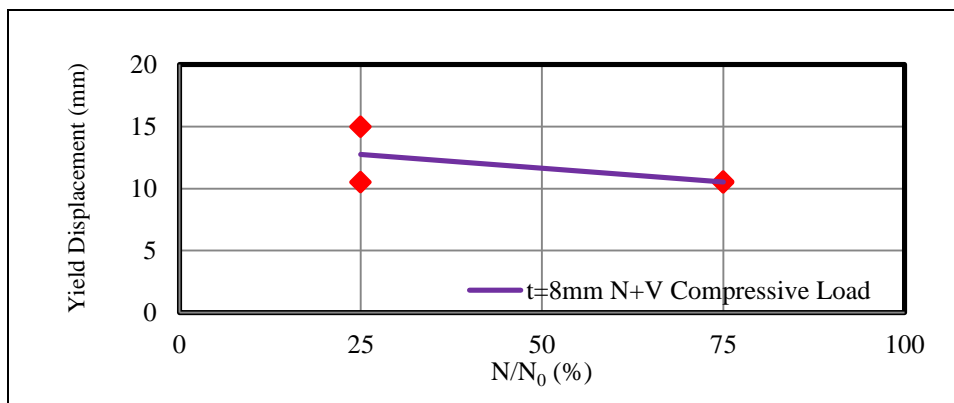


**Figure 3.118 :** Yield displacement trend for 8mm thick specimen under increase of compressive axial load.

### 3.5.3 Initial stiffness

The trend line of initial stiffness for 3mm, 5mm and 8mm thick specimens under increase of compressive axial loads from  $N/N_0=25\%$  to  $75\%$  in bi-directional cyclic shear and axial test are displayed test in Figure 3.119, 3.120 and Figure 3.121, respectively. The initial stiffness increases for 3mm thick specimen as compressive axial load increases, as shown in Figure 3.119.

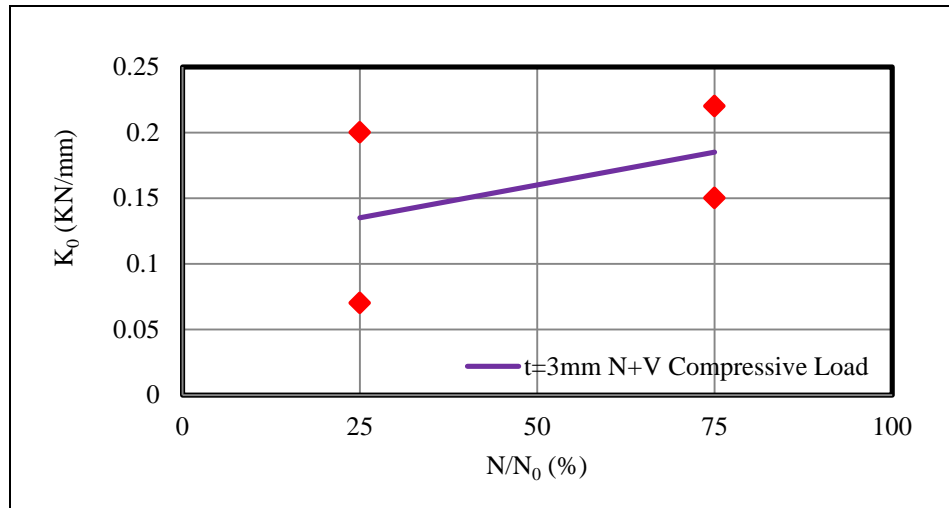


**Figure 3.119** : Initial stiffness trend for 3mm thick specimen under increase of compressive axial load.

The initial stiffness increases for 5mm thick specimen as compressive axial load increases, as shown in Figure 3.120.

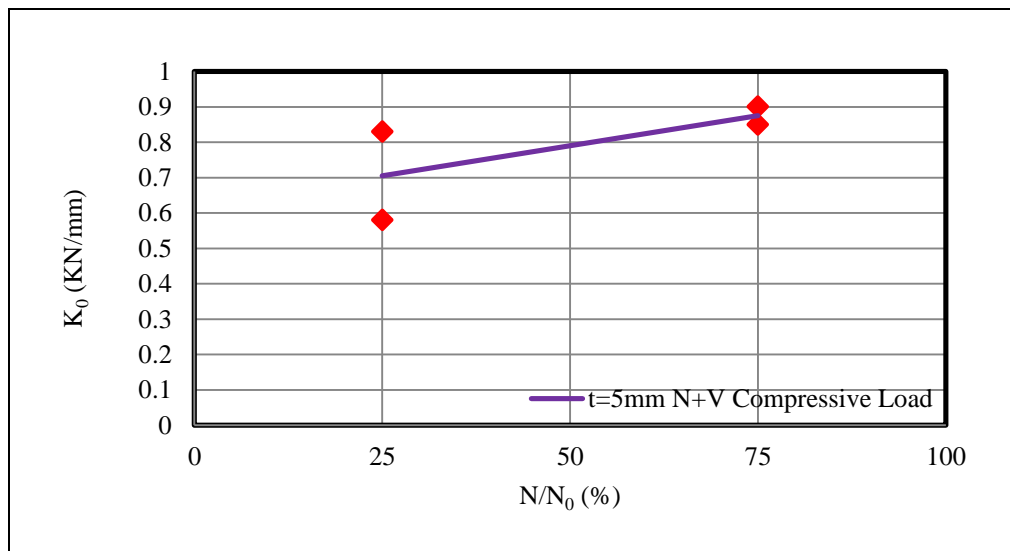


**Figure 3.120** : Initial stiffness trend for 5mm thick specimen under increase of compressive axial load.

The initial stiffness remains constant for 8mm thick specimen as compressive axial load increases, as shown in Figure 3.121.

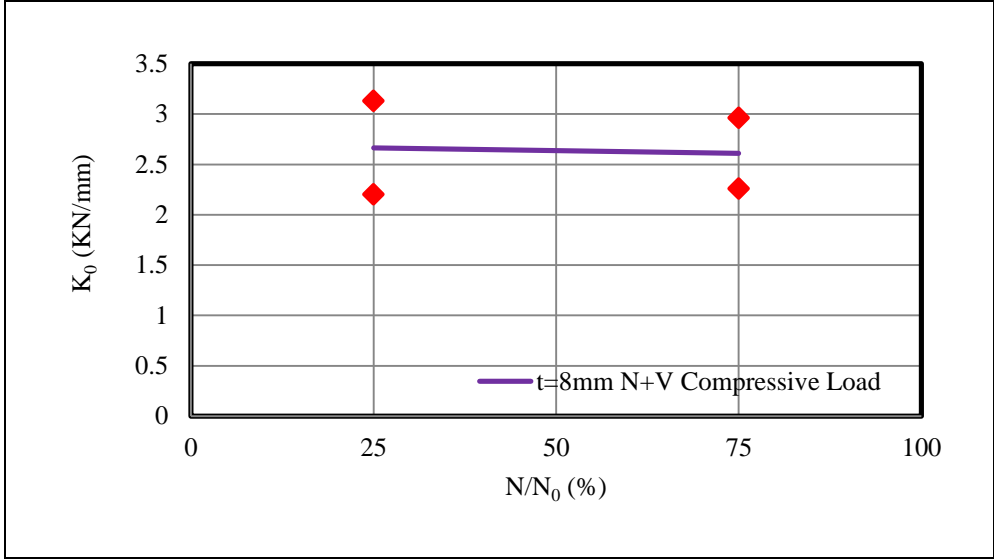


**Figure 3.121 :** Initial stiffness trend for 8mm thick specimen under increase of compressive axial load.

**3.5.4 Maximum shear force**

The trend line of maximum force for 3mm, 5mm and 8mm thick specimens under increase of compressive axial loads from N/N<sub>0</sub>=25% to 75% in bi-directional cyclic shear and axial test are displayed test in Figure 3.122, 3.123 and Figure 3.124 respectively. The maximum force remains constant for 3mm thick specimen as compressive axial load increases, as shown in Figure 3.122.

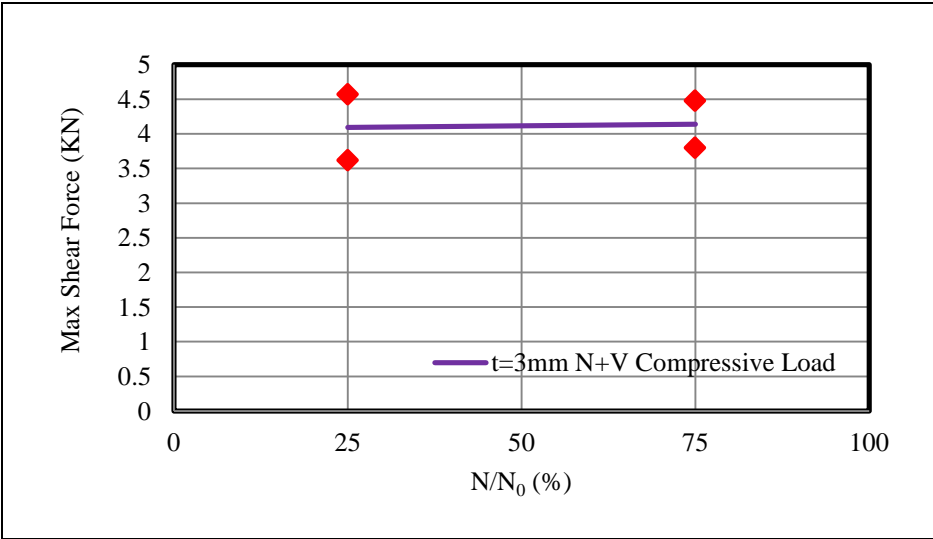


**Figure 3.122 :** Maximum force trend for 3mm thick specimen under increase of compressive axial load.

The maximum force increases for 5mm thick specimen as compressive axial load increases, as shown in Figure 3.123.

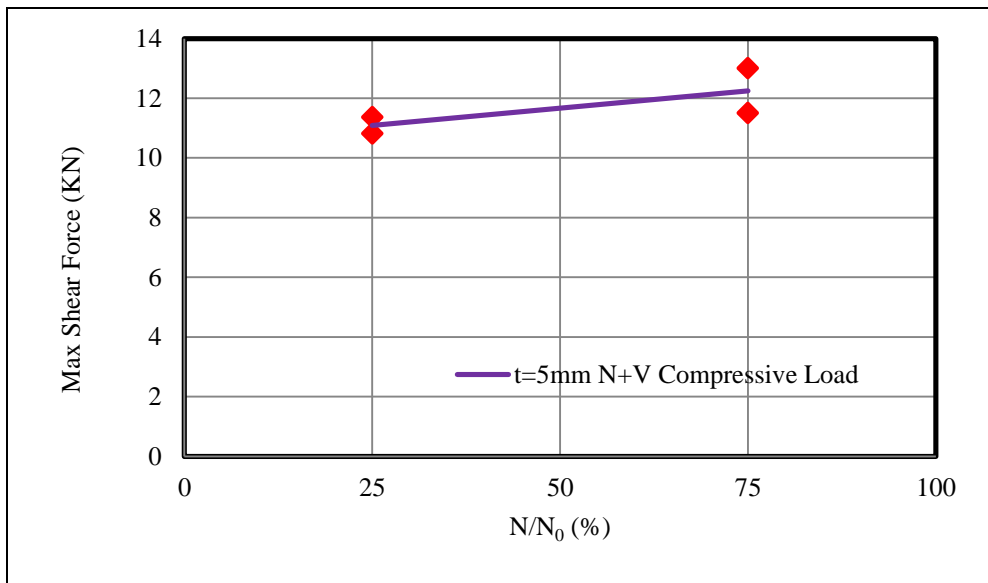


**Figure 3.123** : Maximum force trend for 5mm thick specimen under increase of compressive axial load.

The maximum force increases for 8mm thick specimen as compressive axial load increases, as shown in Figure 3.124.

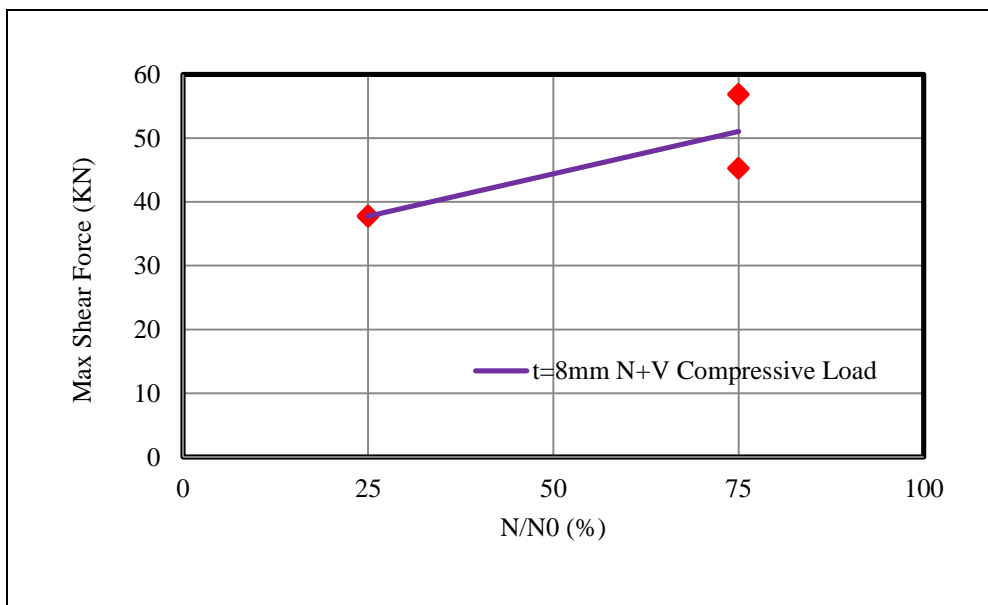


**Figure 3.124** : Maximum force trend for 8mm thick specimen under increase of compressive axial load.

### 3.6 Interaction Diagrams

The relation between axial force and maximum shear force for three distinct specimens are plotted in Figure 3.125. The enclosed area of the interaction diagram for the steel cushion with higher thickness is bigger. The interaction diagrams are formed by trend lines. It should be noted that the axial load in the positive part of y-axis is tensile load and the axial load in negative part of y-axis is compressive load.

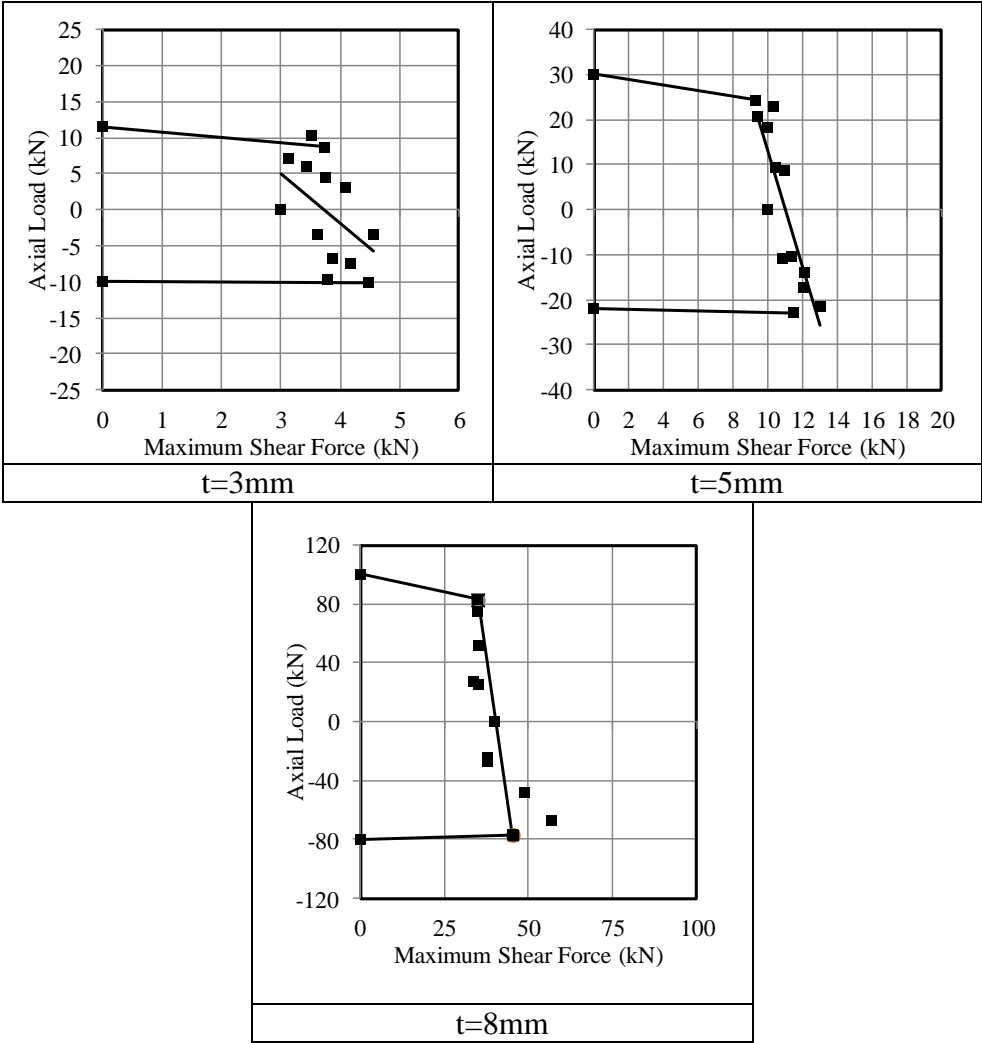


**Figure 3.125** : Interaction diagram for three distinct specimens.

According to interaction diagrams, the compressive axial load increases the maximum shear force; in contrast, the tensile axial load decreases the maximum shear force. Depending on interaction curves, it seems that there is an optimum bandwidth in which the steel cushions have the reasonable shear capacity. This bandwidth may be proposed as +/- 25% of the maximum axial load capacity.

#### 4. CYCLIC TEST OF CLADDING PANELS EQUIPPED WITH STEEL CUSHIONS (SYSTEM TESTS)

In this chapter the cyclic test of cladding panels equipped with steel cushions are discussed. This chapter divided into two sections. In the first section, the experimental results of each system test are presented and discussed. In the second section, the experimental results of each system test are compared with each other.

##### 4.1 Introduction

A total number of four system tests were carried out to evaluate the flexural deformation capacity of the steel cushions and obtain the optimum arrangement of the steel cushions among concrete cladding panels. Since the steel cushions are great deal source of energy dissipation under wind and earthquake, the main part of input energy dissipated by these devices and no significant damage exists in other structural elements such as columns and concrete cladding panels during the excitation. The main parameters of the tests were the thickness and arrangement of steel specimens. There were two kinds of test performed named single steel cushion and double steel cushion tests. The single and double terms indicate the number of steel cushions at the base as the support for concrete cladding panels as shown in Figure 4.1.

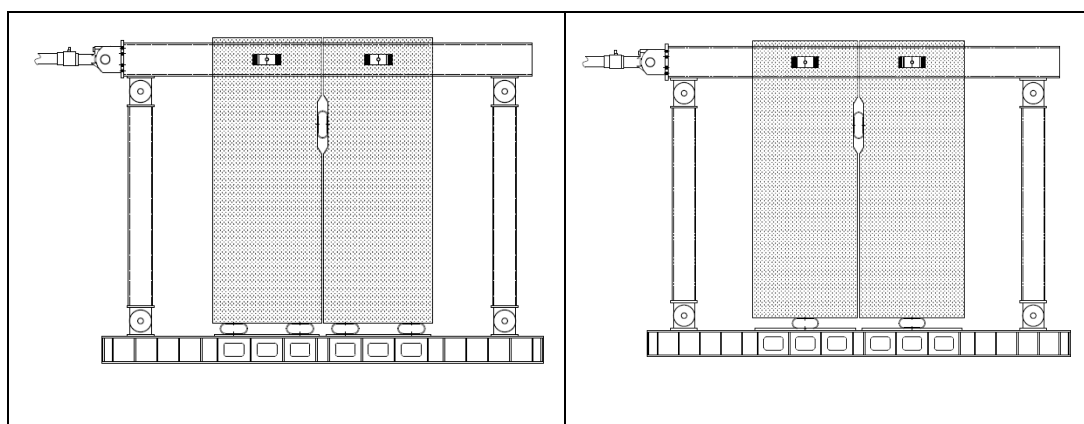


**Figure 4.1** : Double and single cushion tests

### 4.2 System Test Set-Up

The system tests performed to investigate the behavior of steel cushions in the claddings of industrial buildings. The test set up consisted of RC cladding panels and fully pinned swaying steel frame to transfer the lateral load to RC walls, equipped with steel cushions in different location as connector, such as in panel to support, in panel to panel and in panel to beam connections. The steel cushions were assembled through the bolting to structural element such as panels, foundation and the top beam. The dimensions of the test set-up are shown for single cushion and double cushion test types in Figure 4.2 and 4.3 respectively.

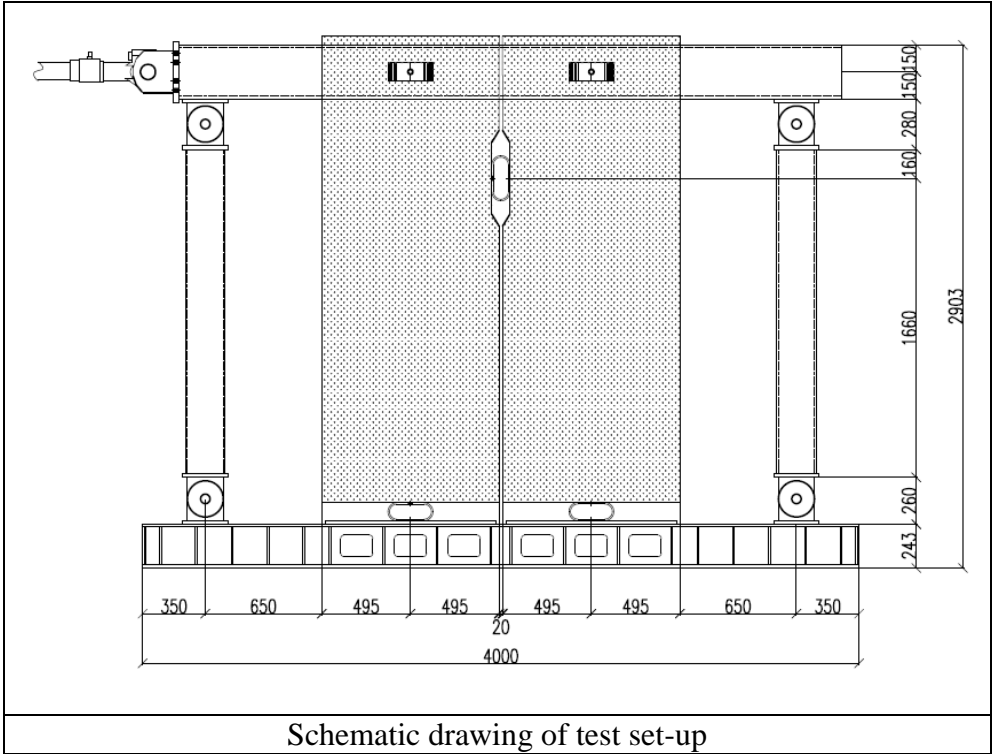


**Figure 4.2 :** Typical dimension of single cushion test set-up.

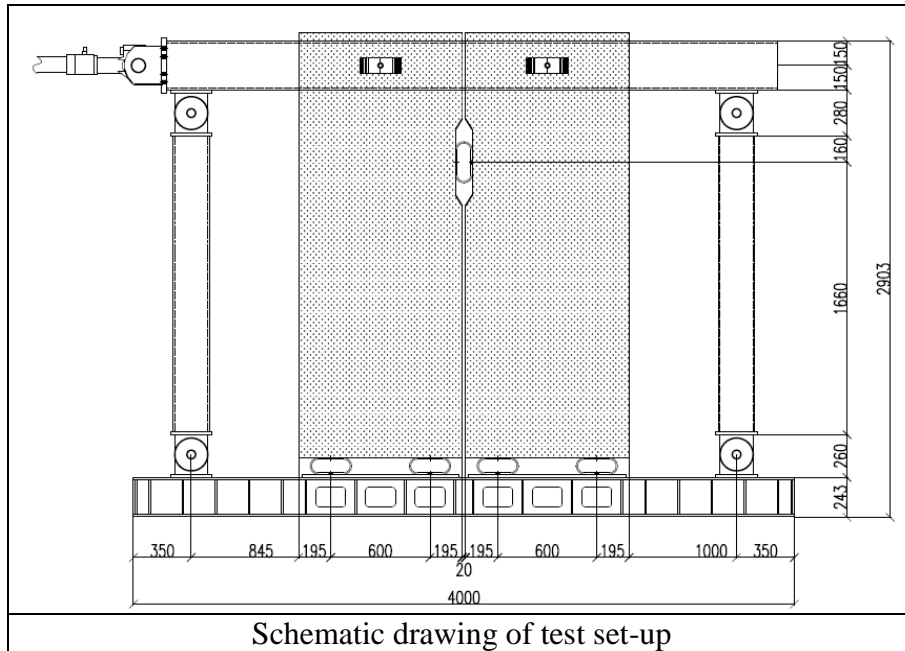


**Figure 4.3 :** Typical dimension of double cushion test set-up.

Due to zero lateral stiffness and strength of loading steel frame, which is caused by its own mechanism condition, the steel channel bracings are used for security and they are removed before the test. The steel bracings are shown in Figure 4.4. Two identical panel systems used at both sides of the actuator axis, to arise symmetry for test set-up for elimination of any out of plane forces, for sake of eccentricity of actuator with respect to panels as shown in Figure 4.5.

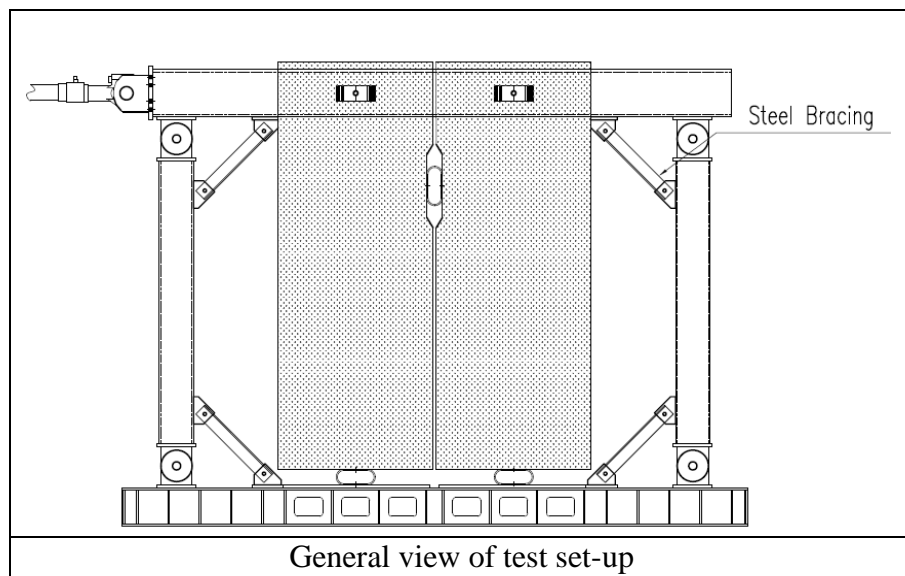


**Figure 4.4 :** Steel bracing in the loading frame.

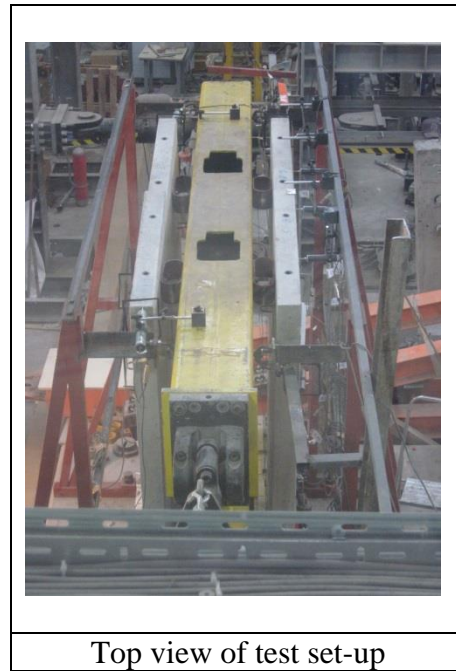


**Figure 4.5 :** Two pairs of concrete panel at two sides.

The horizontal actuator located at tip of the specimen directly applied the drift based cyclic loading pattern. The upper steel beam of the testing frame was fixed to the swivel head of the actuator in order to apply the loading protocol as shown in Figure 4.6. To avoid the out of plane movement of loading frame, two truss systems utilized per side as shown in Figure 4.7.

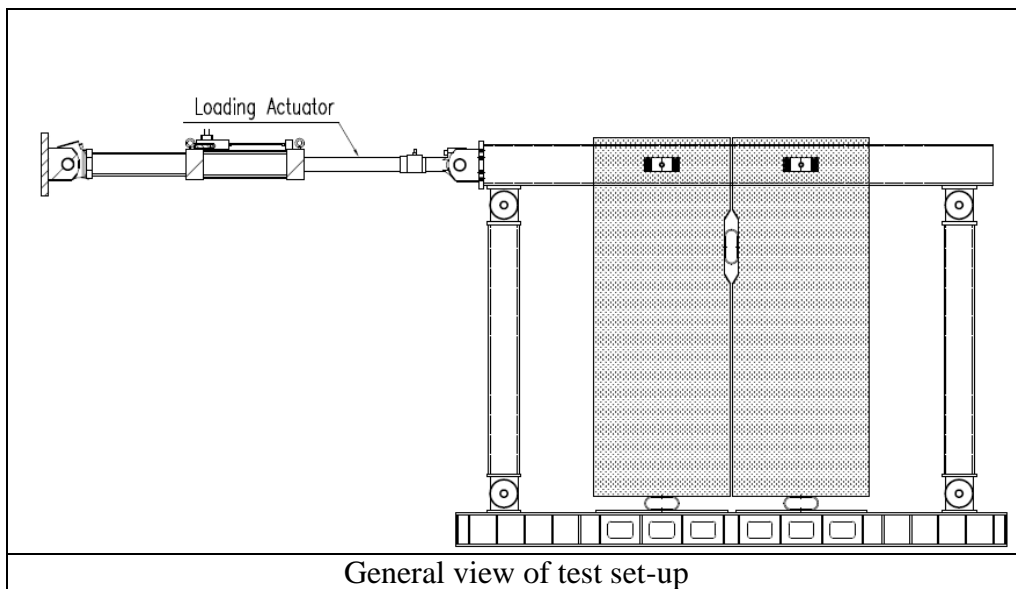


**Figure 4.6 :** Loading actuator.

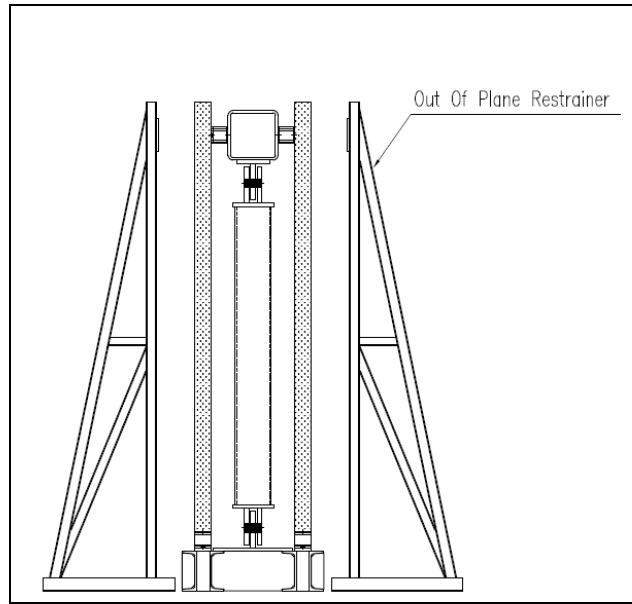


**Figure 4.7 :** Truss system used for possible out of plane movements.

The dimension of the concrete cladding panels and the location of panel to support, panel to panel and panel to beam steel cushions, are dimensioned in Figure 4.8. In addition, the concrete panels are designed according to the design specification of the concrete cladding panels in industrial buildings (TS 9967, 1992). The reinforcement steel details in cladding panels are shown in Figure 4.9 and 4.10.

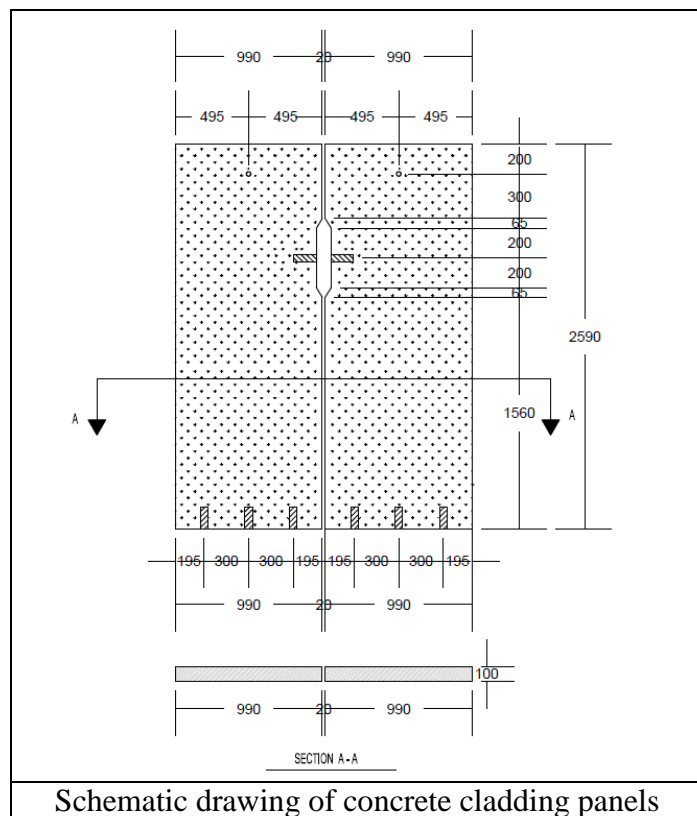


**Figure 4.8 :** Typical dimension of concrete cladding panels.



### 4.3 System Test Loading Protocol

The testing protocols selected in accordance with the recommendations placed in FEMA 461, which actually based on the expected maximum drift ratios. The target displacements derived by multiplying the “ $a_i/a_{10}$ ” ratios to targeted maximum deformation amplitude of the loading history ( $\Delta_m$ ), (FEMA 461, 2007). The ratios to determine target displacement amplitudes defined in Table 4.1. Ten diverse amplitude levels exist in the table. Two full cycles applied for each displacement target.

**Table 4.1 :** Relative loading history deformation amplitude, (FEMA 461, 2007).

step	1	2	3	4	5	6	7	8	9	10	11	12	13
$a_i/a_{10}$	0.018	0.025	0.035	0.048	0.068	0.095	0.133	0.186	0.26	0.364	0.51	0.714	1.0

The above table has been taken into account for creating loading protocol with assuming  $\Delta_m$  is equal to 30 cm. The displacement protocol is illustrated in Figure 4.11.

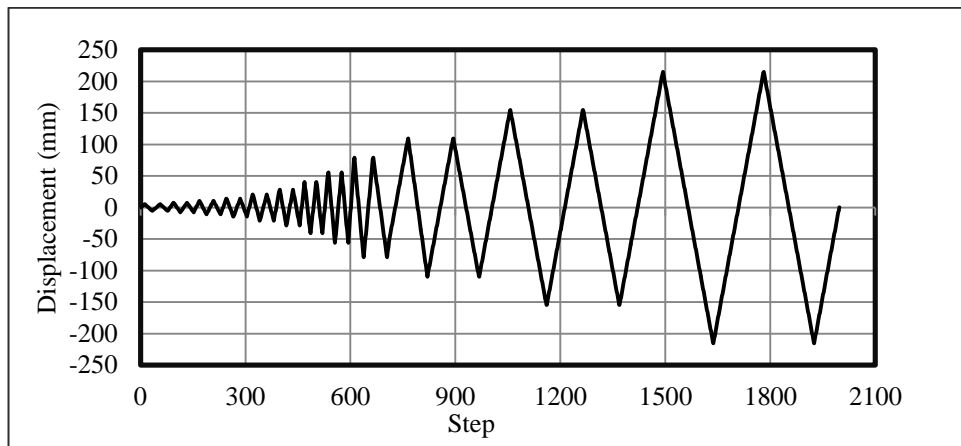


**Figure 4.11 :** Drift based cyclic loading protocol.

The maximum displacement target was 30 cm, but the cyclic loading protocol can be applied up to 21.5 cm, because of contact of the cladding panels to out of plane restrainers. The values of cyclic displacement protocol are shown in Table 4.2.

**Table 4.2 :** Displacement target values.

Cycle	1	2	3	4	5	6	7	8	9	10	11	12
Displacement target (mm)	5.40	7.55	10.58	14.29	20.95	28.28	40.64	55.75	78.98	109.64	154.64	215.35

### 4.4 System Test I (Single Cushion Test)

The system test I was single cushion test. 8 mm cushions were used as panel to support connection (one cushion per panel); 5mm steel devices in panel-to-panel connection and, 8mm ones in panel to beam connection were utilized. Totally, four 8mm, two 5mm, and four 8 mm at the bottom, in the middle, and on the top level were used respectively. This arrangement is shown at Figure 4.12.

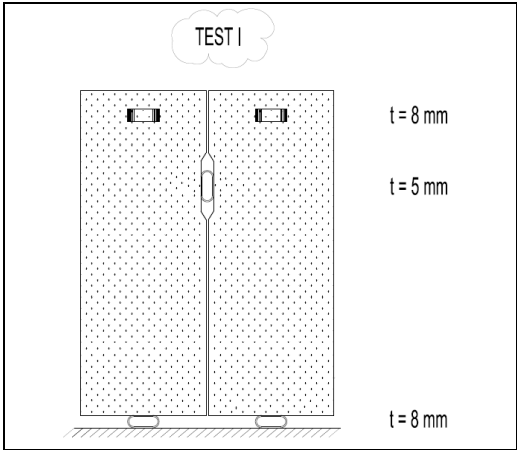


**Figure 4.12 :** Arrangements of steel cushions in system test I.

For evaluation of steel cushions yielding, the used strain gauge locations were as follows. At the base to panel connection, the strain gages were located at two vertices of 8mm steel cushions. In panel to panel connection, the location of strain gages were at the bottom, in the middle, and on the top side of steel cushions, to assess strain history of steel cushions in axial and shearing direction. Eventually, in panel to beam connection, the strain gages were located at two vertices of steel cushions, to evaluate the strain history in shearing direction, plus in the middle of steel cushion next to panels in one side, and next to beam in another side to investigate the strain history in axial direction. The location of strain gages are shown in Figure 4.13.

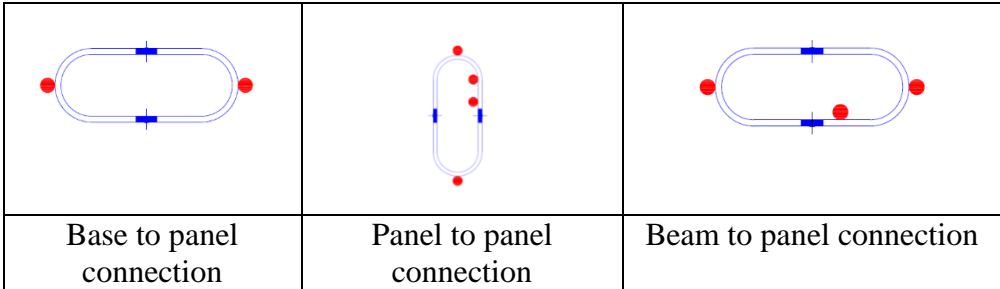


**Figure 4.13 :** Location of strain assessment devices in system test I.

Transducers and their locations are illustrated in Figure 4.14 and 4.15. In this test, to measure the out of plane movement, transducers were utilized on the top parts of panel 3 and panel 4.

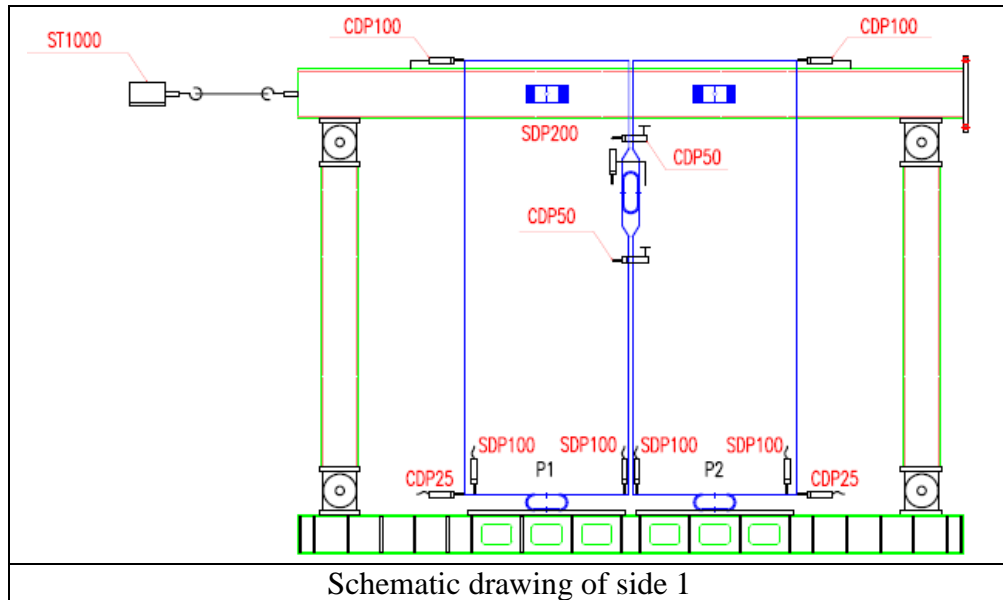


**Figure 4.14 :** Location of transducers in side 1 in system test I.

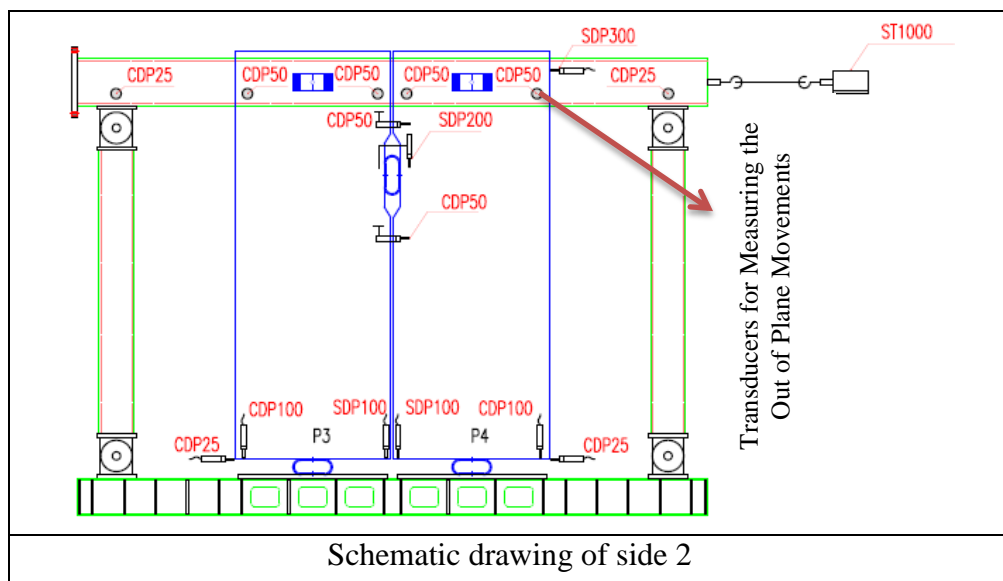


**Figure 4.15 :** Location of transducers in side 2 in system test I.

#### 4.4.1 Evaluation of experimental results obtained from system test I

In this section, the experimental results are presented and discussed.

##### 4.4.1.1 Actuator force-top displacement relation

The experimental actuator force in terms of displacement and drift derived from the system Test I are shown in Figure 4.16 and 4.17.

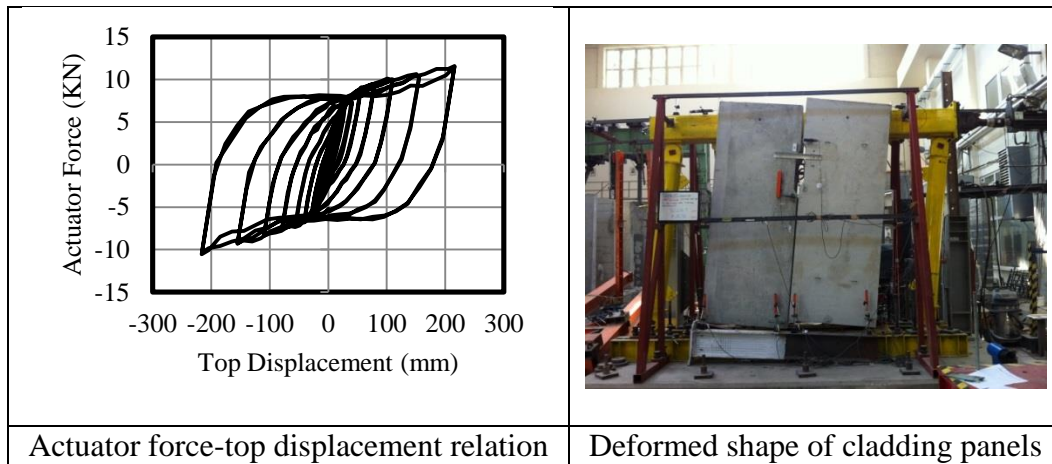


**Figure 4.16 :** Force-Top displacement Relation obtained from system test I.

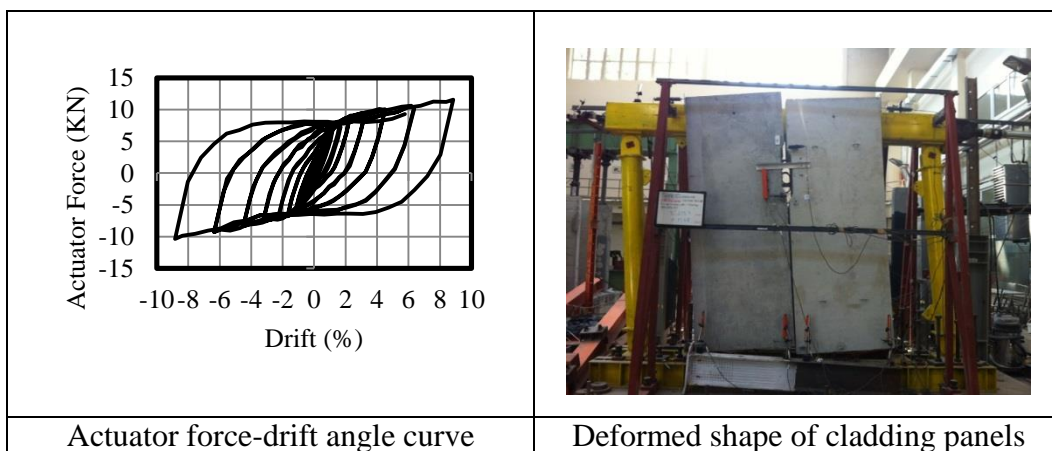


**Figure 4.17 :** Force-Drift angle curve obtained from system test I.

The experimental results obtained from system test I are summarized in Table 4.3. The force – drift angle relation of Figure 4.17 shows a stable hysteresis behavior. Any damages were not observed on steel cushions and cladding panels. The cladding panels remain in the elastic range and the steel devices showed the inelastic behavior. The increase of strength is observed after 1.16% drift angle at load vs. drift curve in other word after the yield drift the strength increases as the drift increases.

**Table 4.3 :** Summary of test results obtained from system test I.

Yielding Force (KN)	Max Force (KN)	Yielding Drift (%)	Max Drift (%)
6.1	11.58	1.16	8.84

#### 4.4.1.2 Energy dissipation

The dissipated energy is measured by the area encased by load-drift angle. Cumulative dissipative energy hysteresis curve vs. the drift angle is presented in Figure 4.18. As the dissipative devices in panel-to-panel connection had the

maximum shear deformation, thus they had the biggest contribution in dissipative energy, the devices yielded after 1.16% drift angle. The device dissipated approximately 354 KN.mm energy at the drift angle less than 1.16%, when the devices started to yield. At the drift angle lower than 1.16%, the energy has been dissipated by the visco-elastic behavior of steel devices. At the drift angle larger than 1.16% the dissipative energy increased considerably due to yielding of the energy dissipative devices. The device dissipated the maximum dissipative energy amount of 23102 KN.mm at the maximum drift angle of 8.8%.

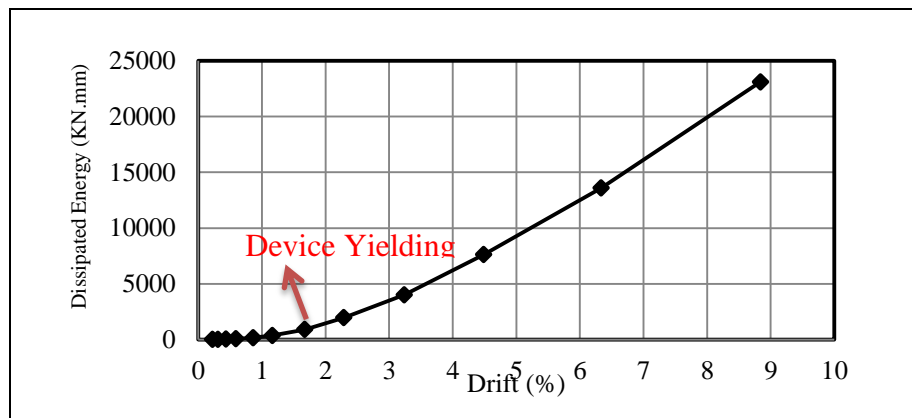


**Figure 4.18 :** Cumulative energy vs. drift curve obtained from system test I.

#### 4.4.1.3 Equivalent viscous damping

According to Figure 4.19, the equivalent damping ratio increases with increase of drift angle of system. Particularly between the drift angle of 1.16% and 1.67%, there is significant increase for the sake of dissipative devices' yielding at panel-to-panel connection. In addition, the equivalent damping reaches to the maximum value of 30%.

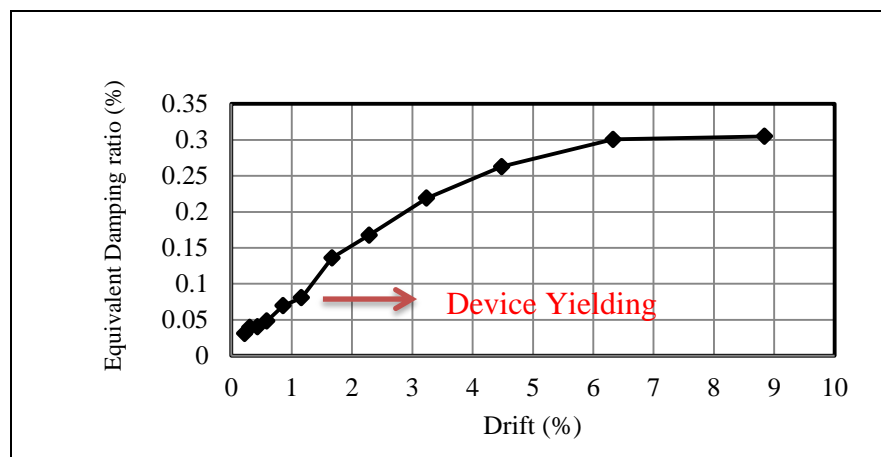


**Figure 4.19 :** Equivalent damping ratio vs. drift curve obtained from system test I.

**4.4.1.4 Effective (secant) stiffness**

The system possess the initial stiffness amount of 0.31 KN/mm at the drift angle of 0.22%, as the drift angle increases the secant stiffness declines and reaches to the value of 0.0507 KN/mm at the maximum drift angle, this shows approximately 84% reduction. The secant stiffness vs. drift relation is displayed in Figure 4.20.

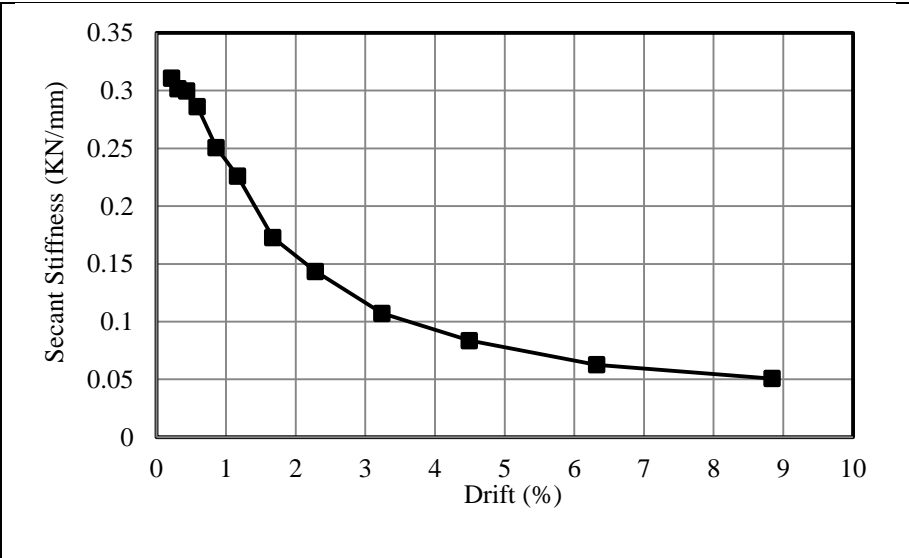


**Figure 4.20 :** Secant stiffness vs. drift relation obtained from system test I.

**4.4.1.5 Relative vertical displacement of panel to panel steel cushions**

The actuator force vs. relative displacement and drift relations for steel cushion in panel 1 to panel 2 connections are presented in Figure 4.21. The steel cushion in panel 1 to panel 2 connection is denoted by S12. The maximum relative displacements of S12 is 90.26 mm at the actuator force of 11.58 KN.

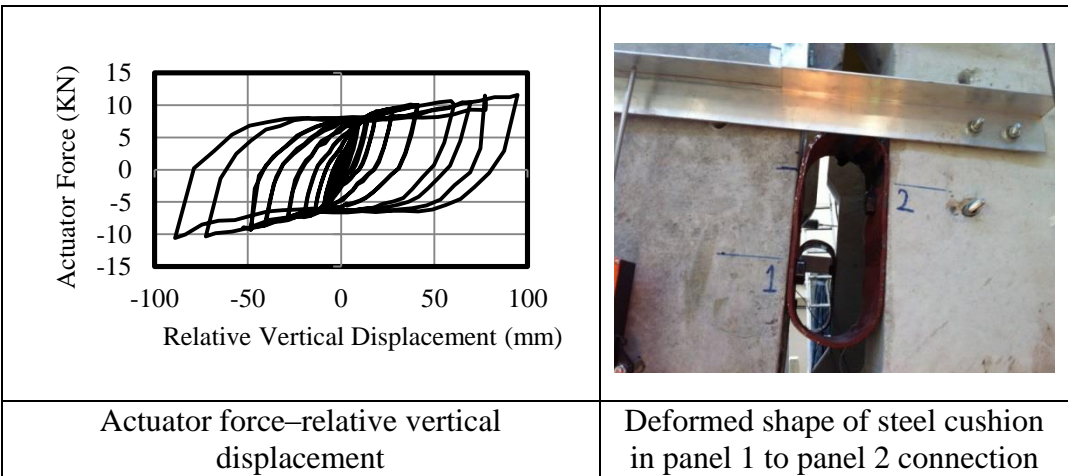


**Figure 4.21 :** Actuator force vs. relative displacement relation for steel cushion in panel 1 to panel 2 connection obtained from system test I.

The strain gauges locations on the specimens in panel-to-panel connections are shown in Figure 4.22.

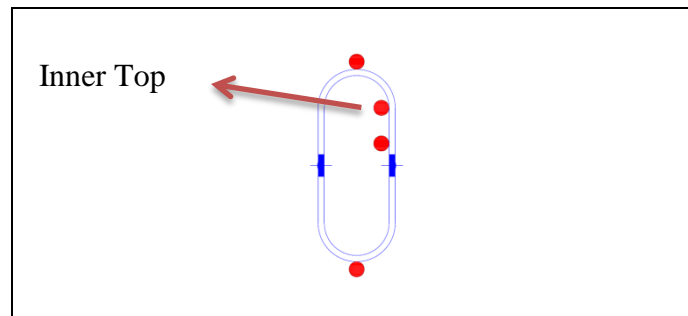


**Figure 4.22 :** Strain gauges location on steel cushions in panel-to-panel connection obtained from system test I.

The specimen yields at the drift angle of 1.16%. Location of the first yielding is the beginning of the arc section of specimen (inner top). The strain vs. drift angle relation for inner top point is presented in Figure 4.23.

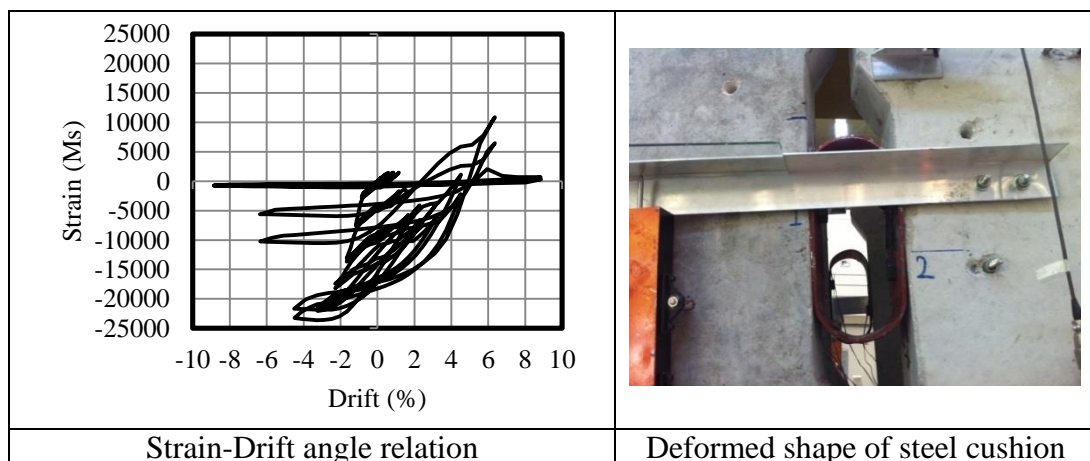


**Figure 4.23 :** Strain vs. drift angle relation for steel cushion in panel 1 to panel 2 connection obtained from system test I.

The actuator force vs. relative displacement and drift relations for steel cushion in panel 3 to panel 4 connection is presented in Figure 4.24. The steel cushion in panel 3 to panel 4 connection is denoted by S34, The maximum relative displacements of S34 is 87.66 mm at the actuator force of 11.58 KN.

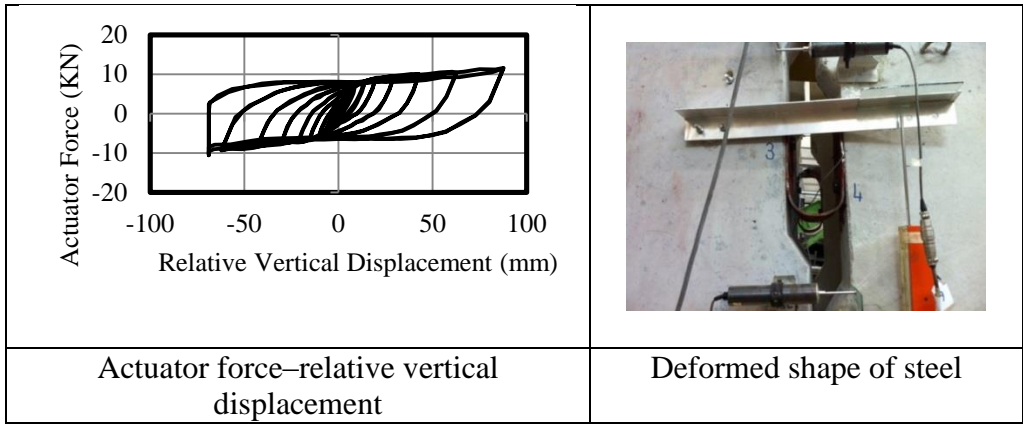


**Figure 4.24 :** Actuator force vs. relative displacement relation for steel cushion in panel 3 to panel 4 connection obtained from system test I.

The specimen yields at the drift angle of 1.16%. Location of the first yielding is the beginning of the arc section of specimen (inner top). The strain vs. drift angle relation for inner top point is presented in Figure 4.25.

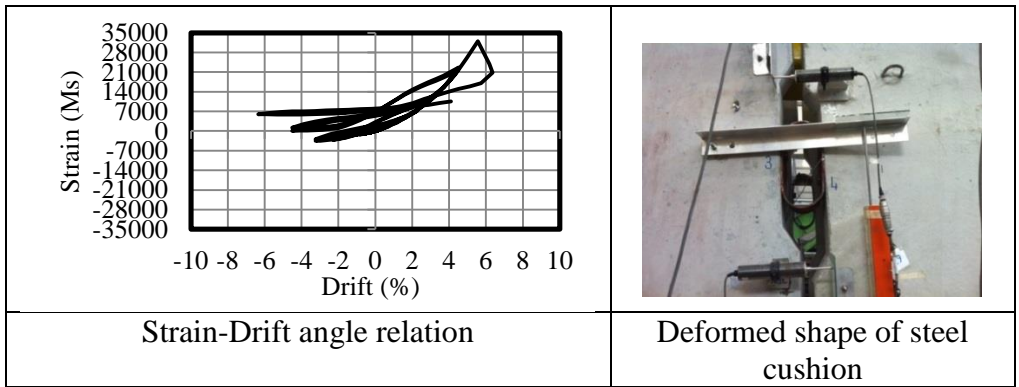


**Figure 4.25 :** Strain vs. drift angle relation for steel cushion in panel 3 to panel 4 connection obtained from system test I.

Two cushions between two adjacent panels behaved nearly symmetrically the actuator force vs. relative displacement relation for two steel devices are compared in Figure 4.26.

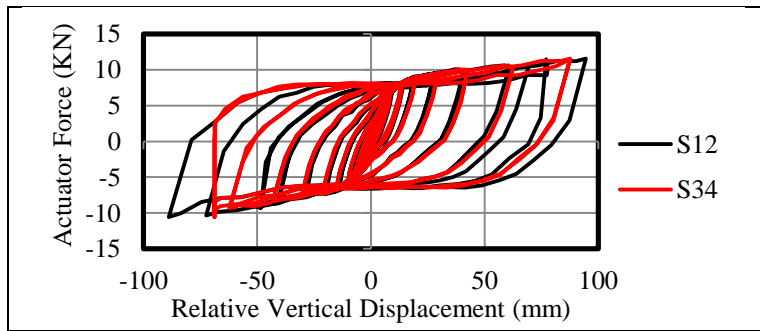


**Figure 4.26 :** Comparison of actuator force vs. relative displacement of S12 and S34 obtained from system test I.

#### 4.4.1.6 Relative horizontal displacement of panel to support steel cushions

To examine the shear displacement of steel cushion beneath panel 1, the actuator force vs. relative displacement relation is presented in Figure 4.27. This steel cushion is denoted by S1. The maximum relative displacement for S1 is 13.45 mm at the actuator force of 11.22 KN. However as the transducer was installed at level of 20 cm from the panel base, the steel device horizontal displacement is smaller than this value. In fact, the recorded horizontal tip displacement is formed by combination of the panel rotation and horizontal displacement of steel cushions although; contribution of rotation is more than horizontal displacement of steel cushions. In addition, the behavior is asymmetric.

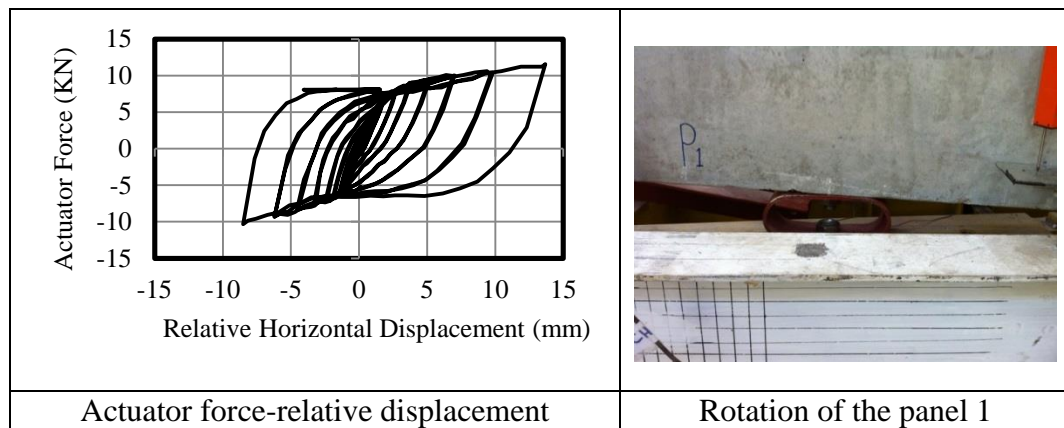


**Figure 4.27 :** Actuator force vs. relative displacement relation for steel cushion beneath panel 1 obtained from system test I.

According to Figure 4.27, the panel 1 rotated which forced the steel cushion to rotate. The strain gauges locations for the support steel devices are shown in Figure 4.28. According to the strain history, the steel device did not yield i.e. the steel cushion remained in elastic range.

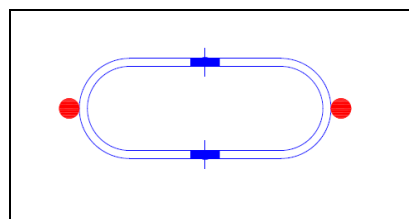


**Figure 4.28 :** Strain gauge location steel cushions in panel to support connection obtained from system test I.

The actuator force vs. relative displacement relation is presented in Figure 4.29 this steel cushion is denoted by S2. The maximum relative displacement for S2 is 6.6 mm at the actuator force of 8.33 KN. However as the transducer was installed at level of 20 cm from the panel base, the steel device horizontal displacement is smaller than this value. In fact, the recorded horizontal displacement is formed by combination of the panel base rotation and horizontal displacement of steel cushions although; contribution of rotation is more than horizontal displacement of steel cushions. In addition, the behavior is asymmetric. It should be noted that the relevant transducer was removed after the 6.6mm for the sake of insufficient capacity.

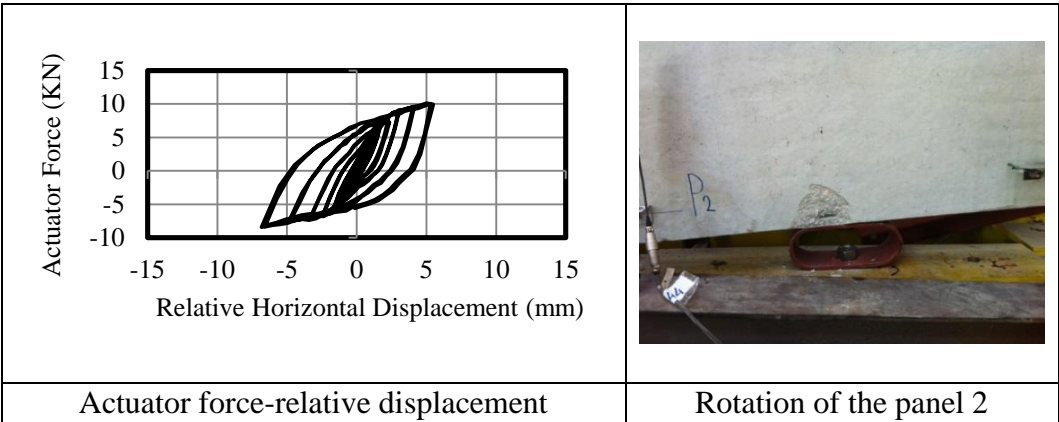


**Figure 4.29 :** Actuator force vs. relative displacement relation for steel cushion beneath panel 2 obtained from system test I.

According to Figure 4.29, the panel 2 rotated which forced the steel cushion to rotate. According to the strain gauges history, the steel device did not yield i.e. the steel cushion remained in elastic range.

The actuator force vs. relative displacement relation is presented in Figure 4.30. This steel cushion is denoted by S3. The maximum relative displacement for S3 is 10.99 mm at the actuator force of 9.94 KN. However as the transducer was installed at level of 20 cm from the panel base, the steel device horizontal displacement is smaller than this value. In fact, the recorded horizontal displacement is formed by combination of the panel rotation and horizontal displacement of steel cushions although contribution of rotation is more than horizontal displacement of steel cushions. In addition, the behavior is asymmetric.

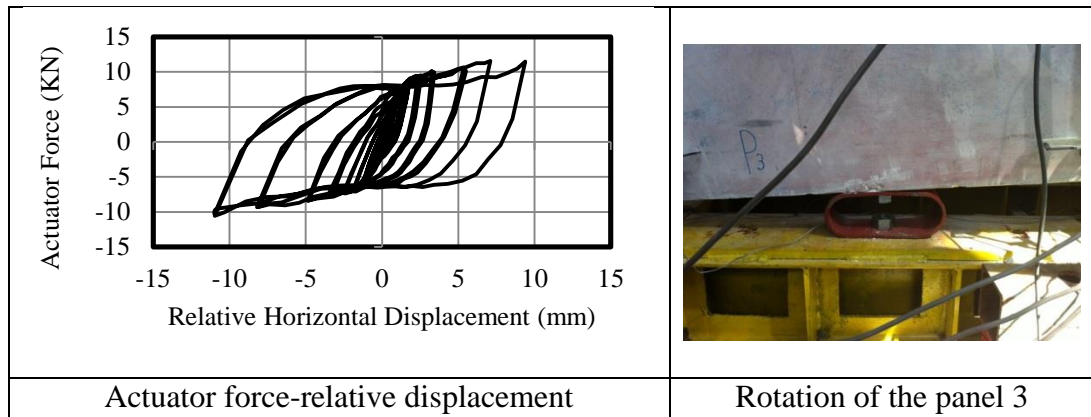


**Figure 4.30 :** Actuator force vs. relative displacement relation for steel cushion beneath panel 3 obtained from system test I.

According to Figure 4.30, the panel 3 rotated which forced the steel cushion to rotate. According to the strain gauges history, the steel device did not yield i.e. the steel cushion remained in elastic range.

The actuator force vs. relative displacement relation is presented in Figure 4.31. This steel cushion is denoted by S4. The maximum relative displacement for S4 is 13.49 mm at the actuator force of 11.24 KN. However as the transducer was installed at level of 20 cm from the panel base, the steel device horizontal displacement is smaller than this value. In fact, the recorded horizontal displacement is formed by combination of the panel rotation and horizontal displacement of steel cushions although contribution of rotation is more than horizontal displacement of steel cushions. In addition, the behavior is asymmetric.

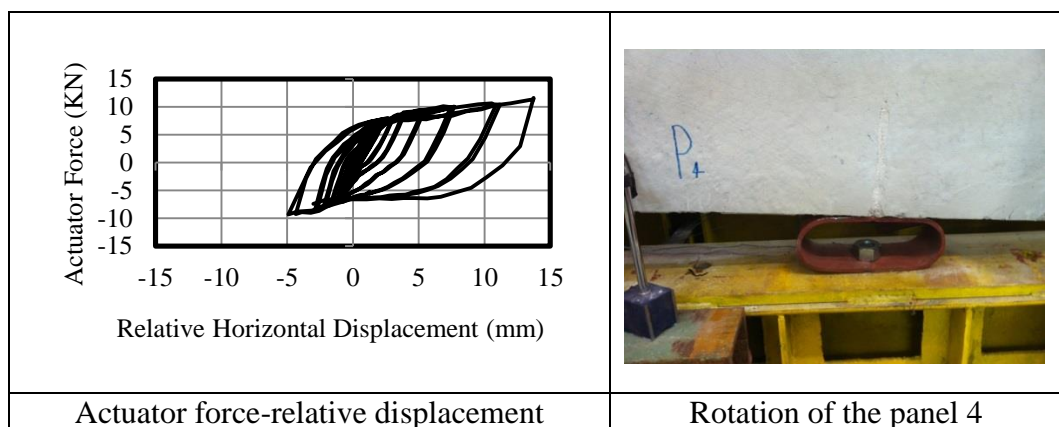


**Figure 4.31 :** Actuator force vs. relative displacement relation for steel cushion beneath panel 4 obtained from system test I.

According to Figure 4.31, the panel 4 rotation caused the rotation of steel cushion. According to the strain gauges history, the steel device did not yield i.e. the steel cushion remained in elastic range.

To investigate whether the steel cushions beneath two symmetric panels, behaved symmetrically or not, actuator force-relative horizontal displacement relations for S1 and S4 are compared in Figure 4.32. According to this Figure the panel 1 and panel 4 behaved asymmetrically as a result the S1 and S4 represented the asymmetrical behavior. It should be mentioned that the transducer that measured the panel 4 horizontal displacement was removed at the last displacement targets because of insufficient capacity. Therefore, it could not be able to record some data.

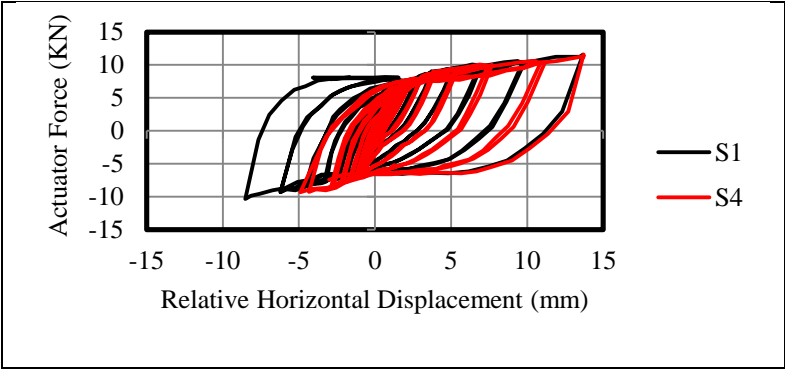


**Figure 4.32 :** Comparison of actuator force-relative displacement relation for S1 and S4 obtained from system test I.

According to Figure 4.33 the panel 2 and panel 3 behaved asymmetrically as a result the S2 and S3 represented the asymmetrical behavior. It should be mentioned that the transducer, which measured the panel 2 horizontal displacement, was removed at the last displacement targets because of insufficient capacity. Therefore, it could not be able to record some data.

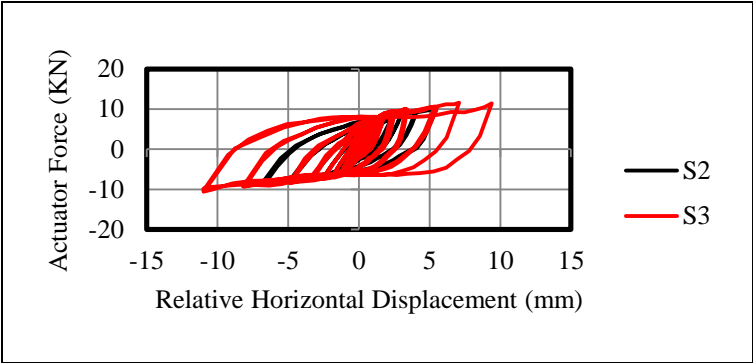


**Figure 4.33 :** Comparison of actuator force-relative displacement relation for S2 and S3 obtained from system test I.

#### 4.4.1.7 Relative horizontal displacement of panel to beam steel cushions

To investigate the behavior of steel cushion in panel 1 to beam connection, the actuator force vs. relative displacement of steel cushion relation are presented in Figure 4.34. This steel cushion is denoted by S1\*. The maximum relative displacement between panel 2 and beam is 11.46 mm at the actuator force of 10.38 KN. According to the strain history relevant to this steel device, yielding is not observed, which indicate the steel device horizontal displacement must be less than 100mm, while the relative displacement between panel 1 and beam is 11.46 mm so this is caused by the rotation of the panel and it does not represent the steel device real horizontal displacement.

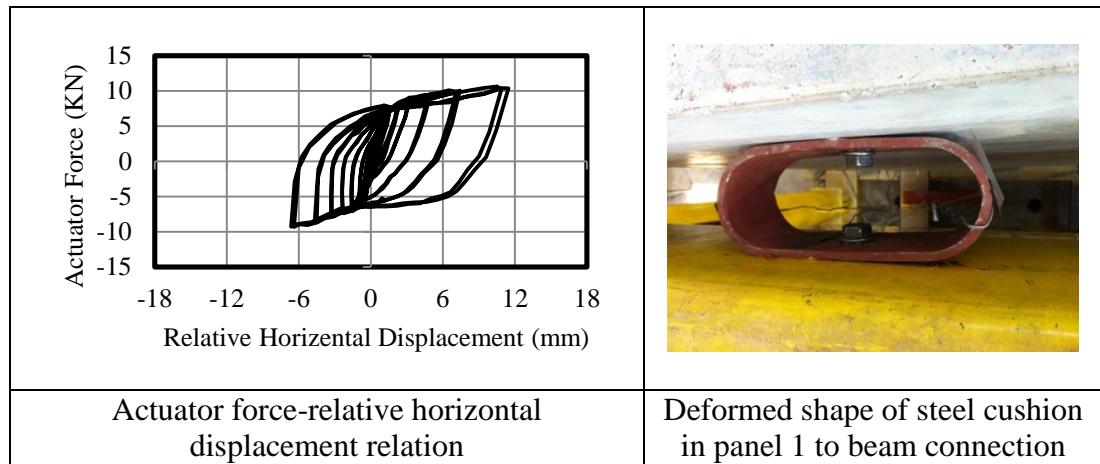


**Figure 4.34 :** Relation of the actuator force vs. relative displacement between panel 1 and beam obtained from system test I.

To investigate the behavior of steel cushion in panel 2 to beam connection, the actuator force vs. relative displacement of steel cushion relation are presented in Figure 4.35. This steel cushion is denoted by S2\*. The maximum relative displacement between panel 2 and beam is 31.94 mm at the actuator force of 10.35 KN. According to the strain history relevant to this steel device it does not yield, which indicate the steel device horizontal displacement must be less than 100mm, while the relative displacement between panel 1 and beam is 31.94 mm this is caused by the rotation of the panel and it doesn't represent the steel device real horizontal displacement.

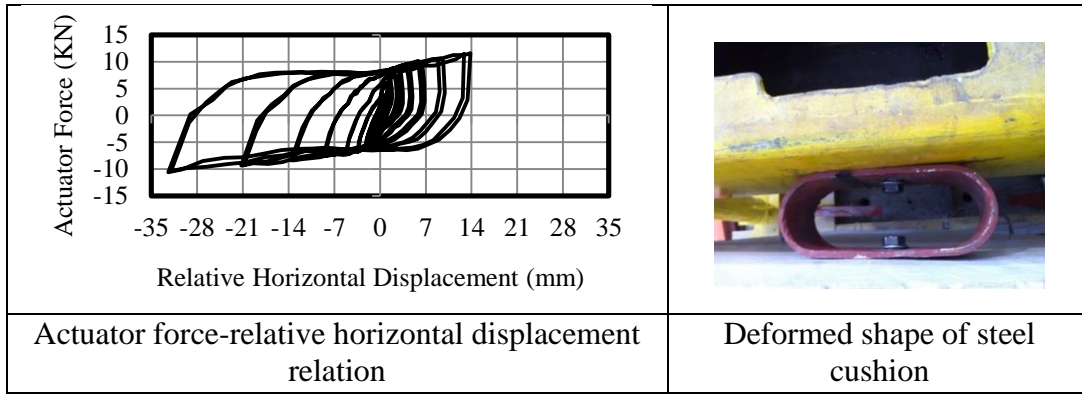


**Figure 4.35 :** Relation of the actuator force vs. relative displacement between panel 1 and beam obtained from system test I.

The steel device in panel 3 to beam connection is denoted by S3\*. According to the Figure 4.36, S3\* horizontal displacement was so small and yielding S3\* did not yield, in fact the panel 3 rotated easily and S3\* acted such a hinge connection. In addition at the last displacement targets S3\* twisted around the connected bolt.



**Figure 4.36 :** Top view of S3\* at final displacement target obtained from system test I.

The steel device in panel 4 to beam connection is denoted by S4\*. According to the Figure 4.37, S4\* horizontal displacement was so small and S4\* did not yield, in fact the panel 4 rotated easily and S4\* acted such a hinge connection. In addition at the last displacement targets S4\* twisted around the connected bolt.



**Figure 4.37 :** Top view of S4\* at final displacement target obtained from system test I.

The strain gauges locations on the steel cushion in panel to beam connection are shown in Figure 4.38.

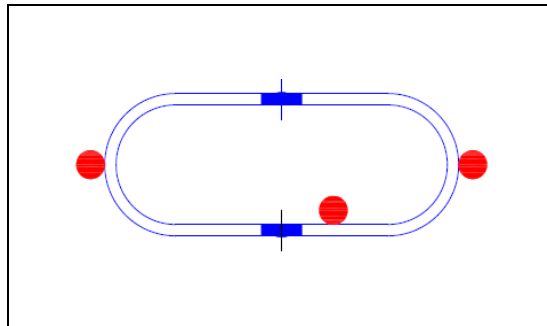


**Figure 4.38** : Strain gauge location of steel devices in panel to beam connection obtained from system test I.

#### 4.4.1.8 Cladding panels rotation

The rotation of each panel is calculated by the help of two transducers installed at the end part of each panel according to Figure 4.39. The rotation can be calculated from the Equation (4.1).

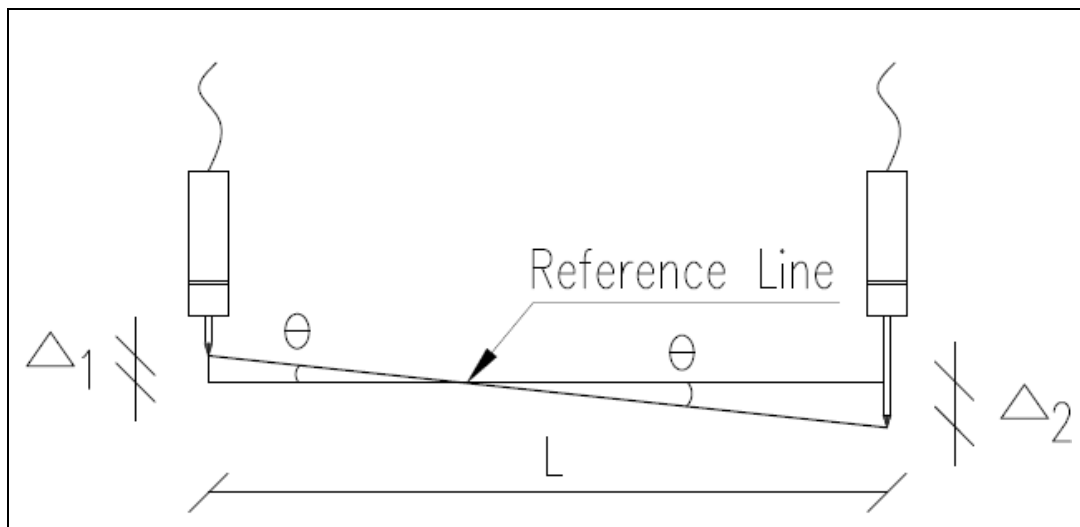


**Figure 4.39** : Cladding panels rotation.

$$\Theta = \frac{\Delta_1 + \Delta_2}{L} \quad (4.1)$$

The rotation of panel 3 and 4 in terms of step numbers are illustrated in Figure 4.40 and 4.41 respectively. The maximum rotation of panel 3 and panel 4 is 0.0821 rad and 0.0872 rad, respectively.

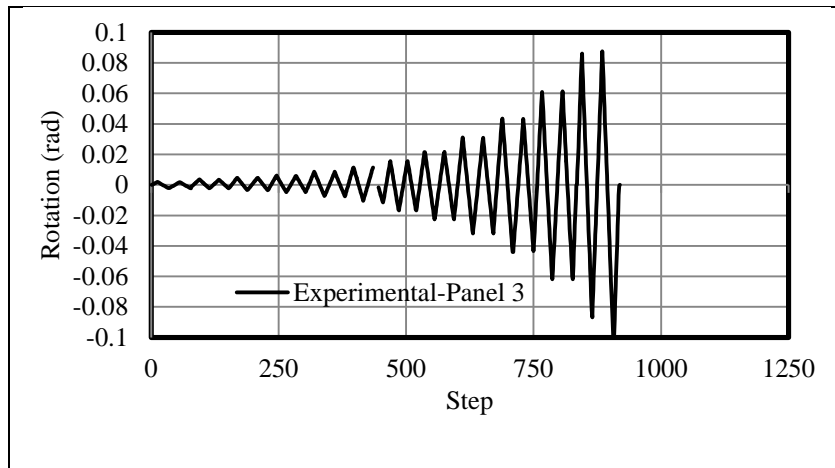


**Figure 4.40 :** Rotation in terms of step numbers for panel 3

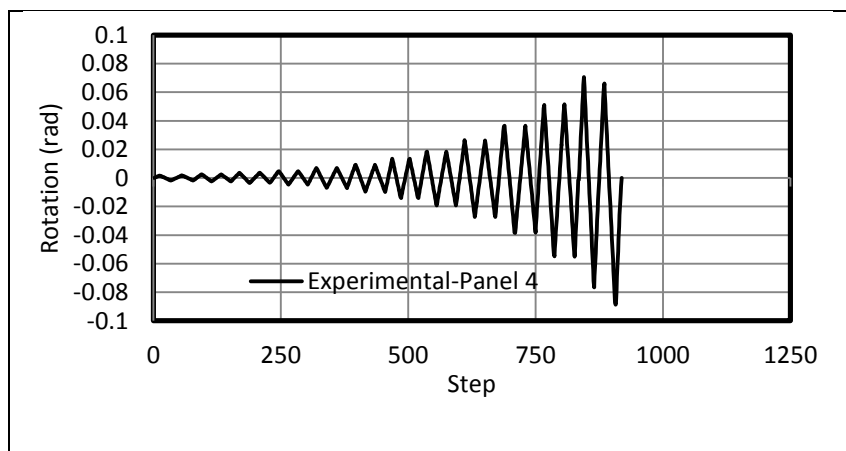


**Figure 4.41 :** Rotation in terms of step numbers for panel 4

#### 4.4.1.9 Total behavior of panels

The cladding panels twisted around the axis parallel to height of the panel. The deformed shape of panels at the end of test is illustrated in Figure 4.42.



**Figure 4.42 :** Deformed shape of cladding panels obtained from system test I.

To investigate the amount of out of plane displacement, the out of plane displacement of panel 3 and panel 4 vs. actuator displacement curve are presented in Figure 4.43 and 4.44. According to Figure 4.43, the amount of out of plane displacement of panel 3 is small enough.

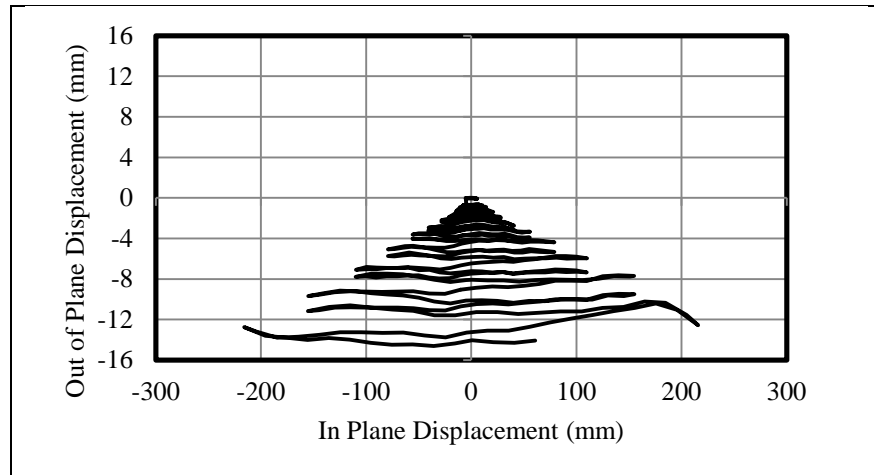


**Figure 4.43 :** Out of plane displacement of panel 3 in terms of in plane displacement obtained from system test I.

According to Figure 4.44 the amount of out of plane displacement of panel 4 is few as well, However the out of plane displacement for panel 4 is greater than corresponding value for panel 3.

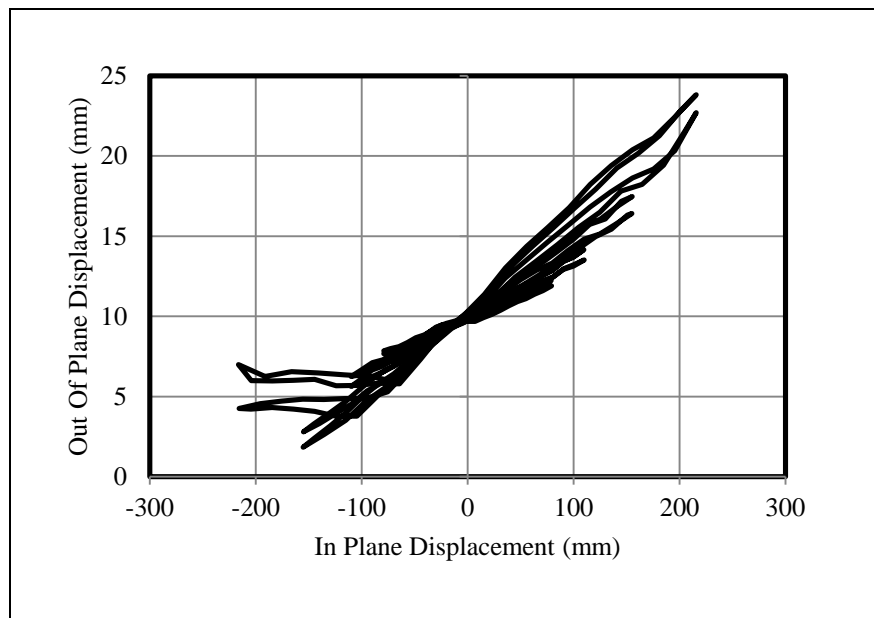


**Figure 4.44 :** Out of plane displacement of panel 4 in terms of in plane displacement obtained from system test I.

**4.5 System Test II (Double Cushion Test)**

Two steel cushions are used at the bottom of each cladding. 3mm steel cushions are assembled in base to panel connection, 8mm ones in the beam to panel connection, besides 5mm steel device assembled in panel to panel connection. Therefore, 8 pieces of 3mm, 2 pieces of 5mm and four pieces of 8 mm steel cushions are used at the base, in the middle, and on the top level, respectively. This arrangement is shown in Figure 4.45.

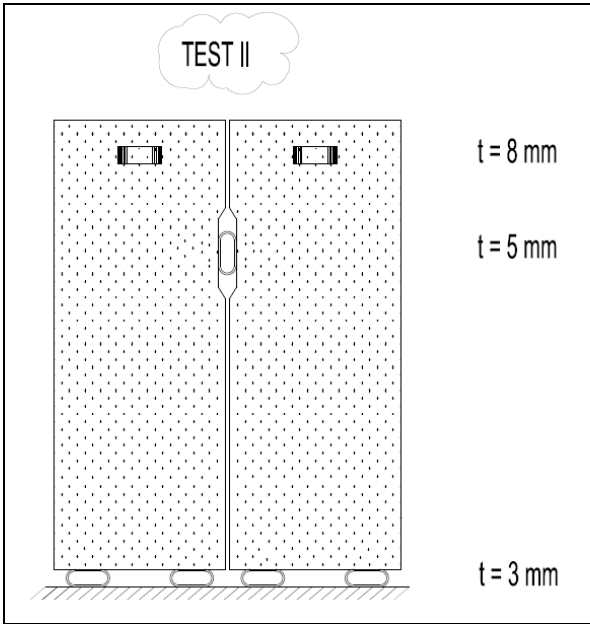


**Figure 4.45 :** Arrangements of steel cushions in system test II.

Location of strain gauges in panel to support, panel to panel and panel to beam connections, are illustrated in Figure 4.46.

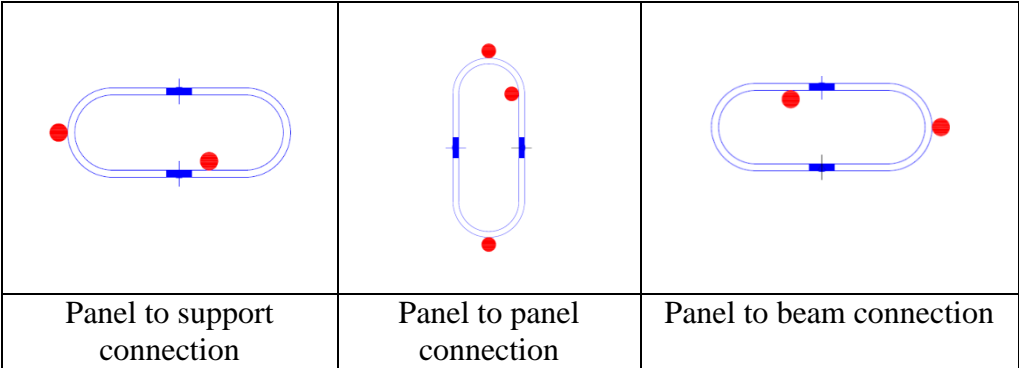


**Figure 4.46 :** Location of strain assessment devices in system test II.

Transducers and their locations are illustrated in Figures 4.47 and 4.48.

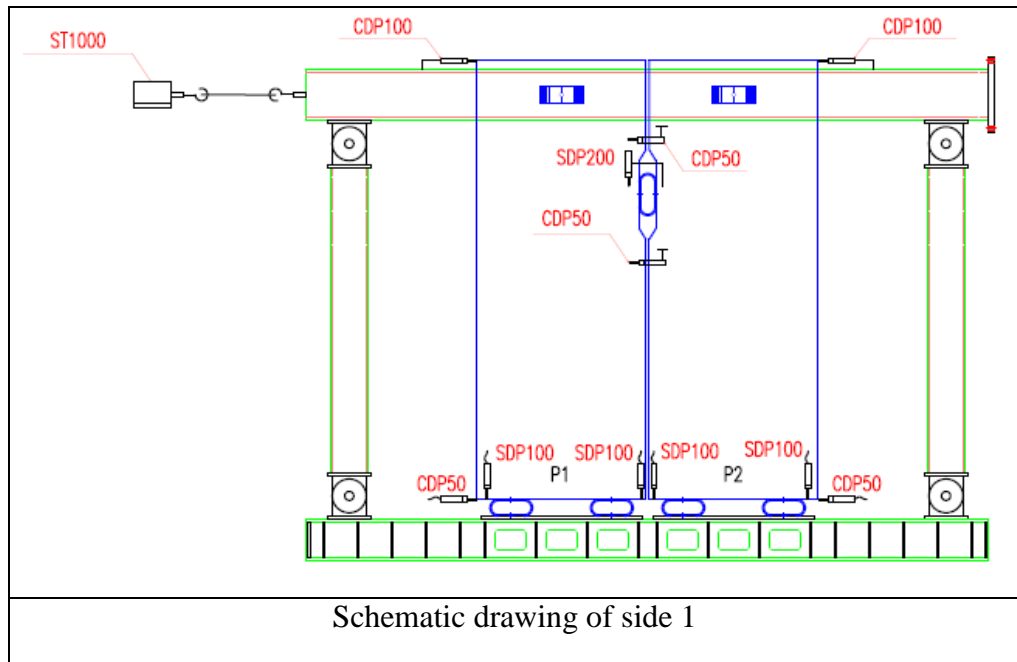


**Figure 4.47** : Location of transducers in side 1 in system test II.

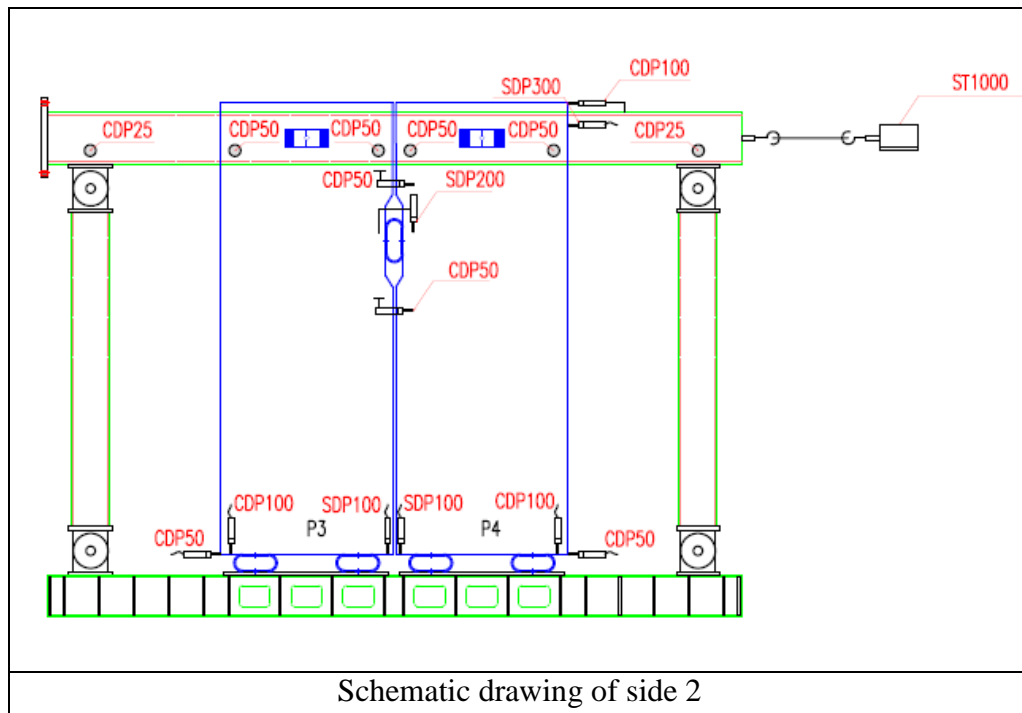


**Figure 4.48** : Location of transducers in side 2 in system test II.

#### 4.5.1 Evaluation of experimental results obtained from system test II

In this part, the experimental results of system test II are presented and discussed.

##### 4.5.1.1 Actuator force-top displacement relation

The experimental actuator force in terms of displacement and drift derived from system test II are shown in Figures 4.49 and 4.50.

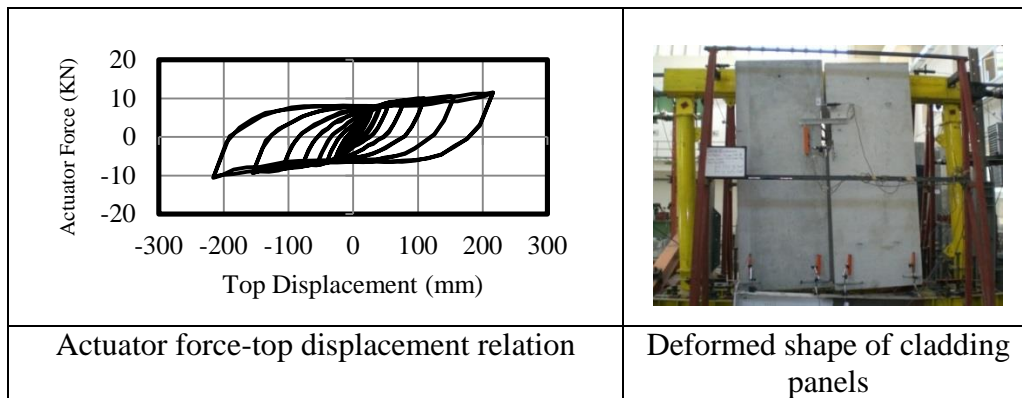


**Figure 4.49 :** Force-Top displacement relation obtained from system test II.

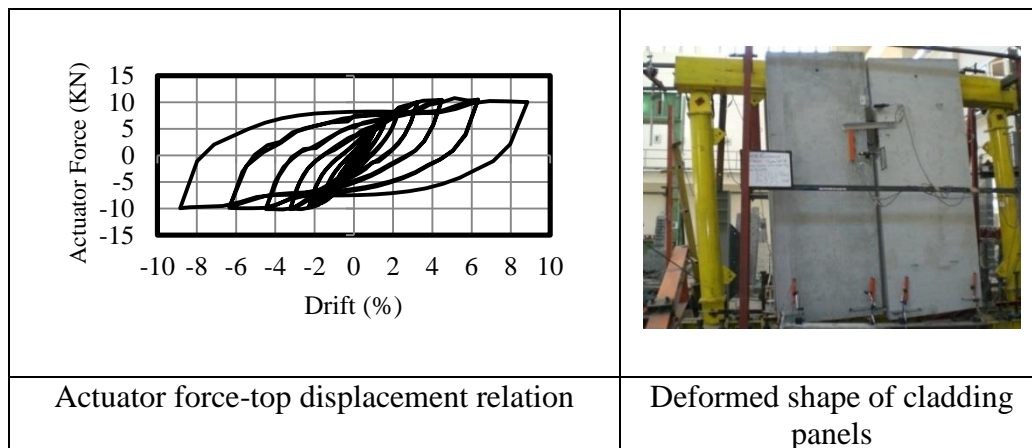


**Figure 4.50 :** Force-Drift angle curve obtained from system test II.

The experimental results obtained from system test II are summarized in Table 4.4. The force–drift angle relation of Figure 4.50 shows a stable and symmetric hysteresis behavior. Any damages were not observed on steel cushions and cladding panels.

**Table 4.4 :** Summary of test results obtained from system test II.

Yielding Force (KN)	Max Force (KN)	Yielding Drift (%)	Max Drift (%)
7.27	10.80	1.67	8.64

#### 4.5.1.2 Energy dissipation

Cumulative dissipative energy hysteresis curve vs. the drift angle is presented in Figure 4.51. Except the panel to beam connection steel device, the steel devices in panel to panel and panel to support connections yielded, therefore they contributed in the cumulative dissipative energy and equivalent damping. The steel devices in panel-to-panel connection had the most contribution in cumulative energy and equivalent damping. According to Figure 4.51 after the yield drift of 1.67% there is a sharp increase with respect to the previous drifts. The cumulative energy at the yielding drift is 1517 KN.mm. After the yielding with increase of drift, the cumulative energy increases significantly, so that at the maximum drift of 8.64 the cumulative energy equals to 22846 KN.mm.

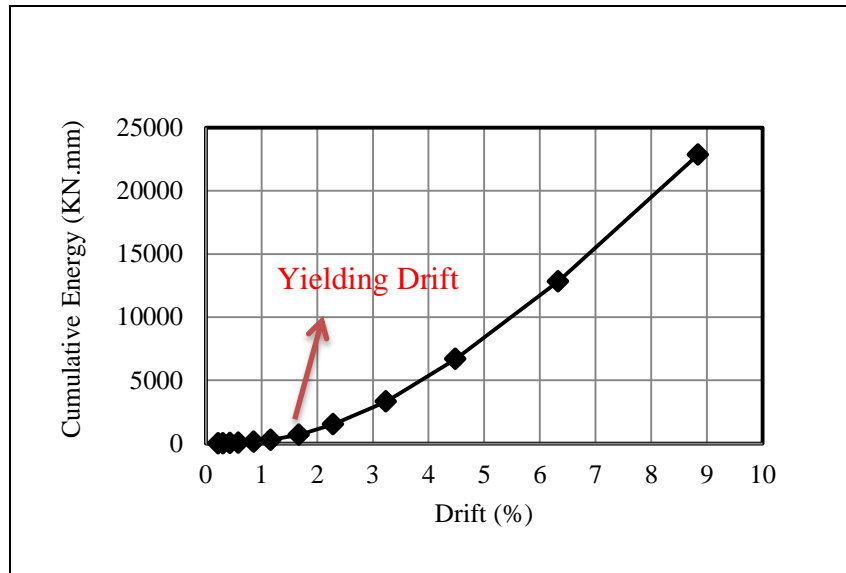


**Figure 4.51** : Cumulative energy vs. drift curve obtained from system test II.

#### 4.5.1.3 Equivalent viscous damping

According to Figure 4.52, the equivalent damping ratio increases with increase of drift angle of system. Particularly after the drift angle of 1.67%, there is a significant increase. The equivalent damping ratio is 10.63 % at yielding drift, after the yielding with increase of drift the equivalent damping ratio increases significantly, so that at the maximum drift of 8.64 the equivalent damping ratio equals to 37.39 %.

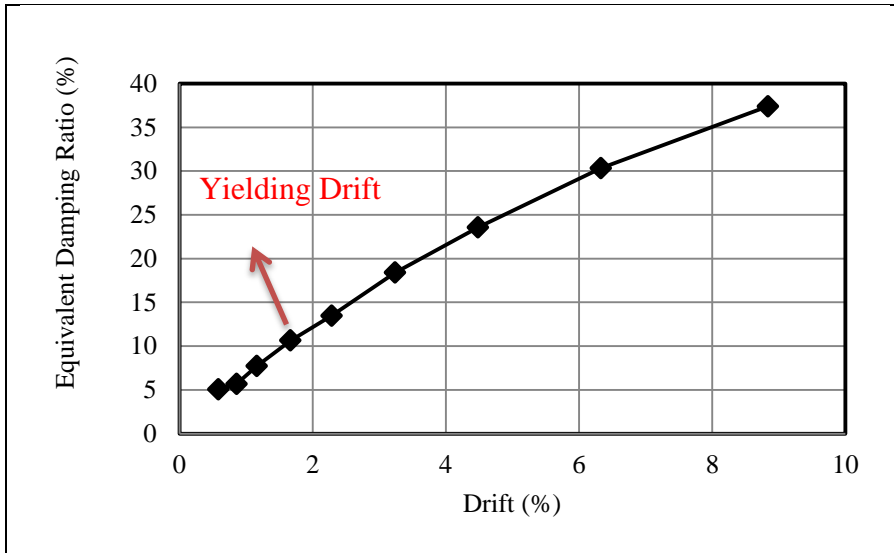


**Figure 4.52 :** Equivalent damping ratio vs. drift curve obtained from system test II.

#### 4.5.1.4 Effective (secant) stiffness

The structural system has the initial stiffness amount of 0.33 KN/mm at the drift angle of 0.22%, as the drift angle increases the secant stiffness declines and reaches to the value of 0.046 KN/mm at the maximum drift angle, this shows approximately 86% reduction. The secant stiffness vs. drift relation is displayed in Figure 4.53.

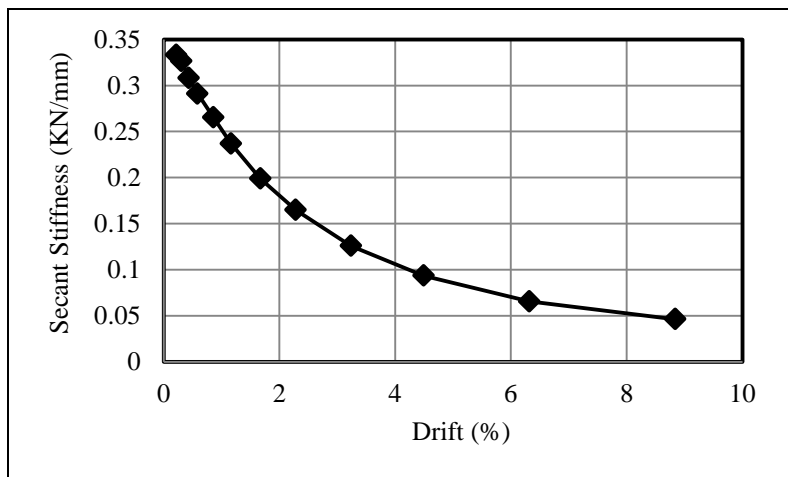


**Figure 4.53 :** Secant stiffness vs. drift relation obtained from system test II.

#### 4.5.1.5 Relative vertical displacement of panel to panel steel cushions

The actuator force vs. relative displacement relation, for steel cushion in panel 1 to panel 2 connection is presented in Figure 4.54. The steel device used in the panel 1 to panel 2 connection is denoted by S12. The maximum relative displacements of S12 is 82.46 mm at actuator force of 9.4 KN.

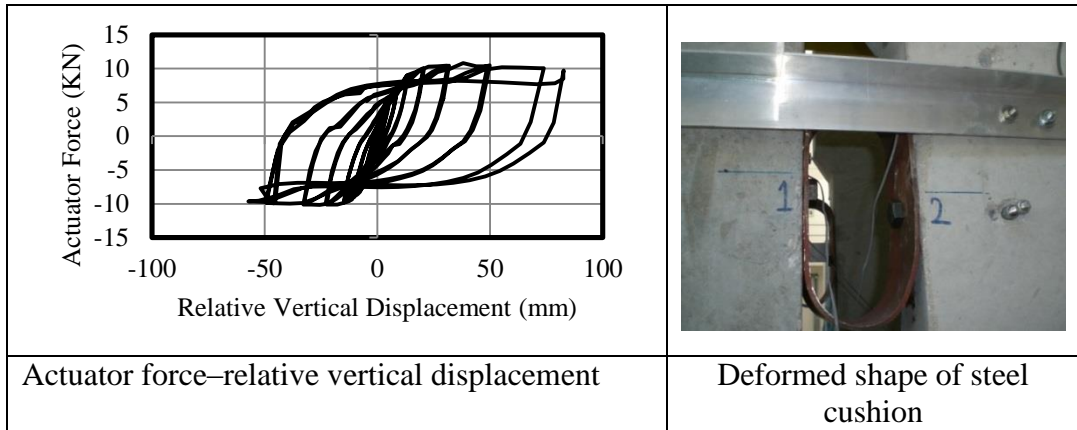


**Figure 4.54 :** Actuator force vs. relative displacement relation for steel cushion in panel 1 to panel 2 connection obtained from system test II.

The strain gauges locations on the specimens in panel-to-panel connections are shown in Figure 4.55.

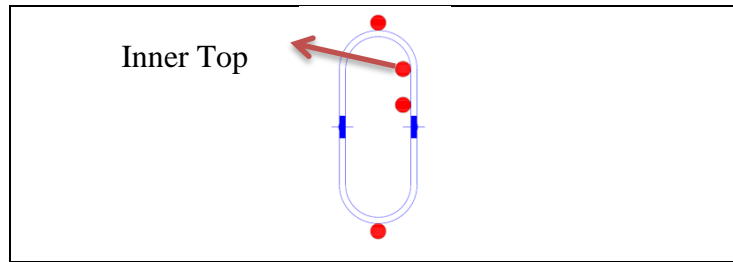


**Figure 4.55 :** Strain gauges location on steel cushions in panel-to-panel connection obtained from system test II.

The specimen yields at the drift angle of 2.28%. Location of the first yielding is the beginning of the arc section of specimen (inner top). The strain vs. drift angle relation for inner top point is presented in Figure 4.56.

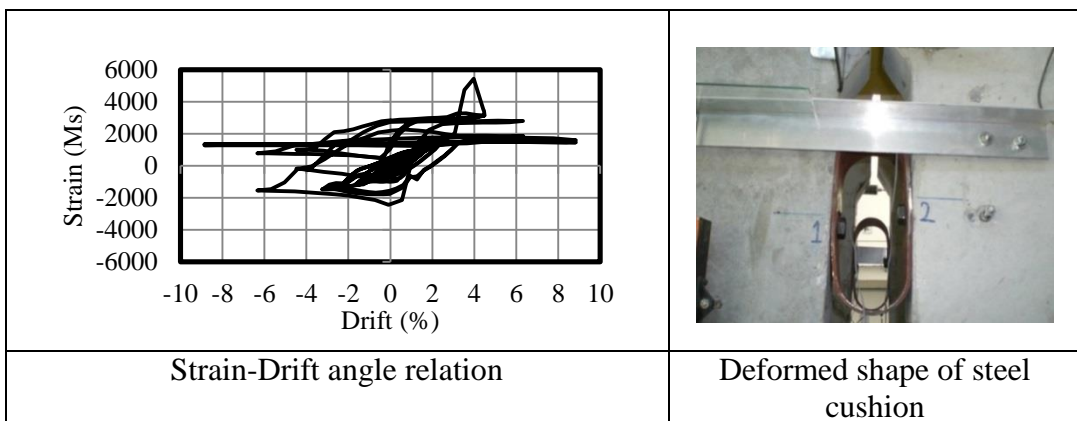


**Figure 4.56 :** Strain vs. drift angle relation for steel cushion in panel 1 to panel 2 connection obtained from system test II.

The actuator force vs. relative displacement relation for steel cushion in panel 3 to panel 4 connection is presented in Figure 4.57. The steel device in panel 3 to panel 4 connection is denoted by S34. The maximum relative displacements of S34 is 73.5 mm at the actuator force of 9.4 KN.

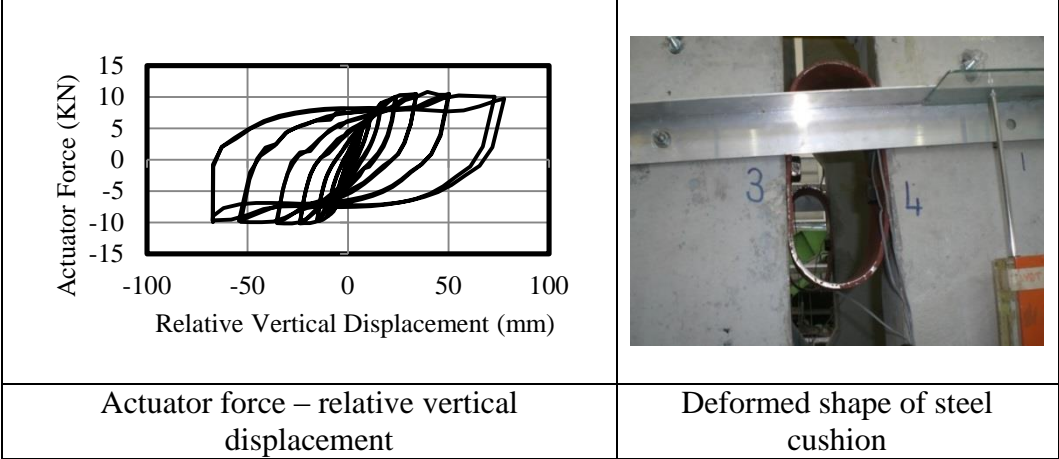


**Figure 4.57 :** Actuator force vs. relative displacement relation for steel cushion in panel 3 to panel 4 connection obtained from system test II.

The specimen yields at the drift angle of 2.28%. Location of the first yielding is the beginning of the arc section of specimen (inner top). The strain vs. drift angle relation for inner top point is presented in Figure 4.58.

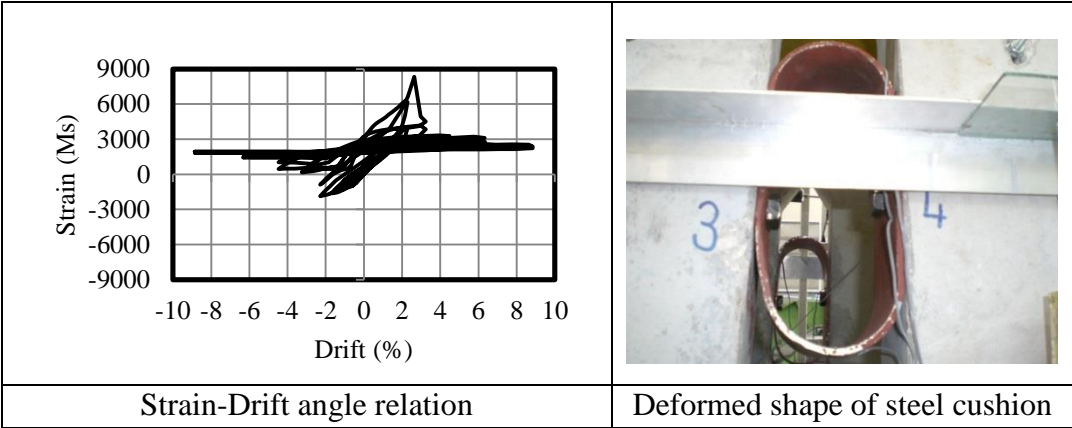


**Figure 4.58 :** Strain vs. drift angle relation for steel cushion in panel 3 to panel 4 connection obtained from system test II.

Two cushions between two adjacent panels behaved nearly symmetrically the actuator force vs. relative vertical displacement relation for two steel devices are compared in Figure 4.59.

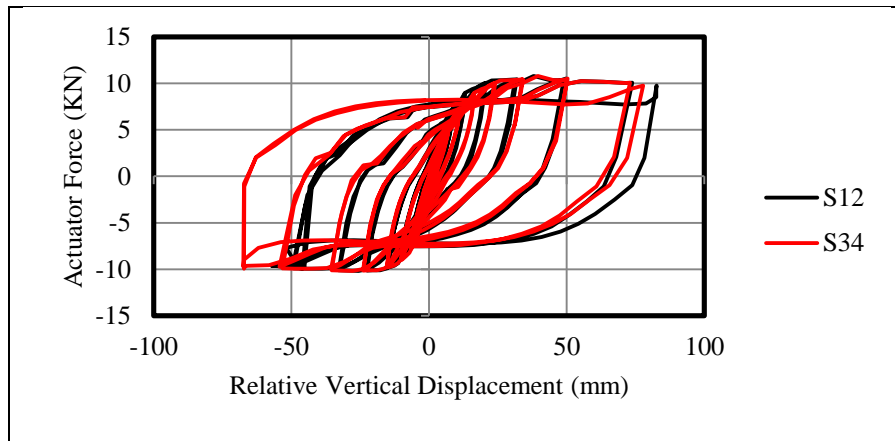


**Figure 4.59 :** Comparison of actuator force vs. relative displacement of S12 and S34 obtained from system test II.

#### 4.5.1.6 Relative horizontal displacement of panel to support steel cushions

To examine the shear displacement of steel cushion beneath panel 1 the relation between actuator force and total relative displacement of steel cushions beneath panel 1 is presented in Figure 4.60. The maximum relative displacement is 38.56 mm at the actuator force of 9.75 kN. However as the transducer was installed at level of 20 cm from the panel base, the steel device horizontal displacement is smaller than this value. According to the deformed shape of steel cushion besides the horizontal displacement the steel cushion rotated. In fact, this value of the horizontal tip displacement is formed by combination of the rotation of panel and horizontal displacement of steel cushions, although the rotation contribution in the horizontal displacement is more than steel cushions horizontal displacement. In addition, the behavior is asymmetric.

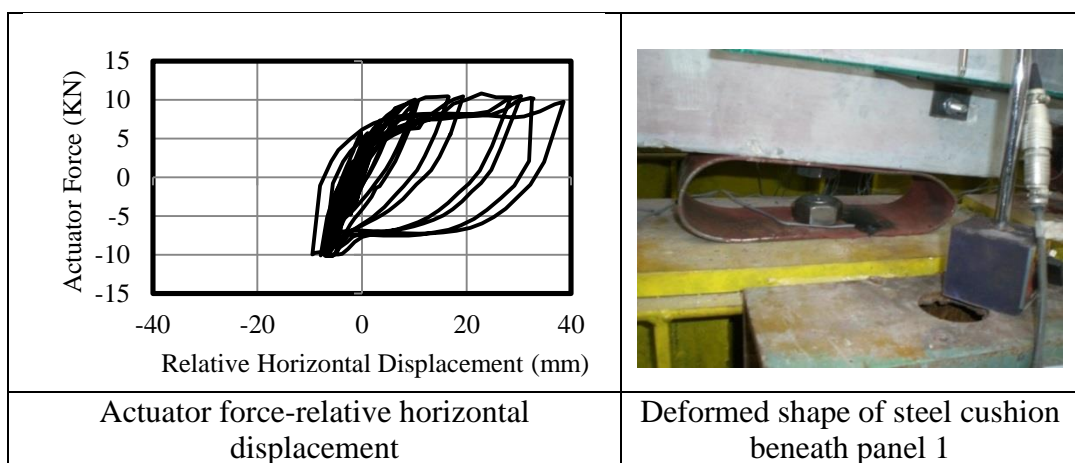


**Figure 4.60 :** Actuator force vs. relative horizontal displacement relation for steel cushions beneath panel 1 obtained from system test II.

The strain gauges locations for steel devices in panel to support connection are shown in Figure 4.61. According to the strain history, yielding occurred at all three points, the first yielding occurred at 0.85% system drift angle. The location of first yielding was the specimen vertex point.

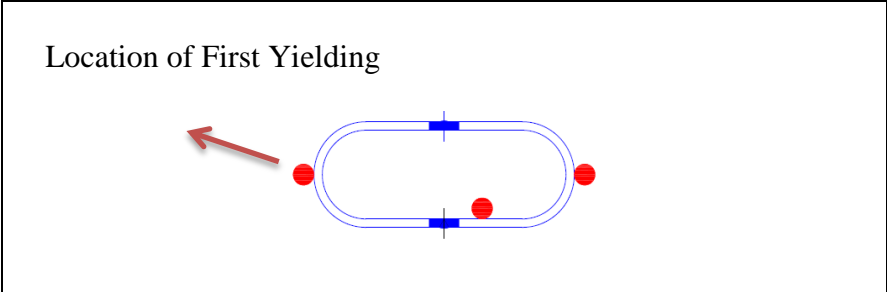


**Figure 4.61** : Location of strain gauges on steel cushions in panel to support connection obtained from system test II.

The relation between the actuator force and total relative displacement of steel cushions beneath panel 2, is presented in Figure 4.62. The maximum relative displacement is 43.06 mm at the actuator force of 9.75 KN. However as the transducer was installed at level of 20 cm from the panel base, the steel device horizontal displacement is smaller than this value. According to the deformed shape of steel cushion besides the horizontal displacement, the steel cushion rotated. In fact, this value of the horizontal displacement is formed by combination of the rotation of panel and horizontal displacement of steel cushions, although the rotation contribution in the horizontal displacement is more than steel cushions horizontal displacement. In addition, the behavior is asymmetric.

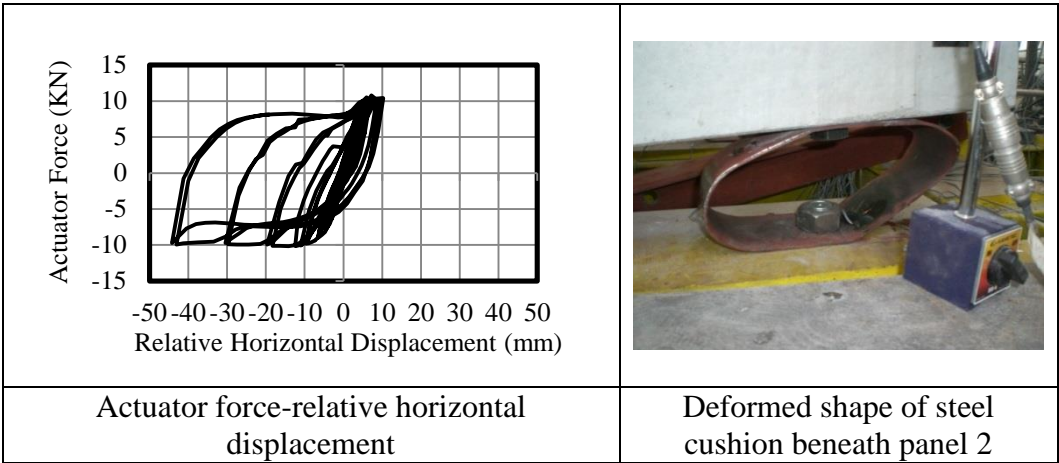


**Figure 4.62** : Actuator force vs. relative horizontal displacement relation for steel cushions beneath panel 2 obtained from system test II.

According to the strain gauges history, yielding occurred at all three points, the first yielding occurred at 1.16 % system drift angle. The location of first yielding was the specimen vertex point.

The relation between the actuator force and total relative displacement of steel cushions beneath panel 3 is presented in Figure 4.63. The maximum relative displacement is 14.05 mm at the actuator force of 10.10 KN. However as the transducer was installed at level of 20 cm from the panel base, the steel device horizontal displacement is smaller than this value. According to the deformed shape of steel cushion, besides the horizontal displacement, the steel cushion rotated. In fact, this value of the horizontal displacement is formed by combination of the rotation of panel and horizontal displacement of steel cushions, although the rotation contribution in the horizontal displacement is more than steel cushions horizontal displacement. In addition, the behavior is asymmetric. The data obtained from transducer interrupted after the displacement target of 109.23 mm.

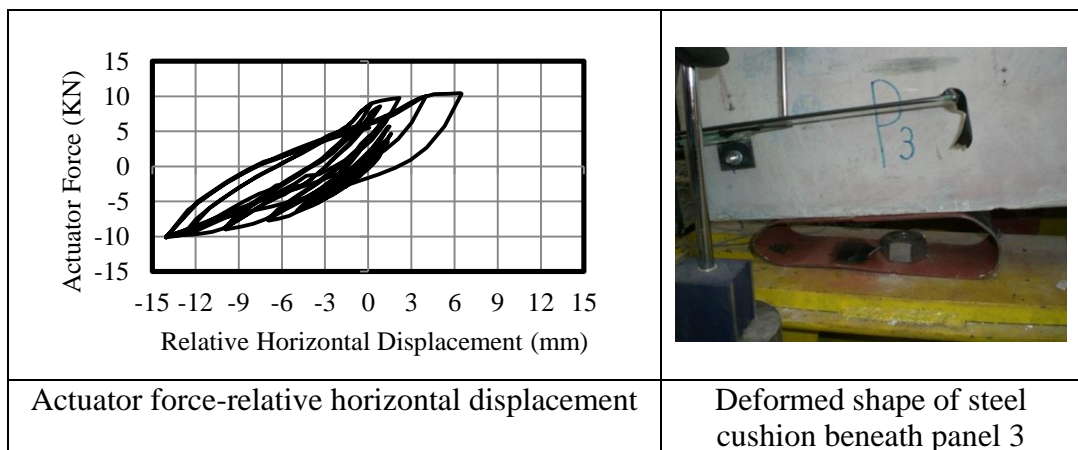


**Figure 4.63 :** Actuator force vs. relative horizontal displacement relation for steel cushions beneath panel 3 obtained from system test II.

According to the strain gauges history, yielding occurred at all three points, the first yielding occurred at 1.66 % system drift angle. The location of first yielding was the specimen vertex point.

The relations between actuator force and total relative displacement of steel cushions beneath panel 4, is presented in Figure 4.64. The maximum relative displacement is 12.93 mm at the actuator force of 10.1 KN. However as the transducer was installed at level of 20 cm from the panel base, the steel device horizontal displacement is smaller than this value. According to the deformed shape of steel cushion, besides

the horizontal displacement, the steel cushion rotated. In fact, this value of the horizontal displacement is formed by combination of the rotation of panel and horizontal displacement of steel cushions, although the rotation contribution in the horizontal displacement is more than steel cushions horizontal displacement. In addition, the behavior is asymmetric. The data obtained from transducer interrupted after the displacement target of 109.23 mm.

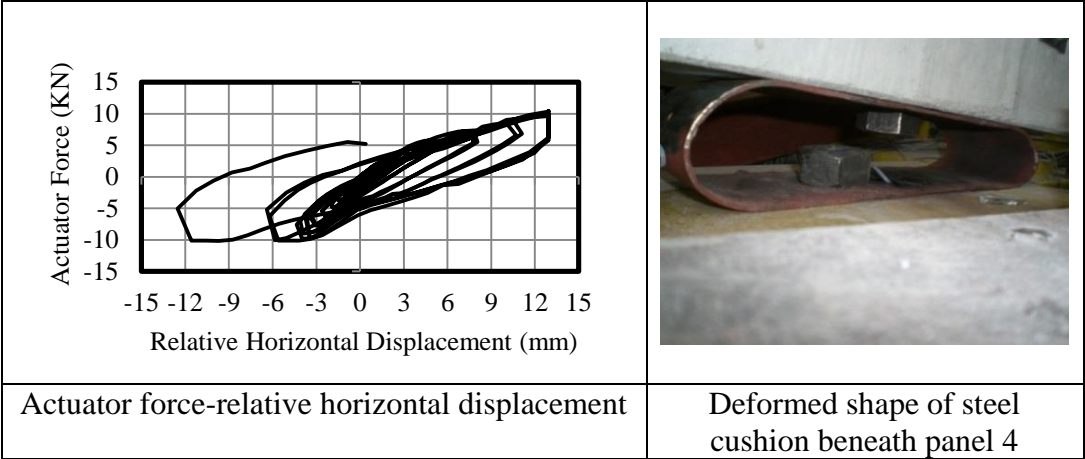


**Figure 4.64 :** Actuator force vs. relative horizontal displacement relation for steel cushions beneath panel 4 obtained from system test II.

According to the strain gauges history, yielding occurred at all three points, the first yielding occurred at 0.86 % system drift angle. The location of first yielding was the specimen vertex point.

To investigate whether the Steel cushions beneath two symmetric panels, behaved symmetrically or not, actuator force-relative horizontal displacement relations for steel cushion beneath panel 1 and panel 4 are compared in Figure 4.65. According to Figure 4.65, panel 1 and panel 4 behaved asymmetrically as a result, the steel cushions below panel 1 and panel 4 represented the asymmetrical behavior. It should be mentioned that the data obtained from transducer, which measured the panel 4 horizontal displacement, was interrupted after the displacement target of 109.23 mm.

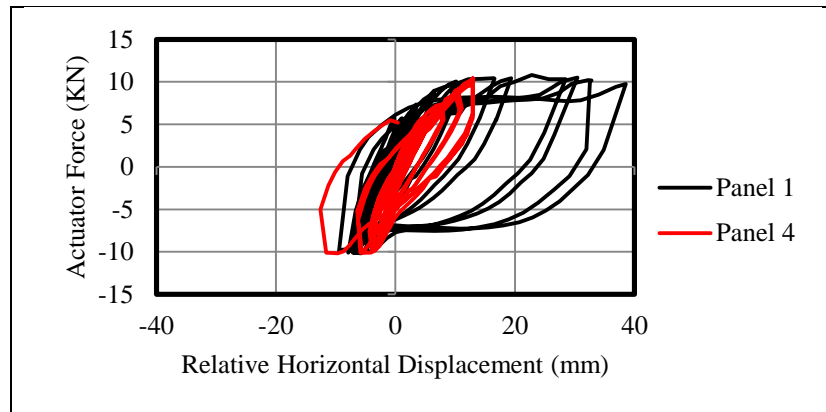


**Figure 4.65 :** Comparison of actuator force-relative displacement relation for steel cushions beneath panel 1 and panel 4 obtained from system test II.

Actuator force-relative horizontal displacement relations for steel cushion beneath panel 2 and panel 3 are compared in Figure 4.66. According to Figure 4.66, panel 2 and panel 3 behaved asymmetrically as a result, the steel cushions below panel 2 and panel 3 represented the symmetrical behavior. It should be mentioned that the data obtained from transducer, which measured the panel 3 horizontal displacement, was interrupted after the displacement target of 109.23 mm.

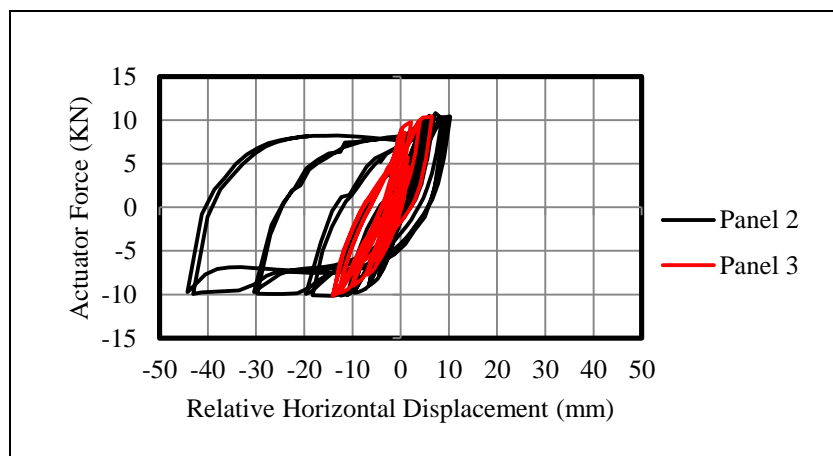


**Figure 4.66 :** Comparison of actuator force-relative displacement relation for steel cushions beneath panel 2 and panel 3 obtained from system test II.

#### 4.5.1.7 Relative horizontal displacement of panel to beam steel cushions

To investigate the behavior of steel cushion in panel 1 to beam connection the relation of the actuator force vs. relative displacement between panel 1 and beam is presented in Figure 4.67. The steel cushion is denoted by S1\*. The maximum relative displacement between panel 1 and beam is 7.66 mm at the actuator force of 10.045 KN. According to the strain history relevant to this steel device the device did not yield, which indicate the steel device horizontal displacement must be less than

100mm, while the relative displacement between panel 1 and beam is 7.66 mm, this is caused by the rotation of the panel and it does not represent the steel device real horizontal displacement.

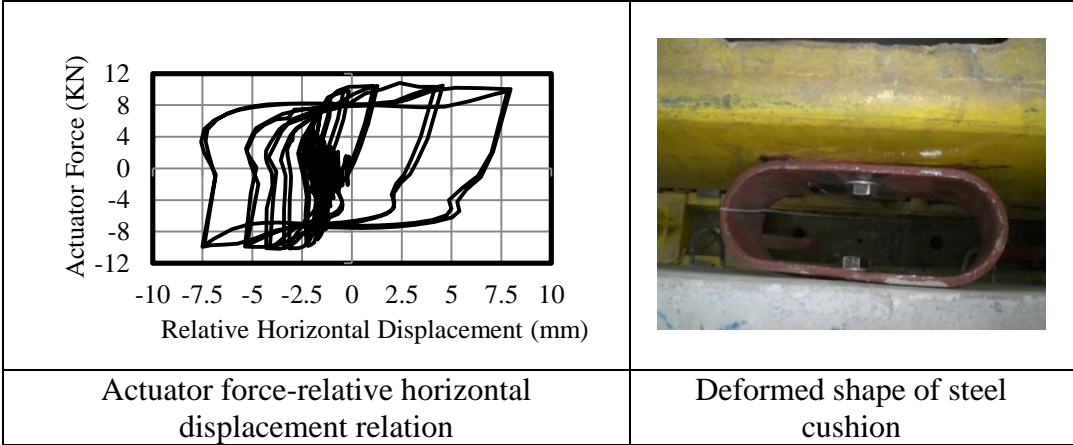


**Figure 4.67 :** Relation of the actuator force vs. relative displacement between panel 1 and beam obtained from system test II.

The steel device in panel 2 to beam connection is denoted by S2\*. The relation of the actuator force vs. relative displacement between panel 2 and beam is presented in Figure 4.68. The maximum relative displacement between panel 2 and beam is 13.25 mm at the actuator force of 9.93 kN. According to the strain history relevant to this steel device, the yielding does not yield, which indicate the steel device horizontal displacement must be less than 100 mm, while the relative displacement between panel 2 and beam is 13.25 mm, so this is caused by the rotation of the panel and it does not represent the steel device real horizontal displacement.

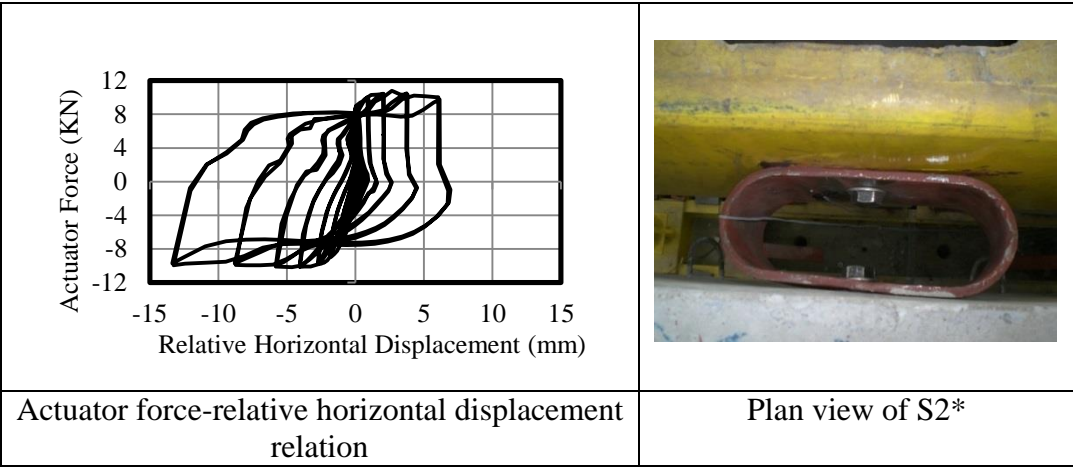


**Figure 4.68 :** Relation of the Actuator force vs. relative displacement between panel 2 and beam obtained from system test II.

The steel device in panel 3 to beam connection, is denoted by S3\*. According to the Figure 4.69, S3\* horizontal displacement was so small. In fact the panel 3 rotated easily and S3\* acted such a hinge connection. In addition at the final displacement targets S3\* twisted around the connected bolt.

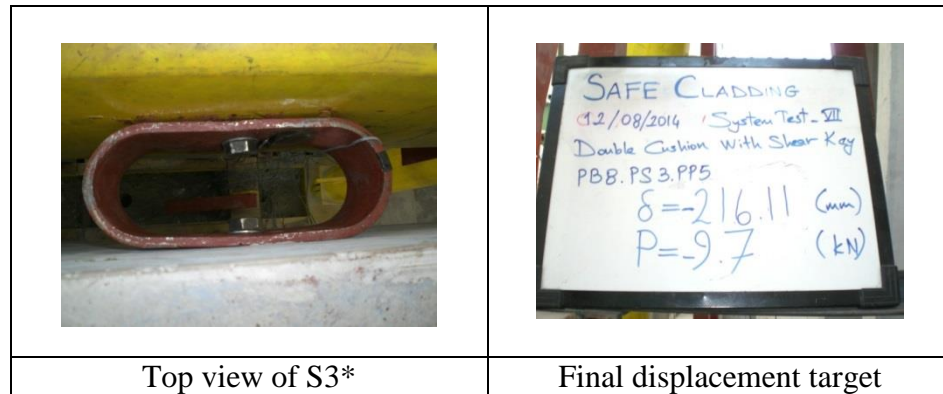


**Figure 4.69 :** Top view of S3\* at final displacement target obtained from system test II.

The steel device in panel 4 to beam connection is denoted by S4\*. According to the Figure 4.70, S4\* horizontal displacement was so small. In fact the panel 3 rotated easily and S4\* acted such a hinge connection. In addition at the last displacement targets S4\* twisted around the connected bolt.

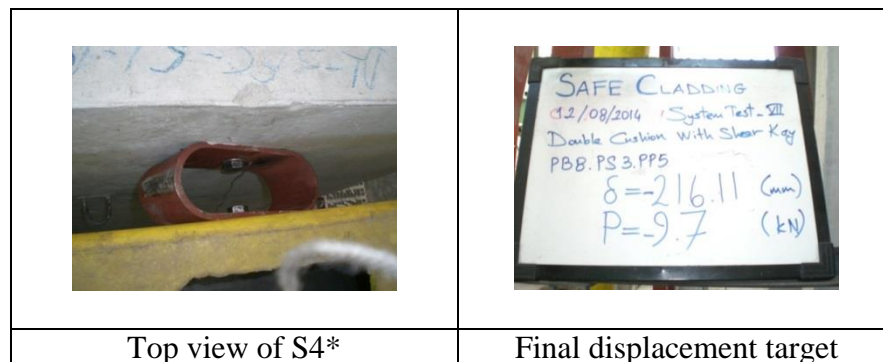


**Figure 4.70 :** Top view of S4\* at final displacement target obtained from system test II.

The locations of strain gauges in panel to beam steel cushions are illustrated in Figure 4.71.

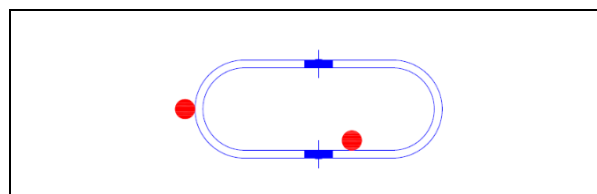


**Figure 4.71 :** location of strain gauges on steel device in system test II.

#### 4.5.1.8 Cladding panels rotation

The rotation of panel 3 and 4 in terms of step numbers are illustrated in Figures 4.72 and 4.73, respectively. The maximum rotation of panel 3 and panel 4 is 0.0839 rad and 0.0702 rad, respectively.

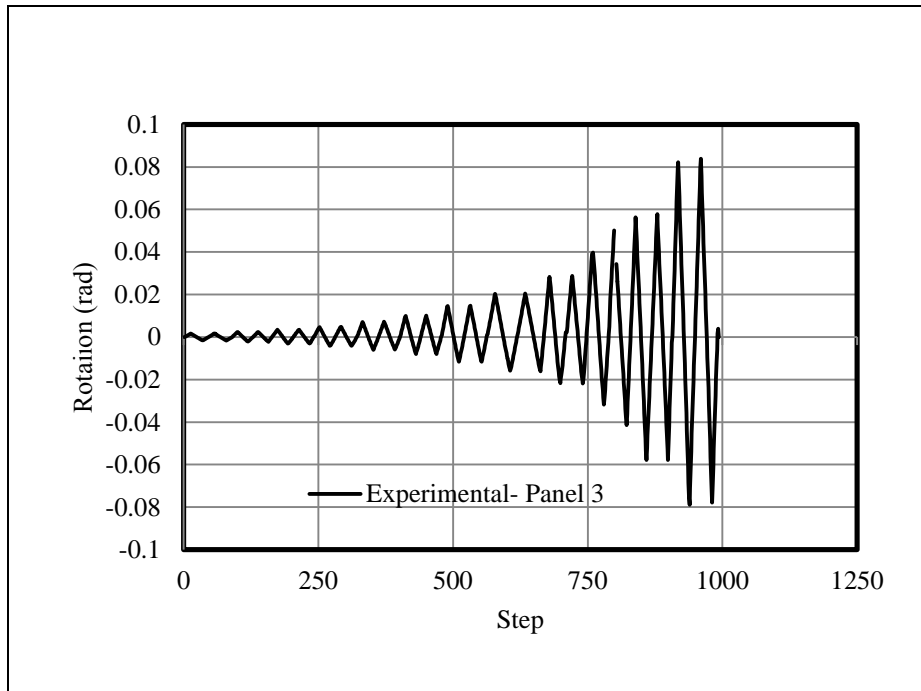


**Figure 4.72 :** Rotation in terms of step numbers for panel 3.

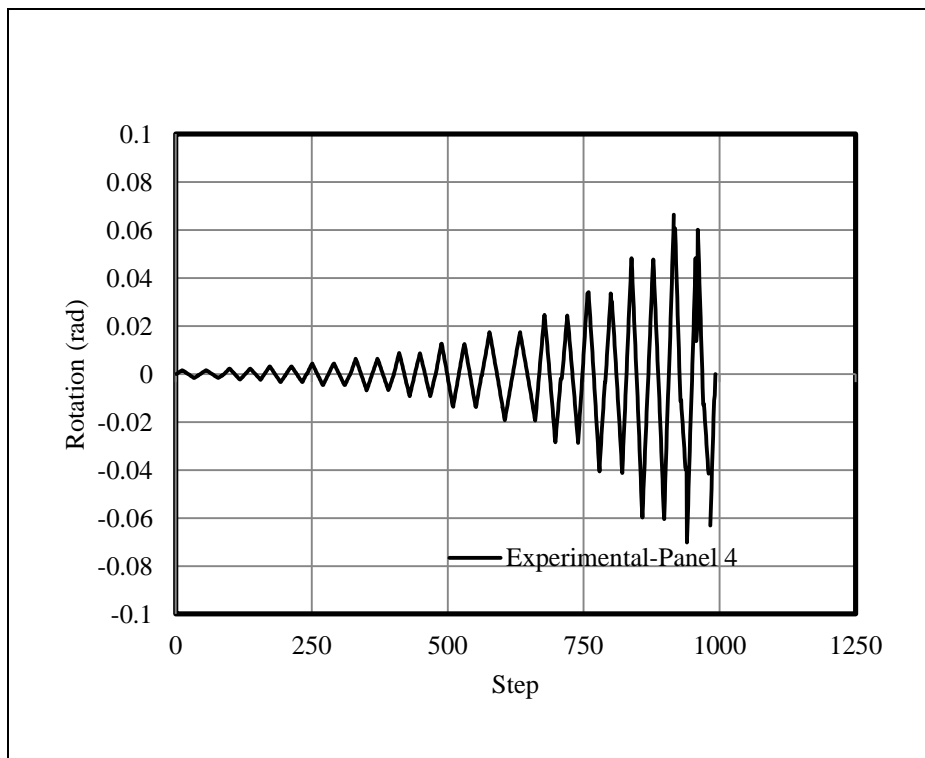


**Figure 4.73 :** Rotation in terms of step numbers for panel 4.

#### 4.5.1.9 Total behavior of panels

To investigate the amount of out of plane displacement, the out of plane displacement of panel 3 and panel 4 vs. actuator displacement curve are presented in Figures 4.74 and 4.75. According to Figure 4.74, the amount of out of plane displacement of panel 3 is small enough.

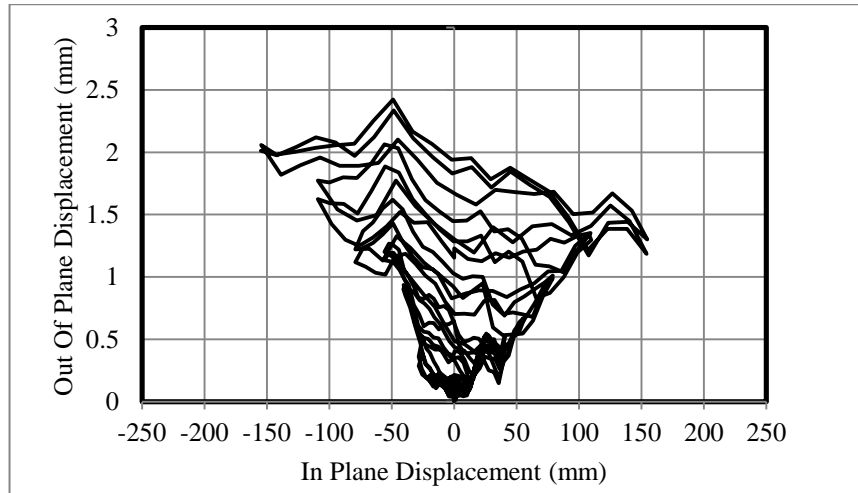


**Figure 4.74 :** Out of plane displacement of panel 3 in terms of in plane displacement obtained from system test II.

According to Figure 4.75, the amount of out of plane displacement of panel 4 is few as well. However, the out of plane displacement for panel 4 is higher than corresponding value for panel 3.

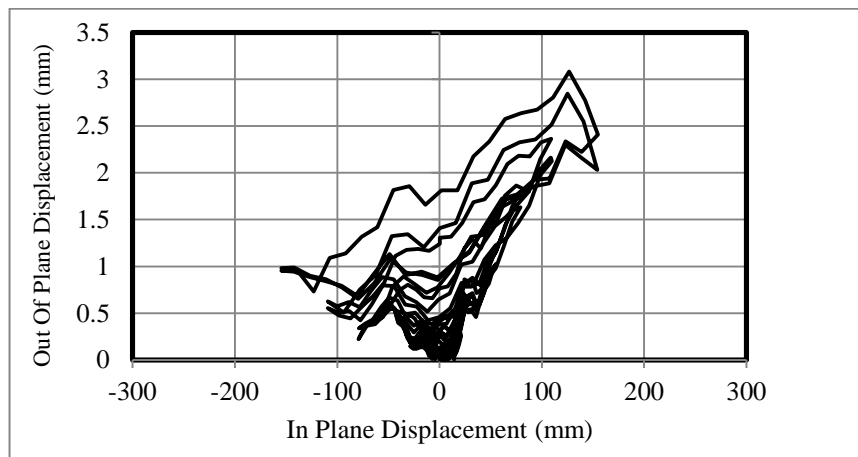


**Figure 4.75 :** Out of plane displacement of panel 4 in terms of in plane displacement obtained from system test II.

In total the out of plane displacement of panels are minimal as a result, the steel device in panel to beam connection were not subjected to significant tensile stress. Moreover, any twisting of panels was not observed during the test.

**4.6 System Test III (Double Cushion Test)**

Two steel cushions are used at the bottom of each cladding. In this test, 5mm thick steel cushions were assembled in panel to support connection. The steel device in panel-to-panel connection and panel to beam connection were 5mm and 8mm thick steel cushions, respectively. Totally, fourteen steel devices including eight 5mm steel cushions as support ( two cushions per panel), two 5mm steel cushions as middle connection ( one cushion between two panels ), and four 8mm cushions in beam to panel connection ( one cushion per panel) were used. This arrangement is shown in Figure 4.76.

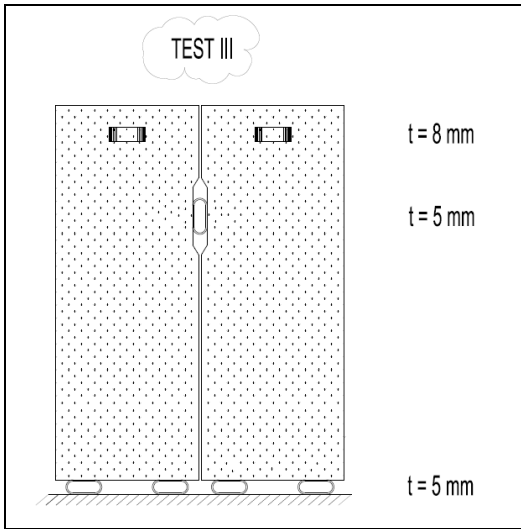


**Figure 4.76 :** Arrangements of steel cushions in system test III.

The location of the strain gauges were analogues to test II, as illustrated in Figure 4.77.

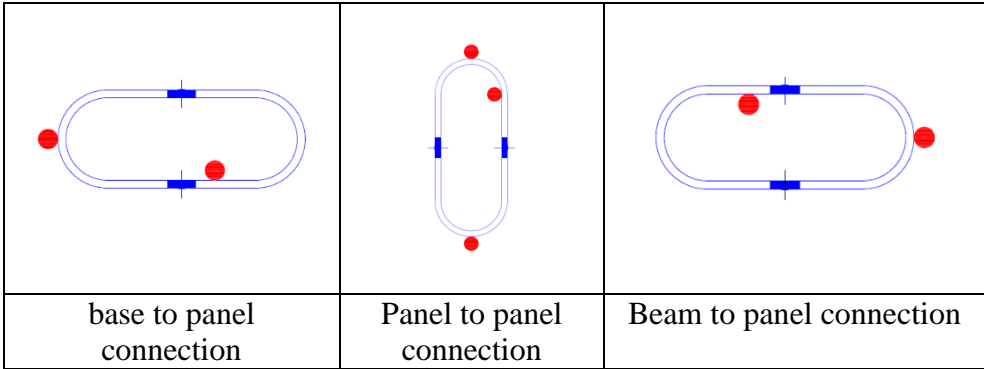


**Figure 4.77 :** Location of strain assessment devices in system test III.

Transducers and their locations are illustrated in Figure 4.78 and 4.79.

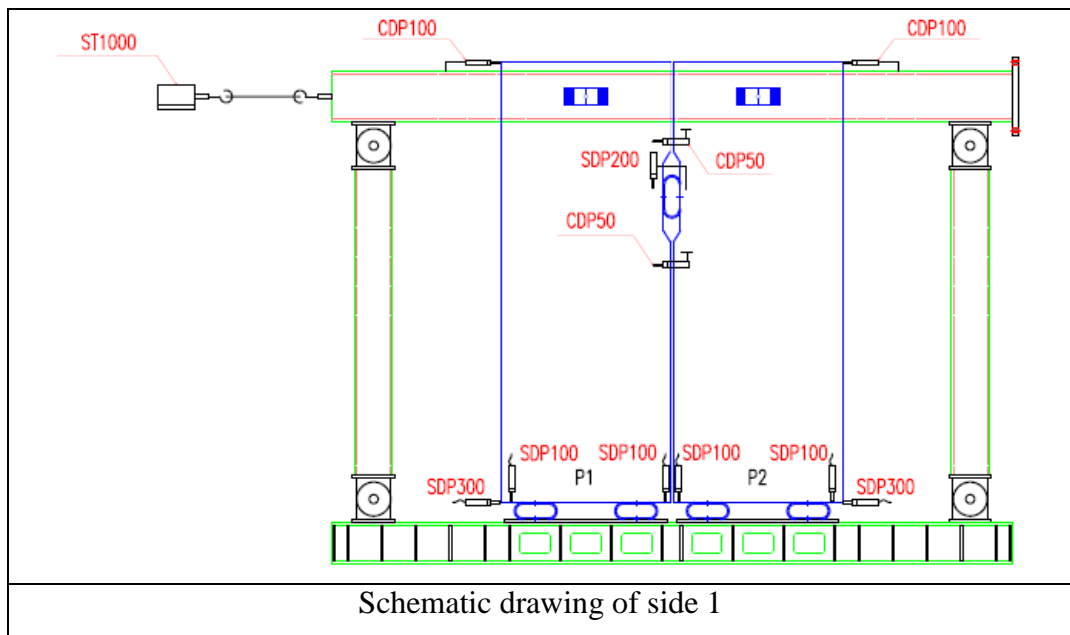


**Figure 4.78 :** Location of transducers in side 1 in system test III.

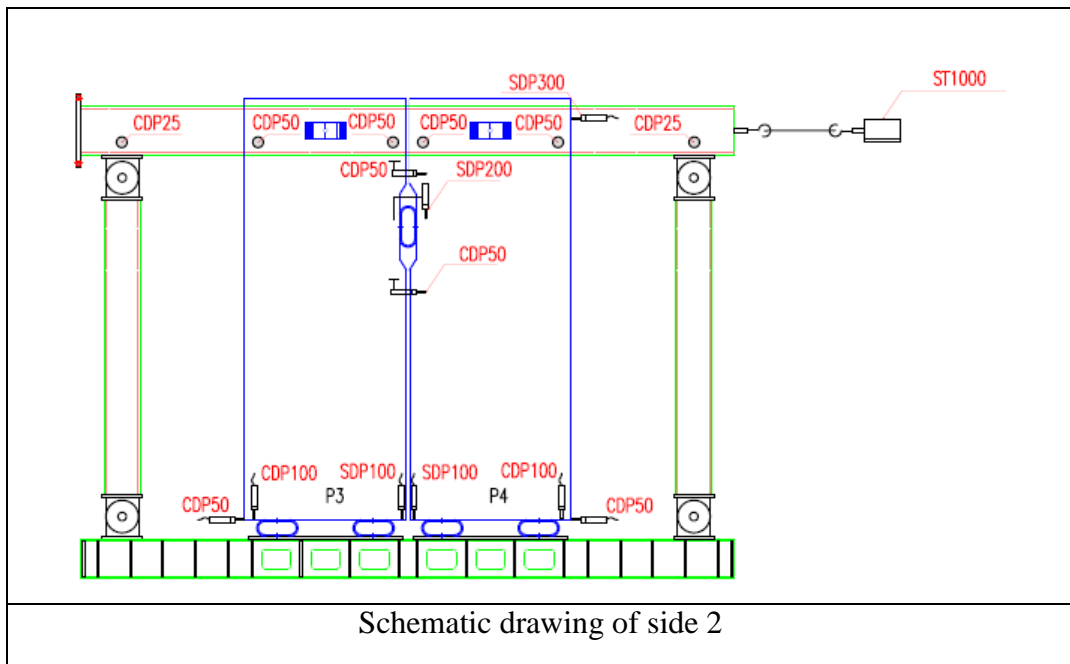


**Figure 4.79 :** Location of transducers in side 2 in system test III.

#### 4.6.1 Evaluation of experimental results obtained from system test III

In this section, the experimental results are presented and discussed.

##### 4.6.1.1 Actuator force-top displacement relation

The experimental actuator force in terms of displacement and drift derived from the system test III are shown in Figure 4.80 and 4.81.

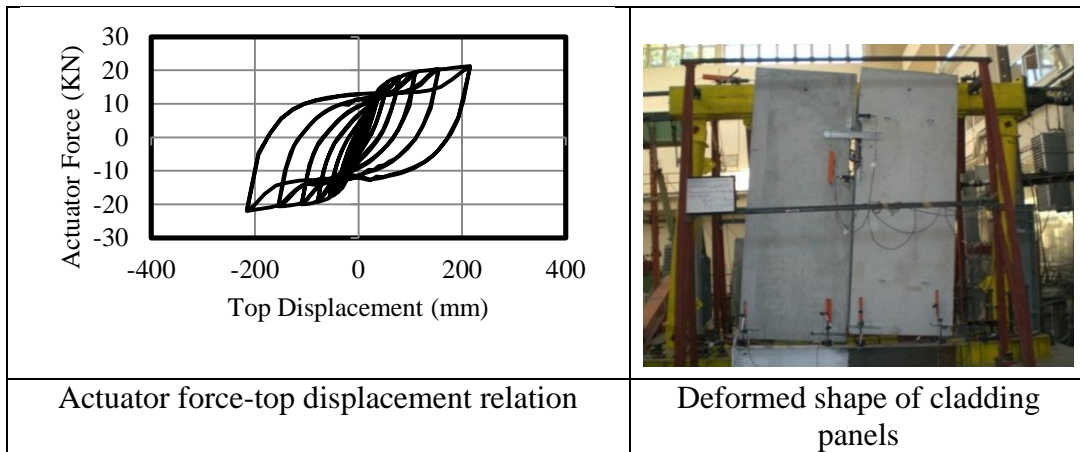


**Figure 4.80 :** Force-Top displacement relation obtained from system test III.

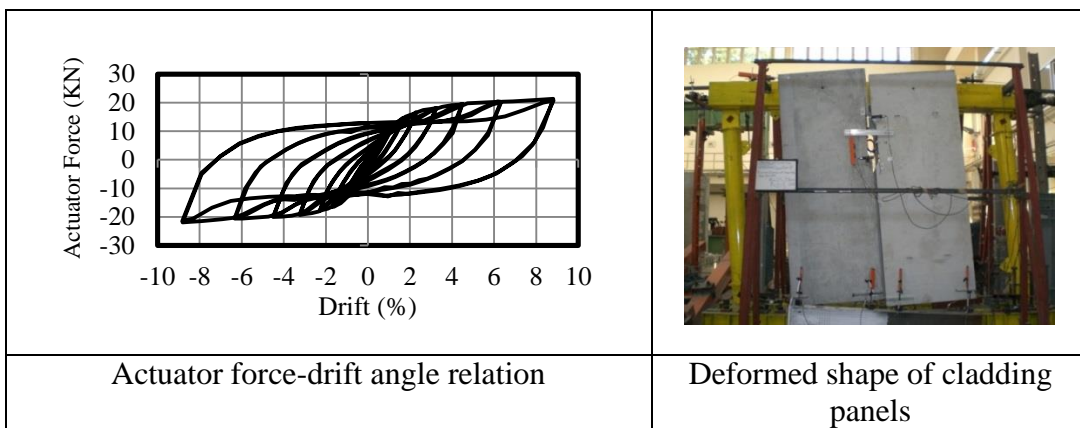


**Figure 4.81 :** Force-Drift angle curve obtained from system test III.

The experimental results obtained from system test III are summarized in Table 4.5. The force–drift angle relation of Figure 4.81 shows a stable and symmetric hysteresis behavior. Any damages were not observed on steel cushions and cladding panels.

**Table 4.5 :** Summary of test results obtained from system test III.

Yielding Force (KN)	Max Force (KN)	Yielding Drift (%)	Max Drift (%)
16.40	21.07	2.28	8.83

#### 4.6.1.2 Energy dissipation

Cumulative energy hysteresis curve vs. the drift angle is presented in Figure 4.82. Except the panel to beam connection steel device, which they did not yield, the steel devices in panel-to-panel and panel to support connection yielded, therefore they contributed in the Cumulative energy capacity. According to Figure 4.82 after the yield drift of 2.28% there is a sharp increase with respect to the previous drifts the energy value at the yielding drift is 2754 KN.mm. After the yielding with increase of

drift, the energy amount increases significantly, so that at the maximum drift of 8.83 the cumulative energy equals to 40131 KN.mm.

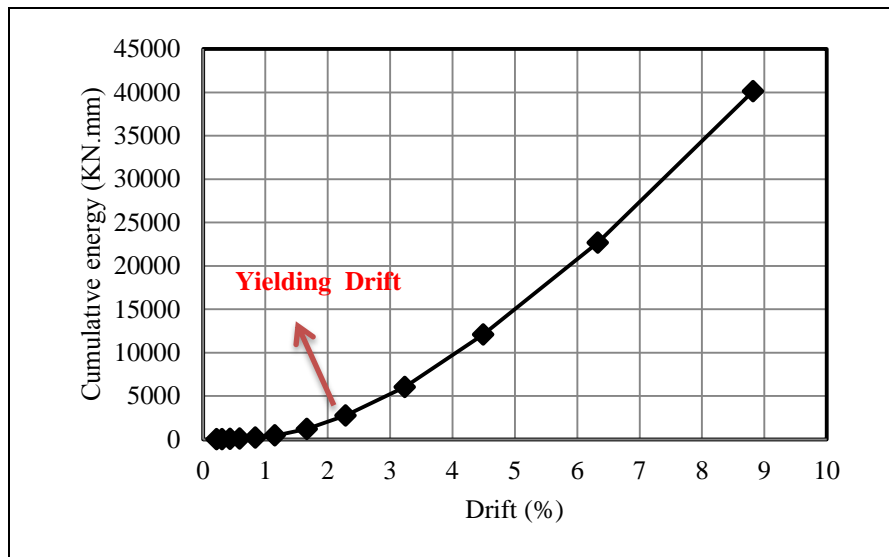


**Figure 4.82 :** Cumulative energy vs. drift curve obtained from system test III.

#### 4.6.1.3 Equivalent viscous damping

According to Figure 4.83, the equivalent damping ratio increases with increase of drift angle of system. Particularly after the drift angle of 2.28%, there is significant, increase. The equivalent damping ratio is 13.51% at yielding drift, after the yielding with increase of drift the equivalent damping ratio increases significantly, so that at the maximum drift of 8.82% the amount of the equivalent damping ratio equals to 30.71 %.

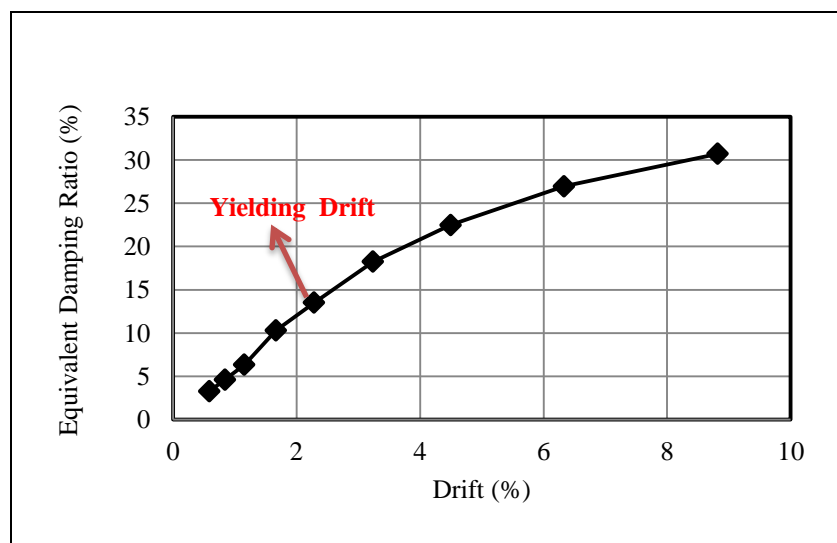


**Figure 4.83 :** Equivalent damping ratio vs. drift curve obtained from system test III.

**4.6.1.4 Effective (secant) stiffness**

The structural system has the initial stiffness of 0.63 KN/mm at the drift angle of 0.22%, as the drift angle increases the secant stiffness declines and reaches to the value of 0.1 KN/mm at the maximum drift angle, this shows approximately 84% reduction. The secant stiffness vs. drift relation is displayed in Figure 4.84.

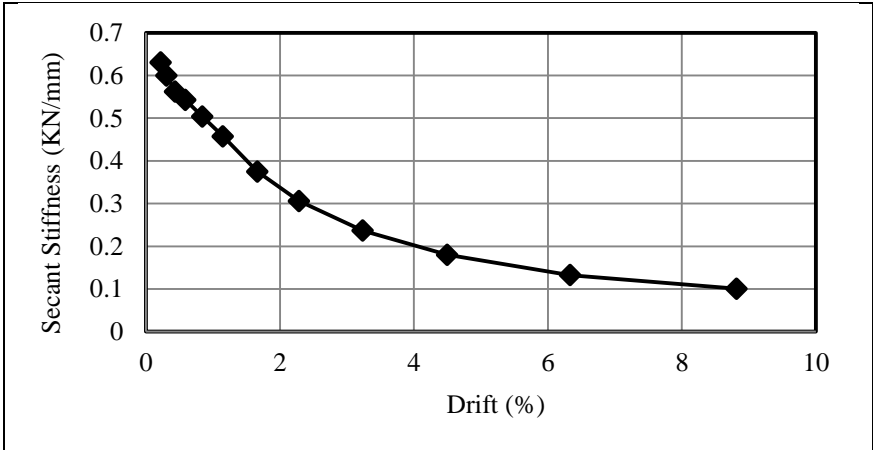


**Figure 4.84 :** Secant stiffness vs. drift relation obtained from system test III.

**4.6.1.5 Relative vertical displacement of panel to panel steel cushions**

The actuator force vs. relative displacement relation, for steel cushion in panel 1 to panel 2 connection is presented in Figure 4.85. The steel device used in the panel 1 to panel 2 connection is denoted by S12. The maximum relative displacement of S12 is 59.52 mm at actuator force of 21.27 KN.

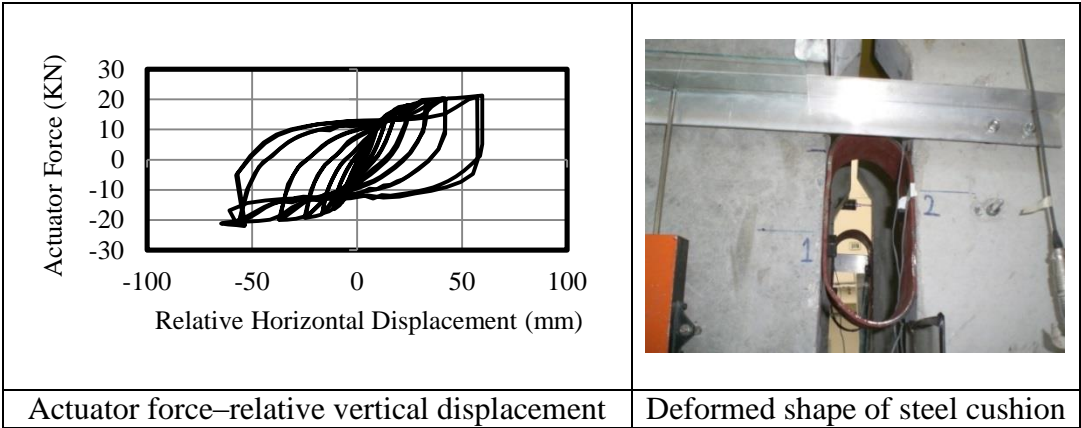


**Figure 4.85 :** Actuator force vs. relative displacement relation for steel cushion in panel 1 to panel 2 connection obtained from system test III.

The strain gauges locations on the specimens in panel-to-panel connections are shown in Figure 4.86.

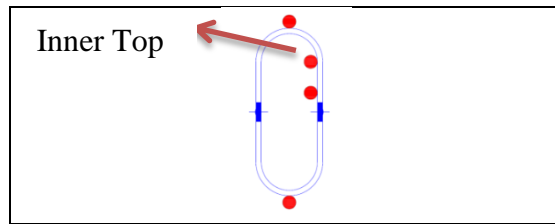


**Figure 4.86 :** Strain gauges location on steel cushions in panel-to-panel connection obtained from system test III.

The specimen yields at the drift angle of 3.23%. Location of the first yielding is the beginning of the arc section of specimen (inner top). The strain vs. drift angle relation of inner top point is presented in Figure 4.87.

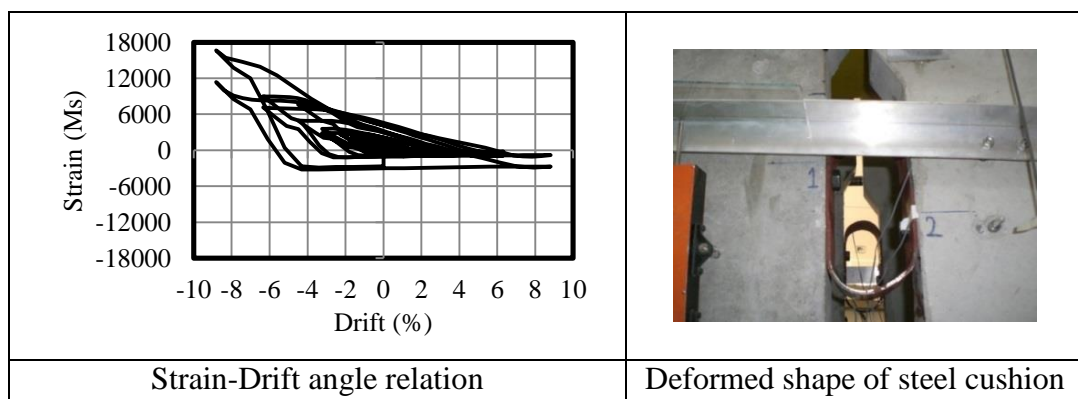


**Figure 4.87 :** Strain vs. drift angle relation for steel cushion in panel 1 to panel 2 connection obtained from system test III.

The actuator force vs. relative displacement relation for steel cushion in panel 3 to panel 4 connection is presented in Figure 4.88. The steel device in panel 3 to panel 4 connection, is denoted by S34. The maximum relative displacement of S34 are 79.6 mm at the actuator force of 21.26 KN.

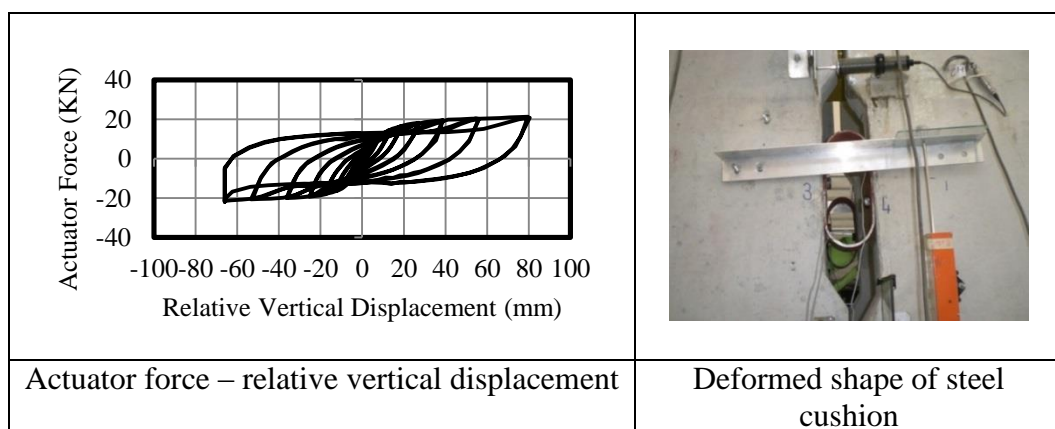


**Figure 4.88 :** Actuator force vs. relative displacement relation for steel cushion in panel 3 to panel 4 connection obtained from system test III.

The specimen yields at the drift angle of 1.15%. Location of the first yielding is the beginning of the arc section of specimen (inner top). The strain vs. drift angle relation of inner top point is presented in Figure 4.89.

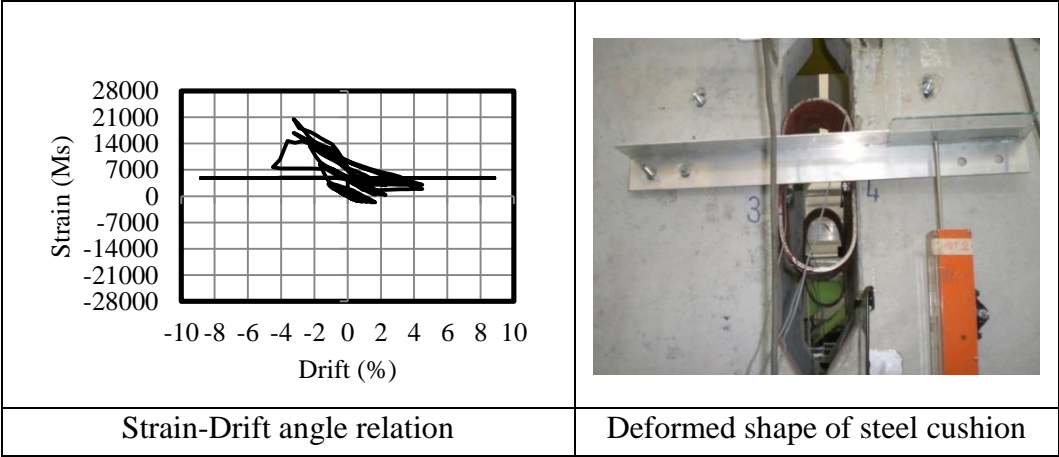


**Figure 4.89 :** Strain vs. drift angle relation for steel cushion in panel 3 to panel 4 connection obtained from system test III.

Two cushions between two adjacent panels behaved nearly symmetrically the actuator force vs. relative vertical displacement relation for two steel devices are compared in Figure 4.90.

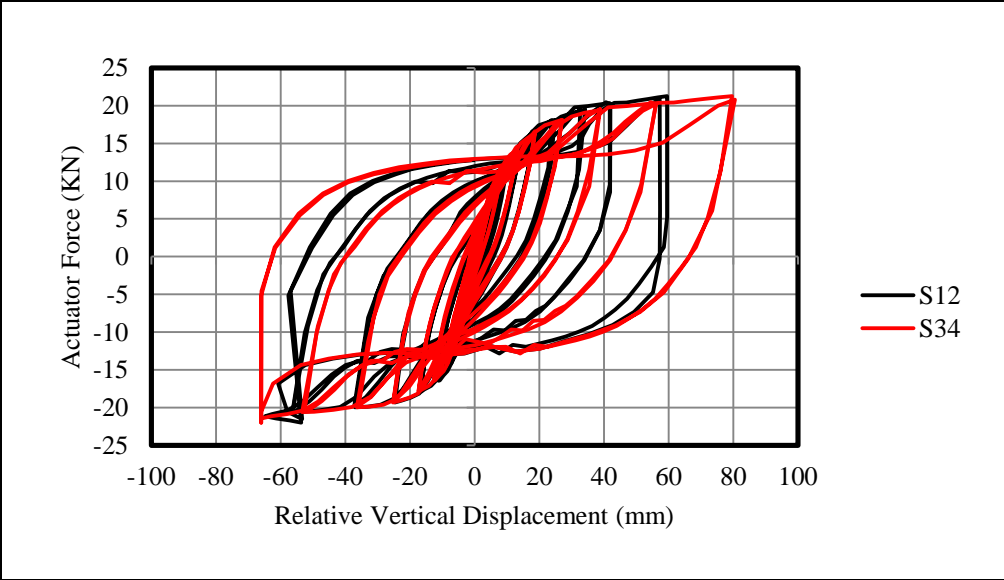


**Figure 4.90 :** Comparison of actuator force vs. relative displacement of S12 and S34 obtained from system test III.

#### 4.6.1.6 Relative horizontal displacement of panel to support steel cushions

To examine the shear displacement of steel cushion beneath panel 1 the relation between the actuator force and total relative displacement of steel cushions beneath panel 1 is presented in Figure 4.91. The maximum relative displacement is 27.84 mm at the actuator force of 21.07 KN, However as the transducer was installed at level of 20 cm from the panel base, the steel device horizontal displacement is smaller than this value. According to the deformed shape of steel cushion, besides the horizontal displacement the steel cushion rotated. In fact, this value of the horizontal displacement is formed by combination of the rotation of panel and horizontal displacement of steel cushions, although the rotation contribution in the horizontal displacement is more than steel cushions horizontal displacement. In addition, the behavior is asymmetric.

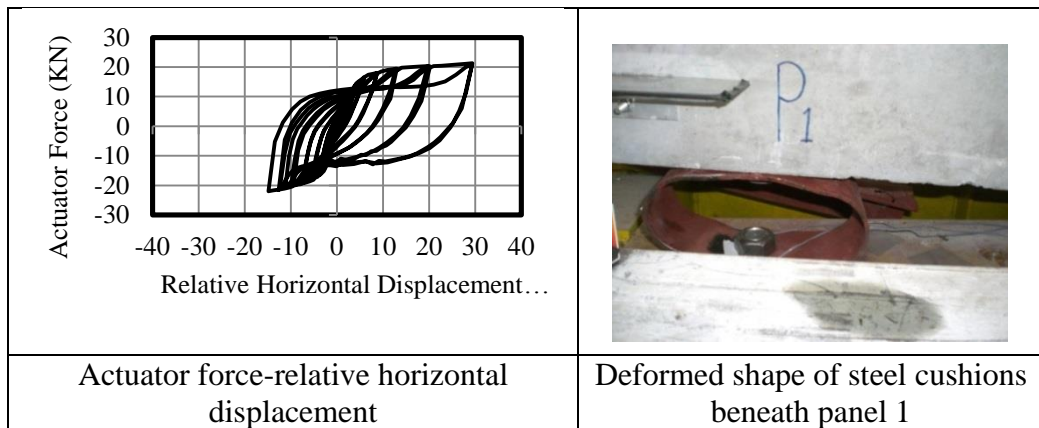


**Figure 4.91 :** Actuator force vs. relative horizontal displacement relation for steel cushions beneath panel 1 obtained from system test III.

The strain gauges locations for steel devices in panel to support connection are shown in Figure 4.92. According to the strain history, yielding occurred at all three points, the first yielding occurred at 1.66% system drift angle. The location of first yielding was the specimen vertex point.

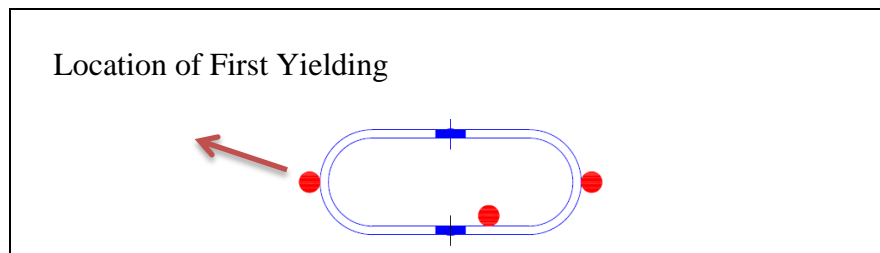


**Figure 4.92 :** Location of strain gauges on steel cushions in panel to support connection obtained from system test III.

The relation between the actuator force and total relative displacement of steel cushions beneath panel 2, is presented in Figure 4.93. The maximum relative displacement is 29.94 mm at the actuator force of 21.67 KN, However as the transducer was installed at level of 20 cm from the panel base, the steel device horizontal displacement is smaller than this value. According to the deformed shape of steel cushion, besides the horizontal displacement the steel cushion rotated. In fact, this value of the horizontal displacement is formed by combination of the rotation of panel and horizontal displacement of steel cushions, although the rotation contribution in the horizontal displacement is more than steel cushions horizontal displacement. In addition, the behavior is asymmetric.

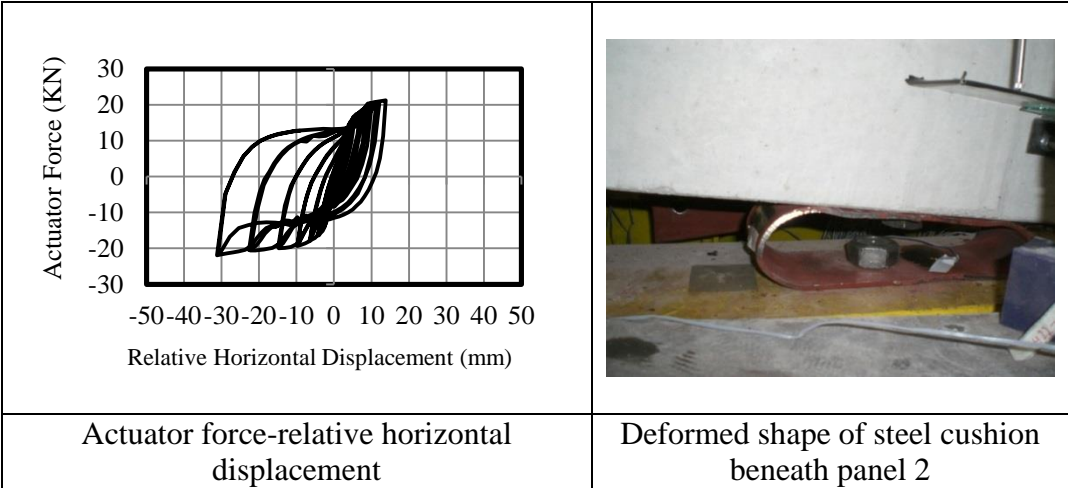


**Figure 4.93 :** Actuator force vs. relative horizontal displacement relation for steel cushions beneath panel 2 obtained from system test III.

According to the strain history, yielding occurred at all three points, the first yielding occurred at 1.16 % system drift angle. The location of first yielding was the specimen vertices.

The relation between the actuator force and total relative displacement of steel cushions beneath panel 3 is presented in Figure 4.94. The maximum relative displacement is 25.29mm at the actuator force of 20.60 KN, However as the transducer was installed at level of 20 cm from the panel base, the steel device horizontal displacement is smaller than this value. According to the deformed shape of steel cushion, besides the horizontal displacement the steel cushion rotated. In fact, this value of the horizontal displacement is formed by combination of the rotation of panel and horizontal displacement of steel cushions, although the rotation

contribution in the horizontal displacement is more than steel cushions horizontal displacement. In addition, the behavior is asymmetric.

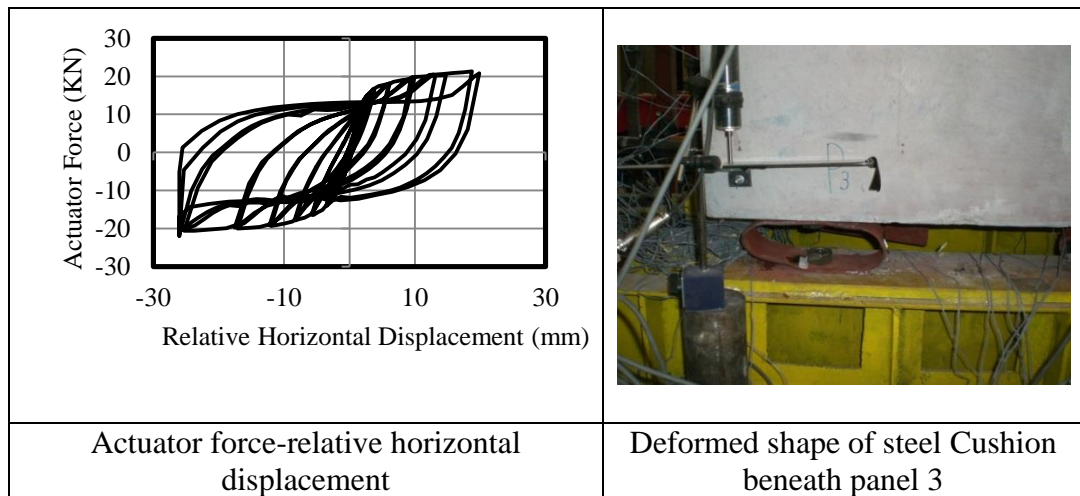


**Figure 4.94 :** Actuator force vs. relative horizontal displacement relation for steel cushions beneath panel 3 obtained from system test III.

According to the strain history, yielding occurred at all three points, the first yielding occurred at 1.66 % system drift angle. The location of first yielding is illustrated in Figure 4.95.

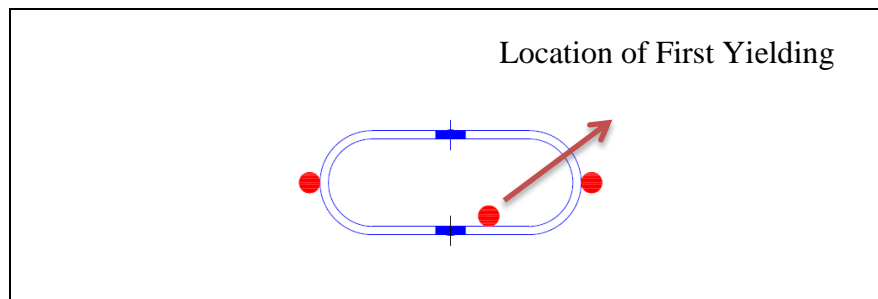


**Figure 4.95 :** Location of strain gages on steel cushions in panel to support connection obtained from system test III.

The relation between the actuator force and total relative displacement of steel cushions beneath panel 4 is presented in Figure 4.96. The maximum relative displacement is 26.09 mm at the actuator force of 20.67 KN, However as the transducer was installed at level of 20 cm from the panel base, the steel device horizontal displacement is smaller than this value. According to the deformed shape of steel cushion, besides the horizontal displacement the steel cushion rotated. In fact, this value of the horizontal displacement is formed by combination of the rotation of panel and horizontal displacement of steel cushions, although the rotation

contribution in the horizontal displacement is more than steel cushions horizontal displacement. In addition, the behavior is asymmetric.

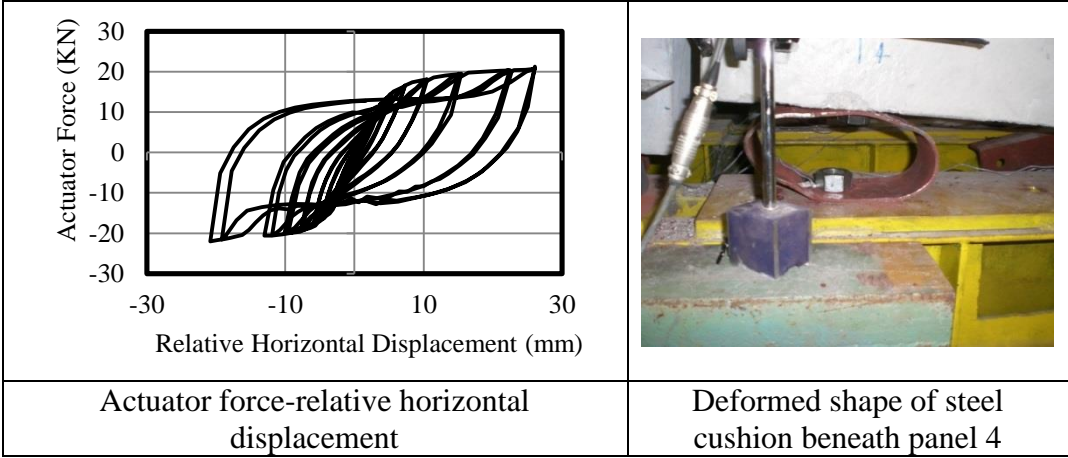


**Figure 4.96 :** Actuator force vs. relative horizontal displacement relation for steel cushions beneath panel 4 obtained from system test III.

According to the strain history, yielding occurred at all three points, the first yielding occurred at 2.28 % system drift angle. The location of first yielding was the specimen vertex point.

To investigate whether the Steel cushions beneath two symmetric panels, behaved symmetrically or not, actuator force-relative horizontal displacement relations for steel cushion beneath panel 1 and panel 4 are compared at Figure 4.97. According to Figure 4.97 the panel 1 and panel 4 almost behaved symmetrically as a result, the steel cushions below panel 1 and panel 4 represented the nearly symmetrical behavior.

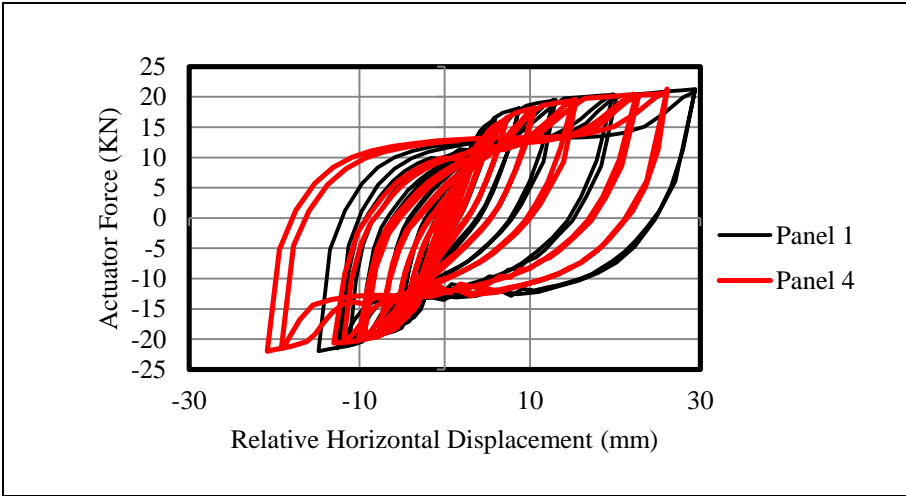


**Figure 4.97 :** Comparison of actuator force-relative displacement relation for steel cushions beneath panel 1 and panel 4 obtained from system test III.

Actuator force-relative horizontal displacement relations for steel cushion beneath panel 2 and panel 3 are compared in Figure 4.98. According to Figure 4.98 the panel 2 and panel 3 almost behaved symmetrically as a result, the steel cushions below panel 2 and panel 3 represented the nearly symmetrical behavior.

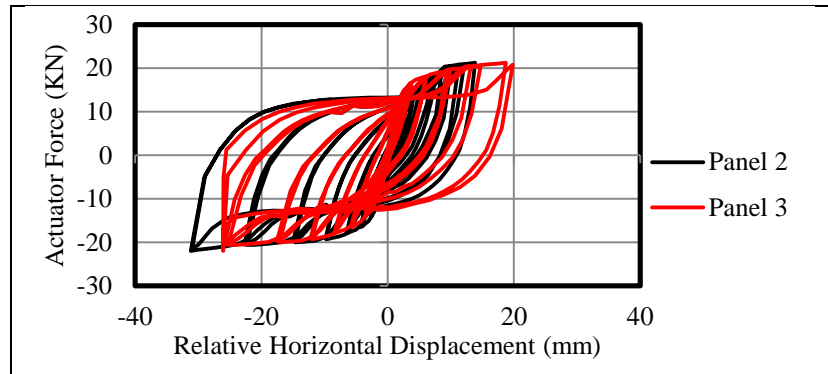


**Figure 4.98 :** Comparison of actuator force-relative displacement relation for steel cushions beneath panel 2 and panel 3 obtained from system test III.

#### 4.6.1.7 Relative Horizontal Displacement of Panel to Beam Steel Cushions

To investigate the behavior of steel cushion in panel 1 to beam connection, the relation of actuator force vs. relative displacement between panel 1 and beam is presented in Figure 4.99. This steel cushion is denoted by S1\*. The maximum relative displacement between panel 1 and beam is 12.01 mm at the actuator force of 21.07 KN. According to the strain history relevant to this steel device the yielding is not observed, which indicate the steel device horizontal displacement must be less than 100 mm, while the relative displacement between panel 1 and beam is 12.01 mm, so this is caused by the rotation of the panel and it does not represent the steel device real horizontal displacement.

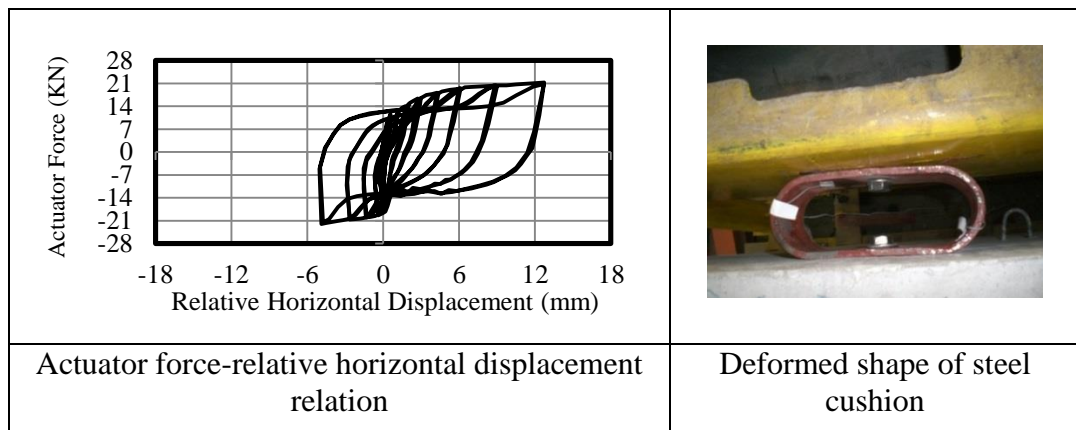


**Figure 4.99 :** Relation of the actuator force vs. relative displacement between panel 1 and beam obtained from system test III.

The steel device in panel 2 to beam connection is denoted by S2\*. The relation of the actuator force vs. relative displacement between panel 1 and beam is presented in Figure 4.100. The maximum relative displacement between panel 2 and beam is 20.22 mm at the actuator force of 21.67 KN in other word the S2\* displaced up to 20.22% its drift angle. According to the strain history relevant to this steel device yielding is not observed, which indicate the steel device horizontal displacement must be less than 100 mm, while the relative displacement between panel1 and beam is 20.22 mm, so this is caused by the rotation of the panel and it doesn't represent the steel device real horizontal displacement.

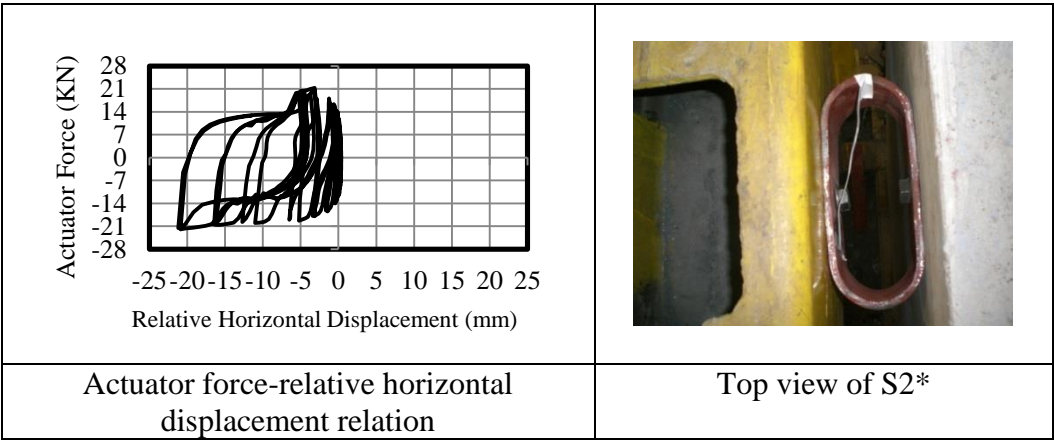


**Figure 4.100 :** Relation of the actuator force vs. relative displacement between panel 2 and beam obtained from system test III.

The steel device in panel 3 to beam connection is denoted by S3\*. According to the Figure 4.101, S3\* horizontal displacement was so small. In fact the panel 3 rotated easily and S3\* acted such a hinge connection.



**Figure 4.101 :** Top view of S3\* at final displacement target obtained from system test III.

The steel device in panel 4 to beam connection is denoted by S4\*. According to the Figure 4.102, S4\* horizontal displacement was so small. In fact the panel 3 rotated easily and S4\* acted such a hinge connection.

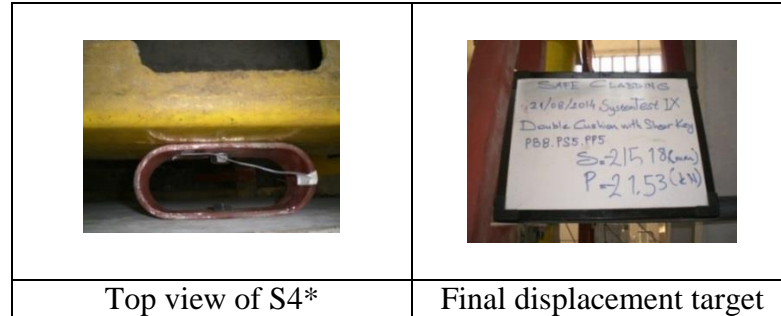


**Figure 4.102 :** Top view of S4\* at final displacement target obtained from system test III.

The locations of strain gauges in panel to beam steel cushions are illustrated in Figure 4.103.

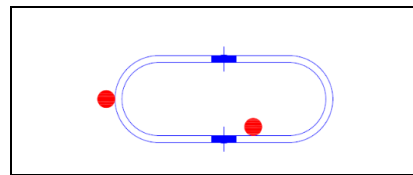


**Figure 4.103 :** location of strain gauges on steel device in system test III.

#### 4.6.1.8 Cladding Panels Rotation

The rotation of panel 3 and 4 in terms of step numbers are illustrated in Figure 4.104 and 4.105, respectively. The maximum rotation of panel 3 and panel 4 is 0.0831 rad and 0.0743 rad, respectively.

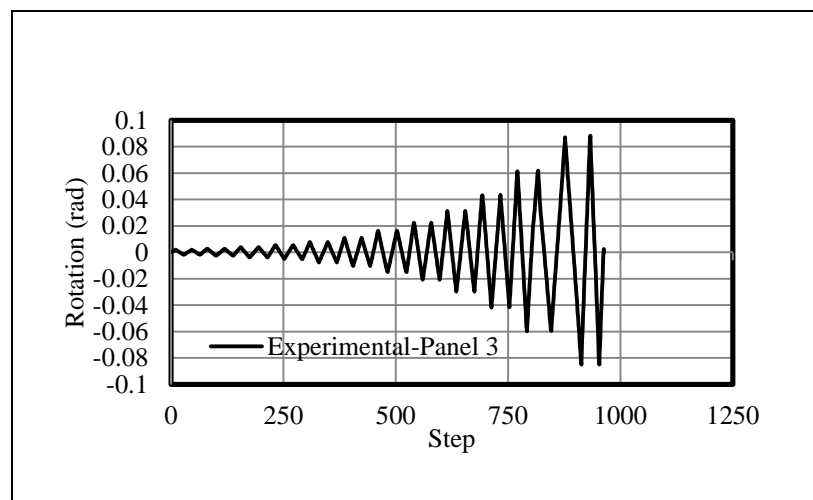


**Figure 4.104 :** Rotation in terms of step numbers for panel 3.

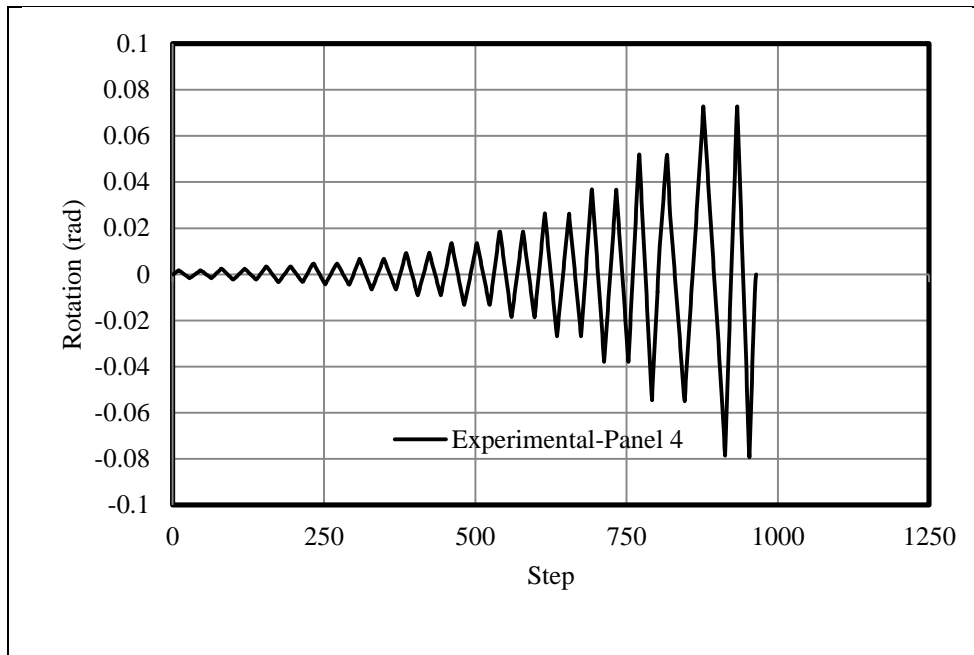


**Figure 4.105 :** Rotation in terms of step numbers for panel 4.

#### 4.6.1.9 Total behavior of panels

To examine the amount of out of plane displacement, the out of plane displacement of panel 3 and panel 4 vs. actuator displacement curves are presented in Figures 4.106 and 4.107. According to Figure 4.106, the amount of out of plane displacement of panel 3 is small enough.

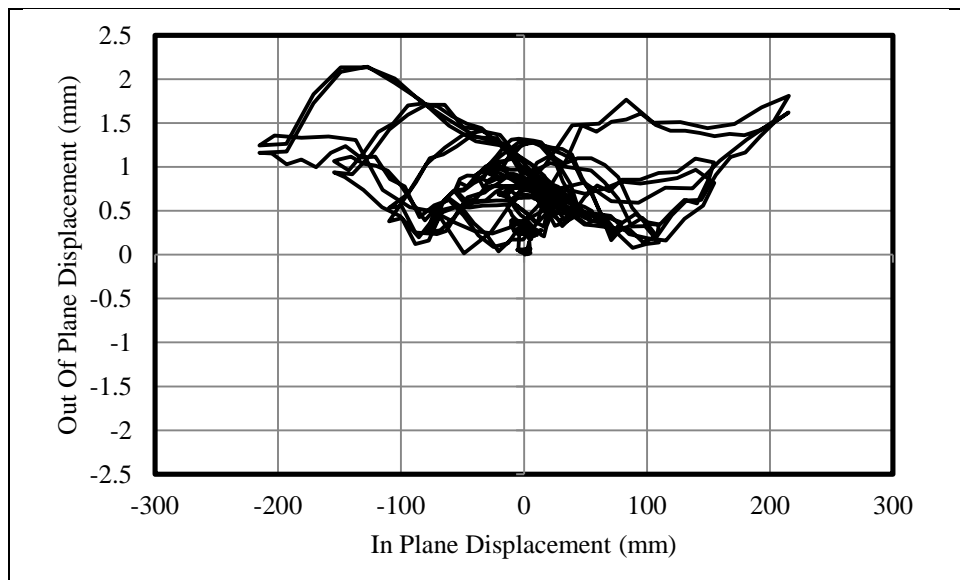


**Figure 4.106 :** Out of plane displacement of panel 3 in terms of in plane displacement obtained from system test III.

According to Figure 4.107, the amount of out of plane displacement of panel 4 is small as well. However, the out of plane displacement for panel 4 is higher than corresponding value for panel 3.

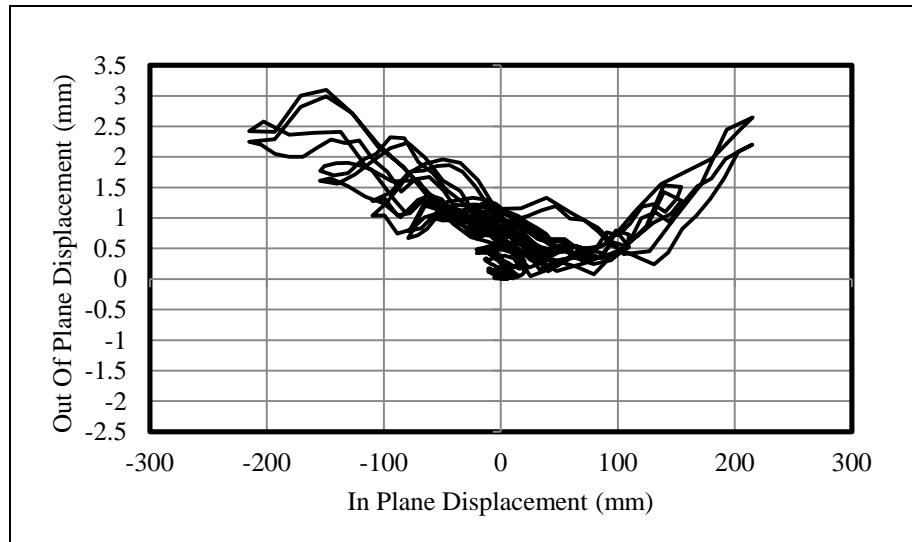


**Figure 4.107 :** Out of plane displacement of panel 4 in terms of in plane displacement obtained from system test III.

In total the out of plane displacement of panels are minimal as a result the steel device in panel to beam connection were not subjected to significant tensile stress. Moreover any twisting of panels or steel cushions were not observed during the test. The deformed shapes of the steel cushions are shown in Figure 4.108.

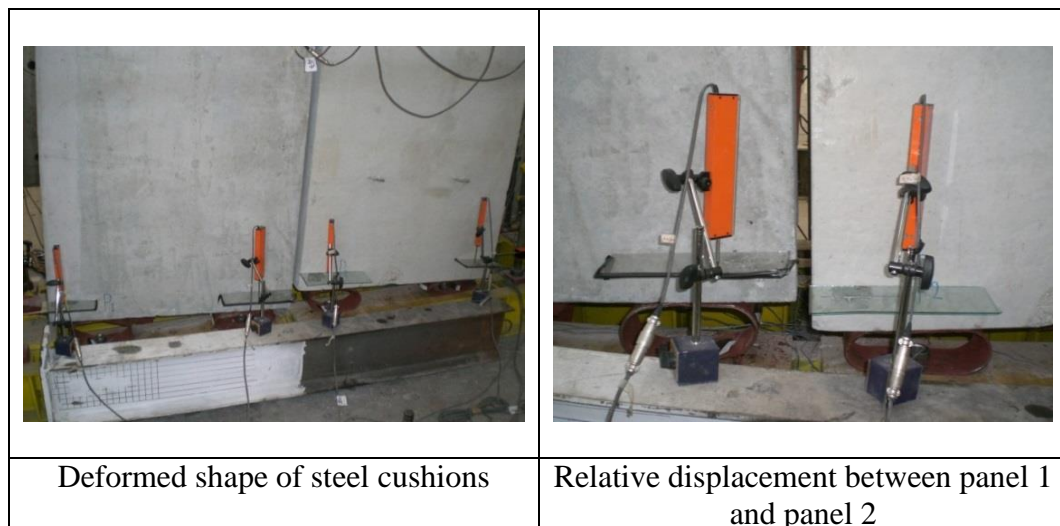


**Figure 4.108 :** Deformed shape of the steel cushions obtained from system test III.

**4.7 System Test IV (Double Cushion Test)**

Two steel cushions were used at the bottom of each cladding. 5mm steel cushions were used at the support to panel connection, 3mm ones in panel-to-panel connection and 8mm steel devices in beam to panel connection. Totally four pieces of 5mm cushions at the supporting level (two ones per panel), two pieces of cushions in the mid-level (one cushion between two panels) and four pieces of steel cushions on the top level (one cushion per panel) were utilized. This arrangement is shown in Figure 4.109.

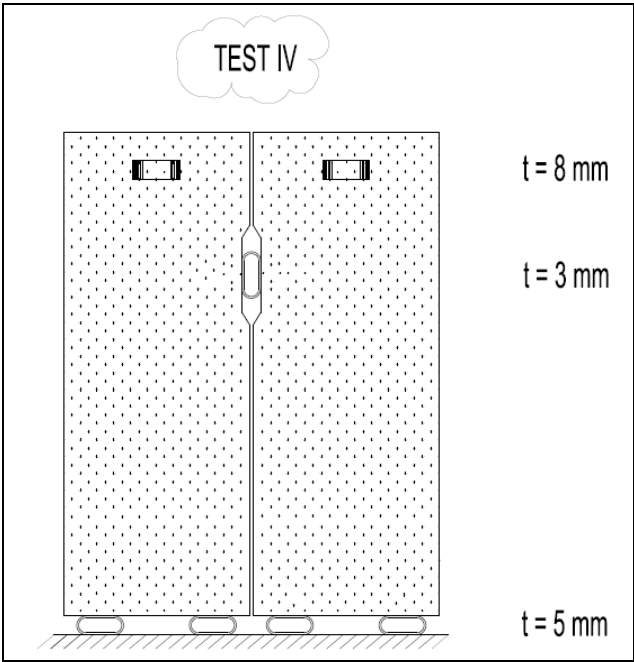


**Figure 4.109 :** Arrangements of steel cushions in system test IV.

The location of the strain gauges are illustrated in Figure 4.110.

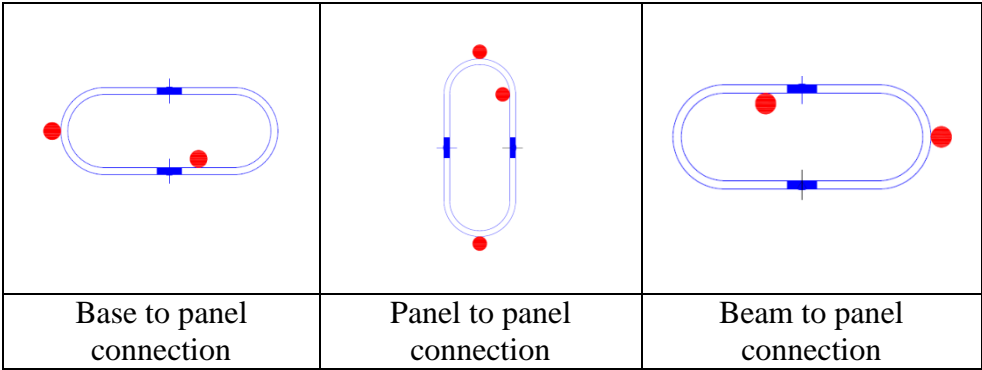


**Figure 4.110 :** Location of strain assessment devices in system test IV.

Transducer and their locations are illustrated in Figure 4.111 and 4.112.

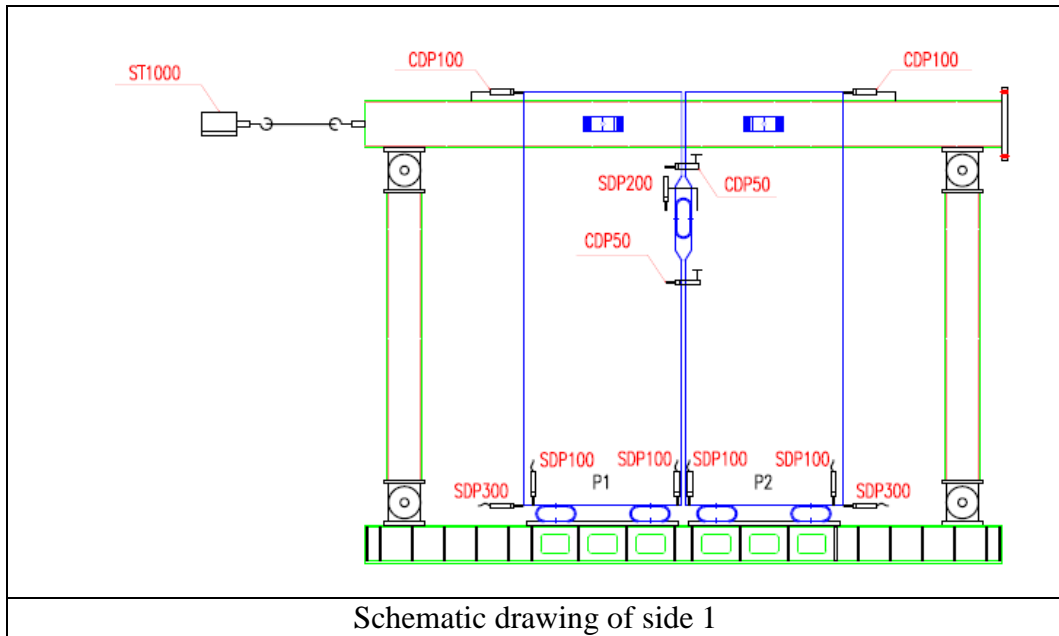


**Figure 4.111** : Location of transducers in side 1 in system test IV.

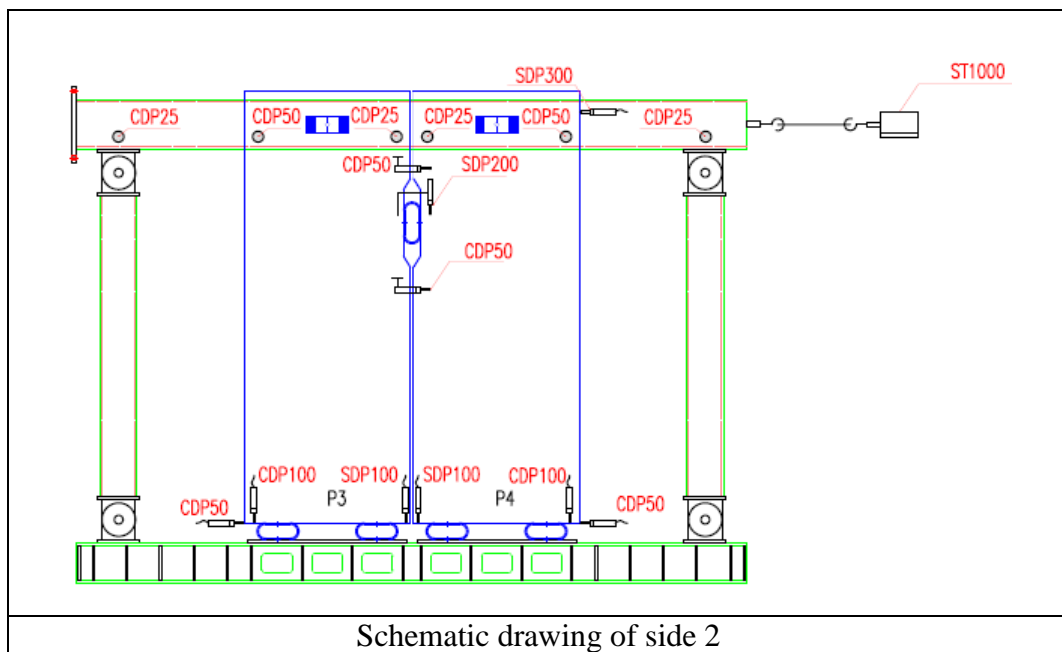


**Figure 4.112** : Location of transducers in side 2 in system test IV.

#### 4.7.1 Evaluation of experimental results obtained from system test IV

In this section, the experimental results are presented and discussed.

##### 4.7.1.1 Actuator force-top displacement relation

The experimental actuator force in terms of displacement and drift derived from the system test IV are shown in Figure 4.113 and 4.114.

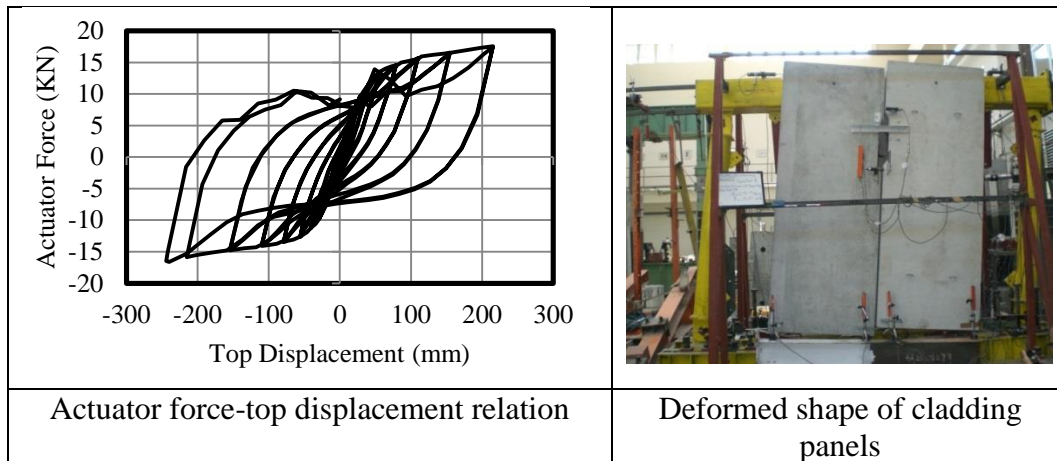


**Figure 4.113 :** Force-Top displacement relation obtained from system test IV.

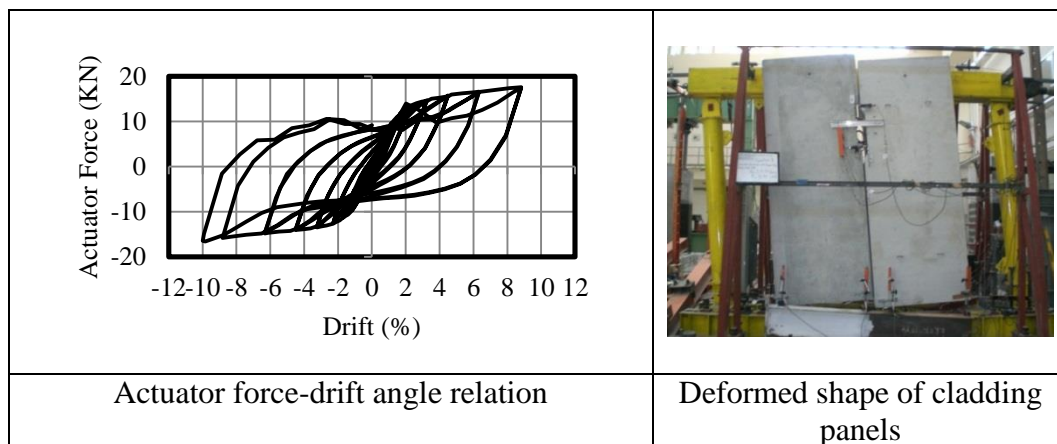


**Figure 4.114 :** Force-Drift angle curve obtained from system test IV.

The experimental results obtained from system test IV are summarized in Table 4.6. The Force–drift angle relation of Figure 4.114 shows a stable and symmetric hysteresis behavior. Any damages were not observed on steel cushions and cladding panels.

**Table 4.6 :** Summary of test results obtained from system test IV.

Yielding Force (KN)	Max Force (KN)	Yielding Drift (%)	Max Drift (%)
11.60	17.59	1.67	8.82

#### 4.7.1.2 Energy dissipation

Cumulative energy dissipation hysteresis curve vs. the drift angle is presented in Figure 4.115. Except the panel to beam connection steel devices, which they did not yield, the steel devices in panel to panel and panel to support connection yielded, therefore they contributed in the Cumulative energy capacity and. According to Figure 4.115, after the yield drift of 1.67%, there is a sharp increase with respect to the previous drifts. The energy value at the yielding drift is 679 KN.mm. After the

yielding with increase of drift angle, the cumulative energy increases significantly, so that at the maximum drift of 8.82% the cumulative energy equals to 27119 KN.mm.

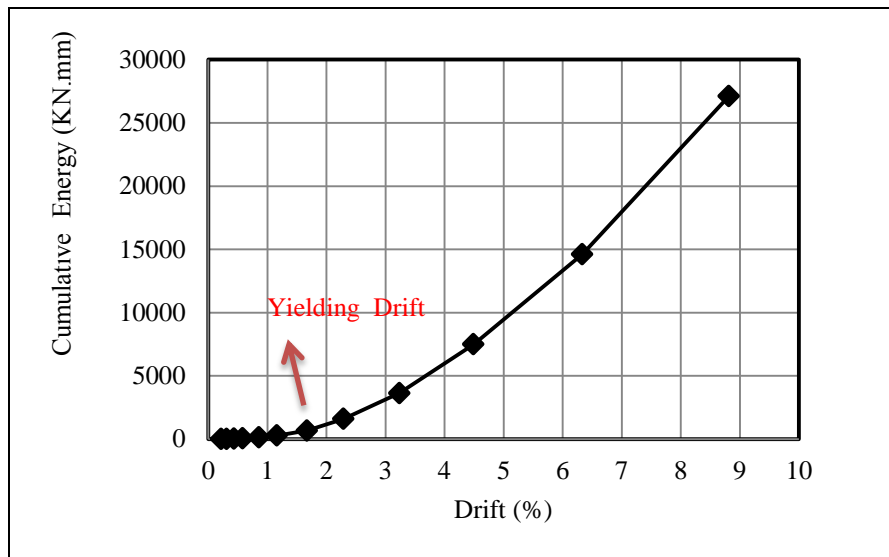


**Figure 4.115 :** Cumulative energy vs. drift curve obtained from system test IV.

#### 4.7.1.3 Equivalent viscous damping

According to Figure 4.116, the equivalent damping ratio increases with increase of drift angle of system. Particularly after the drift angle of 1.67%, there is significant, increase. The equivalent damping ratio is 6.69% at yielding drift, after the yielding with increase of drift the equivalent damping ratio increases significantly, so that at the maximum drift of 8.82% the equivalent damping ratio equals to 26.42 %.

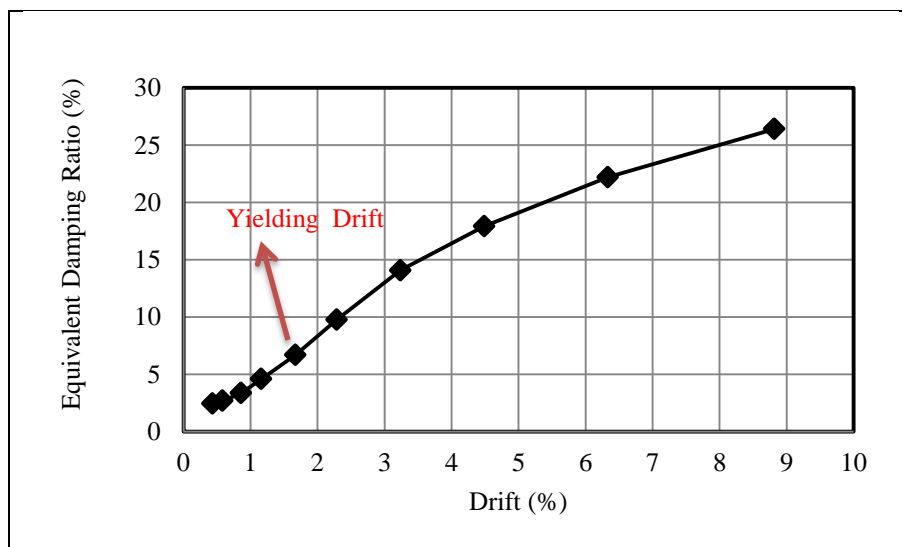


**Figure 4.116 :** Equivalent damping ratio vs. drift curve obtained from system test IV.

**4.7.1.4 Effective (secant) stiffness**

The structural system has the initial stiffness of 0.45 KN/mm at the drift angle of 0.22%. As the drift angle increases the secant stiffness declines and reaches to the value of 0.08 KN/mm at the maximum drift angle, this shows approximately 83% reduction. The secant stiffness vs. drift relation is displayed in Figure 4.117.

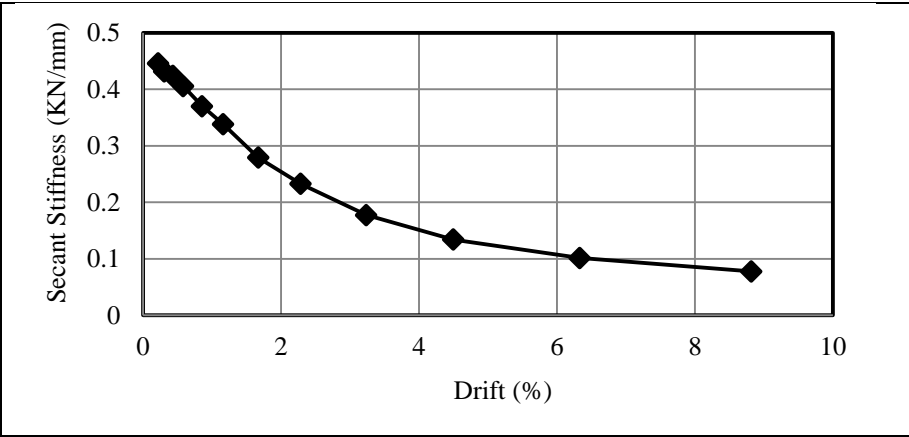


**Figure 4.117 :** Secant stiffness vs. drift relation obtained from system test IV.

**4.7.1.5 Relative vertical displacement of panel to panel steel cushions**

The actuator force vs. relative displacement relation, for steel cushion in panel 1 to panel 2 connection is presented in Figure 4.118. The steel device in panel 1 to panel 2 connection is denoted by S12. The maximum relative displacements of S12 is 83.38 mm at the actuator force of 17.59 KN.

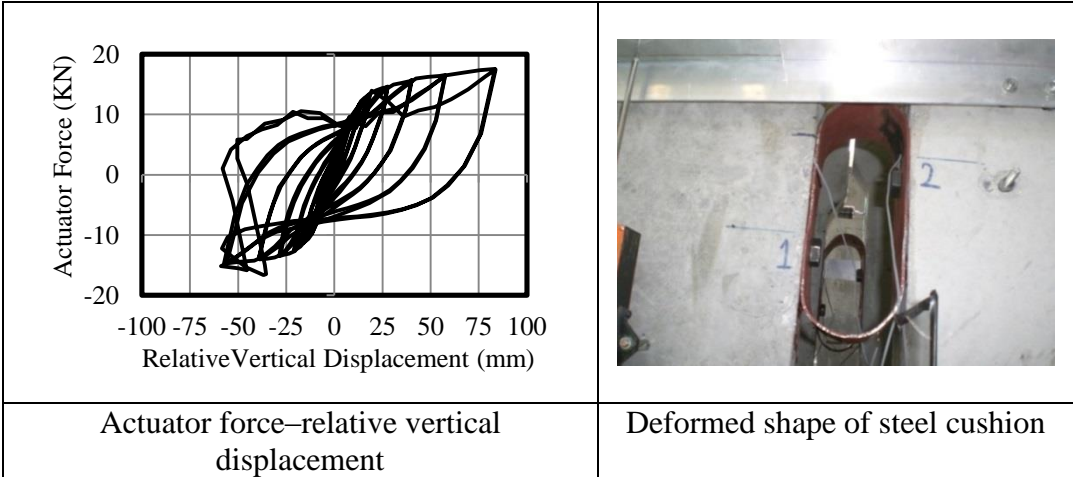


**Figure 4.118 :** Actuator force vs. relative displacement relation for steel cushion in panel 1 to panel 2 connection obtained from system test IV.

The strain gauges locations on the specimens in panel-to-panel connections are shown in Figure 4.119.

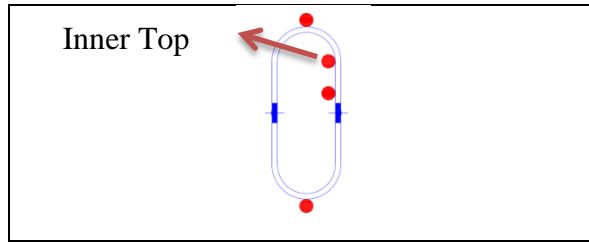


**Figure 4.119 :** Strain gauges location on steel cushions in panel-to-panel connection obtained from system test IV.

The specimen yields at the system drift angle of 2.28%. Location of the first yielding is the beginning of the arc section of specimen (inner top). The strain vs. drift angle relation of inner top point is presented in Figure 4.120.

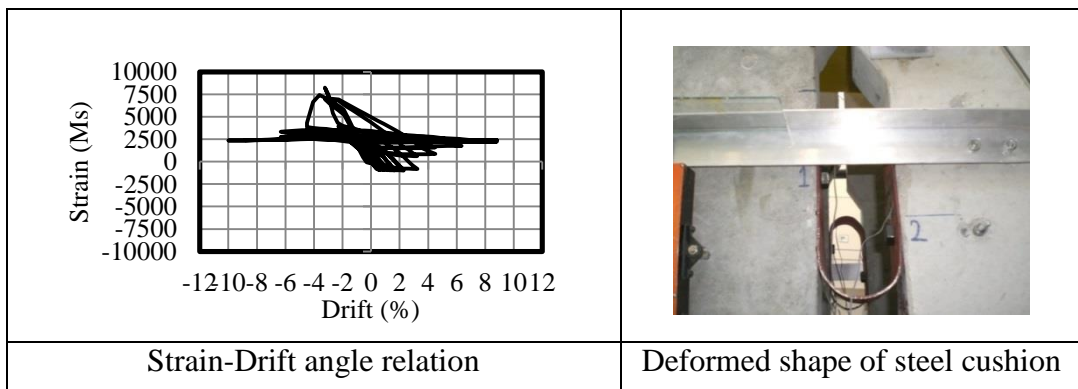


**Figure 4.120 :** Strain vs. drift angle relation for steel cushion in panel 1 to panel 2 connection obtained from system test IV.

The actuator force vs. relative displacement relation for steel cushion in panel 3 to panel 4 connection is presented in Figure 4.121. The steel device in panel 3 to panel 4 connection is denoted by S34. The maximum relative displacements of S34 is 83.3 mm at the actuator force of 17.59KN.

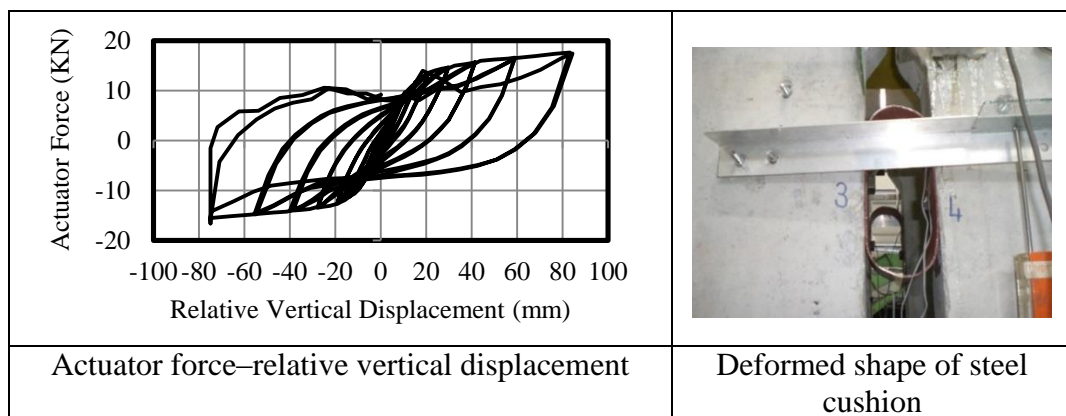


**Figure 4.121 :** Actuator force vs. relative displacement relation for steel cushion in panel 3 to panel 4 connection obtained from system test IV.

The specimen yields at the drift angle of 4.49%. Location of the first yielding is the beginning of the arc section of specimen (inner top). The strain vs. drift angle relation of inner top point is presented in Figure 4.122.

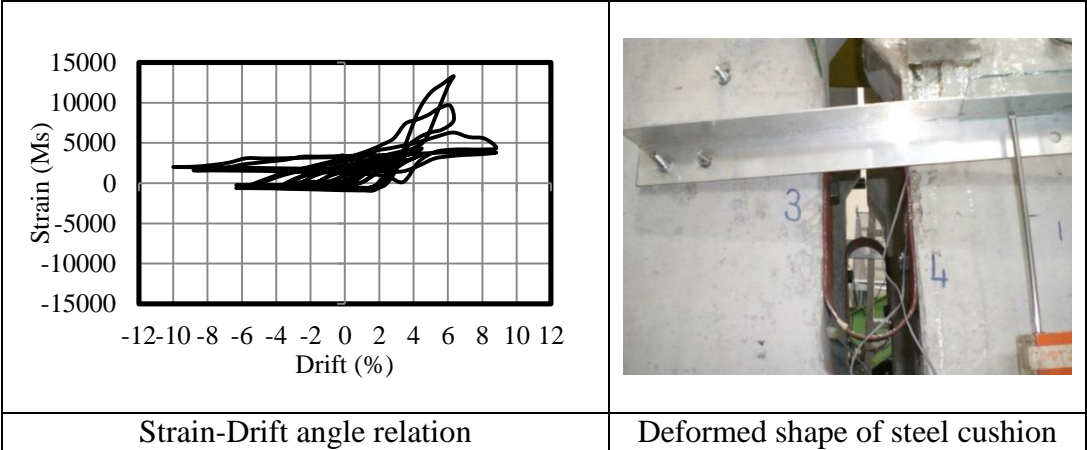


**Figure 4.122 :** Strain vs. drift angle relation for steel cushion in panel 3 to panel 4 connection obtained from system test IV.

Two cushions between two adjacent panels behaved nearly symmetrically the actuator force vs. relative vertical displacement relation for two steel devices are compared in Figure 4.123.

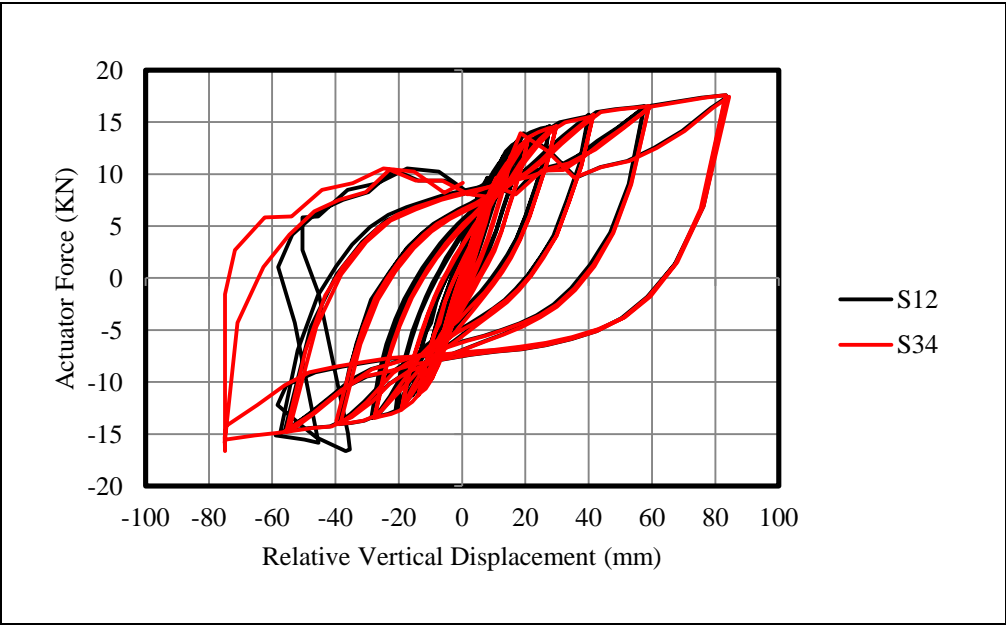


**Figure 4.123 :** Comparison of actuator force vs. relative displacement of S12 and S34 obtained from system test IV.

#### 4.7.1.6 Relative horizontal displacement of panel to support steel cushions

To examine the shear displacement of steel cushion beneath panel 1 the relation between the actuator force and total relative displacement of steel cushions beneath panel 1 is presented in Figure 4.124. The maximum relative displacement is 20.82 mm at the actuator force of 17.59KN, However as the transducer was installed at level of 20 cm from the panel base, the steel device horizontal displacement is smaller than this value. According to the deformed shape of steel cushion, besides the horizontal displacement the steel cushion rotated. In fact, this value of the horizontal displacement is formed by combination of the rotation of panel and horizontal displacement of steel cushions, although the rotation contribution in the horizontal displacement is more than steel cushions horizontal displacement. In addition, the behavior is asymmetric.

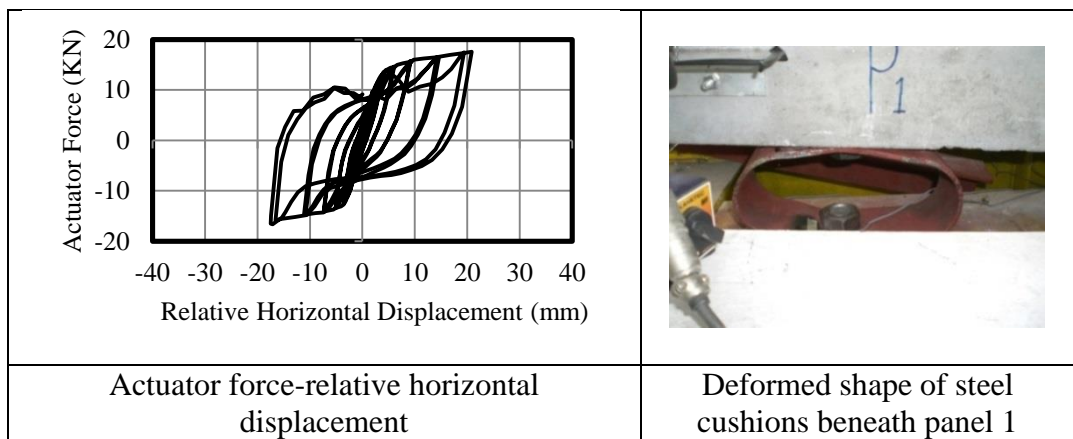


**Figure 4.124 :** Actuator force vs. relative horizontal displacement relation for steel cushions beneath panel 1 obtained from system test IV.

The strain gauges locations for steel devices in panel to support connection are shown in Figure 4.125. According to the strain history, yielding occurred at all three points, the first yielding occurred at 2.83% system drift angle. The location of first yielding was the specimen vertex point.

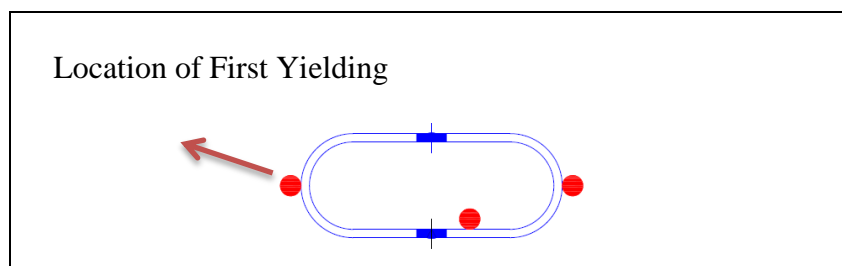


**Figure 4.125 :** Location of strain gauges on steel cushions in panel to support connection obtained from system test IV.

The relation between the actuator force and total relative displacement of steel cushions beneath panel 2 is presented in Figure 4.126. The maximum relative displacement is 26.25mm at the actuator force of 16.63 KN, However as the transducer was installed at level of 20 cm from the panel base, the steel device horizontal displacement is smaller than this value. According to the deformed shape of steel cushion, besides the horizontal displacement the steel cushion rotated. In fact, this value of the horizontal displacement is formed by combination of the rotation of panel and horizontal displacement of steel cushions, although the rotation contribution in the horizontal displacement is more than steel cushions horizontal displacement. In addition, the behavior is asymmetric.

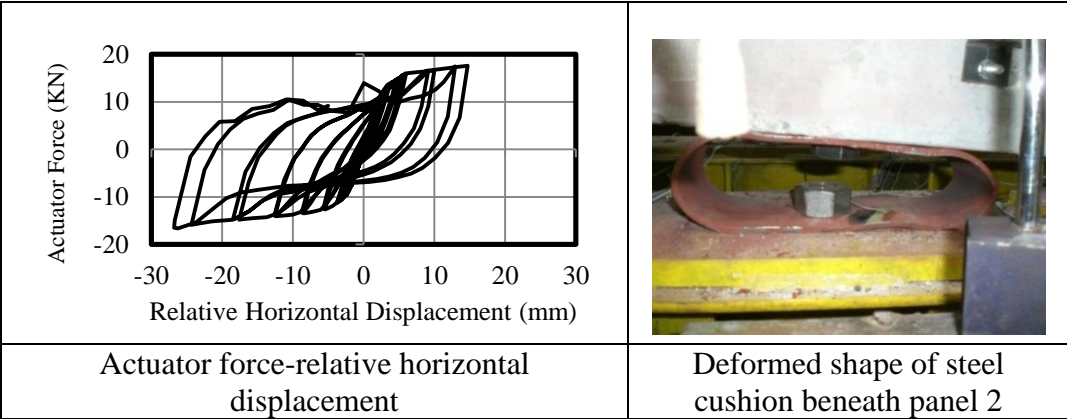


**Figure 4.126 :** Actuator force vs. relative horizontal displacement relation for steel cushions beneath panel 2 obtained from system test IV.

According to the strain history, yielding occurred at all three points, the first yielding occurred at 1.16 % system drift angle. The location of first yielding was the specimens vertices.

The relation between the actuator force and total relative displacement of steel cushions beneath panel 3 is presented in Figure 4.127. The maximum relative displacement is 26.89mm at the actuator force of 16.63 KN, However as the transducer was installed at level of 20 cm from the panel base, the steel device horizontal displacement is smaller than this value. According to the deformed shape of steel cushion, besides the horizontal displacement the steel cushion rotated. In fact, this value of the horizontal displacement is formed by combination of the rotation of panel and horizontal displacement of steel cushions, although the rotation contribution in the horizontal displacement is more than steel cushions horizontal displacement. In addition, the behavior is asymmetric.

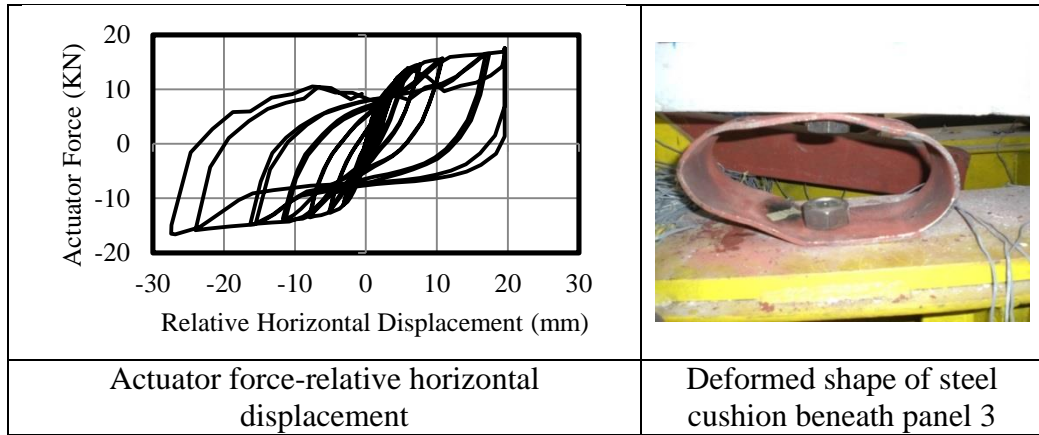


**Figure 4.127 :** Actuator force vs. relative horizontal displacement relation for steel cushions beneath panel 3 obtained from system test IV.

According to the strain history, yielding occurred at all three points, the first yielding occurred at 1.67% system drift angle. The location of first yielding is illustrated in Figure 4.128.

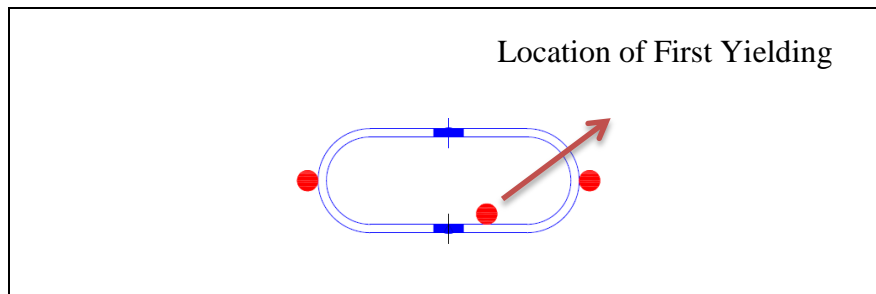


**Figure 4.128 :** Location of strain gauges on steel cushions in panel to support connection obtained from system test IV.

The relation between the actuator force and total relative displacement of steel cushions beneath panel 4 is presented in Figure 4.129. The maximum relative displacement is 26.05 mm at the actuator force of 17.59 KN, However as the transducer was installed at level of 20 cm from the panel base, the steel device horizontal displacement is smaller than this value. According to the deformed shape of steel cushion, besides the horizontal displacement the steel cushion rotated. In fact, this value of the horizontal displacement is formed by combination of the rotation of panel and horizontal displacement of steel cushions, although the rotation contribution in the horizontal displacement is more than steel cushions horizontal displacement. In addition, the behavior is asymmetric.

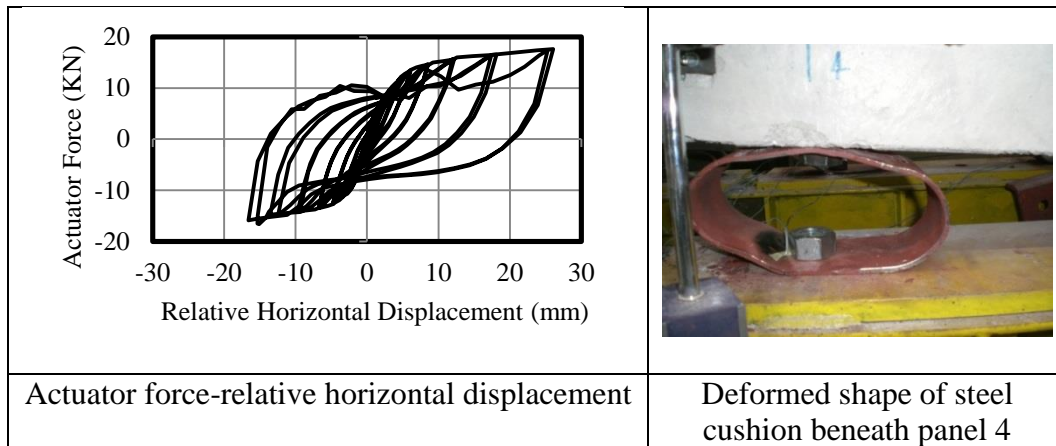


**Figure 4.129** : Actuator force vs. relative horizontal displacement relation for steel cushions beneath panel 4 obtained from system test IV.

According to the strain history, yielding occurred at all three points, the first yielding occurred at 1.67 % system drift angle. The location of first yielding was the specimen vertex point.

To investigate whether the Steel cushions beneath two symmetric panels, behaved symmetrically or not, actuator force-relative horizontal displacement relations for steel cushion beneath panel 1 and panel 4 are compared in Figure 4.130. According to Figure 4.130, panel 1 and panel 4 almost behaved symmetrically as a result the steel cushions below panel 1 and panel 4 represented almost symmetrical behaviors.

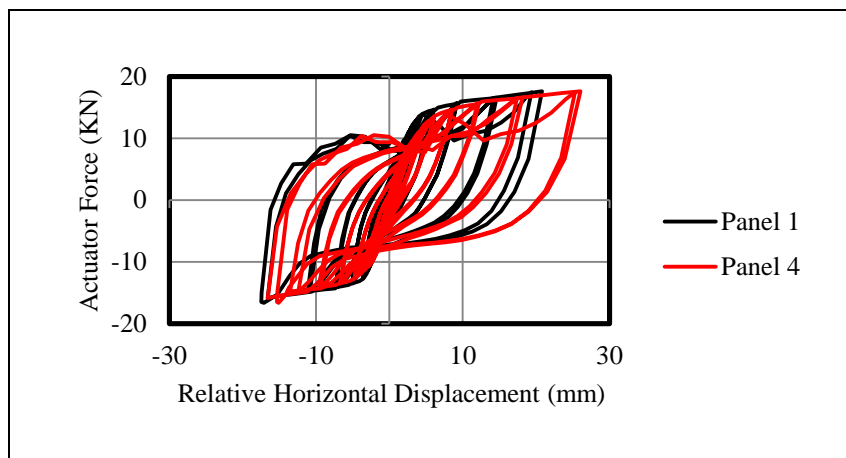


**Figure 4.130** : Comparison of actuator force-relative displacement relation for steel cushions beneath panel 1 and panel 4 obtained from system test IV.

Actuator force-relative horizontal displacement relations for steel cushion beneath panel 2 and panel 3 are compared at Figure 4.131. According to Figure 4.131, panel 2 and panel 3 nearly behaved symmetrically as a result the steel cushions below panel 2 and panel 3 represented almost symmetrical behaviors.

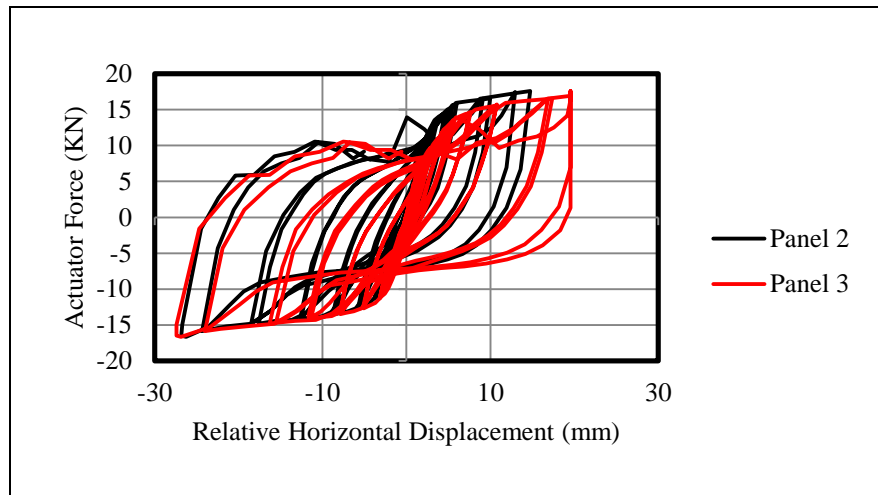


**Figure 4.131 :** Comparison of actuator force-relative displacement relation for steel cushions beneath panel 2 and panel 3 obtained from system test IV.

#### 4.7.1.7 Relative horizontal displacement of panel to beam steel cushions

To investigate the behavior of steel cushion in panel 1 to beam connection the relation of actuator force vs. relative displacement between panel 1 and beam is presented in Figure 4.132. The steel cushion is denoted by S1\*. The maximum relative displacement of between panel 1 and beam is 8.95 mm at the actuator force of 16.63 KN. According to the strain history relevant to this steel device yielding in not observed, which indicate the steel device horizontal displacement must be less than 100mm, while the relative displacement between panel1 and beam is 8.95 mm, so this is caused by the rotation of the panel and it does not represent the steel device real horizontal displacement.

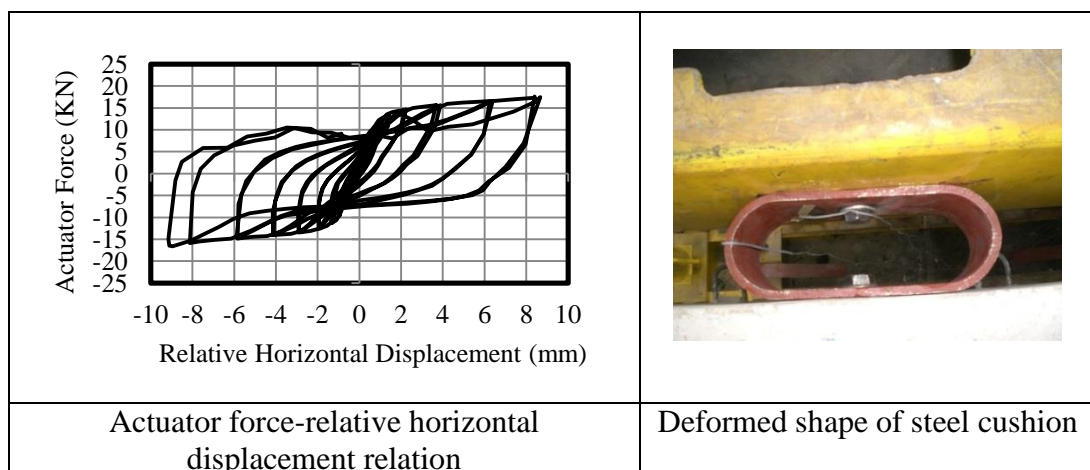


**Figure 4.132 :** Relation of the actuator force vs. relative displacement between panel 1 and beam obtained from system test IV.

The steel device in panel 2 to beam connection is denoted by S2\*. The relation of the actuator force vs. relative displacement between panel 2 and beam is presented in Figure 4.133. The maximum relative displacement between panel 2 and beam is 7.29 mm at the actuator force of 14.265 KN. According to the strain history relevant to this steel device yielding is not observed, which indicate the steel device horizontal displacement must be less than 100mm, while the relative displacement between panel1 and beam is 7.29 mm, so this is caused by the rotation of the panel and it does not represent the steel device real horizontal displacement.

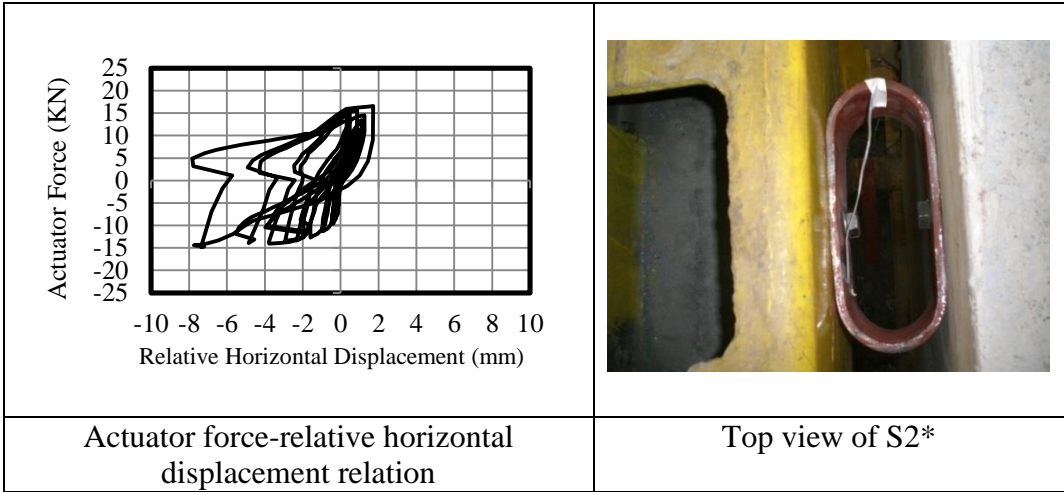


**Figure 4.133 :** Relation of the actuator force vs. relative displacement between panel 2 and beam obtained from system test IV.

The steel device in panel 3 to beam connection is denoted by S3\*. According to the Figure 4.134, S3\* horizontal displacement was so small. In fact the panel 3 rotated easily and S3\* acted such a hinge connection.

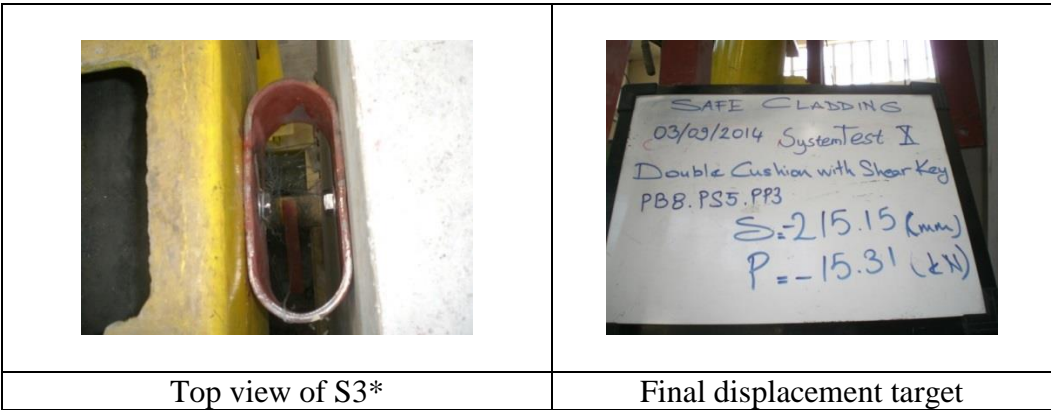


**Figure 4.134 :** Top view of S3\* at final displacement target obtained from system test IV.

The steel device in panel 4 to beam connection is denoted by S4\*. According to the Figure 4.135, S4\* horizontal displacement was so small. In fact the panel 3 rotated easily and S4\* acted such a hinge connection.

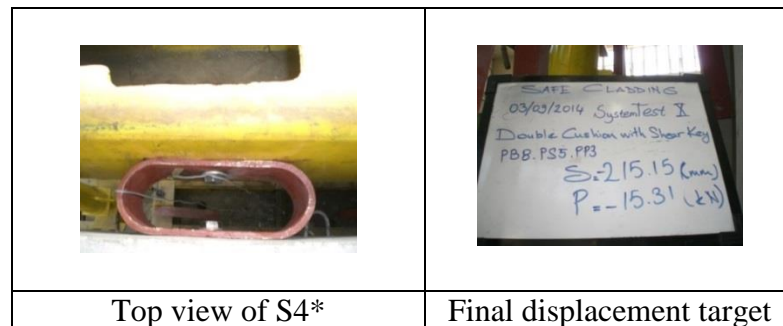


**Figure 4.135** : Top view of S4\* at final displacement target obtained from system test IV.

The locations of strain gauges on panel to beam steel cushions are illustrated in Figure 4.136.

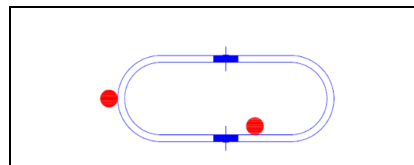


**Figure 4.136** : location of strain gauges on steel device in system test IV.

#### 4.7.1.8 Cladding panels rotation

The rotation of panel 3 and 4 in terms of step numbers are illustrated in Figure 4.137 and 4.138, respectively. The maximum rotation of panel 3 and panel 4 is 0.0984 rad and 0.0872 rad, respectively.

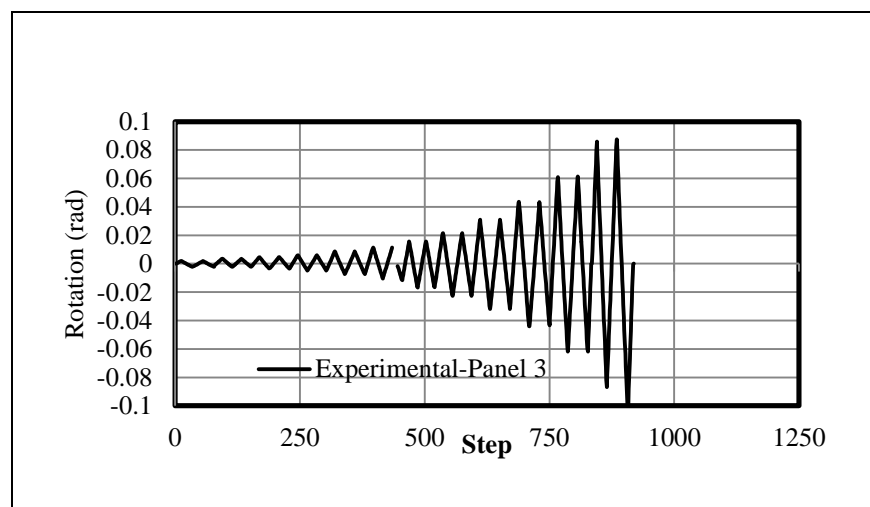


**Figure 4.137** : Rotation in terms of step numbers for panel 3.

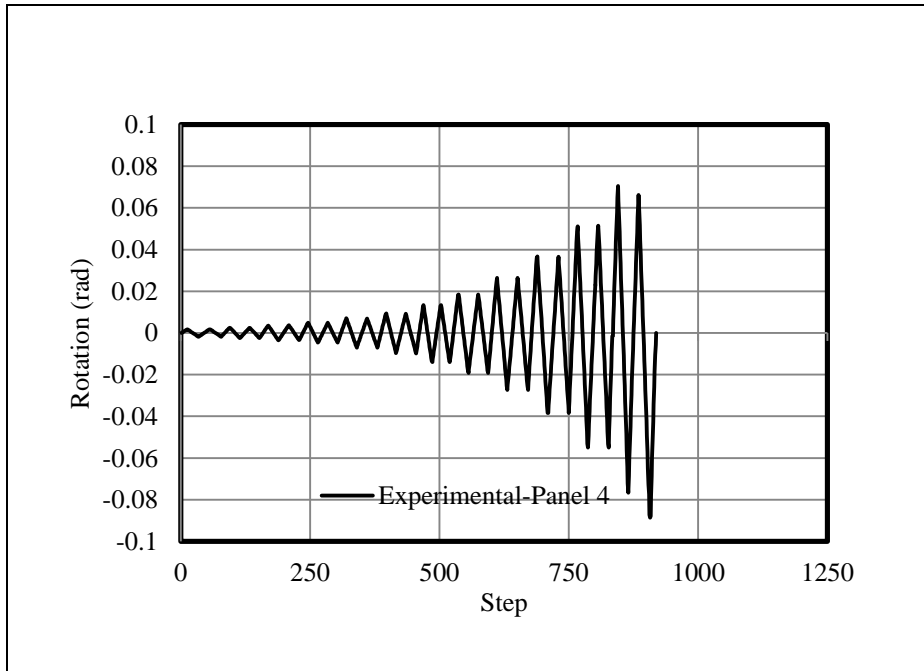


**Figure 4.138 :** Rotation in terms of step numbers for panel 4.

#### 4.7.1.9 Total behavior of panels

To examine the amount of out of plane displacement, the out of plane displacement of panel 3 and panel 4 vs. actuator displacement curves are presented in Figure 4.139 and 4.140. According to the Figure 4.136, the amount of out of plane displacement of panel 3 is small enough.

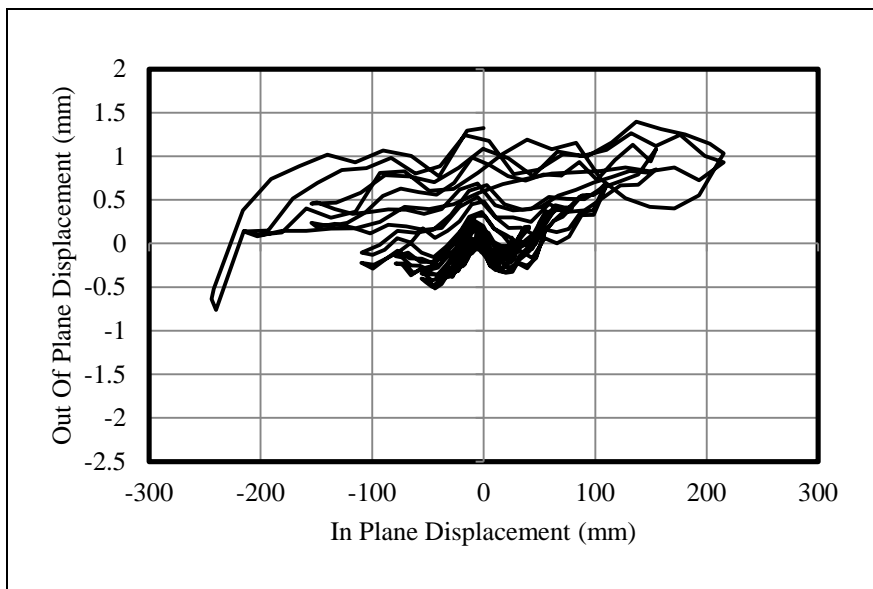


**Figure 4.139 :** Out of plane displacement of panel 3 in terms of in plane displacement obtained from system test IV.

According to Figure 4.140, the amount of out of plane displacement of panel 4 is small as well, however the out of plane displacement for panel 4 is higher than corresponding value for panel 3.

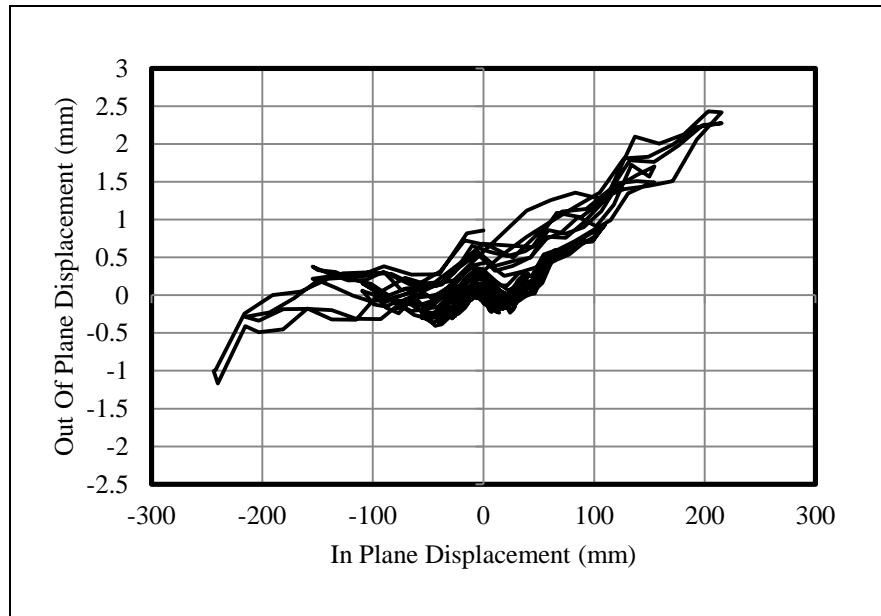


**Figure 4.140 :** Out of plane displacement of panel 4 in terms of in plane displacement obtained from system test IV.

In total the out of plane displacement of panels are minimal as a result the steel device in panel to beam connection were not subjected to significant tensile stress. Moreover any twisting of panels or steel cushions were not observed during the test. The deformed shapes of the steel cushions are shown in Figure 4.141.

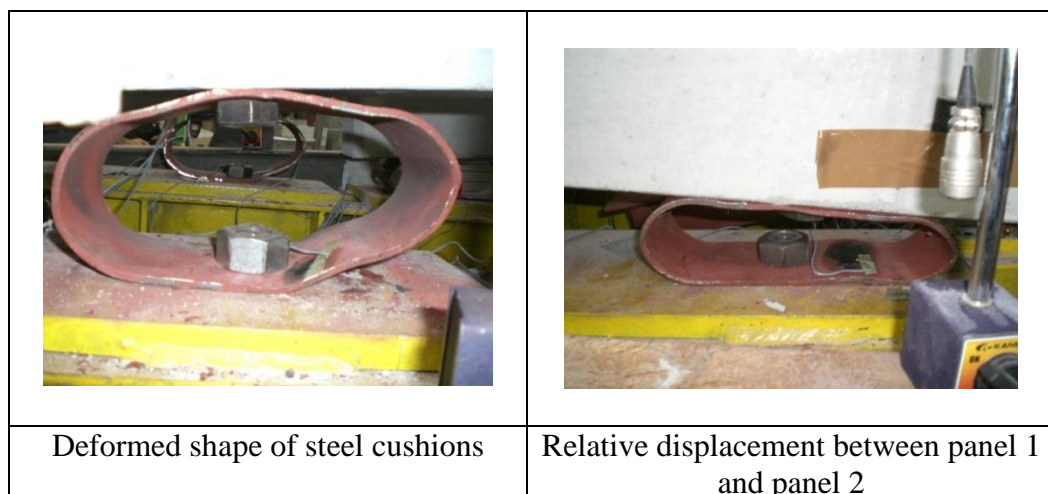


**Figure 4.141 :** Deformed shape of the steel cushions obtained from system test IV.

### 4.8 Comparison of System Tests Experimental Results

In this part, the experimental results of system tests are compared with each other.

#### 4.8.1 Comparison of system test I and II experimental results

The experimental results obtained from the system test I and II are compared, system test I is single cushion type and the system test II is double steel cushions type. In system test I 8mm thick cushions, 5mm thick cushions and 8mm thick, cushions were utilized in panel to support, panel to panel and panel to beam connections, respectively. In system, test II 3mm thick cushions, 5mm thick cushions and 8mm thick cushions were utilized in panel to support, panel to panel and panel to beam connections, respectively.

##### 4.8.1.1 Actuator force-top displacement relation

The actuator force vs. drift relation derived from two mentioned tests are compared in Figure 4.143. It is obvious from Figure 4.142, that the value of strength and the area enclosed by force–drift relation are approximately equal. The experimental results derived from the system test I and II are presented at Table 4.7.

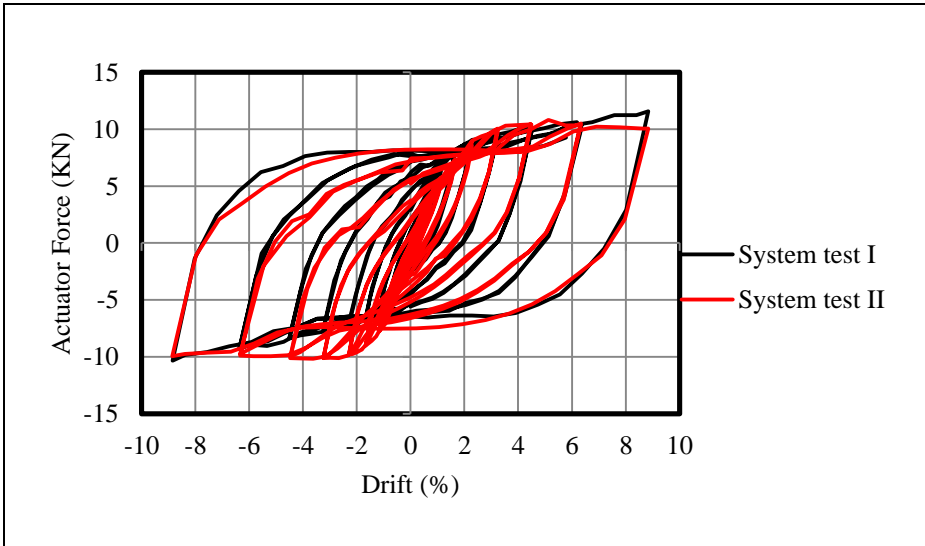


**Figure 4.142 :** Comparison of actuator force vs. drift relations of system test I and II.

**Table 4.7 :** Experimental results derived from system tests I and II.

System Test Number	Yielding Force (KN)	Max Force (KN)	Yielding Drift (%)
I	6.1	11.58	1.16
II	7.3	10.80	1.67

According to Table 4.7, the values of yielding force, maximum force and yielding drift derived from the system test I are nearly equal to the corresponding quantities derived for the system test II.

#### 4.8.1.2 Energy dissipation

According to Figure 4.143, cumulative energy capacities are very similar.

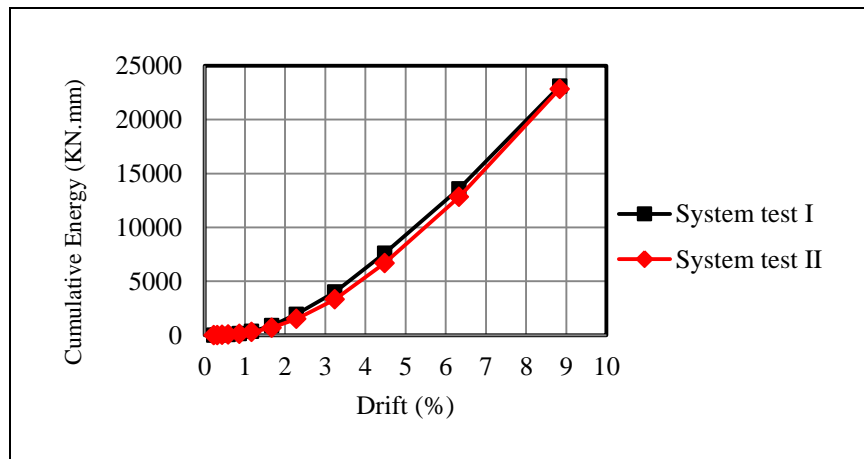


**Figure 4.143 :** Comparison of energy dissipation capacity in terms of drift for system test I and II.

#### 4.8.1.3 Equivalent viscous damping

The equivalent damping ratios are compared in Figure 4.144. The damping ratio derived from the system test II is higher than the corresponding value derived from system test I. In other word the maximum equivalent damping ratio increases from 30.48% to 37.39% by utilizing a pair of 3mm thick cushions at the base panels rather than utilizing single 8mm thick cushion at the base of panels. The increment is about 22.67 %.

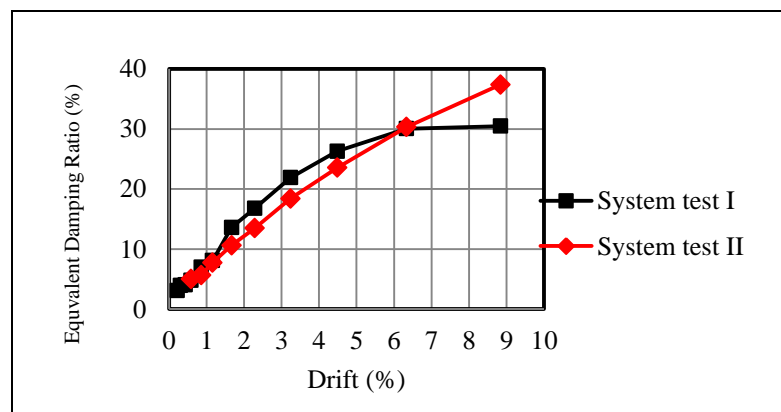


**Figure 4.144 :** Comparison of equivalent damping ratios in terms of drift for system test I and II.

**4.8.1.4 Effective (secant) stiffness**

The initial stiffness values are 0.33 and 0.31 KN/mm for system test II and I respectively. Thus, the values of effective stiffness are approximately equal. The reduction of effective stiffness is 84% and 86% in system test I and II, respectively according to Figure 4.145.

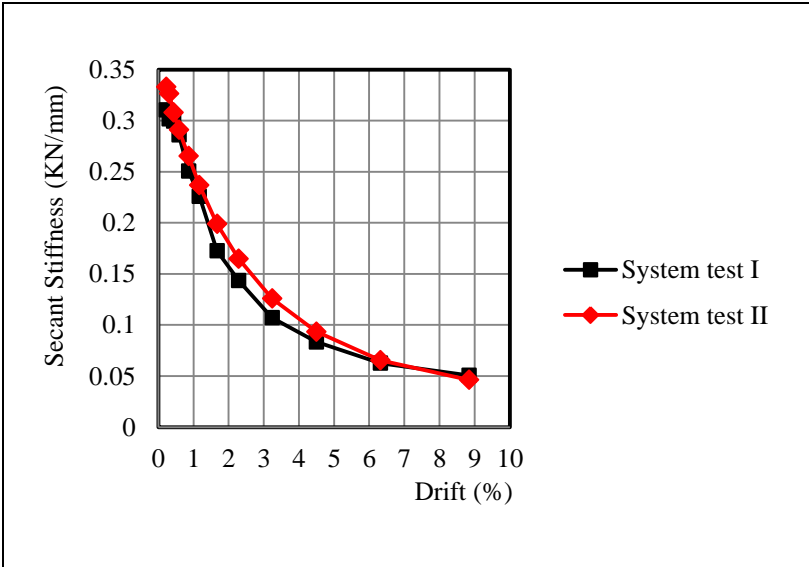


**Figure 4.145 :** Comparison of secant stiffness in terms of drift for of system test I and II.

The rate of stiffness decaying for two system tests is identical and independent arrangement of steel devices and thickness according to the Figure 4.146.

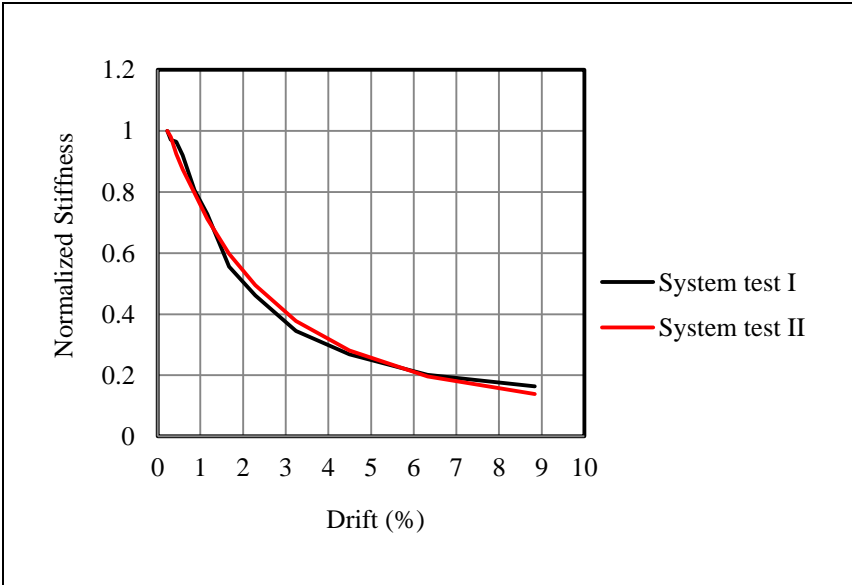


**Figure 4.146 :** Comparison of normalized stiffness in terms of drift for system test I and II.

#### 4.8.1.5 Relative vertical displacement of panel to panel steel cushions

Maximum relative vertical displacements in panel-to-panel elements are 90.26 mm in system test I and 82.54 mm in system test II. Figure 4.147 represents the comparison of S12 elements in system tests II and I.

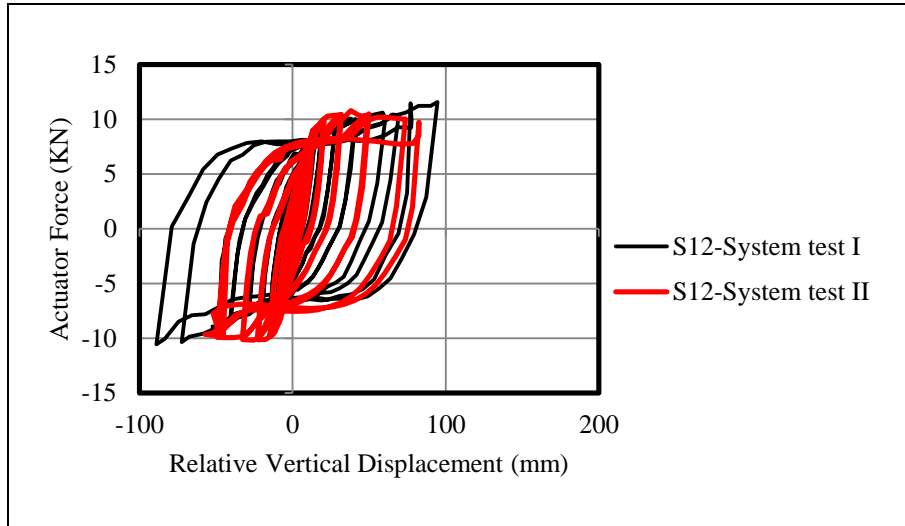


**Figure 4.147 :** Comparison of relative vertical displacements in S12 elements in system test I and II.

#### 4.8.1.6 Relative horizontal displacement of panel to support steel cushions

Maximum relative horizontal displacements in panel to support elements are 11.88 mm and 43.06 mm in system test II and I, respectively. However, they are formed by combination of panel rotation and horizontal displacement of steel cushions. The maximum horizontal displacement of panel to support connection for two-mentioned system tests are compared in Figure 4.148.

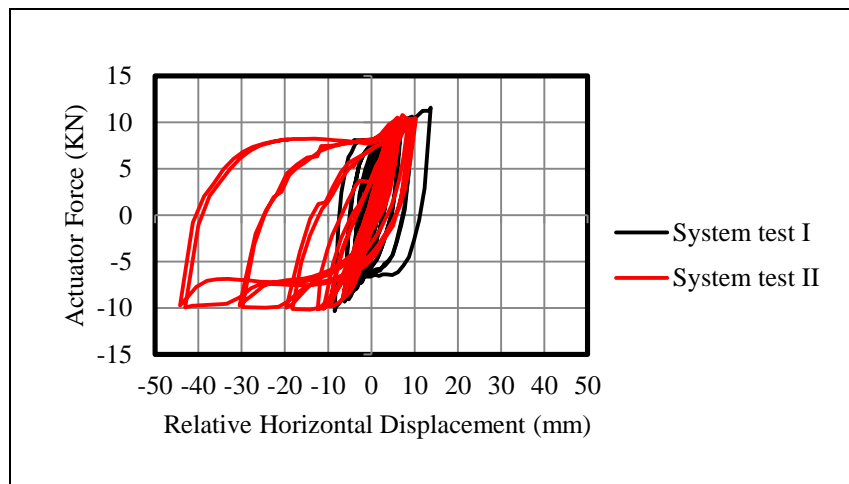


**Figure 4.148 :** Comparison of relative horizontal displacements in panel to support steel devices in system test I and II.

#### 4.8.1.7 Maximum rotation of cladding panels

The maximum rotation of panels obtained from system test I and II are presented and compared in Table 4.8. According to Table 4.8 the maximum rotation of panels in the system test, I and II are almost equaled.

**Table 4.8 :** Maximum rotation of panels obtained from system test I and II.

System Test	Maximum Rotation (rad)
I	0.0872
II	0.0839

#### 4.8.2 Comparison of system test I and III experimental results

The experimental results obtained from the system test I and III are compared. The system test I is single cushion type and the system test III is double steel cushions type. In the system test I 8mm thick cushions, 5mm thick cushions and 8mm thick cushions were utilized in panel to support, panel to panel and panel to beam connections, respectively. In system test III, 5mm thick cushions, 5mm thick cushions and 8mm thick cushions were utilized in panel to support, panel to panel and panel to beam connections, respectively.

##### 4.8.2.1 Actuator force-top displacement relation

The actuator force vs. drift relation derived from two mentioned tests are compared in Figure 4.149. It is obvious from Figure 4.149 that the value of strength and the area enclosed by force–drift relation in the system test III are bigger than corresponding parameters in the system test I. The experimental results derived from the system test I and III are presented at Table 4.9.

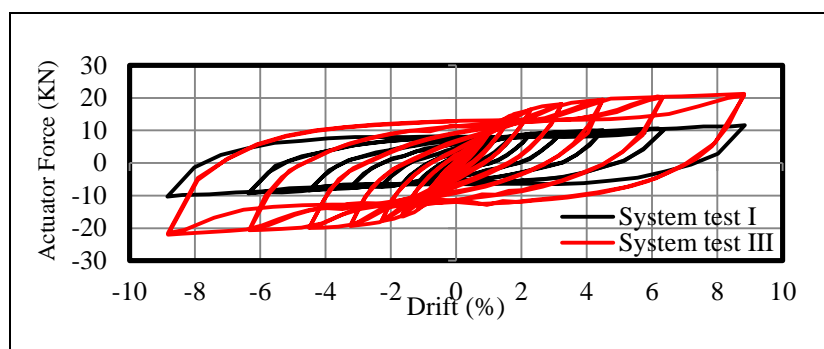


**Figure 4.149 :** Comparison of actuator force vs. drift relations of system test I and II.

**Table 4.9 :** Experimental results derived from system tests I and III.

System Test Number	Yielding Force (KN)	Max Force (KN)	Yielding Drift (%)
I	6.1	11.58	1.16
III	16.4	21.07	2.28

According to Table 4.9, the values of yielding force, maximum force and yielding drift derived from the system test III are more than the corresponding quantities derived from the system test I.

#### 4.8.2.2 Energy dissipation

According to Figure 4.150 cumulative energy capacity increases from 23102 KN.mm in system test I to 40131 KN.mm in system test III with increment of 73%.

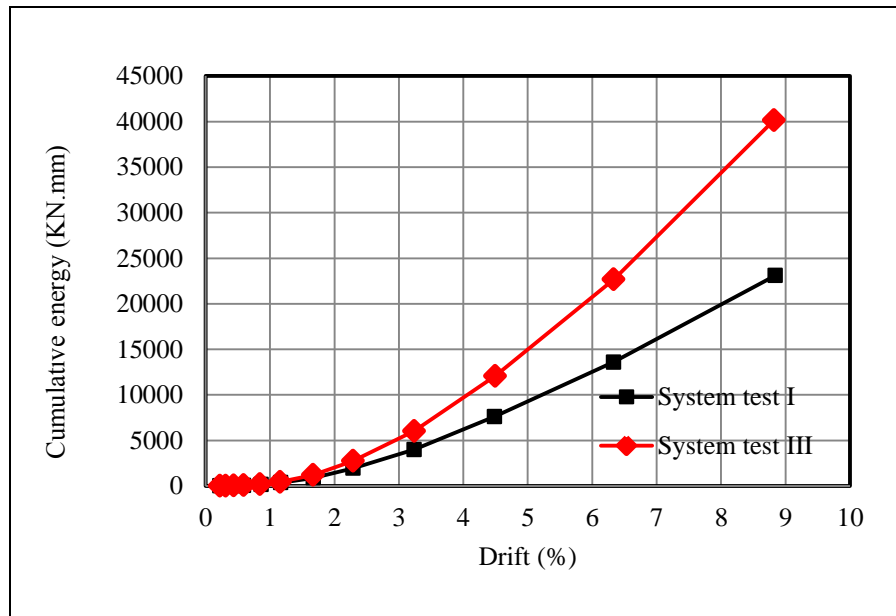


**Figure 4.150 :** Comparison of energy dissipation capacity in terms of drift for system test I and III.

#### 4.8.2.3 Equivalent Viscous Damping

The equivalent damping ratios are compared in Figure 4.151. The maximum damping ratio derived from the system test I is equaled with the corresponding value derived from system test III.

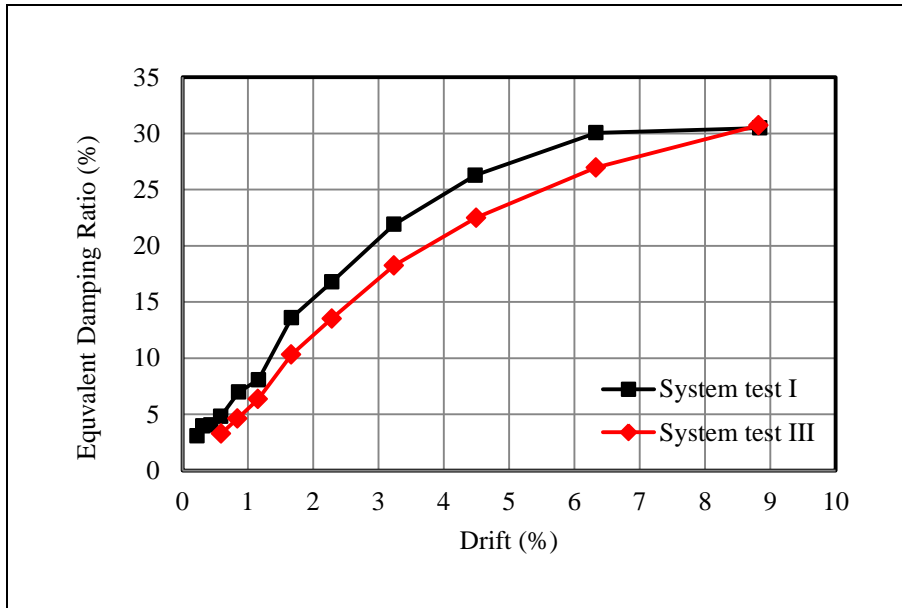


**Figure 4.151 :** Comparison of equivalent damping ratios in terms of drift for system test I and III.

#### 4.8.2.4 Effective (secant) stiffness

The initial stiffness values are 0.63 and 0.31 KN/mm for system test III and I respectively. The reduction of effective stiffness is 84% for both specimens as shown in Figure 4.152.

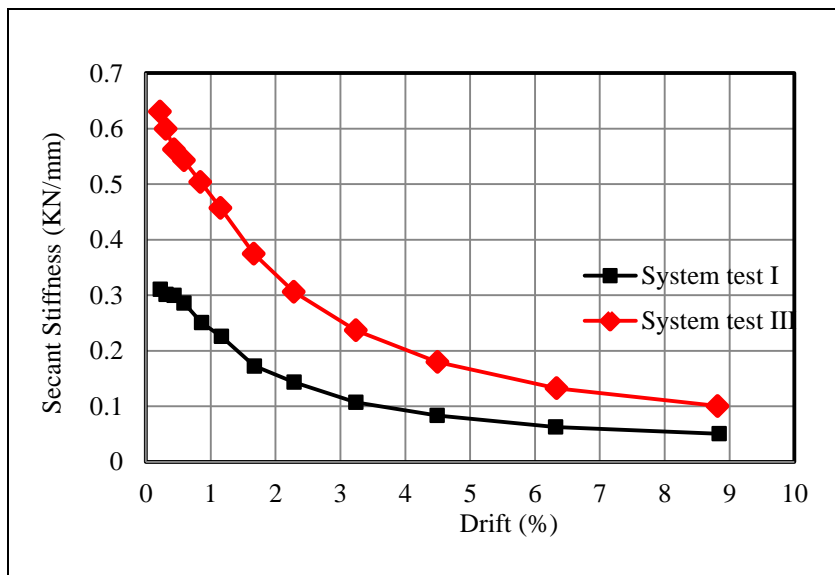


**Figure 4.152 :** Comparison of secant stiffness in terms of drift for of system test I and III.

The rate of stiffness reduction for two specimens is identical and independent from the arrangement of steel devices and thickness according to the Figure 4.153.

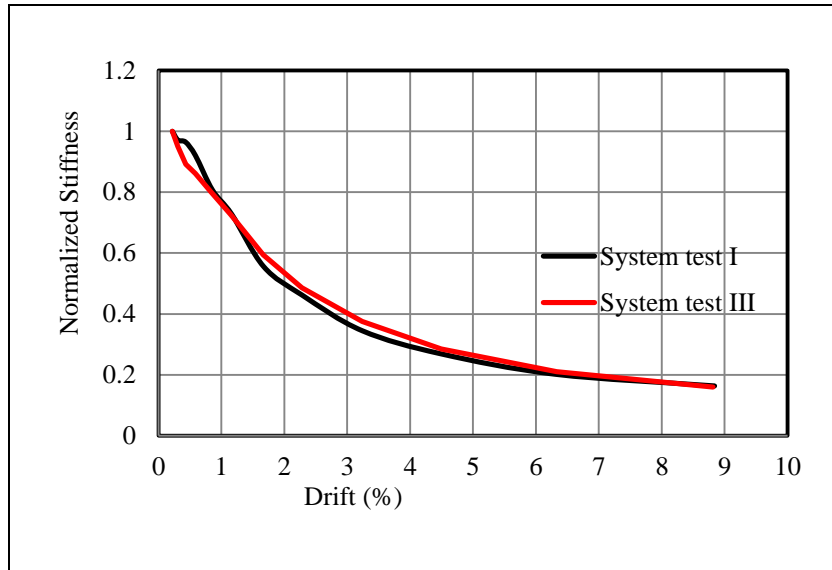


**Figure 4.153** : Comparison of normalized stiffness in terms of drift for system test I and III.

#### 4.8.2.5 Relative vertical displacement of panel to panel steel cushions

Maximum relative vertical displacements in panel-to-panel elements are 90.26 mm in system test I and 79.6 mm in system test II. Figure 4.154 represents the comparison of steel cushions relative displacement in panel-to-panel connections in system tests III and I.

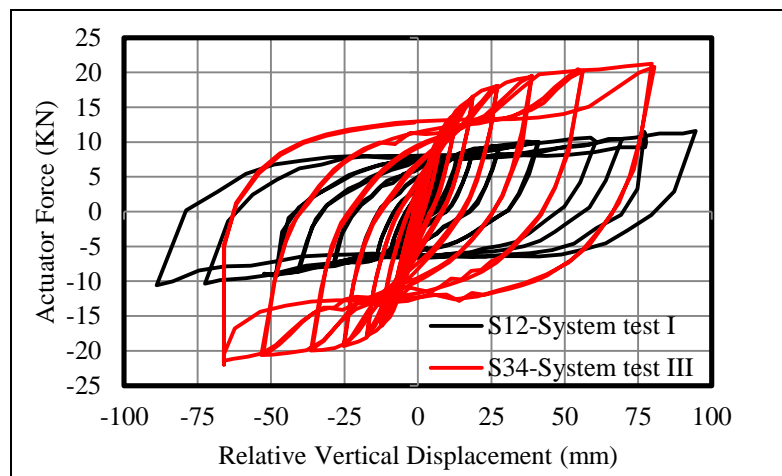


**Figure 4.154** : Comparison of relative vertical displacements in the steel cushions in panel-to-panel connection in system test I and III.

#### 4.8.2.6 Relative horizontal displacement of panel to support steel cushions

Maximum relative horizontal displacements in panel to support elements are 11.88 mm and 31.2 mm in system test III and I, respectively. These quantities are formed by combination of panel rotation and horizontal displacement of steel cushions. The

maximum horizontal displacement of panel to support connection for two-mentioned system tests are compared in Figure 4.155.

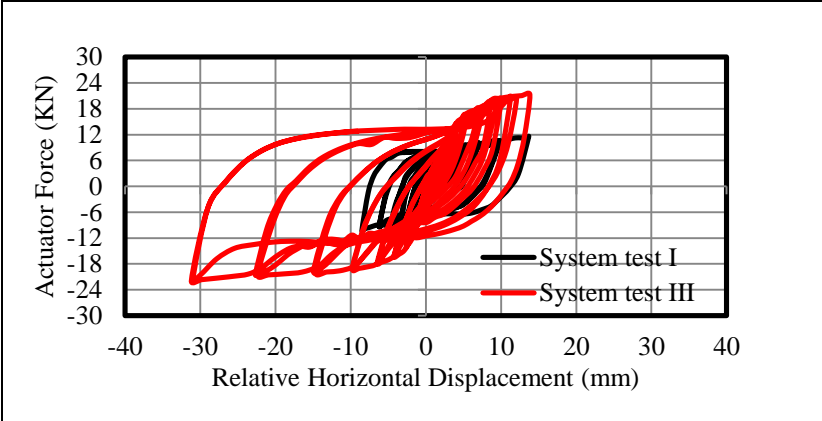


**Figure 4.155 :** Comparison of relative horizontal displacements in panel to support steel devices in system test I and III.

**4.8.2.7 Maximum rotation of cladding panels**

The maximum rotation of panels obtained from system test I and III are presented and compared in Table 4.10. According to Table 4.10 the maximum rotation of panels in the system test, I and III are almost equaled.

**Table 4.10 :** Maximum rotation of panels obtained from system test I and III.

System Test	Maximum Rotation (rad)
I	0.0872
III	0.0831

**4.8.3 Comparison of system test II and III experimental results**

The experimental results obtained from the system test II and III are compared. System test II and III are double steel cushions type specimens. The unique difference is the panel to support steel cushions thickness. In the system test II, the panels to support cushions had 3mm thickness, whereas the corresponding steel devices thickness were 5mm in system test III.

**4.8.3.1 Actuator force-top displacement relation**

The actuator force vs. drift relation derived from two mentioned tests are compared in Figure 4.156. It is obvious from Figure 4.156 that the value of strength and the area enclosed by force–drift relation increase using the thicker steel devices at the

base of each panel. The experimental results derived from the system test II and III are presented at Table 4.11.

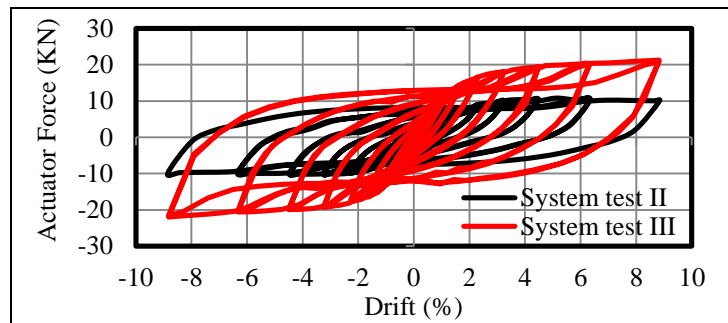


**Figure 4.156 :** Comparison of actuator force vs. drift relations of system test II and III.

**Table 4.11 :** Experimental results derived from system tests II and III.

System Test Number	Yielding Force (KN)	Max Force (KN)	Yielding Drift (%)
II	7.27	10.80	1.67
III	16.40	21.07	2.28

According to Table 4.11, the values of yielding force, maximum force and yielding drift derived from the system test III are higher than corresponding quantities derived from the system test II because of the existence of 5mm thick steel cushions in panel to support connections.

#### 4.8.3.2 Energy dissipation

According to Figure 4.157, cumulative energy capacity increases from 22846 KN.mm in system test II to 40131 KN.mm in system test III, with an increment of 50%.

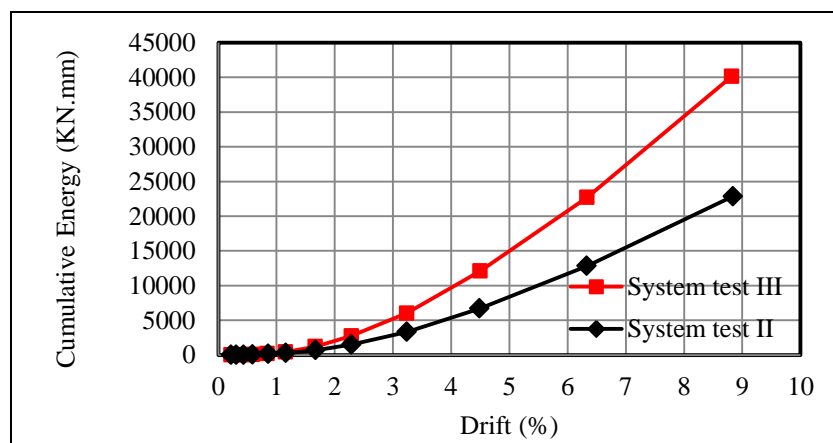


**Figure 4.157 :** Comparison of energy dissipation capacity in terms of drift for system test II and III.

**4.8.3.3 Equivalent viscous damping**

The equivalent damping ratios are compared in Figure 4.158. The maximum damping ratio derived from the system test II is higher than the corresponding value derived from system test III. In other word, the maximum equivalent damping ratio increases from 30.71% to 37.39% by utilizing the 3mm thick cushions at the base level rather than 5mm thick ones, the increment is about 21.75 %.

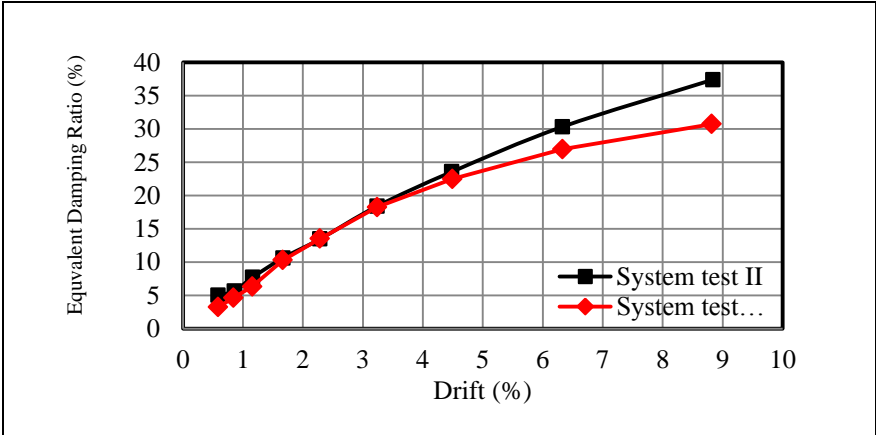


**Figure 4.158 :** Comparison of equivalent damping ratios in terms of drift for system test II and III.

**4.8.3.4 Effective (secant) stiffness**

The initial stiffness values are 0.63 and 0.33 KN/mm for system test III and II, respectively. The values of effective stiffness are higher in system test III than the corresponding quantities in system test II. The reduction of effective stiffness is 84% in system test III, whereas the stiffness reduction is 86% in system test II according to Figure 4.159.

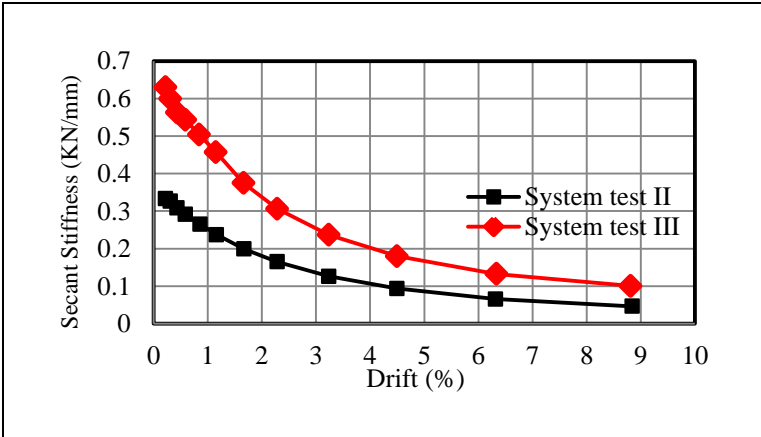


**Figure 4.159 :** Comparison of secant stiffness in terms of drift for of system test II and III.

The rate of stiffness reduction for two systems is identical and independent from the thickness of the cushions used at the base level according to Figure 4.160.

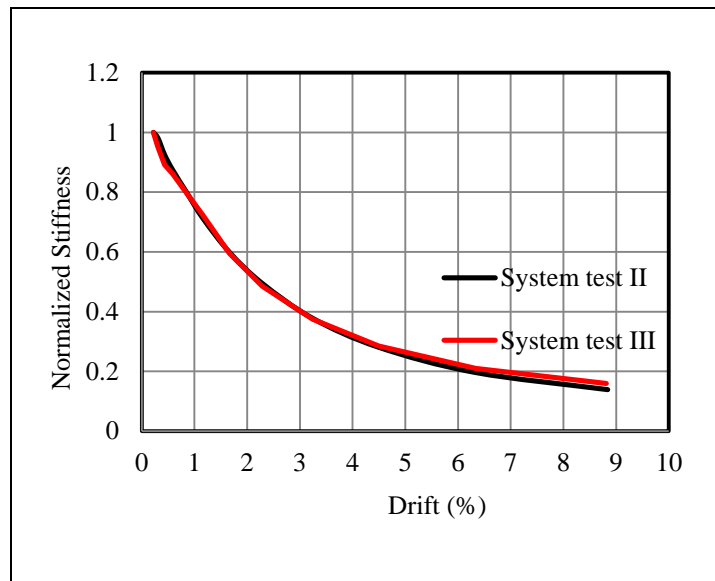


**Figure 4.160 :** Comparison of normalized stiffness in terms of drift for system test II and III.

#### 4.8.3.5 Relative vertical displacement of panel to panel steel cushions

Maximum relative vertical displacements in panel-to-panel connections are 78.78 mm in system test II and 75.34 mm in system test III. They are almost equal. Figure 4.161 represents the comparison of S34 in system tests II and III.

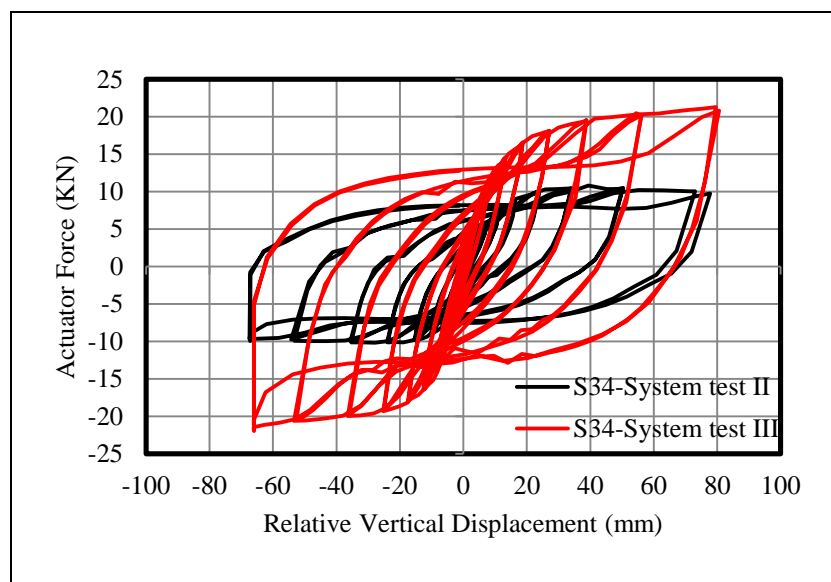


**Figure 4.161 :** Comparison of relative vertical displacements in S34 elements in system test II and III.

**4.8.3.6 Relative horizontal displacement of panel to support steel cushions**

Maximum relative horizontal displacements in panel to support elements are 43.06 mm and 31.2 mm in system test II and III, respectively. They are formed by combination of panel rotation and horizontal displacement of steel cushions. The maximum relative horizontal displacements of panel to support connections are compared in Figure 4.162.

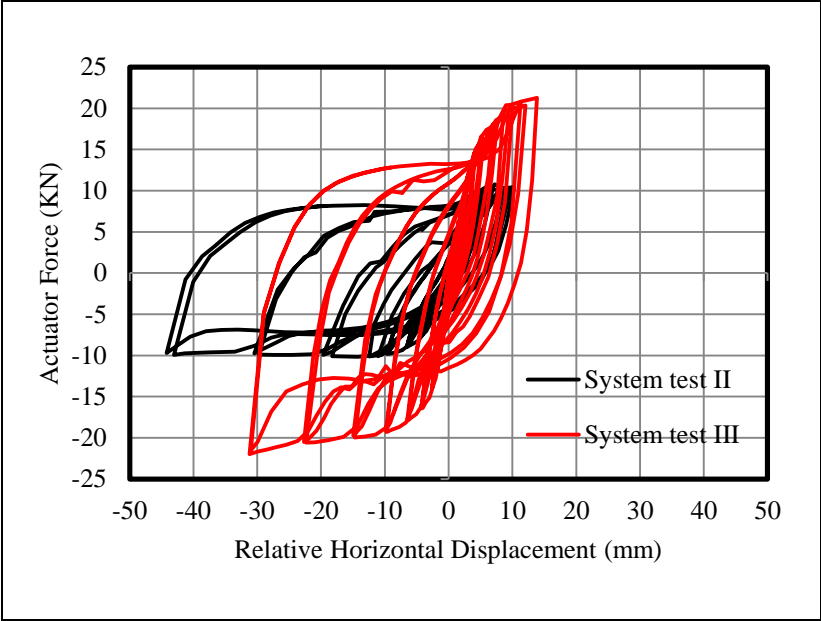


**Figure 4.162 :** Comparison of relative horizontal displacements in panel to support steel devices in system test II and III.

**4.8.3.7 Maximum rotation of cladding panels**

The maximum rotation of panels obtained from system test II and III are presented and compared in Table 4.12. According to Table 4.12 the maximum rotation of panels in the system test, II and III are almost equal.

**Table 4.12 :** Maximum rotation of panels obtained from system test II and III.

System Test	Maximum Rotation (rad)
II	0.0839
III	0.0831

**4.8.4 Comparison of system test III and IV experimental results**

The experimental results obtained from the system test III and IV are compared here. System test III and IV are double steel cushions type. The unique difference is the

panel-to-panel steel cushions thickness. In the system test III, the panel-to-panel steel cushions had a thickness of 5mm whereas the corresponding steel cushions thickness, are 3 mm in system test IV.

#### 4.8.4.1 Actuator force-top displacement relation

The actuator force vs. drift relation derived from two mentioned tests are compared in Figure 4.163. It is obvious from the Figure 4.163, that the value of strength and the area enclosed by force–drift relation increase using the thicker steel cushions in the panel-to-panel connection. The experimental results derived from the system test III and IV are presented at Table 4.13.

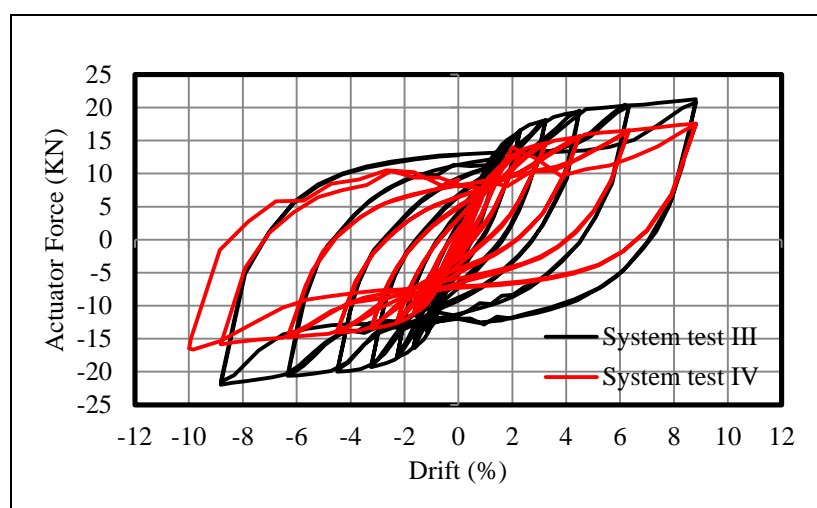


**Figure 4.163 :** Comparison of actuator force vs. drift relations of system test III and IV.

**Table 4.13 :** Experimental results derived from system tests III and IV.

System Test Number	Yielding Force (KN)	Max Force (KN)	Yielding Drift (%)
III	16.40	21.07	2.28
IV	11.60	17.59	1.67

According to Table 4.13, the values of yielding force, maximum force and yielding drift derived from the system test III are higher than the corresponding quantities derived from the system test IV because of the existence of 5mm thick steel cushions in panel-to-panel connections.

#### 4.8.4.2 Energy dissipation

According to Figure 4.164, cumulative energy capacity increases from 27119 in system test IV to 40131 KN.mm in system test III with an increment of 48%.

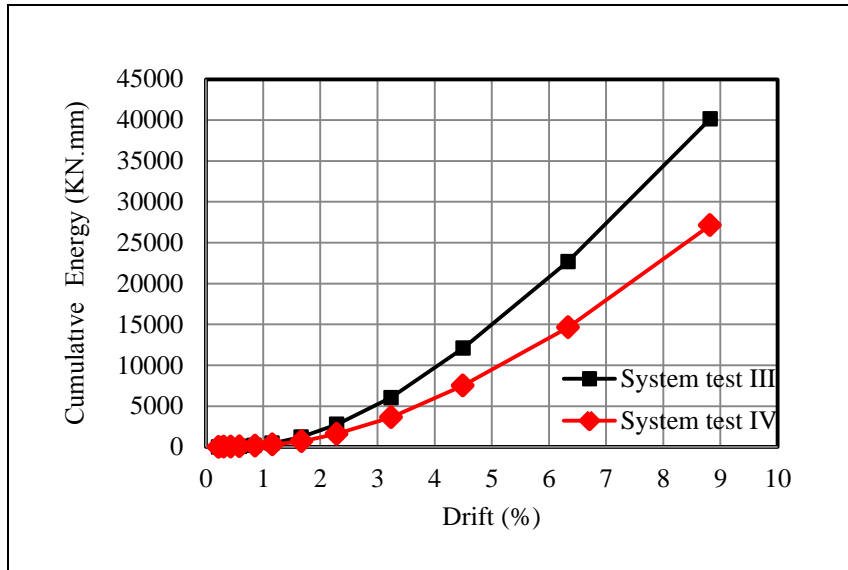


**Figure 4.164 :** Comparison of energy dissipation capacity in terms of drift for system test III and IV.

#### 4.8.4.3 Equivalent viscous damping

The equivalent damping ratios are compared in Figure 4.165. The maximum damping ratio derived from the system test III is higher than the corresponding value derived from system test IV. In other word, the maximum equivalent damping ratio increases from 26.42% to 30.71% by utilizing 5mm thick cushions in panel to panel connections rather than 3mm thick ones, the increment is 16.24 %.

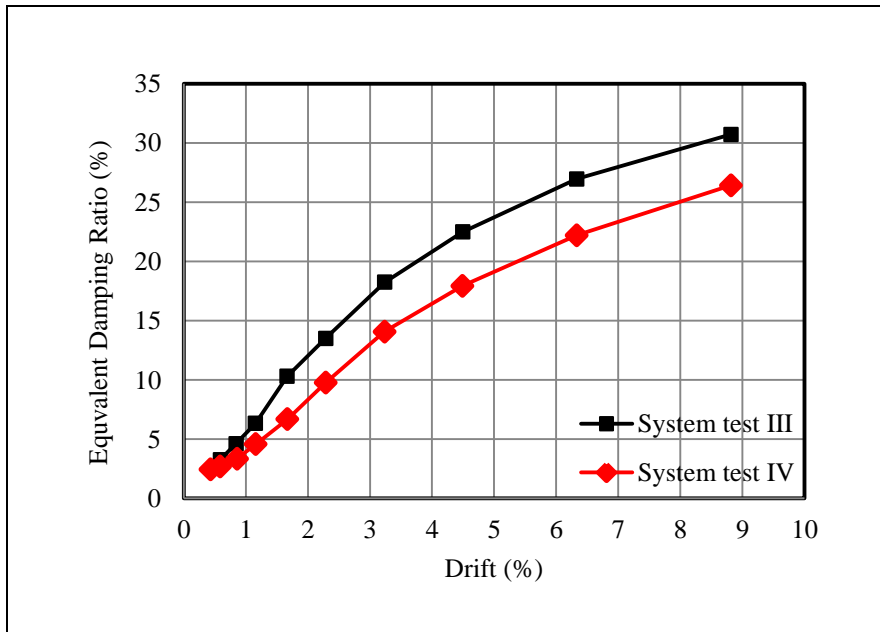


**Figure 4.165 :** Comparison of equivalent damping ratios in terms of drift for system test III and IV.

#### 4.8.4.4 Effective (secant) stiffness

The initial stiffness values are 0.63 and 0.45 KN/mm for system test III and IV, respectively. The values of effective stiffness are higher in system test III than the corresponding quantities in system test IV. The reduction of effective stiffness is 84% in system test III whereas the stiffness reduction is 83% in system test IV according to Figure 4.166.

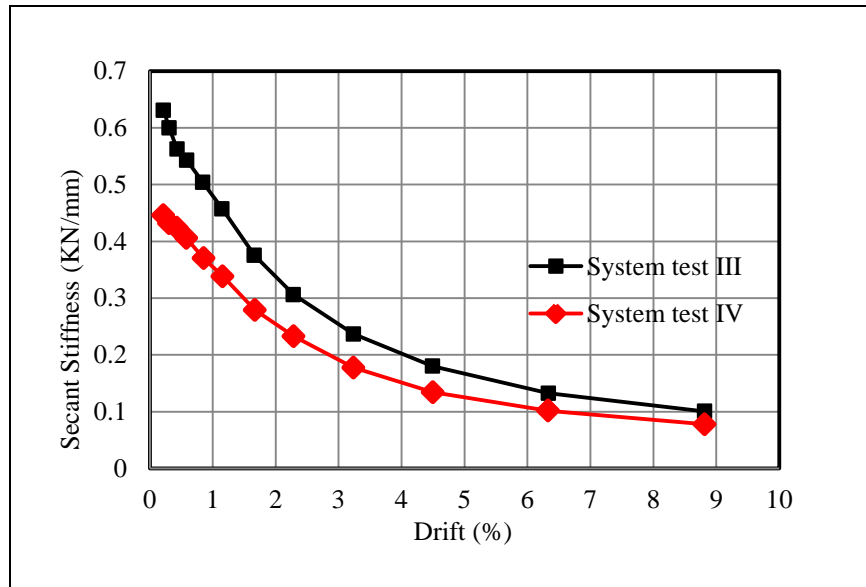


**Figure 4.166 :** Comparison of secant stiffness in terms of drift for of system test III and IV.

The rate of stiffness reduction for two system tests is identical and independent from the steel cushions thickness used at the base level according the Figure 4.167.

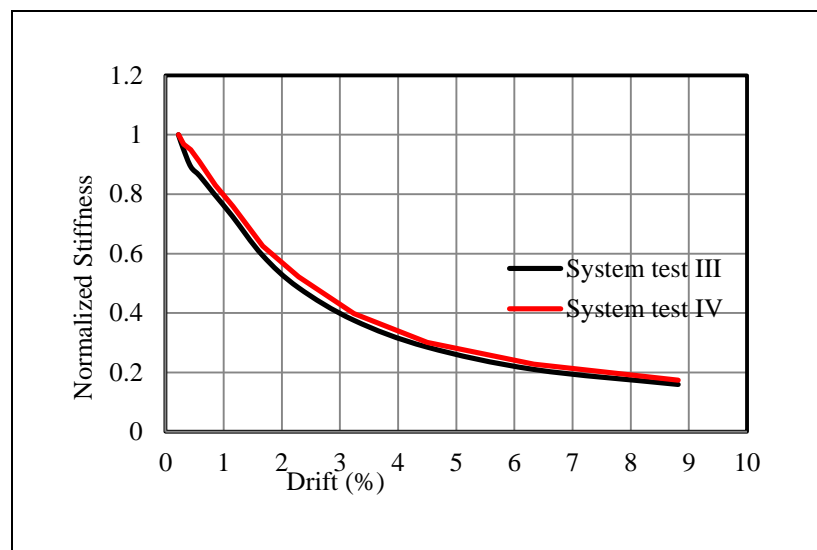


**Figure 4.167 :** Comparison of normalized stiffness in terms of drift for system test III and IV.

**4.8.4.5 Relative vertical displacement of panel to panel steel cushions**

Maximum relative vertical displacements in panel-to-panel elements are 75.34 mm in system test III and 83.3 mm in system test IV. Figure 4.168 represents the comparison of relative vertical displacement in system tests II and III.

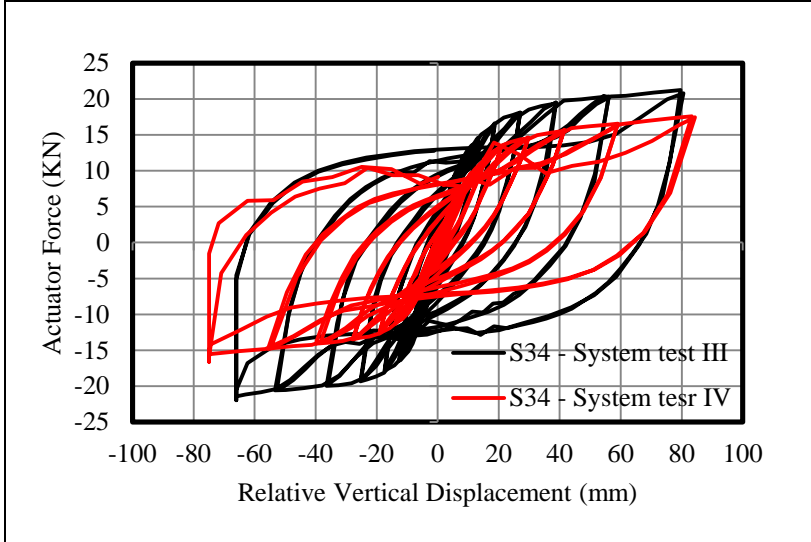


**Figure 4.168 :** Comparison of relative vertical displacements in S34 elements in system test III and IV.

**4.8.4.6 Relative horizontal displacement of panel to support steel cushions**

Maximum relative horizontal displacements in panel to support elements are 31.02 mm and 26.25 mm in system test III and IV respectively. The maximum relative horizontal displacements of panel-to-panel connections are compared in Figure 4.169.

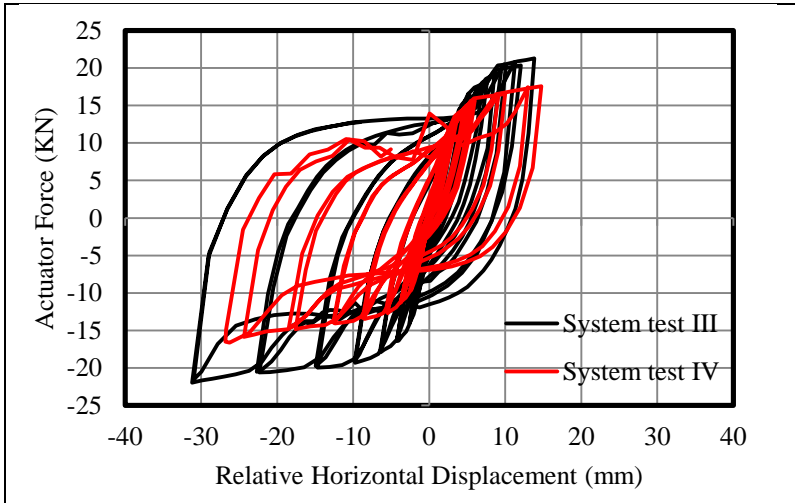


**Figure 4.169 :** Comparison of relative horizontal displacements in panel to support steel devices in system test III and IV.

#### 4.8.4.7 Maximum rotation of cladding panels

The maximum rotation of panels obtained from system test III and IV are presented and compared in Table 4.14. According to Table 4.14 the maximum rotation of panels in the system test IV is higher than the corresponding value in system test III.

**Table 4.14 :** Maximum rotation of panels obtained from system test III and IV

System Test	Maximum Rotation (rad)
III	0.0831
IV	0.0984



## 5. ANALYTICAL STUDY OF CONCRETE CLADDING PANELS EQUIPPED WITH ENERGY DISSIPATIVE STEEL CUSHIONS

### 5.1 Introduction

This chapter is divided into two sections. In the first section, the steel cushions are modeled by link element in the SeismoStruct program v 6.0, and two response curves are suggested for modeling of axial and shear behavior of steel cushions. In the second part, the concrete cladding panels equipped with steel cushions are modeled in the program and analytical and experimental results are compared. Force-displacement relations for panel to panel and panel to support steel devices are obtained from the analytical study leading to calculation of each steel cushion contribution in the energy dissipation capacity.

### 5.2 SeismoStruct Program Version 6.0

In the analytical study, the SeismoStruct program v 6.0 was used. SeismoStruct program is a finite element program is able to analyze three and two-dimensional structures under static and dynamic effects with consideration of the geometric and material nonlinearities. The program contains three main modulus: Pre-Processor in which the user define the analytical model and assign the loads and structural properties. Processor, in which the analysis is run and Post- Processor in which the user is able to gain the analysis results, the structure of the software is illustrated in Figure 5.1.

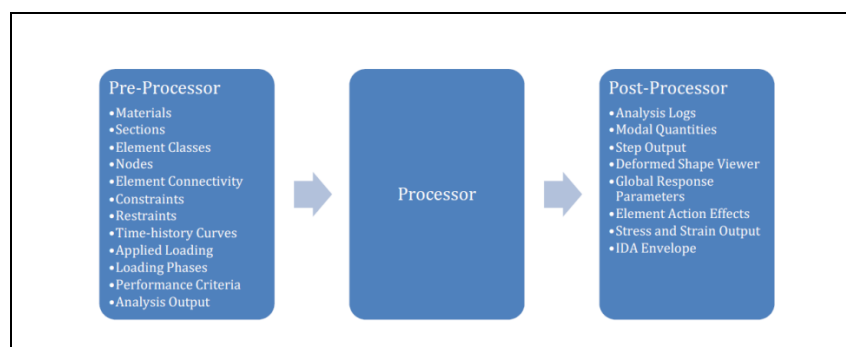


**Figure 5.1 :** Structure of software, (SeismoStruct v 6.0 user manual, 2012).

### 5.3 Response Curve for Modeling Shear and Axial Behaviors of Steel Cushions

The steel cushions are modeled by link element in the SeismoStruct program v 6.0, and two response curves are suggested for modeling of axial and shear behavior of steel cushions. In this section the suggested response curves are described.

#### 5.3.1 Response curve for modeling shear behavior of steel cushions

At the first stage, the steel cushions are modeled analytically under the shear effects. The steel specimens are modeled with the link element with Ramberg- Osgood response curve, the curve is shown in Figure 5.2. Four parameters are required to define Ramberg-Osgood curve as illustrated in Figure 5.3.

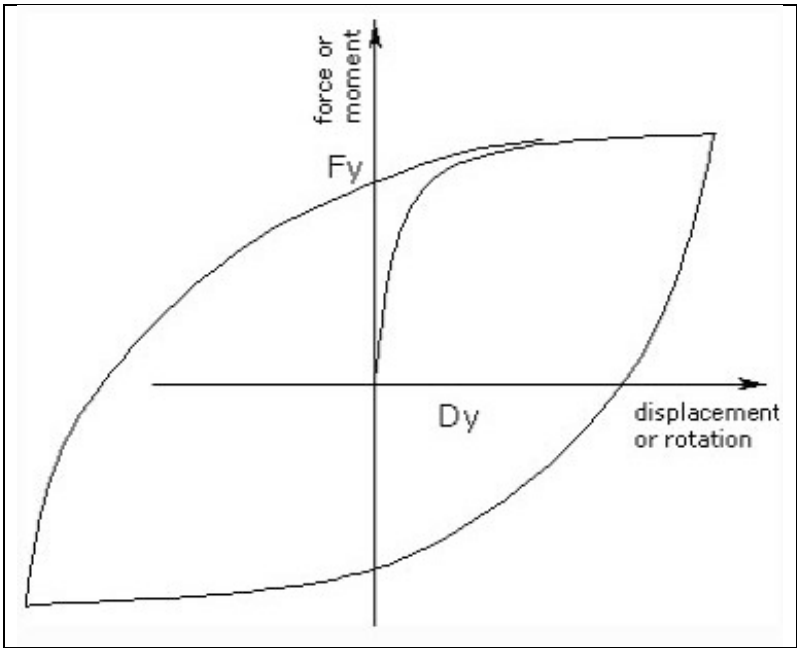


**Figure 5.2 :** Ramberg-Osgood curve, (SeismoStruct v 6.0 user manual, 2012).

Curve Properties	Typical values	Default values
Yield strength - $F_y$	-	500 (-)
Yield displacement - $D_y$	-	0.0025 (-)
Ramberg-Osgood parameter - $\gamma$	-	1.5 (-)
Convergence limit for the Newton-Raphson procedure - $\beta_1$	-	0.001 (-)

**Figure 5.3 :** Required parameters for definition of Ramberg-Osgood curve, (SeismoStruct v 6.0 user manual, 2012).

The values of yield force and yield displacement are obtained experimentally. Ramberg-Osgood parameter is denoted by  $\gamma$  the loading curve may vary from linear elastic line for  $\gamma=1.0$ , to an elasto-plastic bilinear segment for  $\gamma=$  infinity, SeismoStruct v 6.0. Ramberg-Osgood is obtained by comparing the experimental and analytical results and the default value is considered for  $\beta_1$  parameter.

For definition of the link element, it is necessary to define two structural nodes with the identical coordinates and one non-structural nod for determination of local axis directions. In addition, each link element has the six degree of freedoms in which depending on the boundary and supporting condition the appropriate behavior is assigned as shown in the Figure 5.4.

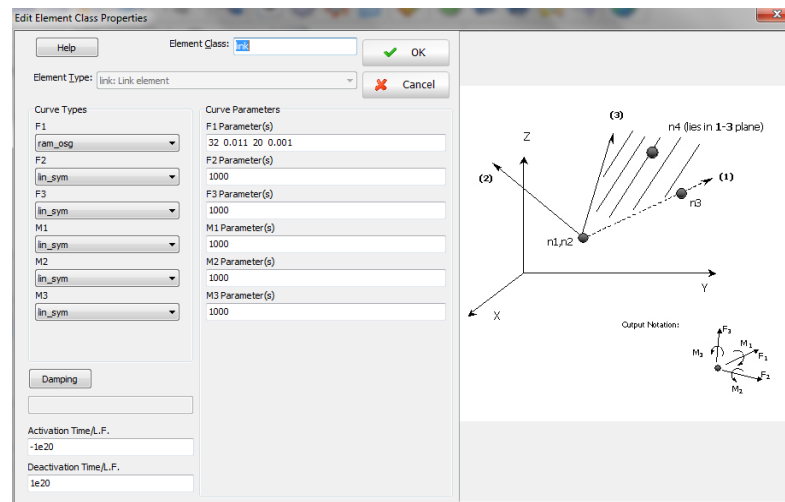


**Figure 5.4 :** Degree of freedoms for definition of element.

The analytical model for definition of steel cushions under shear effect in SeismoStruct program is shown in Figure 5.5. The blue square presents the steel cushions. The rigid elastic element bar is defined to apply the displacement protocol.

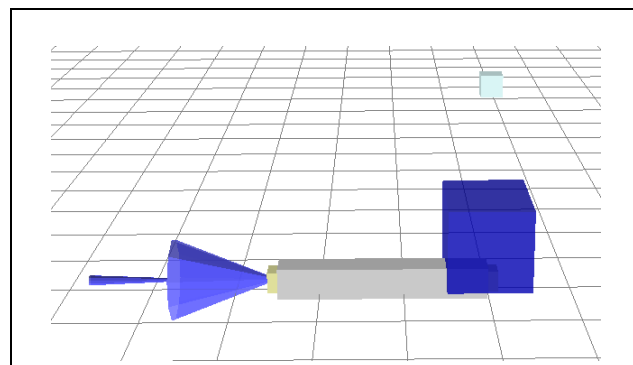


**Figure 5.5 :** Analytical model for definition of steel cushions under shear effect.

The structural and non-structural nodes are defined in the Nods module as shown in Figure 5.6.

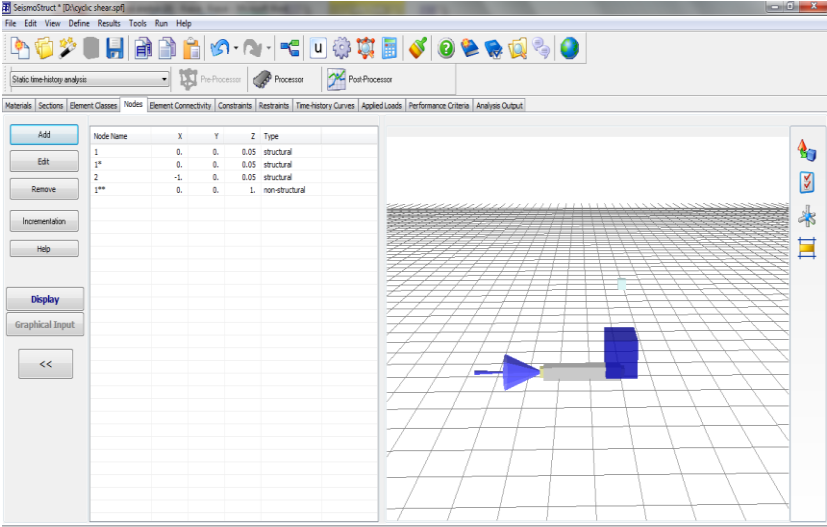


Figure 5.6 : Definition of structural and non-structural nodes.

The link element and the elastic element with high stiffness are defined in the element class module as shown in Figure 5.7.

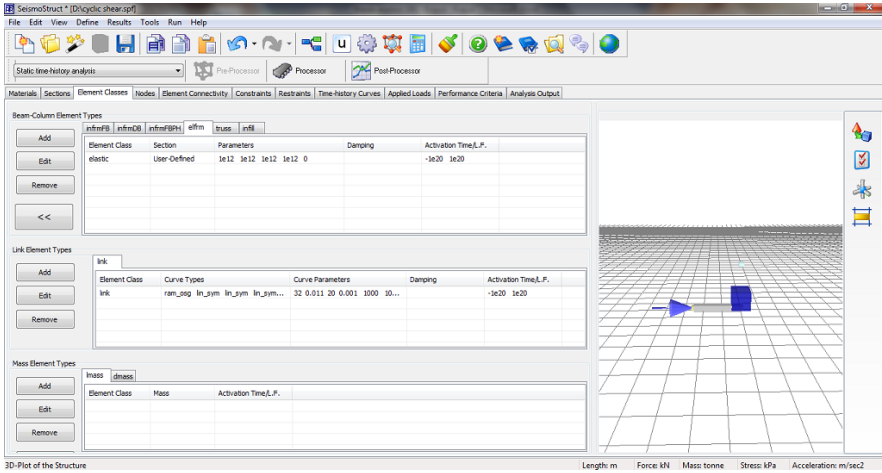
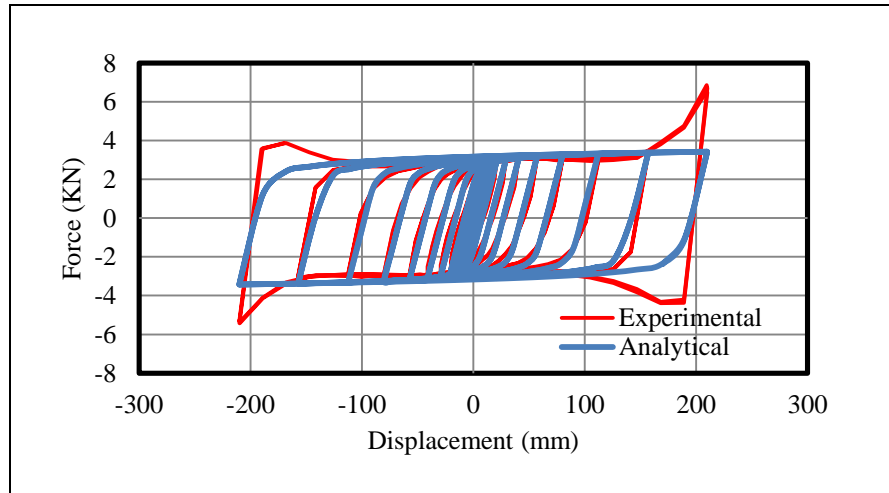


Figure 5.7 : Definition of elastic and link element.

The elements are assigned in the Element Connectivity module and the supporting conditions are assigned in Restraints module. It should be noted that the link models are restrained by the fixed support. The displacement protocol is added in the Time History Curve Module and assigned to analytical module in the applied loads module. The none-linear static time history analysis was run for three distinct steel specimens.

### 5.3.1.1 Comparison of analytical and experimental results for three distinct steel cushions under shear effect

The experimental and analytical force-displacement relations for 3mm thick specimens under shear effect are compared in Figure 5.8. Ramberg-Osgood curve parameters are summarized in Table 5.1.



**Figure 5.8 :** Comparison of experimental and analytical force-displacement relation for 3mm thick steel cushions under shear effects.

**Table 5.1 :** Ramberg-Osgood curve parameters for 3mm specimens.

Fy (KN)	Dy (mm)	$\gamma$	$\beta$
2.77	13.50	20	0.001

The experimental and analytical force-displacement relations for 5mm thick specimens under shear effect are compared in Figure 5.9. Ramberg-Osgood curve parameters are summarized in Table 5.2.

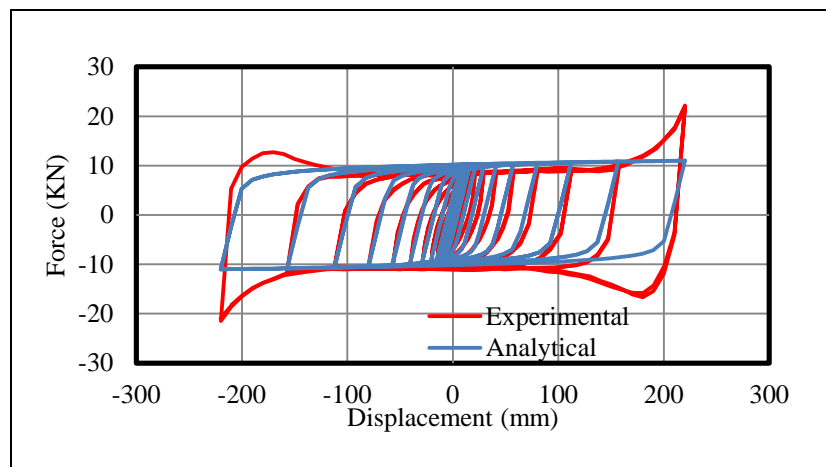


**Figure 5.9 :** Comparison of experimental and analytical force-displacement relation for 5mm thick steel cushions under shear effects.

**Table 5.2 :** Ramberg-Osgood curve parameters for 5mm specimens.

Fy (KN)	Dy (mm)	$\gamma$	$\beta$
7.84	11.0	20	0.001

The experimental and analytical force-displacement relations for t=8mm thick specimens under shear effect are compared in Figure 5.10. Ramberg-Osgood curve parameters are summarized in Table 5.3.

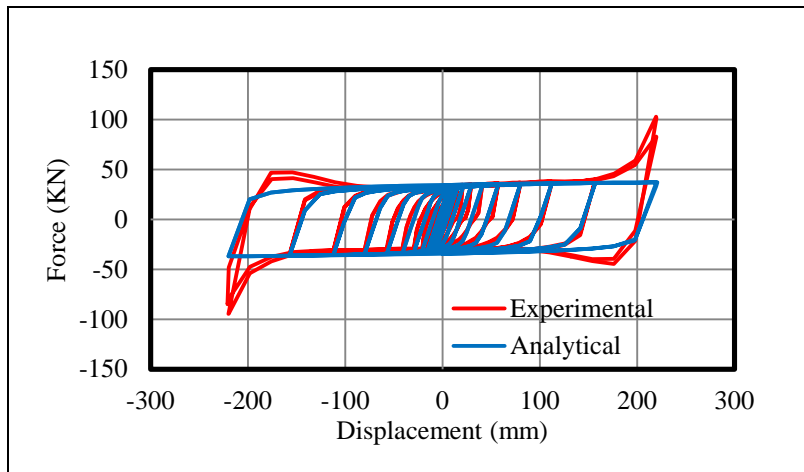


**Figure 5.10 :** Comparison of experimental and analytical force-displacement relation for 8mm thick steel cushions under shear effects.

**Table 5.3 :** Ramberg-Osgood curve parameters for 8mm specimens.

Fy (KN)	Dy (mm)	$\gamma$	$\beta$
27.82	11.0	20	0.001

### 5.3.2 Response curve for modeling axial behavior of steel cushions

The analytical model under the axial effect is shown in Figure 5.11. The differences between analytical models subjected to shear and axial effects are the direction of the applied displacement protocol and the direction of applied protocol, the other properties are identical for two models.

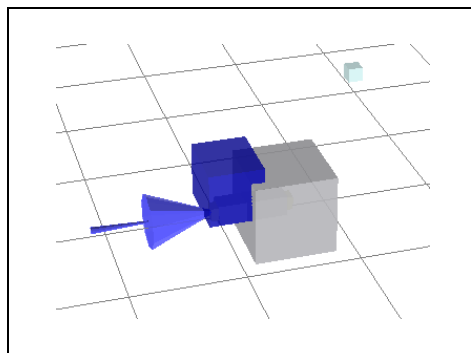


**Figure 5.11 :** Analytical model for definition of steel cushions under axial effect.

For definition of the axial behavior of steel cushions, *asymmetric bi-linear model* is utilized. The bi-linear model is shown in Figure 5.12. Required parameters for definition of asymmetric bi-linear curve are summarized in Figure 5.13.

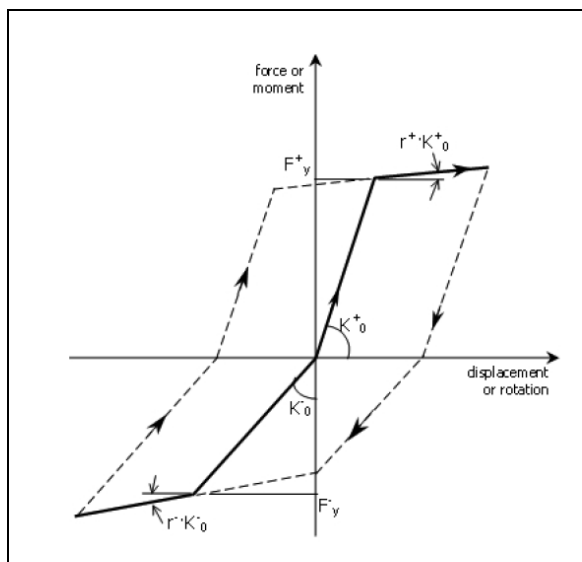


**Figure 5.12 :** Asymmetric bi-linear curve, (SeismoStruct v 6.0 user manual, 2012).

Curve Properties	Typical values	Default values
Initial stiffness in positive region - $K_{0(+)}$	-	20000 (-)
Yield force in positive region - $F_{y(+)}$	-	1000 (-)
Post-yield hardening ratio in positive region - $r_{(+)}$	-	0.005 (-)
Initial stiffness in negative region - $K_{0(-)}$	-	10000 (-)
Yield force in negative region - $F_{y(-)}$	-	-1500 (-)
Post-yield hardening ratio in negative region - $r_{(-)}$	-	0.01 (-)

**Figure 5.13 :** Required parameters for definition of asymmetric bi-linear curve, (SeismoStruct v 6.0 user manual, 2012).

The values of yield force and stiffness are obtained experimentally, the values of post-yield hardening ratios are obtained by comparing the experimental and analytical results.

### 5.3.2.1 Comparison of analytical and experimental results for three distinct steel cushions under axial effect

The experimental and analytical force-displacement relations for  $t=3\text{mm}$  thick specimens under shear effect are compared in the Figure 5.14. Asymmetric bi-linear curve parameters are summarized in Table 5.4.

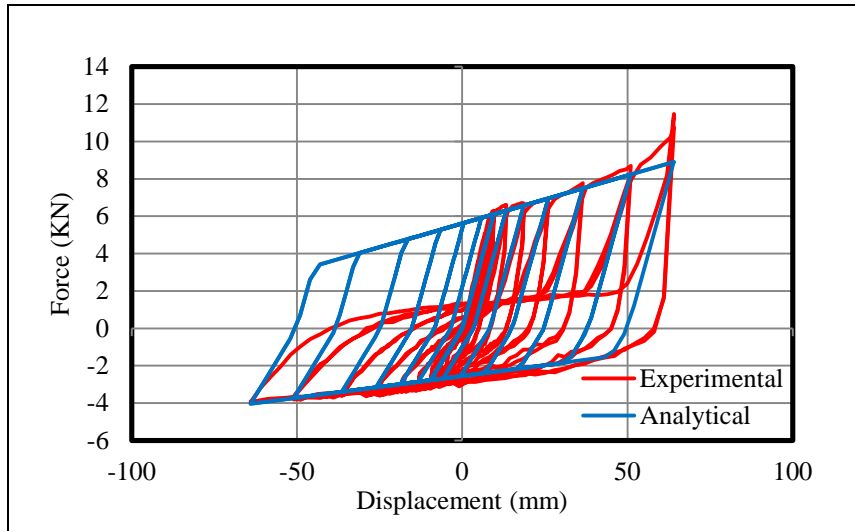


**Figure 5.14 :** Comparison of experimental and analytical force-displacement relation for 3mm thick steel cushions under axial effect.

**Table 5.4 :** Asymmetric bi-linear curve parameters for t=3mm specimens.

$K_{0(+)}$ (KN/m)	$F_{y (+)}$ (KN)	$r_{ (+)}$	$K_{0(-)}$ (KN/m)	$F_{y (-)}$ (KN)	$r_{ (-)}$
290	2.77	0.08	640	6.11	0.08

The experimental and analytical force-displacement relations for t=5mm thick specimens under shear effect are compared in Figure 5.15. Asymmetric bi-linear curve parameters are summarized in Table 5.5.

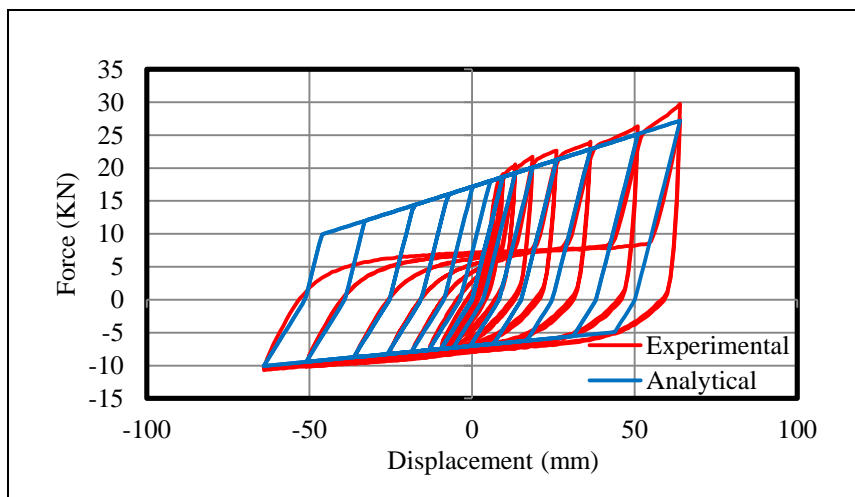


**Figure 5.15 :** Comparison of experimental and analytical force-displacement relation for 5mm thick steel cushions under axial effect.

**Table 5.5 :** Asymmetric bi-linear curve parameters for t=5mm specimens.

$K_{0(+)}$ (KN/m)	$F_{y (+)}$ (KN)	$r_{ (+)}$	$K_{0(-)}$ (KN/m)	$F_{y (-)}$ (KN)	$r_{ (-)}$
790	7.47	0.06	1960	18.65	0.08

The experimental and analytical force-displacement relations for 8mm thick specimens under shear effect are compared in Figure 5.16. Asymmetric bi-linear curve parameters are summarized in Table 5.6.

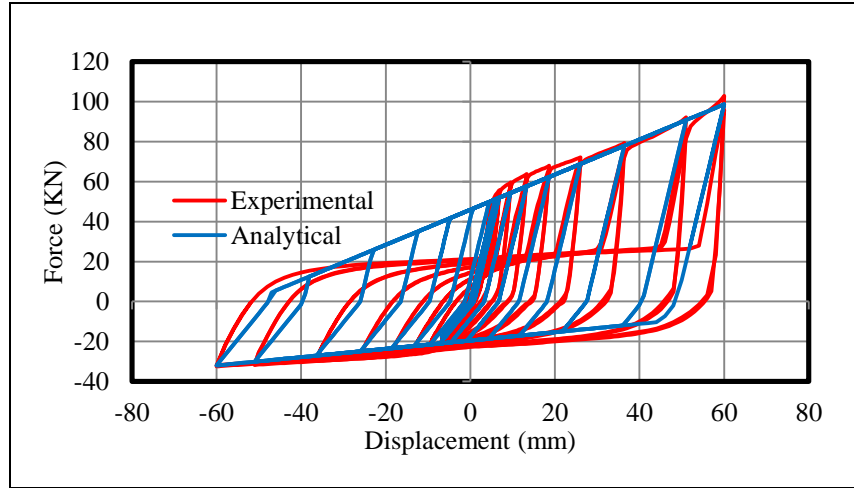


**Figure 5.16 :** Comparison of experimental and analytical force-displacement relation for 8mm thick steel cushions under axial effect.

**Table 5.6 :** Asymmetric bi-linear curve parameters for t=8mm specimens.

$K_0 (+)$ (KN/m)	$F_y (+)$ (KN)	$r (+)$	$K_0 (-)$ (KN/m)	$F_y (-)$ (KN)	$r (-)$
2600	21.18	0.08	8780	51.02	0.1

#### 5.4 Analytical Study of System Tests

In this section, the system tests are represented by analytical model and the analytical results are compared with the experimental results. The column, beam and concrete cladding panels are defined as the elastic element with their structural properties, as any yielding, cracking or non-linear deformation did not occur for these elements. All of the structural sections are defined in the Sections module. The structural elements are connected to the link element through the rigid elastic elements. The static time history analysis was run and the geometrical nonlinearity and material inelasticity are taken into account. At the end of the columns the link element with the in-plane rotational stiffness of zero are utilized to release the end moments.

##### 5.4.1 Analytical study of system test I

In this section analytical model of system test I is presented and the analytical and experimental results are compared.

**5.4.1.1 Definition of link elements**

In this model, 8mm thick cushions axial and shear behaviors are assigned to base and top-level link elements and 5mm thick cushions properties are assigned in panel-to-panel link elements. At the base level, one link element is utilized beneath per panel. The parameters that are assigned in the support link element are illustrated in Figure 5.17. According to Figure 5.17, in F1 and F3 directions the asymmetric bi-linear and Ramberg-Osgood response curves are assigned respectively. For other directions, the linear elastic response curves are assigned. The stiffness value of 10 KN/m is assigned to in- plane rotational stiffness. It should be noted that F1 is the axial direction and F3 is the shear direction.

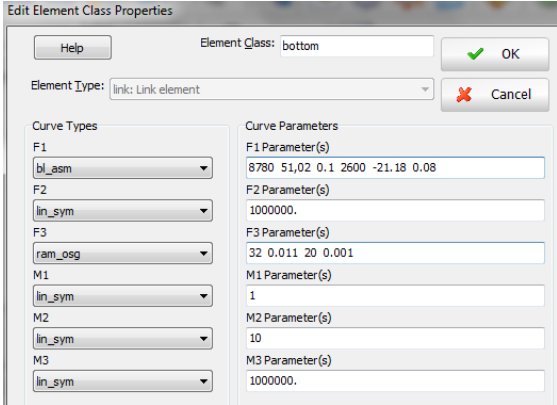


**Figure 5.17 :** Definition of the support link elements for system test I.

Parameters, which are assigned in the panel-to-panel link elements, are illustrated in Figure 5.18. According to Figure 5.18, in F1 and F2 directions the bi-linear asymmetric and Ramberg-Osgood response curves are assigned respectively. In other directions the linear elastic response curves are assigned. It should be noted that F1 is the axial direction and F2 is the shear direction.

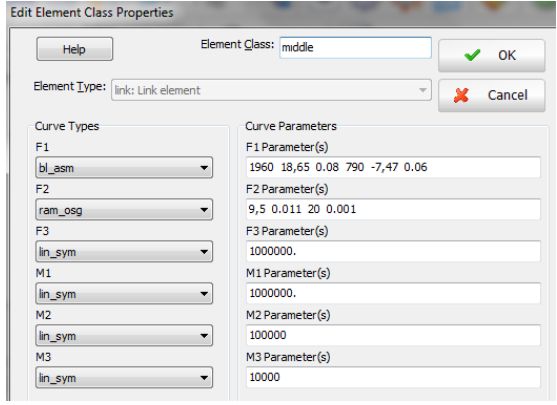


**Figure 5.18 :** Definition of the panel-to-panel link elements for system test I.

Parameters, which are assigned in the panel to beam link elements, are illustrated in Figure 5.19. According to Figure 5.19, in F1 and F2 directions the bi-linear asymmetric and Ramberg-Osgood response curves are assigned respectively. In other directions the linear elastic response curves are assigned. It should be noted that F1 is axial direction and F2 is shear direction.

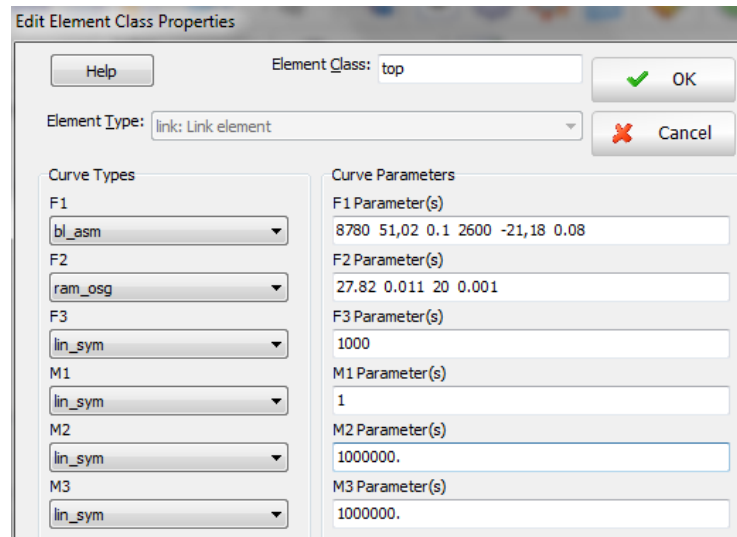


**Figure 5.19** : Definition of the panel to beam link elements for system test I.

#### 5.4.1.2 Actuator force-top displacement relation

The experimental and analytical actuator force-top displacement relations are compared in Figure 5.20. They are comprised with each other.

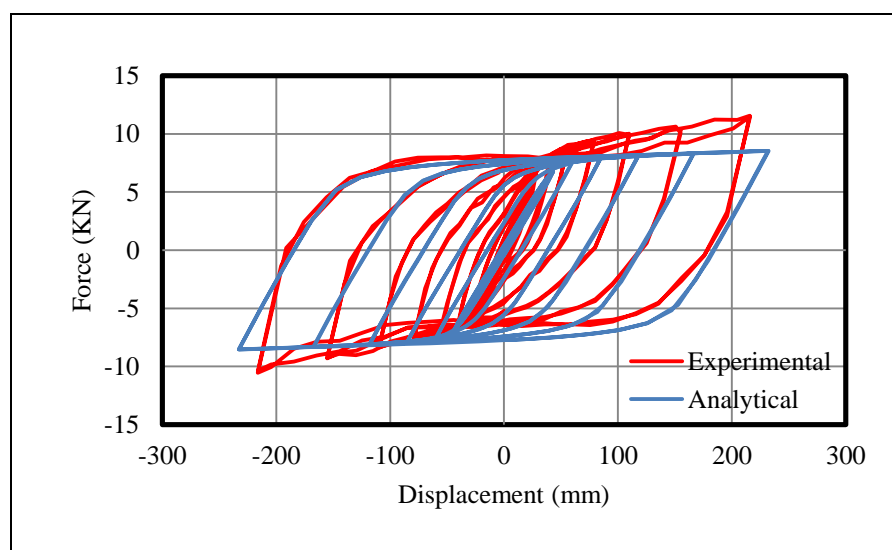


**Figure 5.20** : Comparison of the experimental and analytical actuator force-top displacement relations in the system test I.

**5.4.1.3 Force-Displacement relation of panel to panel steel cushion**

Analytical force versus vertical displacement relation for panel-to-panel steel cushion is illustrated in Figure 5.21. It should be noted that units of force and displacement are KN and m, respectively. The maximum displacement is about 8cm in the force of 10 KN.

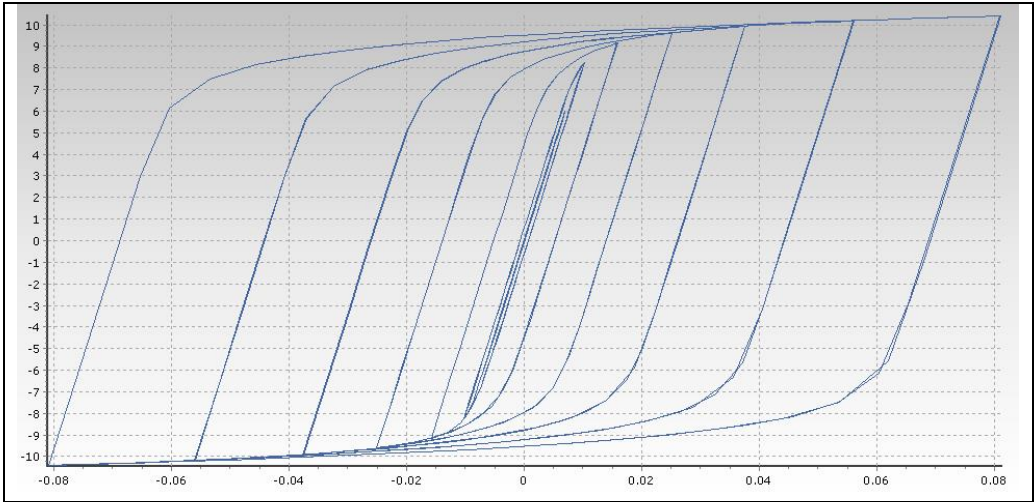


**Figure 5.21 :** Analytical force versus vertical displacement relation for panel-to-panel steel cushion in system test I.

The relative vertical displacement history in the panel-to-panel steel cushion obtained from the test and analytical study are compared in Figure 5.22.

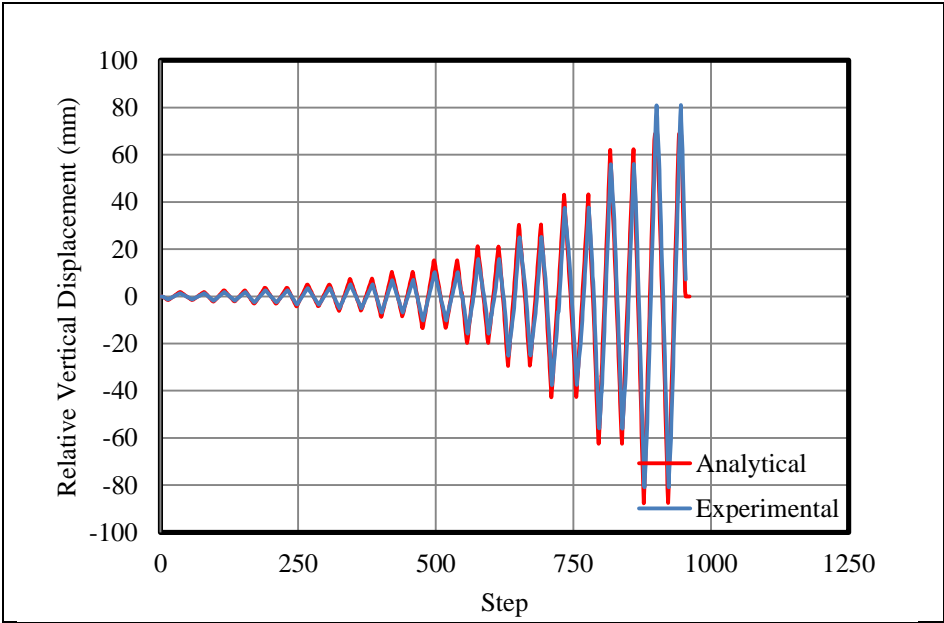


**Figure 5.22 :** Comparison of the experimental and analytical relative vertical displacement history in the panel-to-panel steel cushion.

#### 5.4.1.4 Force-Displacement relation of panel to support steel cushion

The relations of force- displacement for the steel cushions beneath the panel 1 and panel 2 are shown in the Figure 5.23 and 5.24, respectively. These are the force-displacement relations in the axial direction of steel cushions. In the shear direction the steel cushions relative horizontal displacements are negligible and the force-displacement relation remains elastic. It should be noted that units of force and displacement are KN and m respectively.

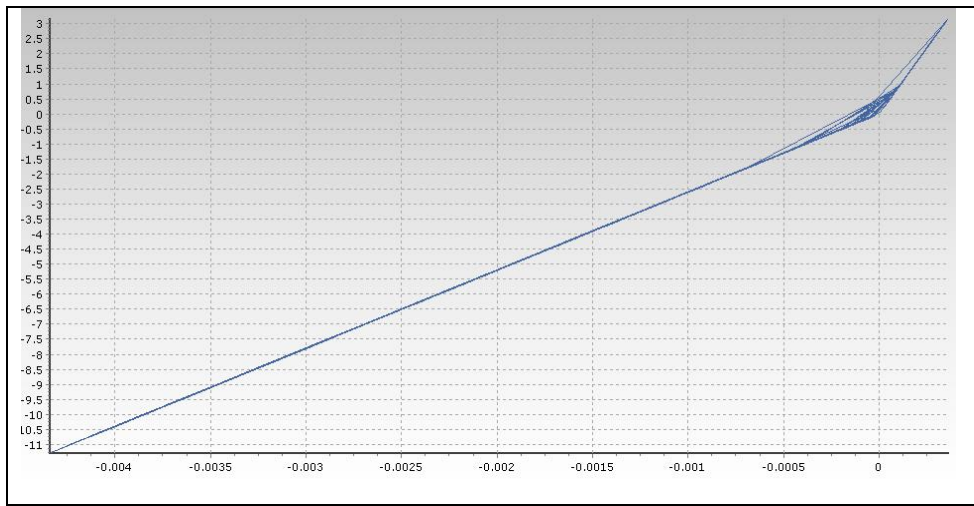


**Figure 5.23 :** Force-Displacement relation panel to support link element under the rotation of the panel 1 for system test I.

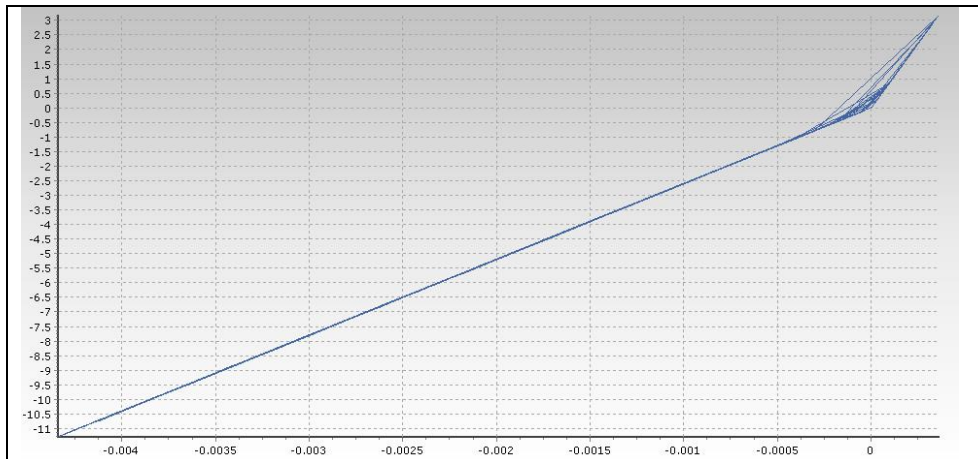


**Figure 5.24 :** Force-Displacement relation panel to support link element under the rotation of the panel 2 for system test I.

The steel cushions beneath each panel did not behave symmetrically. The maximum vertical displacement are 5.0mm for steel cushions beneath the panel 1 and panel 2.

**5.4.1.5 Rotation of cladding panels**

The rotation history of the panel 3 and panel 4 obtained from the analytical and experimental studies are compared in Figure 5.25 and 5.26, respectively. The maximum values of analytical rotations are about 0.1 rad for panel 1 and 3.

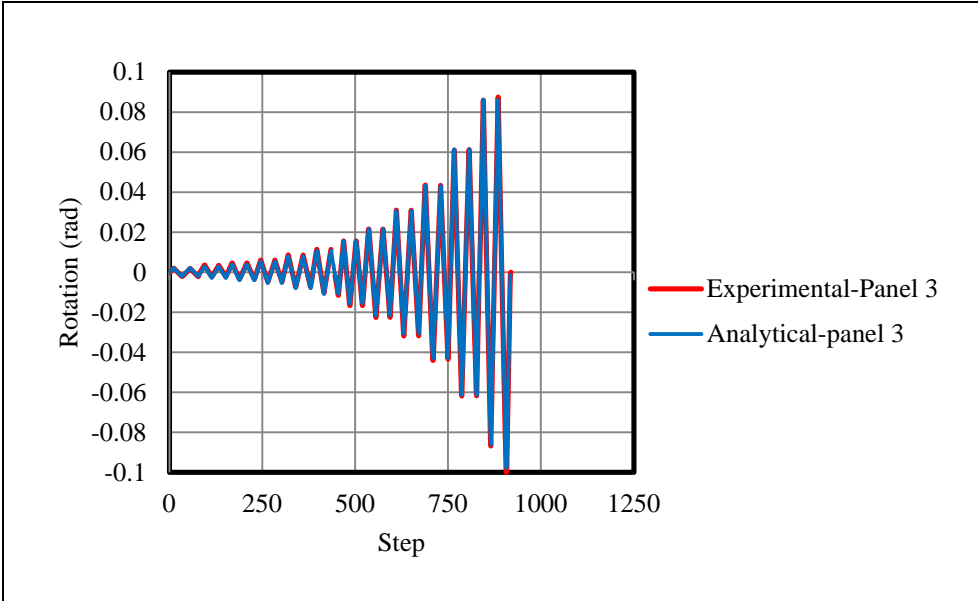


**Figure 5.25 :** Comparison of the experimental and analytical rotation history for panel 3 in system test I.

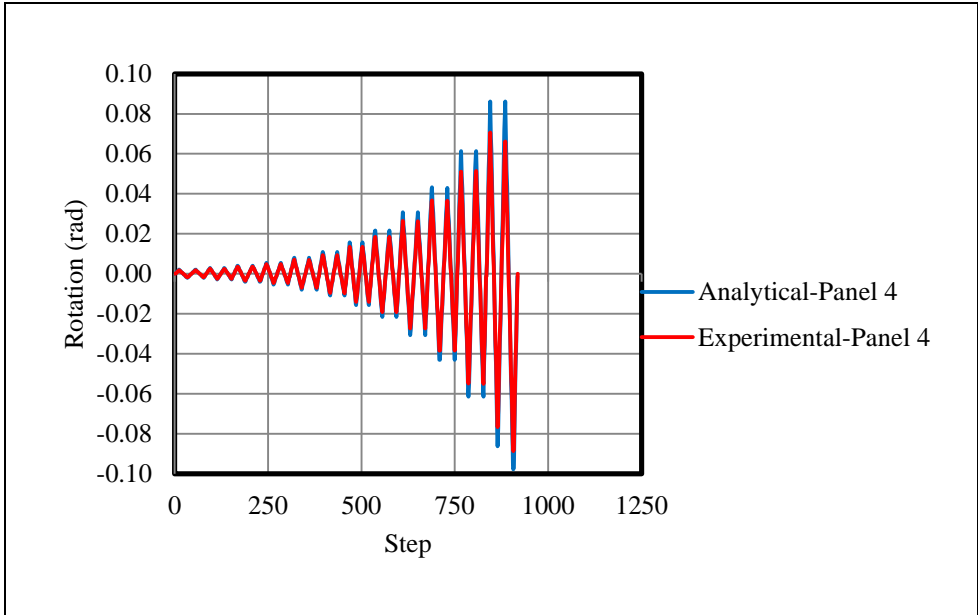


**Figure 5.26 :** Comparison of the experimental and analytical rotation history for panel 4 in system test I.

As it is obvious from Figures 5.25 and 5.26, the analytical and experimental rotation histories are comprised with each other.

#### 5.4.1.6 Moment-Rotation relation of cladding panels

The moment-rotation relation at the base of panel 3 and 4 are shown in Figure 5.27 and 5.28. The maximum base moment value is 5.0 KN.m for panel 3 and 4.

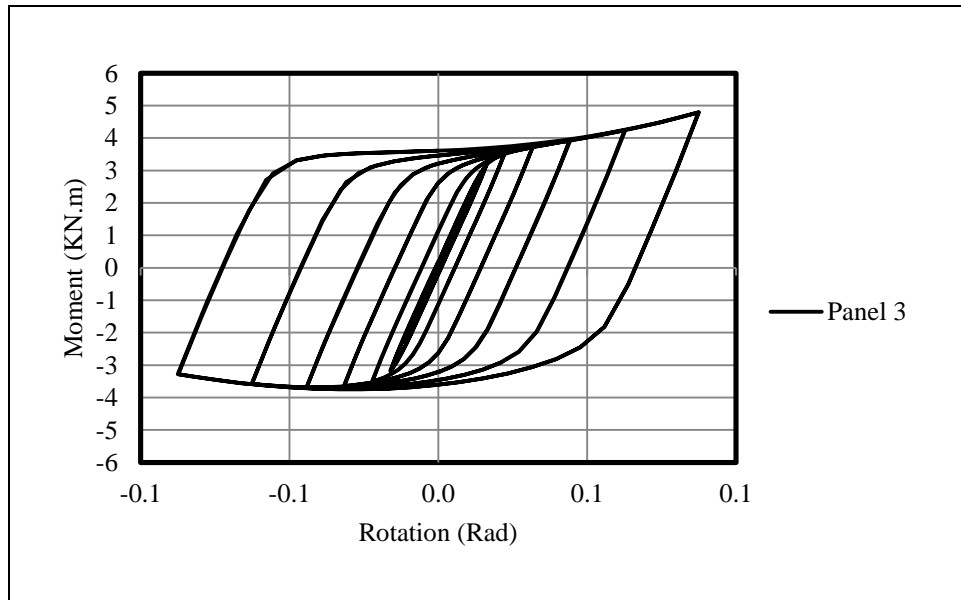


**Figure 5.27 :** Moment-Rotation relation at the base of panel 3 in system test I.

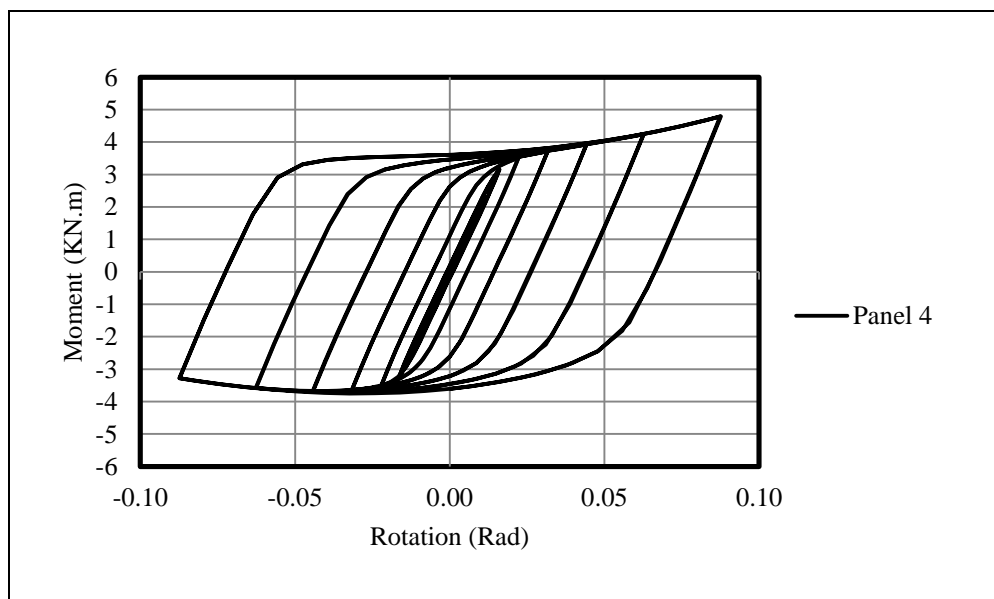


**Figure 5.28 :** Moment-Rotation relation at the base of panel 4 in system test I.

#### 5.4.1.7 Energy analysis

The total cumulative energy is 21523 KN.mm. The cumulative energy obtained from the panel-to-panel steel cushions are dissipated all the input energy.

**5.4.1.8 Deformed shape of structural system**

The deformed shape of the structural system is illustrated in Figure 5.29.

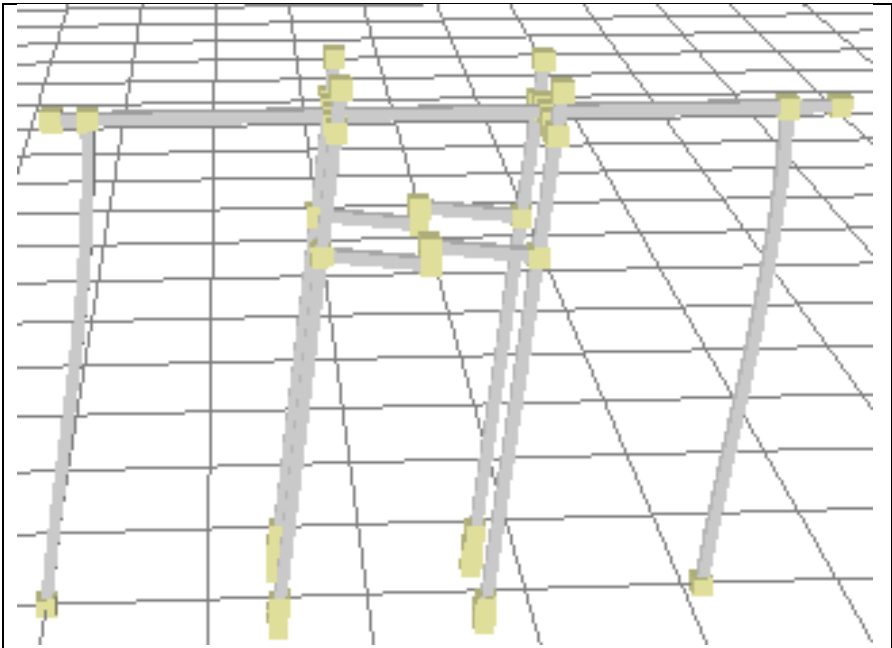


**Figure 5.29 :** Deformed shape of the structural system I.

**5.4.2 Analytical study of system test II**

In this section, analytical model of system test II is presented and the analytical and experimental results are compared. The mathematical model for system test II is illustrated in Figure 5.30.

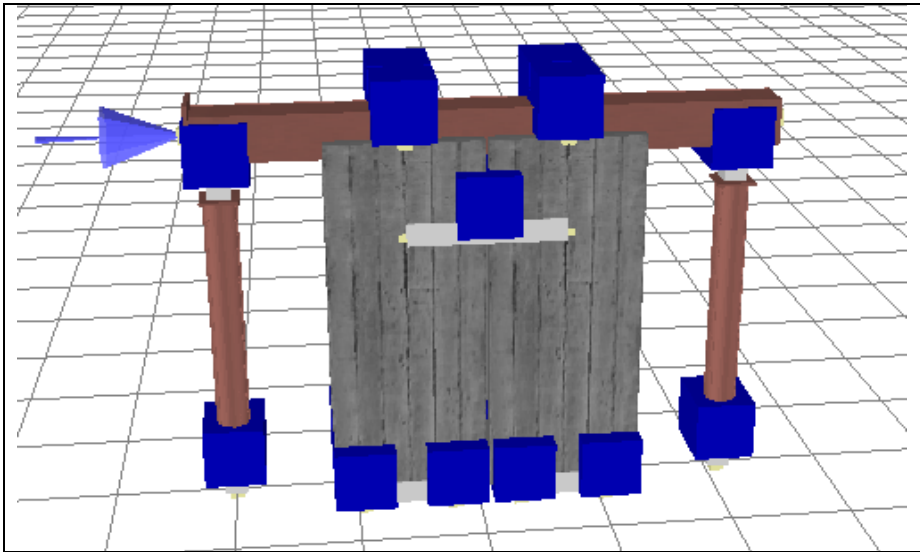


**Figure 5.30 :** Overview of the mathematical model for system test II.

### 5.4.2.1 Definition of link elements

Parameters, which are assigned in the support link elements, are illustrated in Figure 5.31. According to Figure 5.31, in F1 and F3 directions the asymmetric bi-linear and Ramberg-Osgood response curves are assigned respectively. For other directions, the linear elastic response curves are assigned. It should be noted that F1 is the axial direction and F3 is the shear direction.

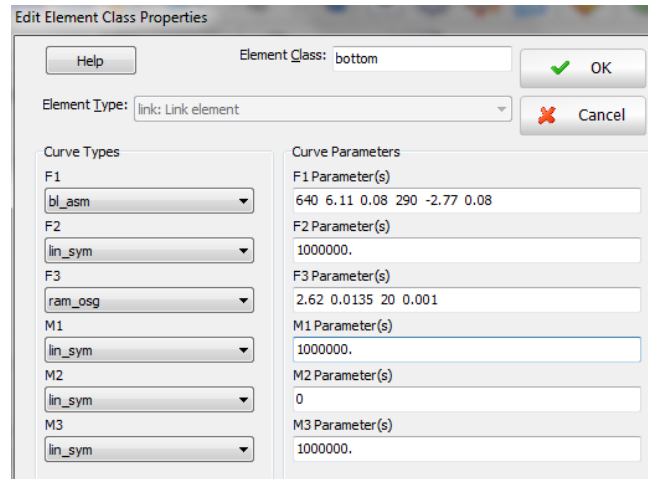


**Figure 5.31** : Definition of the support link elements for system test II.

Parameters, which are assigned in the panel-to-panel link elements, are illustrated in Figure 5.32. According to Figure 5.32, in the F1 and F2 directions the asymmetric bi-linear and Ramberg-Osgood response curves are assigned respectively. In other directions the linear elastic response curves are assigned. It should be noted that F1 is the axial direction and F2 is the shear direction.

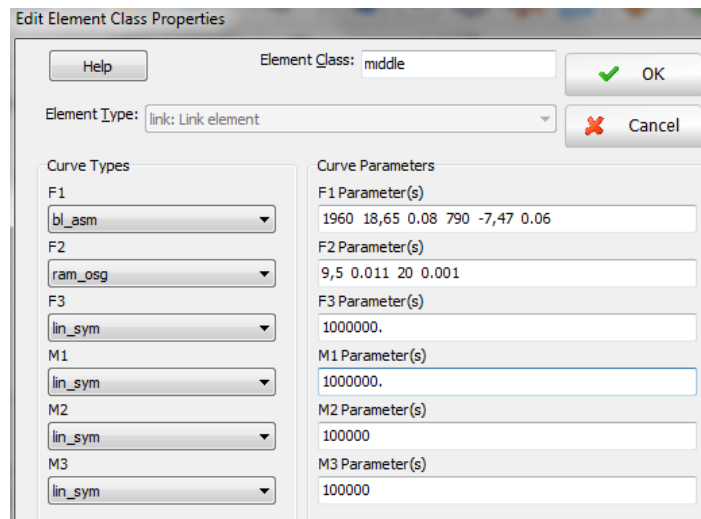


**Figure 5.32** : Definition of the panel-to-panel link elements for system test II.

Parameters, which are assigned in the panel to beam link elements, are illustrated in Figure 5.33. According to Figure 5.33, in F1 and F2 directions asymmetric bi-linear and Ramberg-Osgood response curves are assigned respectively. In other directions, the linear elastic response curves are assigned. It should be noted that F1 is axial direction and F2 is shear direction.

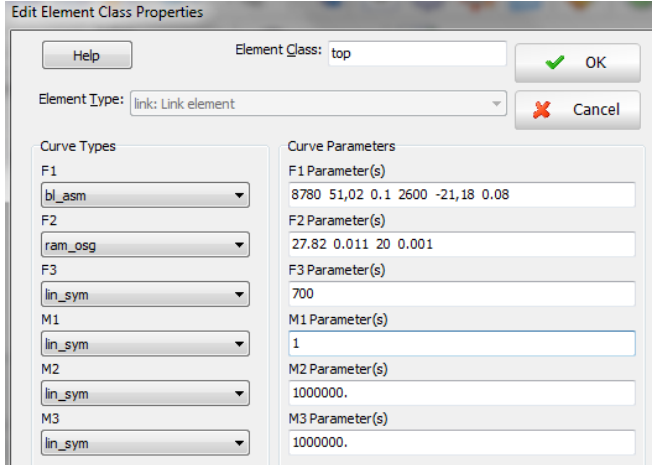


**Figure 5.33 :** Definition of the panel to beam link elements for system test II.

**5.4.2.2 Actuator force-top displacement relation**

The experimental and analytical actuator force-top displacement relations are compared in Figure 5.34. They are comprised with each other.

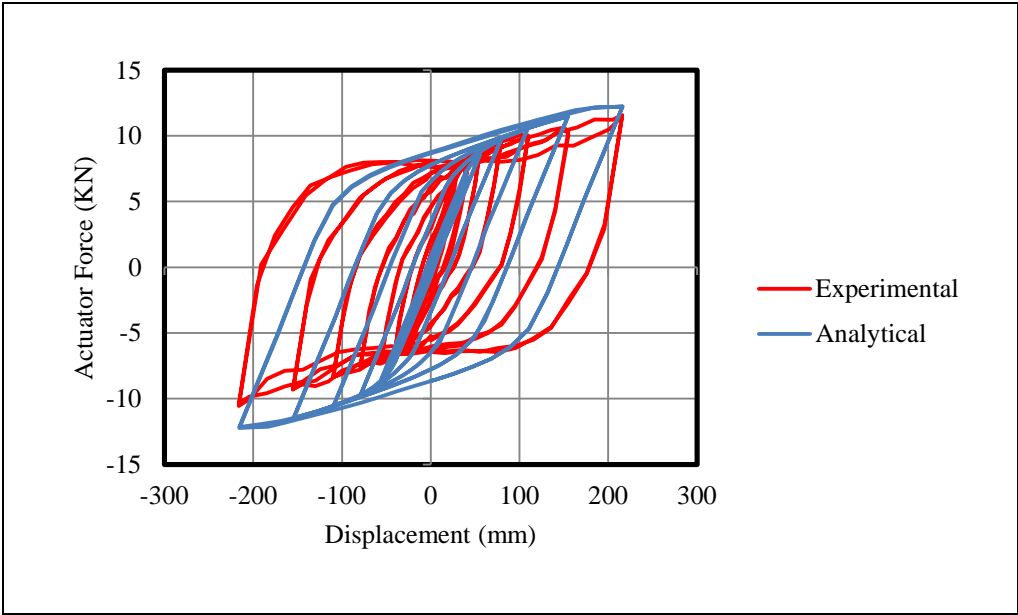


**Figure 5.34 :** Comparison of the experimental and analytical actuator force-top displacement relations in the system test II.

### 5.4.2.3 Force-Displacement relation of panel to panel steel cushion

Analytical force versus vertical displacement relation for panel to panel steel cushion is illustrated in Figure 5.35 it should be noted that units of the force and displacement are KN and m, respectively. The maximum displacement is about 6.5cm in the force of 10KN.

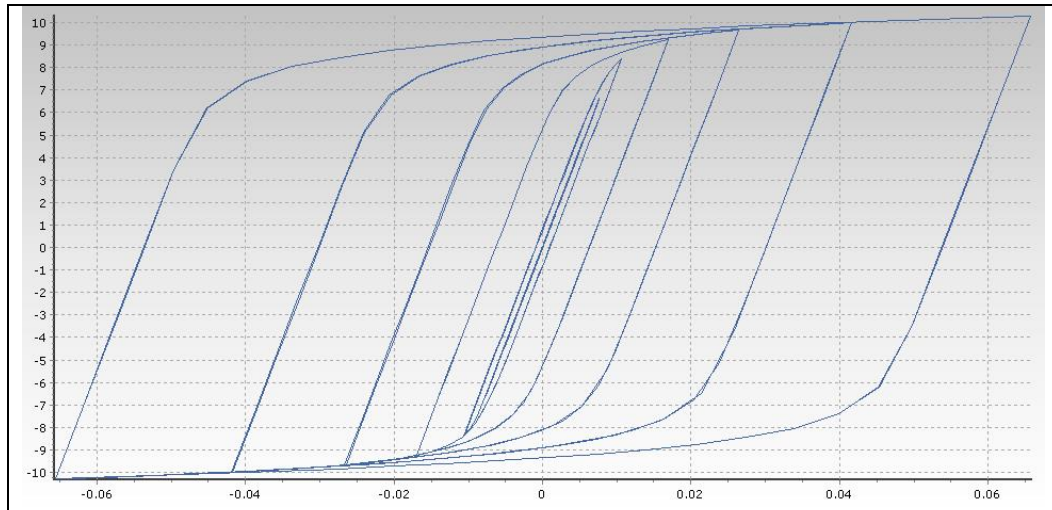


**Figure 5.35 :** Analytical force versus vertical displacement relation for panel-to-panel steel cushion in system test II.

The relative vertical displacement history in the panel-to-panel steel cushion obtained from the test and analytical study are compared in Figure 5.36.

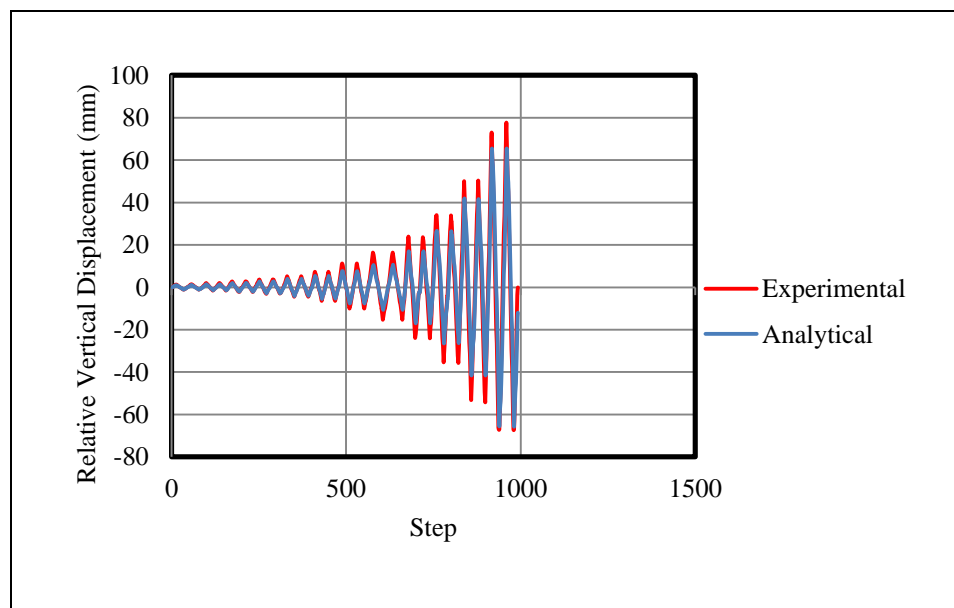


**Figure 5.36 :** Comparison of the experimental and analytical relative vertical displacement history in the panel-to-panel steel cushion.

**5.4.2.4 Force-Displacement relation of panel to support steel cushion**

Force- displacement relations for the steel cushions beneath panel 1, are shown in the Figure 5.37 and 5.38. These relations are caused by the rotation of the panel 1. In the shear direction the steel cushions relative horizontal displacements are negligible and the force-displacement relation remains elastic. It should be noted that units of force and displacement are KN and m, respectively.

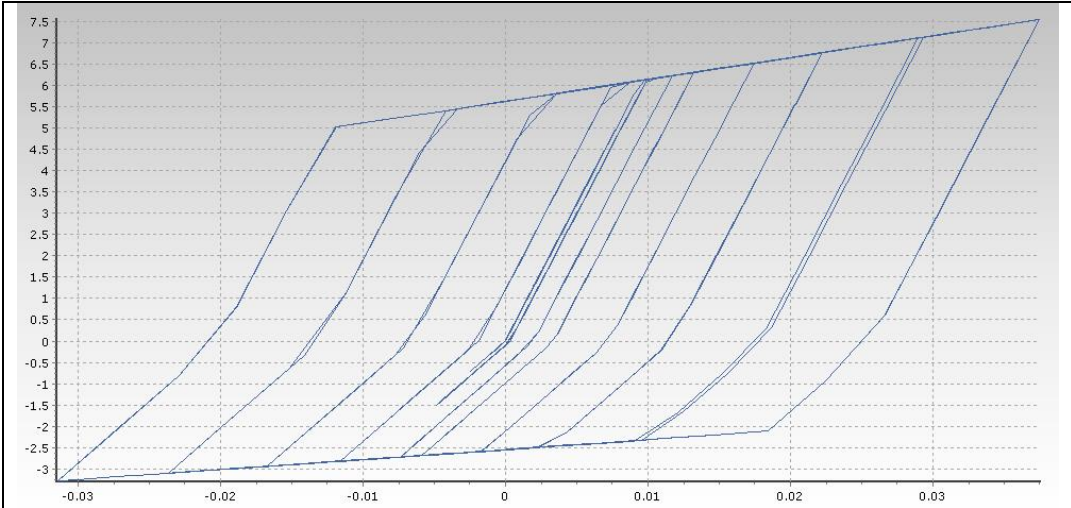


**Figure 5.37 :** Force-Displacement relation panel to support link element in under the rotation of the panel 1 for system test II.

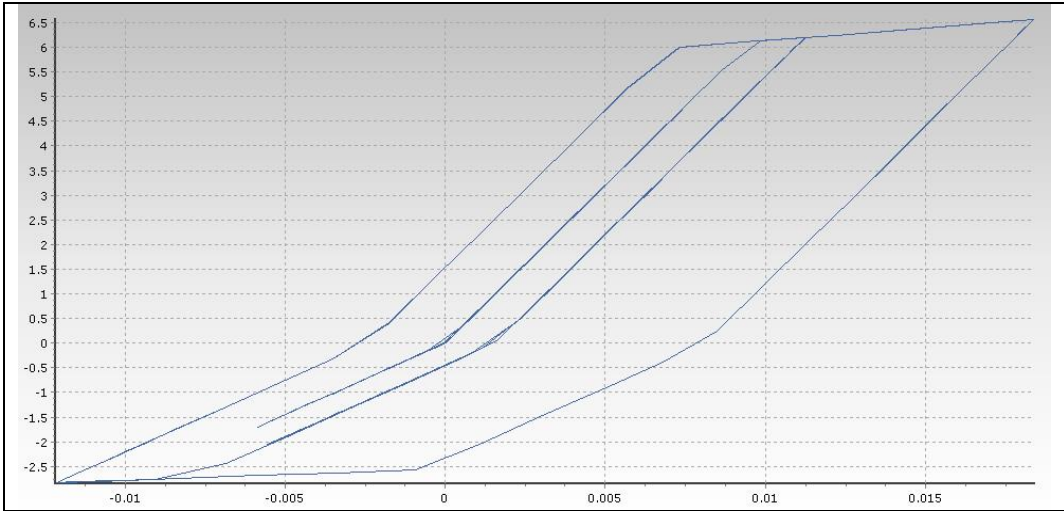


**Figure 5.38 :** Force-Displacement relation panel to support link element under the rotation of the panel 1 for system test II.

Force displacement relations for the steel cushions beneath panel 2, are shown in Figure 5.39 and 5.40. These relations are caused by the rotation of the panel 2, in shear direction the steel cushions relative horizontal displacements are negligible and

the force-displacement relation remains elastic. It should be noted that units of force and displacement are KN and m, respectively.

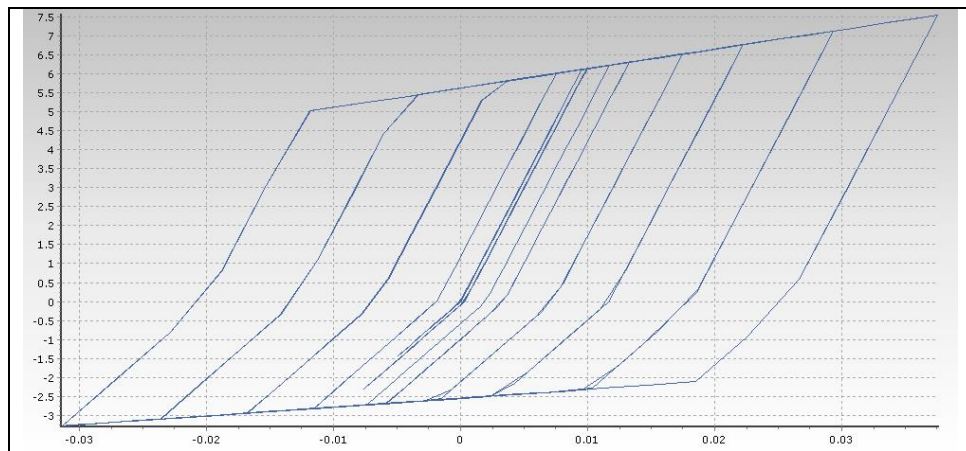


**Figure 5.39 :** Force-Displacement relation panel to support link element under the rotation of the panel 2 for system test II.

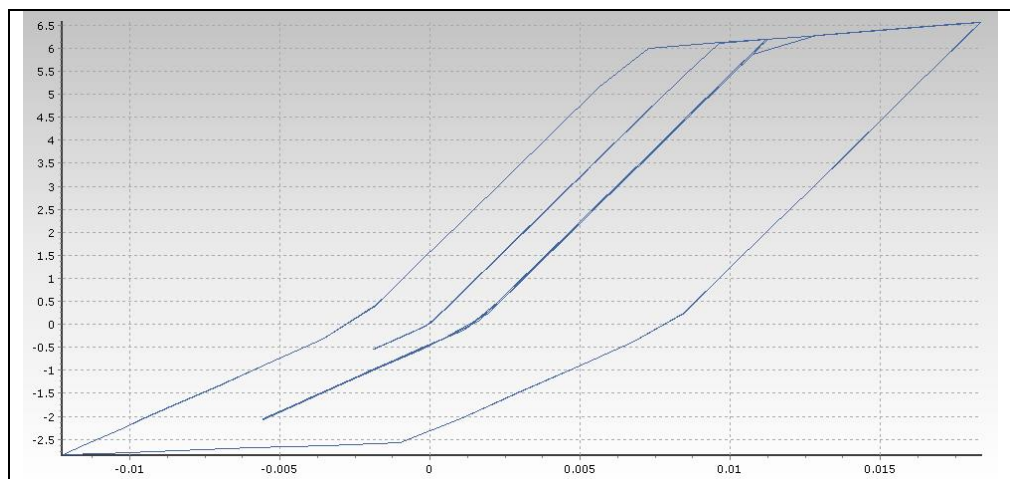


**Figure 5.40 :** Force-Displacement relation panel to support link element under the rotation of the panel 2 for system test II.

The steel cushions beneath each panel did not behave symmetrically. The maximum vertical displacement are almost 3.5cm for one steel cushion and 2 cm for another one in panel 1 and 2.

#### 5.4.2.5 Rotation of cladding panels

The rotation history of the panel 3 and panel 4 obtained from the analytical and experimental studies are compared in Figure 5.41 and 5.42, respectively. The maximum value of analytical rotation is about 0.08 rad.

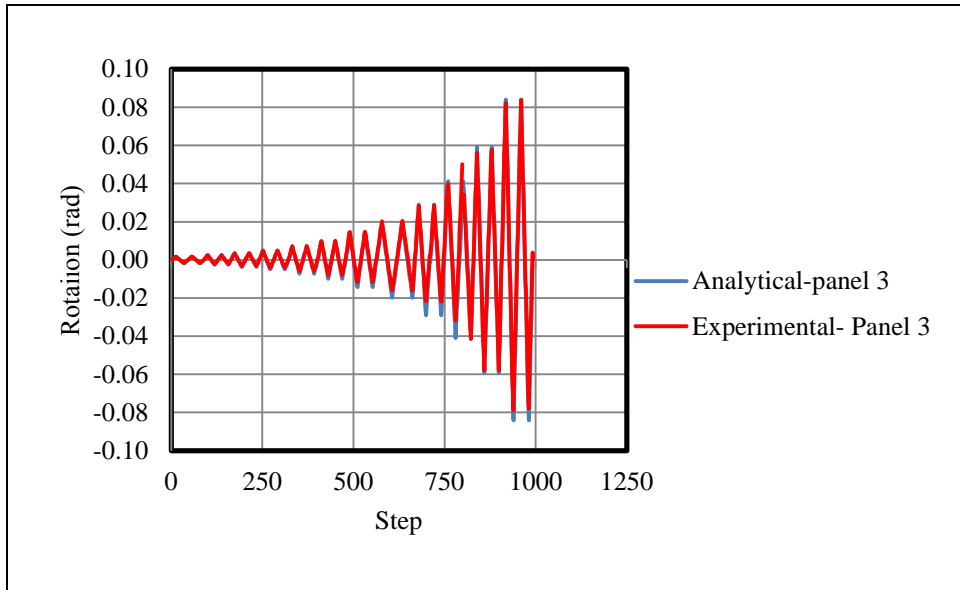


**Figure 5.41 :** Comparison of the experimental and analytical rotation history for panel 3 in system test II.

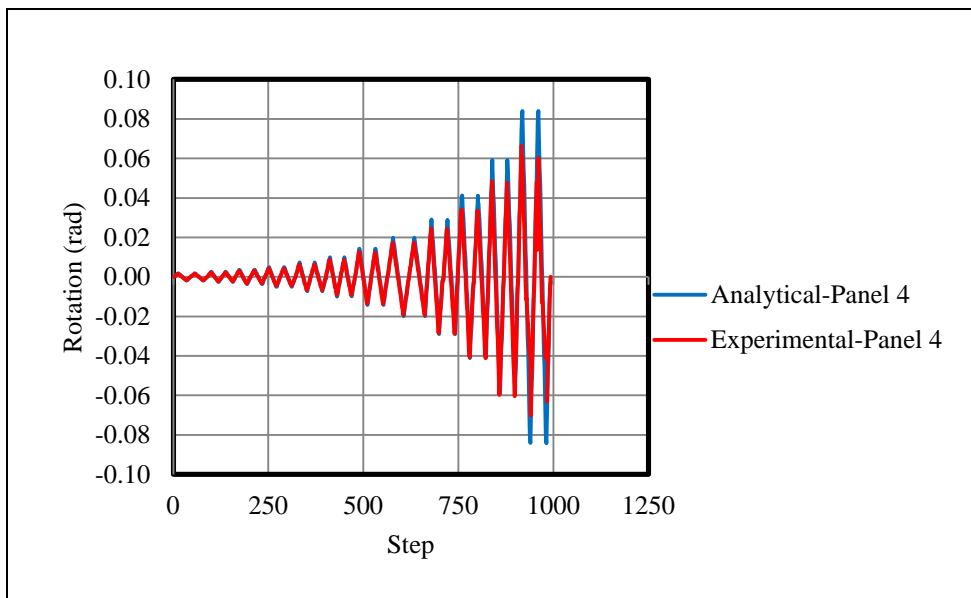


**Figure 5.42 :** Comparison of the experimental and analytical rotation history for panel 4 in system test II.

As it is obvious from Figures 5.41 and 5.42, the analytical and experimental rotation histories are compared with each other.

#### 5.4.2.6 Moment-Rotation relation of cladding panels

The moment-rotation relation at the base of panel 3 and 4 are shown in Figure 5.43 and 5.44. The maximum base moment value is 4 KN.m for panel 3 and 4.

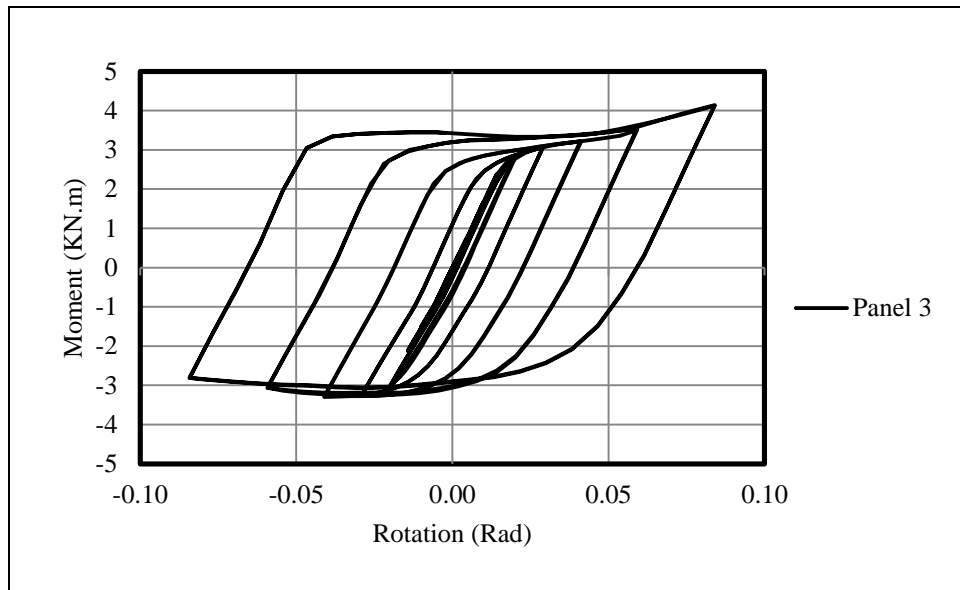


**Figure 5.43 :** Moment-Rotation relation at the base of panel 3 in system test II.

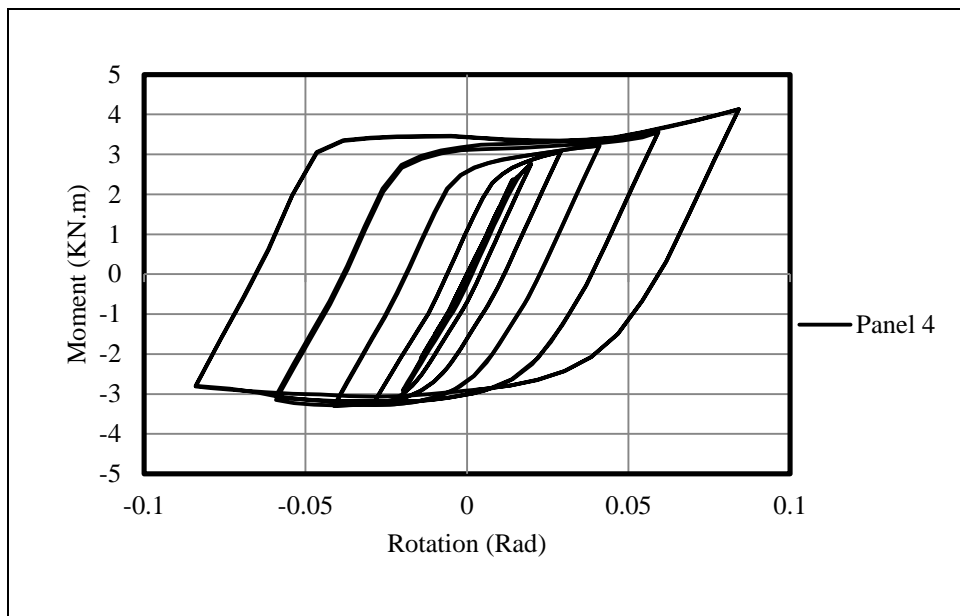


**Figure 5.44 :** Moment-Rotation relation at the base of panel 4 in system test II.

#### 5.4.2.7 Energy analysis

The total cumulative energy is 19476 KN.mm. The cumulative energy obtained from the steel cushions beneath the panels is 7573 KN.mm and the cumulative energy obtained from the panel to panel steel cushions is 12474 KN.mm. Thus 38.88% of the total cumulative energy is dissipated by the steel cushions in the base level and 64.05% of the total cumulative energy is dissipated by the panel to panel steel device.

### 5.4.2.8 Deformed shape of structural system

The deformed shape of the structural system is illustrated in Figure 5.45.

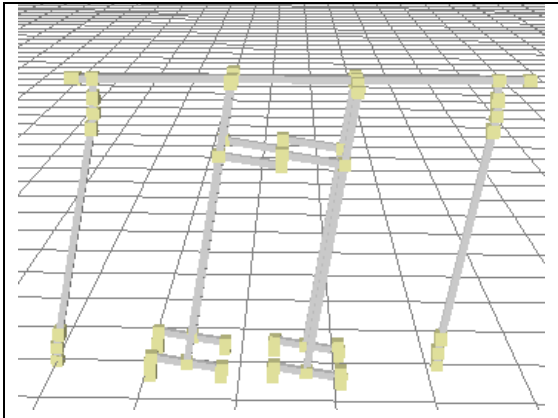


Figure 5.45 : Deformed shape of the structural system II.

### 5.4.3 Analytical study of system test III

In this section, analytical model of system test III is presented and the analytical and experimental results are compared.

#### 5.4.3.1 Definition of link elements

All the analysis setting are identical with system test II the only difference is the utilizing the link element which is related to the 5mm thick steel cushions in panel to support connection rather than 3mm ones. The parameters, which are assigned in the support link elements, are illustrated in Figure 5.46. According to Figure 5.46, in F1 and F3 directions the asymmetric bi-linear and Ramberg-Osgood response curves are assigned respectively. For other directions, the linear elastic response curves are assigned. It should be noted that F1 is axial direction and F3 is shear direction.

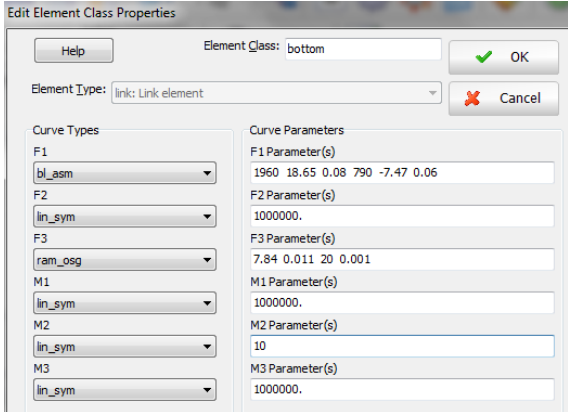
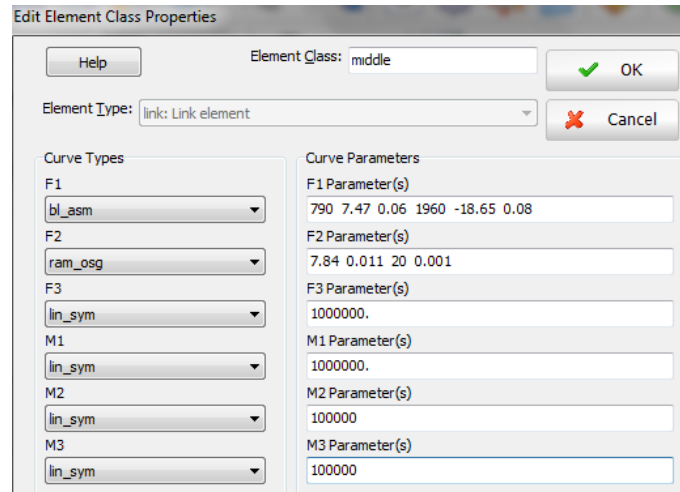


Figure 5.46 : Definition of the support link elements for system test III.

Parameters, which are assigned in the panel-to-panel link elements, are illustrated in Figure 5.47. According to Figure 5.47, in F1 and F2 directions the asymmetric bi-linear and Ramberg-Osgood response curves are assigned respectively. In other directions, the linear elastic response curves are assigned. It should be noted that F1 is axial direction and F2 is shear direction.



**Figure 5.47** : Definition of the panel-to-panel link elements for system test III.

Parameters, which are assigned in the panel to beam link elements, are illustrated in Figure 5.48. According to Figure 5.48, in F1 and F2 directions the asymmetric bi-linear and Ramberg-Osgood response curves are assigned respectively. In other directions, the linear elastic response curves are assigned. It should be noted that the F1 is axial direction and F2 is shear direction.

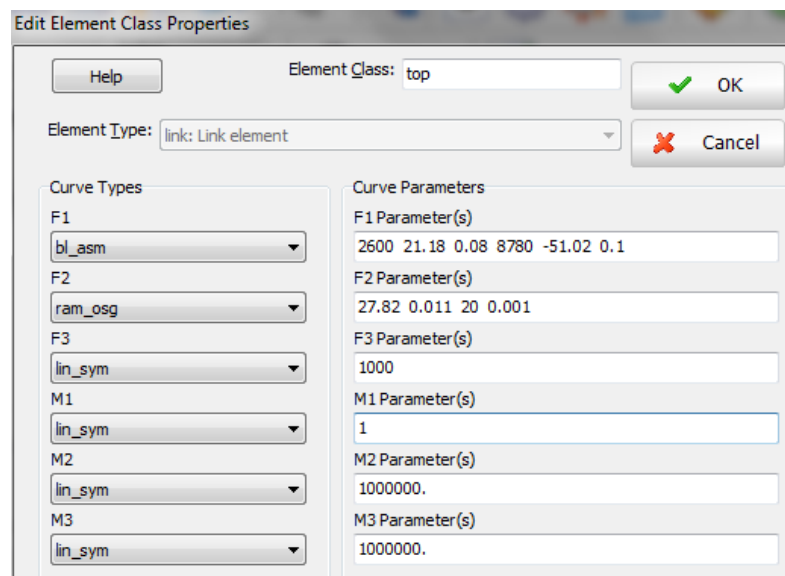


**Figure 5.48** : Definition of the panel to beam link elements for system test III.

**5.4.3.2 Actuator force-top displacement relation**

The experimental and analytical actuator force-displacement relations are compared in Figure 5.49. They are comprised with each other.

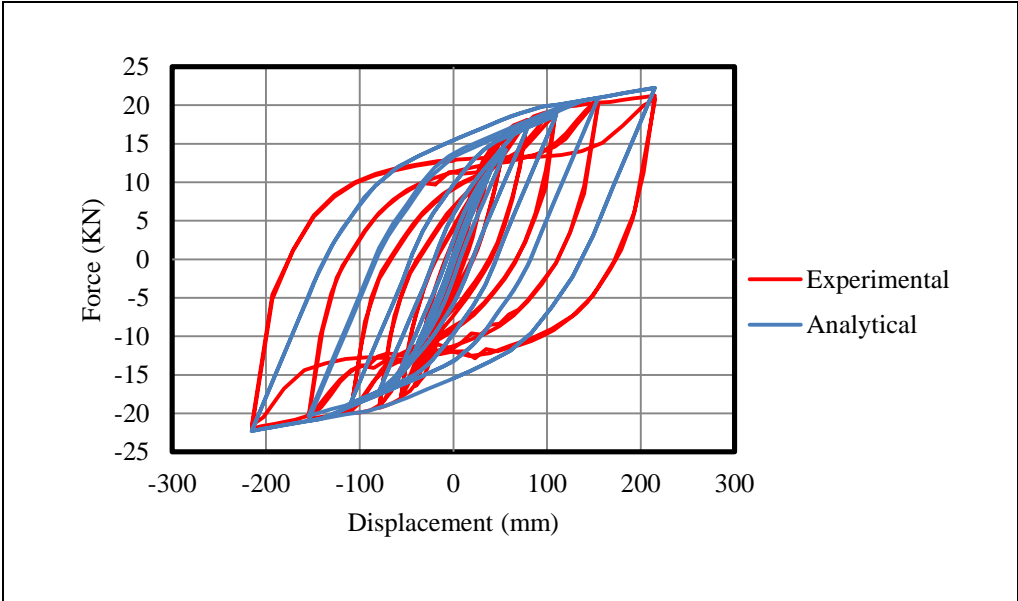


**Figure 5.49 :** Comparison of the experimental and analytical actuator force-displacement relations in the system test III.

**5.4.3.3 Force-Displacement relation of panel to panel steel cushion**

Analytical force versus vertical displacement relations for panel-to-panel steel cushion is illustrated in Figure 5.50. It should be noted that units of force and displacement are KN and m, respectively. The maximum displacement is about 6.5cm in the force of 8KN.

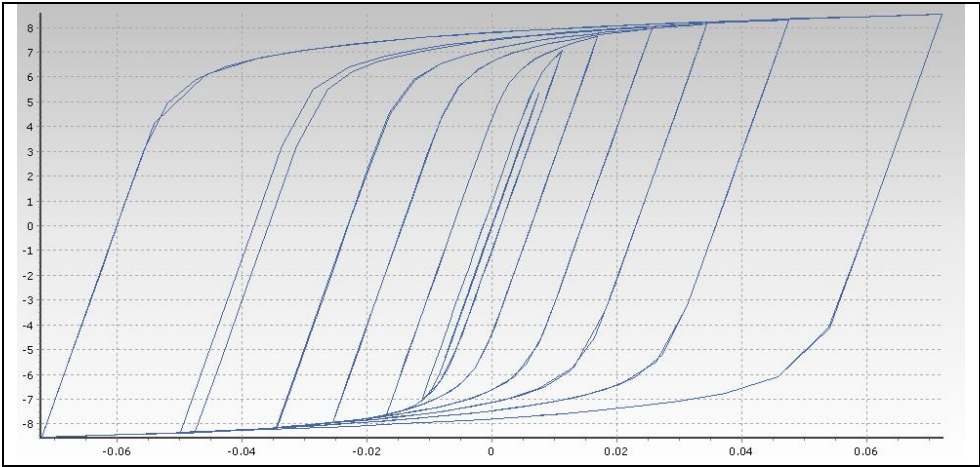


**Figure 5.50 :** Analytical force versus vertical displacement relations for panel-to-panel steel cushion in system test III.

The relative vertical displacement history in the panel-to-panel steel cushion obtained from the test and analysis are compared in Figure 5.51.

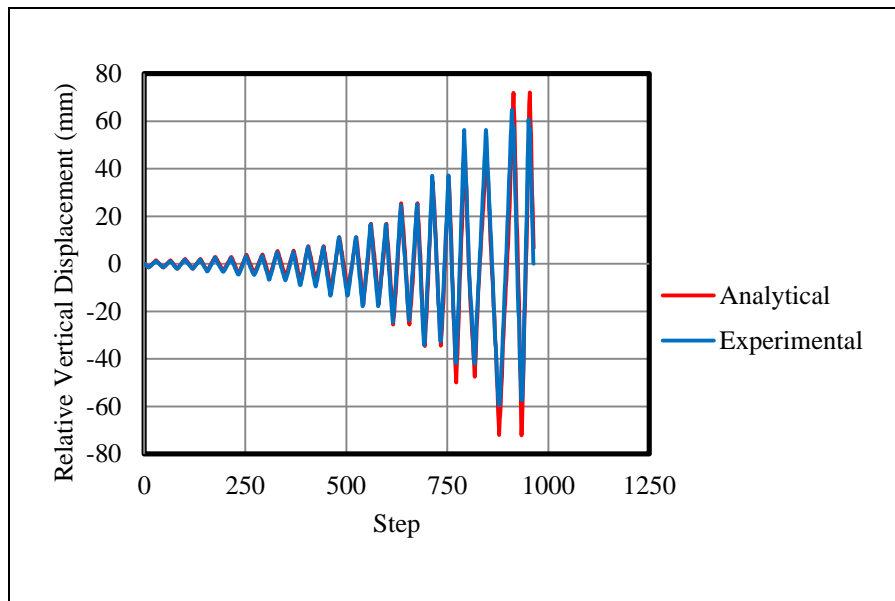


**Figure 5.51 :** Comparison of the experimental and analytical relative vertical displacement history in the panel-to-panel link element.

#### 5.4.3.4 Force-Displacement relation of panel to support steel cushion

Force displacement relations for the steel cushions beneath the panel 1, are shown in the Figure 5.52 and 5.53. These relations are caused by the rotation of the panel 1, in shear direction the steel cushions relative horizontal displacements are negligible and the force-displacement relation remains elastic . It should be noted that units of force and displacement are KN and m, respectively.

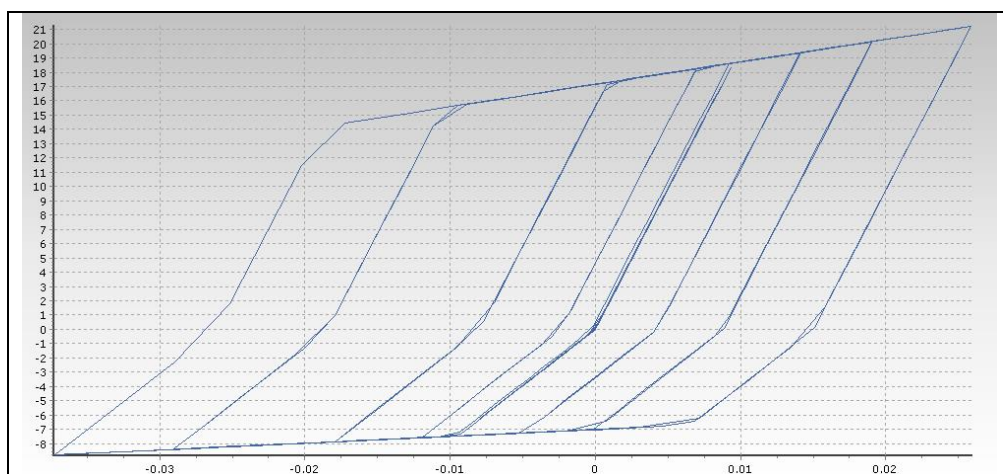


**Figure 5.52 :** Force-Displacement relation panel to support link element under the rotation of the panel 1 for system test III.

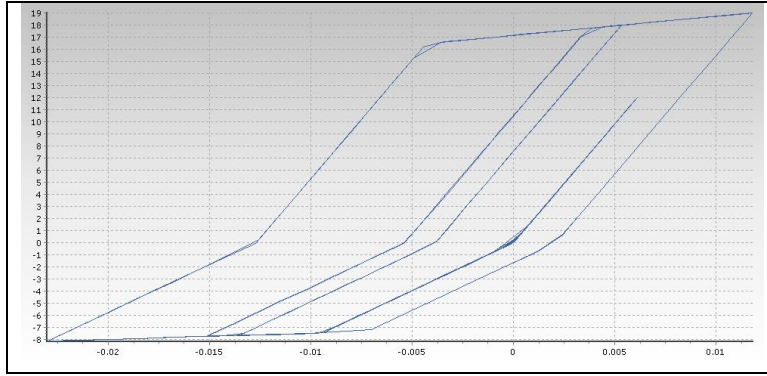


**Figure 5.53 :** Force-Displacement relation panel to support link element under the rotation of the panel 1 for system test III.

Force displacement relations for the steel cushions beneath the panel 2, are shown in Figure 5.54 and 5.55. These relations are caused by the rotation of the panel 2, in shear direction the steel cushions relative horizontal displacements are negligible and the force-displacement relation remains elastic. It should be noted that units of the force and displacement are KN and m, respectively.

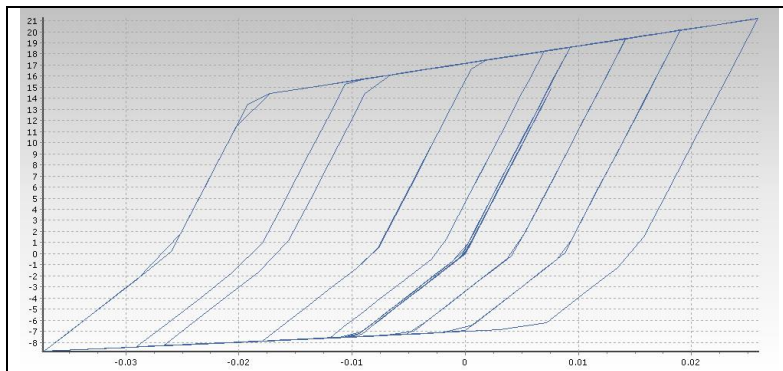


**Figure 5.54 :** Force-Displacement relation panel to support link element under the rotation of the panel 2 for system test III.

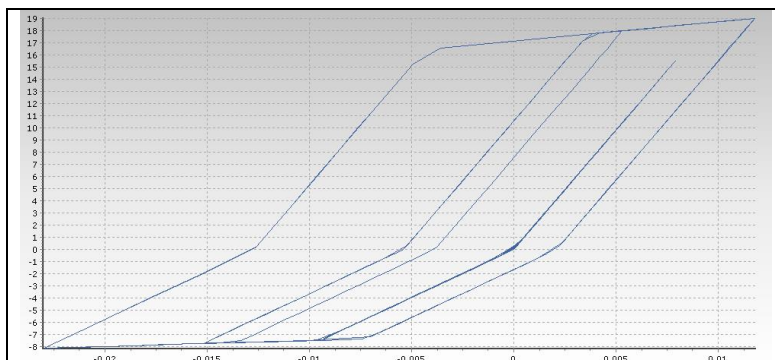


**Figure 5.55 :** Force-Displacement relation panel to support link element under the rotation of the panel 2 for system test III.

The steel cushions under each panel did not behave symmetrically. The maximum vertical displacements are nearly 4cm for one steel cushion and 3cm for another one.

### 5.4.3.5 Rotation of cladding panels

The rotation histories of panel 3 and panel 4 obtained from the analytical and experimental studies are compared in Figure 5.56 and 5.57, respectively. The maximum values of rotation are about 0.09 and 0.08 rad for panel 1 and 3 respectively.

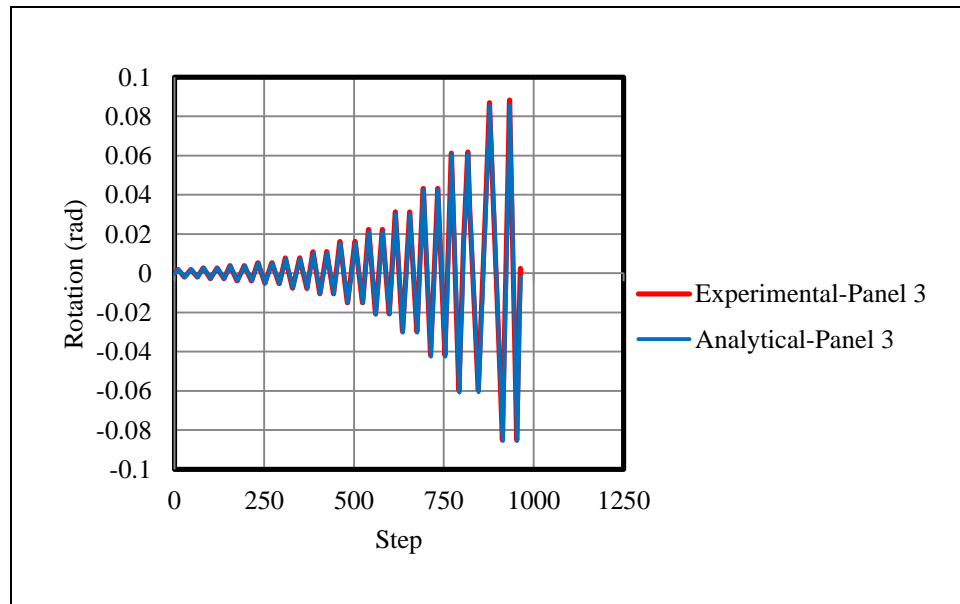


**Figure 5.56** : Comparison of the experimental and analytical rotation history for panel 3 in system test III.

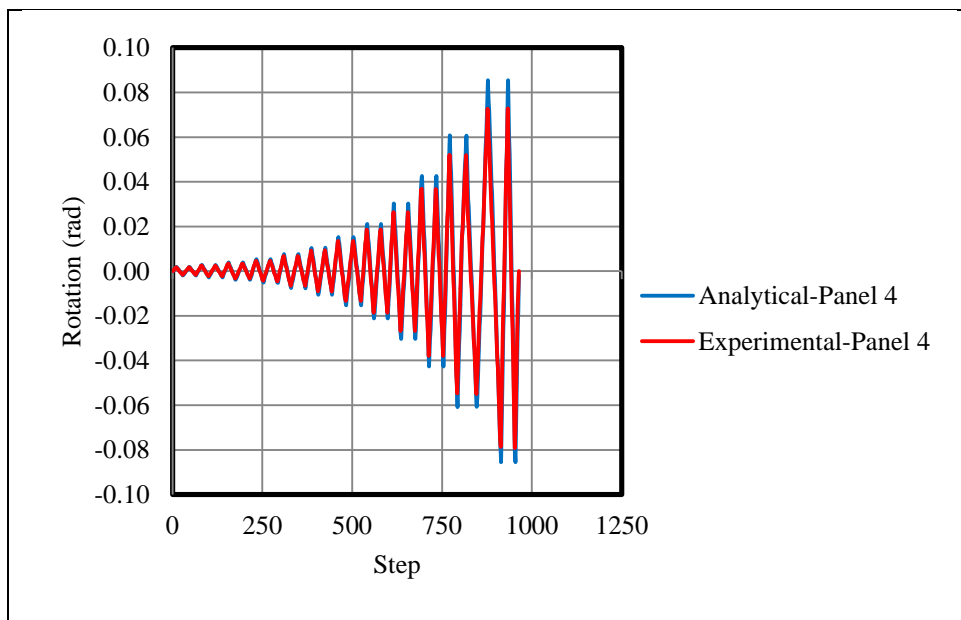


**Figure 5.57** : Comparison of the experimental and analytical rotation for panel 4 in system test III.

**5.4.3.6 Moment-Rotation relation of cladding panels**

The moment-rotation relation at the base of panel 3 and 4 are shown in Figure 5.58 and 5.59. The maximum base moment value is 10 KN.m for panel 3 and 4.

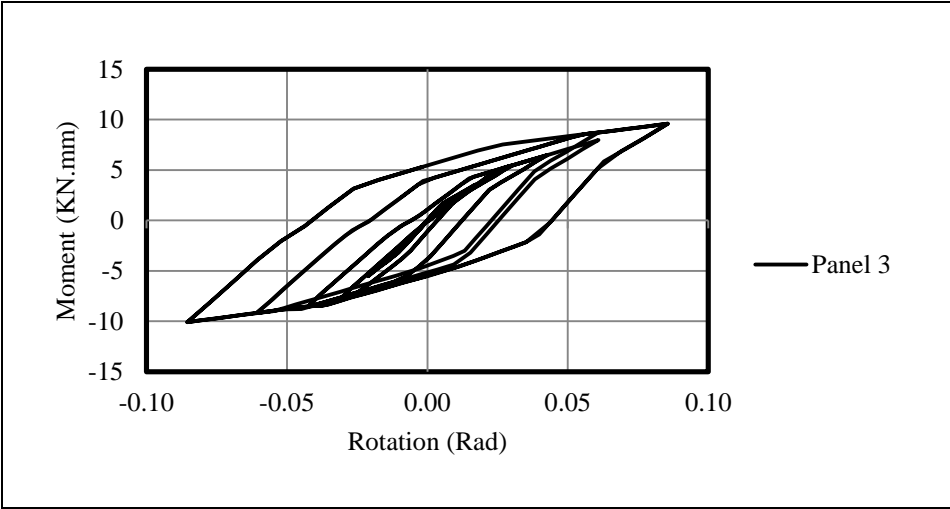


**Figure 5.58 :** Moment-Rotation relation at the base of panel 3 in system test III.

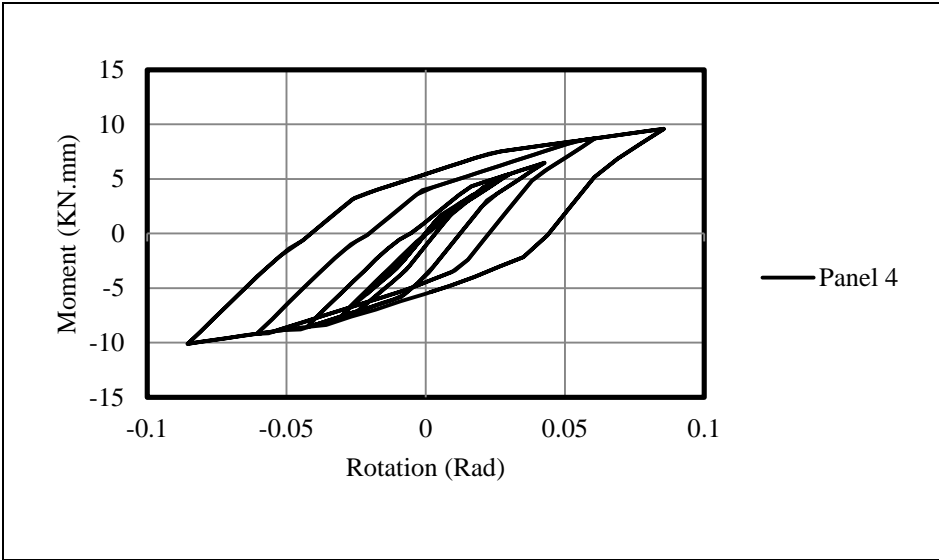


**Figure 5.59 :** Moment-Rotation relation at the base of panel 4 in system test III.

**5.4.3.7 Energy analysis**

The total cumulative is 34710 KN.mm. The cumulative energy obtained from the steel cushions beneath the panels is 17434 KN.mm and the cumulative energy obtained from the panel-to-panel steel cushions is 16088 KN.mm. Thus 50.23% of the total cumulative energy is dissipated by the steel cushions in the base level and 49.77% of the total cumulative energy is dissipated by the panel to panel steel cushions.

### 5.4.3.8 Deformed shape of structural system

The deformed shape of the structural system is illustrated in Figure 5.60

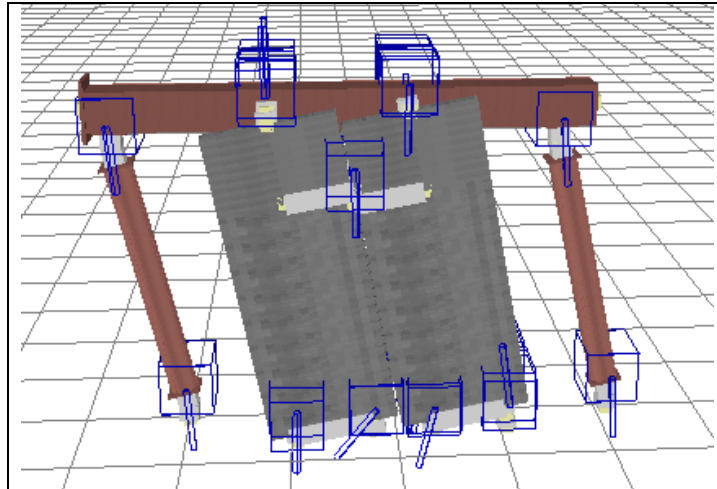


**Figure 5.60 :** Deformed shape of the structural system III.

### 5.4.4 Analytical study of system test IV

In this section, analytical model of system test IV is presented and the analytical and experimental results are compared.

#### 5.4.4.1 Definition of link elements

Parameters, which are assigned in the support link elements, are illustrated in Figure 5.61. According to Figure 5.61, in F1 and F3 directions the asymmetric bi-linear and Ramberg-Osgood response curves are assigned respectively. For other directions the linear elastic response curves are assigned. It should be noted that the F1 is axial direction and F3 is shear direction.

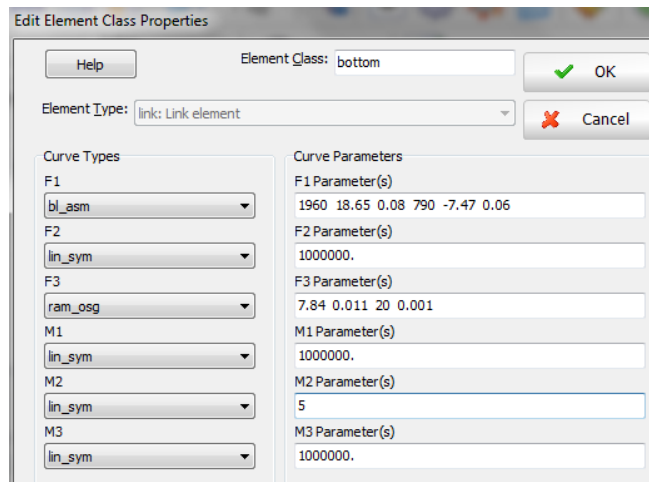


**Figure 5.61 :** Definition of the support link elements for system test IV.

The parameters, which are assigned in the panel-to-panel link, are illustrated in Figure 5.62. According to Figure 5.62, in F1 and F2 directions the asymmetric bi-linear and Ramberg-Osgood response curves are assigned respectively. In other directions, the linear elastic response curves are assigned. It should be noted that the F1 is axial direction and F2 is shear direction.

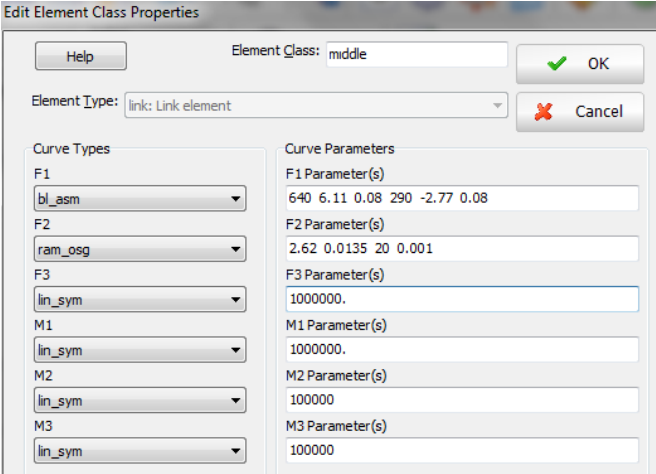


**Figure 5.62 :** Definition of the panel-to-panel link elements for system test IV.

The parameters, which are assigned in the panel to beam link elements, are illustrated in Figure 5.63. According to Figure 5.63, in F1 and F2 directions the asymmetric bi-linear and Ramberg-Osgood response curves are assigned respectively. In other directions, the linear elastic response curves are assigned. It should be noted that the F1 is axial direction and F2 is shear direction.

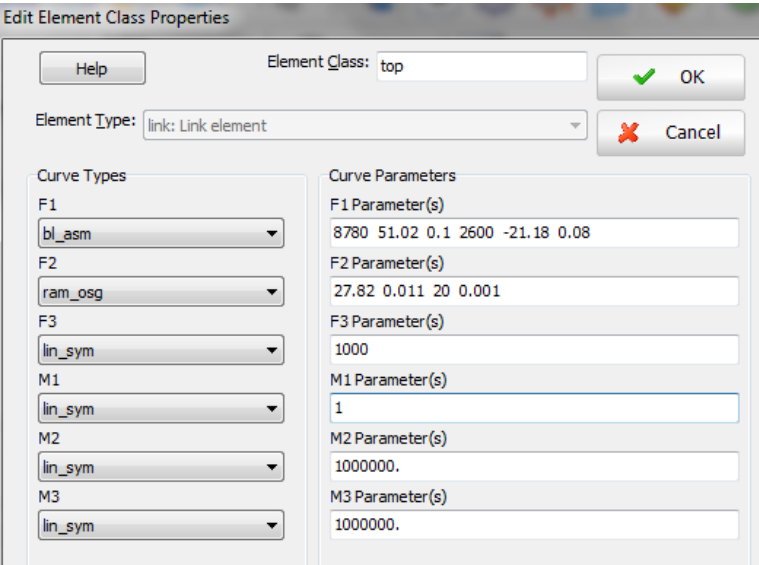


**Figure 5.63 :** Definition of the panel to beam link elements for system test IV.

#### 5.4.4.2 Actuator force-top displacement relation

The experimental and analytical actuator force-top displacement relations are compared in Figure 5.64. They are comprised with each other.

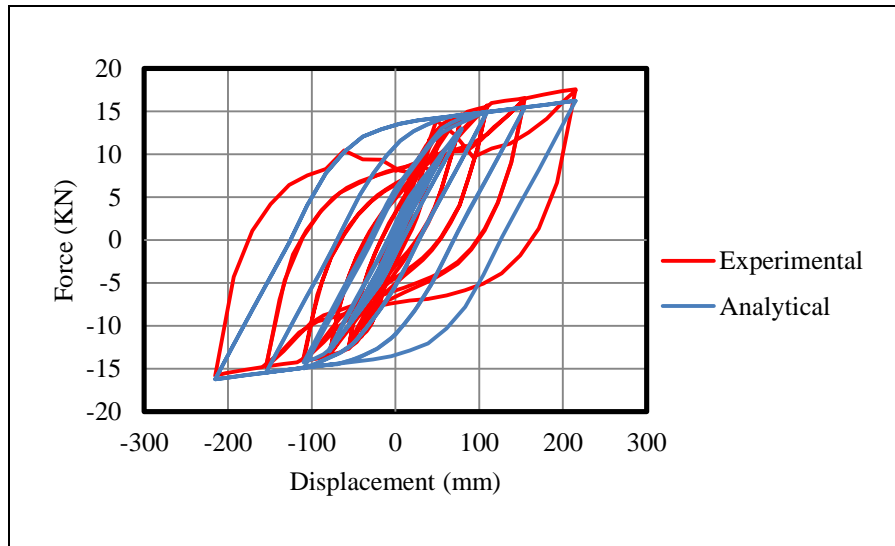


**Figure 5.64 :** Comparison of the experimental and analytical actuator force-top displacement relations in the system test IV.

#### 5.4.4.3 Force-Displacement relation of panel to panel steel cushion

Analytical force versus vertical displacement relations for panel-to-panel steel cushion is illustrated in Figure 5.65. It should be noted that units of the force and displacement are kN and m, respectively. The maximum displacement is about 8cm in the force of 2.8kN.

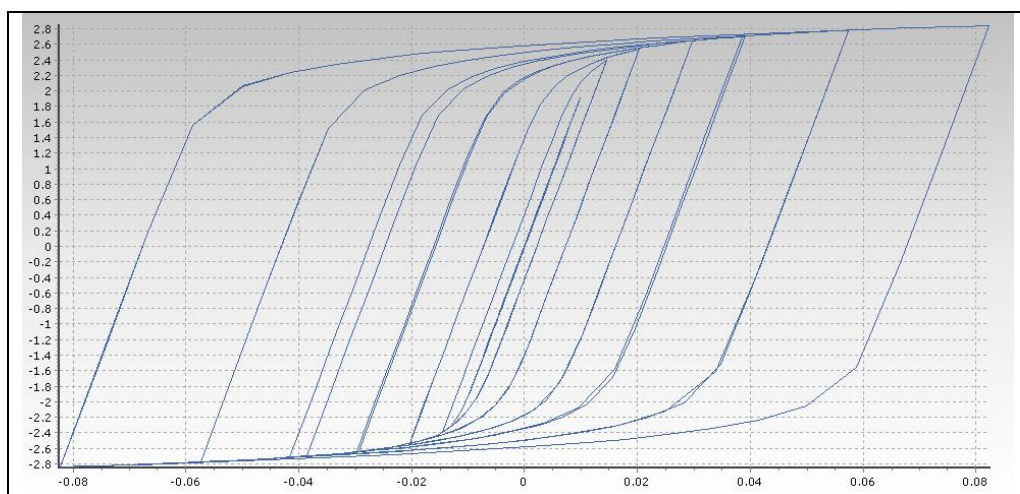


**Figure 5.65 :** Analytical force versus vertical displacement relations for panel-to-panel steel cushion in system test IV.

The relative vertical displacement history in the panel-to-panel steel cushion obtained from the test and analytical study are compared in Figure 5.66.

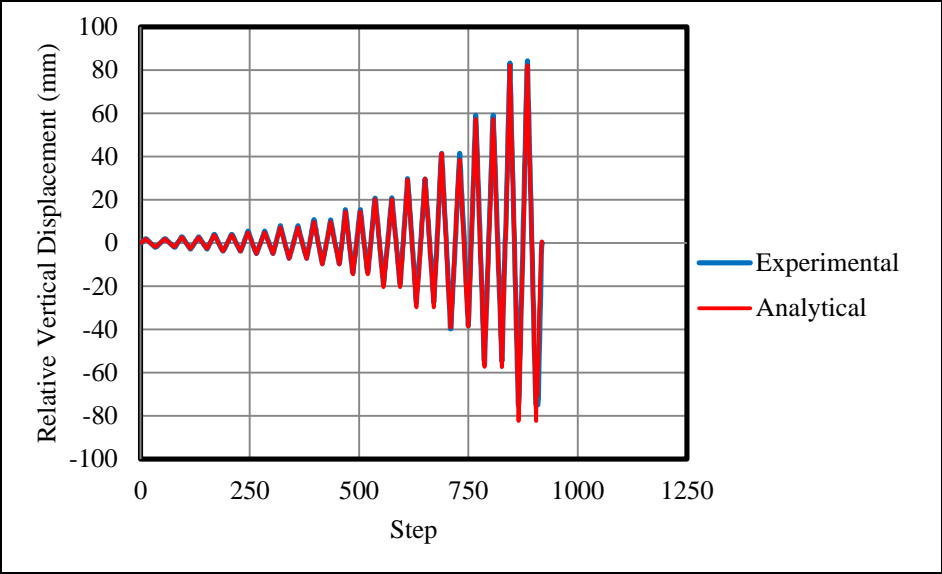


**Figure 5.66 :** Comparison of the experimental and analytical relative vertical displacement history in the panel-to-panel steel cushion.

**5.4.4.4 Force-Displacement Relation of Panel to Support Steel Cushion**

Force-displacement relations for the steel cushions beneath the panel 1, are shown in Figure 5.67 and 5.68. These relation are caused by the rotation of the panel 1, in shear direction the steel cushions relative horizontal displacements are negligible and the force-displacement relation remains elastic. It should be noted that units of force and displacement are KN and m, respectively.

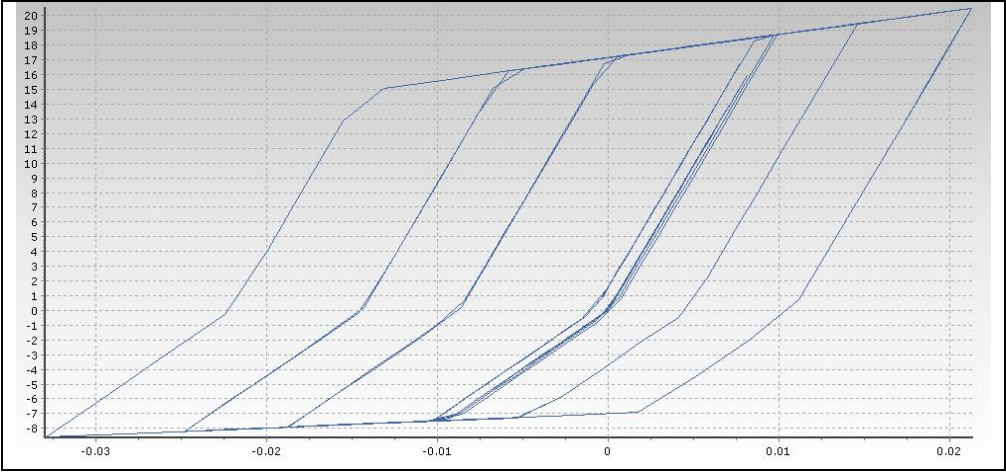


**Figure 5.67 :** Force-Displacement relation panel to support link element under the rotation of the panel 1 for system test IV.

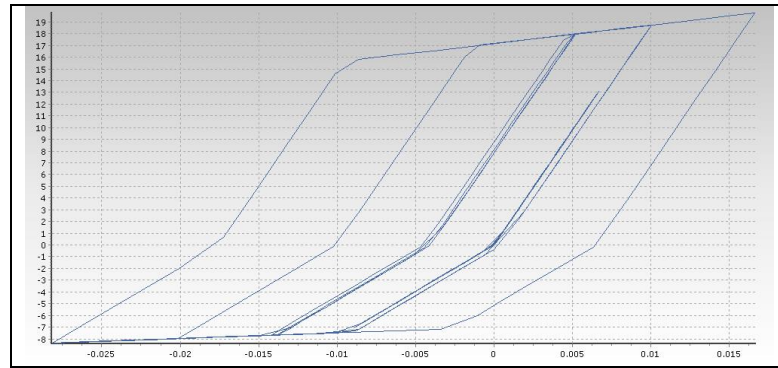


**Figure 5.68 :** Force-Displacement relation panel to support link element under the rotation of the panel 1 for system test IV.

Force displacement relations for the steel cushions beneath the panel 2, are shown in Figure 5.69 and 5.70. These relations are caused by the rotation of the panel 2, in shear direction the steel cushions relative horizontal displacements are negligible and the force-displacement relation remains elastic. It should be noted that units of the force and displacement are KN and m, respectively.

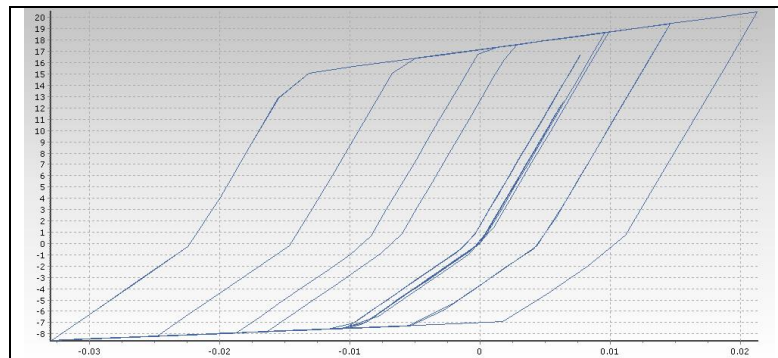


**Figure 5.69 :** Force-Displacement relation panel to support link element under the rotation of the panel 2 for system test IV.

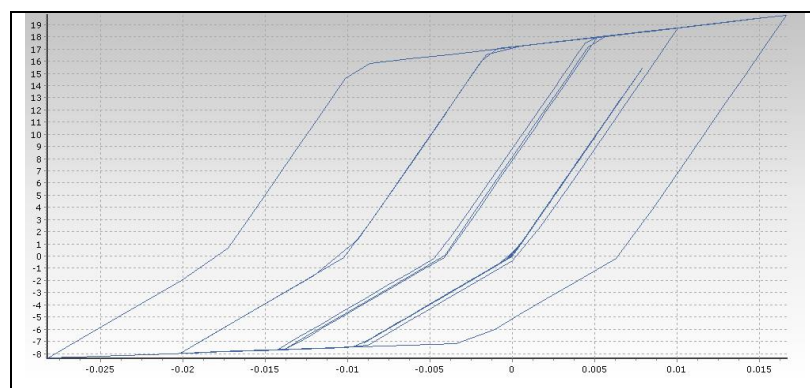


**Figure 5.70 :** Force-Displacement relation panel to support link element under the rotation of the panel 2 for system test IV.

The steel cushions under each panel did not behave symmetrically. The maximum vertical displacement is almost 3.5cm for one steel cushion and 3 cm for another.

**5.4.4.5 Rotation of cladding panels**

The rotation history of panel 3 and panel 4 obtained from the analytical and experimental studies are compared in Figure 5.71 and 5.72, respectively. The maximum values of rotation are about 0.1 rad for panel 1 and 3.

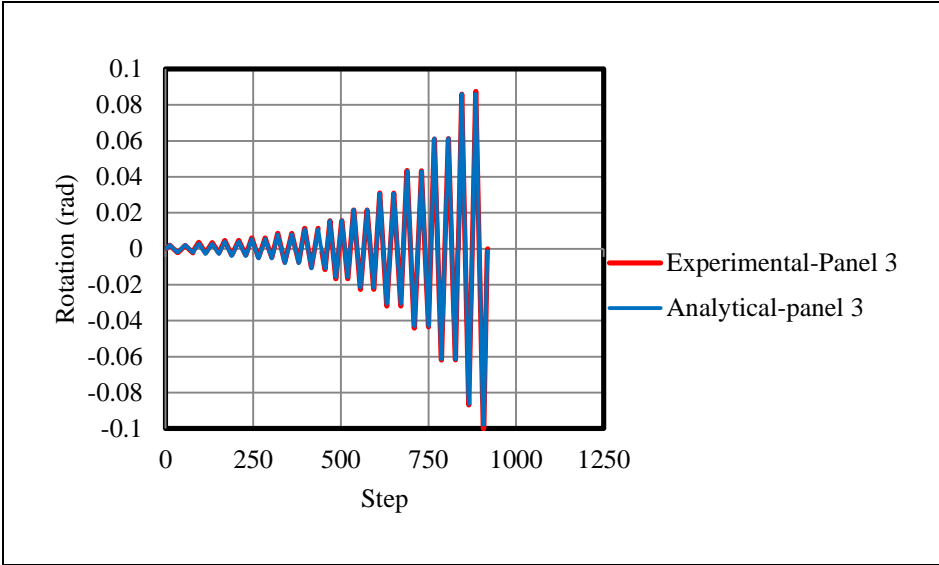


**Figure 5.71 :** Comparison of the experimental and analytical rotation history for panel 3 in system test IV.

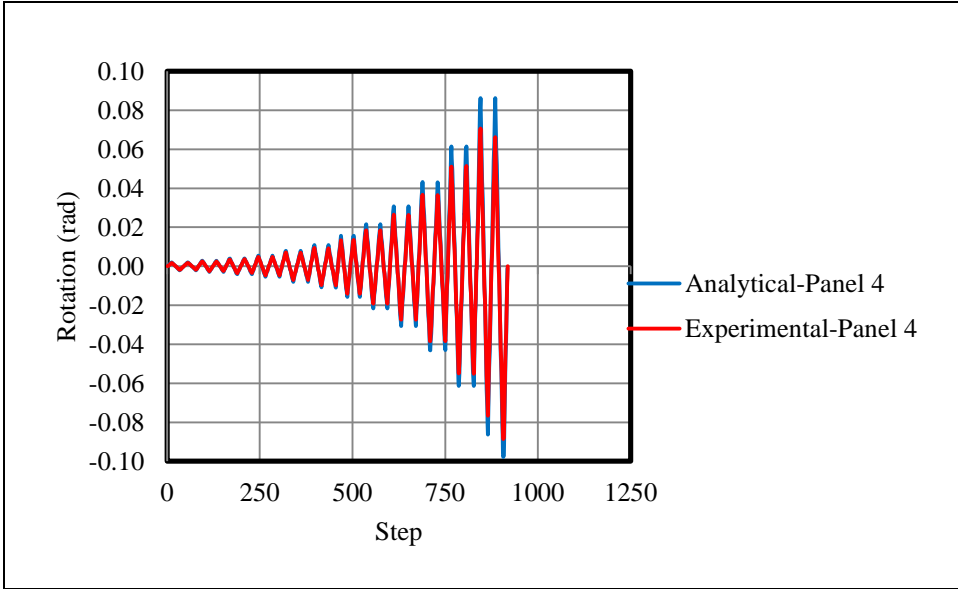


**Figure 5.72 :** Comparison of the experimental and analytical rotation history for panel 4 in system test IV.

The analytical and experimental rotation histories are comprised with each other.

#### 5.4.4.6 Moment-Rotation relation of cladding panels

The moment-rotation relation at the base of panel 3 and 4 are shown in Figure 5.73 and 5.74. The maximum base moment value is 9.0 and 9.24 KN.m for panel 3 and 4, respectively.

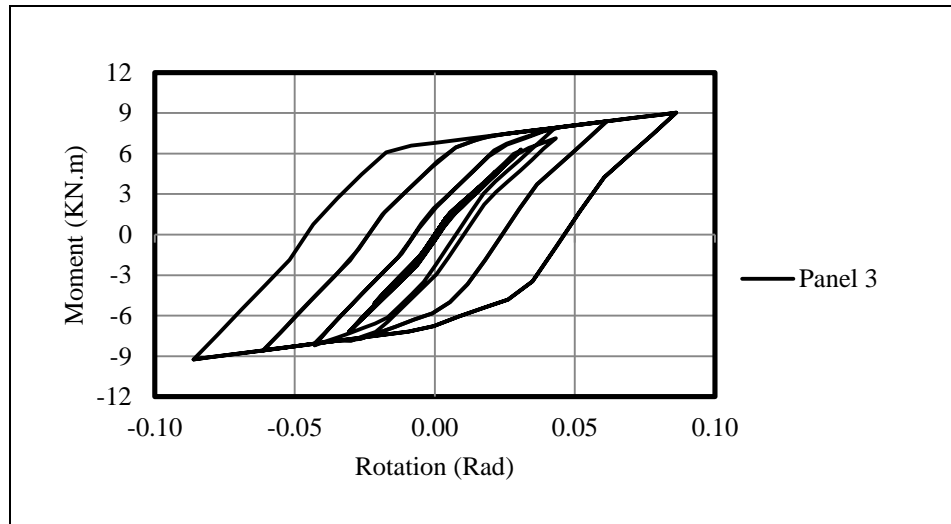


**Figure 5.73 :** Moment-Rotation relation at the base of panel 3 in system test IV.

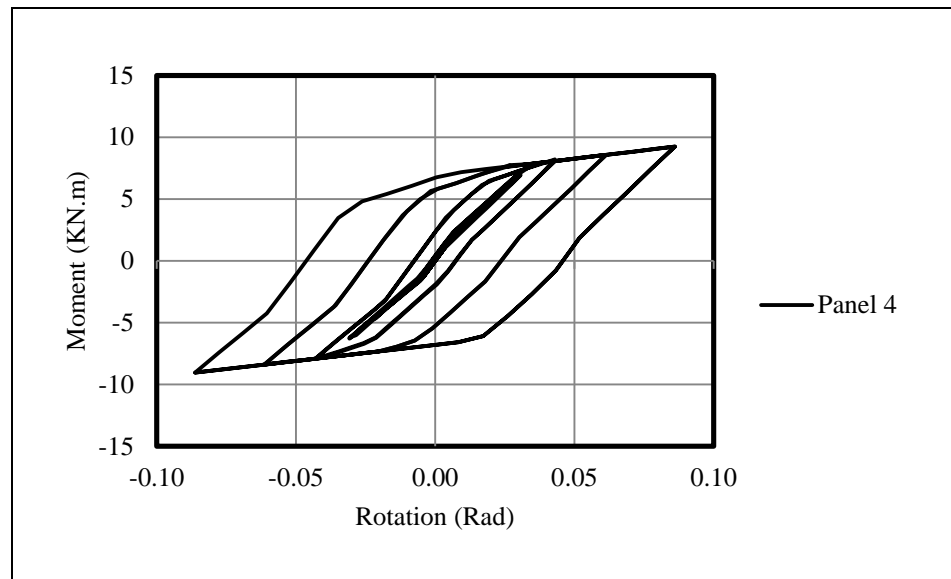


**Figure 5.74 :** Moment-Rotation relation at the base of panel 4 in system test IV.

#### 5.4.4.7 Energy analysis

The total cumulative energy is 17381 KN.mm. The cumulative energy obtained from the steel cushions beneath the panels is 12903 KN.mm and the cumulative energy obtained from the panel-to-panel steel cushions is 4737 KN.mm. Thus 74.24% of the total cumulative energy is dissipated by panel to support steel cushions and 27.25% of the total cumulative energy is dissipated through the panel to panel steel device.

**5.4.4.8 Deformed shape of structural system**

The deformed shape of the structural system is illustrated in Figure 5.75.

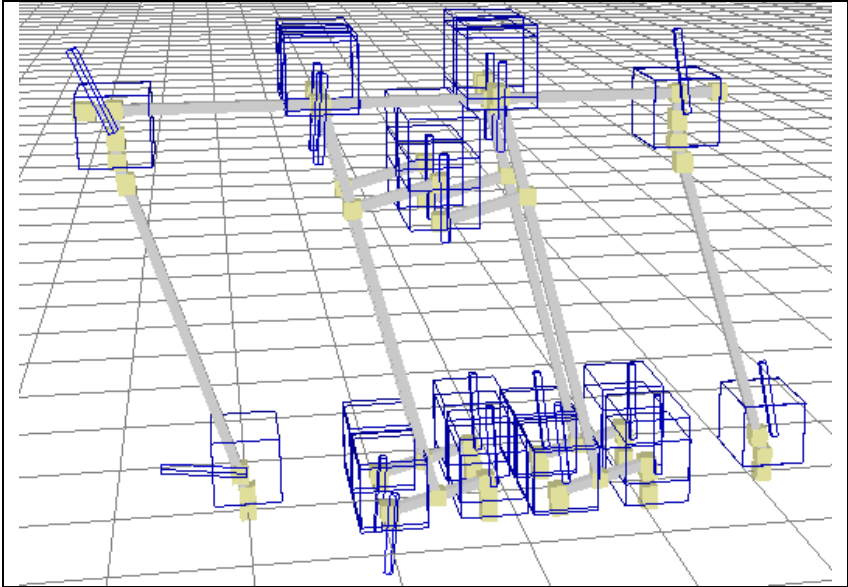


**Figure 5.75 :** Deformed shape of the structural system IV.

## **6. CONCLUSIONS AND RECOMMENDATIONS**

This chapter is divided into two sections. In the first section, conclusions, which obtained from various element and system tests, are presented. In the second section, recommendations are presented for further works.

### **6.1 Conclusions**

In this section conclusions, which obtained from various element and system tests, are presented.

#### **6.1.1 Uniaxial test**

1. The cyclic shear tests represent that the steel cushions have large energy dissipative capacity with stable force-displacement cycles.
2. The displacement capacity of steel cushions is two times of their height i.e. 200 mm.
3. Thickness of steel cushions affects the general behavior of steel devices, so that the thicker steel cushions have more strength, stiffness, and energy dissipation capacity.
4. The ductility of steel cushions increases with the increasing thickness.

#### **6.1.2 Bi-Directional shear and axial test**

1. The direction of loading is an effective factor on the general behavior of steel cushions with different thickness; somehow, with the increment of compression load the damping ratio and energy dissipation capacity increases, while in the case of tension axial load, the parameters change inversely.
2. The thick specimen behaves in much more stable manner than the thin specimen under the compression and tension loads.

3. The thick steel device behaves in much more ductile manner than thin one under tension axial loading whereas, the thin steel cushion behaves in more ductile manner in comparison with thick one under compression axial loading.
4. The ductility increases for thick steel device with increasing axial load level, in contrast the ductility decreases for thin device with increasing tension axial load level.
5. The optimum level of axial load range may be proposed as  $\pm 25\%$  of maximum axial load capacity of specimen because at the higher level it can affect the general behavior of steel cushions.

### **6.1.3 System test and analytical study**

1. Since the plastic hinges concentrated in the steel devices, no damages or cracking were observed in the structural elements.
2. The proposed steel devices are cost-effective and they can be replaced easily after earthquake effect.
3. In all systems test the rotation of the concrete panel were nearly identical, and the horizontal displacement of panels at the base were negligible, indicating that the dominant behavior of panels were rotation. Therefore, the shear behavior of steel devices in panel-to-panel connections and the axial behavior of steel devices in panel to support connections have the largest contribution in the energy dissipation capacity.
4. In the case of single cushion test type, there is out of plane movement so that it affects the general behavior of system however, there is high-energy dissipation capacity.
5. It is necessary to select the optimum thickness for steel cushions in panel to panel and panel to support connections i.e. the yielding must occurred because the proposed steel device dissipate the imparted input energy by means of yielding.
6. The steel device in panel to beam connections did not yield, thus they do not have any contribution in energy dissipation capacity and they acted such a simple hinge connections. It would be better to change the top-level steel cushions with plane hinge connection.

## 6.2 Recommendations

1. In total , the double cushion test types represent the more appropriate performance than the single cushion test types, as the out of plane movement of panels in double cushion test types are negligible therefore it is recommended to utilize the double cushion test type in the further studies.
2. The steel cushions in the panel to beam connections have negligible contribution in the energy dissipation capacity as they do not yield and act such a simple hinge connection. It should be better to replace them with two dimensional simple hinge connections.
3. Since the steel cushions in panel-to-panel and panel to support connections dissipate the input energy by means of shear an axial behavior respectively, the rotation of panels is dominant behavior. Thus, we can convert our problem into the simpler problem, so that the panel to support and panel to beam connections should be replaced with the two dimensional simple hinge connections and only the panel-to-panel steel cushions would be utilized in the structural system. This work has two advantages. First, the out of plane movement of panels can be limited by using two dimensional hinge connections at the base and top levels. Second, as only panel-to-panel steel devices would be utilized, therefore the energy dissipation capacity can be control just by adjusting the thickness and number of steel cushions in the panel-to-panel connections.



## REFERENCES

- Baird, A., Palermo, A., and Pampanin, S.** (2013). Controlling Seismic Response using Passive Energy Dissipating Cladding Connections. New Zealand Society for Earthquake Engineering Conference. 2013, Christchurch, New Zealand.
- Chopra, A. K.** (1995). Dynamics of Structures – Theory and Application to Earthquake Engineering. Prentice Hall, New Jersey, U.S.A.
- Chan, R., Albermani, F., and Williams, M.** (2009). Evaluation of Yielding Shear Panel Device for Passive Energy Dissipation. Journal of Constructional Steel Research. Vol. 65, pp. 260–268.
- Dindar, A.** (2009). Matlab Code for Calculation of Energy Dissipation in Force-Displacement Hysteresis.
- FEMA-461.** (2007). Federal Management Emergency Agency, Interim Testing Protocols For Determining the Seismic Performance Characteristics of Structural and Nonstructural Components, FEMA 461, Washington, DC.
- Ghabraie, K., Chan, R., Huangb, X., and Xie, Y. M.** (2010). Shape Optimization of Metallic Yielding Devices for Passive Mitigation of Seismic Energy. Journal of Engineering Structures Research. Vol. 32, pp. 2258-2267.
- Henry, R. S., Aaleti, S., Sritharan, S., and Ingham, J. M.** (2008). Design of a Shear Connector for a New Self-Centring Wall System. The 14<sup>th</sup> World Conference on Earthquake Engineering, October 12-17, 2008, Beijing, China.
- Henry, R. S., Aaleti, S., ASCE, S., and ASCE, J. M.** (2010). Concept and Finite-Element Modeling of New Steel Shear Connectors for Self-Centering Wall Systems. Journal of Engineering Mechanics.
- Kim, J., Choi, S., Oh, H., and Kang, H.** (2012). Comparative Study on Seismic Performance of Conventional RC Coupling Beams and Hybrid Energy Dissipative Coupling Beams used for RC Shear Walls. The 15<sup>th</sup> World Conference on Earthquake Engineering, 2012, LISBOA.
- Kelly, J. M., Skinner, R. I., and Heine, A. J.** (1972). Mechanisms of Energy Absorption in Special Devices for use in Earthquake Resistant Structures. Bulletin of the New Zealand Society for Earthquake Engineering. Vol. 5, no. 3, pp. 63-73.
- Maleki, S., Bagheri, S.** (2010). Pipe Damper, Part I. Experimental and Analytical Study. Journal of Constructional Steel Research. Vol. 66, pp. 1088\_1095.

- Maleki, S., Mahjoubi, S.** (2013). Dual-Pipe Damper. *Journal of Constructional Steel Research*. Vol. 85, pp. 81–91.
- MATLAB and Statistics Toolbox Release 2012b**, The MathWorks, Inc., Natick, Massachusetts, United States.
- Nakaki, S. D., Stanton, J. F., and Sritharan, S.** (1999). An overview of the PRESSSS five-story precast test building. *PCI J.*, Vol. 44, no. 2, pp. 26–39.
- Priestley, M. J. N.** (1991). Overview of PRESSSS Research Program. *Journal of Precast Concrete Institute*. Vol. 36, no. 4, pp. 50-57.
- Priestley, M. J. N., Sritharan, S., Conley, J., and Pampanin, S.** (1999). Preliminary Results and Conclusions from the PRESSSS Five-Story Precast Concrete Test Building. *Journal of Precast Concrete Institute*. Vol. 44, no 6, pp. 42-67.
- Seismosoft [2012], SeismoStruct v 6.0**, A Computer Program for Static and Dynamic Nonlinear Analysis of Framed Structures.
- Shultz, A. E., and Magana, R. A.** (1996). Seismic Behavior of Connections in Precast Concrete Walls. *Proceedings of Mete A. Sozen Symposium*, ACI SP 162, American Concrete Institute, Farmington Hills, Mich.
- TS 9967**, 1992 . Specifications for Design of Prefabricated Concrete Structures, Turkish Standards Institute, Ankara.

## **CURRICULUM VITAE**

**Name Surname: Arastoo KHAJEHDEHI**

**Place and Date of Birth: IRAN 19.09.1983**

**E-Mail: arastookhajehehi@yahoo.com**

**B.Sc.: ISLAMIC AZAD UNIVERSITY**

### **List of Publications and Patents:**

- ÖZKAYNAK H., GÜLLÜ A., GÖKÇE T., **KHAJEHDEI A.**, MAHDAVI A., AZIZISALES F., Engin BAL I., SYMROU E., YÜKSEL E., KARADOĞAN F., 2014: ENERGY DISSIPATOR STEEL CUSHIONS. *Second European Conference on Earthquake Engineering and Seismology*, AUG 25-29, 2014 Istanbul, Turkey.
- **KHAJEHDEHI A.**, GÜLLÜ A., GÖKÇE T., ÖZKAYNAK H., YÜKSEL E., KARADOĞAN F., 2014: CYCLIC TEST of the PRECAST PANELS EQUIPPED with STEEL CUSHIONS. *Poster Presentation in Second European Conference on Earthquake Engineering and Seismology*, AUG 25-29, 2014 Istanbul, Turkey.

